JOURNAL OF BIOLOGICAL REGULATORS & HOMEOSTATIC AGENTS
Volume 35, No. 3, May - June, 2021

CONTENTS

Editorials

T.C. Theoharides and P. Conti. Be aware of SARS-CoV-2 spike protein: There is more than meets the eye 833

R.G. Bellomo, C.E. Gallenga, Al. Caraffa, G. Tetè, G. Ronconi and P. Conti. Anaphylaxis is a rare reaction in COVID-19 vaccination 839

S. Gangemi, A. Allegra and M. Di Gioacchino. Management of patients at risk of anaphylaxis after COVID 19 vaccination 843

Reviews

G.L. Marseglia, M. Benazzo, P. Biasci, F. Blasi, C. Cricelli, M. Doria, S. Leonardi, D.G. Peroni, F. Scaglione and G. Ciprandi. OM-85 in the prevention of respiratory infections: State-of-the-art and future perspectives in clinical practice 847

M. Abaidullah, S. Peng, M. Kamran, X. Song, A. Ali Sher, Y. Chen, A. Rehman, L. Lin, R. Jia and Z. Yin. Phageome-based vaccination and human innate immune modulation could be a useful strategy to control human Coronavirus infections 865

Original Articles

C. Sitzia, L. Pistelli, R. Cardani, L.V. Renna, M. Ranucci, M. Carrara, S. Borlini, P. Clerici, B. Rampoldi, M. Cornetta and M.M. Corsi-Romanelli. Sensitivity of serology assay in Covid-19 diagnosis: does the antigen matter? 881

L. Zhang, H.J. Hong, B.D. Duan, Y. Zhang, C. C. Shao, L.N. Wang, X. Jiao, Y.J. Du, Y.Q. Zou and Y.Y. Ma. Neutrophil-lymphocyte ratio and hypersensitive C-reaction protein are associated with miscarriage during the second trimester of pregnancy 889

R.A. Compton, A.R. Lonergan, I. Tsillioni, P. Conti, G. Ronconi, D. Lauritano, E.E. Rebeiz† and T.C. Theoharides. Neurohormonal markers in chronic rhinosinusitis 901

C.S. Yu, Y.B. Wang, Q. Li, E.L. Yang and B.B. Dong. Long non-coding RNA OIP5-AS1 serves as a competing endogenous RNA to modulate X-linked inhibitor of apoptosis protein expression via adsorbing miR-429 in papillary thyroid cancer 909

XH. Kong, SF. Shi, HJ. Hu and JX. Wang. MicroRNA-20a suppresses RANKL-modulates osteoclastogenesis and prevents bone erosion in mice with rheumatoid arthritis through the TLR4/p38 pathway 921

PF. Rui, JH. Wang and J. Xu. Long non-coding NEAT1 weakens the protective role of sevoflurane on myocardial ischemia/reperfusion injury by mediating the microRNA-140/RhoA axis 933

YH. Luo, L. Zhang, MY. Wang, J. Fang, JY. Xia and XL. Yu. Anti-cancer effects of baicalein on cervical carcinoma cells through down-regulation of the ERK/p38/MAPK pathway 945

CG. Chen, BS. Luo and C. Wang. Potential role of miR-425, miR-155 and miR-33 in *Streptococcus pneumoniae* pneumonia by using bioinformatics analysis and experimental validation 953

Y. Li, J. Yang, Q. Feng, S.-Q. Li, Y. Lang, X.-F. Zhang and C. Ye. High cyclic tensile stress disrupts the extracellular matrix in human chondrocyte by F-actin cytoskeletal polymerization and reactive oxygen species production 965

F. Zhou, AX. Chen, HY. Lv, DH. Liang and HS. Yu. Establishment of an immune-related gene prognostic model for head and neck tumors 975

N. Zhao, MJ. Yu, J. Xu, HY. Wang, B. Liang, L. Ding, YX. Zhang, K. Du and BL. Leng. microRNA-29b mediates Th17/Treg imbalance in chronic obstructive pulmonary disease by targeting IL-22 987

XH. Yan, QL. Dong, G. Jin, YN. Zhu and LP. Zhang. Effect of interleukin-17 gene on glomerular ultrastructure and podocyte injury in adriamycin nephropathy rat models 1001

ZY. Gu, XY. Miao, LC. Ma, JJ. Gao, YP. Gong and CL. Li. Maintenance of cellular annexin A1 level is essential for PI3K/AKT/mTOR-mediated proliferation of pancreatic beta cells 1011

ZQ. Li, Z. Wang, Y. Zhang, C. Lu, QL. Ding, R. Ren, BB. Cheng and LX. Lou. CircRNA_103801 accelerates proliferation of osteosarcoma cells by sponging miR-338-3p and regulating HIF-1/Rap1/PI3K-Akt pathway 1021

Y. Peng, P. Cai, SF. Zou, M. Jia, WT. Zhong, Y. Wang and XK. Wang. High dose insulin promotes the proliferation of vascular smooth muscle cells via AP-1/SM-α pathway 1029

Letters to the Editor

G. Di Spigna, FW. Rossi, I. Mormile, P. Ladogana, L. Buonavolontà, B. Covelli, S. Salzano, F. Napolitano, A. Giannini and L. Postiglione. Serum Metalloprotease 3 (MMP-3) biomarker of therapeutic efficacy during treatment of rheumatoid arthritis 1041

W-L. Zhang, G-Q. Sun, L-F. Zhang and Z-B. Meng. Efficacy of different drug-eluting stents and their influence on inflammation and prognosis in elderly patients with acute myocardial infarction 1047

M. Marogna and G Ciprandi. Pidotimod as add-on therapy in patients with pollen-induced allergic rhinitis and asthma and associated respiratory infections 1053

Q. Liu, J-Y. Zhao, H-Y. Liu, T-T. Li, Y-X. Guo and Y-H. Liu. Diagnostic value and correlation of miRNA-499 and miR-18A in patients with acute myocardial infarction 1059

J. Pu, MJ. Zhou, JW. Shao, ST. Xiang, Q. He, W. Su, SZ. He, CW. Mao, RG. Ruan and BL. Song. High resolution computerized tomography quantitative evaluation of the correlation between central airway and pulmonary function grading in chronic obstructive pulmonary disease 1067

N. Setaro and A. Gigante. Conservative treatment of partial rotator cuff tears, comparison between infiltrative treatment with corticosteroids, medium molecular weight hyaluronic acid and high molecular weight hyaluronic acid: a prospective study 1073

WX. Xie, MF. Chen, L. Gao and ZK. Feng. A 12-year follow-up study of mucoepidermoid carcinoma-associated membranous nephropathy 1081

Notarnicola, I. Covelli, L. Moretti, S. Setti, F. De Terlizzi and B. Moretti. Predictors of responsiveness to biostimulation treatments (PEMFs and/or shockwaves) in patients with complex regional pain syndrome type I of the ankle 1087

S.E. Aragona, G. Ciprandi and Study Group on Urinary Infections. Acute uncomplicated cystitis management in clinical practice: a nationwide survey 1097

N. Cao, H. Shi, C. Chen, L. Zheng and C. Yu. Inhibition of the TLR9-dependent p38 MAPK signaling pathway improves the pathogenesis of primary Sjögren's syndrome in the NOD/Ltj mouse 1103

SL. Wang, XW. Dong, F. Zhao and CX. Li. MiR-203 inhibits cell proliferation, invasion, and migration of ovarian cancer through regulating RGS17 1109

XL. Hu, J. Ding and XM. Zhang. Long non-coding RNA MIAT increases malignancy of prostate cancer cells through the microRNA-203/glutaminase axis 1117

D-Y. Han, Y-F. Zhang, Z-M. Wang, Y-C. Chang and X-S. Wang. Screening of hub genes for prognosis of gastric cancer based on bioinformatics 1127

HY. Chen, Y. Bao, JJ. Zou, XL. Cong, XX. Zhang, JY. Zheng, XF. Chen and YQ. Shi. Activated Th9 cells in diabetic coronary heart disease 1137

M. De Amici, F. Barocci, A. Licari, S. Caimmi, A. Marseglia, G. Testa, C. Torre and G.L. Marseglia. Latex allergy: advantages of molecular diagnostics during coronavirus 1145

G. Ciprandi, I. La Mantia, F.P. Brunese, Al. Varricchio and At. Varricchio. Hypertonic saline with xylitol and hyaluronate may shorten the viral shedding duration in asymptomatic COVID-19 positive subjects: a pilot study 1151

At. Varricchio, I. La Mantia, F.P. Brunese, Al. Varricchio and G. Ciprandi. Viral shedding in symptomatic patients with mild COVID-19: an experience with nebulized nasal treatment 1155

G. Laskarin, M. Rakić, V. Sotošek, D. Travica Samsa, V. Peršić, T. Kehler, D. Gobić, L. Zaputović and D. Rukavina. Immunoregulatory role of circulating endothelial vWF positive cells in patients after acute myocardial infarction 1159

L.-J. Zhao, X.-L. Sun, J. Qiu, B.-L. Xiao, X.-Y. Fan, T. Wang and C.-L. Li. ARA290 inhibits high glucose-induced apoptosis of NRK-52E cells 1169

R.Y. Ye, X.Y. Kuang, N. Shao, S.M. Wang and Y. Lin. Downregulation of NPTX1 induces cell cycle progression through Wnt/β-catenin signaling in breast cancer 1177

T-W. Shi, N. Bai, J-A. Zhang, F. Lu, X-D. Kong, J-B. Yu and S-S. Zhang. Androgen receptor expression in the skin appendages of patients with acne inversa harboring a mutation in the γ-secretase gene NCSTN 1185

A. Migliore, E. Graziano, L.S.M. Martín, A. Sorbino, M. Raichi and G. Boni. Three-year management of hip osteoarthritis with intra-articular polynucleotides: a real-life cohort retrospective study 1189

U. Rafi, S. Ahmad, A. Zia, S.S. Bokhari, M.A. Iqbal and N. Roohi. Contribution of apolipoprotein estimations to cardiovascular risk assessment in women with endometriosis 1195

EDITORIAL

Be aware of SARS-CoV-2 spike protein: There is more than meets the eye

T.C. Theoharides[1,2,3] and P. Conti[4]

[1]Laboratory of Molecular Immunopharmacology and Drug Discovery, Department of Immunology, Tufts University School of Medicine, Boston. MA, USA; [2]School of Graduate Biomedical Sciences, Tufts University School of Medicine, Boston, MA, USA; [3]Department of Internal Medicine, Tufts University School of Medicine and Tufts Medical Center, Boston, MA, USA; [4]Postgraduate Medical School, University of Chieti, Chieti, Italy

The COVID-19 pandemic necessitated the rapid production of vaccines aimed at the production of neutralizing antibodies against the COVID-19 spike protein required for the corona virus binding to target cells. The best well-known vaccines have utilized either mRNA or an adenovirus vector to direct human cells to produce the spike protein against which the body produces mostly neutralizing antibodies. However, recent reports have raised some skepticism as to the biologic actions of the spike protein and the types of antibodies produced. One paper reported that certain antibodies in the blood of infected patients appear to change the shape of the spike protein so as to make it more likely to bind to cells, while other papers showed that the spike protein by itself (without being part of the corona virus) can damage endothelial cells and disrupt the blood-brain barrier. These findings may be even more relevant to the pathogenesis of long-COVID syndrome that may affect as many as 50% of those infected with SARS-CoV-2. In COVID-19, a response to oxidative stress is required by increasing anti-oxidant molecules. In this regard, it is known that polyphenols are natural anti-oxidants with with anti-inflammatory properties. Hence, there are even more reasons to intervene with the use of anti-oxidant compounds, such as luteolin, in addition to available vaccines and anti-inflammatory drugs to prevent the harmful actions of the spike protein.

Infection with the recent Coronavirus [severe acute respiratory syndrome (SARS)-CoV2] leads to COVID-19, the severity of which derives from the host's immune response (1), especially the release of a storm (2, 3) of pro-inflammatory cytokines (4-10) and prothrombotic molecules, such as platelet activating factor (PAF), leading to microemboli (11, 12).

The SARS-CoV-2 coronavirus infects cells by first binding to its surface receptor, Angiotensin Converting Enzyme 2 (ACE2), via its corona spike protein (13, 14). The spike protein is made up of the S1 subunit containing a receptor-binding domain (RBD) that attaches to ACE2 and the S2 subunit containing a transmembrane anchor that mediates fusion of viral and host cell membranes. A number of vaccines for COVID-19 were developed rapidly using either mRNA or adenovirus vector technology aimed at directing cells to produce the spike protein so that the body will generate neutralizing antibodies (15, 16). However, recent papers have reported intriguing, but also disturbing, findings concerning detrimental actions of the spike protein (Table I).

One paper still in preprint stage at Cell reported that certain antibodies in the blood of patients infected

Key words: ACE2; antibodies; blood-brain barrier; blood vessels; corona virus; endothelial cells; receptor; spike protein

Corresponding Author:
Theoharis C. Theoharides, MS, MPhil, PhD, MD
Department of Immunology,
Tufts University School of Medicine,
136 Harrison Avenue, Suite 304,
Boston, MA 02111, USA
Tel.: +1 (617) 636 6866 - Fax: +1 (617) 636 2456
e-mail: theoharis.theoharides@tufts.edu

0393-974X (2021)
Copyright © by BIOLIFE, s.a.s.
This publication and/or article is for individual use only and may not be further reproduced without written permission from the copyright holder. Unauthorized reproduction may result in financial and other penalties
DISCLOSURE: ALL AUTHORS REPORT NO CONFLICTS OF INTEREST RELEVANT TO THIS ARTICLE.

Table I. *Detrimental effects of spike protein*

• SARS-CoV-2 entry into target cells
• Endothelial damage
• Proinflammatory cytokine release
• TLR activation
• Microglia stimulation
• Molecular mimicry with chaperon and heat shock proteins

with SARS-CoV-2 appear to change the shape of the spike protein so as to make it more likely to bind to cells and infect them. Evidently, antibodies against the RBD are protective, but antibodies against the N-terminal domain (NTD) induced the open conformation of the RBD enhancing the binding ability and infectivity (https://www.cell.com/cell/pdf/S0092-8674(21)006620.pdf). Another paper reported that the spike protein shares antigenic epitopes with human molecular chaperons resulting in autoimmunity against endothelial cells (17). In fact, the spike protein by itself (without being part of the corona virus) was shown to damage endothelium in an animal model via impaired mitochondrial function (18). A fourth paper reported that the spike protein could alter barrier function in an in-vitro model of the blood-brain barrier (BBB); in particular, the S1 protein promoted loss of barrier ability in an advanced 3D microfluidic model of the human BBB (19). Finally, S1 protein was reported to actually cross the BBB and enter the brain of mice (20), possibly leading to neuroinflammation (21). In fact, another recent study reported blood vessel damage and inflammation, but no infection, in brains of patients with COVID-19 (22).

These findings may help explain the pathogenesis of COVID-associated neurological (23-26) and mental (27-31) symptoms, especially "brain fog" (32, 33). Moreover, these results could be central in our understanding of Long-COVID syndrome (34, 35) that may affect over 50% of COVID patients (32, 36, 37) and is characterized by neurologic (38) and psychiatric (39) symptoms (32, 34, 35, 40), as well as persistent fatigue apparently independent of the severity of the initial symptoms (41). Symptoms

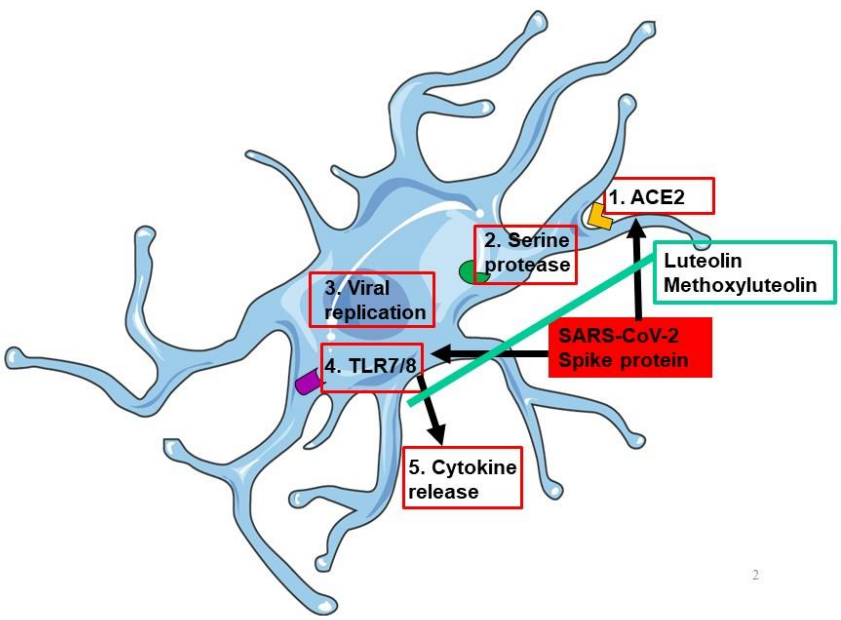


Fig. 1. *Diagrammatic representation of how luteolin and methoxyluteolin could block SARS-CoV-2 Spike protein from stimulating microglia. The biologic action of SARS-CoV-2 Spike protein could be via different steps (red rectangles): (1) Spike protein binding to its ACE2 receptor; (2) Activation of serine proteinases responsible for "priming" the Spike protein for entry into the cells; (3) Viral replication within the nucleus; (4) Activation of TLR7/8 found in the endosomes by single-stranded RNA viruses like SARS-CoV-2; (5) Production of proinflammatory cytokines. Luteolin and methoxyluteolin could protect against SARS-CoV-2 Spike protein-associated damage by interfering (green line) at practically all steps.*

experienced by Long-COVID syndrome patients are similar (42, 43) to those present in patients with Mast Cell Activation Syndrome (MCAS) (44, 45).

Emerging evidence suggests mast cell activation or a dysfunctional response play a role in COVID-19 via the release of multiple pro-inflammatory cytokines (1, 2, 4-10) and prothrombotic mediators (11, 12), especially since mast cells are stimulated by viruses (46). The result is inflammation around brain blood vessels (22) that may generate a vicious cycle or autoimmune loop of neuroimmune processes casing L-COVID. In fact, preliminary reports suggest that mast cells may be involved in COVID-19 (47-49) and that individuals taking substances interfering with the mast cells or their mediators are less likely to suffer severe COVID-19 (33, 43). COVID-19 can also affect the hypothalamic-pituitary-adrenal (HPA) axis (50), which is typically activated by stress (51), but also has pro-inflammatory effects via stimulation of mast cells by corticotropin-releasing hormone (CRH) (53). Mast cells can interact with microglia in the brain, leading to their activation with subsequent neuroinflammation (52-54) and cognitive dysfunction (55). Microglia express Toll-like receptors (TLRs) (56), activated by damage associated molecular patterns (DAMPs) and were recently implicated in COVID-19 (57-60).

Given the above, it is reasonable to consider preventing the detrimental actions of the spike protein (Table I). This could be accomplished by the use of liposomal formulations (61) of the natural flavonoids luteolin and methoxyluteolin (62-64), which are safe (65, 66) and have broad anti-viral properties (67) by acting at different steps (Fig. 1): Spike protein binding to its ACE2 receptor; 2) Activation of serine proteinases responsible for “priming” the Spike protein for entry into the cells; 3) Viral replication within the nucleus; 4) Activation of TLR7/8 found in the endosomes by single-stranded RNA viruses like SARS-CoV-2; 5) Production of proinflammatory cytokines.

Furthermore, luteolin and methoxyluteolin better penetrate into the brain, inhibiting both microglia (68-70) and mast cells (71, 72), while they also reduce neuroinflammation (66, 73, 74) and cognitive dysfunction (75, 76), especially brain fog (77, 78).

REFERENCES

1. Brodin P. Immune determinants of COVID-19 disease presentation and severity. Nat Med 2021; 27(1):28-33.
2. Canna SW, Cron RQ. Highways to hell: Mechanism-based management of cytokine storm syndromes. J Allergy Clin Immunol 2020; 146(5):949-59.
3. Moore JB, June CH. Cytokine release syndrome in severe COVID-19. Science 2020; 368(6490):473-4.
4. Ye Q, Wang B, Mao J. The pathogenesis and treatment of the `Cytokine Storm' in COVID-19. J Infect 2020; 80(6):607-13.
5. Chen G, Wu D, Guo W et al. Clinical and immunological features of severe and moderate coronavirus disease 2019. J Clin Invest 2020; 130(5):2620-9.
6. Conti P, Ronconi G, Caraffa A et al. Induction of pro-inflammatory cytokines (IL-1 and IL-6) and lung inflammation by Coronavirus-19 (COVI-19 or SARS-CoV-2): anti-inflammatory strategies. J Biol Regul Homeost Agents 2020; 34(2):327-31.
7. Giamarellos-Bourboulis EJ, Netea MG, Rovina N et al. Complex immune dysregulation in COVID-19 patients with severe respiratory failure. Cell Host Microbe 2020; 27(6):992-1000.
8. Tang Y, Liu J, Zhang D, Xu Z, Ji J, Wen C. Cytokine Storm in COVID-19: The current evidence and treatment strategies. Front Immunol 2020; 11:1708.
9. Paces J, Strizova Z, Smrz D, Cerny J. COVID-19 and the immune system. Physiol Res 2020; 69(3):379-88.
10. Ragab D, Salah EH, Taeimah M, Khattab R, Salem R. The COVID-19 Cytokine Storm; What we know so far. Front Immunol 2020; 11:1446.
11. Theoharides TC, Antonopoulou S, Demopoulos CA. Coronavirus 2019, microthromboses, and platelet activating factor. Clin Ther 2020; 42(10):1850-2.
12. Demopoulos C, Antonopoulou S, Theoharides TC. COVID-19, microthromboses, inflammation, and platelet activating factor. Biofactors 2020; 46(6):927-33.
13. Tai W, He L, Zhang X, et al. Characterization of the receptor-binding domain (RBD) of 2019 novel coronavirus: implication for development of RBD protein as a viral attachment inhibitor and vaccine. Cell Mol Immunol 2020; 17(6):613620.
14. Hoffmann M, Kleine-Weber H, Schroeder S. et

al. SARS-CoV-2 cell entry depends on ACE2 and TMPRSS2 and is blocked by a clinically proven protease inhibitor. Cell 2020; 181(2):271-80.
15. Dai L, Gao GF. Viral targets for vaccines against COVID-19. Nat Rev Immunol 2021; 21(2):73-82.
16. Theoharides TC, Lauritano D, Ronconi G, Calvisi V, Conti P. Antibodies for COVID-19 - which, when and how long? J Biol Regul Homeost Agents 2021; 35(2).
17. Paladino L, Vitale AM, Caruso BC et al. The role of molecular chaperones in virus infection and implications for understanding and treating COVID-19. J Clin Med 2020; 9(11).
18. Lei Y, Zhang J, Schiavon CR, et al. SARS-CoV-2 Spike protein impairs endothelial function via downregulation of ACE 2. Circ Res 2021; 128(9):1323-6.
19. Buzhdygan TP, DeOre BJ, Baldwin-Leclair A, et al. The SARS-CoV-2 spike protein alters barrier function in 2D static and 3D microfluidic in-vitro models of the human blood-brain barrier. Neurobiol Dis 2020; 146:105131.
20. Rhea EM, Logsdon AF, Hansen KM, et al. The S1 protein of SARS-CoV-2 crosses the blood-brain barrier in mice. Nat Neurosci 2021; 24(3):368-78.
21. Tremblay ME, Madore C, Bordeleau M, Tian L, Verkhratsky A. Neuropathobiology of COVID-19: The role for glia. Front Cell Neurosci 2020; 14:592214.
22. Lee MH, Perl DP, Nair G et al. Microvascular injury in the brains of patients with Covid-19. N Engl J Med 2021; 384(5):481-3.
23. Helms J, Kremer S, Merdji H et al. Neurologic features in severe SARS-CoV-2 Infection. N Engl J Med 2020; 382(23):2268-70.
24. Fotuhi M, Mian A, Meysami S, Raji CA. Neurobiology of COVID-19. J Alzheimers Dis 2020; 76(1):3-19.
25. Najjar S, Najjar A, Chong DJ, et al. Central nervous system complications associated with SARS-CoV-2 infection: integrative concepts of pathophysiology and case reports. J Neuroinflammation 2020; 17(1):231.
26. Singh AK, Bhushan B, Maurya A, Mishra G, Singh SK, Awasthi R. Novel coronavirus disease 2019 (COVID-19) and neurodegenerative disorders. Dermatol Ther 2020; 33(4):e13591.
27. Ongur D, Perlis R, Goff D. Psychiatry and COVID-19. JAMA 2020; 324(12):1149-50.
28. Vindegaard N, Benros ME. COVID-19 pandemic and mental health consequences: Systematic review of the current evidence. Brain Behav Immun 2020; 89:531-42.
29. Pfefferbaum B, North CS. Mental health and the Covid-19 pandemic. N Engl J Med 2020; 383(6):510-2.
30. Xiang YT, Yang Y, Li W et al. Timely mental health care for the 2019 novel coronavirus outbreak is urgently needed. Lancet Psychiatry 2020; 7(3):228-9.
31. Gordon JA, Borja SE. The COVID-19 Pandemic: setting the mental health research agenda. Biol Psychiatry 2020; 88(2):130-1.
32. Nalbandian A, Sehgal K, Gupta A, et al. Post-acute COVID-19 syndrome. Nat Med 2021; 27(4):601-15.
33. Theoharides TC, Cholevas C, Polyzoidis K, Politis A. Long-COVID syndrome-associated brain fog and chemofog: Luteolin to the rescue. Biofactors 2021; 47(2):232-41.
34. Huang C, Huang L, Wang Y, et al. 6-month consequences of COVID-19 in patients discharged from hospital: a cohort study. Lancet 2021; 397(10270):220-232.
35. Higgins V, Sohaei D, Diamandis EP, Prassas I. COVID-19: from an acute to chronic disease? Potential long-term health consequences. Crit Rev Clin Lab Sci 2020; 1-23.
36. Moreno-Perez O, Merino E, Leon-Ramirez JM, et al. Post-acute COVID-19 Syndrome. Incidence and risk factors: a Mediterranean cohort study. J Infect 2021; 82(3):378-83.
37. Montagne A, Nation DA, Sagare AP, et al. APOE4 leads to blood-brain barrier dysfunction predicting cognitive decline. Nature 2020; 581(7806):71-76.
38. Nazari S, Azari JA, Mirmoeeni S, et al. Central nervous system manifestations in COVID-19 patients: A systematic review and meta-analysis. Brain Behav 2021; e02025 doi: 10.1002/brb3.2025.
39. Taquet M, Luciano S, Geddes JR, Harrison PJ. Bidirectional associations between COVID-19 and psychiatric disorder: retrospective cohort studies of 62 354 COVID-19 cases in the USA. Lancet Psychiatry 2021; 8(2):130-40.
40. Baig AM. Deleterious Outcomes in Long-Hauler COVID-19: The Effects of SARS-CoV-2 on the CNS in Chronic COVID Syndrome. ACS Chem Neurosci 2020; 11(24):4017-20.
41. Townsend L, Dyer AH, Jones K, et al. Persistent

fatigue following SARS-CoV-2 infection is common and independent of severity of initial infection. PLoS ONE 2020; 15(11):e0240784.
42. Theoharides TC, Conti P. COVID-19 and multisystem inflammatory syndrome, or is it mast cell activation syndrome? J Biol Regul Homeost Agents 2020; 34(5):1633-6.
43. Afrin LB, Weinstock LB, Molderings GJ. Covid-19 hyperinflammation and post-Covid-19 illness may be rooted in mast cell activation syndrome. Int J Infect Dis 2020; 100:327-32.
44. Akin C, Valent P, Metcalfe DD. Mast cell activation syndrome: Proposed diagnostic criteria. J Allergy Clin Immunol 2010; 126(6):1099-104.
45. Theoharides TC, Tsilioni I, Ren H. Recent advances in our understanding of mast cell activation - or should it be mast cell mediator disorders? Expert Rev Clin Immunol 2019; 15(6):639-56.
46. Marshall JS, Portales-Cervantes L, Leong E. Mast cell responses to viruses and pathogen products. Int J Mol Sci 2019; 20(17):4241.
47. Conti P, Caraffa A, Tete G, et al. Mast cells activated by SARS-CoV-2 release histamine which increases IL-1 levels causing cytokine storm and inflammatory reaction in COVID-19. J Biol Regul Homeost Agents 2020; 34(5):1629-32.
48. Theoharides TC. COVID-19, pulmonary mast cells, cytokine storms, and beneficial actions of luteolin. Biofactors 2020; 46(3):306-8.
49. Theoharides TC. Potential association of mast cells with COVID-19. Ann Allergy Asthma Immunol 2020; 126(3):217-8.
50. Steenblock C, Todorov V, Kanczkowski W, et al. Severe acute respiratory syndrome coronavirus 2 (SARS-CoV-2) and the neuroendocrine stress axis. Mol Psychiatry 2020; 25(8):1611-7.
51. Chrousos GP. The hypothalamic-pituitary-adrenal axis and immune-mediated inflammation. N Engl J Med 1995; 332:1351-62.
52. Skaper SD, Facci L, Zusso M, Giusti P. Neuroinflammation, mast cells, and glia: dangerous liaisons. Neuroscientist 2017; 23(5):478-98.
53. Hendriksen E, van BD, Oosting RS, Redegeld FA. Mast cells in neuroinflammation and brain disorders. Neurosci Biobehav Rev 2017; 79:119-33.
54. Zhang X, Wang Y, Dong H, Xu Y, Zhang S. Induction of microglial activation by mediators released from mast cells. Cell Physiol Biochem 2016; 38(4):1520-31.
55. Zhang X, Dong H, Li N, et al. Activated brain mast cells contribute to postoperative cognitive dysfunction by evoking microglia activation and neuronal apoptosis. J Neuroinflammation 2016; 13(1):127.
56. Jack CS, Arbour N, Manusow J, et al. TLR signaling tailors innate immune responses in human microglia and astrocytes. J Immunol 2005; 175(7):4320-30.
57. Vargas G, Medeiros Geraldo LH, Gedeao SN, Viana PM, Regina Souza LF, Carvalho Alcantara GF. Severe acute respiratory syndrome coronavirus 2 (SARS-CoV-2) and glial cells: Insights and perspectives. Brain Behav Immun Health 2020; 7:100127.
58. Murta V, Villarreal A, Ramos AJ. Severe acute respiratory syndrome coronavirus 2 impact on the central nervous system: Are astrocytes and microglia main players or merely bystanders? ASN Neuro 2020; 12:1759091420954960.
59. Sheridan SD, Thanos JM, De Guzman RM, et al. Umbilical cord blood derived microglia-like cells to model COVID-19 exposure. Transl Psychiatry 2021; 11(1):179.
60. Tremblay ME, Madore C, Bordeleau M, Tian L, Verkhratsky A. Neuropathobiology of COVID-19: The role for glia. Front Cell Neurosci 2020; 14:592214.
61. Theoharides TC. Luteolin supplements: All that glitters is not gold. Biofactors 2020; 47(2):242-4.
62. Seelinger G, Merfort I, Schempp CM. Anti-oxidant, anti-inflammatory and anti-allergic activities of luteolin. Planta Med 2008; 74(14):1667-77.
63. Jager AK, Saaby L. Flavonoids and the CNS. Molecules 2011; 16(2):1471-85.
64. Leyva-Lopez N, Gutierrez-Grijalva EP, mbriz-Perez DL, Heredia JB. Flavonoids as cytokine modulators: A possible therapy for inflammation-related diseases. Int J Mol Sci 2016; 17(6).
65. Harwood M, nielewska-Nikiel B, Borzelleca JF, Flamm GW, Williams GM, Lines TC. A critical review of the data related to the safety of quercetin and lack of evidence of in vivo toxicity, including lack of genotoxic/carcinogenic properties. Food Chem Toxicol 2007; 45(11):2179-205.
66. Theoharides TC, Conti P, Economu M. Brain inflammation, neuropsychiatric disorders, and

immunoendocrine effects of luteolin. J Clin Psychopharmacol 2014; 34(2):187-9.
67. Russo M, Moccia S, Spagnuolo C, Tedesco I, Russo GL. Roles of flavonoids against coronavirus infection. Chem Biol Interact 2020; 328:109211.
68. Calis Z, Mogulkoc R, Baltaci AK. The Roles of flavonols/flavonoids in neurodegeneration and neuroinflammation. Mini Rev Med Chem 2020; 20(15):1475-88.
69. Jang S, Kelley KW, Johnson RW. Luteolin reduces IL-6 production in microglia by inhibiting JNK phosphorylation and activation of AP-1. Proc Natl Acad Sci USA 2008; 105(21):7534-9.
70. Patel AB, Tsilioni I, Leeman SE, Theoharides TC. Neurotensin stimulates sortilin and mTOR in human microglia inhibitable by methoxyluteolin, a potential therapeutic target for autism. Proc Natl Acad Sci U S A 2016; 113:E7049-E7058.
71. Weng Z, Patel AB, Panagiotidou S, Theoharides TC. The novel flavone tetramethoxyluteolin is a potent inhibitor of human mast cells. J Allergy Clin Immunol 2015; 135(4):1044-52.
72. Patel AB, Theoharides TC. Methoxyluteolin inhibits neuropeptide-stimulated proinflammatory mediator release via mTOR activation from human mast cells. J Pharmacol Exp Ther 2017; 361(3):462-71.
73. Ashaari Z, Hadjzadeh MA, Hassanzadeh G, et al. The flavone luteolin improves central nervous system disorders by different mechanisms: A review. J Mol Neurosci 2018; 65(4):491-506.
74. Kempuraj D, Thangavel R, Kempuraj DD, et al. Neuroprotective effects of flavone luteolin in neuroinflammation and neurotrauma. Biofactors 2020; 47(2):190-7.
75. Devi SA, Chamoli A. Polyphenols as an effective therapeutic intervention against cognitive decline during normal and pathological brain aging. Adv Exp Med Biol 2020; 1260:159-74.
76. Gratton G, Weaver SR, Burley CV, et al. Dietary flavanols improve cerebral cortical oxygenation and cognition in healthy adults. Sci Rep 2020; 10(1):19409.
77. Theoharides TC, Stewart JM, Hatziagelaki E, Kolaitis G. Brain "fog," inflammation and obesity: key aspects of 2 neuropsychiatric disorders improved by luteolin. Front Neurosci 2015; 9:225.
78. Theoharides TC, Cholevas C, Polyzoidis K, Politis A. Long-COVID syndrome-associated brain fog and chemofog: Luteolin to the rescue. Biofactors 2021; 47(2):232-41.

EDITORIAL

Anaphylaxis is a rare reaction in COVID-19 vaccination

R.G. Bellomo[1], C.E. Gallenga[2], Al. Caraffa[3], G. Tetè[4], G. Ronconi[5] and P. Conti[6]

[1]University of Study of Urbino Carlo Bo, Department of Biomolecular Sciences, Urbino, Italy; [2]Molecular Medicine, Department of Morphology, Surgery, Experimental Medicine, University of Ferrara, Ferrara, Italy; [3]School of Pharmacy, University of Camerino, Camerino, Italy; [4]Specialization School in Oral Surgery, Vita-Salute San Raffaele University, Milan, Italy; [5]Policlinico Universitario A. Gemelli IRCCS, Università Cattolica del Sacro Cuore, Rome, Italy; [6]Postgraduate Medical School, University of Chieti, Chieti, Italy

Anaphylaxis is a severe multisystem reaction that occurs rapidly after the introduction of an antigen that would otherwise be a harmless substance. It is characterized by airway and respiratory problems, cardiovascular collapse, mucosal inflammation, and other complications, all severe symptoms that can cause death. IgE-dependent anaphylaxis involves mast cells (MCs) which are the main sources of biologically active mediators that contribute to the pathological and lethal phenomena that can occur in anaphylaxis. Antibody-mediated anaphylaxis can follow multiple pathways such as that mediated by MCs carrying the FceRI receptor, which can be activated by very small amounts of antigen including a vaccine antigen and trigger an anaphylactic reaction. In addition, anaphylaxis can also be provoked by high concentrations of IgG antibodies that bind to the FcγR receptor present on basophils, neutrophils, macrophages and MCs. For this reason, the IgG concentration should be kept under control in vaccinations. Activation of MCs is a major cause of anaphylaxis, which requires immediate treatment with epinephrine to arrest severe lethal symptoms. MCs are activated through the antigen binding and cross-linking of IgE with release of mediators such as histamine, proteases, prostaglandins, leukotrienes and inflammatory cytokines. The release of these compounds causes nausea, vomiting, hives, wheezing, flushing, tachycardia, hypotension, laryngeal edema, and cardiovascular collapse. mRNA and viral vector vaccines have been cleared by the United States, Food and Drug Administration (FDA), generating hope of prevention and cure for COVID-19 around the world. Scientists advise against giving the vaccine to individuals who have had a previous history of anaphylaxis. The US Centers for Disease Control and Prevention (CDC) advises people with a previous history of any immediate allergic reaction to remain under observation for approximately 30 minutes after COVID-19 vaccination. To date, vaccines that prevent SARS-CoV-2 infection have not raised major concerns of severe allergic reactions, although, in some cases, pain and redness at the injection site and fever have occurred after administration of the vaccine. These reactions occur in the first 24-48 hours after vaccination. It has been reported that probable forms of anaphylaxis could also occur, especially in women approximately 40 years of age. But after tens of millions of vaccinations, only a few patients had this severe reaction with a low incidence. Anaphylactic and severe allergic reactions can also occur to any component of the vaccine including polysorbates and polyethylene glycol. To date, there is no precise information on allergic reactions to COVID-19 vaccines. Individuals with MCs and complement with higher activation than others may be at greater allergic risk. Moreover, the reactions called anaphylactoids, are those not mediated by IgE because they do not involve this antibody and can

Corresponding Author:
Dr. Pio Conti,
Professor of Immunology,
Post Graduate School of Medicine,
University of Chieti-Pescara, University Zone,
Viale Unità d'Italia, 73, 66013 Chieti, Italy
Tel./Fax: +39 0871 574136
e-mail: piocontieditor@biolifesas.org

0393-974X (2021)
Copyright © by BIOLIFE, s.a.s.
This publication and/or article is for individual use only and may not be further reproduced without written permission from the copyright holder.
Unauthorized reproduction may result in financial and other penalties
DISCLOSURE: ALL AUTHORS REPORT NO CONFLICTS OF INTEREST RELEVANT TO THIS ARTICLE.

also occur in COVID-19 vaccination. These not-IgE-mediated reactions occur through direct activation of MCs and complement with tryptase production, but to a lesser extent than IgE-mediated anaphylaxis. However, at the moment it is not known exactly which component of the vaccine causes the allergic reaction and which vaccine causes the most side effects, including anaphylaxis. Thus, individuals who have a known allergy to any component of the vaccine should not be vaccinated. However, should an anaphylactic reaction occur, this requires immediate treatment with epinephrine to arrest severe lethal symptoms. In conclusion, the purpose of this editorial is to encourage the population to be vaccinated in order to extinguish this global pandemic that is afflicting the world population, and to reassure individuals that anaphylactic reactions do not occur with a higher incidence than other vaccinations.

Key words: COVID-19; anaphylaxis; vaccine; SARS-CoV-2; immunity; inflammation; allergy

It has been clearly confirmed and reported that the new coronavirus SARS-CoV-2 causes COVID-19 disease. The virus has provoked a global pandemic, hospitalizing millions of individuals in intensive care (1). Fortunately, precautions and treatments have been taken that have avoided a greater number of infections, and therefore deaths. The serious pathological situations were caused by lung inflammation and thromboembolism with consequent asphyxiation. SARS-CoV-2 is biologically formed from RNA and N-proteins, while outside the membrane it made up of two proteins, E and M, lipids and the glycoprotein (S) spike (2). Coronavirus-19 infects humans, usually starting in the airways, nose and mouth, binding to the target cell ACE2 receptor and the immune cell TLR. Once SARS-CoV-2 has entered the cell and therefore the human body, it replicates quickly, carrying out its pathogenic action with the release of interferon that stimulates immune cells such as T and B lymphocytes, neutrophils, macrophages and mast cells. The production of pro-inflammatory cytokines such as IL-1, IL-6 and TNF is essentially given by macrophages and mast cells causing edema, bleeding, intravascular coagulation, thrombosis, respiratory failure and patient death.

Vaccines induced by microbial antigens prevent the spread of infectious diseases and reduce disease and mortality. On December 11, 2020, Pfizer-BioNTech and Moderna mRNA vaccines packaged in lipid nanoparticles**,** were cleared for emergency use (EUA) by the United States Food and Drug Administration (FDA), generating hope of prevention and cure for COVID-19 worldwide. After tens of millions of vaccinations, only a small number of patients had a severe allergic reactions with an incidence of 1 in 100,000, about 10 times higher than that of other vaccinations (3).

During the protective vaccination foe SARS-CoV-2 allergic phenomena can occur and, in very rare cases, anaphylaxis, with serious consequences. The anaphylactic reaction is a severe pathological advent that can arise in a few minutes, but also after up to eight hours, leading to cardio-vascular collapse and insufficient pulmonary activity. These cases involve the activation of MCs through the FcεRI receptor, a reaction activated by IgE. Mast cells are immune but also inflammatory cells which perform a biological action partially overlapping that of basophilic granulocytes. When IgE binds to its FcεRI receptor it aggregates and activates the cell to immediately release biological mediators stored in its cytoplasmic granules (4). The mediators released by MCs in the tissue provoke an allergic reaction with local and systemic inflammatory problems. SARS-CoV-2 vaccines can cause an allergic response mediated by MCs which are activated by the binding of IgE with part of the vaccine, but also the allergic reaction can be non-IgE mediated. MC mediators such as histamine, heparin (and other proteoglycans), proteases (such as carboxypeptidase A3, tryptase and chymase), as well as the cytokine TNF, are released in seconds; while the products of arachidonic acid metabolism such as prostaglandins, cysteinyl leukotrienes, and cytokines/chemokines and growth factors are transcriptionally up-regulated, generated and released (5). MCs can also be activated by complement products such

as C3a and C5a, cytokines (IL-33), some peptides (substance P) and by products of microorganisms, all independent of IgE. These allergy-intervening immune cells contribute to host defense in the type 2 response of antigen-activated T helper lymphocytes, resulting the production of IgE antibodies against the antigen in B-cell.

After delayed allergic reactions 48-92 hours after vaccination, delayed allergic cell-mediated reactions may occur, not dependent on IgE antibodies, but due to the abnormal reaction of T cells, macrophages and MCs (without degranulation) with release of pro-inflammatory cytokines. These reactions result in endothelial and tissue damage, inflammation and, in severe cases, death of the patient.

Allergies are inflammatory immune responses against any antigen and can cause severe host harm, including death. They are known to affect about 25 of the world population and trigger an acquired type 2 response involving $CD4^+$ helper T cells. Antigens such as viral antigens can also sensitize individuals by causing an IgE-mediated anaphylactic allergic reaction. Anaphylaxis is an immediate systemic hypersensitivity reaction that can be triggered by any antigen (very rarely by SARS-CoV-2 vaccine) (6). It is characterized by diffuse edema and drop in blood pressure due to a strong vasodilatation spread throughout the body. The antigen introduced into the body by injection, insect bite or absorption by the intestinal mucosa, activates MCs simultaneously in many tissues which first release inflammatory chemical mediators and then pro-inflammatory cytokines, with serious damage to the organism that can even lead to death. The release of the mediators of inflammation causes plasma loss, a drop in blood pressure and anaphylactic shock which can be fatal. To these effects are often added constriction of the airways, hypersecretion of mucus (both in the intestine and in the lungs), hypersensitivity and cutaneous urticaria.

In severe allergic reactions mediated by tryptases and pro-inflammatory cytokines, renal failure and brain damage can also occur which can lead to death (7).

Mast cells (MCs)

MCs can mediate inflammatory phenomena with consequent implications of acute and sub-acute pathological processes. Therefore, MCs can participate in immediate or delayed immunological reactions as primary or secondary effector cells. The IgE antibody binds on the MC surface on which the antigen binds, leading to degranulation, which is the basis of the allergy. Activation of MCs can cause leaky gut and promote anaphylaxis. These reactions induce the release of IL-33 and IL-25 which synergize by activating the ILC2 innate lymphoid cells with consequent production of IL-4 and expansion of MCs, all phenomena that can favor the onset of anaphylaxis. Therefore, the release of IL-33 from sensitized tissue can activate ILC2 cells which release IL-4 and IL-13 and activate the multiplication of inflammatory MCs. The proliferation in the marrow of MCs is also due to other cytokines, such as IL-5 and IL-9, which can play a redundant role with IL-4 and IL-13 (8).

Mast cells can enhance the innate response to antigen, contributing to acquired resistance. Therefore, it is pertinent to think that these cells and IgE help protect individuals from foreign antigens, including viruses.

It has long been known that vaccines very rarely cause anaphylaxis. In fact, the administration of

Table I. *Some excipients contained in mRNA and viral vector vaccines*

Moderna: Acetic acid, lipids, SM-102, polyethylene glycol, cholesterol, and 1,2-distearoyl-sn-glycero-3-phosphocholine, sodium acetate, sucrose(sugar), tromethamine, tromethamine hydrochloride.
Pfizer: Electrolytes potassium chloride, monobasic potassium phosphate, sodium chloride, dibasic sodium phosphate dehydrate, lipids, polyethylene glycol, sucrose(sugar), saline (sodium chloride).
AstraZeneca vaccine: histidine, L-histidine hydrochloride monohydrate, magnesium chloride hexahydrate, polysorbate 80, ethanol, sucrose (sugar), sodium chloride, disodium edetate dihydrate, water.

anti-COVID-19 vaccines has caused a small number of allergic reactions, causing apprehension in the world population (9). Vaccines can provoke, albeit in very few instances, severe acute systemic IgE or IgG-mediated and anaphylactic reactions with complement participation. These can also cause severe delayed systemic reactions mediated by $CD4^+$ T helper cells. The allergic reaction can occur either due to the active components of the vaccine or, more frequently, against excipients, substances which pharmacologically should be inactive and used to improve the absorption, stability and solubility of the active compounds present in vaccines (10). Several types of excipients could be added to the vaccine to better stimulate the immune response with a more copious production of antigen-neutralizing antibodies. Thus, in the vaccination process, excipients are the main culprits of IgE-mediated allergic reactions (Table I).

It has been reported that in viral vector vaccines the compound most suspected of allergic reactions is polysorbate; while in mRNA vaccines it appears to be polyethylene glycol (11).

In conclusion, the reactions described above must in no way hinder the anti-SARS-CoV-2 vaccination process as, as already mentioned, they occur very rarely and the benefit of vaccination is much greater than the risks of serious allergic reactions, including anaphylactic shock.

REFERENCES

1. Gandhi RT, Lynch JB, Del Rio C. Mild or Moderate Covid-19. N Engl J Med 2020; 383(18):1757-66.
2. Ramasamy S, Subbian S. Critical determinants of cytokine storm and Type I interferon response in COVID-19 pathogenesis. Clin Microbiol Rev 2021; 34(3):e00299-20.
3. Harvey WT, Carabelli AM, Jackson B, et al. SARS-CoV-2 variants, spike mutations and immune escape. Nat Rev Microbiol 2021; 19(7):409-24.
4. Galli SJ, Gaudenzio N, Tsai M. Mast cells in inflammation and disease: recent progress and ongoing concerns. Annu Rev Immunol 2020; 38:49-77.
5. Taracanova A, Alevizos M, Karagkouni A, et al. SP and IL-33 together markedly enhance TNF synthesis and secretion from human mast cells mediated by the interaction of their receptors. Proc Natl Acad Sci U S A 2017; 114(20):E4002-E4009.
6. Reber LL, Hernandez JD, Galli SJ. The pathophysiology of anaphylaxis. J Allergy Clin Immunol 2017; 140(2):335-48.
7. Kalesnikoff J, Galli SJ. Anaphylaxis: mechanisms of mast cell activation. Chem Immunol Allergy 2010; 95:45-66.
8. Galli SJ, Tsai M, Piliponsky AM. The development of allergic inflammation. Nature 2008 Jul 24;454(7203):445-54.
9. Conti P, Pregliasco FE, Calvisi V, et al. Monoclonal antibody therapy in COVID-19. J Biol Regul Homeost Agents 2021; 35(2):423-27.
10. Mukai K, Karasuyama H, Kabashima K, Kubo M, Galli SJ. Differences in the importance of mast cells, basophils, IgE, and IgG versus that of CD4(+) T cells and ILC2 cells in primary and secondary immunity to Strongyloides venezuelensis. Infect Immun 2017; 85(5):e00053-17.
11. Kounis NG, Koniari I, de Gregorio C, et al. allergic reactions to current available COVID-19 vaccinations: pathophysiology, causality, and therapeutic considerations. Vaccines (Basel) 2021; 9(3):221.

EDITORIAL

Management of patients at risk of anaphylaxis after COVID 19 vaccination

S. Gangemi[1], A. Allegra[2] and M. Di Gioacchino[3,4]

[1]School and Operative Unit of Allergy and Clinical Immunology, Department of Clinical and Experimental Medicine, University of Messina, Messina, Italy; [2]Division of Hematology, Department of Human Pathology in Adulthood and Childhood "Gaetano Barresi", University of Messina, Messina, Italy; [3]Center Advanced Science and Technology, G. d'Annunzio University, Chieti, Italy; [4]Institute for Clinical Immunotherapy and Advanced Biological Treatments, Pescara, Italy

The success of a vaccination campaign depends on the possibility of guaranteeing not only a wide distribution of effective vaccines, but also on their safety and acceptance by the population. Vaccine safety questions should be answered by correct, unbiased and evidence-based reports, and by addressing all possible problems including allergic reactions. Despite the fact that many COVID-19 vaccines are free from the majority of potentially sensitizing components, an allergic reaction can occur even in the form of a severe, life-threatening anaphylaxis. The frequency of allergic reactions against COVID vaccine is greater than that observed for other vaccinations. National and international allergology societies have proposed specific guidelines for individuals at risk of anaphylaxis by vaccine. Vaccines, like all the pharmaceutical preparations, are submitted to great safety and efficacy valuations, however, even the greatest pre-licensure experimentations are insufficient to evaluate the vaccine's potential to provoke anaphylaxis. Therefore, post-market surveillance is essential to analyze, record and characterize all adverse events. To this purpose, specific algorithms should be used as a monitoring strategy of adverse events in patients undergoing vaccination against COVID 19.

The hope in controlling SARS-Cov-2 lies on the effectiveness of vaccines at present available and the many under investigation, as the drugs being currently used are unable to limit the pandemic (1). Vaccines reduce morbidity and mortality from infections and block the diffusion of infections when applied on a large scale: the "herd protection" mechanism (2). WHO states that vaccines save 1-3 million lives globally every year and will save 25 million more in the next ten years. Furthermore, it has been reported that for every dollar expended in vaccines, 16 dollars are spared in health care expenses, and reduction of productivity (3).

A successful COVID-19 vaccine campaign is presently the world's principal urgency, and production of vaccine is progressing at an incredible speed. To accelerate the fast implementation of diverse candidate vaccines, drug regulatory agencies have dedicated facilitated regulatory pathways. The European Medicines Agency (https://www.ema.europa.eu/en/authorisation-procedures) guaranties an 'emergency procedure', which allows for fast-track approval of a vaccine around 70 days instead of the usual 210 days.

At present, 164 vaccine candidates, of which 48 in clinical evaluation, have been tested, and

Key words: COVID-19; vaccination; anaphylaxis; management of allergic reaction

Corresponding Author:
Mario Di Gioacchino
Center Advanced Science and Technology,
G. d'Annunzio University,
66100 Chieti, Italy
Tel +39 3280122862
e-mail: mario.digioacchino@unich.it

0393-974X (2021)
Copyright © by BIOLIFE, s.a.s.
This publication and/or article is for individual use only and may not be further reproduced without written permission from the copyright holder.
Unauthorized reproduction may result in financial and other penalties
DISCLOSURE: ALL AUTHORS REPORT NO CONFLICTS OF INTEREST RELEVANT TO THIS ARTICLE.

four vaccines have recently cleared phase III trials reporting very positive results (4, 5). Russia and China have early initiated programmatic roll-out of COVID-19 vaccines, despite the perplexity on the quality of performed trials (6). Furthermore, four vaccines, mRNA-1273 (Moderna), BNT162b2 (Pfizer), Vaxzevria (Astra Zeneca) and Ad26. COV2-S (Jansen), have been demonstrated to be safe and very efficacious in inhibiting symptomatic COVID-19, and others are under investigation (7).

The US, UK, Israel, EU and many other countries are in an advanced phase of the vaccination campaign, however, the success of the vaccination campaign will depend on the possibility of guaranteeing not only a wide distribution of effective vaccines but also their safety and acceptance by the population (8, 9). Vaccine diffidence is strictly linked to its safety: inoculating a theoretically dangerous organism is instinctively experienced as a menace that inspires skepticism towards vaccines, particularly when untrue statements of adverse reactions are widespread (9, 10). Therefore, vaccine safety questions should be answered by correct, unbiased and evidence-based reports, and by addressing all possible problems including allergic reactions (9, 10). Many vaccine constituents, such as viral proteins and toxoids, additives and preservatives, albumin salts, eggs or yeast as culture media, antibiotics, gelatin or albumin stabilizers, PEG, polysorbate and latex can act as sensitizing agents (10, 11), and epidemiological and

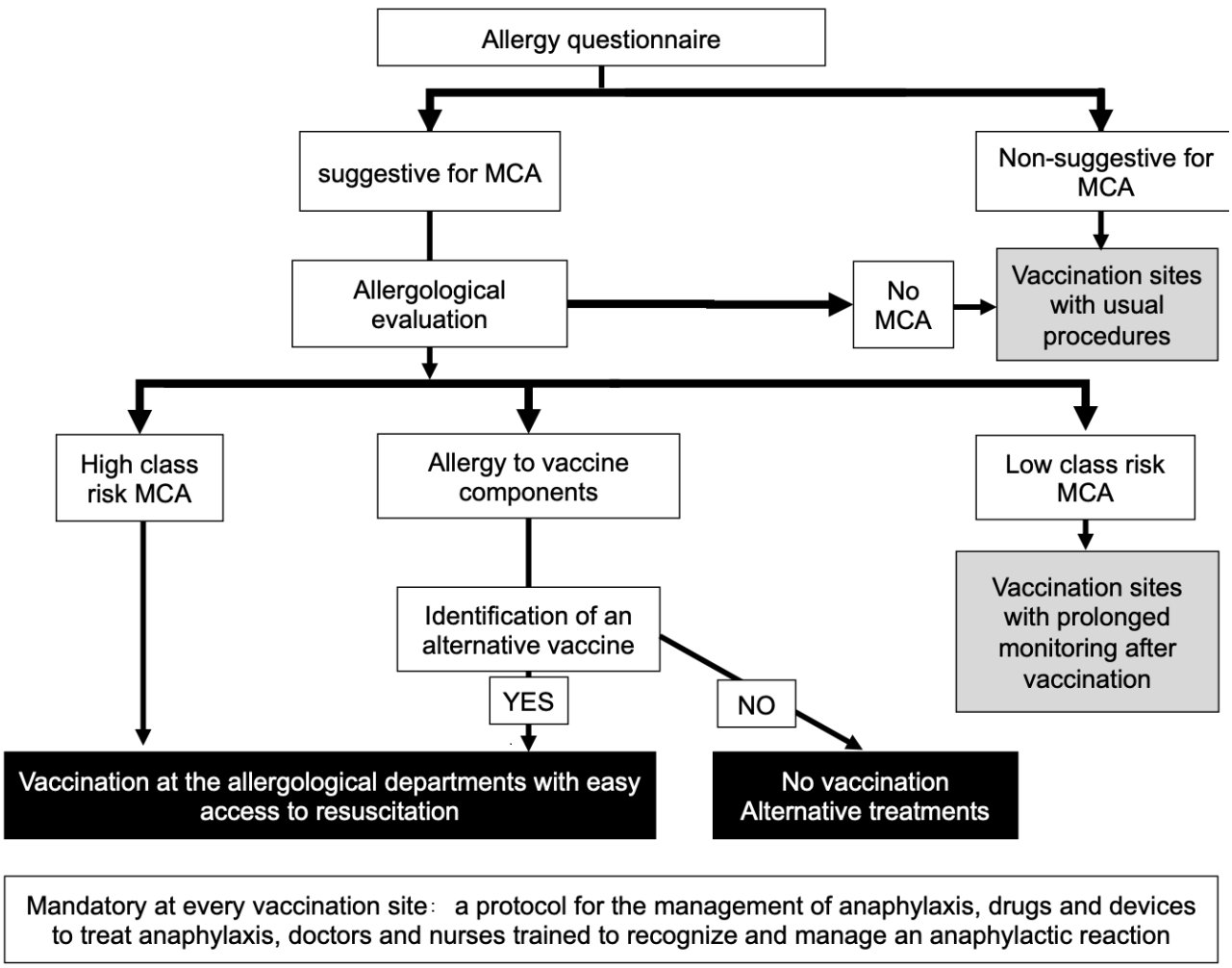


Fig. 1. *Flow chart for the management of subjects with suspected or verified allergic reaction to vaccines. MCA: Mast cell activation conditions: risk class described in the text.*

mechanistic proofs strongly established a causal relationship between anaphylaxis and vaccine (11, 12). However, despite many COVID-19 vaccines being free from most of these potentially sensitizing components, an allergic reaction can occur even in the form of a severe, life-threatening anaphylaxis, as occurred in the UK, US and recently in Italy, or as reported by manufacturers during clinical trials. In England, the Chief Executive of the Medicines and Healthcare products Regulatory Agency, following the first allergic reaction observed after BNT162b2 vaccine, at first suggested "*Any person with a history of anaphylaxis to a vaccine, medicine or food should not receive the vaccine*"; but after updated: "*Anyone with a previous history of allergic reactions to the ingredients of the vaccine should not receive it, but those with any other allergies such as a food allergy can now have the vaccine"*. (https://www.gov.uk/government/news/confirmation-of-guidance-to-vaccination-centres-on-managing-allergic-reactions-following-covid-19-vaccination-with-the-pfizer-biontech-vaccine). Many allergology societies proposed specific guidelines for the management of individuals at risk of anaphylaxis, in particular against polyethylene glycol (PEG) and polysorbate, that seem responsible for the observed allergic reactions (12, 13),

Vaccine-caused anaphylaxis is a rare event (1.31 per million during 2009–2011, in US), COVID vaccines seem to induce a greater number of events; in Italy, to date, there have been 3 cases of allergic reactions in about 800,000 vaccinations, and the incidence of 11.1 allergic reactions per million doses in the US has been reported (14). We should consider that COVID-19 vaccination will be conducted on a global scale, so the number of possible anaphylaxis cases could be enormous. Every effort is therefore required to possibly prevent reactions or minimize their outcome. Besides factors strictly inherent to the composition of vaccines, other host-related characteristics can be relevant to the onset and severity of anaphylaxis. At present, 60% of cases of anaphylaxis had a pre-existing atopic disease, a condition characterized by mast cell activation (MCA). In general, all conditions characterized by MCA, including IgE-dependent diseases, other immunologic and inflammatory reactions, primary mast cell disorders, and hereditary alpha tryptasemia, must be taken into account as factors facilitating and worsening an allergic or pseudoallergic reaction (15). Therefore, how COVID-19 vaccines will be administered should be modulated according to severity of coexisting MCA syndromes.

Subjects with a history of reaction to previous vaccines or to drug-containing ingredients present in COVID vaccines or reacting to the first dose of COVID vaccine should be evaluated by allergologists, in particular for PEG and polysorbate; those most at risk (with mastocytosis, previous systemic anaphylaxis, prescription of self-injectable adrenaline, severe asthma, with multiple severe drug reactions, elevated tryptase) should be vaccinated in allergology departments, with easy access by resuscitators; those with lesser risk (with non-anaphylactic allergic reactions, chronic urticaria, severe atopic dermatitis, allergic to single drugs) should be monitored at the vaccination site for at least 30 minutes. Vaccinators should be trained to manage anaphylactic conditions and have all the devices and drugs available to deal with such an emergency. A specific flowchart based on risk classification is proposed in Fig. 1.

Vaccines, like all the pharmaceutical preparations, are submitted to great safety and efficacy evaluations, however, even the greatest pre-licensure experimentations are insufficient to evaluate the vaccine's potential to provoke anaphylaxis. Therefore, post-market surveillance is essential to analyze, record and characterize all adverse events. To this purpose, specific algorithms should be used as a monitoring strategy of adverse events in patients undergoing vaccination against COVID 19; for example, a Natural Language Processing (NLP) system was applied with good results to identify reports of anaphylaxis in the Vaccine Adverse Event Reporting System database after H1N1 vaccine with 98.5% specificity, 75% sensitivity, 66.7% positive predictive value, and 99% negative predictive value (16).

In conclusion, vaccines presently employed for the general population have an exceptional safety profile overall and offer protection against infections to individuals and the general population (17). To

attain population-wide diminutions in transmission, COVID-19 vaccines would need to demonstrate effectiveness against infection and transmission and not just against disease, possess wide uptake, and display a convincing safety profile. In any case, the possibility of an unpredictable allergic reaction must be foreseen, and every effort must be made to minimize its outcome by implementing a correct management of the vaccination campaign.

REFERENCES

1. Saeed H, Osama H, Madney YM, et al. COVID-19; current situation and recommended interventions. Int J Clin Pract 2020:e13886.
2. Frederiksen LSF, Zhang Y, Foged C, Thakur A. The long road toward COVID-19 herd immunity: vaccine platform technologies and mass immunization strategies. Front Immunol 2020; 11:1817.
3. Ozawa S, Clark S, Portnoy A, et al. Return on investment from childhood immunization in lowand middle-income countries, 2011-20. Health Affairs 2016; 35:199-207.
4. Mishra SK, Tripathi T. One year update on the COVID-19 pandemic: Where are we now? Acta Trop 2020; 214:105778.
5. Amant F, Krammer F. SARS-CoV-2 Vaccines: Status Report. Immunity 2020; 52:583-9.
6. Balakrishnan VS. The arrival of Sputnik V. Lancet Infect Dis 2020; 20:1128.
7. Bisgin A, Sanlioglu AD, Eksi YE, Griffith TS, Sanlioglu S. Current update on SARS-CoV-2 vaccine development with a special emphasis on gene therapy viral vector design and construction for vaccination. Hum Gene Ther 2021 doi:10.1089/hum.2021.052. Online ahead of print.
8. Shah A, Marks PW, Hahn SM. Unwavering regulatory safeguards for COVID-19 vaccines. JAMA 2020; 324:931-32.
9. Tau N, Yahav D, Shepshelovich D. Vaccine safety – is the SARS-CoV-2 vaccine any different? Hum Vaccin Immunother 2020; 1-4. On line ahead of print
10. Yang HJ. Allergic reactions to vaccine components. Allergy Asthma Respir Dis 2014; 2:157-64.
11. Committee to Review Adverse Effects of Vaccines; Institute of Medicine; Stratton K, Ford A, Rusch E, Clayton EW. Adverse effects of vaccines; evidence and causality. Washington (DC), National Academies Press (US); 2011.
12. Turner PJ, Ansotegui IJ, Campbell DE, et al. COVID-19 vaccine-associated anaphylaxis: A statement of the World Allergy Organization Anaphylaxis Committee. World Allergy Organ J 2021; 14:100517.
13. Patella V, Delfino G, Florio G, et al. Management of the patient with allergic and immunological disorders in the pandemic COVID-19 era. Clin Mol Allergy 2020; 18:18.
14. Banerji A, Wickner PG, Saff R, et al. RNA vaccines to prevent COVID-19 disease and reported allergic reactions: Current evidence and approach. J Allergy Clin Immunol In Practice. Online ahead of print.
15. Valent P, Akin C, Nedoszytko B, et al. Diagnosis, Classification and Management of Mast Cell Activation Syndromes (MCAS) in the Era of Personalized Medicine. Int J Mol Sci 2020; 21:9030
16. Yu W, Zheng C, Xie F, et al. The use of natural language processing to identify vaccine-related anaphylaxis at five health care systems in the Vaccine Safety Datalink. Pharmacoepidemiol Drug Saf 2020; 29:182-8.
17. Dudley MZ, Halsey NA, Omer SB, et al. The state of vaccine safety science: systematic reviews of the evidence. Lancet Infect Dis 2020; 20:e80-e89.

REVIEW

OM-85 in the prevention of respiratory infections: State-of-the-art and future perspectives in clinical practice

G.L. Marseglia[1], M. Benazzo[2], P. Biasci[3], F. Blasi[4], C. Cricelli[5], M. Doria[3], S. Leonardi[6], D.G. Peroni[7], F. Scaglione[8] and G. Ciprandi[9]

[1]Pediatric Clinic, Fundation IRCCS Policlinico San Matteo, University of Pavia, Pavia, Italy; [2]Otorhinolaryngoiatric Clinic, Foundation IRCCS Policlinico San Matteo, University of Pavia, Pavia, Italy; [3]Italian Federation of Pediatricians, Rome, Italy; [4]Department of Pathophysiology and Transplant, University of Milan, Italy; [5] The Italian Society of General Medicine, Florence, Italy; [6]Department of Clinical and Experimental Medicine, University of Catania, Catania, Italy; [7] Pediatric Unit, University of Pisa, Pisa, Italy; [8]Department of Oncology and Onco-Hematology, University of Milan, Milan, Italy; [9]Casa di Cura Villa Montallegro, Genoa, Italy

Received March 22, 2021 – Accepted May 25, 2021

Respiratory infections (RI) significantly burden patients, their families, and society. Respiratory infection recurrence (RRI) usually depends on a defect of the immune response, which can be more or less transient and/or selective. In particular, children, older people, heavy smokers, and patients with chronic diseases, characterized by an inadequate immune response, may be at risk of developing RRI. In this context, OM-85 could represent a valuable option in the management of RRI. OM-85 is a bacterial lysate containing the extracts of some common pathogens, including *Branhamella catarrhalis, Klebsiella pneumoniae, Klebsiella ozaenae, Streptococcus pneumoniae, Streptococcus pyogenes, Streptococcus viridans*, and *Staphylococcus aureus*. Methodologically rigorous studies have documented the mechanism of action, efficacy, and safety of OM-85. OM-85 enhances the natural and acquired immune response through multifaceted mechanisms. Substantial evidence has shown that OM-85 can prevent respiratory infections, reduce the number of COPD exacerbations, and shorten the disease duration at home or in hospital. OM-85 can enhance the effectiveness of the 'flu vaccination without affecting the vaccine tolerability. The preventive use of OM-85 can reduce the use of antibiotics, contributing to contrast antibiotic resistance and saving the high cost of chronic respiratory diseases. Further studies should define the ideal candidate to OM-85 treatment.

Epidemiology of respiratory infections

Respiratory infections (RI) represent a relevant public health issue, mainly concerning children and older people (1). As a result, the socio-economic burden of respiratory infections is particularly relevant.

Acute respiratory infections (ARI) affect the upper airways (rhinitis, rhinopharyngitis, rhinosinusitis, tonsillitis, laryngitis, and otitis media) and/or the lower airways (tracheitis, bronchitis, bronchiolitis, and pneumonia), with very varied clinical pictures depending on the organ(s) involved, the patient's age, and the general clinical condition (2, 3). ARI have a notable impact on morbidity and mortality and direct and indirect healthcare costs (4-

Key words: recurrent respiratory infections; immune defect; bacterial lysate; OM-85; vaccinations

Corresponding Author:
Prof. Giorgio Ciprandi,
Allergy Clinic,
Casa di Cura Villa Montallegro,
Genoa, Italy
e-mail: gio.cip@libero.it

0393-974X (2021)
Copyright © by BIOLIFE, s.a.s.
This publication and/or article is for individual use only and may not be further reproduced without written permission from the copyright holder.
Unauthorized reproduction may result in financial and other penalties
DISCLOSURE: ALL AUTHORS REPORT NO CONFLICTS OF INTEREST RELEVANT TO THIS ARTICLE.

6). Respiratory infections are the second cause of death in children under five years of age, just after prematurity, as documented by the WHO report (7).

The incidence of upper airway respiratory infections is inversely proportional to age. Children usually have 6-8 episodes per year, while adults tend to have 1-2 respiratory infections yearly (4). Moreover, it was estimated that approximately 6% of Italian children under six years of age had recurrent RI (RRI), defined by the presence of at least one of the following conditions: i) ≥ six annual RI; ii) one or more monthly RI from October to February; iii) ≥ 3 RI involving lower airways (8). The prevalence of ARI reaches 25% among children under one year of age, decreasing to 18% in those between 1 and 4 years of age (9). Respiratory infections represent approximately one-third of all pediatric visits and constitute 8-18% of pediatric hospitalizations (10).

Chronic obstructive pulmonary disease (COPD) is one of the most common diseases in the elderly, such as those over 65 years. It is often associated with several comorbidities, including diabetes mellitus, cardiovascular disease, arterial hypertension, obesity, cancer, and impaired immune response (11). In addition, COPD is worsened by various unfavorable situations, namely malnutrition, prolonged hospitalization, and poor hygienic conditions (11, 12). In the US, COPD is the fourth most common cause of morbidity; it is the reason for more than 17 million medical visits per year and 13% of all hospital admissions, and the fourth cause of death (13, 14). Respiratory infections significantly affect COPD patients as they induce an exacerbation of respiratory symptoms and deterioration of the disease (15, 16). Furthermore, each COPD exacerbation irreversibly accelerates the respiratory functional decline and worsens the quality of life of patients and their families (11-13).

Etiology and pathophysiology

Viral respiratory infections are the most common cause of ARI, so much so that they represent up to 80% of all infectious forms affecting the respiratory system (17). Rhinoviruses are the most common cause of ARI in all age groups; other virus families, frequently responsible for respiratory infections, are adenoviruses, influenza viruses, and coronaviruses (17, 18). The coronavirus family has been deeply investigated in the era of the pandemic caused by the SARS-CoV-2 coronavirus (19).

As a rule, viral infections tend to resolve in a short time and, in the majority of cases, spontaneously; sometimes, however, they can be accompanied or followed by bacterial over-infections. It has been estimated that 60% of patients with upper respiratory tract infections, whose symptoms last for more than ten days, have bacterial over-infection, which is associated with additional damage to the respiratory tissues (20). In particular, the so-called "10-day" sign has been proposed: if infectious rhinitis (the common cold) lasts for more than ten days or gets worse after the first five days, acute rhinosinusitis must be suspected.

Viruses and bacteria are capable of inducing transient modifications of the immune system. In particular, a viral infection is associated with a state of relative immunodeficiency, obviously transient in the immunocompetent subject. This phenomenon explains the susceptibility to contract other infections, both viral and bacterial, occurring during and/or after a viral infection. As a consequence, the immune system requires some time to restore its normal functionality after a viral infection. Bacteria also implement mechanisms to contrast the host defenses; for example, they carry out a proteolytic activity against secretory immunoglobulin A (IgA), reduce the complement system's opsonizing capacity, and inhibit chemotaxis (20).

The extremes of life share a reduced ability of the immune system to defend the body from infectious agents. In addition, the clinical situation becomes more complicated in the elderly as numerous comorbidities worsen infectious diseases. Combining these factors explains the greater susceptibility to infections in children and the elderly (21, 22).

Children require several years to achieve adequate immunological competence, i.e., a sufficient repertoire of specific memory cells. The maturation of the immune system occurs linearly with the growth, as documented, for example, by the number of alveolar macrophages: minimal in the first years of life, but progressively increasing

over time (22). Furthermore, numerous risk factors play a pathogenetic role in children, such as certain environmental conditions ("cold" season, exposure to passive smoke, outdoor and indoor pollution, early socialization, promiscuity, and kinship groups), pathophysiological elements (reduced validity of the tussive reflex, low levels of secretory IgA, IgG2, and IgG4, inadequate antibody response to polysaccharide antigens, reduced complement activity, and granulocyte function), anatomical elements (reduced airway caliber and length as well as horizontalization of the Eustachian tube) and, obviously, the genetic predisposition of having an altered immunological function (23-25).

Older adults with COPD usually have a reduction of immunological defenses, often related to smoking and mechanical alterations of the airways due to underlying inflammation and the accumulation of endobronchial secretions (26). Moreover, in elderly subjects, a high risk of reduced immunological response is characterized by a low level of B lymphocytes, an increase in CD8+/CD28-/CD57+ cells (suppressor and cytotoxic lymphocytes), high levels of pro-inflammatory interleukins (IL-1 and IL-6), low T lymphocyte function, and cytomegalovirus seropositivity (27). This immunopathological scenario emphasizes the concept that pro-inflammatory cytokines play an important role. Healthy adults display a balance between pro-inflammatory and anti-inflammatory cytokines. On the contrary, the elderly present a series of pathogenetic factors (stress, continuous exposure to antigens, metabolic and chronic diseases) that create a situation which has been defined as "inflammaging," that is a low-level chronic inflammatory state linked to aging. Inflammaging in turn causes a predisposition to the onset of inflammatory diseases, such as atherosclerosis, type 2 diabetes, obesity, arterial hypertension, and sarcopenia (28). In addition, the incidence of autoimmune and neoplastic diseases is also increased in the elderly, again due to a defect in the immune response, particularly the so-called regulatory response. This immunopathological setting creates a vicious circle, such as a defective immune system promotes the onset of chronic diseases, which also depresses the immune function.

Treatment strategies

One of the main problems in treating respiratory infections is indirectly linked to the high rate of inappropriate antibiotic prescriptions in subjects with viral infections. In Italy, 70% of antibiotic prescriptions concern patients with ARI, mainly affecting the upper airways (mostly pharyngotonsillitis and rhinosinusitis). Italy is among the European countries in which the use of antibiotics in childhood is the highest. Indeed, 88.7% of the total number of antibiotic prescriptions are prescribed by the family pediatrician (61.2%) or by the general practitioner (27.5%); the remaining antibiotics are prescribed by various specialists (29-32). Unfortunately, this excessive use of antibiotics results in a continuous increase in resistance to the antibiotics themselves, which significantly reduces their effectiveness, especially in children and the elderly.

Different strategies are available to prevent RI in clinical practice. Vaccinations currently represent the most effective, safest, and best documented way for preventing infections. The Italian Ministry of Health has prepared a vaccination calendar that includes a series of mandatory and optional vaccinations for all ages of life. In particular, the latest ministerial newsletter recommended the flu vaccine in subjects 65 years of age or over, in children, and a number of subjects at risk. To confirm the preventive value of vaccinations, in the present phase of the SARS-CoV-2 pandemic, the Ministry of Health had issued a more stringent recommendation regarding the 2020-2021 anti-flu vaccination (33). Moreover, an immense vaccination program against COVID-19 is implementing.

The clinical response to vaccines depends on the age of subjects as it is reduced in children and older people (34-36). In particular, antibody production tends to decline over time. The degree of response to a vaccine depends on several factors, some intrinsic to the vaccine itself, its composition, while others are related to the host. In this respect, there is a very close correlation between the efficacy of the influenza vaccine and the age of the vaccinated subject. Concerning the coverage efficacy, vaccine effectiveness is detectable in approximately 70-90% of healthy people under 65 years of age, obviously depending on the type of vaccine used (37, 38).

However, a much lower efficacy is observed in the elderly, up to only 30-40% in elderly adults in assisted residences (37, 38). Seroprotection ranges from 42 to 91% one month after vaccination and from 16 to 84% five months after vaccination (38). Therefore, the problem of an adequate response to vaccinations requires adequate attention, mainly in subjects with vulnerability, such as frail patients affected by multiple debilitating chronic diseases.

Apart from vaccines, many other products have been tested, but the outcomes rarely were reliable because of methodological drawbacks that arose in the study design or during the study conduction. Nevertheless, a long list of substances is commonly used in daily clinical practice to stimulate the immune system to prevent infections and enhance the response to vaccinations. In this regard, probiotics have been used to bolster the response to vaccines. The definition of probiotic is a live microorganism that confers a benefit to the health of the host when administered in adequate quantities. A meta-analysis has shown that probiotics (and prebiotics, i.e., the metabolic substrate of probiotics) effectively increased the immunogenicity of influenza vaccination in healthy adult subjects by increasing seroconversion rates and seroprotection (39). The effectiveness of probiotics depends on the gut-lung axis, such as the cross-talk between the intestinal tube and the respiratory tract, mainly concerning the activation of the immune system (40). From a conceptual point of view, the existence of this gut-lung axis also allows us to understand how an oral immunomodulator can act on the airways (41). A microorganism taken orally, after coming into contact with the immunocompetent cells of the enteric mucosa, initiates a cascade of phenomena at this level which, also thanks to the bloodstream and lymphatic vessels, allows the passage of cells, mediators, and cytokines from one organ to another, thus also determining effects “at a distance”.

In the broad class of substances with presumed adjuvant activity on the immune system, bacterial lysates are the most commonly used in daily practice (41). Different mixtures of purified bacterial antigens, derived from various inactivated pathogens, are available in the market. The antigens are obtained by chemical or mechanical lysis, after which the extract is lyophilized to be stored for a long time. In this context, OM-85 has been deeply investigated.

OM-85 is obtained by the chemical lysis of a series of common Gram-positive and Gram-negative respiratory pathogens (42). The list of pathogens contained in OM-85, therefore, includes extracts of *Branhamella catarrhalis*, *Klebsiella pneumoniae*, *Klebsiella ozaenae*, *Streptococcus pneumoniae*, *Streptococcus pyogenes*, *Streptococcus viridans*, and *Staphylococcus aureus*. All these pathogens are suitably inactivated and purified. The lyophilized extract is administered orally and contains proteins, peptides, and traces of sugars, fatty acids, lipoiteic acids, and inactivated lipopolysaccharides (43). The pediatric formulation of OM-85 contains 3.5 mg of bacterial extracts, while the adult formulation contains 7 mg.

OM-85: mechanism of action

OM-85 has a multifaceted and complex mechanism of action (Fig. 1) that can play an important role in preventing recurrent bacterial and viral respiratory infections in the pediatric and adult populations and elderly subjects. OM-85 activates both the innate and adaptive immune responses through the gut-lung axis (41, 42). In detail, OM-85 induces an upregulation of the antiviral cytokine interferon-gamma (IFN-γ), associated with the type 1 immune response and, at the same time, a downregulation of type 2 cytokines, including IL-4, IL-5, and IL-13, produced by specific Th2 cells. This rebalancing of the immunological response also leads to a reduction in IgE levels in allergic subjects, as documented by several studies (44-51).

OM-85 induces the homing of immune cells in the so-called bronchus-associated lymphoid tissue (BALT) and their subsequent activation against viral and bacterial agents (44-46). OM-85 promotes interferon-α and interferon-β and has a dual effect on IL-1 (47). OM-85 reduces IL-1β during the inflammatory response, dampening the inflammation, whereas it induces IL-1β expression in the absence of inflammation, thus ensuring prompt immune response in case of need (48). OM-85 stimulates IL-6 and tumor necrosis factor-alpha (TNF-α) production, allowing a greater macrophage capacity to eliminate

invading bacteria (49, 50). OM-85 promotes the development of $CD4^+/CD25^+/Foxp3^+$ regulatory cells in the respiratory mucosa, exerting an anti-inflammatory activity and mitigating the airway hyperreactivity (51). OM-85 selectively induces nuclear transcription factor NF-κβ and mitogen-associated protein kinases (MAPKs) in dendritic cells, thus increasing the release of the chemokines involved in the migration of macrophages and neutrophils, and of cytokines activating B cells, such as IL-10 and TGF-β, which can control the excessive expression of the pro-inflammatory mediators involved in the tissue damage observed in COPD patients (47). OM-85 downregulates the expression of ICOSL (Inducible T Cell Co-stimulator Ligand), connected to the Th2-mediated immune response, thus diminishing allergic reaction (49, 52). In addition, OM-85 increases nitric oxide production (NO) with a consequent increase in ciliary beating, a crucial element of the physiological mucociliary clearance, which serves to eliminate all harmful agents from the mucous membranes (53). The NO-mediated antibacterial activity is a very intriguing issue. The NO receptors are highly represented in children and are involved in pathogen recognition mechanisms, thus triggering an immune response. These receptors are also involved in the recognition of taste which in turn is connected to the cough receptors. This scenario could open new interesting pathophysiological consequences.

Another intriguing aspect is the transplacental immune modulation; two animal studies, conducted

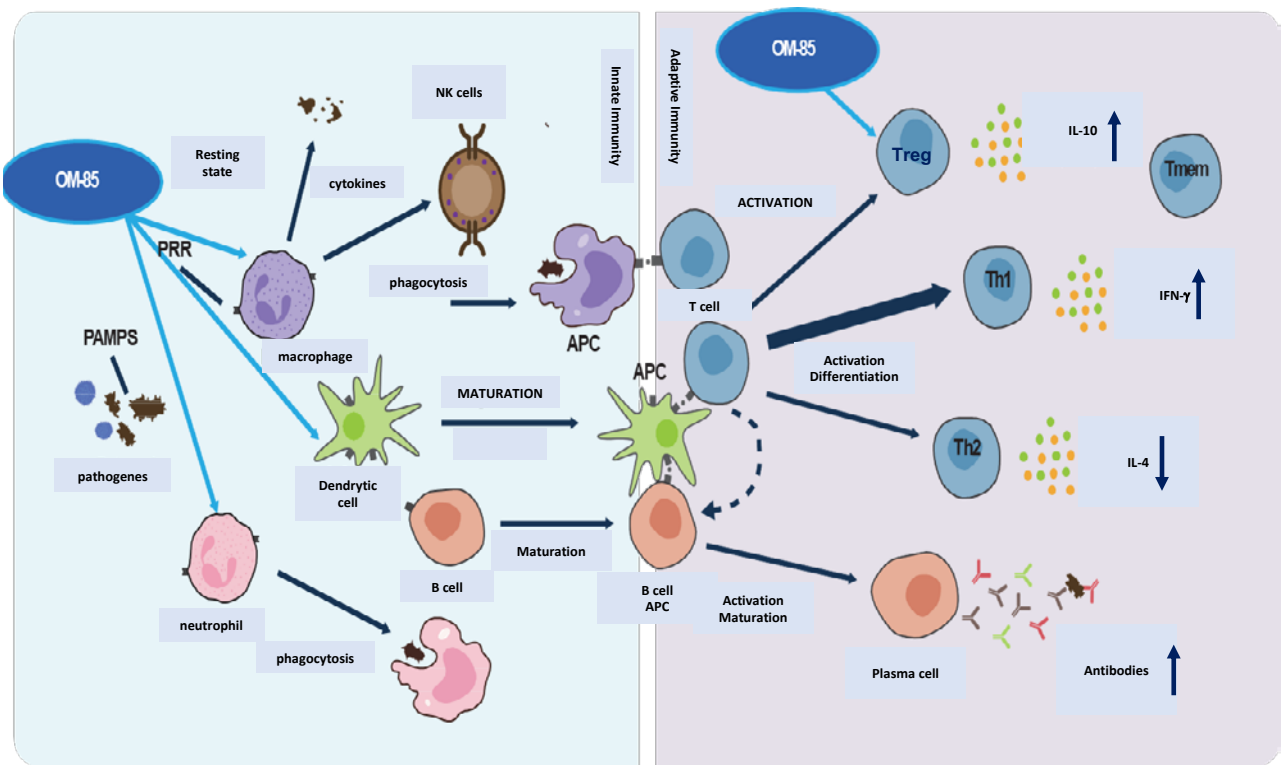


Fig. 1. *Schematic representation of the mechanism of action of OM-85 (Adapted from Scaglione, ref 45). Left panel: effect on innate immunity; Right panel: effect on acquired immunity. PAMPS: pathogen associated molecular patterns; PRR: pattern recognition receptors; NK: natural killer; APC: antigen presenting cell; Tmem: T memory cell; Th: T helper cells; Treg: T regulatory cell; IFN: interferon; IL: interleukin. OM-85 exerts direct effects (blue arrows) on macrophages, dendritic cells, and neutrophils. These cells send signals to NK cells, APC, B cells that activate maturation of APC and macrophages. These effects promote the specific immunity acting on T effector cells, including memory cells, and plasma cells. OM-85 stimulates (dotted arrow) T helper 1 to release of IFN-gamma, plasma cells to produce antibodies (mainly the A class), and T regulatory cells to release IL-10. OM-85 suppresses Th2 reducing IL-4 release.*

by the same research team, provided promising results. The first study demonstrated that OM-85, supplemented to pregnant mice, prevented the development of experimental allergic inflammation (54). Offspring presented an enhanced dendritic cell-dependent mechanism of respiratory surveillance function resulting in more efficient T regulatory activity, preventing induced allergic inflammation. Further study explored the pathways involved in the transplacental innate immunity training (55). OM-85 administration to the mother enhanced the offspring's XBP1-ERN1 signaling axis, fundamental for the survival and maturation of dendritic cells.

Post-viral bacterial co-infections are a common challenge in clinical practice, as a bacterial superinfection frequently occurs after acute viral respiratory infection. In this regard, OM-85 pretreatment in mice prevented *S pneumoniae* co-infection after experimental influenza (56). OM-85 induced a significant increase of $CD8^+$ cells that

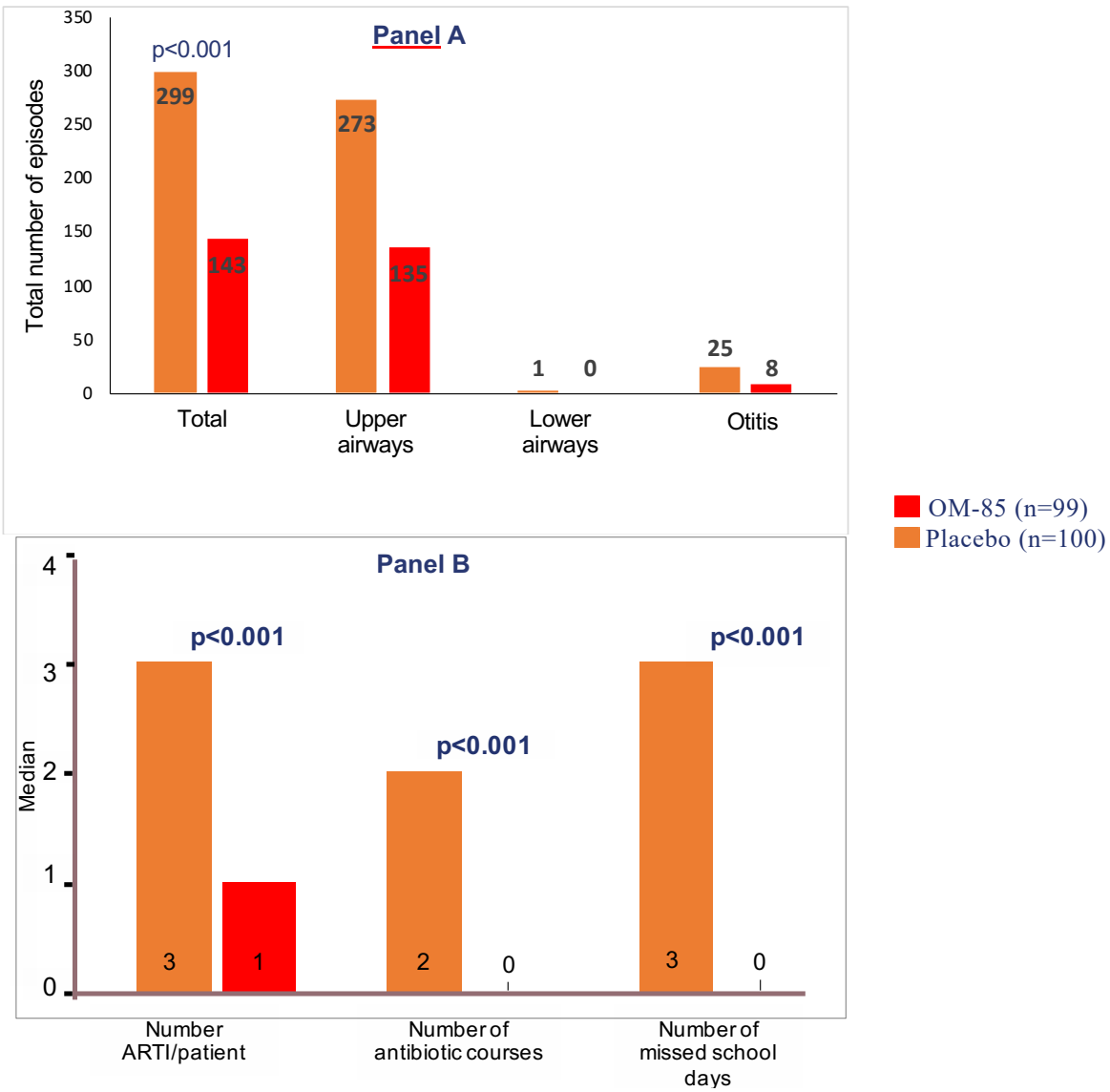


Fig. 2. *Rate of episodes of total acute respiratory infections according to type (Panel A), the median rate of episodes of infection per patient, the median number of days of antibiotic treatment, and median number of days of absence from school (Panel B) in female children of school age living with foster families, and treated with OM-85 or a placebo (Adapted from Jara-Pèrez, ref. 59).*

provided the reduced susceptibility to the secondary bacterial infection. These findings were supported by an *in vitro* study demonstrating that OM-85 pretreatment reduced the viral load and increased dendritic cell maturation and activation (57).

OM-85: clinical efficacy

The clinical development program of OM-85 has included more than 8,000 patients, of whom approximately 2,000 were enrolled in more than 40 randomized controlled clinical trials. These studies demonstrated that OM-85 reduced the number and duration of ARI and antibiotics use.

Evidence in childhood

One of the first studies involved 116 children over six months of age with recurrent respiratory infections (58). The study considered a three-month OM-85 treatment (3.5 mg/day) or placebo for ten days per month for three consecutive months, followed by a

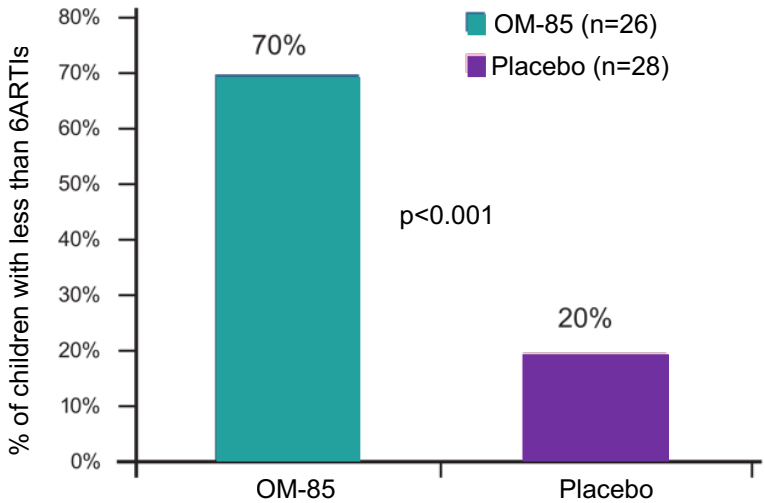


Fig. 3. *Percentage of patients experiencing fewer than 6 acute respiratory infections (RIs) over the 12-month study period of OM-85 treatment vs a placebo (Adapted from Gutiérrez-Tarango, ref. 60)*

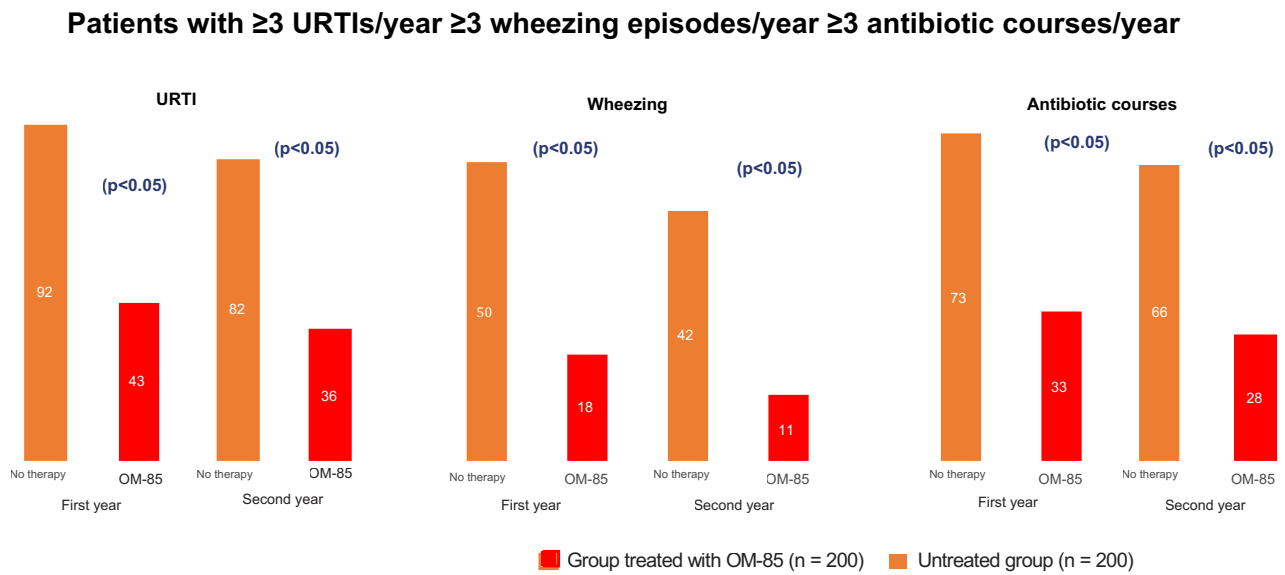


Fig. 4. *Percentage of patients with recurrent respiratory infections (RRIs (treated for two years with OM-85 or a placebo. (Adapted from Esposito, ref. 62).*

3-month follow-up (58). This study showed that OM-85 significantly ($p < 0.01$) prevented RI: 39.5% of the subjects taking OM-85 and 16.5% of subjects treated with placebo remained free from respiratory infections. Furthermore, 44% of children treated with OM-85 did not require antibiotic therapy as compared to 23.5% of the placebo group ($p < 0.05$). The differences were even more pronounced in the subgroup of children six years of age and younger [34% *vs* 3.5% for the absence of infections ($p < 0.01$) and 37% *vs* 10% for the need for antibiotics, respectively ($p < 0.05$)].

Jara-Pèrez and colleagues evaluated a population of 200 girls, between 6 and 13 years of age, living in an orphanage and with RRI (59). The OM-85-treated group (3.5 mg/day for ten days per month for three consecutive months, followed by three months of follow-up) had 143 episodes of ARI as compared to 299 infections observed in the placebo group ($p < 0.001$) at the end of the 6-month study. The median number of RI episodes per patient was 1 in the OM-85 group and 3 in the placebo group ($p < 0.001$). The study also showed statistically significant benefits in terms of the reduction in antibiotic prescriptions (2 in the placebo group *vs* 0 in the OM-85 group; $p < 0.001$), days with disease (19 in the placebo group *vs* 5 in the OM-85 group; $p < 0.001$), and days of school absence (3 in the placebo group *vs* 0 in the OM-85 group; $p < 0.001$), as shown in Fig. 2.

The study of Gutiérrez-Tarango included 54 children, 1 to 12 years of age, with a high number of respiratory infection recurrences in the 12 months preceding the start of the study: mean RRI = 12 (60). Over 12 months, the enrolled subjects received two cycles of OM-85 (3.5 mg) or placebo, both taken for ten days per month, for three consecutive months, with a first cycle at the start of the study and a second cycle after six months. The results showed that the median number of RIs per patient was 5.04 in the OM-85 group compared to 8 in the placebo group ($p < 0.001$). The proportion of patients experiencing less than six acute RI episodes during the study period was also significantly higher in the OM-85 group than the placebo group (70% *vs* 20%, respectively; $p < 0.001$), as shown in Fig. 3. Treatment with two courses of OM-85 also significantly reduced the number of days with the disease as compared to the placebo (35.23 days *vs* 60.75 days, respectively; $p < 0.001$) as well as the mean number of antibiotic courses (2.46 *vs* 4.46, respectively; $p < 0.001$).

A recent study enrolled 288 children, 1-6 years of age, with a history of RRIs (61). The children were treated with OM-85 (3.5 mg/day) or placebo for ten consecutive days per month for three months, after which the children were followed up for a further three months. The treatment started in October. The results demonstrated the effectiveness of OM-85 in reducing the number of RI. OM-85 treated children experienced less RI than placebo-treated ones (33% *vs* 65.1%, respectively; $p < 0.0001$). The percentage of patients with antibiotic prescriptions was also lower in the actively-treated group than the placebo group (25% *vs* 50.5%, respectively; $p = 0.0002$). In addition, the mean number of upper respiratory tract infections and acute otitis media, was approximately lower in the OM-85 group than in placebo group (0.33 ± 0.61 *vs* 0.65 ± 0.55, $p < 0.0001$, and 0.24 ± 0.41 *vs* 0.78 ± 0.73, $p = 0.006$, respectively). The sub-analysis of subjects with at least three episodes of upper respiratory tract RRI or acute otitis media showed a significant effect of OM-85 (21% with OM-85 *vs* 52% with placebo; $p < 0.05$). A further study, conducted by the same authors, investigated the long-term efficacy of OM-85 (62). The study lasted two years, during which OM-85 (3.5 mg/day) was administered for ten days per month for three consecutive months each year. The inclusion criterion was a clinical history of at least six episodes of RI/year. The subjects treated with OM-85 had significantly fewer respiratory infections, wheezing episodes, and antibiotic prescriptions than the control subjects ($p < 0.05$ for all parameters), as shown in Fig. 4. Furthermore, the proportion of children without infections during the study was significantly higher in the OM-85 group. Interestingly, there was no difference between the first and second years of treatment.

The same study group investigated the possible "adjuvant" effect of OM-85 on influenza vaccination (63). This randomized trial recruited 68 preschool children with RRI. The children must have received at least one dose of inactivated influenza vaccine. The study aimed to identify the correct timing

of the administration of OM-85, such as prior to vaccination or at the same time. In addition to vaccination, a group of children also took a course of OM-85 (3.5 mg/day for ten days per month for three consecutive months). Children treated with OM-85 had a significant reduction of RI episodes and antibiotic courses compared to the group of subjects who received only the inactivated influenza vaccine ($p < 0.05$ for both).

Razi and colleagues evaluated the post-viral wheezing in 75 preschool children with RRI (64). This randomized, placebo-controlled study demonstrated that a course of OM-85 (3.5 mg/day for ten days per month for three consecutive months) reduced both RI and wheezing episodes by 38% in 12 months. The mean cumulative frequency of wheezing episodes was also statistically lower in OM-85-treated children than a placebo (-22.4 days/year; $p < 0.001$), as reported in Fig. 5.

There is evidence that OM-85 is effective even in infants at risk of respiratory infections. A randomized placebo-controlled study recruited 59 infants (3 to 9 months of age); the primary endpoint was the development of severe respiratory tract infections (65). The study, despite being undersized, documented the OM-85 safety in infants and demonstrated a reduction of respiratory infections.

Another interesting application of the OM-85 prophylaxis could be the recurrent tonsillitis model. Children suffering from recurrent tonsillitis undergo tonsillectomy surgery, exposing them to the risks and costs associated with this invasive procedure. In this regard, a long-term retrospective observational study collected 5-year data from a population of 131 children (1 to 15 years of age) with recurrent tonsillitis (66). OM-85 (3.5 mg/day) was prescribed ten days per month for three consecutive months. The results documented either a total (defined as a > 50% reduction in acute tonsillitis episodes) or partial (i.e., a ≤ 50% reduction) response in 67 and 32 children, respectively. The total or partial response resulted in a significant reduction in tonsillectomy: none of the 67 patients with total response underwent tonsillectomy, while only 4 of the 32 patients with a partial response required tonsillectomy. A clinical report concerned a child with pulmonary arterial sling presenting as pneumonia by inhalation of a foreign body, the child was successfully treated

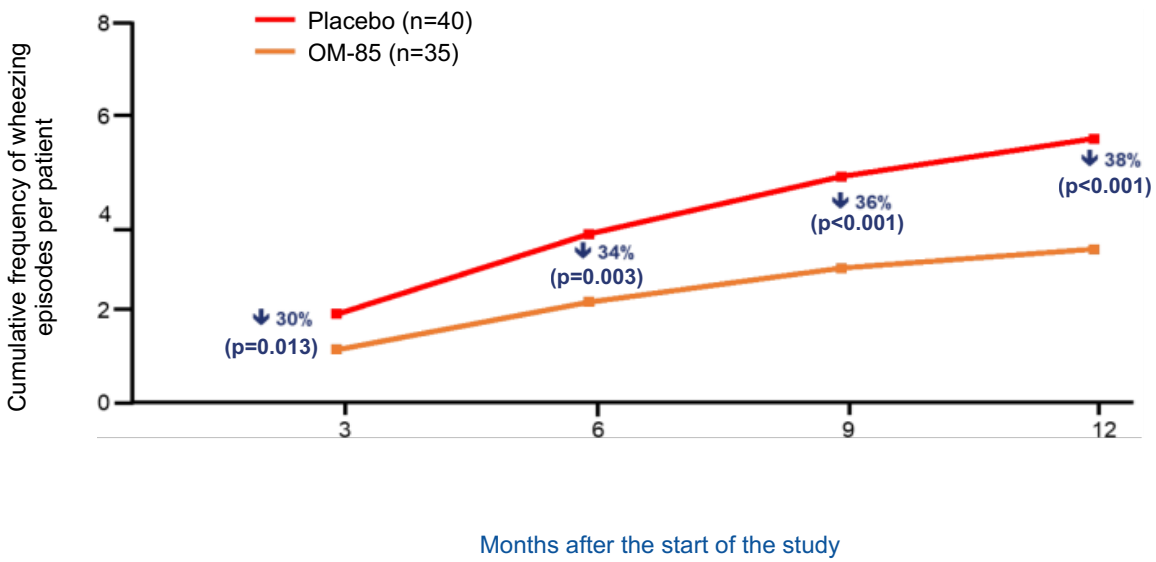


Fig. 5. *Benefits of OM-85 on the average cumulative frequency of wheezing episodes (Adapted from Razi, ref. 64).*

with a preventive 3-month OM-85 course (67). On the contrary, a pilot study showed that OM-85 did not prevent respiratory infections in 54 children (six months to five years old) with no past history of RRI attending a daycare center in Brazil (68). However, the study had some limitations, including the small size, uncertainty about treatment adherence, and the lack of the identification of risk factors associated with the explored outcomes. Moreover, some narrative reviews and meta-analyses have confirmed the efficacy and safety of OM-85 in childhood. A meta-analysis selected eight randomized, placebo-controlled studies which evaluated the impact of 1 or 2 courses of OM-85 on preventing respiratory infections in children (69). The duration of the studies lasted up to 12 months. Globally, 851 children (between 1 month and 12 years of age, mean age six years) with at least three infectious episodes in the six months preceding each study were evaluated. This meta-analysis documented a significant difference in the onset of respiratory infections between the children treated with OM-85 and the children treated with placebo. Only 32% of the children treated with OM-85 developed an RI compared with 58.2% of the children in the placebo group ($p < 0.001$). There was also a 35.5% reduction in the mean total number of acute RI compared to a placebo. A further meta-analysis confirmed the OM-85 preventive effect of RI (70). This meta-analysis included 35 studies, nine placebo-controlled and 4 with high methodological quality. The analysis included 437 children treated with OM-85 and 415 children treated with placebo. The OM-85-treated group reported a 35.9% reduction of RI episodes compared to the control group; in absolute terms, the children treated with OM-85 developed 1.12 RI less than the children treated with placebo. Another meta-analysis examined 53 studies concerning 1 or 2 OM-85 cycles and compared with placebo; the observation time lasted up to 12 months (71). A total of 4,851 patients up to 16 years of age were analyzed. This meta-analysis documented a 52% reduction in acute RI episodes (on average 2.33 episodes less), a 42% reduction in the duration of the antibiotic therapy (on average 4.1 days shorter), a 45% reduction in the duration of infection (on average 3.13 days less), and a 49% reduction in fever (2.91 days less with fever). A recent review pointed out the preventive effect

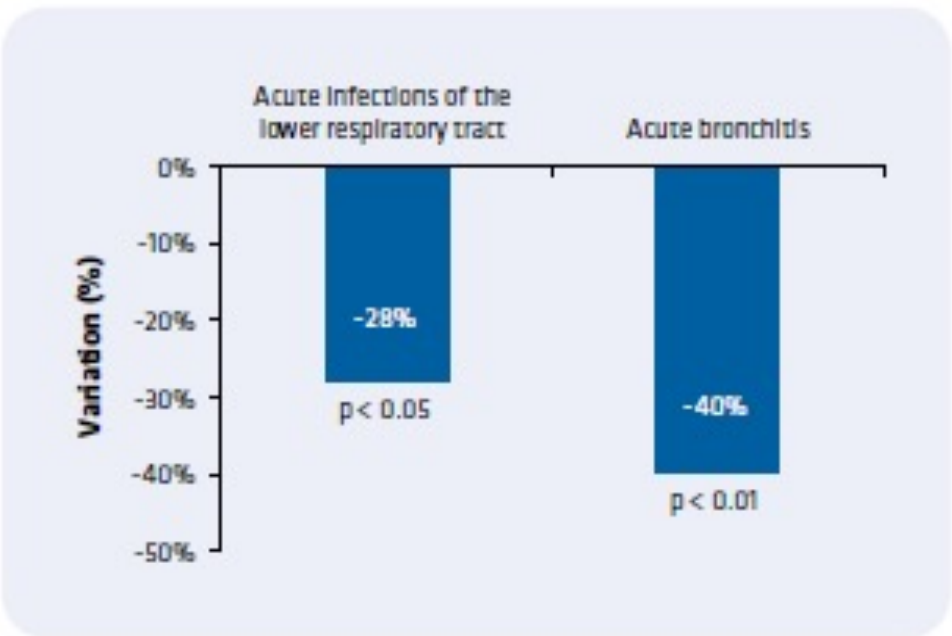


Fig. 6. *Frequency of lower respiratory tract infections with OM-85 vs placebo in elderly adults with chronic bronchitis (Adapted from Orcel, ref. 77).*

of OM-85 in respiratory infections in childhood (72). Consistently, a pharmacoeconomic study has shown that the use of OM-85 was characterized by a favorable cost/benefit ratio (73). The study estimated a saving of approximately $85 regarding the cost of each IR episode when using OM-85 as compared to standard care. The cost reduction considered both direct and indirect costs, as well as the reduced use of antibiotics and days of work lost by parents to care for the ill child (73).

Cardinale and colleagues underlined the OM-85 effectiveness in modulating the *in vivo* immune response against different pathogens, including influenza and respiratory syncytial virus; OM-85 also reduced the wheezing rate and attack duration in wheezing-prone children (74).

An expert consensus from the World Association of Infectious Diseases and Immunological Disorders summarized the characteristics of OM-85, underlining its limitation consisting in the absence of biomarkers predicting the best responder profile in the context of the precision medicine (75). The expert consensus stated that OM-85 should be recommended for preventing respiratory recurrence in RRI-prone children ($\geq$ 6 months old). A very recent meta-analysis evaluated 14 studies including 1,859 children, 890 treated with OM-85 (76). The results showed that OM-85 use was significantly related to lower frequency of respiratory tract infections ($p< .001$), lower total duration of respiratory tract infections ($p< .001$), lower incidence of respiratory tract infections (OR 0.40; p .006), lower number of antibiotic courses ($p= .03$), and lower antibiotic use (OR 0.38; $p< .001$). Moreover, OM-85 use was not significantly related to adverse event rate (OR 1.02; $p= 0.94$) or to wheezing attack frequency ($p= 0.14$). The authors concluded that OM-85 is recommended for children with high risk of RRI.

Evidence in adulthood

Several experimental and observational studies evaluated the role of OM-85 in reducing the care burden, clinical severity, and costs of respiratory diseases in adult patients. In particular, the study model was mainly represented by COPD and/or chronic bronchitis, evaluated by randomized, double-blind, placebo-controlled trials.

A historic study involved 354 elderly institutionalized patients with chronic bronchitis who had had more than four episodes of lower RI in the six months prior to enrollment (77). The patients were followed-up for six months, including three months of treatment with OM-85 (7 mg/day) or placebo, for ten days per month for three consecutive months, followed by a 3-month follow-up. This study demonstrated a significant ($p<0.05$) reduction in the number of lower respiratory tract infections in patients treated with OM-85 (112 events in 147 patients) as compared to the placebo group (156 events in 143 patients). The OM-85 treatment affected acute bronchitis episodes but not pneumonia. Furthermore, the number of antibiotic prescriptions was also 28% lower in the OM-85 group than the placebo group ($p <0.05$), as shown in Fig. 6.

Another randomized, double-blind, placebo-controlled, 6-month study enrolled 381 long-term heavy smokers or former smokers with severe COPD (78). The purpose of the study was to evaluate the efficacy of OM-85 in preventing COPD exacerbations. Patients received OM-85 (7mg/day) or placebo for 30 days the first month, followed by ten days per month from the 3rd to the 5th month). The frequency of exacerbations was similar between the two groups (44.5% *vs* 43.7%, respectively), but the number of hospitalization days for respiratory disease was 55% lower in the OM-85 group (287 days) as compared to the placebo group (642 days), as shown in Fig. 7. In addition, the number of hospitalizations was also decreased by the OM-85 prophylaxis, but not by placebo (44 *vs* 57 hospitalizations, respectively). Finally, the mean days of hospitalization for respiratory problems were significantly lower in the OM-85 group (1.5 days) than in the placebo group (3.4 days).

The effectiveness of OM-85 was more evident in smokers, as documented by a multicentric, randomized, double-blind, placebo-controlled study that involved 273 patients with a recent history of chronic bronchitis or mild COPD (79). The patients were randomized to receive treatment with OM-85 (7 mg/day) or placebo for 30 consecutive days in the first month and ten days per month from the 3rd to the 5th month. At the end of the treatment, the frequency

of respiratory infections was 29% lower in subjects treated with OM-85 than in the placebo group (0.61 *vs* 0.86, respectively; p = 0.03). This outcome was even more relevant in the subpopulation of smokers and former smokers: the mean cumulative frequency of exacerbations was approximately 40% lower in the OM-85 group than the placebo group (0.62 exacerbations with OM-85 and 1.04 with placebo; p <0.01). Another multicentric, randomized, double-blind, placebo-controlled study, lasting five and a half months, enrolled 428 patients with chronic bronchitis or COPD (80). The patients took OM-85 (7 mg/day) or placebo for ten days/month for three consecutive months. The percentage of smokers or former smokers was very high (approximately 60%). The study evaluated the proportion of patients with exacerbations. The OM-85 group had a more significant reduction than the placebo group (-10%) after the end of treatment at 12 weeks (23.4% for OM-85 *vs* 33.3% for the placebo; p = 0.03). This trend in favor of OM-85 was maintained in the follow-up period (32.8% in the OM-85 group *vs* 38.0% in the placebo group; p = 0.277).

Some studies were also performed in clinical practice (the so-called real-life studies). A 12-month study involved 84 patients with chronic respiratory disease and RRIs; 29 had allergic rhinitis, 28 asthma, and 27 COPD (81). During the first nine months, the patients received standard therapy for COPD. Later, the standard therapy was associated with OM-85 add-on treatment (7 mg/day for ten consecutive days per month for three months), then, a 6-month follow-up ensued. The RI frequency decreased from 69 episodes to 38 (p<0.05), and exacerbations decreased by 36%. This study also demonstrated an increase in serum and secretory IgA levels. Another 130 patients with acquired immunodeficiency (HIV) and RRI were investigated in a single-center, observational, retrospective study lasting six years (82). The patients were stratified into various subgroups: patients with COPD and/or sinusitis (n = 42), recurrent sinusitis (n = 21), recurrent otitis media (n = 5), and smokers (n = 62). The number of respiratory infections, antibiotic use, and antibiotic cost before (2005-2006) and after (2008-2011) preventive treatment with OM-85 was compared longitudinally. The RI

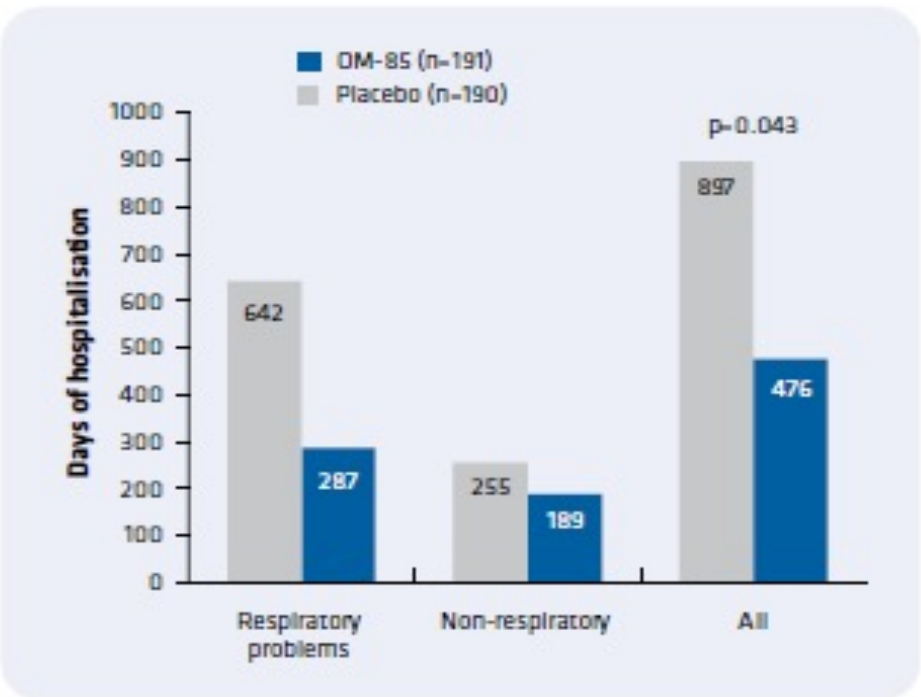


Fig. 7. *Impact of OM-85 on the reduction of hospitalizations in subjects with COPD (Adapted from Collet, ref. 78).*

frequency had decreased in all the subgroups. This finding was even more pronounced in COPD and/or sinusitis patients and smokers. There was also a reduction in the use of antibiotics.

Very recently, Gao and colleagues evaluated the preventive effect of a 3-month OM-85 treatment, compared to placebo, in patients with bronchiectasis (83). There was no significant difference between treatments concerning the number of exacerbations and the time to the first pulmonary exacerbation. However, the safety profile of OM-85 was good and the majority of adverse events was mild in both arms.

Safety of OM-85

OM-85 has been shown to have a particularly favorable safety profile, similar to that observed in patients treated with a placebo in both pediatric and adult studies. The Schaad's systematic review showed that OM-85 had a rate of adverse events similar to placebo (63). Specifically, minor adverse events were observed in 17.7% of patients treated with OM-85 compared with 18.2% of placebo patients. Serious adverse events were reported in 1% of subjects treated with OM-85 and 0.5% of patients taking placebo. The withdrawal rate from clinical trials for adverse events was 1.3% in the active treatment groups and 0.7% in the placebo groups. The most common minor adverse events were nausea, abdominal pain, and common cold. Nevertheless, it has to be noted that no causal relationship has been established between the adverse events observed and the use of OM-85 in the various studies considered (72).

OM-85 was also well tolerated by the various patient subpopulations, including patients with autoimmune nephrotic syndrome (84), HIV (81), COPD (78, 79), and chronic bronchitis (77-79). Furthermore, OM-85 was well tolerated even when administered in combination with a vaccine, as it did not interfere with seroconversion, seroprotection, and B memory cells (63).

CONCLUSIONS

The management of respiratory infections represents an ongoing challenge in clinical practice. Respiratory infections also represent a significant burden for the patients and society. Children and older people have a defective immune response, and aging is frequently associated with comorbidities. As a result, these age classes have a sustained susceptibility to respiratory infections and a reduced response to vaccinations. Therefore, the use of immunomodulating agents could be a valuable strategy to prevent RI and enhance the response to vaccines. This concept may be even more cogent in the era of the COVID-19 pandemic. In this regard, OM-85 may claim to have relevant evidence concerning the mechanism of action, clinical effectiveness, safety, and tolerability, documented by methodologically rigorous studies.

OM-85 can enhance the natural and acquired immune responses through a multifaceted mechanism of action. OM-85 can represent a preventive strategy in RI management, especially in frail subjects, such as children, including infants, older people, smokers, and subjects with immunodeficiency.

Robust evidence has shown that OM-85 can prevent recurrent respiratory infections, reduce the number of COPD exacerbations, and shorten disease duration at home or in the hospital. In addition, OM-85 can enhance the effectiveness of the flu vaccination without affecting vaccine tolerability. Finally, the preventive use of OM-85 can reduce the use of antibiotics, contributing to contrasting the antibiotic resistance and saving the high cost of chronic respiratory diseases. Further studies should identify the profile of the ideal candidate to OM-85, using specific biomarkers in the context of the precision and personalized medicine.

CONFLICT OF INTEREST: The paper was finalized with the unconditioned contribution from Angelini Pharma, Rome, Italy. The authors do not have any conflicts of interest related to the present paper.

REFERENCES

1. GBD 2015 LRI Collaborators. Estimates of the global, regional, and national morbidity, mortality, and aetiologies of lower respiratory tract infections in 195 countries: a systematical analysis for the Global Burden of Disease Study 2015. Lancet Infect

Dis 2017; 17:1133-61.
2. Jain N, Lodha R, Kabra SK. Upper respiratory tract infections. Indian J Pediatr 2001; 68:1135-8.
3. Grief SN. Upper respiratory infections. Prim Care 2013; 40(3):757-70.
4. Moellering RC Jr. The continuing challenge of lower respiratory tract infections. Clin Infect Dis 2002; 34(Suppl 1):S1-3.
5. Adams PF, Hendershot GE, Marano MA. Current estimates from the National Health Interview Survey. Vital Health Stat 1999; 10:1996.
6. Ferkol T, Schraufnagel D. The global burden of respiratory disease. Ann Am Thorac Soc 2014; 11(3):404-6.
7. https://www.who.int/docs/default-source/gho-documents/world-health-statistic-reports/6-june-18108-world-health-statistics-2018.pdf Last access May 2021.
8. de Martino M, Ballotti S. The child with recurrent respiratory infections: normal or not? Pediatr Allergy Immunol 2007; 18 Suppl 18:13-18.
9. Heikkinen T, Järvinen A. The common cold. Lancet 2003; 361(9351):51-59.
10. Hay AD, Heron J, Ness AALSPAC study team. The prevalence of symptoms and consultations in pre-school children in the Avon Longitudinal Study of Parents and Children (ALSPAC): a prospective cohort study. Fam Pract 2005; 22:367-74.
11. Negewo NA, Gibson PG, McDonald VM. COPD and its comorbidities. Respirology 2015; 20:1160-71.
12. Poh TY, Mac Aogáin M, Chan AK, et al. Understanding COPD-overlap syndromes. Expert Rev Respir Med 2017; 11(4):285-98.
13. Mannino DM, Kiriz VA. Changing the burden of COPD mortality. Int J Chron Obstruct Pulmon Dis 2006; 1(3):219-33.
14. Lopez AD, Shibuya K, Rao C, et al. Chronic obstructive pulmonary disease: current burden and future projections. Eur Respir J 2006; 27:397-412.
15. ISTAT. Stime per l'anno 2018. Indicatori Demografici. https://www.istat.it/it/files/2019/02/Report-Stime-indicatori-demografici.pdf.
16. Cherniak, NS. Chronic Obstructive Pulmonary Disease. W. B. Saunders, Philadelphia; 1991.
17. Elliott SP, Ray CG. Viral infections of the lower respiratory tract. Pediatric Respiratory Medicine 2008; 481-9. doi: 10.1016/B978-032304048-8.50037-2.
18. Schaad U B, Esposito S, Razi C H. Diagnosis and Management of Recurrent Respiratory Tract Infections in Children: A Practical Guide. Arch Pediatr Infect Dis 2016; 4(1):e31039.
19. Zhou MY, Xie XL, Peng YG, et al. From SARS to COVID-19: What we have learned about children infected with COVID-19. Int J Infect Dis 2020; 96:710-14.
20. Sviriaeva EN, Korneev KV, Drutskaya MS, Kuprash DV. Mechanisms of changes in immune response during bacterial coinfections of the respiratory tract. Biochemistry (Mosc) 2016; 81(11):1340-9.
21. Meyer KC. The role of immunity and inflammation in lung senescence and susceptibility to infection in the elderly. Semin Respir Crit Care Med 2010; 31(5):561-74
22. Grigg J, Riedler J, Robertson CF, Boyle W, Uren S. Alveolar macrophage immaturity in infants and young children. Eur Respir J 1999; 14(5):1198-205.
23. Karevold G, Kvestad E, Nafstad P, Kvaerner KJ. Respiratory infections in schoolchildren: co-morbidity and risk factors. Arch Dis Child 2006; 91:391-98.
24. Forssel G, Hakansson A, Mansson NO. Risk factors for respiratory tract infections in children aged 2–5 years. Scand J Prim Health Care 2001: 19:122–5.
25. Brims F, Chauhan AJ. Air quality, tobacco smoke, urban crowding and day care: modern menaces and their effects on health. Pediatr Infect Dis J 2005: 24:152–6.
26. Shaw AC, Goldstein DR, Montgomery RR. Age-dependent dysregulation of innate immunity. Nat Rev Immunol 2013; 13(12):875-87.
27. Valiathan R, Ashman M, Asthana D. Effects of ageing on the immune system: infants to elderly. Scand J Immunol 2016; 83(4):255-66.
28. Boren E, Gershwin ME. Inflamm-aging: autoimmunity, and the immune-risk phenotype. Autoimmun Rev 2004; 3(5):401-6.
29. Zetts RM, Stoesz A, Smith BA, Hyun DY. Outpatient antibiotic use and the need for increased antibiotic stewardship efforts. Pediatrics 2018; 141(6):e20174124.
30. King LM, Fleming-Dutra KE, Hicks LA. Advances in optimizing the prescription of antibiotics in outpatient settings. BMJ 2018; 363:k3047.
31. Chiappini E, Mazzantini R, Bruzzese E, et al. Rational

use of antibiotics for the management of children's respiratory tract infections in the ambulatory setting: an evidence-based consensus by the Italian Society of Preventive and Social Pediatrics. Paediatr Respir Rev 2014; 15(3):231-6.
32. Guitor AK, Wright GD. Antimicrobial resistance and respiratory infections. Chest 2018; 154(5):1202-12.
33. http://www.salute.gov.it/portale/news/p3_2_1_1_1.jsp?menu=notizie&id=4859
34. Saso A, Kampmann B. Vaccine responses in newborns. Semin Immunopathol 2017; 39(6):627642.
35. Buchy P, Badur S. Who and when to vaccinate against influenza. Int J Infect Dis 2020; 93:375-87.
36. Pera A, Campos C, López N, et al. Immunosenescence: implications for response to infection and vaccination in older people. Maturitas 2015; 82(1):50-5.
37. Palache A, Oriol-Mathieu V, Abelin A, Music T, and Influenza Vaccine Supply task force (IFPMA IVS). Seasonal influenza vaccine dose distribution in 157 countries (2004-2011). Vaccine 2014; 32(48):6369-76.
38. Brydak LB, Machała M, Myśliwska J, Myśliwski A, Trzonkowski P. Immune response to influenza vaccination in an elderly population. J Clin Immunol 2003; 23(3):214-22.
39. Lei WT, Shih PC, Liu SJ, Lin CY, Yeh TL. Effect of probiotics and prebiotics on immune response to influenza vaccination in adults: a systematic review and meta-analysis of randomized controlled trials. Nutrients 2017; 9(11):1175.
40. Marsland BJ, Trompette A, Gollwitzer ES. The gut-lung axis in respiratory disease. Ann Am Thorac Soc 2015; 12 (Suppl 2):S150–S156.
41. Esposito S, Soto-Martinez ME, Feleszko W, Jones MH, Shen KL, Schaad UB. Nonspecific immunomodulators for recurrent respiratory tract infections, wheezing and asthma in children: a systematic review of mechanistic and clinical evidence. Curr Opin Allergy Clin Immunol 2018; 18(3)198-209.
42. Scaglione F. Meccanismo d'azione ed efficacia di OM-85 nella prevenzione delle infezioni respiratorie. Farmaci 2017; 16:1.
43. Suárez N, Ferrara F, Rial A, Dee V, Chabalgoity JA. Bacterial lysates as immunotherapies for respiratory infections: methods of preparation. Front Bioeng Biotechnol 2020; 8:545
44. Parola C, Salogni L, Vaira X, et al. Selective activation of human dendritic cells by OM-85 through a NF-kB and MAPK dependent pathway. PLoS One 2013; 8:e82867.
45. Rozy A, Chorostowska-Wynimko J. Bacterial immunostimulants—mechanism of action and clinical application in respiratory diseases. Pneumonol Alergol Pol 2008; 76:353–9.
46. Kearney SC, Dziekiewicz M, Feleszko W. Immunoregulatory and immunostimulatory responses of bacterial lysates in respiratory infections and asthma. Ann Allergy Asthma Immunol 2015; 114:364–9.
47. Rossi GA, Esposito S, Feleszko W, et al. Immunomodulation therapy – clinical relevance of bacterial lysates OM-85. Eur Respir Pulm Dis 2019; 15(1):17–23.
48. Dang AT, Pasquali C, Ludigs K, et al. OM-85 is an immunomodulator of interferon-beta production and inflammasome activity. Sci Rep 2017; 7:43844.
49. Huber M, Mossmann H, Bessler WG. Th1-orientated immunological properties of the bacterial extract OM-85-BV. Eur J Med Res 2005; 10(5):209-17.
50. Luan H, Zhang Q, Wang L, et al. OM85-BV induced the productions of IL-1beta, IL-6, and TNF-alpha via TLR4- and TLR2-mediated ERK1/2/NF-kappaB pathway in RAW264.7 cells. J Interferon Cytokine Res 2014; 34:526-36.
51. Strickland DH, Judd S, Thomas JA, et al. Boosting airway T-regulatory cells by gastrointestinal stimulation as a strategy for asthma control. Mucosal Immunol 2011; 4:43-52.
52. Pasquali C, Salami O, Taneja M, et al. Enhanced mucosal antibody production and protection against respiratory infections following an orally administered bacterial extract. Front Med (Lausanne) 2014; 1:41.
53. Triantafillou V, Workman AD, Patel NN, et al. Broncho-Vaxom® (OM-85 BV) soluble components stimulate sinonasal innate immunity. Int Forum Allergy Rhinol 2019; 9(4):370-7.
54. Mincham KT, Scott NM, Lauzon-Joset JF, et al. Transplacental immune modulation with a bacterial-derived agent protects against allergic airway inflammation. J Clin Invest 2018; 128:4856-69.
55. Mincham KT, Jones AC, Bodinier M, et al. Transplacental innate immune training via maternal

microbial exposure: role of. XBP1-ERN-1 axis in dendritic cell precursor programming. Front Immunol 2020; 11:601494.
56. Rossi GA, Bessler W, Ballarini S, Pasquali C. Evidence that a primary anti-viral stimulation of the immune response by OM-85 reduces susceptibility to a secondary respiratory bacterial infection in mice. It J Pediatr 2018; 44:112.
57. Roth M, Khameneh HJ, Fang L, et al. Distinct antiviral porperties of two different bacterial lysates. Can Respir J 2021; 2021:8826645.
58. Paupe J. Immunotherapy with an oral bacterial extract (OM-85 BV) for upper respiratory infections. Respiration 1991; 58(3-4):150-4.
59. Jara-Pérez JV, Berber A. Primary prevention of acute respiratory tract infections in children using a bacterial immunostimulant: a double-masked, placebo-controlled clinical trial. Clin Ther 2000; 22(6):748-59.
60. Gutiérrez-Tarango MD, Berber A. Safety and efficacy of two courses of OM-85 BV in the prevention of respiratory tract infections in children during 12 months. Chest 2001; 119(6):1742-8.
61. Esposito S, Bianchini S, Bosis S, et al. A randomized, placebo-controlled, double-blinded, single-centre, phase IV trial to assess the efficacy and safety of OM-85 in children suffering from recurrent respiratory tract infections. J Transl Med 2019; 17(1):284.
62. Esposito S, Bianchini S, Polinori I, Principi N. Impact of OM-85 given during two consecutive years to children with a history of recurrent respiratory tract infections: a retrospective study. Int J Environ Res Public Health 2019; 16(6):1065.
63. Esposito S, Marchisio P, Prada E, et al. Impact of a mixed bacterial lysate (OM-85 BV) on the immunogenicity, safety and tolerability of inactivated influenza vaccine in children with recurrent respiratory tract infection. Vaccine 2014; 32(22):2546-52.
64. Razi CH, Harmancı K, Abacı A, et al. The immunostimulant OM-85 BV prevents wheezing attacks in preschool children. J Allergy Clin Immunol 2010; 126(4):763-9.
65. Sly PD, Galbraith S, Islam Z, Holt B, Troy N, Holt PG. Primary prevention of severe lower respiratory illnesses in at-risk infants using the immunomodulator OM-85. J Allergy Clin Immunol 2019; 144(3):870-.2
66. Bitar MA, Saade R. The role of OM-85 BV (Broncho-Vaxom) in preventing recurrent acute tonsillitis in children. Int J Pediatr Otorhinolaryngol 2013; 77(5):670-3.
67. Luo S, Rao H. Pulmonary artery sling presenting as pneumonia and inhalation of a foreign body. Case Rep Infect Dis 2019; 8912136.
68. Souza FC, Mocellin M, Ongaratto R, et al. OM-85 BV for primary prevention of recurrent airway infections: a pilot randomized, double-blind, placebo-controlled study. Einstein (Sao Paulo) 2020; 18:eAO5262.
69. Schaad UB. OM-85 BV, an immunostimulant in pediatric recurrent respiratory tract infections: a systematic review. World J Pediatr 2010; 6(1):5-12.
70. Berber A, Del-Rio-Navarro BE. Cost-effectiveness analysis of OM-85 vs placebo in the prevention of acute respiratory tract infections (ARTIs) in children that attend day-care centers. Health Econ Rev 2019; 9(1):12.
71. Yin J, Xu B, Zeng X, Shen K. Broncho-Vaxom in pediatric recurrent respiratory tract infections: a systematic review and meta-analysis. Int Immunopharmacol 2018; 54:198-209.
72. Marengo R, Ortega Martell JA, Esposito S. Paediatric Recurrent ear, nose and throat infections and complications: can we do more? Infect Dis Ther 2020; 9(3):697-700.
73. Del-Rio-Navarro BE. Cost-effectiveness analysis of OM-85 vs placebo in the prevention of acute respiratory tract infections (ARTIs) in children that attend day-care centers. Health Econ Rev 2019; 9(1):12.
74. Cardinale F, Lombardi E, Rossi O, et al. Epithelial dysfunction, respiratory infections and asthma: the importance of immunomodulation. A focus on OM-85. Expert Rev Respir Med 2020; 14(10):1019-26.
75. Esposito S, Jones MH, Feleszko W, et al. Prevention of new respiratory episodes in children with recurrent respiratory infections: an expert consensus statement. Microorganisms 2020; 8(11):1810.
76. Cao C, Wang J, Li Y, et al. Efficacy and safety of OM-85 in paediatric recurrent respiratory tract infections which could have a possible protective effect on COVID-19 pandemic: A meta-analysis. Int J Clin Pract 2021; 75(5):e13981.
77. Orcel B, Delclaux B, Baud M, Derenne JP. Oral immunization with bacterial extracts for protection

against acute bronchitis in elderly institutionalized patients with chronic bronchitis. Eur Respir J 1994; 7(3):446-52.

78. Collet JP, Shapiro P, Ernst P, Renzi T, Ducruet T, Robinson A. Effects of an immunostimulating agent on acute exacerbations and hospitalizations in patients with chronic obstructive pulmonary disease. The PARI-IS Study Steering Committee and Research Group. Prevention of Acute Respiratory Infection by an Immunostimulant. Am J Respir Crit Care Med 1997; 156(6):1719-24.
79. Solèr M, Mütterlein R, Cozma G; Swiss-German OM-85 Study Group. Double-blind study of OM-85 in patients with chronic bronchitis or mild chronic obstructive pulmonary disease. Respiration 2007; 74(1):26-32.
80. Tang H, Fang Z, Saborío GP, Xiu Q. Efficacy and safety of OM-85 in patients with chronic bronchitis and/or chronic obstructive pulmonary disease. Lung 2015; 193(4):513-19.
81. Koatz AM, Coe NA, Cicerán A, Alter AJ. Clinical and immunological benefits of OM-85 bacterial lysate in patients with allergic rhinitis, asthma, and COPD and recurrent respiratory infections. Lung 2016; 194(4):687-97.
82. Capetti A, Cossu MV, Carenzi L, Rizzardini G. Four years of immunization with OM-85 BV to prevent respiratory infections in HIV+ patients. Hum Vaccin Immunother 2013; 9(9):1849-51.
83. Gao J, Li L, Jiang N, et al. Effect of OM-85 BV on reducing bronchiectasis exacerbation in Chinese patients: the iPROBE study. J Thor Dis 2021; 13:1641-51.
84. Zhang M, Luan H, Zhang Q, et al. Prevention of infection in immunosuppressive patients with autoimmune nephrosis by using an immunostimulating bacterial lysate Broncho-vaxom. Hum Vaccin Immunother 2012; 8(12):1802-7.

REVIEW

Phageome-based vaccination and human innate immune modulation could be a useful strategy to control human Coronavirus infections

M. Abaidullah[1], S. Peng[1], M. Kamran[2], X. Song[1], A. Ali Sher[3], Y. Chen[1], A. Rehman[4], L. Lin[1], R. Jia[5] and Z. Yin[1]

[1]Natural Medicine Research Center, College of Veterinary Medicine, Sichuan Agricultural University, Chengdu, China; [2]Queensland Alliance for Agriculture and Food Innovation, University of Queensland, Brisbane, Australia; [3]College of Veterinary Medicine, Michigan State University, East Lansing, Michigan, USA; [4]College of Veterinary and Animal Sciences, Jhang, Pakistan; [5]Key laboratory of Animal Disease and Human Health of Sichuan Province, Sichuan Agricultural University, Chengdu, China

Received October 12, 2020 – Accepted April 7, 2021

Human Coronavirus (CoV) infections, including SARS-COV, MERS-COV, and SARS-CoV-2, usually cause fatal lower and upper respiratory tract infections due to exacerbated expression of pro-inflammatory cytokines and chemokines. We aim to summarize different aspects, such as CoV immune evasion mechanisms and host innate immune response to these infections, and their role in pathogenesis. We have also elaborated the up-to-date findings on different vaccine development strategies and progress against CoVs in both humans and non-human models. Most importantly, we have described the Phageome-human immune interaction, its therapeutic usage as anti-viral, anti-inflammatory agent, and implications for multiple vaccine development systems. The data suggest that endogenous phages might play a vital role in eliminating the infection and regulating the body's immune system. Considering the innate-immune-induced pathogenesis against CoVs and the therapeutic aptitude of phageome, we propose that the prophylactic administration of phages and phage-based vaccines could be a useful strategy to control the emerging CoV infections

Public health is always challenged by emerging, re-emerging, and highly transmissible pathogens globally (1). It has been observed that enveloped RNA coronaviruses are distributed among birds, mammals, and humans, causing respiratory, hepatic, neurological, and enteric diseases (2, 3). Six known species of coronavirus cause human diseases. Four coronavirus strains, HKU1, 229E, NL63, and OC43, often cause cold symptoms in immunocompromised patients (4). The other two are zoonotic strains, Middle East Respiratory Syndrome Coronavirus (MERS-CoV) and Severe Acute Respiratory Syndrome Coronavirus (SARS-CoV) that sometimes produce fatal illnesses (5). During 2002 and 2003, outbreaks of a severe acute respiratory syndrome caused by SARS-CoV were reported in the Chinese province of Guangdong (6-8). Similarly, the first outbreaks of MERS, another severe respiratory disease, were reported in the Middle Eastern countries in 2012 (9). SARS-CoV caused around 8,422 cases and 916

Key words; cytokines; chemokines; pathogenesis; anti-inflammatory; anti-viral

Corresponding Author:
Prof. Dr. Zhongqiong Yin,
Natural Medicine Research Center,
College of Veterinary Medicine, Sichuan Agricultural University,
Chengdu, 611130, China
Tel.: +86 2886291162
e-mail: yinzhongq@163.com

0393-974X (2021)
Copyright © by BIOLIFE, s.a.s.
This publication and/or article is for individual use only and may not be further reproduced without written permission from the copyright holder.
Unauthorized reproduction may result in financial and other penalties
DISCLOSURE: ALL AUTHORS REPORT NO CONFLICTS OF INTEREST RELEVANT TO THIS ARTICLE.

deaths, while MERS-CoV caused 2,122 cases and 740 deaths (10, 11). Different factors contributing to the wide distribution and prevalence of coronaviruses include huge genetic diversity, frequent human-animal interaction, and genomic recombination that can cause periodic emergence in humans due to cross-species infections and rare spillover events (5, 12). Local health authorities reported groups of people with symptoms of pneumonia by unknown causes in late December 2019 at Wuhan, Hubei Province, China, and epidemiological studies linked it to wholesale markets of wet animals and seafood in Wuhan (13). Health authorities of China confirmed the causative agent as novel Coronavirus, Covid-19, on January 7, 2020 (14). Although reported cases were initially associated with seafood exposure in Wuhan, person-to-person transmission of SARS-CoV-2 was confirmed in recent epidemiological studies (15, 16). Globally 37,109,851 confirmed cases with 1,070,355 deaths had been reported up to October 12, 2020 (17).

The SARS-CoV-2 infection has a limited clinical spectrum. In China, cardiac injury and respiratory failure have been reported following health complications such as severe pneumonia, and acute respiratory distress syndrome (ARDS) (18). Similarities have been found between clinical features of SARS-CoV-2 and previous beta coronavirus infections. CoV-infected patients presented with clinical signs including dry cough, bilateral ground-glass opacities shown by chest CT scans, fever, and dyspnea (19). It seems that all three coronaviruses, SARS-CoV-2, SARS-CoV, and MERS-CoV, primarily transmit through the mouth, eyes, and nose (20, 21). An essential role of the respiratory tract in virus transmission and disease onset suggests a strategy against coronavirus to immunize respiratory mucosa for immunoprophylaxis (22).

Cytokine storm and cytokine release syndrome are life-threatening systemic inflammatory syndromes involving elevated levels of circulating cytokines and immune cell hyperactivation triggered by various therapies, pathogens, cancers, autoimmune conditions, and monogenic disorders (23). Likewise, aggravation of ARDS and multiple-organ failure is caused by cytokine storms (24). Cytokine storm suppression could be an effective strategy to save the lives of human coronavirus (HCoVs)-infected patients, as cytokine storm is frequently detected in clinical studies of those patients (25).

Bacteriophages are widely distributed entities occupying different ecological niches from the ocean to the gut microbiome (26, 27). Phage therapy was taken as a promising treatment after bacteriophage discovery in 1915 and Felix d'Herelle's conformation in 1917. Phage was applied in treating several clinical cases, but its application decreased after the discovery of antibiotics and their use in the Second World War (28). The phage-encoded virulence factors are exotoxins but the specificity of phages towards host bacteria without infecting non-host bacterial strains is evident. It makes phages an ideal candidate for treating specific bacterial infections without infecting non-bacterial targets and mammalian cells (28-30). Phage therapy was at the top as an alternative product to control infections in a review commissioned by the Prime Minister of the UK on antimicrobial resistance in 2016 (31). Many phage biology studies focused on bacterial cells and bacteriophage interactions as bacteriophage can interact with mammalian cell populations, specifically immune cells (32). Eukaryotic host initial contact and response to phage are through the innate immune system cells. The innate immune system consists of granulocytes, phagocytes, and complement proteins, which opsonize foreign particles to increase phagocytic uptake (33). Microbe-specific material is sensed by innate immune system cells, such as bacterial endotoxin, by the pathogen recognition receptor (PRR) family that can recognize pathogen-associated molecular patterns (PAMPs) (34).

The production of various cytokines is significantly affected by phages, as shown by subsequent studies (35, 36). In the intestinal tract, NF-κB activity inhibition can be mediated by probiotic-like and immunomodulatory functions by phages, as previously proposed (37). The probiotic-like role of phages in other parts of the body could be due to their translocation from the intestine (35, 37). It is interesting that some data also suggest the role of bacteriophages as an inhibitor of pathogenic

'virus' infections (38). Nevertheless, its anti-viral effects have not yet been confirmed. Phage anti-viral activity was related to the ability of phage virion components to specifically induce interferon production by nucleic acids (39). Henceforth, possible phage-virus interaction and its use as human viral infection treatment could be a matter of great debate for scientists.

Keeping in view the pathogenesis, exuberated innate immune response to HCoVs and anti-viral, anti-inflammatory, immunomodulatory properties of phageome and their high safety profile for vaccine development against several human viral diseases, we proposed that prophylactic phageome-based human innate immune modulation could be an effective tool to control HCoV infection.

Host innate immune response to CoV and its role in the pathogenesis

Initially, invading viruses are differentiated from cellular molecules by innate immune signaling to alert host cells about the presence of pathogens (40). Signaling cascade is initiated after recognition of viral PAMPs by the host pattern recognition receptors (PRRs). As a result of this signaling, an anti-viral state is established in cells (40). Viral RNA is detected by RIG-I-like receptors that are cytoplasmic sensors. An *in vitro*, SARS-CoV infection transcribed melanoma differentiation-associated protein 5(MDA5) and Retinoic acid-inducible gene (RIG-1)-like receptors (RLRs), that induces the Interferon-stimulated gene (ISGs) expression (41). Immune responses to invading pathogens may include chemokines, the most of which are interferon stimulatory factors (ISFs) and pro-inflammatory cytokines. However, an aggravated expression of these factors is associated with acute respiratory distress syndrome (ARDS) and immunopathology (42). ARDS pathogenesis is linked to pro-inflammatory cytokines, whose transcription is mediated by NF-κB (43). In *vitro* SARS-CoV infection showed a higher expression of IL-6 and IL-8 mediated by NF-κB expression as compared to the control group (41). Similarly, in a macaque model, aged macaques with severe lung injury had shown a higher expression of genes induced by NF-κB than the young adult macaques (44).

An association is found in earlier studies of SARS patients having massive lung damage and pulmonary inflammation with higher pro-inflammatory cytokines level in serum (e.g., IFN-γ, IL-1β, MCP1, IL-6, IL-10, and IL-12) (Fig. 1) (45). Likewise, higher pro-inflammatory cytokine levels in susceptible aged mice due to SARS-CoV infection are associated with ARDS involving IL-1β, TNF-α, and IL-6 (43). An exacerbated serum cytokine and chemokine level in severe MERS infected patients were reported as compared to mild to moderate MERS cases (46). MERS-CoV infections of Dendritic cells (DCs) and macrophages result in robust production of pro-inflammatory cytokines and chemokines, such as IL-17, IL-15, IFN-γ TNF-α, IL-6, CXCL-10, CCL-2, CCL-3, CCL-5, and IL-8, as compared to non-infected groups (11).

SARS-CoV-2 infected patients, compared with non-ICU, patients were found with higher concentrations of pro-inflammatory cytokines/ chemokines (e.g., IL-1β, IL-2, IL-7, IL-8, IL-9, IL-10, IL-17, G-CSF, GM-CSF, IFN-γ, TNF-α, IP10, MCP1, MIP1A, and MIP1B.1) (47, 48) that might lead to activated T helper 1 (Th1) cell responses (25). Lung injury due to higher infiltration of monocytes and neutrophils is due to the cytokine recruitment of inflammatory cells. Rapid progression of MERS-CoV, SARS-CoV-2, and SARS-CoV is due to the higher response of cytokines and chemokines that are dysregulated due to these viral infections (49). Avoiding cellular PRR detection, SARS-CoV can evade the host innate immune responses. Viral dsRNA segregates during the replication cycle of SARS-CoV that intermediates in double-membrane vesicle (DMV) interior which has the potential to shield viral PAMPs from cytosolic PRR recognition (50, 51). The production of IFN-I or IFN-α/β is the natural immune defense response against viral infections (49, 52). The delayed release of IFNs in the early stages of coronavirus infection hinders the body's antiviral response (53). Eight proteins encoded by SARS-CoV can antagonize the host IFN responses (54). SARS-CoV evades immune responses manifested by lymphopenia and higher viral loads during the first 10 days of SARS. Infected cells with a deficiency of IFN-β responses have been reported

in *in-vitro* studies (20). One study anticipated an immune evasion mechanism by SARS-CoV in DCs that reduced the expression of anti-viral cytokines (IL-12p40, IFN-α, IFN-y, and IFN-β), moderated overexpression of pro-inflammatory cytokines (TNF-α and IL-6), and remarkably upregulated pro-inflammatory chemokines (MCP-1, MIP-1, IP-10, and RANTES).

Furthermore, it has been shown that SARS-CoV prevents IFN-β induction by interfering with IFN regulatory factor 3 (IRF3) activation (55). These results support the point of view that following HCoVs infection, high virus titers and dysregulation of cytokine/chemokine response cause a life-threatening inflammatory cytokine storm. Immunopathological changes in the lungs accompany the inflammatory cytokine storm.

HCoV vaccination

Disease and infection prevention by vaccines in vulnerable populations is explained by the exposure of specific pathogens of interest (52). In the perspective of the HCoV epidemics, numerous vaccination approaches have been tried on animal models, however, few current vaccines are permitted for human use against MERS-CoV, SARS-CoV, and SARS-CoV-2. We analyzed the information publicly available on different scientific websites and documents due to the scarcity of peer-reviewed literature. These trials were projected to complete in June 2020 at the University of Queensland and Moderna, December 2020, in Russia and December 2021 in Germany, as reviewed by Pang et al. (52).

To date, one study is available published on the MERS-CoV vaccine by GeneOne Life Science & Inovio Pharmaceuticals (56). Also, the US National Institute of Allergy and Infectious Diseases conducted one SARS vaccine trial. Positive results from Phase I clinical trials are reported by both institutes, but Phase 2 trial proceedings are announced by the US National Institute of Allergy and Infectious Diseases (57).

There are five types of vaccine platforms currently available for the development of a vaccine, i.e., DNA vaccines, viral vector vaccines (Rabies, (NC)-based vaccine, parainfluenza, MVA-vaccinia, Adenovirus), subunit vaccines and live attenuated and inactivated vaccine (58, 59). Numerous studies were focused on the development of active immunization. DNA vaccines, vaccinia virus Ankara, rhabdo virus-based vectors, adenoviral vectors, inactivated virions, and recombinant parainfluenza virus type 3 vectors, and recombinant antigen are under examination. In mice, systemic humoral immunity was prompted by inactivated SARS vaccines and elevated titers of spike-specific antibodies causing blockage of binding receptors and virus entrance was reported in cell culture (60-62).

It is described that in rhesus monkeys, mucosal and humoral immunity was induced by inactivated SARS-CoV to combat the challenges of SARS-CoV (63). Through DNA immunization, nucleocapsid (64) and RS-CoV spike (65) and membrane glycoprotein (66) work as candidate vaccines in mice. Excitingly, in mouse model against SARS-CoV, humoral and cellular immunity can be induced by DNA vaccination. It is also revealed that T-cell and neutralizing antibody responses were induced by codon-optimized SARS spike glycoprotein encoded DNA vaccine. Humoral immune response enabled protection from SARS-CoV challenge but not by a T-cell-dependent mechanism (67).

Adenovirus-based vaccination approaches for anti-SARS-CoV have also been reported using replication-defective adenovirus type 5 vectors expressing structural SARS proteins (S1, M, and N) (68). Antibody responses against fragment S1 of a spike, T-cell responses against nucleocapsid, and virus-neutralizing antibody responses were developed by vaccinated rhesus macaques (68). Likewise, it is also proven that vaccination of C57B/L6 mice with adenovirus type5-expressing nucleocapsid elicited SARS-CoV-specific humoral and T-cell-mediated immune responses in C57B/L6 mice (69). Vaccination trial by using the mouse, attenuated, and modified vaccinia virus Ankara (MVA) has been used to prompt the spike glycoprotein of SARS-CoV (70). It was shown that SARS-CoV spike protein encoded MVA administration *via* intramuscular and intranasal routes in BALB/c mice led to the reduction of viral titers and stimulation of humoral immune response. Dynamic antibody response was observed in ferrets when they were vaccinated with

spike or nucleocapsid encoded MVA., however, viral infection and dissemination did not stop (71, 72).

In hamsters, recombinant bovine-human parainfluenza virus type 3 vector (BHPIV3) expressing SARS-CoV structural protein (S, M, and N) alone or in combination has been assessed for immunogenicity. It supports both SARS-CoV and BHPIV3 replication in the lungs. Administration of BHPIV3 expressing the SARS-CoV spike protein *via* intranasal route induced high titer of SARS-CoV neutralizing antibodies but merely two-fold fewer as compared to SARS-CoV infection-induced antibodies. No obvious SARS-CoV-neutralizing antibody response was observed by expression of M, N, or E in the absence of spike protein. Complete and partial protection in the lower and upper respiratory tract was reported by immunization with BHPIV3 expressing spikes, respectively (22, 73). Recombinant rabies virus was exhibiting the spike or the nucleocapsid protein of SARS CoV in mice; these vectors induced a neutralizing antibody reaction. For anti-SARS vaccination, rabies virus vectors usage as vaccines may give promising results. An attenuated vesicular stomatitis virus vector has been developed that encodes the SARS-CoV spike. Vesicular stomatitis virus S vaccinated mice showed the development of SARS-CoV-neutralizing antibodies and competed with the SARS-CoV challenge even after a single vaccination (60, 74). In rabbits, mice, and non-human primates, robust antibody and immune response were shown by full length S protein immunogens to lead to reduced MERS-CoV infection severity. Vaccination by adjuvanted MERS-CoV Spike protein subunit in dromedary camels led to reduced viral shedding in upper airways and the presence of lower titers of serum neutralizing antibodies (75). Ma et al. compared the systemic humoral, local mucosal immune responses, and cellular immune responses via subcutaneous (s.c) and intranasal (i.n) vaccination of recombinant receptor-binding domain (RBD) protein comprising residues 377–662 of MERS-CoV S joined with Fc of human IgG (RBDFc). Nonetheless, we observed that systemic humoral immune response was induced by MERS-CoV RBD-Fc, comprising neutralizing antibodies comparable to the subcutaneous vaccination-induced response, however, in vaccinated mice, more cellular response and higher local (lung) mucosal immune response were observed (76).

Phage-based stimulation of host innate immune cells

Bacteriophages are the most abundant and diverse living creatures on this planet (77). They are naturally present in the mammalian gut and have coevolved with millions of bacteria and host cells for many centuries (35). A graphical interaction of phages with immune cells in the gut is shown in Fig. 2. They are often found very close to the mucosal surface of the intestine that is enriched with innate immune cells and signaling molecules. Bacteriophages as microorganisms have several epitopes that can be recognized by pattern recognition receptors (PRRs) of innate immune cells (78, 79) through the following mechanisms: extracellular recognition, endocytic recognition, and cytoplasmic recognition (80, 81). The study showed that bacteriophages are likely to have initial contact with innate immune cells at the mucosal surface, where some specific protein domains for mucin sugar residues are expressed (82).

Interestingly, bacteriophage alone can activate multiple TLRs and other PRRs and efficiently trigger different downstream inflammatory cascades. Bacteriophages can trigger both cytotoxic and adaptive immune responses based on antigenic molecule presentation on major histocompatibility complex molecules (MHC-I and MHC-II) (83, 84). If epitopes of the phage genome are loaded into MHC-I molecules, it will activate cytotoxic T cell lymphocytes (CTLs); otherwise, the phage genome loaded into MHC-II molecules will trigger T helper cells, which further initiate adaptive immune response through B lymphocytes. Overall, bacteriophages can stimulate both types of immune responses, pro- and anti-inflammatory cascades, but they often dampen the inflammatory responses. Moreover, no study has reported any bacteriophage-driven damage into host cells (85, 86).

Bacteriophages as anti-inflammatory agents

Phage therapy has shown anti-inflammatory responses in the host. A retrospective study reported

a significant decrease in leukocyte counts and the mean of C reactive protein in patients treated with bacteriophages (87). It was observed that phage treatment diminished the expression of the NF-κB transcription factor, which commonly induces the expression of adhesion molecules and pro-inflammatory cytokines and chemokines (88). Cytokines of the IL-10 family (IL-28A, IL-20, IL-28B, IL-24, IL-10, IL-26, IL-22, and IL-19) are known for having anti-inflammatory characteristics and tissue protection (89). It was found that cytokine IL-10, having anti-inflammatory properties, was up-regulated after stimulation of phage PNM (Log2 fold change of 4.3) and *P. aeruginosa* (Log2 ratio of 4.3) (36). IL-10 also blocked pro-inflammatory cytokine expression, including CC chemokines, IL-1, IFN-γ, TNF-α, IL-12, and CXC (Fig. 1) (36). Another study reported that TH1 cells, macrophages, and NK cell activity were inhibited by anti-inflammatory cytokine, IL-10 (90) (Fig.2). Macrophages are considered critical for initiating both innate and adaptive immune responses in the host. There are two populations of macrophages, M1, and M2, known as classically and alternatively activated macrophages, respectively (91). M1 macrophages are recognized for releasing pro-inflammatory cytokines and M2 macrophages for anti-inflammatory cytokines (92). An *in-vivo* study on *P. aeruginosa* (PAO1)-infected mouse group reported that PAO1 and filamentous Pf bacteriophage (Pf4)-infected bone marrow-derived macrophages (BMDMs) expressed the M2 markers IL10 and Arg1 at higher levels than only PAO1-infected BMDMs without pf4 infection, which indicates Pf4 infection leads to diminished inflammatory response, reduced phagocytosis, and less tissue injury (93). It has been observed that the pro-inflammatory effect of LPS was counteracted by tail adhesion protein (gp12) of T4 phage in *in vivo* mouse model. Protein gp12 inhibited the leukocyte infiltration into the spleen, liver, and lungs, and reduced the production of pro-

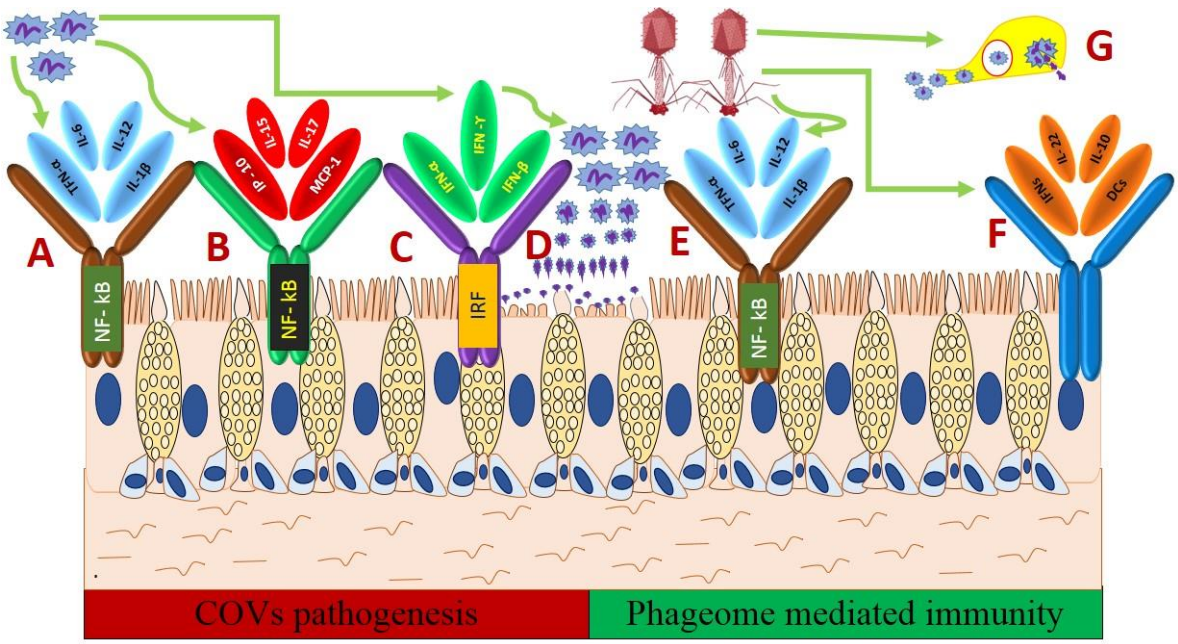


Fig. 1. *Host Innate immune response mediated pathogenesis against CoVs and role of bacteriophages to modulate the different anti-inflammatory and anti-viral mechanisms in the human population.* ***A, B****) CoVs infection stimulates the exuberated host innate immune response which leads to the frenzied production of pro-inflammatory cytokines e.g., IL-1β, TNF- α IL-6, IL12, IL-15, IL-17, IP10, and MCP1.* ***C****) Overstimulation of NF-κB and exuberated innate immune response dampens the interferon production including IFN-α, IFN-β and IFN-γ.* ***D****) Evasion of CoVs from interferon regulatory mechanisms leads to uncontrolled viral replication.* ***E****) Bacteriophages stifle the NF-κB activation which results in decreased production of pro-inflammatory cytokines such as IL-1β, TNF- α IL-6, IL-12.* ***F****) Bacteriophage interaction with host innate immune cells enhances dendritic cells production and activation of interferon and anti-inflammatory cytokines such as IL-10 and IL-22.* ***G****) Bacteriophage interaction to host innate immune cells that leads to the increased phagocytosis of pathogenic viral particles.*

inflammatory cytokines including IL-6 and IL-1α in blood serum (86).

Many other anti-inflammatory properties of phages have been reported in the past. Phage treatment inhibited the generation of reactive oxygen species by bacteria or endotoxin-mediated stimulation of polymorphonuclear leukocytes (83). Bacteriophages reduced the activation of NF-κB in human mononuclear cells by treating them with human herpesvirus-1 (84). Bacteriophages decreased T-cell and platelet adhesion to fibrinogen and extracellular matrix (94). A significant decline in classical inflammatory marker, C-reactive protein (CRP) (95), serum concentration, and WBCs in patients with phage lysate treatment suggests anti-inflammatory effects of phage therapy (87). All these findings suggest that phages have a high potential of modulating the immune system and drive anti-inflammatory response in the host without harming local tissues.

Phages as an anti-viral agent

In 1965, it was found that a substance, "phagicin", was produced by K-12 *E. coli* when infected with bacteriophage λ. Phagicin was found active against herpes simplex virus in both *in-vivo* and *in-vitro* conditions. It affected the viral replication process inside the host cell (96). Viral DNA synthesis was inhibited by phagicin, and no effect was found on host-DNA synthesis by Meek and Takahashi investigations in 1968 (97). Depending on the dose, human adenovirus (HAdV) replication and adsorption were significantly inhibited by T4 phage by blocking and suppressing the expression of cellular receptors or co-receptors that are used by the virus to attach to and enter into cells (98). It was observed that ϕ80

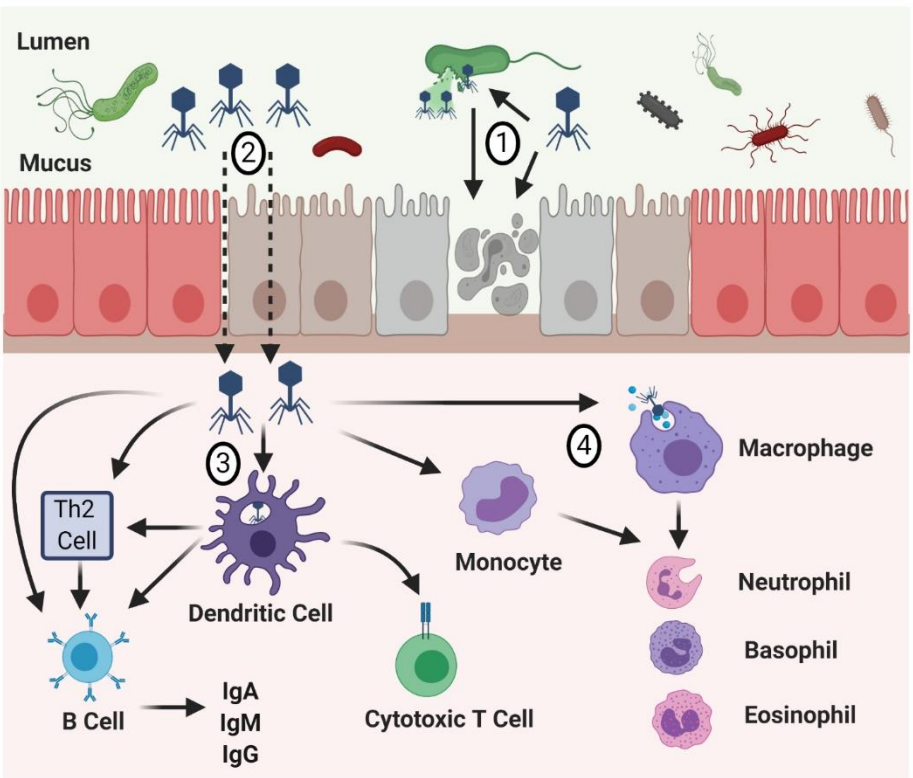


Fig. 2. *Phages are abundantly present in the gut microbiota. Phages can interact with immune cells by multiple interfaces:* ***1****) phags can cause bacteriolysis and induce immune cells by releasing immunogenic bacterial peptides;* ***2****) phage can cross the epithelial cells and directly interact with immune cells;* ***3****) in this direct interaction, phage can be engulfed by dendritic cells and presented to Th2 cells which can further induce B lymphocytes to produce antibodies or phage can directly activate Th3 cells, B lymphocytes to initiate adaptive response,* ***4****) phage can also bind to macrophages and monocytes which can activate neutrophil, basophil and eosinophil.*

bacteriophage had activity against herpes simplex virus (HSV), and λ phage has anti-VSV action (99). Chickens were challenged with a virulent Newcastle disease virus (NDV), and significant protection against infection was observed in chickens treated with lysate of *Brucella* bacteriophage type *abortus* strain 3. The control group of untreated birds had 88% mortality while the study groups showed a mortality of 31% when given oral doses in the first week and 17% when intramuscular preparation was administered (100). An *in-vivo* study showed that double-stranded RNA of ϕ6 bacteriophage inhibited HSV type 1 and type 2-based infection in fetal rhesus monkey kidney cells (MA104) (101). The higher anti-viral activity was observed in the duck hepatitis B virus (DHBV) model where single-stranded DNA extracted from M13 phage significantly inhibited hepatitis B (HB) acute infection compared to a well-known anti-DHBV agent, acyclovir (102). Similarly, tail lesions caused by the Vaccinia virus were decreased by administering M13 single-stranded decreased DNA intravenously 24 hours before infection of the virus (39). Mice were protected from encephalomyocarditis and herpes simplex virus infection by treating with dsRNA of R17 *E. coli* phage mutant form amB11 (103). Anti-HBsAg antibody response was significantly higher in the group of mice that were given an intramuscular injection of whole bacteriophage λ-gt11 particles having the gene for surface antigens of hepatitis B (104). A lytic Pf4 phage stimulation showed an anti-viral response in the mouse model, however, it suppressed bacterial infection clearance from the body (105).

An interaction model suggests a direct competition for cellular receptors between viruses and bacteriophages to enter the host cell (106). Viruses use integrins as adhesion receptors such as Hantaviruses, adenoviruses, rotaviruses, (107) foot and mouth disease virus (FMDV) and (108) HIV type 1 (109). Blocking the viral adhesion receptors inhibits viral replication and infection (110). The study showed that bacteriophage capsid having gp24 head corner protein-containing Lys-Gly-Asp motif (aIIbB3 integrin-binding KGD sequence) can effectively bind to beta3 integrin receptor and block downstream signaling pathways (111). Even phages displaying integrin ligand showed an efficient binding ability. It was examined that filamentous fd phage displaying cyclic-RGD peptide (RGD-4C) bound to avB5 and avB3 integrins gathered in inflamed synovium, and reduced arthritis (112). Hantavirus entry was prevented by blocking B3 integrins with KGD+ bacteriophages (113). Virus infection can be inhibited by other cellular receptors using phage-based chemokines (114).

Role of bacteriophages in vaccine development

Bacteriophages have huge potential to be an effective tool for developing vaccines against emerging infectious diseases. Phage-based vaccines can be developed in two ways: phage DNA vaccine and phage displaying external DNA vaccine. As discussed above, phage DNA itself carries immunogenic properties and can induce both innate and adaptive immune responses. Whole filamentous phages having antigenic peptides were first used in 1998 as a vaccine by Vida et al. to initiate immune responses in rabbits against *Plasmodium falciparum* (115). Since then, several studies have been conducted to investigate the potential of phage-based vaccines (116). Phages have a strong adjuvant and immunostimulatory capacity (117) that qualify them for vaccine delivery with superior immunogenicity (118). Moreover, phages can deliver DNA vaccine combining expression cassette of protective antigens or imitating epitopes into a phage genome (77). In phage display technology, a unique peptide sequence is displayed along with phage surface protein to trigger the immune response. This technique provides an opportunity to identify and select protein or functional polypeptides with desired immunogenic characteristics (119, 120). The immunogenicity of phage-displayed vaccines depends on the displayed peptides and methods. To bioengineer phages for phage display technique, two approaches are used - either the direct display of antigen by transcriptional fusion with coat protein, or secondary display of antigens to capture antigens using pre-displayed antigen-binding peptide (121). Often, the direct approach of phage display vaccines is used. Multiple phage display systems have been studied that include filamentous phages, T7 phage,

phage lambda, T4 phage, and few RNA phage display systems (77). Filamentous phages (f1, M13, and fd) can infect Gram-negative bacteria using F pilus assembled from the ssDNA genome and coat proteins. The sidewall of coat proteins includes one or two thousand copies of major coat protein (pVIII), and tips of nanofibers contain five copies of each minor protein (pVII, pIII, pIX, and pVI) (122). The peptide display results from fusion to pVIII (123) or pIII (124) phage proteins. Although M13 phage is an effective and commonly used display system, it has one drawback as it possesses a nonlytic proliferation mechanism (77). T4 phage infects *E. coli* and is a lytic bacteriophage having a double-stranded (ds) DNA genome with icosahedral capsid tail and twelve tail fibers (125). The Head of the T4 phage comprises different proteins (9~19), of which, some are highly antigenic, especially highly outer capsid (HOC) protein and small outer capsid protein (SOC), thus, it is commonly used to display foreign immunogens (126). T4 phage having HOC capsid proteins were fused with single and multiple antigens by Sathaliyawala et al. using phage display technology. T4 surface was exposed with single and multiple copies of HIV antigens, and elicited a strong broad-spectrum neutralizing antibody-based immune response. An effective HIV vaccine can therefore have T4 phage displaying an engineered antigen (127). Like T4 phage, T7 phage is also lytic in nature and has a dsDNA encapsulated in an icosahedral capsid. The two capsid proteins, i.e 10A and 10B, are commonly used to display peptides or proteins in T7 phage system (77). T7 phage was used for vaccine delivery against viral infections such as Influenza A virus (IAV) and foot and mouth disease virus (FMDV). Gene encoding the antigenic site (G-H loop of protein structu) of FMDV was inserted into T7 phage genome. The recombinant T7 phage displaying G-H loop peptide produced a more pronounced immune response as compared to the commercially available vaccine (PepVac and InactVac) in pig model (128). Against the IAVs, phage (f88M2e2-16) can be a substitute vaccine to trigger the protective immune responses (129). Overall, T7 phage has rapid proliferation as compared to filamentous and lambda phages (130). Lambda phage has a characteristic isometric head of ~50 nm in diameter and ~150 nm long tail. To fuse foreign protein or peptide, D head capsid protein, and tail protein termed as pV can be used (131, 132). However, the N-or C-terminal of D head protein is commonly used as a display site compared to pV protein because D-head-based display does not disturb the phage multiplication and produces a higher copy number (77).

M13 phage surface protein was fused with two Hepatitis B virus antigens. HBcAg (hepatitis B core antigen) gene was inserted into pIII of M13 phage that resulted in pIII and HBcAg fusion at the surface of the phages. Antigenicity and immunogenicity were tested by injecting whole HBcAg-displaying recombinant phages into the tail vein of BALB/c mice that established effective immunization (133). Similarly, epitope 28−39 of Hepatitis B virus was displayed in M13 phage. Effective cytotoxic T lymphocyte (CTL) responses specific to the hepatitis B virus were triggered *in vivo* by reconstructed phages in mice models (134). The phage-displayed vaccine was also constructed against other viral infections, such as papillomavirus, using M13 phage (135) and white spot syndrome virus (136).

Phage-based vaccines can also be used in animal vaccinations. The shrimp industry can be impacted globally by the white spot syndrome virus (WSSV). WSSV full-length protein, VP28, was expressed on M13 phage surface in a phage-displayed vaccine by Lucero and colleagues. Lower mortality was observed in the vaccinated group compared to the untreated group after challenge (136). Recombinant filamentous phages used as phage DNA vaccine can also be used as vehicles for DNA vaccine delivery. Recently, a recombinant filamentous phage was constructed by inserting the HSV-1 glycoprotein D expression cassette of Herpes simplex into the genome of M13 phage. Cost-effectiveness and purification of the procedure showed that filamentous phages are the best candidate as a vehicle for DNA vaccines (137). Phage DNA vaccines triggerred an elevated antibody response against hepatitis B HBsAg compared to commercial vaccines in a rabbit model (104, 138). The phage lambda system was also successfully applied in designing the phage

DNA vaccines against hepatitis C virus (139).

Phages can be an effective vaccine delivery tool to induce a robust immunogenic response (140). Antigen-presenting cells (APC) can efficiently engulf phage DNA and express phage genomic DNA as epitopes on MHC molecules (77). Viral infections can be mainly treated with vaccines and anti-viral drugs, however, a high frequency of genomic mutability in viruses helps them evade immune responses such as HIV and coronaviruses. These viral characteristics limit the scope of developing anti-viral drugs against particular viral targets (77). Protection against viral infections with effective immune responses induced by reconstructed phages is evident. Many other phages having the potential for the phage display technique have been reviewed in another study (141).

Phage therapy showed a decrease in T cell activation by binding with the CD3-TCR complex (142). Pseudomonas PMN phage treatment up-regulated anti-inflammatory IL-1 and IL-10 cytokines, and also downregulated TLR4 gene that induces a pro-inflammatory response in the host (36). Though immune responses against different phages vary, phage therapy still could be an efficient tool to develop vaccines against an infectious agent such as SARS-CoV-2 and cancer.

DISCUSSION

Historically, coronaviruses have always posed serious challenges for both public health and modern medicine due to their acute onset, high transmission, and significant fatality rate among humans. Among seven human CoVs, SARS-CoV, MERS-CoV, and SARS-CoV-2 are mainly associated with zoonotic infections with fatal outcomes. The detailed underlying mechanisms of cellular pathogenesis triggered by CoV infection remain less understood. A proposed model for CoV pathogenesis suggested the three phases of pathogenesis: pulmonary destruction, viral replication, and immune hyperactivity. Hyperactive innate immune responses of the host against these three CoVs lead to exacerbated expressions of pro-inflammatory cytokines and chemokines, including NF-κB, TNF-α IL-1α, IL-1β, IL-2, IL6, IL12, IL-15, 1L-17, IP10, and MCP1, which play a primary role in the disease pathogenesis. Considering the upregulation of pro-inflammatory cytokines, the initial treatment procedures for CoV-infected patients involved the administration of anti-inflammatory agents or stimulation of anti-inflammatory cytokines within the host body, for which we propose phage-based therapeutics that could modulate the host immune responses to combat CoVs infections. Phages are natural entities that can stimulate the anti-inflammatory response against multiple viral infections by suppressing the above-mentioned pro-inflammatory cytokines secreted in response to CoV infections. Phages also trigger anti-inflammatory cytokines that belong to the IL-10 family i.e. IL-10, IL-19, IL-20, IL-22, IL-24, IL-26, IL-28A, and IL-28B. These anti-inflammatory cytokines can inhibit the release of pro-inflammatory response during CoV infection in the host. Besides their anti-inflammatory properties, phages also possess direct anti-viral effects against different eukaryotic pathogenic viruses.

Vaccine development against CoV infection is the most reliable way to control the current SARS-CoV-2 pandemic. To date, several vaccines based on different molecular approaches are under clinical trials. However, no phage-based vaccine has yet been proposed and tested against SARS-COV, MERS-CoV, and SARS-CoV-2 yet. Keeping in view the potential of bacteriophages in vaccine development technology, we propose that phages could be an effective and economical source to develop vaccines against different CoVs. Both phage DNA vaccine and phage-display vaccine techniques can be used for developing vaccines against SARS-CoV-2. These phage-based techniques have shown significant results against other infectious diseases such as influenza, and hepatitis. In brief, the anti-viral, anti-inflammatory and vaccine delivery potential of phages make them a strong candidate for anti-viral therapeutics against CoVs infections. There should be a collaborative effort by the scientific community to further investigate the potential of different phages in treating and developing vaccines against emerging and re-emerging viral infections among humans.

ACKNOWLEDGEMENTS

This work was supported by the Sichuan Veterinary Medicine and Drug Innovation Group of China Agricultural Research System (CARS-SVDIP) and the Science and Technology Project of Sichuan Province (Grant Nos. 2018NZ0043 and 2018NZ0064). We also wish to thank Dr. Sohaib Iqbal Bandehsa, Asad Riaz and Muhammad Ahsan Asghar for technical assistance

REFERENCES

1. Gao GF. From ""A"" IV to ""Z"" IKV: attacks from emerging and re-emerging pathogens. Cell 2018; 172:1157-9.
2. Weiss SR, Leibowitz JL. Coronavirus pathogenesis. Adv Virus Res 2011; 81:85-164.
3. Alluwaimi AM, Alshubaith IH, Al-Ali AM, Abohelaika S. The Coronaviruses of Animals and Birds: Their Zoonosis, Vaccines, and Models for SARS-CoV and SARS-CoV2. Front Vet Sci 2020; 7:655.
4. Su S, Wong G, Shi W, et al. Epidemiology, genetic recombination, and pathogenesis of coronaviruses. Trends Microbiol 2016; 24:490-502.
5. Cui J, Li F, Shi ZL. Origin and evolution of pathogenic coronaviruses. Nat Rev Microbiol 2019; 17:181-92.
6. Zhong N, Zheng B, Li Y, et al. Epidemiology and cause of severe acute respiratory syndrome (SARS) in Guangdong, People's Republic of China, in February, 2003. Lancet 2003; 362:1353-8.
7. Ksiazek TG, Erdman D, Goldsmith CS, et al. A novel coronavirus associated with severe acute respiratory syndrome. N Engl J Med 2003; 348:1953-66.
8. Drosten C, Günther S, Preiser W, et al. Identification of a novel coronavirus in patients with severe acute respiratory syndrome. N Engl J Med 2003; 348:1967-76.
9. Zaki AM, Van Boheemen S, Bestebroer TM, Osterhaus AD, Fouchier RA. Isolation of a novel coronavirus from a man with pneumonia in Saudi Arabia. N Engl J Med 2012; 367:1814-20.
10. Chan-Yeung M, Rui-Heng XU. SARS: epidemiology. Respirology 2003; 8:9-14.
11. Mahallawi WH, Khabour OF, Zhang Q, Makhdoum HM, Suliman BA. MERS-CoV infection in humans is associated with a pro-inflammatory Th1 and Th17 cytokine profile. Cytokine 2018; 104:8-13.
12. Wong G, Liu W, Liu Y, Zhou B, Bi Y, Gao GF. MERS, SARS, and Ebola: the role of super-spreaders in infectious disease. Cell Host Microbe 2015; 18:398-401.
13. Commission WMH. Report of clustering pneumonia of unknown etiology in Wuhan City. Published December 31, 2019.
14. Organization WH. Novelcoronavirus — China. https://www who int/ csr/ don/ 12 -january-2020-novel-coronavirus-china/en/. 2020.
15. Chan JF, Yuan S, Kok KH, et al. A familial cluster of pneumonia associated with the 2019 novel coronavirus indicating person-to-person transmission: a study of a family cluster. Lancet 2020; 395:514-23.
16. Phan LT, Nguyen TV, Luong QC, et al. Importation and human-to-human transmission of a novel coronavirus in Vietnam. N Engl J Med 2020; 382:872-4.
17. Organization WH. Coronavirus disease 2019 (COVID-19) Situation Report – 226. https://ncdc.gov.ng/themes/common/files/sitreps/8a72a13340d906f9fce9c7814f963ace.pdf. 202.
18. Chen N, Zhou M, Dong X, et al. Epidemiological and clinical characteristics of 99 cases of 2019 novel coronavirus pneumonia in Wuhan, China: a descriptive study. Lancet 2020; 395:507-13.
19. Assiri A, Al-Tawfiq JA, Al-Rabeeah AA, et al. Epidemiological, demographic, and clinical characteristics of 47 cases of Middle East respiratory syndrome coronavirus disease from Saudi Arabia: a descriptive study. Lancet Infect Dis 2013; 13:752-61.
20. Law HK, Cheung CY, Ng HY, et al. Chemokine up-regulation in sars-coronavirus–infected, monocyte-derived human dendritic cells. Blood 2005; 106:2366-74.
21. Guan W, Xian J. The progress of 2019 Novel Coronavirus (2019-nCoV) event in China. J Med Virol 2020; 92:468-472.
22. Bukreyev A, Lamirande EW, Buchholz UJ, et al. Mucosal immunisation of African green monkeys

(Cercopithecus aethiops) with an attenuated parainfluenza virus expressing the SARS coronavirus spike protein for the prevention of SARS. Lancet 2004; 363:2122-7.
23. Fajgenbaum DC, June CH. Cytokine storm. N Engl J Med 2020; 383:2255-73.
24. Chousterman BG, Swirski FK, Weber GF. Cytokine storm and sepsis disease pathogenesis. Semin Immunopathol 2017; 39:517-28.
25. Min CK, Cheon S, Ha NY, et al. Comparative and kinetic analysis of viral shedding and immunological responses in MERS patients representing a broad spectrum of disease severity. Sci Rep 2016; 6:1-12.
26. Suttle CA. Viruses in the sea. Nature. 2005; 437:356-61.
27. Mills S, Shanahan F, Stanton C, Hill C, Coffey A, Ross RP. Movers and shakers: influence of bacteriophages in shaping the mammalian gut microbiota. Gut Microbes 2013; 4:4-16.
28. Loc C, Abedon ST. Pros and cons of phage therapy. Bacteriophage. 2011; 1:111-4.
29. Keen EC. A century of phage research: bacteriophages and the shaping of modern biology. Bioessays 2015; 37:6-9.
30. Wagner PL, Waldor MK. Bacteriophage control of bacterial virulence. Infect Immun 2002; 70:3985-93.
31. O'Neill J. Tackling Drug-resistant infections globally: final report and recommendations–the review on antimicrobial resistance chaired by Jim O'Neill. Wellcome Trust and HM Government, London. 2016.
32. 'd'Herelle F. Opsonic power of the lysins. In ""Bacteriophage: 'It's Role in Immunity". Williams & Wilkins, Baltimore; 1922.
33. Holers VM. Complement and its receptors: new insights into human disease. Annu Rev Immunol 2014; 32:433-59.
34. Abaidullah M, Peng S, Kamran M, Song X, Yin Z. Current findings on gut microbiota mediated immune modulation against viral diseases in chicken. Viruses 2019; 11:681.
35. Górski A, Ważna E, Dąbrowska BW, Dąbrowska K, Świtała JK, Międzybrodzki R. Bacteriophage translocation. FEMS Immunol Med Microbiol 2006; 46:313-9.
36. Van Belleghem JD, Clement F, Merabishvili M, Lavigne R, Vaneechoutte M. Pro-and anti-inflammatory responses of peripheral blood mononuclear cells induced by Staphylococcus aureus and Pseudomonas aeruginosa phages. Sci Rep 2017; 7:1-13.
37. Górski A, Weber DB. The potential role of endogenous bacteriophages in controlling invading pathogens. Cell Mol Life Sci 2005; 62:511.
38. Miedzybrodzki R, Fortuna W, Weber DB, Gorski A. Bacterial viruses against viruses pathogenic for man?. Virus Res 2005; 110:1-8.
39. Mori K, Kubo T, Kibayashi Y, Ohkuma T, Kaji A. Anti-vaccinia virus effect of M13 bacteriophage DNA. Antiviral Res 1996; 31:79-86.
40. Rathinam VA, Fitzgerald KA. Cytosolic surveillance and anti-viral immunity. Curr Opin Virol 2011; 1:455-62.
41. Yoshikawa T, Hill TE, Yoshikawa N, et al. Dynamic innate immune responses of human bronchial epithelial cells to severe acute respiratory syndrome-associated coronavirus infection. PLoS One 2010; 5:8729.
42. Pugin J, Ricou B, Steinberg KP, Suter PM, Martin TR. Proinflammatory activity in bronchoalveolar lavage fluids from patients with ARDS, a prominent role for interleukin-1. Am J Respir Crit Care Med 1996; 153:1850-6.
43. Galani V, Tatsaki E, Bai M, Kitsoulis P, Lekka M, Nakos G, Kanavaros P. The role of apoptosis in the pathophysiology of Acute Respiratory Distress Syndrome (ARDS): an up-to-date cell-specific review. Pathol Res Pract 2010; 206:145-50.
44. Smits SL, de LA, Van den BJM, et al. Exacerbated innate host response to SARS-CoV in aged non-human primates. PLoS Pathog 2010; 6:1000756.
45. Chien JY, Hsueh PR, Cheng WC, Yu CJ, Yang PC. Temporal changes in cytokine/chemokine profiles and pulmonary involvement in severe acute respiratory syndrome. Respirology 2006; 11:715-22.
46. Kim ES, Choe PG, Park WB, et al. Clinical progression and cytokine profiles of Middle East respiratory syndrome coronavirus infection. J Korean Med Sci 2016; 31:1717-25.
47. Huang C, Wang Y, Li X, et al. Clinical features of patients infected with 2019 novel coronavirus in Wuhan, China. Lancet 2020; 395:497-506.
48. Xu Z, Shi L, Wang Y, et al. Pathological findings of COVID-19 associated with acute respiratory distress syndrome. Lancet Respir Med 2020; 8:420-22.

49. Ye Q, Wang B, Mao J. Cytokine storm in COVID-19 and treatment. J Infect 2020; 80:607-613.
50. Knoops K, Kikkert M, van den Worm SH, et al. SARS-coronavirus replication is supported by a reticulovesicular network of modified endoplasmic reticulum. PLoS Biol 2008; 6:226.
51. Snijder EJ, Van DMY, Zevenhoven-Dobbe J, Onderwater JJM, Van DMJ, Koerten HK, Mommaas AM. Ultrastructure and origin of membrane vesicles associated with the severe acute respiratory syndrome coronavirus replication complex. J Virol 2006; 80:5927-40.
52. Pang J, Wang MX, Ang IYH, et al. Potential rapid diagnostics, vaccine and therapeutics for 2019 novel Coronavirus (2019-ncoV): a systematic review. J Clin Med 2020; 9:623.
53. Frieman M, Baric R. Mechanisms of severe acute respiratory syndrome pathogenesis and innate immunomodulation. Microbiol Mol Biol Rev 2008; 72:672-85.
54. Totura AL, Baric RS. SARS coronavirus pathogenesis: host innate immune responses and viral antagonism of interferon. Curr Opin Virol 2012; 2:264-75.
55. Spiegel M, Pichlmair A, Martínez-Sobrido L, Cros J, García-Sastre A, Haller O, Weber F. Inhibition of beta interferon induction by severe acute respiratory syndrome coronavirus suggests a two-step model for activation of interferon regulatory factor 3. J Virol 2005; 79:2079-86.
56. Modjarrad K, Roberts CC, Mills KT, et al. Safety and immunogenicity of an anti-Middle East respiratory syndrome coronavirus DNA vaccine: a phase 1, open-label, single-arm, dose-escalation trial. Lancet Infect Dis 2019; 19:1013-22.
57. Mumbai I. 'Inovio's Positive First-Inhhuman Mers Vaccine Results Published in the Lancet Infectious Diseases. https://www.prnewswire.com/news-releases/inovios-positive-first-in-human-mers-vaccine-results-published-in-the-lancet-infectious-diseases-300890842.html. 2019.
58. Modjarrad K. MERS-CoV vaccine candidates in development: The current landscape. Vaccine 2016; 34:2982-7.
59. Wang C, Horby PW, Hayden FG, Gao GF. A novel coronavirus outbreak of global health concern. Lancet 2020; 395:470-3.
60. Faber M, Lamirande EW, Roberts A, Rice AB, Koprowski H, Dietzschold B, Schnell MJ. A single immunization with a rhabdovirus-based vector expressing severe acute respiratory syndrome coronavirus (SARS-CoV) S protein results in the production of high levels of SARS-CoV-neutralizing antibodies. J Gen Virol 2005; 86:1435.
61. Takasuka N, Fujii H, Takahashi Y, et al. A subcutaneously injected UV-inactivated SARS coronavirus vaccine elicits systemic humoral immunity in mice. Int Immunol 2004; 16:1423-30.
62. Tang L, Zhu Q, Qin E, et al. Inactivated SARS-CoV vaccine prepared from whole virus induces a high level of neutralizing antibodies in BALB/c mice. DNA Cell Biol 2004; 23:391-4.
63. Zhou J, Wang W, Zhong Q, et al. Immunogenicity, safety, and protective efficacy of an inactivated SARS-associated coronavirus vaccine in rhesus monkeys. Vaccine 2005; 23:3202-9.
64. Zhao P, Cao J, Zhao LJ, et al. Immune responses against SARS-coronavirus nucleocapsid protein induced by DNA vaccine. Virology 2005; 331:128-35.
65. Zeng F, Chow KYC, Hon CC, et al. Characterization of humoral responses in mice immunized with plasmid DNAs encoding SARS-CoV spike gene fragments. Biochem Biophys Res Commun 2004; 315:1134-9.
66. Wang Z, Yuan Z, Matsumoto M, Hengge UR, Chang YF. Immune responses with DNA vaccines encoded different gene fragments of severe acute respiratory syndrome coronavirus in BALB/c mice. Biochem Biophys Res Commun 2005; 327:130-5.
67. Yang ZY, Kong WP, Huang Y, Roberts A, Murphy BR, Subbarao K, Nabel GJ. A DNA vaccine induces SARS coronavirus neutralization and protective immunity in mice. Nature 2004; 428:561-4.
68. Gao W, Tamin A, Soloff A, et al. Effects of a SARS-associated coronavirus vaccine in monkeys. Lancet 2003; 362:1895-6.
69. Zakhartchouk AN, Viswanathan S, Mahony JB, Gauldie J, Babiuk LA. Severe acute respiratory syndrome coronavirus nucleocapsid protein expressed by an adenovirus vector is phosphorylated and immunogenic in mice. J Gen Virol 2005; 86:211-5.
70. Bisht H, Roberts A, Vogel L, et al. Severe acute

respiratory syndrome coronavirus spike protein expressed by attenuated vaccinia virus protectively immunizes mice. Proc Natl Acad Sci U S A 2004; 101:6641-6.
71. Weingartl HM, Copps J, Drebot MA, et al. Susceptibility of pigs and chickens to SARS coronavirus. Emerg Infect Dis 2004; 10:179.
72. Weingartl H, Czub M, Czub S, et al. Immunization with modified vaccinia virus Ankara-based recombinant vaccine against severe acute respiratory syndrome is associated with enhanced hepatitis in ferrets. J Virol 2004; 78:12672-6.
73. Buchholz UJ, Bukreyev A, Yang L, Lamirande EW, Murphy BR, Subbarao K, Collins PL. Contributions of the structural proteins of severe acute respiratory syndrome coronavirus to protective immunity. Proc Natl Acad Sci U S A 2004; 101:9804-9.
74. Kapadia SU, Rose JK, Lamirande E, Vogel L, Subbarao K, Roberts A. Long-term protection from SARS coronavirus infection conferred by a single immunization with an attenuated VSV-based vaccine. Virology 2005; 340:174-82.
75. Adney DR, Wang L, van DN, et al. Efficacy of an adjuvanted Middle East respiratory syndrome coronavirus spike protein vaccine in dromedary camels and alpacas. Viruses 2019; 11:212.
76. Ma C, Li Y, Wang L, et al. Intranasal vaccination with recombinant receptor-binding domain of MERS-CoV spike protein induces much stronger local mucosal immune responses than subcutaneous immunization: Implication for designing novel mucosal MERS vaccines. Vaccine 2014; 32:2100-8.
77. Bao Q, Li X, Han G, Zhu Y, Mao C, Yang M. Phage-based vaccines. Adv Drug Deliv Rev 2019; 145:40-56.
78. Dąbrowska K, Miernikiewicz P, Piotrowicz A, et al. Immunogenicity studies of proteins forming the T4 phage head surface. J Virol 2014; 88:12551-7.
79. Dabrowska K, Switała JK, Opolski A, Weber DB, Gorski A. Bacteriophage penetration in vertebrates. J Appl Microbiol 2005; 98:7-13.
80. Gorski A, Dabrowska K, Switala JK, et al. New insights into the possible role of bacteriophages in host defense and disease. Med Immunol 2003; 2:2.
81. Wenger S, Turner J, Petricciani J. The cytogenetic, proliferative and viability effects of four bacteriophages on human lymphocytes. In Vitro 1978; 14:543-9.
82. Barr JJ, Auro R, Furlan M, et al. Bacteriophage adhering to mucus provide a non–host-derived immunity. Proc Natl Acad Sci U S A 2013; 110:10771-6.
83. Kieser KJ, Kagan JC. Multi-receptor detection of individual bacterial products by the innate immune system. Nat Rev Immunol 2017; 17:376.
84. Thaiss CA, Zmora N, Levy M, Elinav E. The microbiome and innate immunity. Nature. 2016; 535:65-74.
85. Przerwa A, Zimecki M, Świtała-Jeleń K, et al. Effects of bacteriophages on free radical production and phagocytic functions. Med Microbiol Immunol 2006; 195:143-50.
86. Miernikiewicz P, Kłopot A, Soluch R, et al. T4 phage tail adhesin gp12 counteracts LPS-induced inflammation in vivo. Front Microbiol 2016; 7:1112.
87. Międzybrodzki R, Fortuna W, Weber DB, Górski A. A retrospective analysis of changes in inflammatory markers in patients treated with bacterial viruses. Clin Exp Med 2009; 9:303.
88. Górski A, Kniotek M, Perkowska PA, et al. Bacteriophages and transplantation tolerance. Transplant Proc 2006; 38:331-3.
89. Ouyang W, Rutz S, Crellin NK, Valdez PA, Hymowitz SG. Regulation and functions of the IL-10 family of cytokines in inflammation and disease. Annu Rev Immunol 2011; 29:71-109.
90. Couper KN, Blount DG, Riley EM. IL-10: the master regulator of immunity to infection. J Immunol 2008; 180:5771-7.
91. Sica A, Mantovani A. Macrophage plasticity and polarization: in vivo veritas. J Clin Invest 2012; 122:787-95.
92. Benoit M, Desnues B, Mege JL. Macrophage polarization in bacterial infections. J Immunol 2008; 181:3733-9.
93. Secor PR, Michaels LA, Smigiel KS, et al. Filamentous bacteriophage produced by Pseudomonas aeruginosa alters the inflammatory response and promotes noninvasive infection in vivo. Infect Immun 2017; 85:00648-16.
94. Kniotek M, Ahmed A, Dabrowska K, Switala JK, Opolski A, Gorski A. Bacteriophage interactions with T cells and platelets. Immunol 2004:189-93.

95. Mc VCS, Velásquez M, Fralick JA. Phage therapy of Pseudomonas aeruginosa infection in a mouse burn wound model. Antimicrob Agents Chemother 2007; 51:1934-8.
96. Centifanto Y. A Therapeutic Antiviral from an Extract of A Infected E. coli (Phagicin). Proc Soc Exp Biol Med 1965; 120:607-11.
97. Meek E, Takahashi M. Differential inhibition by phagicin of DNA synthesis in cells infected with vaccinia. Nature 1968; 220:822.
98. Przybylski M, Borysowski J, Jakubowska ZR, Weber DB, Górski A. T4 bacteriophage-mediated inhibition of adsorption and replication of human adenovirus in vitro. Future Microbiol 2015; 10:453-60.
99. Merril CR. Interactions of bacterial viruses and bacterial genes with animal systems. 1977.
100. Keyhani M. Protection against experimental Newcastle disease in chickens given Brucella bacteriophage. Vet Rec 1969; 84:657-8.
101. Vales N, Barron BL, Padilla JA, Sandoval H, Sotelo J. Effect of dsRNA from π6 Bacteriophage on Herpetic Infection in Cell Culture and an Animal Model. J Interferon Res. 1991; 11:271-4.
102. Iizuka A, Watanabe T, Kubo T, Yamamoto M, Ogawa K, Ohkuma T, Kaji A. M13 bacteriophage DNA inhibits duck hepatitis B virus during acute infection. Hepatol 1994; 19:1079-87.
103. Feldmane G, Loza V, Duks A, et al. Nucleic acid as interferon inducer. Its anti-viral and antitumor activity. Arch Immunol Ther Exp 1977; 25:693.
104. March JB, Clark JR, Jepson CD. Genetic immunisation against hepatitis B using whole bacteriophage λ particles. Vaccine 2004; 22:1666-71.
105. Sweere JM, Van Belleghem JD, Ishak H, et al. Bacteriophage trigger anti-viral immunity and prevent clearance of bacterial infection. Science 2019; 363:1416.
106. Schneider SJ. Cellular receptors for viruses: links to tropism and pathogenesis. J Gen Virol 2000; 81:1413-29.
107. Triantafilou K, Triantafilou M. Mechanisms of integrin-mediated virus attachment and internalization process. Crit Rev Immunol 2001; 21:311–322.
108. Jackson T, Mould AP, Sheppard D, King AM. Integrin αvβ1 is a receptor for foot-and-mouth disease virus. J Virol 2002; 76:935-41.
109. Lafrenie RM, Lee SF, Hewlett IK, Yamada KM, Dhawan S. Involvement of integrin αvβ3 in the pathogenesis of human immunodeficiency virus type 1 infection in monocytes. Virology 2002; 297:31-8.
110. Hippenmeyer PJ, Ruminski PG, Rico JG, Lu HS, Griggs DW. Adenovirus inhibition by peptidomimetic integrin antagonists. Antivir Res 2002; 55:169-78.
111. Dabrowska K, Opolski A, Wietrzyk J, et al. Antitumor activity of bacteriophages in murine experimental cancer models caused possibly by inhibition of beta3 integrin signaling pathway. Acta Virol 2004; 48:241-8.
112. Gerlag DM, Borges E, Tak PP, et al. Suppression of murine collagen-induced arthritis by targeted apoptosis of synovial neovasculature. Arthritis Res Ther 2001; 3:357.
113. Gavrilovskaya IN, Brown EJ, Ginsberg MH, Mackow ER. Cellular entry of hantaviruses which cause hemorrhagic fever with renal syndrome is mediated by β3 integrins. J Virol 1999; 73:3951-9.
114. Hartley O, Dorgham K, Perez BD, et al. Human immunodeficiency virus type 1 entry inhibitors selected on living cells from a library of phage chemokines. J Virol 2003; 77:6637-44.
115. De LCV, Lal A, Mc CTF. Immunogenicity and epitope mapping of foreign sequences via genetically engineered filamentous phage. J Biol Chem 1988; 263:4318-22.
116. Asadi GM, Ghaemmaghami M, Klimka A, Javanmardi M, Navari M, Rasaee MJ. Cancer immunotherapy by a recombinant phage vaccine displaying EGFR mimotope: an in vivo study. Immunopharmacol Immunotoxicol 2015; 37:274-9.
117. Aghebati ML, Bakhshinejad B, Baradaran B, et al. Phage display as a promising approach for vaccine development. J Biomed Sci 2016; 23:66.
118. Bartolacci C, Andreani C, Curcio C, et al. Phage-based anti-HER2 vaccination can circumvent immune tolerance against breast cancer. Cancer Immunol Res 2018; 6:1486-98.
119. Shi H, Dong S, Zhang X, Chen X, Gao X, Wang L. Phage vaccines displaying YGKDVKDLFDYAQE epitope induce protection against systemic candidiasis in mouse model. Vaccine 2018; 36:5717-24.
120. Lopes RS, Queiroz MAF, Gomes STM, Vallinoto ACR, Goulart LR, Ishak R. Phage display: an

important tool in the discovery of peptides with anti-HIV activity. Biotechnol Adv 2018; 36:1847-54.
121. Kobayashi N, Oyama H, Nakano M, et al. ""Cleavable"" hapten–biotin conjugates: Preparation and use for the generation of anti-steroid single-domain antibody fragments. Anal Biochem 2009; 387:257-66.
122. Rakonjac J, Bennett NJ, Spagnuolo J, Gagic D, Russel M. Filamentous bacteriophage: biology, phage display and nanotechnology applications. Curr Issues Mol Biol 2011; 13:51.
123. Smith GP. Filamentous fusion phage: novel expression vectors that display cloned antigens on the virion surface. Science 1985; 228:1315-7.
124. Benhar I. Biotechnological applications of phage and cell display. Biotechnol Adv 2001; 19:1-33.
125. Yap ML, Rossmann MG. Structure and function of bacteriophage T4. Future Microbiol. 2014; 9:1319-27.
126. Wu J, Tu C, Yu X, et al. Bacteriophage T4 nanoparticle capsid surface SOC and HOC bipartite display with enhanced classical swine fever virus immunogenicity: a powerful immunological approach. J Virol Methods 2007; 139:50-60.
127. Sathaliyawala T, Rao M, Maclean DM, Birx DL, Alving CR, Rao VB. Assembly of human immunodeficiency virus (HIV) antigens on bacteriophage T4: a novel in vitro approach to construct multicomponent HIV vaccines. J Virol 2006; 80:7688-98.
128. Xu H, Bao X, Lu Y, et al. Immunogenicity of T7 bacteriophage nanoparticles displaying GH loop of foot-and-mouth disease virus (FMDV). Vet Microbiol 2017; 205:46-52.
129. Deng L, Ibañez LI, Van den Bossche V, et al. Protection against influenza A virus challenge with M2e-displaying filamentous Escherichia coli phages. PLoS One 2015; 10:0126650.
130. Takakusagi Y, Ohta K, Kuramochi K, Morohashi K, Kobayashi S, Sakaguchi K, Sugawara F. Synthesis of a biotinylated camptothecin derivative and determination of the binding sequence by T7 phage display technology. Bioorganic Med Chem Lett 2005; 15:4846-9.
131. Santini C, Brennan D, Mennuni C, Hoess RH, Nicosia A, Cortese R, Luzzago A. Eficient display of an HCV cDNA expression library as C-terminal fusion to the capsid protein D of bacteriophage lambda. J Mol Biol 1998; 282:125-35.
132. Mikawa YG, Maruyama IN, Brenner S. Surface display of proteins on bacteriophage λ heads. J Mol Biol 1996; 262:21-30.
133. BahadirAO, Balcioglu BK, Uzyol KS, Hatipoglu I, Sogut I, Basalp A, Erdag B. Phage displayed HBV core antigen with immunogenic activity. Appl Biochem Biotechnol 2011; 165:1437-47.
134. Wan Y, Wu Y, Bian J, et al. Induction of hepatitis B virus-specific cytotoxic T lymphocytes response in vivo by filamentous phage display vaccine. Vaccine 2001; 19:2918-23.
135. Lidqvist M, Nilsson O, Holmgren J, Hall C, Fermér C. Phage display for site-specific immunization and characterization of high-risk human papillomavirus specific E7 monoclonal antibodies. J Immunol Methods 2008; 337:88-96.
136. Solís LG, Manoutcharian K, Hernández LJ, Ascencio F. Injected phage-displayed-VP28 vaccine reduces shrimp Litopenaeus vannamei mortality by white spot syndrome virus infection. Fish Shellfish Immunol 2016; 55:401-6.
137. Hashemi H, Bamdad T, Jamali A, Pouyanfard S, Mohammadi MG. Evaluation of humoral and cellular immune responses against HSV-1 using genetic immunization by filamentous phage particles: a comparative approach to conventional DNA vaccine. J Virol Methods 2010; 163:440-4.
138. Clark JR, Bartley K, Jepson CD, Craik V, March JB. Comparison of a bacteriophage-delivered DNA vaccine and a commercially available recombinant protein vaccine against hepatitis B. Fems Immunol Med Mic 2011; 61:197-204.
139. Clark JR, March JB. Bacteriophage-mediated nucleic acid immunisation. Fems Immunol Med Mic 2004; 40:21-6.
140. Tao P, Mahalingam M, Zhu J, et al. A bacteriophage T4 nanoparticle-based dual vaccine against anthrax and plague. MBio. 2018; 9:01926.
141. Hess KL, Jewell CM. Phage display as a tool for vaccine and immunotherapy development. Bioeng Transl Med 2020; 5:10142.
142. Górski A, Międzybrodzki R, Borysowski J, et al. Phage as a modulator of immune responses: practical implications for phage therapy. Adv Virus Res 2012; 83:41-71.

Sensitivity of serology assay in Covid-19 diagnosis: does the antigen matter?

C. Sitzia[1*#], L. Pistelli[2*], R. Cardani[3], L.V. Renna[3], M. Ranucci[4], M. Carrara[2], S. Borlini[2], P. Clerici[5], B. Rampoldi[6], M. Cornetta[6] and M.M. Corsi-Romanelli[1,6]

[1]Department of Biomedical Sciences for Health, University of Milan, Milan, Italy; [2]Residency Program in Clinical Pathology and Clinical Biochemistry, University of Milan, Milan, Italy; [3]Biobank BioCor, Service of Laboratory Medicine1-Clinical Pathology, IRCCS Policlinico San Donato, San Donato Milanese, Milan, Italy; [4]Department of Cardiothoracic and Vascular Anesthesia and Intensive Care Unit, IRCCS Policlinico San Donato, San Donato Milanese, Milan, Italy; [5]Microbiology Unit, Hospital of Legnano, ASST Ovest Milanese, Italy; [6]Operative Unit 1-Clinical Pathology, Department of Pathology and Laboratory medicine, I.R.C.C.S. Policlinico San Donato, San Donato Milanese, Milan, Italy

Received March 26, 2021 – Accepted June 17, 2021

[*]These authors equally contributed to this work

Since the spreading of Sar-CoV-2 in March 2020, many serologic tests have been developed to identify antibody responses. Indeed, different commercial kits are directed against different antigens and could utilise different methods thereby triggering confusion and criticism. Here, we compared two Food and Drug Administration (FDA)-approved automatized assays that detect IgG responses against spike or nucleocapsid protein of Sars-Cov-2 virus in 127 subjects among healthcare workers of IRCCS Policlinico San Donato (MI), Italy. We observed different kinetics of IgG responses, demonstrating the importance of timing of sampling to correctly interpret the results both for infection diagnosis and for epidemiologic studies. We observed that Anti-N response starts earlier than Anti-S1/S2 response but also decreases earlier, affecting the sensitivity of the tests at different time points. Combining two different assays, designed against different antigens, could reduce false negative results. Finally, we observed a patient who produced anti-nucleocapsid IgG, but not anti-spike IgG. In conclusion, we investigated antibody responses in Covid-19 disease, aiming to direct clinicians and laboratory scientists to correctly interpret serologic results by always paying attention to clinical history correlation, timing of sampling, methods and antigens used, to avoid false negative results and obtain relevant epidemiologic data.

New Sars-Cov-2 infection was first reported in December 2019, after the discovery of pneumonia cases of unknown origin: clinical features and mortality varied, depending on the age of patients and comorbidities (1, 2). Since the spreading of Sars-Cov-2 pandemic in March 2020, many methods to assess antibody responses have emerged. The multitude of available commercial kits triggered confusion and criticism about their reliability, that relies on both analytical performance, timing of

Key words: IgG kinetics; Sars-Cov-2; antibody responses; long-term immunity; serological test

[#]*Corresponding Author:*
Clementina Sitzia MD,
Via Luigi Mangiagalli, 31
20133 Milan, Italy
Tel.: +39 02 503 15384/02 503 15387
e-mail: clementina.sitzia@unimi.it

0393-974X (2021)
Copyright © by BIOLIFE, s.a.s.
This publication and/or article is for individual use only and may not be further reproduced without written permission from the copyright holder.
Unauthorized reproduction may result in financial and other penalties
DISCLOSURE: ALL AUTHORS REPORT NO CONFLICTS OF INTEREST RELEVANT TO THIS ARTICLE.

sampling and the antigen targeted (3). Sensitivity ranges from 72.7-100% depending on the antigen tested, the method used and the timing of sampling, while specificity varies from 98.7 to 100%. Some manufacturers declared cross-interaction with other coronavirus strains or interference due to Rheumatoid Factor (RF) and antinuclear antibody (ANA) (4, 5). Antibody responses could be detected as early as 4 days after the onset of symptoms; however, their levels increase during the second and third weeks, reaching the maximum of sensitivity in the first month of illness (3). IgM response starts early while IgG response increases when IgM starts to decline, but they can be found simultaneously, together with viral particles in nasopharyngeal swabs (6). The comparison of methods is problematic due to different antigenic targets of the tests. In this sense, the nucleocapsid protein (N) is abundantly expressed during infection so that N-based assays seem to be more sensitive than S1-subunit-based assays (4), which target the spike protein, important for attachment to host cells. Conversely, antibodies against receptor binding domain (RBD) of S protein seem to be more specific and are expected to be neutralizing (3, 7). However, some manufacturer did not even declare the epitope used. Different studies have compared diagnostic performance of serologic assays (8, 9), however due to the multitude of methods (ELISA, CMIA, Immunochromatographic), different targeted epitopes, different classes of IG (IgM, IgG, IgA) and heterogeneous groups of subjects analysed, the reported sensitivity varied.

In this sense, the majority of these studies focused on hospitalised patients with severe symptoms, and as antibody titre could correlate with symptom severity, the reported sensitivity could result higher than in asymptomatic patients. In a study by Naaber et al. the sensitivity of tests varied from 65 to 92% when applied to different groups (10). Furthermore, sampling time influences the sensitivity of the test, both at the beginning of infection (median seroconversion time between 6 and 14 days from symptom onset) and during convalescence. Some studies reported high IgG levels for at least 7 weeks, but after 3-4 months a decline was observed. However, as mentioned previously, asymptomatic patients could present a more rapid decline due to low IgG titer (11, 12).

In the present study, two Food and Drug Administration (FDA)-approved, automated chemiluminescent assays for IgG anti Sars-Cov-2 were evaluated in 127 voluntary subjects among healthcare workers of IRCCS Policlinico San Donato, Milan (Italy). The two assays differ in the antigen targeted: one is directed against nucleocapsid protein (N) from Abbott (Ireland) and the other is directed against spike protein (S1/S2) from DiaSorin (Italy). We calculated sensitivity, specificity, accuracy and overall agreement between the two tests. Finally, IgG kinetics in serial serum samples were evaluated to highlight any difference in test sensitivity related to timing of sampling from a positive nasopharyngeal swab.

MATERIALS AND METHODS

Subjects

One hundred and twenty-seven voluntary subjects, among healthcare workers of IRCCS Policlinico San Donato, Milan (Italy), were included in this study; there were 74 females and 53 males with a median age of 45 years (20-68 years). Subjects were included during routine screening of healthcare workers which was performed two times: the first in May 2020 when the test became available, and the second in September 2020 when the epidemic started to spread again in Italy. A positive serologic result entailed the obligation to perform a swab testing within 48 h and the abstention from work. A positive RT-PCR result implied the mandatory quarantine and the screening of co-workers. A negative RT-PCR result implied resolved infection. The study was performed at IRCCS Policlinico San Donato, Milan (Italy) in accordance with the Declaration of Helsinki. All subjects included in the study gave signed informed consent. Exclusion criteria were the presence of declared concomitant chronic conditions (e.g., Cancer, chronic liver disease and hematologic diseases). The study was approved by the Local Ethics Committee (75/INT/2020) and carried out on frozen leftover samples stored at Biobank BioCor of IRCCS Policlinico San Donato.

Of the 127 subjects 44 were RT-PCR positives, 33 negatives, 8 had never had a nasopharyngeal swab and

42 samples, collected from December 2017 to April 2018, represented negative controls of background immunity. For the kinetic study 5 RT-PCR+ subjects were included (of the 44 positives). Inclusion criteria was having performed at least 4 serial serum samples over time (min 0 to 135 days after positive nasopharyngeal swab). At onset, these subjects presented fever, headache, dry cough, asthenia and fatigue. The timing of nasopharyngeal swab was performed following the sanitary surveillance guidelines: after 14 days from the first positive swab and every 7 days until obtaining two consecutive negative RT-PCR results.

Chemiluminescent for antibody responses analysis

SARS-CoV-2-IgG (Abbott, Longford, Ireland) is a chemiluminescent microparticle immune assay for qualitative assessment of IgG anti-nucleocapsid protein of SARS-CoV-2 in human serum on the Architect analyser. Briefly, analysis was performed following the manufacturer's instructions. Intensity of chemiluminescence reaction was measured as relative light units (RLU) and results were compared to RLU of the calibrator and transformed as a calculated Index (S/C). The cut-off is 1.4 Index (S/C). Cross-reactivity with the main infectious agents had been excluded by the manufacturer, but other coronavirus strain had not been evaluated by the manufacturer and interference of elevated title of rheumatoid factor was reported by the manufacturer.

LIAISON® SARS-CoV-2 S1/S2 IgG (DiaSorin, Vercelli, Italy) is a fully automated quantitative CLIA analysis to detect S1/S2 antigens of SARS-CoV-2. S1 and S2 proteins are derived from the SARS-CoV-2 spike protein and they are the main target of neutralising antibodies. 94.4% positive agreement to Plaque Reduction Neutralization test (PRNT) was declared by the manufacturer. Cross-reactivity for non-SARS-CoV-2 coronavirus strain HkU1, OC43 had not been observed by the manufacturer. FDA reported performance metrics for both tests: Abbott Architect SARS-CoV-2 IgG sensitivity 100% (95.8%-100%), specificity 99.6% (99.0%-99.9%); Diasorin IgG sensitivity 97.6% (87.4%-99.6%), specificity 99.3% (98.6%-99.6%). These assays were chosen because they had been the earliest to be approved by the FDA and secondly by the Italian Regulatory Agency, therefore they were the only ones automatized in use in laboratories in Italy at the time of sample collection.

Statistical analysis

Data were analysed by Graph Pad software to evaluate sensitivity, specificity, accuracy, overall agreement and Kappa Cohen between the two methods. Confidence intervals were calculated at 95%. RT- PCR analysis was considered as ground truth. For sensitivity and specificity calculation, 8 subjects who did not perform RT-PCR analysis on nasopharyngeal swab were excluded and considered only for overall agreement analysis. Forty-two sera from the pre-Covid era (collected before December 2019) were considered as RT-PCR negative.

RESULTS

Clinical features of study population

Serum was collected from 127 voluntary subjects among healthcare workers of IRCCS Policlinico San Donato (MI), Italy during routine screening for sanitary surveillance. Four subjects needed hospitalization without invasive ventilation, one presented gastrointestinal symptoms, and the remaining subjects, who were treated at home, presented fever and dry cough or were asymptomatic. Thus this population is mainly composed of paucisymptomatic subjects (home-treated, fever <37.5°C, dry cough and fatigue).

Sensitivity, specificity and agreement between the tests

Sensitivity and specificity were evaluated for both tests in 119 of 127 subjects who had nasopharyngeal swabs taken or in pre-Covid-19 negative controls. Samples were collected between day 0 and a maximum of day 95 from RT-PCR analysis (mean: 38 days). The results are shown in Tables I and II. Then agreement between the two tests was evaluated, resulting as good. (Overall Agreement: 0.906 and K Cohen: 0.79)

Time course analysis of antibody responses

Among 44 RT-PCR positive subjects, 10 false negative results were observed, of which 5 subjects were negative to both tests while 2 were negative to anti-S1/S2 and 3 to anti-N IgG tests (Table III) (Positive agreement 0.88 and Kappa Cohen 0.599). Differences existed regarding the timing of sampling from nasopharyngeal swab. To better investigate

these differences, we decided to evaluate IgG antibody kinetics with both tests. We tested 5 RT-PCR positive subjects, choosing those who had had at least 4 serial serum samplings (among 44 RT-PCR positive subjects) (Fig. 1). We observed that the time to develop IgG response from symptom onset varied among subjects. Differences were noted in IgG antibody kinetics: anti-N IgG increased rapidly whilst anti-S1/S2 IgG increased more slowy (Fig. 1). Finally, we noticed a decline of anti-N-IgG titer after 60 days in 4 of 5 subjects analysed, while anti-S1/S2 IgG varied among individuals. Moreover, simultaneous presence of Sars Cov-2 viral RNA in nasopharyngeal swab and early IgG response (Fig. 1) was detected, however RT-PCR tended to turn negative throughout anti-N IgG plateau phase.

Lastly, it is remarkable that subject 5 never developed anti-S1/S2 IgG during the following 10 weeks. Nasopharyngeal swab was repeated in this subject on day 62 because of Covid- 19 associated-symptom onset in his young son. Surprisingly, the result was positive, while she reported two negative RT-PCR analyses on day 18 and 22 from symptom onset.

Thanks to these results we decided to separately evaluate the sensitivity on the basis of the timing of serum sampling from nasopharyngeal swab. We chose two periods from 0 to 4 weeks and from 4 to 14 weeks. Results are shown in Table IV.

DISCUSSION

Serologic analysis could represent a powerful tool to aid the diagnosis of Covid-19 disease, as it is a low-cost test and less time-consuming than molecular analysis. However, the interpretation of results is critical to reach a correct diagnosis both for patients – to isolate cases and to start therapy – and epidemiological studies – to evaluate herd immunity. Indeed, a correct interpretation depends on the knowledge of the test used, of the antigen tested, on the timing of sampling and, even more importantly, on the clinical history of the patient.

We compared data from two FDA approved, automated methods, largely employed in Italy, to evaluate eventual differences related to discrepancies in the antigen tested. There is only slight difference

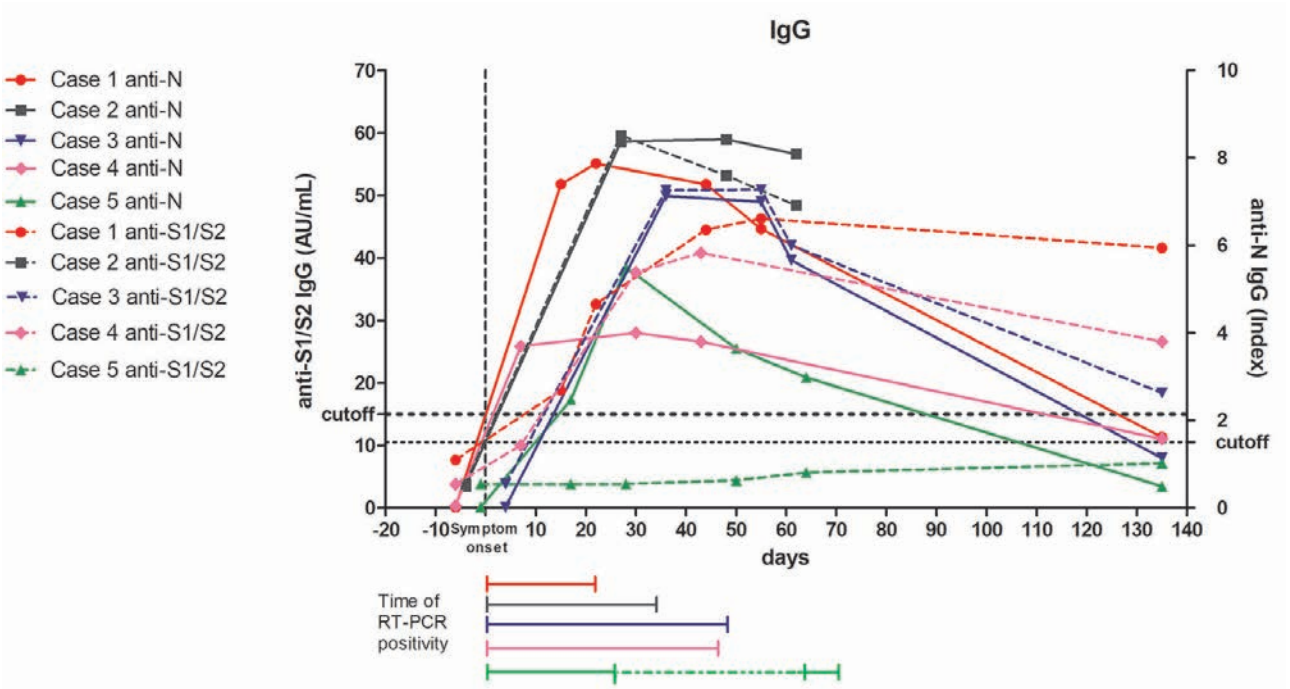


Fig. 1. *Long-term monitoring of antibody responses in 5 RT-PCR+ subjects. On the right axis, anti-nucleocapsid IgG curves are plotted while on the left axis anti-spike protein IgG curves. Lines show presence of viral RNA in nasopharyngeal swab starting from the onset of symptoms.*

from the FDA report in sensitivity between the two tests while specificity does not differ. Reported data for sensitivity from the FDA are higher than those observed in our study, but this finding is in accordance with previously reported data (10). Furthermore, the FDA declared that differences could exists in sensitivity data between the tests because of different times of sampling.

Despite good agreement, we observed discordant results, and deeper investigations revealed that differences relied on different kinetics of IgG responses directed against N or S1/S2 protein, as anti-S-IgG increased later than anti-N-IgG. Conversely, anti-N-IgG seemed to decline earlier than anti-S-IgG. We also observed the simultaneous presence of Sars-Cov-2 RNA on nasopharyngeal swab and IgG responses. These results could depend on high sensitivity of RT-PCR assay to viral RNA fragments; therefore, they could not represent a contagious phase, however further studies are needed to clarify this point (9).

In addition, we observed that subject 5 never developed anti-S1/S2 IgG while producing anti-N-IgG responses. In this sense, spike protein was reported to be a target for neutralizing antibodies, and 94.4% accordance with plaque-reduction neutralization test was reported. However, this point was not investigated due to lack of BSL-3 facility.

According to the literature, re-infection is still a matter of debate (14), however the absence of

Table I. *Features of Anti-N IgG and anti S1/S2 IgG tests*

	Anti-N IgG	Anti-S1/S2 IgG
Sensitivity	81.8 (67.3 - 91.8%)	84.1 (69.9 - 93.4%)
Specificity	97.3 (90.7 - 99.7%)	94.7 (86.9 - 98.5%)
Accuracy	91.6 (85.1 - 95.9%)	90.7 (84 - 95.29%)
Overall agreement	0.906	
K Cohen	0.79	

Table II. S*ensitivity and specificity of anti-N and antiS1/S2 assays*

	RT-PCR+	RT-PCR-	Total
Anti-N IgG +	36	2	38
Anti-N IgG -	8	73	81
Total	44	75	119

	RT-PCR+	RT-PCR-	Total
Anti-S1/S2 IgG +	37	4	41
Anti-S1/S2 IgG -	7	71	78
Total	44	75	119

Table III. *Positive agreement between the two assays*

	Anti-S1/S2 IgG +	Anti-S1/S2 IgG -
Anti-N IgG +	34	2
Anti-N IgG -	3	5
Total	37	7

Table IV. *Sensitivity calculated on two different periods of sampling*

	Sensitivity	
	0-4 weeks	**4-14 weeks**
Anti-N IgG	82.6 (62.9 - 93%)	80.9 (58 - 94.5%)
Anti-S1/S2 IgG	78.3 (58 - 90.3%)	90.5 (71.1 - 98.3%)

	RT-PCR+		Total
	0-4 weeks	**4-14 weeks**	
Anti-N IgG +	19	17	36
Anti-N IgG -	4	4	8
Total	23	21	44

	RT-PCR+		Total
	0-4 weeks	**4-14 weeks**	
Anti-S1/S2 IgG +	18	19	37
Anti-S1/S2 IgG -	5	2	7
Total	23	21	44

anti-S1/S2 antibodies could support this option. Anyway, the high sensitivity of molecular analysis against inactivated virus particles could make the test inadequate to monitor recovery (13).

In conclusion, we observed different kinetics between anti-S1/S2 and anti-N IgG, confirming that the antigen targeted influences the performance of the method. Long-term monitoring of recovered patients is critical to determine the persistence of these antibodies in blood and their role both in the active phase of the disease and in the long-term immunity. Accordingly, we observed a decline of antibody titers over 5 months, dropping to cut-off value.

To date, there are few studies that have evaluated the kinetic of antibodies and, in particular, the majority focused on 1-3 months after infection (15, 16). In accordance with our study, Kutsuma et al. observed a decrease of IgG titer (17). In particular, Dittari et al., who compared two methods targeting different epitopes, observed a significant difference with one test sensitivity that declines rapidly after 45 days and the other one that remains constant till 85 days, confirming our findings (18). Furthermore, Ibarrondo et al reported rapid IgG response decline in persons with mild Covid-19, resembling our population (19).

We strongly recommend paying attention to the antigen targeted and timing of sampling when choosing a serologic method to confirm the absence of anti-Sars-Cov2 response in subjects with a clinical history of exposure and/or COVID-19-related symptoms and in high-risk categories such as healthcare workers. However, a limitation of our study is the exclusion of subjects with concomitant chronic conditions that could influence the results.

It is mandatory to know when the sample has been collected, since each serologic test is differently time-sensitive: anti-N tests showed positive response earlier than anti-S1/S2. Moreover, the life span of antibodies is unknown: therefore, some tests may result negative because the antibody titer has already decreased below cut-off levels, even after 90 days from virus infection.

To avoid the risk of false-negative results, tests related to two different antigens could be undertaken for the same patient, in order to increase the test sensitivity. Multiplex platform enabling the simultaneous detection of diverse antibody responses against N, S1 and RBD, has been developed (20). Adopting this strategy could lead to more accurate and reliable results within a single diagnostic run, especially in low seroprevalence mass-screening programs.

ACKNOWLEDGEMENTS

The authors received specific funding for this work from the Italian Ministry of Health, "Ricerca Corrente".

REFERENCES

1. Cao J, Tu WJ, Cheng W, et al. Clinical features and short-term outcomes of 102 patients with coronavirus disease 2019 in Wuhan, China. Clin Infect Dis 2020; 71(15):748-55.
2. Yang X, Yu Y, Xu J, et al. Clinical course and outcomes of critically ill patients with SARS-CoV-2 pneumonia in Wuhan, China: a single-centered, retrospective, observational study. Lancet Respir Med 2020; 8(5):475-81.
3. Sethuraman N, Jeremiah SS, Ryo A. Interpreting Diagnostic Tests for SARS-CoV-2. Jama 2020; 323(22):2249-51
4. Lee CY, Lin RTP, Renia L, Ng LFP. Serological Approaches for COVID-19: Epidemiologic Perspective on Surveillance and Control. Front Immunol 2020; 11:879.
5. Tang MS, Hock KG, Logsdon NM, et al. Clinical performance of two SARS-CoV-2 serologic assays. Clin Chem 2020; 66(8):1055-62.
6. Wang W, Xu Y, Gao R, et al. Detection of SARS-CoV-2 in Different Types of Clinical Specimens. Jama 2020; 12;323(18):1843-44.
7. Liu W, Liu L, Kou G, et al. Evaluation of Nucleocapsid and Spike Protein-Based Enzyme-Linked Immunosorbent Assays for Detecting Antibodies against SARS-CoV-2. J Clinical Microbiol 2020; 58(6):e00461-20
8. Harritshøj LH, Gybel-Brask M, Afzal S, et al. Comparison of 16 serological SARS-CoV-2 immunoassays in 16 clinical Laboratories. J Clin Microbiol 2021; 59:e02596-20.
9. Andrea Tešija Kuna, Milena Hanžek, Ines Vukasović et al. Comparison of diagnostic accuracy for eight SARS-CoV-2 serological assays. Biochem Med (Zagreb) 2021; 31(1):010708.
10. Naaber P, Hunt K, Pesukova J et al. Evaluation of SARS-CoV-2 IgG antibody response in PCR positive patients: Comparison of nine tests in relation to clinical data. PLoS ONE 2020; 15(10):e0237548.
11. Bastos ML, Tavaziva G, Abidi SK, et al. Diagnostic accuracy of serological tests for covid-19: systematic review and meta-analysis BMJ 2020; 370:m2516.
12. Quan-Xin Long QX, Tang XJ, Shi QL, et al. Clinical and immunological assessment of asymptomatic SARS-CoV-2 infections. Nat Med 2020; 26(8):1200-4 .
13. Wolfel R, Corman VM, Guggemos W, et al. Virological assessment of hospitalized patients with COVID-2019. Nature 2020; 581(7809):465-9.
14. Ota M. Will we see protection or reinfection in COVID-19? Nat Rev Immunol 2020; 20(6):351.
15. Bolke E, Matuschek C, Fischer JC. Loss of anti-SARS-CoV-2 antibodies in mild Covid-19. N Engl J Med 2020; 383:1694-5.
16. Gudbjartsson DF, Norddahl GL, Melsted P, et al. Humoral immune response to SARS-CoV-2 in Iceland. N Engl J Med 2020; 383:1724-34.
17. Kutsuna S, Asai Y, Matsunaga A. Loss of anti-SARS-CoV-2 antibodies in mild covid-19. N Engl J Med 2020; 383:1695-6.
18. Dittadi R, Afshar H, Carraro P, Two SARS-CoV-2 IgG immunoassays comparison and time-course profile of antibodies response. Diagn Microbiol Infect Dis 2021; 99(4):115297.
19. Ibarrondo FJ, Fulcher JA, Goodman-Meza D, et al. Rapid decay of Anti-SARS-CoV-2 antibodies in persons with mild Covid-19. N Engl J Med 2020; 383:1085-7.
20. Fotis C, Meimetis N, Tsolakos N, et al. Accurate SARS-CoV-2 seroprevalence surveys require robust multi-antigen assays. Sci Rep 2021; 11(1):6614.

Neutrophil-lymphocyte ratio and hypersensitive C-reaction protein are associated with miscarriage during the second trimester of pregnancy

L. Zhang[1,2*], H.J. Hong[2*], B.D. Duan[3], Y. Zhang[4,5], C. C. Shao[6], L.N. Wang[7], X. Jiao[8], Y.J. Du[8], Y.Q. Zou[8] and Y.Y. Ma[1]

[1]Department of Obstetrics and gynecology, Qilu Hospital, Cheeloo College of Medicine, Shandong University, Ji'nan, China; [2]Department of Obstetrics, The Second Hospital, Cheeloo College of Medicine, Shandong University, Ji'nan, China; [3]Department of Obstetrics, Zibo Central hospital, Zibo, China: [4]Clinical Epidemiology Unit, Qilu Hospital, Cheeloo College of Medicine, Shandong University, Ji'nan, China; [5]Clinical Research Center, Cheeloo College of Medicine, Shandong University, Ji'nan, China; [6]Center of Evidence-based Medicine, The Second Hospital, Cheeloo College of Medicine, Shandong University, Ji'nan, China; [7]Department of Clinical Laboratory Medicine, The Second Hospital, Cheeloo College of Medicine, Shandong University, Ji'nan, China: [8]School of Medicine, Cheeloo College of Medicine, Shandong University, Ji'nan, China

Received September 30. 2020 -

*These Authors contributed equally to this study

This study investigated whether biomarkers in the second trimester of pregnancy, including the white blood cell (WBC) count, neutrophil-lymphocyte ratio (NLR), hypersensitive C-reactive protein (hs-CRP) concentration, and procalcitonin (PCT) concentration, were associated with miscarriage during the second trimester of pregnancy. Sixty-two asymptomatic patients in their second trimester of pregnancy were included in the control group (group A). Among 67 patients diagnosed with late threatened miscarriage, 46 patients with ongoing pregnancy were included in group B and 21 patients with subsequent miscarriage were included in group C. The serum of these patients was collected and the biomarkers were analyzed. A paired-samples *t*-test was used for the comparison between the groups before and after the miscarriage. Statistical significance was set at $p<0.05$. Receiver operating characteristic curve (ROC) analysis was performed to evaluate the predictive value of different biomarkers for miscarriage during the second trimester of pregnancy. WBC count, neutrophil percentage, and hs-CRP levels were significantly higher in group C than in groups A and B ($p<0.05$). Lymphocyte percentage and albumin levels decreased significantly from group A to group C ($p<0.05$). In contrast, NLR increased significantly from group A to group C ($p<0.05$). There was a significant decrease in the WBC count, neutrophil percentage, hemoglobin concentration, and post-miscarriage NLR among the cases with miscarriage ($p<0.05$). The area under the curve of WBC count, NLR, hs-CRP, and the combination of these three factors for the prediction of late miscarriage varied from 78.0% to 82.6%. The combination of these three factors had the highest specificity of 91.1%, while hs-CRP had the highest sensitivity of 88.9%. WBC count, NLR, and hs-CRP levels are strongly associated with miscarriage during the second trimester of pregnancy, indicating that they are potential predictive biomarkers.

Key words: albumin; C-reactive protein; miscarriage; neutrophil-lymphocyte ratio; procalcitonin; white blood cell count

Corresponding Author:
Dr Y.Y. MA,
Department of Obstetrics and Gynecology, Qilu Hospital,
Cheeloo College of Medicine, Shandong University,
No.107 of Wenhua West Road, Lixia District, Ji'nan,
Shandong Province, China
Fax: +86 0531 82169630 - Tel: +86 0531 82169200
e-mail: yuyanma65@163.com

0393-974X (2021)
Copyright © by BIOLIFE, s.a.s.
This publication and/or article is for individual use only and may not be further reproduced without written permission from the copyright holder.
Unauthorized reproduction may result in financial and other penalties
DISCLOSURE: ALL AUTHORS REPORT NO CONFLICTS OF INTEREST RELEVANT TO THIS ARTICLE.

Threatened miscarriage is common during pregnancy, accounting for approximately 20% of all pregnancies (1). It is diagnosed when a patient presents with vaginal bleeding and a closed cervix before 28 gestational weeks in combination with regular fetal cardiac activity demonstrated by subsequent ultrasound scan. The potential outcomes of threatened miscarriage include miscarriage (delivery before 27 weeks), preterm delivery (delivery between 28 and 36 weeks), and term delivery (delivery between 37 and 41 weeks) (6, 7).

Patients diagnosed with threatened miscarriage are more likely to suffer from depression and anxiety than those with stable pregnancy due to the extreme worry regarding the outcome of the pregnancy (2). Currently, reliable prediction of miscarriage in clinical practice remains a challenge. Many studies have analyzed various peripheral blood biomarkers as predictors for outcomes of threatened miscarriage, as they are non-invasive and easier to study in clinical practice compared to tissue biomarkers. To date, most of these studies have focused on the relationship between circulating biomarkers and pregnancy outcomes during early pregnancy. These biomarkers include traditional markers such as serum β-human chorionic gonadotropin, progesterone, cancer antigen 125, pregnancy-associated plasma protein A, inhibin A, estradiol, estriol, alpha-fetoprotein, human placental lactogen, white blood cell (WBC) count, neutrophil-lymphocyte ratio (NLR), and high-sensitivity C-reactive protein (hs-CRP) (3, 4), as well as novel markers such as placental prokineticin-1, soluble fms-like tyrosine kinase-1, soluble endoglin, and placental growth factor (5). However, there are very few studies on these biomarkers during the second trimester of pregnancy. It is still unknown whether WBC count and serum levels of NLR, hs-CRP, and procalcitonin (PCT) during the second trimester of pregnancy (between 13 and 26 gestational weeks) are related to pregnancy outcome in cases of threatened miscarriage.

Recent studies have shown that mild inflammation is common in normal pregnancies (6). The balance of immunity is essential for implantation and maintenance of pregnancy (7). Although the specific mechanism is still unclear, a shift in this balance and excessive inflammation are related to pregnancy complications such as miscarriage (8-11). Since inflammation is reflected in biomarkers such as WBC count, serum NLR (12, 13), and hs-CRP (14, 15), we hypothesized a correlation between these biomarkers and miscarriage during the second trimester of pregnancy.

As an accurate marker for bacterial infection, PCT is beneficial for differentiating bacterial infections from non-infectious inflammation and viral infections (15). Previous studies have demonstrated that systemic infections caused by bacteria, viruses, and parasites are closely related to 15% of early miscarriages and 66% of late miscarriages (16, 17). Since there are no available data regarding this association, we also included PCT as a biomarker in the present study.

The assessment of the aforementioned markers of systemic inflammation is non-invasive, easy, economical, and quick. Clinicians might find it beneficial to know the predictive biomarker values in cases of threatened miscarriage during the second trimester of pregnancy.

MATERIALS AND METHODS

We retrospectively analyzed 78 patients diagnosed with threatened miscarriage during the second trimester of pregnancy (13−26 gestational weeks) as the test group and 62 asymptomatic controls with term delivery between July 2017 and June 2018 at The Second Hospital of Shandong University, Jinan, Shandong, China.

None of these cases had preterm premature rupture of membranes, hypertension, gestational diabetes mellitus, cervical insufficiency, fetal death, vaginitis, respiratory tract infection, urinary tract infection, intrauterine infection with symptoms (fever, uterine tenderness, increased levels of WBCs and neutrophils), or fetal malformation. In all patients, gestational weeks were calculated from the last menstrual period and confirmed by crown-rump length during the first trimester of pregnancy. Fetal cardiac activity was confirmed every day by an ultrasonic Doppler fetal heartbeat detector, which excluded fetal death in group C. The cervical length of all patients was measured using vaginal ultrasound.

This study was approved by the ethics committee of

the Second Hospital of Shandong University. All samples and data were collected after obtaining informed consent from the participants.

Pregnancy outcomes were acquired from the medical records or telephone follow-ups. Among the 78 cases with late threatened miscarriage, we excluded 10 patients who were lost to follow-up and one patient who underwent unexplained artificial termination of pregnancy. Thus, 67 patients were included in the test group. Based on the pregnancy outcomes, these 67 patients were further divided into two sub-groups: 46 patients with ongoing pregnancy that subsequently ended with live birth (5 cases of late preterm delivery between 34 and 36 gestational weeks and 41 cases of term delivery) (6, 7) and 21 cases with subsequent miscarriage without any surviving infants.

Blood sample tests

Maternal serum samples from group A were obtained at 13–26 gestational weeks. WBC count, red blood cell (RBC) count, serum NLR, hemoglobin, hematocrit, hs-CRP, PCT, and albumin (ALB) were analyzed in the laboratory. For groups B and C, maternal serum samples were routinely obtained as soon as possible after a definite diagnosis was made, and the same biomarkers were analyzed in the laboratory. For group C, maternal serum samples were collected again at 1–3 days after miscarriage to test these biomarkers except ALB. All samples were tested according to the following procedure.

Venous blood samples (2–3 mL) were collected and placed in tubes containing ethylenediaminetetraacetic acid. WBC count, neutrophil and lymphocyte percentages, RBC count, hemoglobin, hematocrit, and hs-CRP levels were determined using an automated blood analyzer (CAL 8000, Mindray, Shenzhen, China).

Venous blood samples (3 mL) were collected and placed in coagulant processing tubes, which were kept for 15 min at room temperature. The serum was separated after centrifugation at 3000 rpm for 10 min at room temperature, the PCT level was examined using the Cobas e602 electrochemiluminescence analyzer (Roche Diagnostics, Basel, Switzerland), and the ALB level was examined using the Cobas c702 electrochemiluminescence analyzer (Roche Diagnostics, Basel, Switzerland).

Statistical analysis

Data collected from the aforementioned tests were analyzed using IBM SPSS Statistics version 24.0 (IBM Corp. Armonk, NY, USA). Data with normal distribution were expressed as mean ± standard deviation. The least significant difference test or Dunnett's T3 test was used for post-hoc multiple comparisons. Data with non-normal distribution were presented as median and interquartile range. The Kruskal-Wallis H test was used for non-normal variables and the *chi*-squared test was used for categorical variables. A paired-samples *t*-test was used to compare the two groups before and after the miscarriage. Statistical significance was set at $p<0.05$.

Diagnostic efficacy was estimated by statistical analysis using the R software, version 3.6.1 (https://www.r-project.org/, The R foundation, Vienna, Austria). The receiver operating characteristic (ROC) curves were plotted using the "pROC" package and 2,000 bootstrap replications were used to compare the area under the ROC curves (AUC).

RESULTS

Basic information of the patients

In this study, 62 patients were included in group A (control group), 46 patients were included in group B, and 21 patients were included in group C. Details of patient inclusion are shown (Fig. 1). In group B, five out of 46 patients underwent preterm labor (late preterm labor, delivery between 34 and 36 gestational weeks) (6, 7). All infants of these five patients survived and exhibited normal growth.

There were no significant differences in age, weight, diastolic blood pressure, cervical length, vaginal bleeding time before the blood test, and gestational weeks among the three groups. Despite a significant difference in systolic blood pressure among the three groups ($p<0.05$), we did not obtain an interpretable pattern. The median time of vaginal bleeding before the blood test was 0 days in groups B and C. There was no significant difference in vaginal bleeding time between the two groups before the blood test. The median time from vaginal bleeding to miscarriage was 5 days in group C (Table I).

Biomarkers of inflammation

Among the biomarkers of systemic inflammation, there was an increase in the WBC count, neutrophil percentage, NLR, and hs-CRP from group A to group

C (all p<0.05). In contrast, ALB and lymphocyte percentage significantly decreased from group A to group C (all p<0.05). No statistically significant difference was observed in the PCT levels among the three groups (p=0.181; Table II and Fig. 2**)**.

Among the biomarkers of anemia, RBC count and hemoglobin level did not differ significantly among the three groups despite higher hematocrit levels in group A than in groups B and C (p=0.026).

Inflammatory biomarkers before and after miscarriage

Statistical analysis was also conducted of the biomarkers of inflammation in group C before and after miscarriage. Since six patients were lost to follow-up after miscarriage, biomarker testing was performed in 15 cases. The results showed a significant decrease in the WBC count, neutrophil percentage, hemoglobin concentration, lymphocyte percentage, and NLR (all p<0.05). However, there was no significant difference between the RBC count, hematocrit, hs-CRP, and PCT levels before miscarriage and those after miscarriage (Table III and Fig. 3).

ROC curve analysis of WBC count, NLR, and hs-CRP for the prediction of late miscarriage

ROC curve analysis was used to estimate the predictive value of WBC count, NLR, and hs-CRP for late miscarriage (Table 4 * ROMAN * MERGEFORMAT). The AUC values of WBC count, NLR, and hs-CRP for predicting late miscarriage were 80.3% (Fig. 4A), 78.0% (Fig. 4B), and 82.6% (Fig. 4C), respectively. Multi-factor ROC curve analysis showed that the AUC of the combination of these three factors was 78.4% (Fig. 4D). No significant difference was observed while comparing any two out of the four AUC results (p>0.05) (Fig. 5). The combination of the three factors had the highest specificity (91.1%), while hs-CRP had the highest sensitivity (88.9%). The cut-off values of WBC count, NLR, hs-CRP, and the combination of

Table I. *Patient characteristics*

Index	Group A (n=62)	Group B (n=46)	Group C (n=21)	***F/Z***	***P***
Age (Year)	29.516 ± 4.152	29.932 ± 5.267	32.048 ± 4.466	2.392	0.096
BMI (kg/m^2)	25.230 ± 4.466	23.807 ± 3.527	24.380 ± 3.691	1.467	0.235
Systolic blood pressure (mmHg)	118.600 ± 8.348	123.682 ± 8.369	118.191 ± 9.714	4.684	0.011
Diastolic blood pressure (mmHg)	70.075 ± 5.740	73.523 ± 6.390	71.143 ± 9.441	2.731	0.070
Gestational weeks (Day)	156.855 ± 28.694	149.500 ± 31.775	139.048 ± 31.027	2.859	0.061
Cervical length	3.715 ± 0.481	3.769 ± 1.074	3.731 ± 0.798	0.061	0.941
Vaginal bleeding time before blood test	-	0 (0, 1.0)	0 (0, 1.0)	-0.185	0.853
Vaginal bleeding occurs to abortion time	-	-	5.0(1.5, 10)	-	-

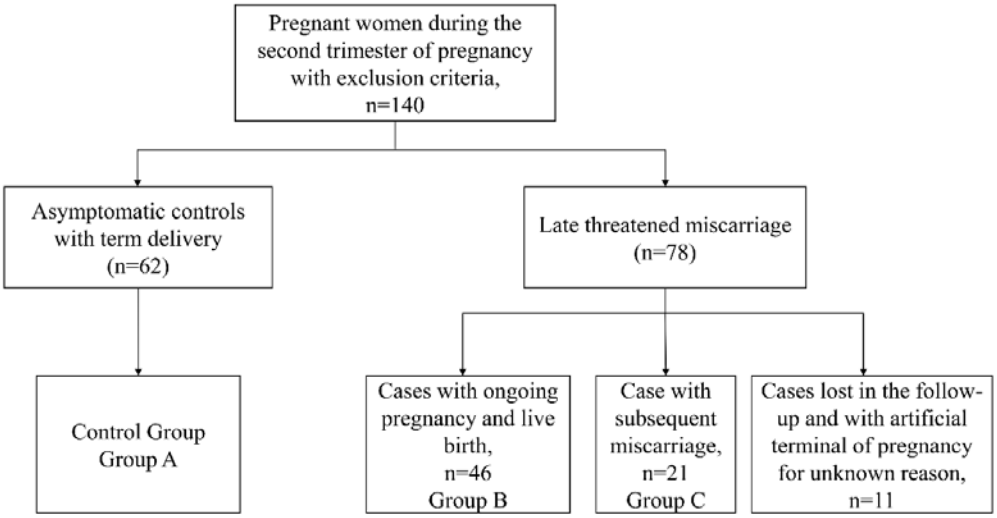


Fig. 1. *Illustration of the inclusion criteria and process*

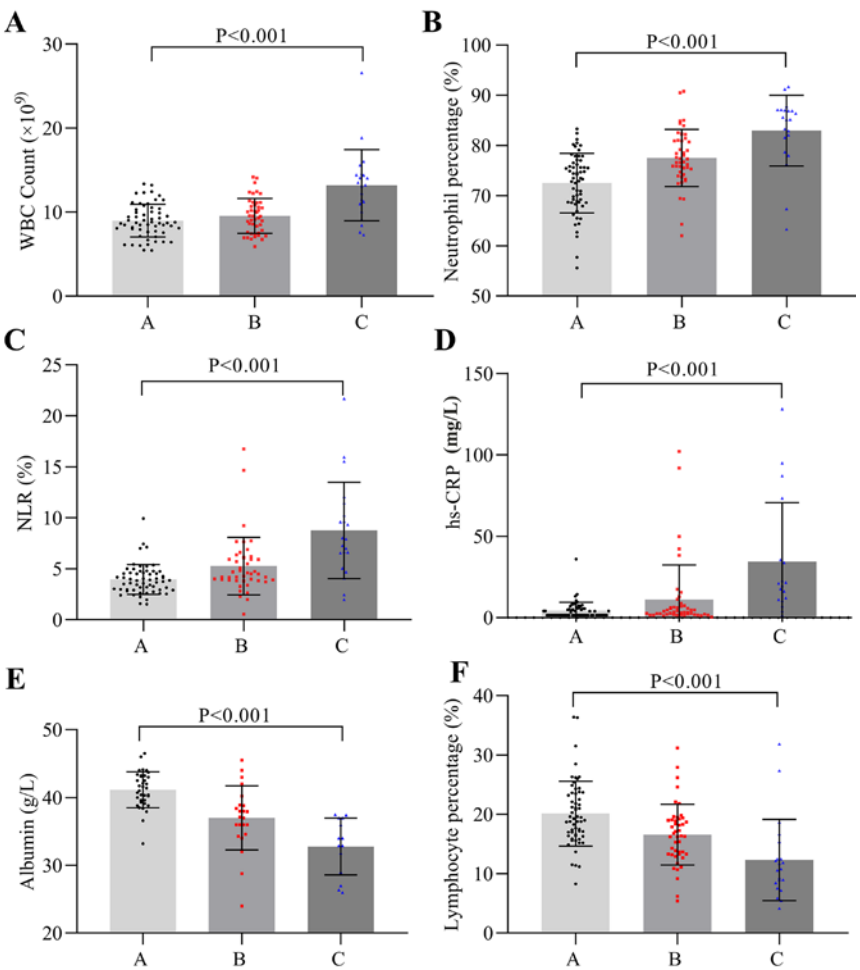


Fig. 2. *Biomarkers of inflammation in the three groups. **A**) White blood cell count (×10⁹), **B**) neutrophil percentage (%), **C**) neutrophil-lymphocyte ratio (%), **D**) hypersensitive C-reactive protein concentration (mg/L), **E**: albumin concentration (g/L), and **F**: lymphocyte percentage (%).*

these three factors were 11.215×10^9/L, 6.474, 7.070 mg/L, and 0.505, respectively.

DISCUSSION

The results of the present study demonstrated that women who suffered miscarriage in the second trimester of pregnancy exhibited significantly higher WBC count, neutrophil percentage, NLR, and hs-CRP and lower lymphocyte percentage than the control group (group A) and the ongoing pregnancy group (group B). In other words, women with late threatened miscarriage who suffered from subsequent miscarriage had a higher WBC count, neutrophil percentage, NLR, and hs-CRP as well as lower lymphocyte percentage than the women from the late threatened miscarriage group with ongoing pregnancy and those with an asymptomatic healthy pregnancy. We also compared the levels of the five biomarkers at the occurrence of the first symptom of threatened miscarriage and those at 2–3 days after miscarriage in women with late miscarriage. The results showed that except for hs-CRP, the remaining four biomarkers showed significant fluctuations. Specifically, the WBC count, neutrophil percentage, and NLR decreased and the lymphocyte percentage increased. We suggest that WBC count, NLR, and hs-CRP during the second trimester of pregnancy are strongly associated with subsequent miscarriage in the second trimester of pregnancy.

Parturition is accompanied by the initiation and activation of WBCs (18, 19) and a large number of inflammatory cells, especially neutrophils and macrophages, that infiltrate the myometrium and the cervix. A previous study (3) reported that NLR, WBC count, neutrophil count, and lymphocyte count at the sixth gestational week were useful in assessing the risk of subsequent spontaneous miscarriage. Our results corroborated the results of previous studies, suggesting that WBC count and NLR showed a

Table II. S*erum levels of biomarkers of the three groups*

Index	Group A (n=62)	Group B (n=46)	Group C (n=21)	F/χ^2	*P*
WBC count	8.982±1.952	9.546±2.081	13.199±4.237	22.467	**<0.001**[b,c]
Neutrophil percentage (%)	72.486±5.903	75.959±11.727	82.938±7.059	25.220	**<0.001**[b,c]
Lymphocyte percentage	20.136±5.458	16.584±5.102	12.310±6.834	16.233	**<0.001**[a,b,c]
NLR	3.954±1.466	5.266±2.822	8.764±4.721	23.753	**<0.001**[a,b,c]
RBC count	3.849±0.353	3.719±0.341	3.700±0.279	2.553	**0.082**
Hemoglobin	117.288±10.891	114.978±9.917	115.000±8.614	0.794	0.454
Hematocrit	34.951±2.798	33.944±2.306	33.352±2.405	3.756	**0.026**[a,b]
CRP	1.600 (1.60, 5.625)	3.480 (2.025, 7.030)	20.460 (10.908, 44.956)	27.703	**<0.001**[b,c]
PCT	0.029 (0.022, 0.040)	0.040(0.020, 0.062)	0.041 (0.020, 0.090)	3.416	0.181
ALB	41.133±2.656	36.978±4.26	32.779±4.187	27.367	**<0.001**[a,b,c]

[a] significant difference between group A and group B, [b] between group A and group C, and [c] between group B and group C. ALB: albumin; HCT: hematocrit value; NLR: neutrophil-lymphocyte ratio; CRP: C-reaction protein; PCT: procalcitonin.

predictive value for miscarriage not only in the first trimester (3) of pregnancy but also in the second trimester. In the present study, the predictive values of WBC count and NLR were comparable (AUC values: 80.3% and 78.0%, respectively) and the specificity of these two biomarkers was also the same (82.2%). However, NLR exhibited higher sensitivity (76.2%) than WBC count. Furthermore, when compared with the specificity and the sensitivity in the first trimester of pregnancy (57% and 67%, respectively) (3), NLR had a much higher specificity and sensitivity for predicting miscarriage in the second trimester.

Moreoer, hs-CRP was also found to be strongly associated with miscarriage in the second trimester

Table III. *The serum level of biomarkers before and after miscarriage in Group C*

Index	Before miscarriage (n=15)	After miscarriage (n=15)	*t/Z*	*P*
WBC count	14.037±3.109	9.937±5.279	2.842	**0.029**
Neutrophil percentage	84.743 ±5.546	71.729±8.540	4.842	**0.003**
Lymphocyte percentage	10.657±4.848	20.643 ±7.701	-3.724	**0.010**
RBC count	3.739±0.280	3.391±0.478	2.190	0.071
Hemoglobin	113.143 ±10.172	101.429 ±14.305	2.461	**0.049**
Hematocrit	33.429±2.252	30.543±3.980	2.086	0.082
CRP	20.460 (10.907, 44.955)	17.400(14.410, 25.100)	-0.936	0.349
PCT	0.041 (0.020, 0.895)	0.067 (0.032, 0.076)	-1.533	0.125
NLR	9.654±4.649	4.407±3.320	3.899	**0.008**

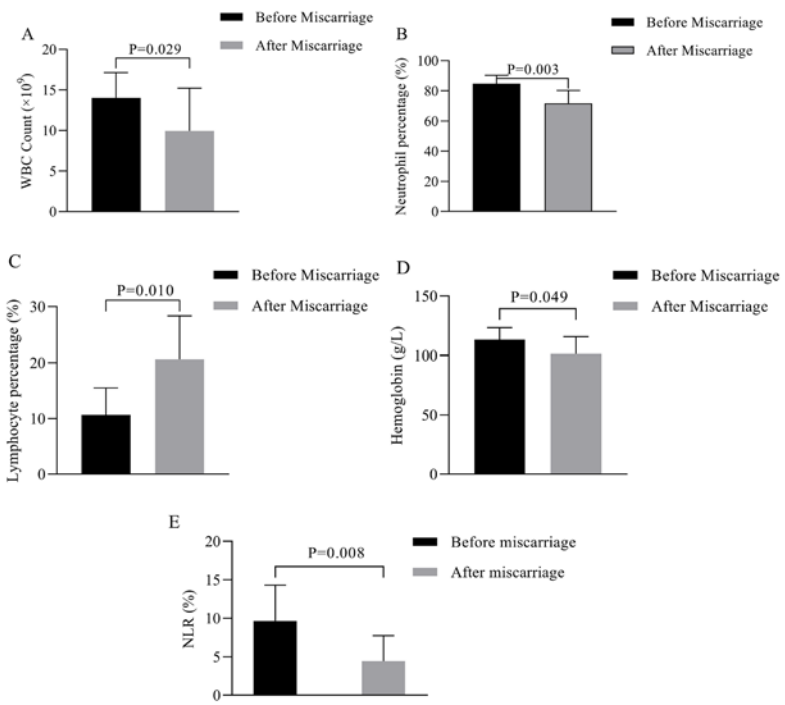


Fig. 3. *Inflammatory biomarkers before and after miscarriage. **A)** White blood cell count (×10⁹), **B)** neutrophil percentage (%), **C)** lymphocyte percentage (%), **D)** hemoglobin concentration (g/L), and **E)** neutrophil-lymphocyte ratio (%).*

Table IV. *ROC curve analysis of WBC count, NLR, CRP and combined biomarkers for late miscarriage*

Factor	AUC (95% CI)	Specificity	Sensitivity	Cut-off value
CRP	0.826 (0.710~0.942)	0.761	0.889	7.070mg/L
WBC	0.803 (0.679~0.927)	0.822	0.714	11.215×10^9/L
NLR	0.780 (0.644~0.916)	0.822	0.762	6.474
Combined biomarkers	0.784 (0.645~0.923)	0.911	0.611	0.505

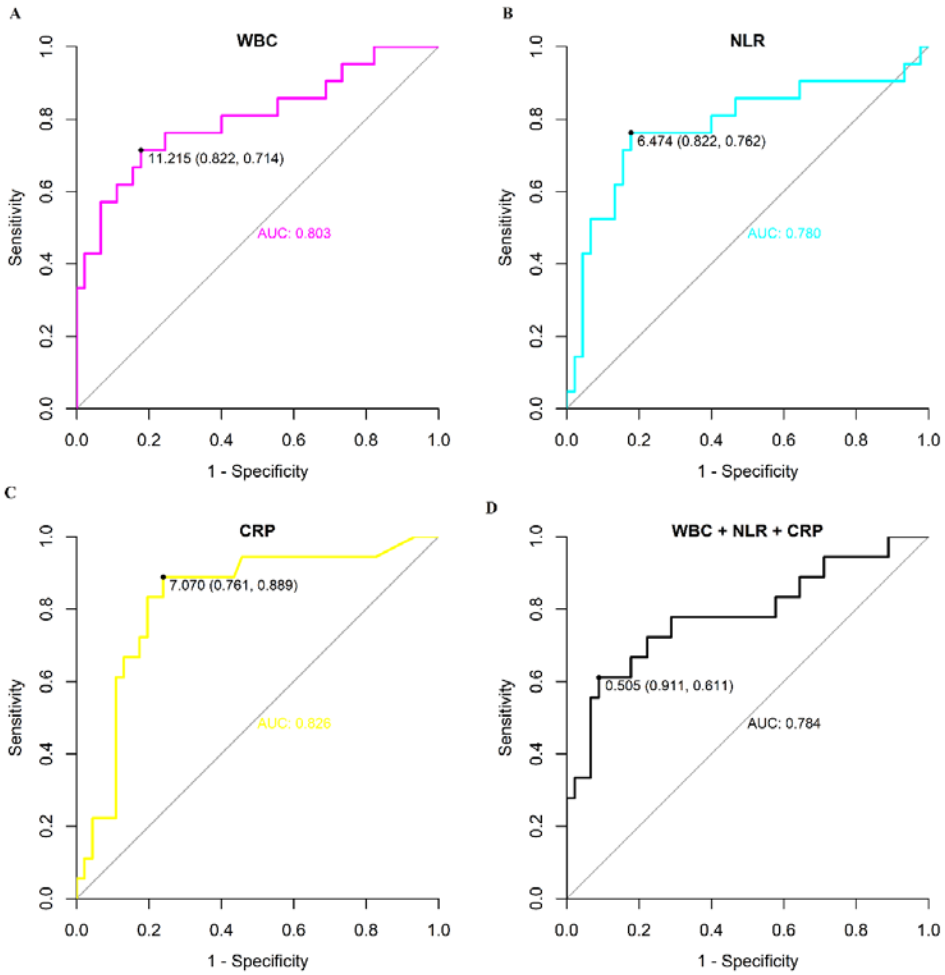


Fig. 4. *Receiver operating curve analysis of white blood cell (WBC) count, neutrophil-lymphocyte ratio (NLR), high-sensitivity C-reactive protein (hs-CRP), and the combination of these three factors for the prediction of late miscarriage.* ***A****) The area under the curve (AUC) of WBC count was 80.3%, with a specificity of 82.2%, sensitivity of 71.4%, and a cut-off value of 11.215×10⁹.* ***B****) The AUC of NLR was 78.0%, with a specificity of 82.2%, sensitivity of 76.2%, and a cut-off value of 6.474.* ***C****) The AUC of hs-CRP was 82.6%, with a specificity of 76.1%, sensitivity of 88.9%, and a cut-off value of 7.070 mg/L.* ***D****) The AUC of the combination of these three factors was 78.4%, with a specificity of 91.1%, sensitivity of 61.1%, and a cut-off value of 0.505.*

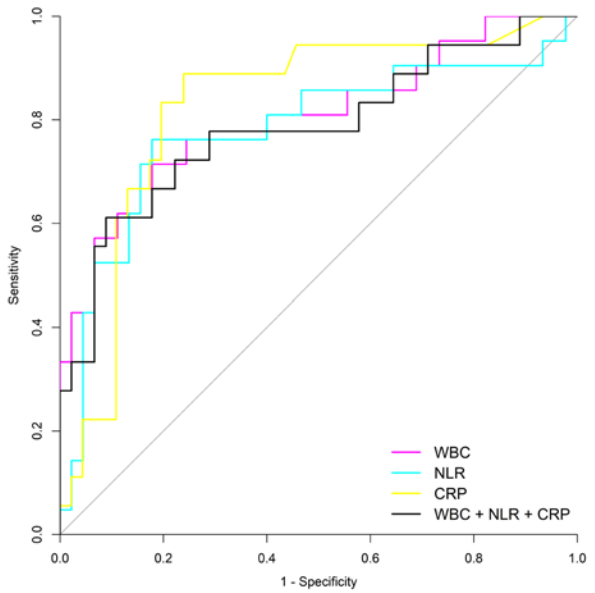


Fig. 5. *Comparison of the area under the curve of white blood cell count, neutrophil-lymphocyte ratio, high-sensitivity C-reactive protein, and the combination of these three factors.*

of pregnancy despite no association with ongoing pregnancy in cases of threatened miscarriage during the second trimester of pregnancy. It is an acute-phase protein produced in response to inflammation caused by infections with bacteria and some types of viruses as well as in response to non-infective tissue injuries. It has been studied extensively in the fields of physiology and pathology of pregnancy. Previous studies indicated that the hs-CRP levels in the serum and in the placenta exhibited good diagnostic performance in the prediction of imminent preterm delivery (20), maternal adverse outcomes (21), and miscarriages (22). We observed significantly higher serum levels of hs-CRP in the present study, echoing the results reported by Kim et al. (22). However, some researchers have reported contradictory results regarding the relationship between hs-CRP levels and miscarriage. Jauniaux et al. indicated that the role of hs-CRP is limited and does not provide additional information for the management of threatened spontaneous abortion (23). Another study (24) reported that the hs-CRP levels in early pregnancy were not associated with miscarriage before 21 gestational weeks. In contrast, we found that the hs-CRP levels during the second trimester of pregnancy were consistently increased in women with subsequent late miscarriage. This inconsistency in findings may be due to the difference in racial and ethnic composition and disparate gestational ages when the serum samples were obtained. Different gestational ages were accompanied by fluctuations in the hs-CRP levels (25), resulting in inconsistencies in the correlation between the hs-CRP levels and miscarriage. In our study, the close relationship between the hs-CRP levels during the second trimester of pregnancy and late miscarriage may be due to the association of chronic intrauterine bleeding with chronic oxidative stress within the gestational sac (26). This results in the release of a potent mix of pro-inflammatory cytokines and trophoblastic aponeurotic debris into the maternal circulation, inducing an increase in the hs-CRP levels. The AUC of hs-CRP was 82.6% and the sensitivity was 88.9%. These values were higher than the AUC and sensitivity of WBC count and NLR, indicating that hs-CRP has valuable application prospects in predicting late miscarriage.

In the present study, WBC count, NLR, and hs-CRP levels during the second trimester of pregnancy were strongly associated with subsequent miscarriage in cases of threatened miscarriage. These biomarkers had a high predictive value with AUC values of 78.0–82.6%. The AUC values of these biomarkers were comparable and hs-CRP had the highest sensitivity of 88.9%, while the combination of these three factors had the highest specificity of 91.1%. These results suggest that a single biomarker and the combination of these biomarkers should be used to achieve the best predictive effect for late miscarriage.

The ALB level was also explored in terms of its correlation with late miscarriage. To the best of our knowledge, there has been no research related to this correlation. Serum ALB level has been mistakenly used as a biomarker of nutritional status in clinical practice, but there is a poor correlation between nutritional intake and serum ALB levels (27, 28). Instead, hypoalbuminemia has been found to be an epiphenomenon of inflammation, which results in

microvascular permeability and increased escape of ALB (29-31). Therefore, hypoalbuminemia reflects the inflammatory state rather than the nutritional state. In the present study, women with late miscarriage showed exacerbated inflammation with a higher WBC count, NLR, and hs-CRP than the other two groups. The severity of this inflammation was also demonstrated by comparing ALB levels among the three groups. Specifically, the ALB levels decreased significantly from group A to group C, indicating a negative correlation between the ALB levels and late threatened miscarriage as well as between the ALB levels and late miscarriage. Theoretically, our data on ALB level, an indicator of a negative association with inflammation, provides more support for the role of inflammation in late miscarriage.

The relationship between PCT and late miscarriage has not been studied previously, thus, the present is the first validation study regarding the predictive role of this biomarker for late miscarriage. The results showed that PCT did not correlate with late threatened miscarriage or late miscarriage. There was no significant difference in PCT levels between groups B and C in the time of vaginal bleeding before the blood test (median: 0 days). This finding indicates that the levels of biomarkers in groups B and C in the present study reflect the inflammatory condition immediately after the occurrence of the first symptom of late threatened miscarriage. Therefore, the PCT levels can reflect the condition of bacterial infection at the time of late miscarriage. The PCT levels in the present study were comparable among the three groups and between the two time points (before and after late miscarriage), demonstrating that bacterial infection was not the primary cause of late miscarriage.

In the present study, none of the patients from the three groups exhibited anemia and the hemoglobin level was not correlated with late miscarriage. Despite the trend of RBC count, hemoglobin, and hematocrit in group A being higher than those in the other two groups, there were no significant differences among the three groups ($p>0.05$). Among women with late threatened miscarriage, there was no consistent pattern regarding differences in the levels of these three biomarkers between patients with live birth and those with late miscarriage. We could not confirm a definite association between hemoglobin level and late miscarriage based on these results. In addition, there was a decrease in the hemoglobin levels after miscarriage in the present study, which was possibly due to bleeding caused by miscarriage.

The limitations of the present study include its retrospective design, the use of data from a single tertiary center, and the limited sample size. These factors limit the ability of the study to calculate the population-based rates. Despite these limitations, this was the first study to evaluate the association between miscarriage and biomarkers such as WBC count, NLR, hs-CRP, and PCT during the second trimester of pregnancy. Further studies are needed to determine the specific mechanisms of late miscarriage.

We found that WBC count, NLR, and hs-CRP levels during the second trimester of pregnancy were strongly associated with miscarriage and had potential predictive value for late miscarriage. However, PCT showed no association with late miscarriage. The predictive value was comparable among WBC count, NLR, hs-CRP, and the combination of these three factors. The combination of these three factors had the highest specificity, while hs-CRP had the highest sensitivity for the prediction of late miscarriage.

Among pregnant women with late threatened miscarriage, those with subsequent miscarriage exhibited higher levels of peripheral blood white blood cell (WBC) count, neutrophil-to-lymphocyte ratio (NLR), high-sensitivity C-reactive protein (hs-CRP), and lower levels of albumin than those with ongoing pregnancy and subsequent live birth. In contrast, procalcitonin levels were comparable between the two groups. The predictive value was comparable among WBC count, NLR, hs-CRP, and the combination of these three factors. The combination of these three biomarkers had the highest specificity, while hs-CRP had the highest sensitivity for the prediction of late miscarriage.

ACKNOWLEDGEMENTS

This work was supported by the National Natural Science Foundation of China (grant numbers

81702538); the Natural Science Foundation of Shandong Province (No. ZR201702160271); and the Foundation for Young Scholars of The Second Hospital of Shandong University(2018YT11).

REFERENCES

1. Lee HJ, Park TC, Kim JH, Norwitz E, Lee B. The influence of oral dydrogesterone and vaginal progesterone on threatened abortion: a systematic review and meta-analysis. Biomed Res Int 2017; 2017:3616875.
2. Zhu CS, Tan TC, Chen HY, Malhotra R, Allen JC, Østbye T. Threatened miscarriage and depressive and anxiety symptoms among women and partners in early pregnancy. J Affect Disord 2018; 237:1-9.
3. Bas FY, Tola EN, Sak S, Cankaya BA. The role of complete blood inflammation markers in the prediction of spontaneous abortion. Pak J Med Sci 2018; 34(6):1381-5.
4. Phupong V, Hanprasertpong T. Combined maternal serum inhibin A and embryonic/fetal heart rate for the prediction of pregnancy outcome in a first-trimester threatened abortion. J Med Assoc Thai 2011; 94(5):529-34.
5. Jayasena CN, Abbara A, Comninos AN, et al, Bloom SR, Dhillo WS. Novel circulating placental markers prokineticin-1, soluble fms-like tyrosine kinase-1, soluble endoglin and placental growth factor and association with late miscarriage. Hum Reprod 2016; 31(12):2681-8.
6. Gomez-Lopez N, Motomura K, Miller D, Garcia-Flores V, Galaz J, Romero R. Inflammasomes: their role in normal and complicated pregnancies. J Immunol 2019; 203(11):2757-69.
7. Raghupathy R, Kalinka J. Cytokine imbalance in pregnancy complications and its modulation. Frontiers in Bioscience: A Journal & Virtual Library 2008; 13:985-94.
8. Kwak-Kim J, Bao S, Lee SK, Kim JW, Gilman-Sachs A. Immunological modes of pregnancy loss: inflammation, immune effectors, and stress. Am J Reprod Immunol 2014; 72(2):129-40.
9. Ehrentraut S, Sauss K, Neumeister R, et al. Human miscarriage is associated with dysregulations in peripheral blood-derived myeloid dendritic cell subsets. Front Immunol 2019; 10:2440.
10. He M, Jiang M, Zhou Y, et al. Impaired Gal-9 Dysregulates the PBMC-Induced Th1/Th2 Imbalance in Abortion-Prone Matings. J Immunol Res 2018; 2018:9517842.
11. Kheshtchin N, Gharagozloo M, Andalib A, Ghahiri A, Maracy MR, Rezaei A. The expression of Th1- and Th2-related chemokine receptors in women with recurrent miscarriage: the impact of lymphocyte immunotherapy. Am J Reprod Immunol 2010; 64(2):104-12.
12. Celikbilek M, Dogan S, Ozbakır O, et al. Neutrophil-lymphocyte ratio as a predictor of disease severity in ulcerative colitis. J Clin Lab Anal 2013; 27(1):72-6.
13. Wang D, Yang JX, Cao DY, et al. Preoperative neutrophil-lymphocyte and platelet-lymphocyte ratios as independent predictors of cervical stromal involvement in surgically treated endometrioid adenocarcinoma. Onco Targets Ther 2013; 6:211-6.
14. Sierra R, Rello J, Bailén MA, Benítez E, Gordillo A, León C, Pedraza S. C-reactive protein used as an early indicator of infection in patients with systemic inflammatory response syndrome. Intensive Care Med 2004; 30(11):2038-45.
15. Simon L, Gauvin F, Amre DK, Saint-Louis P, Lacroix J. Serum procalcitonin and C-reactive protein levels as markers of bacterial infection: a systematic review and meta-analysis. Clin Infect Dis 2004; 39(2):206-17.
16. Giakoumelou S, Wheelhouse N, Cuschieri K, Entrican G, Howie SE, Horne AW. The role of infection in miscarriage. Hum Reprod Update 2016; 22(1):116-33.
17. Srinivas SK, Ma Y, Sammel MD, Chou D, McGrath C, Parry S, Elovitz MA. Placental inflammation and viral infection are implicated in second trimester pregnancy loss. Am J Obstet Gynecol 2006; 195(3):797-802.
18. Yuan M, Jordan F, McInnes IB, Harnett MM, Norman JE. Leukocytes are primed in peripheral blood for activation during term and preterm labour. Mol Hum Reprod 2009; 15(11):713-24.
19. Osman I, Young A, Ledingham MA, Thomson AJ, Jordan F, Greer IA, Norman JE. Leukocyte density and pro-inflammatory cytokine expression in human fetal membranes, decidua, cervix and myometrium before and during labour at term. Mol Hum Reprod

2003; 9(1):41-5.
20. Park H, Park KH, Kim YM, Kook SY, Jeon SJ, Yoo HN. Plasma inflammatory and immune proteins as predictors of intra-amniotic infection and spontaneous preterm delivery in women with preterm labor: a retrospective study. BMC Pregnancy Childbirth 2018; 18(1):146.
21. Vecchié A, Bonaventura A, Carbone F, et al. C-Reactive Protein Levels at the Midpregnancy Can Predict Gestational Complications. Biomed Res Int 2018; 2018:1070151.
22. Kim EN, Yoon BH, Jeon EJ, et al. Placental deposition of C-reactive protein is a common feature of human pregnancy. Placenta 2015; 36(6):704-7.
23. Jauniaux E, Gulbis B, Jamil A, Jurkovic D. Evaluation of the role of maternal serum high-sensitivity C-reactive protein in predicting early pregnancy failure. Reprod Biomed Online 2015; 30(3):268-74.
24. Boggess KA, Lieff S, Murtha AP, Moss K, Jared H, Beck J, Offenbacher S. Maternal serum C-reactive protein concentration early in pregnancy and subsequent pregnancy loss. Am J Perinatol 2005; 22(6):299-304.
25. Kalva-Borato DC, Ribas JT, Parabocz GC, Borba LM, Maciel MAS, Santos FAD, Vellosa JCR. Biomarkers in Non-Complicated Pregnancy: Insights About Serum Myeloperoxidase and Ultrasensitive C-Reactive Protein. Exp Clin Endocrinol Diabetes 2019; 127(9):585-9.
26. Burton GJ, Yung HW, Cindrova-Davies T, Charnock-Jones DS. Placental endoplasmic reticulum stress and oxidative stress in the pathophysiology of unexplained intrauterine growth restriction and early onset preeclampsia. Placenta 2009; 30(S):S43-8.
27. Cederholm T, Bosaeus I, Barazzoni R, et al. Diagnostic criteria for malnutrition-An ESPEN Consensus Statement. Clin Nutr. 2015; 34(3):335-40.
28. Lee JL, Oh ES, Lee RW, Finucane TE. Serum albumin and prealbumin in calorically restricted, nondiseased individuals: a systematic review. Am J Med 2015; 128(9):1023.e1-22.5.
29. Fleck A, Raines G, Hawker F, Trotter J, Wallace PI, Ledingham IM, Calman KC. Increased vascular permeability: a major cause of hypoalbuminaemia in disease and injury. Lancet 1985; 1(8432):781-4.
30. Soeters PB, Wolfe RR, Shenkin A. Hypoalbuminemia: Pathogenesis and Clinical Significance. JPEN J Parenter Enteral Nutr 2019; 43(2):181-93.
31. Soeters PB, Grimble RF. The conditional role of inflammation in pregnancy and cancer. Clin Nutr 2013; 32(3):460-5.

Neurohormonal markers in chronic rhinosinusitis

R.A. Compton[1], A.R. Lonergan[2], I. Tsillioni[3], P. Conti[4], G. Ronconi[5], D. Lauritano[6], E.E. Rebeiz[1†] and T.C. Theoharides[3,7]

[1]Department of Otolaryngology, Tufts Medical Center, Boston, MA, USA; [2]Department of Otolaryngology, University of California Irvine, Orange, CA, USA; [3]Laboratory of Molecular Immunopharmacology and Drug Discovery, Department of Immunology, Tufts University School of Medicine, Boston, MA, USA; [4]Postgraduate Medical School, University of Chieti, Pescara, Italy; [5]Clinica dei Pazienti del Territorio, Fondazione Policlinico Gemelli, Rome, Italy; [6]University of Milan-Bicocca, Medicine and Surgery Department, Centre of Neuroscience of Milan, Italy; [7]School of Graduate Biomedical Sciences, Tufts University School of Medicine, Boston, MA, USA; [†]Deceased

Received June 3, 2021- Accepted June 20, 2021

Chronic rhinosinusitis (CRS), especially with nasal polyps, continues to elude precise pathogenesis and effective treatment. Prior work in our laboratory demonstrated interleukin-33 (IL-33) and Substance P (SP) activation of mast cells, and inhibitory effect of interleukin-37 (IL-37). Our objective is to study the expression of these neurohormonal mediators in mast cell stimulation of nasal polyposis. This was a prospective research study involving collection of nasal lavage fluid and nasal polyp tissue from adult patients with CRS. The study was divided into two arms. First, nasal lavage fluid was collected from normal controls, and patients with allergic rhinitis, CRS, or CRS with nasal polyposis. The second arm was collection of nasal tissue from normal controls undergoing inferior turbinoplasty, or patients with nasal polyposis. Enzyme-linked immunosorbent assay and quantitative polymerase chain reaction techniques were used to determine levels in the lavage fluid and relative gene expression in the tissue of SP, IL-33, and IL-37. In total, 70 lavage and 23 tissue specimens were obtained. The level of SP was highest in patients with polyps; however, gene expression was reduced compared to normal controls. The level of IL-33 was reduced in patients with polyps as compared to patients with allergy and sinusitis, and its gene expression was not significantly different from normal controls. IL-37 was elevated in the lavage fluid of patients with nasal polyps and its gene expression was increased in the polyp tissue. Levels of SP and IL-37 were elevated in the lavage fluid of patients with nasal polyps as compared to normal controls and other sinonasal pathologies, and gene expression of IL-37 was significantly increased in the polyp tissue itself. These findings implicate these neurohormonal molecules in the pathophysiology of nasal polyposis and provide possible novel therapeutic targets.

Nasal polyps are benign inflammatory masses that arise from the nasal mucosa, representing a subgroup of chronic rhinosinusitis (CRS) (1). The pathophysiology of CRS with nasal polyposis (CRSwNP) is complex, involving both host and environmental factors. Proposed mechanisms include

Keywords: nasal polyps; mast cells; chronic sinusitis; inflammation; substance P; interleukin-33; interleukin-37

Corresponding Author:
Theoharis C. Theoharides, MS, MPhil, PhD, MD
Department of Immunology,
Tufts University School of Medicine,
136 Harrison Avenue, Suite J304, Boston, MA 02111, USA
Tel.: +1 617 636 6866 - Fax: +1 617 636 2456
e-mail: theoharis.theoharides@tufts.edu

0393-974X (2021)
Copyright © by BIOLIFE, s.a.s.
This publication and/or article is for individual use only and may not be further reproduced without written permission from the copyright holder.
Unauthorized reproduction may result in financial and other penalties
DISCLOSURE: ALL AUTHORS REPORT NO CONFLICTS OF INTEREST RELEVANT TO THIS ARTICLE.

defects in the airway epithelial barrier, microbial surface colonization, activation of the body's innate and adaptive immune system, and tissue remodeling (2). The mast cell (MC), the body's major effector cell of allergic reactions, is found in high numbers in nasal polyps (3). MC are stimulated via exposure to an antigen that cross-links a specific immunoglobulin, but can also be triggered by cytokines, neuropeptides, and microbes (4). While MC are associated with nasal polyposis, the precise mechanism of this process has not been elucidated (3-7).

Our laboratory has shown that SP, a pro-inflammatory peptide secreted by sensory neurons, can activate MC (8). SP has a widespread distribution in the central and peripheral nervous systems with effects on nearly all organ systems (9). The role of SP in other inflammatory disease processes, such as arthritis, has been studied extensively (10, 11), but there have been few reports describing its role in nasal polyposis (12-14). In a pilot study, we demonstrated that SP was detectable in the nasal lavage fluid of patients with CRSwNP (15). Previous work from our laboratory also reported that the action of SP on vascular endothelial growth factor (VEGF) in MC was enhanced by the "alarmin" cytokine IL-33 (16). The expression of IL-33 was reported to be elevated in nasal polyposis in association with eosinophilia (17), and this is mirrored in other eosinophilic-mediated conditions such as eosinophilic esophagitis and asthma (18-19). In contrast, however, one recent study demonstrated significantly reduced tissue levels of IL-33 in those patients with CRSwNP *versus* those without nasal polyps (CRSsNP) (20). The expected pattern of IL-33 release in nasal polyposis and its relationship to SP-activation of MC is thus not fully defined.

One additional cytokine that warrants study in the mechanism of nasal polyposis is IL-37, a unique anti-inflammatory molecule that binds to the IL-18-receptor and inhibits release of pro-inflammatory cytokines (21). In experimental studies, IL-37 protected mice against inflammation including lung and spinal cord injury, coronary artery disease, and arthritis (22). Mucosal MC-stimulated cellular inflammatory response in the gut could be inhibited by IL-37 (23). IL-37 has been infrequently studied in nasal polyposis. One study showed that IL-37 levels in nasal secretions were reduced in concert with increased eosinophilic inflammation in patients with eosinophilic CRSwNP (24). A similar study reported significantly decreased mRNA and protein expression of IL-37 in nasal polyp tissue (25).

The aim of this study was to investigate levels and gene expression of SP, IL-33, and IL-37 in patients with CRSwNP, CRSsNP, allergic rhinitis, and normal controls.

MATERIALS AND METHODS

Participants

Patients were evaluated in the otolaryngology clinic at Tufts Medical Center (TMC) as part of their clinical care between July 2017 and March 2019. Consent was obtained from all patients participating in the study. Patients were recruited for collection of nasal lavage and collection of nasal tissue. Approval for this study was obtained from the TMC Institutional Review Board.

Nasal lavage

Nasal lavage samples were collected from four groups: (i) normal controls, (ii) allergic rhinitis, (iii) CRSsNP, and (iv) CRSwNP. The controls consisted of patients requiring nasal endoscopy for an unrelated complaint such as epistaxis or patients who were found to have negative allergy testing and no evidence of sinusitis or polyposis. The lavage technique consisted of nasal endoscopy performed with a rigid endoscope to facilitate direct suctioning of 0.5 mL of mucous into a Lukens trap® (Cardinal Health, OH, USA) from along the nasal floor using a rigid suction. The samples were mixed with 1 mL of sterile normal saline to clear any mucous stuck in the trap. The samples were subsequently centrifuged at 350 g for 10 minutes; the supernatant fluid was collected, labeled, and stored at -80°F until further analysis.

Nasal tissue

The second arm of the study consisted of collection of nasal tissue from two groups: (i) normal controls, and (ii) patients with CRSwNP. In both groups, specimens were collected in the operating room as part of the surgical-procedure. Polyps were sampled with a forceps and brought to the laboratory on ice. They were then

cut into two specimens, one of which was treated with RNAlater (Thermo Fisher Scientific, MA); both were stored at -80°F until further analysis. Control tissue in this setting consisted of a small sample of mucosa taken from the anterior face of the inferior turbinate in patients undergoing inferior turbinate reduction. Such tissue was processed similarly to the polyp tissue.

Mediator levels in lavage fluid

To determine the levels of mediators in the lavage fluid, enzyme-linked immunosorbent assay (ELISA) was employed. Specifically, ELISA kits were used to measure lavage SP (Phoenix Pharmaceuticals, Inc., CA, USA), IL-33 and IL-37 (R&D Systems, MN, USA) according to manufacturer's protocols.

Determination of relative gene expression

To determine relative gene expression, 30 mg of specimen that had been stored in RNAlater (Thermo Fisher Scientific, MA, USA) was weighed. Total RNA was then isolated using the RNeasy Mini Kit (Qiagen, CA, USA) per manufacturer's protocol. Reverse transcription was performed with 200 ng of total RNA using the iScript cDNA synthesis kit (Bio-Rad, CA, USA). Quantitative real-time polymerase chain reaction (qPCR) was then performed using TaqMan gene expression assays with validated oligonucleotide primers (Applied Biosystems, CA, USA). Samples were run for 45 cycles using the Applied Biosystems 7300 Real-Time PCR system. Relative mRNA abundance was determined from standard curves run for each experiment. Gene expression was normalized to glyceraldehyde 3-phosphate dehydrogenase endogenous control.

Statistical analysis

All data were validated and inspected for outliers. The results are presented as scattergrams, with symbols representing individual data points and the horizontal lines representing the median and interquartile range for each group. Normality of distribution was checked with the Shapiro-Wilk test. Comparisons between the nasal polyp group and control groups were performed using the nonparametric Mann-Whitney U test. A result was considered significant at a p-value of <0.05. The analysis was performed by using the GraphPad Prism version 8.0 software (GraphPad Software, CA, USA).

RESULTS

Demographics

In total, 70 nasal lavage samples were collected from controls and patients with allergic rhinitis, CRSsNP, and CRSwNP (Table I). The allergic rhinitis group was younger (median age 35 years) and had a greater female representation (84%) than the other groups of patients. Asian ethnicity was represented

Table I. *Demographic profile of groups collected for nasal lavage fluid*

	NC	AR	CRSsNP	CRSwNP
Number	15	19	13	23
Age (median)	56	35	51	56
Gender (N, %)				
Female	7 (47%)	16 (84%)	8 (62%)	8 (35%)
Male	8 (53%)	3 (16%)	5 (38%)	15 (65%)
Ethnicity (N, %)				
Caucasian	9 (60%)	6 (32%)	8 (62%)	12 (52%)
Black or African American	2 (13%)	0 (0%)	0 (0%)	2 (9%)
Asian	2 (13%)	12 (63%)	3 (23%)	7 (30%)
Latino	2 (13%)	1 (5%)	2 (15%)	2 (9%)

NC: normal controls; AR: allergic rhinitis; CRSwNP: chronic rhinosinusitis with nasal polyposis; CRSsNP: chronic rhinosinusitis without nasal polyposis.

to a greater extent in patients with allergic rhinitis (63%) and patients with CRSwNP (30%) than in other groups. For tissue sampling, 20 polyp samples were collected, and three normal control samples were collected from the anterior surface of the inferior turbinate (Table II). The groups were roughly similar in age; however, the normal control subset did not include any female subjects. Caucasian ethnicity was represented in 50% of patients, Asian ethnicity in 30% of patients, and Black or African American ethnicity in 20% of the patients from whom polyp tissue was collected.

Substance P

SP was detected in the nasal lavage fluid from the four study groups (Fig. 1). The median level was highest in the CRSwNP group (2.70 ng/mL), which was significant when compared to patients with allergic rhinitis (0.92 ng/mL, p = 0.001), but not when compared to CRSsNP (2.09 ng/mL) and

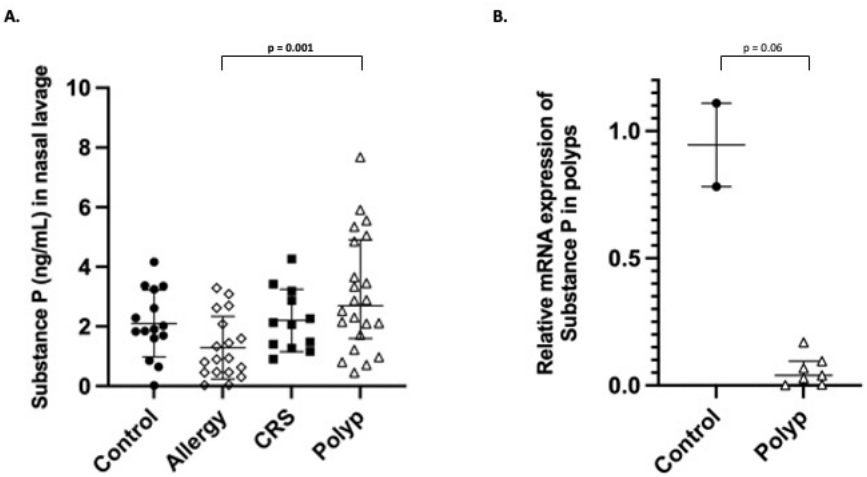


Fig. 1. ***A)*** *Concentrations of substance P in the nasal lavage fluid of patients with nasal polyps versus normal controls, allergy, and chronic rhinosinusitis (CRS).* ***B)*** *Relative mRNA expression in nasal polyp tissue as compared to normal nasal mucosa. Significant differences are denoted with a horizontal bar and p-value.*

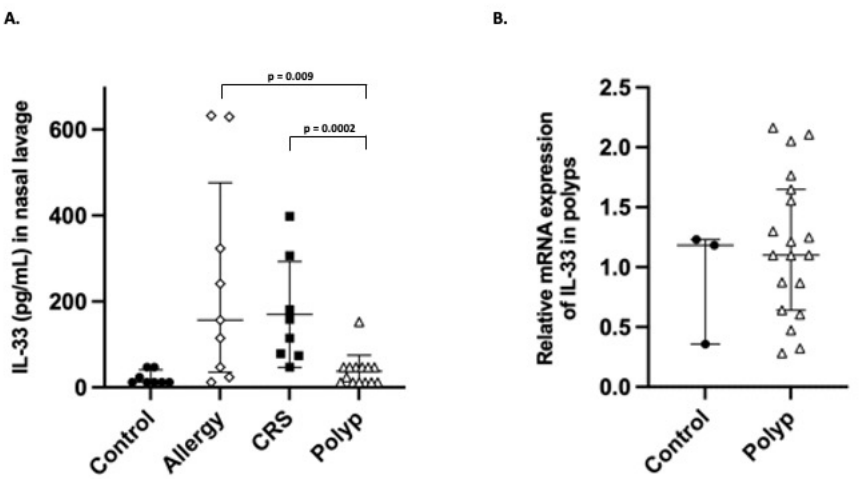


Fig. 2. ***A)*** *Concentrations of interleukin-33 in the nasal lavage fluid of patients with nasal polyps versus normal controls, allergy, and chronic rhinosinusitis (CRS).* ***B)*** *Relative mRNA expression in nasal polyp tissue as compared to normal nasal mucosa. Significant differences are denoted with a horizontal bar and p-value.*

normal controls (1.91 ng/mL). The gene expression of SP trended towards reduced in nasal polyp tissue as compared to normal controls (p = 0.06) (Fig. 1).

Interleukin-33

Median levels of IL-33 were significantly decreased in patients with CRSwNP (35.15 pg/mL) as compared to patients with allergic rhinitis (156.6 pg/mL, p=0.009) and patients with CRSsNP (158.2 pg/mL, p=0.0002) (Fig. 2). There was no statistical difference between levels in patients with CRSwNP as compared to controls (11.70 pg/mL). There was also no difference in relative mRNA expression between polyp tissue and normal nasal tissue (Fig. 2).

Interleukin-37

IL-37 was significantly increased in the lavage fluid of patients with CRSwNP (523.4 pg/mL) as compared to patients with CRSsNP (17.06 pg/mL, p=0.013), allergic rhinitis (20.11 pg/mL, p=0.001), and normal controls (32.42 pg/mL; p = 0.035) (Fig. 3). Relative expression of IL-37 mRNA was significantly increased in the polyp tissue as compared to normal nasal tissue (p= 0.038).

Table II. *Demographic profile of groups collected for tissue sampling*

	Control	Polyp
Number	3	20
Age (median)	53	56
Gender (N, %)		
Female	0 (0%)	6 (30%)
Male	3 (100%)	14 (60%)
Ethnicity (N, %)		
Caucasian	2 (67%)	10 (50%)
Black or African American	0 (0%)	4 (20%)
Asian	0 (0%)	6 (30%)
Latino	1 (33%)	0 (0%)

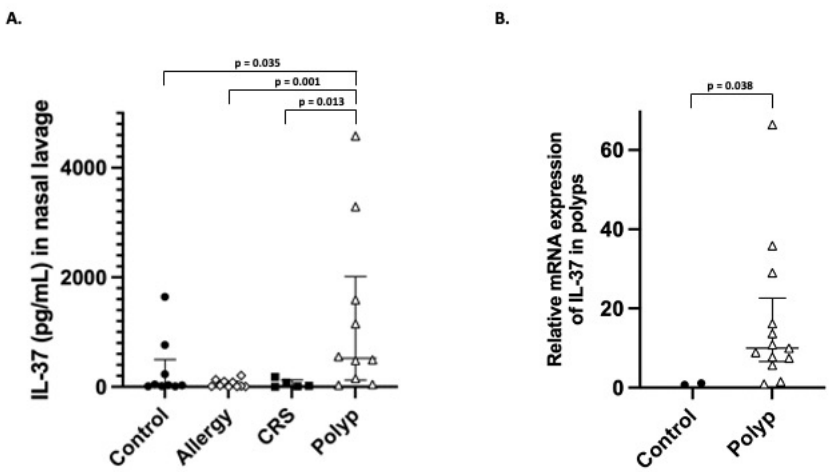


Fig. 3. ***A)*** *Concentrations of interleukin-37 in the nasal lavage fluid of patients with nasal polyps versus normal controls, allergy, and chronic rhinosinusitis (CRS).* ***B)*** *Relative mRNA expression in nasal polyp tissue as compared to normal nasal mucosa. Significant differences are denoted with a horizontal bar and p-value.*

DISCUSSION

In this study, the expression of neuroimmune mediators was studied in nasal lavage fluid and nasal tissue in nasal polyposis. Overall, we found different patterns among the three neuroimmune mediators studied: SP, IL-33, and IL-37.

Other studies have demonstrated SP-positivity in tissue biopsies of nasal polyps (12) and increased levels of SP in nasal polyps relative to serum levels (13). In 1995, Baumgarten et al. studied SP in the nasal mucosa of patients with and without allergies, noting that SP enhances mediator response to allergen (14). Here, we show that SP levels tend to be higher in the nasal lavage fluid of patients with nasal polyps as compared to other types of sinonasal pathology, in particular allergy patients. On the other hand, the gene expression of SP mRNA in the polyp tissue itself is decreased. These findings are at odds with previous findings of elevated SP levels in allergic rhinitis and nasal polyposis, though few reports have studied levels of SP across different disease processes as done in the present study (12-14). In terms of pathogenesis of nasal polyps, these results may suggest one of two possibilities. First, SP may be released into the lavage fluid from the nasal polyp tissue, and therefore is more easily detected in lavage fluid than in the tissue itself. Second, it is possible that nasal polyps are not well-innervated with sensory neurons that produce SP; this molecule might diffuse from other parts of the nasal mucosa.

We show that IL-33 is highest in the nasal lavage fluid of patients with CRSsNP and allergic rhinitis, but not in patients with CRSwNP. Similarly, we did not detect a difference in gene expression of IL-33 in the polyp tissue. These findings suggest that IL-33 is downregulated in the process of nasal polyposis. IL-33 is released primarily from endothelial and epithelial cells. Polyps mostly consist of fibrotic tissue and may not synthesize IL-33, just as this tissue may not synthesize SP. It is not surprising that the patterns of gene expression for both SP and IL-33 are similar, as these two mediators tend to work in concert. Previous papers have reported increased expression of IL-33 in nasal polyposis and have linked this finding to increased eosinophilia in this condition (17-19). However, other research has shown that the composition of nasal polyps may differ according to genetic and environmental factors; in fact, one recent study demonstrated significantly lower eosinophilia in nasal polyps that were collected from second-generation Asian patients as compared to other ethnicities (26). It is possible that the sampled population of nasal polyps in our study manifested a lower tendency of eosinophilia, corresponding with lower levels of IL-33. The patient population sampled for analysis of nasal polyposis in this study had a high representation of Asian ethnicity; 30% of CRSwNP patients sampled for lavage fluid were Asian, and 30% of CRSwNP patients sampled for polyp tissue were Asian.

In our nasal lavage samples, we found a significantly higher amount of IL-37 in the polyp group compared to all other groups. Likewise, we saw significantly increased gene expression of IL-37 in the polyp tissue as compared to a limited number of controls. These findings may reflect the body's efforts to contain inflammation; however, our results are at odds with other reported findings of reduced IL-37 levels in nasal polyposis (24, 25). Nonetheless, a similar increase in IL-37 has been reported in other inflammatory conditions including coronary artery disease (27) and autism spectrum disorder (28). It is possible that IL-37 may play a critical regulatory role in certain types of polyps - perhaps non-eosinophilic polyps - and could represent a novel therapeutic target.

The limitations of this study include demographic differences between study groups and a limited number of normal controls. It is also difficult to completely control study groups, as there may be some overlap between patients with polyps, sinusitis, and allergy. Finally, the control tissue was collected from nasal mucosa that is different in composition from polyp tissue.

In this prospective study, we measured differential levels and gene expression of SP, IL-33, and IL-37 in the lavage fluid and nasal tissue of patients with nasal polyposis and controls. In particular, SP and IL-37 levels were elevated in the lavage fluid of patients with nasal polyps, and IL-37 had increased gene expression in the polyp tissue. This finding may help us better understand and potentially treat CRS.

ACKNLOWLEDGMENTS

We thank the New England Otolaryngology Society for partial funding in the form of a resident research grant to RAC.

REFERENCES

1. Hopkins C. Chronic rhinosinusitis with nasal polyps. N Engl J Med 2019; 381:55-63.
2. Hulse KE, Stevens WW, Tan BK, et al. Pathogenesis of nasal polyposis. Clin Exp Allergy 2015; 45(2):328-46.
3. Patou J, Holtappels G, Affleck K, et al. Syk-kinase inhibition prevents mast cell activation in nasal polyps. Rhinology 2011; 49(1):100-6.
4. Theoharides TC, Valent P, Akin C. Mast Cells, mastocytosis, and related disorders. New Engl J Med 2015; 373(2):163-72.
5. Teranishi Y, Jin D, Takano S, Kishiko S, et al. Decrease in number of mast cells in resected nasal polyps as an indicator for postoperative recurrence of chronic rhinosinusitis. Immun Inflamm Dis 2019; 7(3):191-200.
6. Zhai GT, Li JX, Zhang XH, et al. Increased accumulation of CD30 ligand-positive mast cells associates with eosinophilic inflammation in nasal polyps. Laryngoscope 2019; 129(3):110-7.
7. Baba S, Kondo K, Suzukawa M, et al. Distribution, subtype population, and IgE positivity of mast cells in chronic rhinosinusitis with nasal polyps. Ann Allergy Asthma Immunol 2017; 119(2):120-8.
8. Patel A, Theoharides TC. Methoxyluteolin inhibits neuropeptide-stimulated proinflammatory mediator release via mTOR activation from human mast cells. J Pharmacol Exp Ther 2017; 361(3):462-71.
9. Mashagi A, Marmalidou A, Tehrani M, et al. Neuropeptide substance P and the immune response. Cell Mol Life Sci 2016; 73(22):4249-64.
10. Harrison S, Geppetti P. Substance P. Int J Biochem Cell Biol 2001; 33(6):555-76.
11. Barbosa-Cobbos RE, Lugo-Zamudio G, Flores-Estrada J, et al. Serum substance P: an indicator of disease activity and subclinical inflammation in rheumatoid arthritis. Clin Rheumatol 2018; 37(4):901-8.
12. Beatrice F, Aluffi P, Bottomicca F, et al. Nasal polyps and substance P: a preliminary report. Acta Otorhinolaryngol Ital 1994; 14(Suppl)41:35-9.
13. Drake-Lee A, Jones V, Lewin I, et al. Levels of substance P and IgE decapeptide in nasal polyp fluid and matching sera. J Laryngol Otol 1996; 110:225-7.
14. Baumgarten CR, Witzel A, Kleine-Tebbe J, et al. Substance P enhances antigen-evoked mediator release from human nasal mucosa. Peptides 1996; 17(1):25-30.
15. Lonergan A, Theoharides T, Tsilioni E, et al. Substance P and hemokinin 1 in nasal lavage fluid of patients with chronic sinusitis and nasal polyposis. OTO Open 2019; 3(3).
16. Theoharides TC, Zhang B, Kempuraj D, et al. IL-33 augments substance P-induced VEGF secretions from human mast cells and is increased in psoriatic skin. Proc Natl Acad Sci USA 2010; 107(9):4448-53.
17. Song W, Wang C, Zhou J, et al. IL-33 Expression in chronic rhinosinusitis with nasal polyps and its relationship with clinical severity. ORL J Otorhinolaryngol Relat Spec 2017; 79(6):323-30.
18. Travers J, Rochman M, Caldwell JM, et al. IL-33 is induced in undifferentiated, non-dividing esophageal epithelial cells in eosinophilic esophagitis Sci Rep 2017; 7(1):17563.
19. Tworek D, Majewski S, Szewczyk K, et al. The association between airway eosinophilic inflammation and IL-33 in stable non-atopic COPD. Respir Res 2018; 19(1):108.
20. Ozturan A, Eyigor H, Eygior M, et al. The role of IL-25 and IL-33 in chronic rhinosinusitis with or without nasal polyps. Eur Arch Otorhinolaryngol 2017; 274(1):283-88.
21. Nold MF, Nold-Petry CA, Zepp JA, et al. Interleukin 37 is a fundamental inhibitor of innate immunity. Nat Immunol 2010; 11(11):1014-22.
22. Cavalli G, Dinarello CA. Suppression of inflammation and acquired immunity by IL-37. Immunol Rev 2018; 281(1):179-90.
23. Conti P, Caraffa A, Ronconi G, et al. Impact of mast cells in mucosal immunity of intestinal inflammation: inhibitory effect of IL-37. Eur J Pharmacol 2018; 818(5):294-9.
24. Liu JX, Liao B, Yu QH, et al. The IL-37-Mex3B-Toll-like receptor 3 axis in epithelial cells in patients with eosinophilic chronic rhinosinusitis with nasal polyps. J Allergy Clin Immunol 2020; 145(1):160-72.
25. Cheng J, Quyang H, Du J. Expression and regulation of interleukin-37 in pathogenesis of nasal polyps. Indian

J Otolaryngol Head Neck Surg 2014; 66(4):401-6.
26. Mahdavinia M, Suh LA, Carter RG, et al. Increased non-eosinophilic nasal polyps in chronic rhinosinusitis in U.S. second-generation Asians suggests genetic regulation of eosinophilia. J Allergy Clin Immunol 2015; 135(2):576-9.
27. Li H, Shen C, Chen B, Du J, et al. Interleukin-37 is increased in peripheral blood mononuclear cells of coronary heart disease patients and inhibits inflammatory reaction. Mol Med Rep 2020; 21(1):151-60.
28. Tsilioni I, Patel AB, Pantazopoulos H, et al. IL-37 is increased in brains of children with autism spectrum disorder and inhibits human microglia stimulated by neurotensin. Proc Natl Acad Sci 2019; 116(43):21659-65.

Long non-coding RNA OIP5-AS1 serves as a competing endogenous RNA to modulate X-linked inhibitor of apoptosis protein expression via adsorbing miR-429 in papillary thyroid cancer

C.S. Yu, Y.B. Wang, Q. Li, E.L. Yang and B.B. Dong

Department of Thyroid and Breast Surgery, Yijishan Hospital, Wuhu, Anhui Province, China

Received November 9, 2020 – Accepted May 12, 2021

Papillary thyroid cancer (PTC) is currently one of the most common endocrine tumors worldwide. Long non-coding RNA (LncRNA) is a vital regulator in the biological processes of diverse tumors. Hence, this work aimed to clarify the role and mechanism of lncRNA OIP5-AS1 in PTC progression. OIP5-AS1 and miR-429 expression levels in PTC tissues and cells were examined using qRT-PCR. Immunohistochemical staining (IHC) was applied to detect X-linked inhibitors of apoptosis protein (XIAP) expression in PTC tissues. A dual-luciferase reporter gene experiment was employed to validate the relationship for miR-429 and XIAP, miR-429 and OIP5-AS1. The regulatory effects of OIP5-AS1 on PTC cell proliferation, migration, and invasion was detected using the MTT, BrdU, Transwell and Western blot assays. In this work we reported that OIP5-AS1 expression was up-modulated in PTC tissues and cell lines. OIP5-AS1 overexpression enhanced the proliferation and metastasis of PTC cells, but the transfection of miR-429 mimics reversed the functions of OIP5-AS1 on the proliferation, migration, and invasion of PTC cells. Additionally, OIP5-AS1 was identified as a competitive endogenous RNA (ceRNA) that repressed miR-429, thereby increasing the expression level of XIAP. Taken together, the findings confirm that OIP5-AS1 accelerates PTC progression via modulating the miR-429/XIAP axis and imply that OIP5-AS1 is likely to be a therapeutic target for PTC.

Thyroid cancer (TC) is the most common endocrine tumor, and its morbidity ranks ninth among cancers globally, with nearly 570,000 new cases per year worldwide (1). TC is classified into three main histological subtypes: differentiated, undifferentiated, and medullary TC (MTC). Differentiated TC, accounting for more than 90% of thyroid malignancies, comprises papillary thyroid carcinoma (PTC) and follicular thyroid carcinoma (FTC) (2). Papillary thyroid carcinoma (PTC) is the most common thyroid cancer, and its morbidity has increased dramatically in recent years (2-5). Most PTC patients can be effectively treated with conventional treatment strategies and have a relatively good 5-year survival rate (6). However, recurrence associated with metastasis still occurs in 10-15% of PTC patients, leading to an adverse prognosis (7). It is therefore imperative to clarify the mechanism of PTC pathogenesis and development.

Belonging to non-coding RNAs (ncRNAs), long non-coding RNA (lncRNA) is longer than 200nt. LncRNAs are crucial in regulating many biological processes such as epigenetic modulation, cell cycle progression, differentiation (8). LncRNAs are also

Key words: OIP5-AS1; miR-429; XIAP; papillary thyroid cancer

Corresponding Author:
Dr Ya-bing Wang,
Department of Thyroid and Breast Surgery,
Yijishan Hospital, No. 2, Zheshan West Road,
Jinghu District, Wuhu 2410001, Anhui Province, China
Tel.: +86 13637135553
e-mail: haoliantuo2@163.com

0393-974X (2021)
Copyright © by BIOLIFE, s.a.s.
This publication and/or article is for individual use only and may not be further reproduced without written permission from the copyright holder.
Unauthorized reproduction may result in financial and other penalties
DISCLOSURE: ALL AUTHORS REPORT NO CONFLICTS OF INTEREST RELEVANT TO THIS ARTICLE.

crucial regulators in cancer biology (9-13), and the mechanism by which lncRNAs act as competitive endogenous RNAs (ceRNAs) to regulate tumor progression has been widely reported (13). OIP5 antisense RNA 1 (OIP5-AS1) is a lncRNA which is dysregulated in diverse cancers and serves as a tumor suppressor or promoter (14). Recent studies have reported that OIP5-AS1 is markedly highly expressed in several malignancies, such as gastric, pancreatic, cervical, and hepatocellular carcinomas (15-18). Interestingly, OIP5-AS1 is also reported to be markedly up-modulated in TC, and its up-modulation predicts an unfavorable prognosis and enhances TC cell growth via activating the Wnt/β-catenin signaling pathway (19). Nonetheless, the detailed mechanism of OIP5-AS1 in PTC progression is still undefined.

In the present research, OIP5-AS1 expression in PTC and its regulatory effects on the proliferation, migration, and invasion of PTC cells were investigated to provide a theoretical basis of the pathogenesis of PTC. We reported that OIP5-AS1, as a ceRNA, could probably promote the progression of PTC via regulating miR-429 and X-linked inhibitor of apoptosis (XIAP).

MATERIALS AND METHODS

Samples

Fifty-nine PTC tissues and matched paracancerous non-tumor tissues surgically resected from Yijishan Hospital were collected. None of the subjects had undergone chemotherapy or radiotherapy before the surgery. Immediately after surgical resection, all tissues were frozen in liquid nitrogen until total RNA extraction. This work was endorsed by the Ethics Committee of Yijishan Hospital and was conducted under the guidance of the "Declaration of Helsinki". Before being included in this research, all subjects signed written informed consent.

Cell culture

PTC cell lines (IHH-4, HTH83, TPC-1, NPA87 and K1 cells) and Nthy-ori 3–1 thyroid follicular epithelial cell lines were obtained from the American Type Culture Collection (ATCC, Manassas, VA, USA). The cells were routinely cultured in complete DMEM medium (Thermo, San Jose, CA, USA) with additional 10% fetal bovine serum (FBS), 100 U/mL penicillin and 100 mg/mL streptomycin (Invitrogen, Carlsbad, CA, USA) at 37°C and 5% CO_2.

Cell transfection

The OIP5-AS1 overexpression plasmid was constructed with the pcDNA3.1 plasmid, and the pcDNA3.1 empty vector was used as the control plasmid. OIP5-AS1 overexpressing vector pcDNA3.1-OIP5-AS1 and the empty vector pcDNA3.1 were obtained from GeneChem (Shanghai, China). In addition, miR-628-5p mimics and NC mimics were purchased from GenePharma (Shanghai, China). The transfection was executed using Lipofectamine® 2000 (CAT11668030, Invitrogen, Carlsbad, CA, USA) under the guidance of the protocols.

Quantitative real-time Polymerase Chain Reaction (qRT-PCR)

Total RNA was extracted using TRIzol reagent (CAT15596026, Invitrogen, Carlsbad, CA, USA), and cDNA synthesis was conducted using the PrimeScript™ RT reagent Kit (CATRR037Q, TaKaRa, Dalian, China). qPCR reaction was executed using a SYBR-Green Master Mix Kit (CAT4385610, TaKaRa, Dalian, China) on the MyIQ RT-PCR Detection System (Bio-Rad, Hercules, CA, USA). The relative expression of target genes was calculated by the $2^{-\Delta\Delta Ct}$ method, with GAPDH or U6 as an internal control. The sequences of the primers were displayed as follows: OIP5-AS1, forward primer: 5′-TGCGAAGATGGCGGAGTAAG-3′ and reverse primer: 5′-TAGTTCCTCTCCTCTGGCCG-3′; XIAP, forward primer: 5′-TACCGTGCGGTGCTTTAGTT-3′ and reverse primer: 5′-TTCTGACCAGGCACGATCAC-3′; GAPDH, forward primer: 5′-GGAGCGAGATCCCTCCAAAAT-3-3′ and reverse primer: 5′-GGCTGTTGTCATACTTCTCATGG-3′; miR-429, forward primer: 5′-GGAAGATGAGGAGGTCGCTG-3′ and reverse primer: 5′-GACTTGACTGGAAGGGTGGG-3′; U6, forward primer: 5′CTCGCTTCGGCAGCACA-3′ and reverse primer: 5′AACGCTTCACGAATTTGCGT-3′.

Immunohistochemistry

XIAP protein expression in PTC tissues was examined by the Immunohistochemistry (IHC) method. Briefly, the paraffin-embedded PTC tissue was sectioned, dewaxed and rehydrated with xylene, and then incubated with 0.3% H_2O_2 for 30 min to block the activity of endogenous peroxidase, then incubated in 5% bull serum albumin

(BSA) to block non-specific binding. Subsequently, the slices were incubated overnight with the primary antibody (anti-XIAP, Abcam, ab229050, 1:1000) at 4 ℃, then incubated with the second antibody for 30 min, and then washed thoroughly with PBS solution. Thereafter, DAB staining solution (Wuhan Boster Biological products Technology Ltd, Wuhan, China) was applied to develop the color. Ultimately, the sections were observed and the staining intensity was scored by the pathologist.

MTT

PTC cells were inoculated in 96-well plates at the density of 4×10^3 cells/well. At the specific time points, 20 μL of MTT solution (CAS298-93-1, 5 mg/mL; Beyotime, Shanghai, China) was added to each well. After 4 h, the formazan crystals were dissolved in 150 μL DMSO, and the absorbance (570 nm) of the cells was measured.

Bromodeoxyuridine immunohistochemistry

HTH83 and K1 cells were sub-cultured in a 24-well plate. After the confluence of cells reached about 80%, BrdU solution (10 μM, RiboBio, Guangzhou, China) was supplemented and the cells were incubated at 37℃ for 4 h. Afterwards, the medium was discarded. After the cells were washed 3 times with PBS and 4% paraformaldehyde was applied to fix the cells for 10 min. After the cells were rinsed for 3 times with PBS, HCl solution was supplemented to denature the DNA. Following that, 1% BSA (CAS9048-46-8, Beyotime, Shanghai, China) was supplemented, and the unspecific antigens were blocked for 1 h. Then BrdU monoclonal antibody (ab8152, 1: 300, Abcam, Cambridge, UK) was added into each well, and the cells were incubated at 4 ℃ overnight. After that, the secondary antibody was supplemented to incubate the cells in the dark for 2 h. Thereafter, cell nuclei were stained with DAPI solution (CATYT890, RiboBio, Guangzhou, China), and then the cells were observed using a fluorescent microscope. 10 non-overlapping fields were arbitrarily chosen. The number of BrdU positive cells was then counted and averaged.

Transwell assay

The cells resuspended in 200 μL of serum-free medium were transferred into the upper compartment of Matrigel-uncovered (for migration assay) and Matrigel-covered (for invasion assay) Transwell inserts (8 μM pore size; Corning, Inc., Corning, NY, USA). The lower compartments were loaded with 600 μL of medium containing 10% FBS. After the cells were cultured for 24 h, the cells that had migrated or invaded to the lower compartment were fixed by 4% paraformaldehyde, stained with 0.1% crystal violet solution and photographed under an optical microscope.

Dual-luciferase reporter gene analysis

The wild-type (WT) sequence of OIP5-AS1 and the WT 3′UTR sequence of XIAP containing the predicted binding site of miR-429 were amplified and sub-cloned into the psiCHECK-2 reporter vector (Hanbio Biotechnology, Shanghai, China) to construct the OIP5-AS1-WT and XIAP-WT vectors. The site-directed mutagenesis was performed using a Quick Change Lightning kit (Agilent, Shanghai, China) to construct mutant-type (MUT) OIP5-AS1 and XIAP vectors. With Lipofectamine® 2000 (Invitrogen, Carlsbad, CA, USA) transfection reagent, HTH83 and K1 cells were co-transfected with the above vectors and miR-429 mimic control. After 48 h, the cells were lysed, and the firefly luciferase activity and Renilla luciferase activity were measured using the Dual-Luciferase Reporter Assay System (CATE1910, Promega, Madison, WI, USA). The results were expressed as the ratio of Firefly luciferase activity to Renilla luciferase activity.

RNA binding protein immunoprecipitation (RIP) assay

RIP analysis was performed utilizing the Magna RIP kit (Millipore, Bedford, MA, USA) in accord to the manufacturer's protocol. PTC cells were lysed in the RIP lysis buffer and the mixture was incubated with the antibody against Ago2 (Millipore, Bedford, MA, USA) or normal immunoglobulin G (IgG) (Millipore, Bedford, MA, USA). After that, the samples were mixed with proteinase K, and RNA was extracted by TRIzol reagent. Subsequently, the expression of OIP5-AS1 in the immunoprecipitate was detected by qRT-PCR.

RNA pull-down assay

HTH83 cells were collected and lysed with lysis buffer. Then biotinylated miR-429 (or control biotinylated mimics) was added into the cell lysates and incubated for 12 h, and then the lysates were incubated with M-280 streptavidin magnetic beads (Sigma, Shanghai, China). Then, then the RNA was extracted with TRIzol reagent

(Takara, Dalian, China) and the OIP5-AS1 enrichment was evaluated by qRT-PCR.

Western blotting

Total proteins were extracted using radioimmunoprecipitation assay buffer (1% NP-40, 0.5% sodium deoxycholate, 50 mM Tris-HCl, 0.1% SDS, 150 mM NaCl, pH 7.5) containing 1% protease inhibitor. Protein concentrations were quantified using a BCA protein assay kit (Bio-Rad, Hercules, CA, USA). The proteins (30 μg in each lane) were separated by SDS-PAGE and transferred onto the nitrocellulose membranes (Millipore, Bedford, MA, USA). Next, the membrane was blocked with 5% skimmed milk for 1 h at room temperature and incubated with anti-GAPDH (Abcam, Shanghai, China) (ab9484, 1:3000), anti-XIAP (Abcam, Shanghai, China) (ab229050, 1:1000), anti-Cyclin D1 (Abcam, Shanghai, China) (ab134175, 1:1000), anti-CDK4 (Abcam, Shanghai, China) (ab108375, 1:1000), and anti-CDK6 (Abcam, Shanghai, China) (ab124821, 1:1000) primary antibodies at 4 ˚C for 12 h. Then the membranes were rinsed and then incubated with horseradish peroxidase-conjugated secondary antibody at room temperature for 2 h. Finally, the bands were developed with an ECL substrate kit (Millipore, Billerica, MA, USA) . GAPDH was utilized as an internal control.

Statistical analysis

All the assays were carried out at least 3 times and in independent biological replicates. Statistical analysis was conducted using SPSS v22.0 (SPSS, Inc, Chicago, IL, USA). All measurement data was expressed as "means ± standard deviation". Students' *t*-test and one-way ANOVA were respectively conducted to analyze the differences between two groups and among multiple groups. A Chi-square test was adopted for analyzing the count data. The correlation analysis was analyzed by Pearson's correlation analysis. $P < 0.05$ signified statistical significance.

RESULTS

OIP5-AS1 was up-modulated in PTC tissues and cells

To elaborate on the clinical significance of OIP5-AS1 in PTC, we extracted total RNA from 59 PTC cancer tissues and paracancerous tissues for qRT-PCR analysis. It was found that OIP5-AS1 expression was remarkably higher in PTC tissues than that in normal paracancerous tissues (Fig. 1A). Additionally, OIP5-AS1 expression was notably higher in PTC cell lines (IHH-4, HTH83, TPC-1, NPA87, and K1 cells) than that in Nthy-ori 3-1 thyroid follicular epithelial cell lines (Fig. 1B). However, miR-429 was markedly down-modulated in PTC tissues and cells (Fig. 1 C, D). Furthermore, we also observed remarkable XIAP overexpression in PTC tissues using IHC staining (Fig. 1E). The findings implied that OIP5-AS1 and XIAP could probably exert a cancer-promoting effect in PTC progression while miR-429 could probably exert a tumor-suppressive effect.

OIP5-AS1 enhanced the proliferation, migration, and invasion of PTC cells

OIP5-AS1 expression was relatively low in HTH83 and K1 cells of all tested PTC cell lines. Therefore, the OIP5-AS1 overexpressing plasmid was transfected into HTH83 and K1 cells, and qRT-PCR confirmed that OIP5-AS1 expression was remarkably up-modulated in HTH83 and K1 cells after the transfection (Fig. 2A). Moreover, MTT and BrdU experiments were executed to monitor the proliferation of PTC cells and the Transwell method was used to examine the migration and invasion of PTC cells. The data showed that cell proliferation was remarkably increased in the OIP5-AS1 overexpression group relative to the control group (Fig. 2 B, C). Furthermore, migration and invasion of OIP5-AS1 overexpressing HTH83 and K1 cells were also remarkably enhanced (Fig. 2D). With Western blot, we detected the expression of cell cycle regulators. The results showed that overexpression of OIP5-AS1 promoted the protein expression of cyclin D1, CDK4 and CDK6, suggesting that OIP5-AS1 overexpression promoted the cell cycle progression of PTC cells (Fig. 2E). This data implied that OIP5-AS1 enhanced the proliferation and invasion of PTC cells.

OIP5-AS1 functioned as a sponge for miR-429 in PTC cells

By nuclei-cytoplasm separation, the enrichment of OIP5-AS1 in nuclei and cytoplasm of PTC cells was detected, respectively, and showed that OIP5-AS1 was mainly located in the cytoplasm, suggesting

OIP5-AS1 may be a molecular sponge (Fig. 3A). The ENCORI database predicted that miR-429 was a potential downstream target of OIP5-AS1 (Fig. 3B). To verify whether OIP5-AS1 could bind with miR-429, the wild-type plasmid (OIP5-AS1-WT) or the mutant plasmid (OIP5-AS1-MUT) and miR-429 mimics were co-transfected into HTH83 and K1 cells, respectively. The data of the luciferase reporter gene experiment revealed that the luciferase activity of the OIP5-AS1-WT group was remarkably reduced by miR-429 mimics in PTC cells, whereas the luciferase activity of OIP5-AS1-MUT was not markedly altered (Fig. 3C). RIP analysis showed that the expression of OIP5-AS1 and miR-429 were significantly enhanced in the anti-Ago2 group compared with that in the anti-IgG group (Fig. 3D). Meanwhile, RNA pull-down experiment showed that miR-429 interacted directly with OIP5-AS1 in PTC cells (Fig. 3E). Additionally, qRT-PCR signified that OIP5-AS1 overexpression could induce a remarkable decrease in miR-429 expression in HTH83 cells and K1 cells (Fig. 3F). Collectively, these findings implied that OIP5-AS1 adsorbed miR-429 in PTC cells and negatively modulated its expression.

XIAP was a direct target of miR-429 in the PTC

Bioinformatics analysis was employed to predict the targets of miR-429, and TargetScan was adopted to predict XIAP as a downstream target of miR-429 (Fig. 4A). The data of the luciferase reporter gene

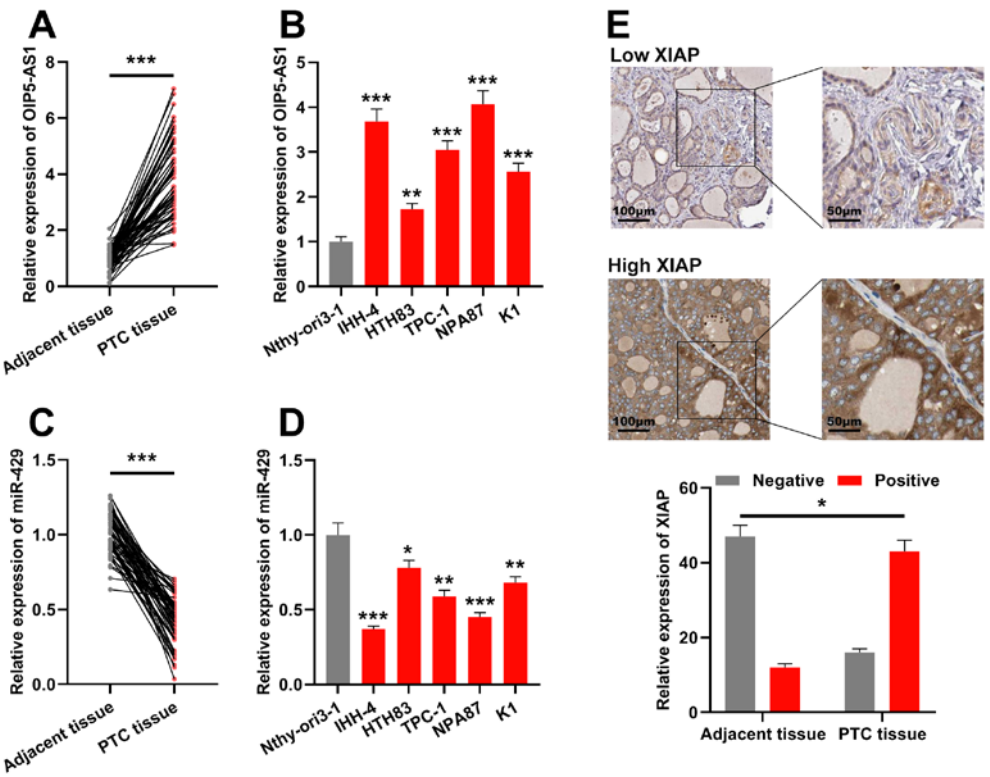


Fig. 1. *OIP5-AS1 was highly expressed in PTC samples and PTC cell lines, while miR-429 was lowly expressed in PTC cell lines.* ***A****) qRT-PCR was used to determine the OIP5-AS1 expression in PTC tumor tissues and matched paracancerous non-tumor tissues (n=59).* ***B****) qRT-PCR was used to determine the OIP5-AS1 expression in Nthy-ori 3-1 thyroid follicular epithelial cell line and five PTC cell lines (IHH-4, HTH83, NPA87, and K1 cells).* ***C****) qRT-PCR was used to determine the miR-429 expression in PTC tumor tissues and paired adjacent paracancerous tissues (n=59).* ***D****) qRT-PCR was used to determine the miR-429 expression in Nthy-ori 3-1 thyroid follicular epithelial cell lines and five PTC cell lines (IHH-4, HTH83, NPA87, and K1 cells).* ***E****) IHC staining was used to detect XIAP expression in PTC tumor tissues and paired paracancerous non-tumor tissues (n=59). All experiments were performed in triplicate. * P < 0.05, ** P < 0.01, *** P < 0.001.*

experiment manifested that the miR-429 mimic reduced the luciferase activity of XIAP-WT reporter, but miR-429 mimics didn't change the luciferase activity of XIAP-MUT reporter (Fig. 4B). Pearson's correlation analysis confirmed that XIAP expression was negatively correlated with miR-429 expression in PTC tissues (R^2=0.4027) (Fig. 4C). Additionally, miR-429 mimics were transfected into HTH83 and K1 cells to construct miR-429 overexpression models (Fig. 4D). Then XIAP expression in PTC cells after the up-modulation of miR-429 was detected by qRT-PCR and Western blot. The data indicated that XIAP expression was decreased at both mRNA and protein levels after miR-429 overexpression (Fig. 4E-F). This data implied that XIAP was a direct target of miR-429 and XIAP could be directly and negatively modulated by miR-429.

OIP5-AS1 modulated the miR-429/XIAP axis to enhance proliferation, migration, and invasion of PTC cells

To probe whether OIP5-AS1 modulates PTC

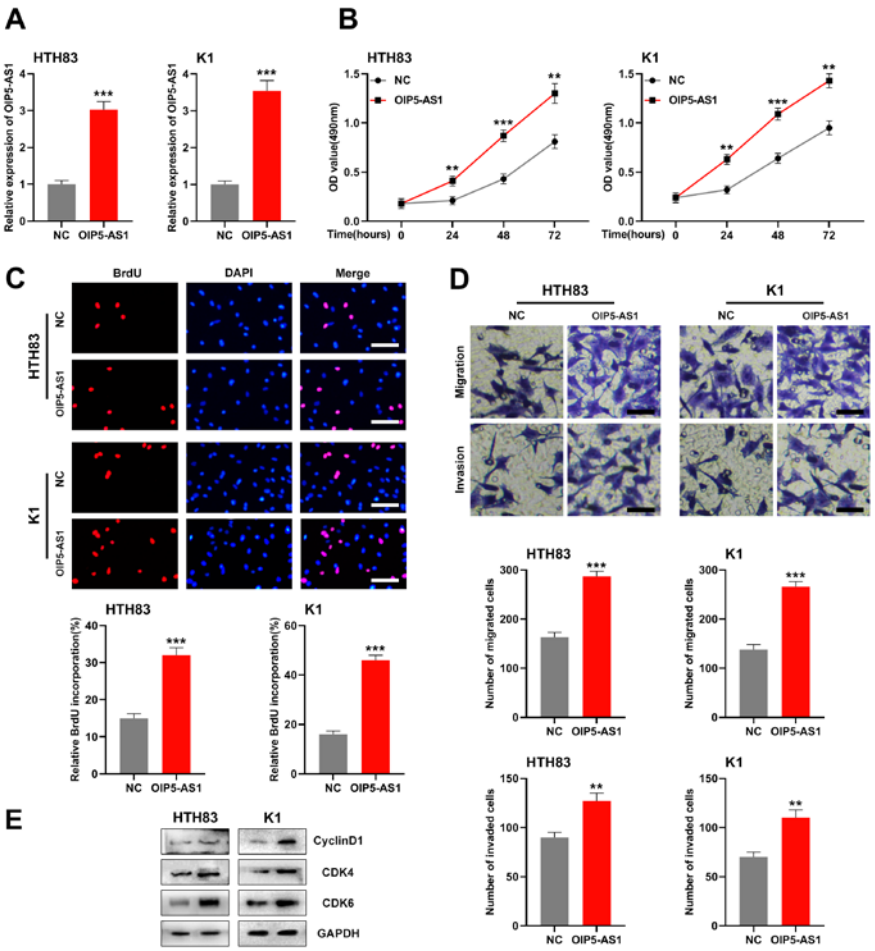


Fig. 2. *OIP5-AS1 enhanced the proliferation, migration, and invasion of PTC cells. **A**) OIP5-AS1 overexpression plasmid and negative control were transfected into HTH83 and K1 cells. qRT-PCR was used to detect the relative expression of OIP5-AS1 in both cells. **B, C**) MTT method and BrdU assay were used to detect the proliferation of OIP5-AS1 overexpressed HTH83 and K1 cells. **D**) Transwell assay was used to detect the migration and invasion of HTH83 and K1 cells after overexpression of OIP5-AS1. **E**) Western blot was used to detect the expression of CyclinD1, CDK4 and CDK6 of HTH83 and K1 cells after overexpression of OIP5-AS1. All experiments were performed in triplicate. ** P < 0.01, *** P < 0.001.*

progression by modulating the miR-429/XIAP axis, we transfected miR-429 mimics and negative controls into OIP5-AS1-overexpressed HTH83 and K1 cells to perform compensation experiments. Western blot revealed that the XIAP protein expression was up-modulated in OIP5-AS1-overexpressed HTH83 and K1 cells, whereas XIAP expression was partially decreased after transfection with miR-429 mimics (Fig. 5A). MTT and BrdU experiments revealed that the proliferation was partially decreased in OIP5-AS1-overexpressed HTH83 and K1 cells after transfection with miR-429 mimics (Fig. 5 B, C). Transwell experiments signified that the migration and invasion were also partially reduced in OIP5-AS1-overexpressed HTH83 and K1 cells after transfection with miR-429 mimics (Fig. 5D). The

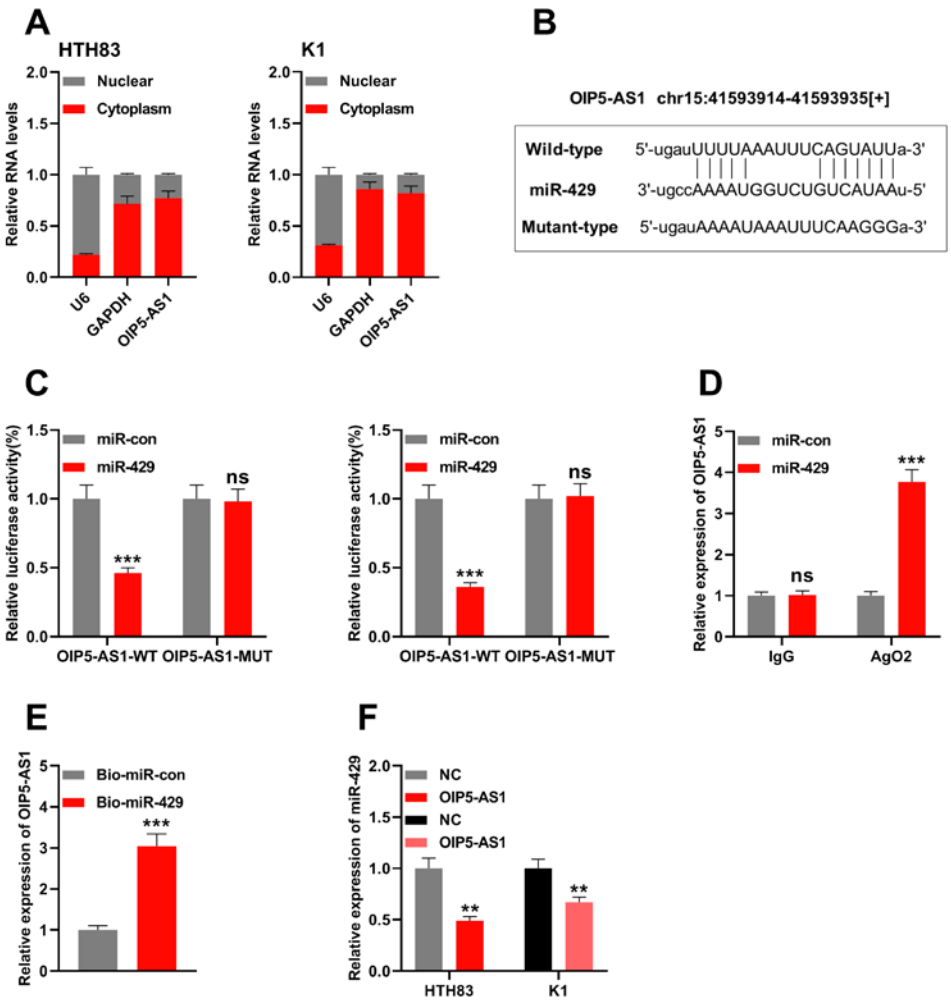


Fig. 3. *miR-429 was a downstream target of OIP5-AS1. **A**) The cellular distribution of OIP5-AS1 was analyzed by cellular RNA fractionation assays. GAPDH was mostly localized in cytoplasm and U6 was mainly localized in the nucleus, which was used as a negative control. **B**) The OIP5-AS1-WT and OIP5-AS1-MUT luciferase reporter gene vectors were constructed. **C**) The miR-429 mimics were co-transfected with OIP5-AS1-WT or OIP5-AS1-MUT into 293T cells. The luciferase activity of each group was then measured by the dual-luciferase reporter gene assay. **D, E**) RIP and RNA pull-down assays were performed to examine the direct interaction between miR-429 and OIP5-AS1 in PTC cells. **F**) The OIP5-AS1 overexpression plasmid was transfected into HTH83 and K1 cells, respectively. qRT-PCR was used to detect the expression of miR-429 in HTH83 and K1 cells. All experiments were performed in triplicate. ** $P < 0.01$, *** $P < 0.001$, The difference in ns was not statistically significant.*

data suggested that the up-modulation of miR-429 partially weakened the promoting effects of OIP5-AS1 overexpression on PTC cell proliferation, migration and invasion. Collectively, OIP5-AS1 could enhance the proliferation, migration and invasion of PTC via repressing miR-429/XIAP axis.

DISCUSSION

The present study confirms that OIP5-AS1 is overexpressed in PTC tissues and cell lines. Additionally, miR-429 expression is down-modulated in PTC tissues, whereas XIAP expression is up-modulated. We demonstrate that there is a regulatory relationship among OIP5-AS1, miR-429 and XIAP in PTC. Functionally, OIP5-AS1 overexpression enhances the proliferation and metastatic potential of PTC cells, whereas miR-429 represses the promoting effects of OIP5-AS1 malignant phenotypes of PTC cells by targeting XIAP.

LncRNA participates in regulating the carcinogenesis, development and metastasis of diverse human malignancies (20). Reportedly, multiple lncRNAs are dysregulated in PTC, and they can serve as potential diagnostic or prognostic biomarkers for PTC (21). For instance, lncRNA SBF2-AS1 expression is higher in PTC tissues relative to that in paracancerous normal tissues, and its high

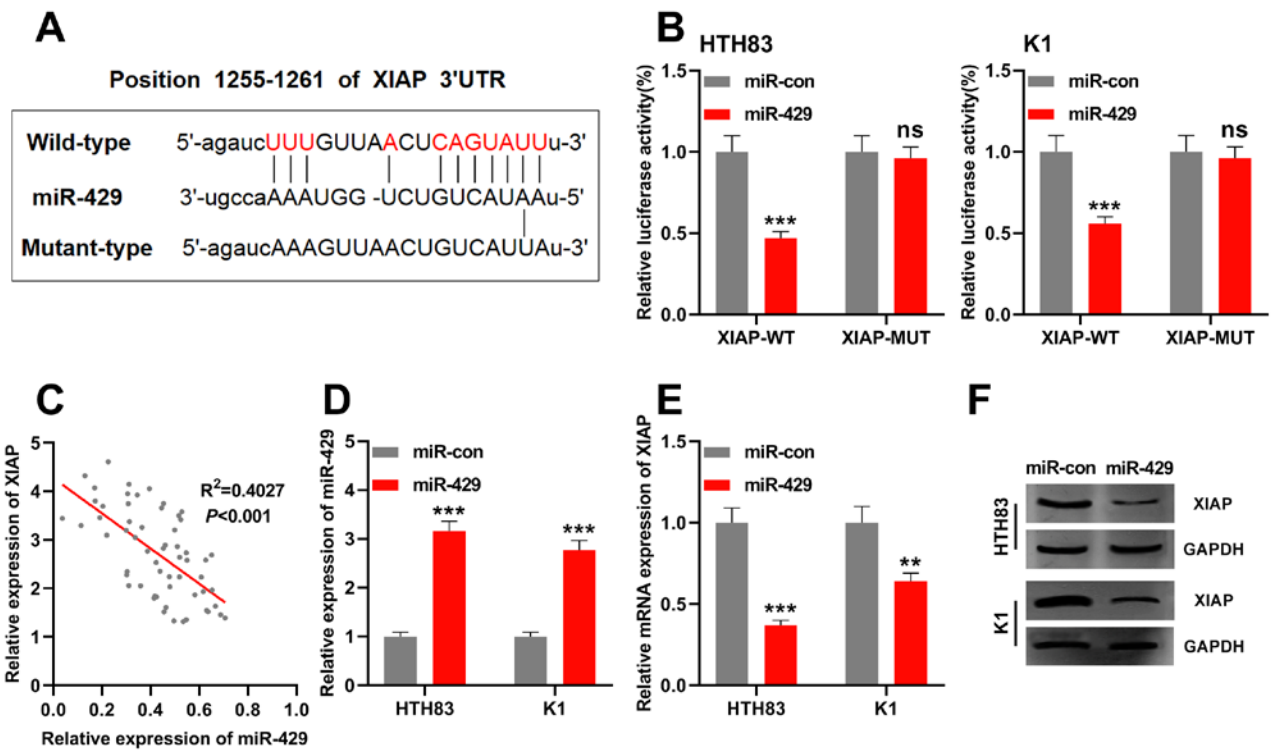


Fig. 4. *XIAP was a downstream target of miR-429.* ***A****) XIAP-WT and XIAP-MUT luciferase reporter gene vectors were constructed.* ***B****) The miR-429 mimic and negative control were co-transfected with XIAP-WT or XIAP-MUT into HTH83 and K1 cells, respectively. The luciferase activity of each group was then determined.* ***C****) Pearson's correlation analysis was used to confirm the correlation between miR-429 and XIAP expression in PTC tissues.* ***D****) The miR-429 mimics and negative control were transfected into HTH83 and K1 cells. qRT-PCR was used to detect the relative expression of miR-429 in both cells.* ***E****) qRT-PCR was used to detect the mRNA expression of XIAP in HTH83 and K1 cells.* ***F****) Western blot was used to detect the protein expression of XIAP in HTH83 and K1 cells. All experiments were performed in triplicate. ** P < 0.01, *** P < 0.001, The difference in ns was not statistically significant.*

expression predicts an unfavorable prognosis for PTC patients; it facilitates PTC cell proliferation and cell cycle progression while suppressing apoptosis (22). LncRNA HOTAIR enhances the proliferation and metastasis of PTC cells by modulating Wnt/catenin pathway-mediated epithelial-mesenchymal transition (EMT) (23). In the present study, we report that OIP5-AS1 is highly expressed in PTC tissues and cell lines. Moreover, this work validates that OIP5-AS1 enhances the proliferation and metastatic potential

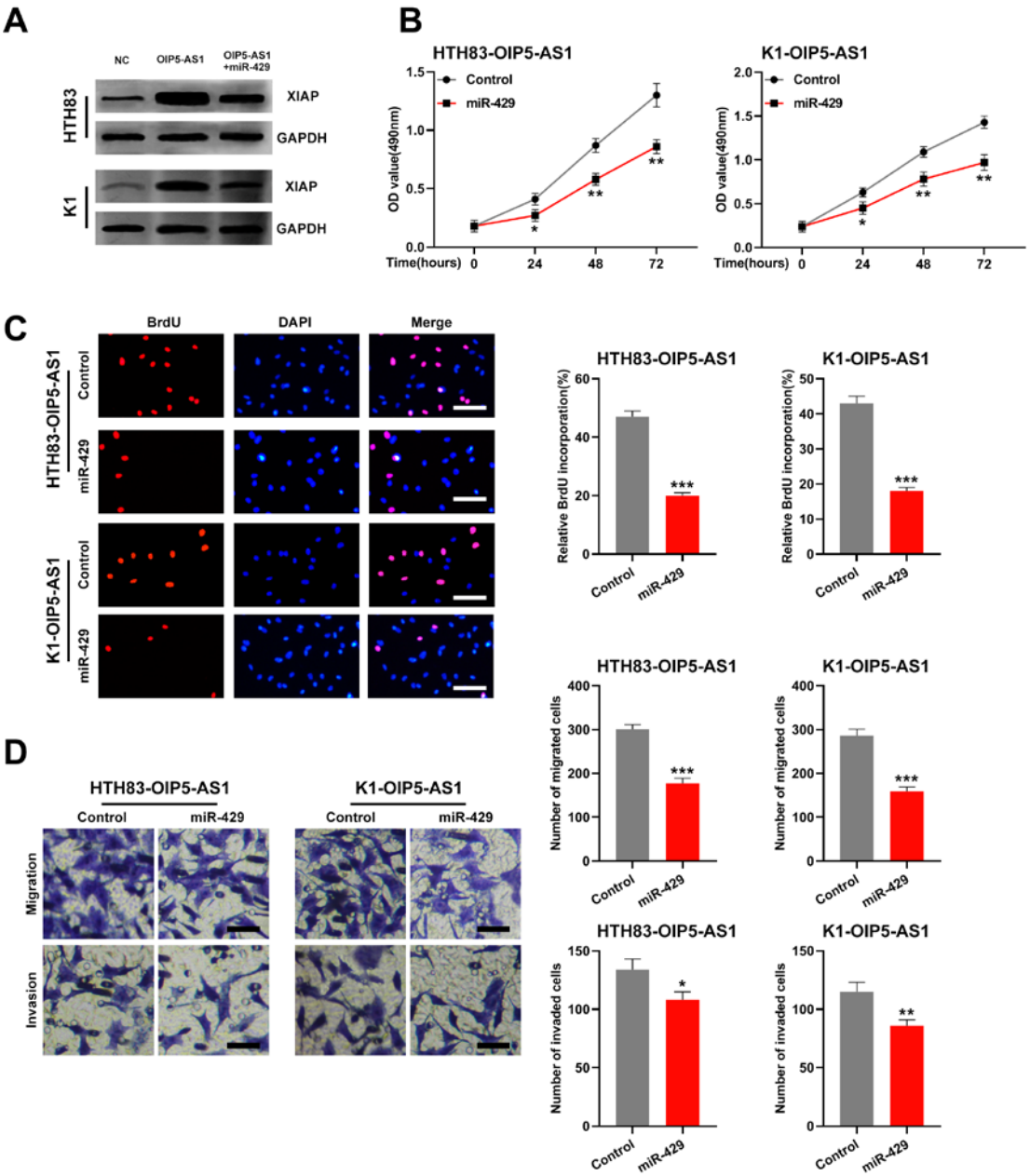


Fig. 5. *OIP5-AS1 modulated the miR-429/XIAP axis to enhance proliferation, migration and invasion of PTC cells. A) The miR-429 mimics were transfected into OIP5-AS1 overexpressed HTH83 and K1 cells. Western blot was used to detect the expression of XIAP in both cells after the transfection.* ***B, C****) MTT method and BrdU assay were used to detect the proliferation of HTH83 and K1 cells after the transfection.*
D*) The Transwell assay was used to detect migration and invasion of HTH83 and K1 cells after the transfection. All experiments were performed in triplicate. * P < 0.05, ** P < 0.01, *** P < 0.001.*

of PTC cells. Our work suggests that OIP5-AS1 is a potential biomarker and therapy target for PTC.

Inhibitor apoptosis proteins (IAPs) are anti-apoptotic proteins, and their high expression is one of the vital mechanisms to prevent apoptosis. XIAP is the most potent caspase inhibitor of the IAP family (24). Reportedly, XIAP contains three baculovirus IAP repeats (BIRs) that act as protein-protein interaction domains to restrain apoptosis by directly binding to caspase-3, caspase-7, and caspase-9, thereby enhancing tumor cell survival during tumor progression (25). Furthermore, it contains a ubiquitin-associated domain that binds to polyubiquitin conjugates and has a loop domain required for E3 ligase activity, and XIAP acts as an E3 ligase to facilitate the degradation of several pro-apoptotic proteins (26). Moreover, XIAP expression is strongly related to adverse clinical outcomes in diverse cancers, including breast cancer (27), renal cell carcinoma (28) and bladder cancer (29). Hence, XIAP is considered to be a promising therapeutic target (30). It is reported that XIAP expression is markedly up-modulated in PTC and that there is a correlation between its high expression and lymph node metastasis (31). Furthermore, another study reports that knocking down XIAP causes a significant decrease in PTC cell proliferation *in vitro* and tumor growth *in vivo* (32). In this study, our IHC staining results reconfirm that XIAP is overexpressed in PTC tissues.

Notably, the ceRNA network theory assumes that lncRNAs and mRNAs can share the same miRNA response element (MRE), and via competitively binding with miRNAs, lncRNA can indirectly promote the expression of downstream genes. Reportedly, OIP5-AS1 activates the ERK pathway through sponging miR-429 and up-modulating forkhead box D1 expression, and modulates the proliferation, migration and EMT of pancreatic ductal adenocarcinoma cells (33). In this work we demonstrate that, in PTC cells, OIP5-AS1 can specifically suppress miR-429 expression, and XIAP is a target gene of miR-429. Additionally, OIP5-AS1 positively modulates the expression of XIAP via repressing miR-429. This data suggests that OIP5-AS1, miR-429 and XIAP form a ceRNA network to modulate the progression of PTC.

In summary, our work suggests that the overexpression of OIP5-AS1 can promote the malignant biological behaviors of PTC cells via modulating the miR-429/XIAP axis. In following studies, more clinical samples should be collected from multiple medical centers to further evaluate the potential of OIP5-AS1 as a biomarker, and *in vivo* models are needed to validate the biological function of OIP5-AS1 in modulating the biological behaviors of PTC cells.

ACKNOWLEDGEMENT

The authors thank Hubei Yican Health Industry Co., Ltd. for its linguistic assistance during the preparation of this manuscript.

REFERENCES

1. Siegel RL, Miller KD, Jemal A. Cancer statistics, 2019. CA Cancer J Clin 2019; 69(1):7-34.
2. Prete A, Borges de Souza P, Censi S, Muzza M, Nucci N, Sponziello M. Update on fundamental mechanisms of thyroid cancer. Front Endocrinol (Lausanne) 2020; 11:102.
3. Chen Y, Jiang B, Wang W, Su D, Xia F, Li X. Identifying the transcriptional regulatory network associated with extrathyroidal extension in papillary thyroid carcinoma by comprehensive bioinformatics analysis. Front Genet 2020; 11:453.
4. Massoni F, Simeone C, Ricci P, Onofri E, Ricci S. Papillary thyroid carcinoma and medicolegal considerations. Minerva Med 2013; 104(4):493-4.
5. Xiao X, Li L, Cui JC, Wang Y. LncRNA FALEC promotes proliferation, migration, and invasion of PTC cells through regulating Wnt/β-catenin signaling pathway. Eur Rev Med Pharmacol Sci 2020; 24(8):4361-7.
6. Liu S, Zhang D, Chen L, Gao S, Huang X. Huang. Long non-coding RNA BRM promotes proliferation and invasion of papillary thyroid carcinoma by regulating the microRNA-331-3p/SLC25A1 axis. Oncol Lett 2020; 19(4):3071-8.
7. Li D, Chai L, Yu X, et al. The HOTAIRM1/miR-107/TDG axis regulates papillary thyroid cancer cell proliferation and invasion. Cell Death Dis 2020; 11(4):227.

8. Zhang J, Zou S, Deng L. Gene Ontology-based function prediction of long non-coding RNAs using bi-random walk. BMC Med Genomics 2018; 11(Suppl 5):99.
9. Bhan A, Soleimani M, Mandal SS. Long mnoncoding RNA and cancer: A new paradigm. Cancer Res 2017; 77(15):3965-81.
10. Ma Y, Zhang J, Wen L, Lin A. Membrane-lipid associated lncRNA: A new regulator in cancer signaling. Cancer Lett 2018; 419:27-9.
11. Renganathan A, Felley-Bosco E. Long noncoding RNAs in cancer and therapeutic potential. Adv Exp Med Biol 2017; 1008:199-222.
12. Kong X, Duan Y, Sang Y, et al. LncRNA-CDC6 promotes breast cancer progression and function as ceRNA to target CDC6 by sponging microRNA-215. J Cell Physiol 2019; 234(6):9105-17.
13. Li R, Yang YE, Jin J, et al. Identification of lncRNA biomarkers in lung squamous cell carcinoma using comprehensive analysis of lncRNA mediated ceRNA network. Artif Cells Nanomed Biotechnol 2019; 47(1):3246-58.
14. Chiu HS, Somvanshi S, Patel E, et al. Pan-cancer analysis of lncRNA regulation supports their targeting of cancer genes in each tumor context. Cell Rep 2018; 23(1):297-312.e12.
15. Bai Y, Li S. Long noncoding RNA OIP5-AS1 aggravates cell proliferation, migration in gastric cancer by epigenetically silencing NLRP6 expression via binding EZH2. J Cell Biochem 2020; 121(1):353-62.
16. Meng X, Ma J, Wang B, Wu X, Liu Z. Long non-coding RNA OIP5-AS1 promotes pancreatic cancer cell growth through sponging miR-342-3p via AKT/ERK signaling pathway. J Physiol Biochem 2020; 76(2):301-15.
17. Yang J, Jiang B, Hai J, Duan S, Dong X, Chen C. Long noncoding RNA opa-interacting protein 5 antisense transcript 1 promotes proliferation and invasion through elevating integrin α6 expression by sponging miR-143-3p in cervical cancer. J Cell Biochem 2019; 120(1):907-16.
18. Shi C, Yang Q, Pan S, et al. LncRNA OIP5-AS1 promotes cell proliferation and migration and induces angiogenesis via regulating miR-3163/VEGFA in hepatocellular carcinoma. Cancer Biol Ther 2020; 21(7):604-14.
19. Li Q, Chen W, Luo R, et al. Upregulation of OIP5-AS1 predicts poor prognosis and contributes to thyroid cancer cell proliferation and migration. Mol Ther Nucleic Acids 2020; 20:279-91.
20. Wang Y, Yang L, Chen T, et al. A novel lncRNA MCM3AP-AS1 promotes the growth of hepatocellular carcinoma by targeting miR-194-5p/FOXA1 axis. Mol Cancer 2019; 18(1):28.
21. ang T, Li H, Chen T, Ren H, Shi P, Chen M. LncRNA MALAT1 depressed chemo-sensitivity of NSCLC cells through directly functioning on miR-197-3p/p120 Catenin Axis. Mol Cells 2019; 42(3):270-83.
22. Wen HL, Xu ZM, Wen D, Lin SY, Liang Y, Xie JP. Long noncoding RNAs SET-binding factor 2-antisense RNA1 promotes cell growth through targeting miR-431-5p/CDK14 axis in human papillary thyroid cancer. Kaohsiung J Med Sci 2020; 36(10):808-16.
23. Wu L, Shi Y, Liu B, Zhao M. Expression of lncRNA-HOTAIR in the serum of patients with lymph node metastasis of papillary thyroid carcinoma and its impact. Oncol Lett 2020; 20(1):907-13.
24. Gholizadeh MA, Shamsabadi FT, Yamchi A, Golalipour M, Jhingan GD, Shahbazi M. Identification of hub genes associated with RNAi-induced silencing of XIAP through targeted proteomics approach in MCF7 cells. Cell Biosci 2020; 10:78.
25. Yang WZ, Zhou H, Yan Y. XIAP underlies apoptosis resistance of renal cell carcinoma cells. Mol Med Rep 2018; 17(1):125-30.
26. Chen F, Yin S, Zhu J, et al. Effects of nuclear factor-κB on the uptake of 131iodine and apoptosis of thyroid carcinoma cells. Mol Med Rep 2018; 17(4):4959-64.
27. Evans MK, Brown MC, Geradts J, et al. XIAP regulation by MNK Links MAPK and NFκB signaling to determine an aggressive breast cancer phenotype. Cancer Res 2018; 78(7):1726-38.
28. Chen C, Zhao SC, Yang WZ, Chen ZP, Yan Y. Potential biological process of X-linked inhibitor of apoptosis protein in renal cell carcinoma based upon differential protein expression analysis. Oncol Lett 2018; 15(1):821-32.
29. Xu J, Hua X, Yang R, et al. XIAP Interaction with E2F1 and Sp1 via its BIR2 and BIR3 domains specific activated MMP2 to promote bladder cancer invasion. Oncogenesis 2019; 8(12):71.
30. Abbas R, Larisch S. Targeting XIAP for promoting

cancer cell death-the story of ARTS and SMAC. Cells 2020; 9(3):663.
31. Yim JH, Yoon JH, Kim SA, et al. Expression of X-linked inhibitor of apoptosis protein in neoplastic thyroid disorder. J Korean Med Sci 2011; 26(9):1191-5.
32. Werner TA, Dizdar L, Nolten I, et al. Survivin and XIAP - two potential biological targets in follicular thyroid carcinoma. Sci Rep 2017; 7(1):11383.
33. Wu L, Liu Y, Guo C, Shao Y. LncRNA OIP5-AS1 promotes the malignancy of pancreatic ductal adenocarcinoma via regulating miR-429/FOXD1/ERK pathway. Cancer Cell Int 2020; 20:296.

MicroRNA-20a suppresses RANKL-modulated osteoclastogenesis and prevents bone erosion in mice with rheumatoid arthritis through the TLR4/p38 pathway

XH. Kong, SF. Shi, HJ. Hu and JX. Wang

Department of Rheumatism, Linyi Central Hospital, Linyi, Shandong, P.R. China

Received October 14, 2020 – Accepted May 18, 2021

Abnormal osteoclast formation plays a significant part in rheumatoid arthritis (RA). As potent therapeutic biomarkers, microRNAs (miRNAs) have obtained increasing attention. Recently, treatment regimens regarding miRNAs have been implicated in skeletal diseases. The aim of this study is to assess the expression and function of miR-20a during osteoclast proliferation and differentiation and its correlation with bone erosion in RA mice. The expression of miR-20a was observed to be diminished in the ankle tissues of RA mice relative to that in normal controls evaluated by RT-qPCR. Hematoxylin and eosin staining, Safranin O-fast green staining, and tartrateresistant acid phosphatase staining were used to evaluate the effects of miR-20a on RA symptoms. The proliferation and differentiation of osteoclasts, and bone erosion were repressed by agomiR-20a injection. 3'UTR luciferase reporter assays were conducted to validate the putative binding between miR-20a and receptor activation of nuclear factor-κB ligand (RANKL). The protein expression and phosphorylation level of toll-like receptor4 (TLR4)/p38 pathway-related factors were detected by Western blot. miR-20a inhibited proliferation and differentiation potentials to osteoclasts partly through the TLR4/p38 pathway. The current work provides evidence that miR-20a hinders proliferation and differentiation of osteoclasts by targeting RANKL through the TLR4/p38 pathway.

Rheumatoid arthritis (RA) is a chronic systemic disorder characterized by inflammation, resulting in joint erosion and cartilage loss (1). Even though novel therapeutic options have substantially delayed the progression of RA and enhanced the quality of life of patients, restrictions on administration methods and the inevitability for frequent long-term dosing culminate in adverse effects and non-compliance (2). In RA, gathering of osteoclasts in synovial tissues and their induction are linked to osteoclastogenic cytokines and chemokines at cartilage erosion sites, implying their possible roles as therapeutic targets (3). As a consequence, a deeper comprehension of the mechanisms involving osteoclasts in homeostatic and disease surroundings will be helpful for developing new and complementary therapeutic options to repress pathologic bone resorption (4).

MicroRNA (miRNAs), short noncoding RNAs (18-24 nucleotides in lengthen) that could interact with one or more mRNAs to modify protein expression, have been extensively studied in the regulation of arthritic diseases via a wide range of cell systems including mesenchymal stromal cells, fibroblast-like synoviocytes as well as osteoclasts (5). Moreover, an increasing number of miRNAs has been clarified to be involved in the formation,

Key words: rheumatoid arthritis; microRNA-20a; RANKL; The TLR4/p38 pathway; osteoclast

Corresponding Author:
Dr Junxia Wang,
Department of Rheumatism, Linyi Central Hospital,
No.17 Jiankang Road, Yishui Town, Linyi 276400,
Shandong, P.R. China
Tel.: +86 0539 2250831
e-mail: wangjunxia@lyhospital-edu.cn

0393-974X (2021)
Copyright © by BIOLIFE, s.a.s.
This publication and/or article is for individual use only and may not be further reproduced without written permission from the copyright holder.
Unauthorized reproduction may result in financial and other penalties
DISCLOSURE: ALL AUTHORS REPORT NO CONFLICTS OF INTEREST RELEVANT TO THIS ARTICLE.

differentiation and resorption of osteoclasts (6). The miR-17-92 cluster, containing miR-17, miR-18a, miR-20a as well as miR-92a, was found to be diminished in lipopolysaccharide-induced fibroblast-like synoviocytes in RA (7). Furthmore, miR-20a was downregulated during hypoxia and was acknowledged as a major candidate for modulating hypoxia-triggered differentiation of osteoclasts (8). Toll-like receptor 4 (TLR4) was recently ascertained as one of the downstream targets of miR-20a, and miR-20a may hold a protective capacity for cardiomyocytes against hypoxia/reoxygenation by blocking the p38 MAPK/JNK pathway (9). p38 participates in varied cellular processes, including cell differentiation, growth and death, and mounting data has specified that it is also a crucial modulator of TLR4-stimulated inflammatory signaling (10). Interestingly, TLR induction in mature osteoclasts elevates their survival and function, and drives osteoclastogenesis, coordinating with receptor activation of nuclear factor-κB ligand (RANKL) (11). The expression of RANKL was detected in osteoblasts, T cells and stromal cells, and was indispensable for the differentiation of osteoclasts (12). Bioinformatics analysis in the present study identified putative binding sites between miR-20a and the 3'untranslated region (3'UTR) of RANKL mRNA. As a consequence, this report aimed to investigate the role of miR-20a in regulating RANKL expression and the TLR4/p38 pathway activation, as well as osteoclast proliferation and differentiation in the settings of induced RA mice and RAW264.7 cells.

MATERIALS AND METHODS

Induction of collagen-induced arthritis (CIA)

A total of 28 male DBA/1 mice (8-10 weeks old) were obtained from the animal center of Linyi Central Hospital and housed under specific pathogen-free conditions. All animals were treated conforming to national and local regulations. All experimental protocols involving mice were reviewed and approved by the Animal Care Committee of Linyi Central Hospital.

Bovine type II collagen was emulsified in 10 mM acetic acid at 4°C for 12 h and then in the same volume of complete or incomplete Freund's adjuvant. CIA was induced in DBA/1 mice by subcutaneous injection at the joints of a 100 μL emulsion containing 200 mg bovine type II collagen (13). After 21 days from the first injection, the bovine II collagen enhancer was injected at the same injection site. Similarly, sham-operated mice were given an equal volume of phosphate buffered saline (PBS). On day 22, the mice were administrated *in situ* weekly with 0.2 mL agomiR-20a or agomir Mock (Shanghai Sangon Biological Engineering Technology & Services Co., Ltd., Shanghai, China) using Invivofectamine (Thermo Fisher Scientific Inc., Waltham, MA, USA). Two independent investigators observed the degree of paw swelling with a Vernier caliper. CIA was assessed and scored from 0 to 4 based on the following standards: 0 point, no signs of arthritis; 1 point, swelling and/or redness of the paw or one digit; 2 points, swelling and/or redness observed in two joints; 3 points, swelling and/or redness observed in more than two joints; 4 points, severe arthritis of the entire paw and all digits (14). Serum samples were harvested before the mice were euthanized with an overdose of pentobarbital sodium at 100 mg/kg, and the hind paws were collected for histological analysis.

Oligonucleotide microarray

Ankle tissues from three RA and sham-operated mice were used for the screening of differentially expressed miRNAs using microarray analysis which was carried out as previously described (15).

Reverse transcription-quantitative PCR (RTqPCR)

Total RNA in tissues was obtained using a Trizol kit (Takara, Kyoto, Japan). Subsequently, the expression of miR-20a was detected using an SYBR Green qPCR Mix (Thermo Fisher) kit with the ABI real-time fluorescence quantitative PCR platform (Thermo Fisher). The relative mRNA expression was calculated by the 2^{-Ct} method and normalized to U6 or glyceraldehyde-3-phosphate dehydrogenase. The primers (Sangon Biotech) used were: miR-20a (forward, 5'-AGTGCTTATAGTGCAGGTAG-3'; reverse, 5'-GAACATGTCTGCGTATCTC-3'); osteoprotegerin (OPG) (forward, 5'-ACCCAGAAACTGGTCATCAGC-3'; reverse, 5'-CTGCAATACACACACTCATCACT-3'); RANK (forward, 5'-GGAGGGAGCACGAAAAACTG-3'; reverse, 5'-GGAAGGGTTGGACACCTGAA-3'); RANKL (forward, 5'-CAGCATCGCTCTGTTCCTGTA-3'; reverse, 5'-CTGCGTTTTCATGGAGTCTCA-3') and GAPDH (forward, 5'-GGAGCGAGATCCCTCCAAAAT-3'; reverse, 5'-GGCTGTTGTCATACTTCTCATGG-3').

Histopathological staining of ankle joints

The ankle joint was fixed, decalcified, embedded in paraffin, cut into 5 μM sections and stained with hematoxylin and eosin (HE) or Safranin O-fast green. The stained sections were then scored on a scale from 0 to 4 as previously reported (16). To investigate the bone resorption activity of osteoclasts, sections and RAW264.7 cells were stained using a tartrate-resistant acid phosphatase (TRAP) using a Sigma-Aldrich (St Louis, MO, USA) kit according to the manufacturer's instructions.

Luciferase assay

The binding relationship between miR-20a and RANKL was detected using a luciferase assay. The RANKL wild-type (WT) and 3'UTR binding sequence mutant (MT) were synthesized by GenePharma (shanghai, China) and inserted into the pMIR-REPORT™ (Thermo Fisher) luciferase reporter vectors. The luciferase activities were tested using a dual-luciferase reporter assay system (Promega, Madison, WI, USA) according to the manufacturer's protocol.

Immunoblotting

Immunoblotting was used to detect the expression of RANKL and the TLR4/p38 pathway-related proteins in tissues. Briefly, joint tissue samples from all mice were coagulated for 2 h, homogenized with 100 μL tissue lysis buffer (Beyotime, Shanghai, China) and protease inhibitor cocktail (Sigma-Aldrich) on ice for 30 min, and centrifuged at 2,000 ×g for 10 min at 4°C. Protein concentrations were determined using the bicinchoninic acid assay. Protein samples (50 μg) were separated by 10-12% sodium dodecyl sulfate-polyacrylamide gel electrophoresis and transferred to a polyvinylidene difluoride membrane. The membranes were blocked with 5% skimmed milk and tris-buffered saline containing Tween-20 at room temperature, followed by incubation with primary antibodies for 2 h at room temperature. Subsequently, the membranes were incubated with the appropriate secondary antibody (1:2,000; cat. no. C2221; Applygen Technologies, Inc., Beijing, China) for 1 h at room temperature. Protein bands were visualized using an enhancedchemiluminescence reagent (Applygen Technologies, Inc.). The blots were quantified using Image J software (National Institutes of Health, Bethesda, MD, USA). All the primary antibodies used in the experiments were purchased from Abcam (Cambridge, UK): RANKL (1:100, ab45039), TLR4 (1:2000, ab13556), p38 (1:5000, ab170099), p-p38^{y182} (1:100, ab47363) and TRAP (1:2000, ab208818).

Cell culture

RAW-264.7 mouse macrophages were purchased from BeNa Culture Collection (Beijing, China) and cultured in a 5% CO_2 incubator at 37°C in Dulbecco's modified Eagle's medium containing 10% fetal bovine serum and 100 IU/mL penicillin/streptomycin. RAW 264.7 cells were transfected with miR-20a mimic or RANKL overexpression plasmids and corresponding controls. After 24 h, the medium was renewed with a differentiated medium supplemented with 50 ng/mL macrophage colony-stimulating factor (M-CSF, Sigma-Aldrich Chemical Company, St Louis, MO, USA).

Differentiation of osteoclasts

After 5 days of cell culture, the medium was removed, and the cells were fixed, permeated, and air-dried. To identify osteoclasts, treated RAW 264.7 cells were subjected to TRAP staining with an acid phosphatase kit (Sigma-Aldrich Chemical Company, St Louis, MO, USA). TRAP$^+$ cells are defined as osteoclasts with more than 3 nuclei.

Statistical analysis

All data were processed by Statistical Product and Service Solutions 21.0 statistical software (IBM SPSS, Chicago, IL, USA). All data were presented as mean ± standard deviation (SD). The statistical differences were assessed using unpaired *t*-test, one-way or two-way analysis of variance (ANOVA), and multiple comparison between the groups was performed by using Tukey's post hoc test, in which $*p < 0.05$ represented as the difference significance.

RESULTS

MiR-20a expresses poorly in RA

The swelling and redness of the paw of the mice in the second week after the modeling as shown in Fig. 1A eased in the fourth week. The swelling degree of the paw of the mice was analyzed, and the results showed (Fig. 1 B, C) that compared with the sham-operated mice, the swelling degree of the CIA

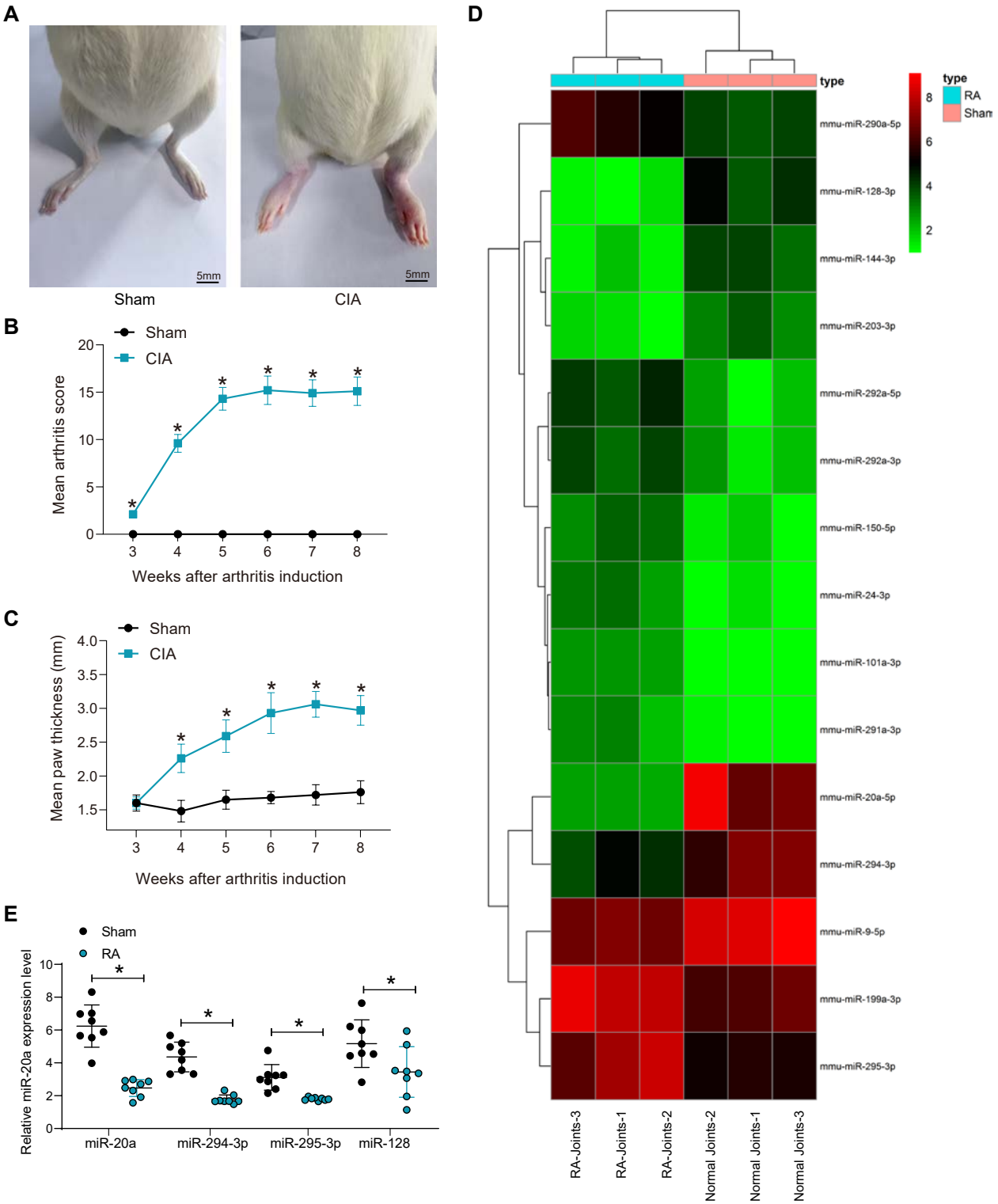


Fig. 1. *miR-20a is downregulated in the CIA mice. **A**) hind paws of RA mice on day 56. **B**) arthritis score of mice at week 3, 4, 5, 6, 7 and 8 after RA induction. **C**) paw thickness of mice at week 3, 4, 5, 6, 7 and 8 after RA induction. **D**) the heatmap for different expressed miRNAs between RA or sham mice. **E**) miR-20a, miR-294-3p, miR-295-3p, and miR-128 expression in knee joints of mice determined by RT-qPCR (each spot represents for a single mouse). The data are expressed as the mean ± SD. One-way ANOVA and Tukey's multiple comparison test or unpaired t test was used to determine statistical significance, *$p < 0.05$.*

mice was aggravated at week 1, 2, 3, and 4 ($p < 0.05$), suggesting the success of the RA model induction.

The differentially expressed miRNAs in ankle tissues from 3 CIA mice were first compared with those from 3 control mice by microarray analysis. By means of homogenization of raw data, 74 miRNAs with Log FoldChange > 2 and p value < 0.05 were selected as the screening conditions using Limma Rstudio package. Among them, 19 miRNAs were downregulated and 55 miRNAs were upregulated. The heatmap in Fig. 1D shows some differentially expressed miRNAs. RT-qPCR was then used to detect miR-20a, miR-294-3p, miR-295-3p and miR-128 expression in bone tissues of mice. It was found that they were significantly downregulated in the bone tissue of CIA mice, with the most pronounced difference in the expression of miR-20a (Fig. 1E).

MiR-20a agomir alleviates symptoms in CIA mice

To evaluate the effect of miR-20a *in vivo*, CIA mice were administrated with miR-20a agomir or agomir Mock (control). The treatment of miR-20a agomir alleviated the symptoms of RA mice, illustrating as lower arthritis scores and significantly decreased paw swelling (Fig. 2 A-D).

MiR-20a agomir inhibits bone erosion in CIA mice

Subsequently, histological staining was used to observe the pathological changes of RA mouse joints. HE staining and Safranin O-fast green staining showed that after miR-20a agomir administration, the number of inflammatory cell infiltration, synovial tissue hyperplasia, cartilage tissue damage and bone erosion in mouse joints were significantly inhibited (Fig. 3 A-E). Moreover, we found that mRNA and protein expression of TRAP, an osteoclast marker in the joints was significantly inhibited after addition of miR-20a agomir treatment (Fig. 3 F, G). As a result, miR-20a agomir inhibited osteoclastogenesis.

MiR-20a decreases osteoclast proliferation and differentiation

To further verify the role of miR-20a in osteoclastogenesis, TRAP staining was carried out. The results revealed that miR-20a agomir-treated mice had fewer TRAP-positive cells (Fig. 4 A, B) in the joints, so it could be further validated that miR-20a agomir inhibited osteoclastogenesis.

MiR-20a targets RANKL to disrupt the TLR4/p38 pathway

To identify the downstream molecular mechanism of miR-20a in RA mice, we predicted targeting mRNAs of miR-20a through StarBase. We then proved that miR-20a targeted RANKL by dual-luciferase reporter gene experiments (Fig. 5 A, B). Subsequently, the expression of RANKL was found significantly increased in the joint tissues of RA mice by immunoblotting experiments, while the that of RANKL was significantly decreased after the administration of miR-20a agomir (Fig. 5C). Moreover, the activation level of the TLR4/p38 pathway in CIA and sham-operated mice was further examined. The TLR4/p38 pathway was abnormally activated in CIA mice *versus* the sham-operated mice, however, after the addition of miR-20a agomir, the activation of the TLR4/p38 pathway was significantly inhibited (Fig. 5 D, E). Based on the above results, we reasoned that miR-20a could lower the expression of RANKL and disrupt the TLR4/p38 pathway in RA mice.

miR-20a inhibits RAW264.7 cell differentiation through targeting RANKL to disrupt the TLR4/p38 pathway

To further validate our conjecture, we overexpressed miR-20a alone or in the presence of oe-RANKL in RAW264.7 macrophages. We validated that cells were transfected successfully by RT-qPCR and Western blot (Fig. 6 A, B). We first used TRAP staining to detect the differentiation of RAW264.7 cells towards osteoclasts. The number of TRAP positive cells in transfected cells was significantly reduced following miR-20a mimic, and after further overexpression of RANKL, the number of TRAP positive cells showed a certain restoration (Fig. 6C). Subsequently, we used RT-qPCR to detect the expression of OPG and RANK in cells and found that the expression of OPG and RANK was significantly increased after miR-20a upregulation, but after further overexpression of RANKL, their expression in cells were significantly decreased (Fig. 6D). We subsequently used immunoblotting

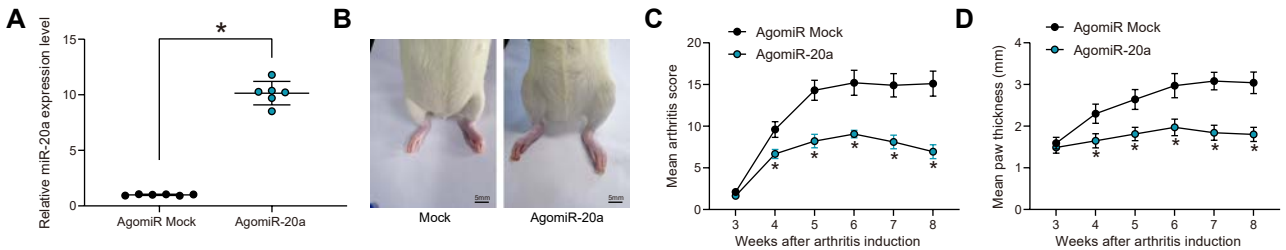


Fig. 2. *miR-20a agomir ameliorates severity of RA in mice. **A**) miR-20a expression in ankle tissues from mice treated with miR-20a agomir or agomir mock (each spot represents for a single mouse). **B**) Hind paws of RA mice on day 56. **C**) Arthritis score of mice at week 3, 4, 5, 6, 7 and 8 after RA induction. **D**) Paw thickness of mice at week 3, 4, 5, 6, 7 and 8 after RA induction. The data are expressed as the mean±SD. One-way ANOVA and Tukey's multiple comparison test or unpaired t test was used to determine statistical significance, *p < 0.05.*

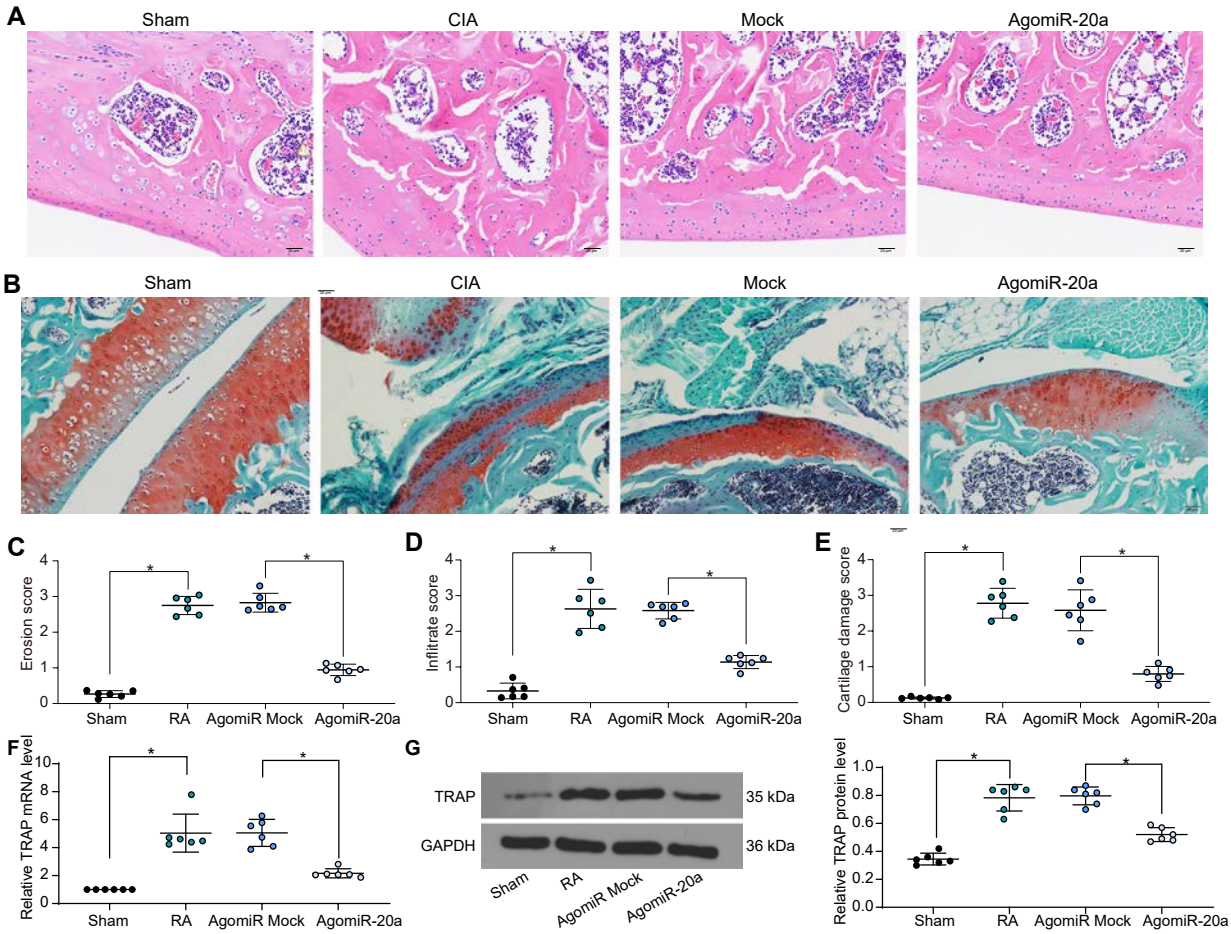


Fig. 3. *miR-20a agomir improves the morphology of arthritic joints. **A**) HE and (**B**) safranin O/fast green staining of the ankle joints in mice. **C**) Erosion score, (**D**) infiltration score and (**E**) cartilage damage score determination. **F**) mRNA and (**G**) protein expression of TRAP in ankle tissues determined by RT-qPCR and immunoblotting. The data are expressed as the mean±SD. One-way ANOVA and Tukey's multiple comparison test was used to determine statistical significance, *p < 0.05. Each spot represents for a single mouse in panel C, D, E and F.*

to detect the expression of TLR4/p38 pathway in cells. After overexpression of miR-20a, the extent of p38 phosphorylation and TLR4 expression in cells were significantly inhibited, but further RANKL overexpression led to promoted extent of p38 phosphorylation and TLR4 expression (Fig. 6E).

DISCUSSION

Osteoclastogenesis is of great importance for bone health, and the expression patterns of genes related to osteoclasts altered significantly in the process of osteoclastogenesis, contributing to differences in the shape and functions of cells (17). In the present study, we found that miR-20a attenuated the severity of RA in developed CIA mice and hindered osteoclastogenesis and osteoclast differentiation in mice and RAW264.7 cells. The mean arthritis scores as well as mean paw thickness in agomir miR-20a-treated mice were significantly lower than those in agomir mock-treated mice. More importantly, we monitored that miR-20a may exert its anti-arthritic

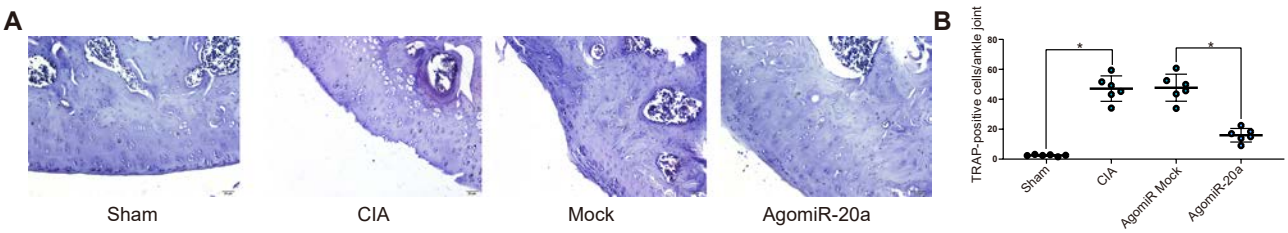


Fig. 4. *miR-20a agomir decreases osteoclast numbers and suppresses osteoclast formation. **A)** Images of TRAP-stained knee sections for mice in each group observed under a light microscope (purple, indicated by the arrows). **B)** The number of TRAP-positive cells in knee sections were counted (each spot represents for a single mouse). The data are expressed as the mean ± SD. One-way ANOVA and Tukey's multiple comparison test was used to determine statistical significance, *p < 0.05.*

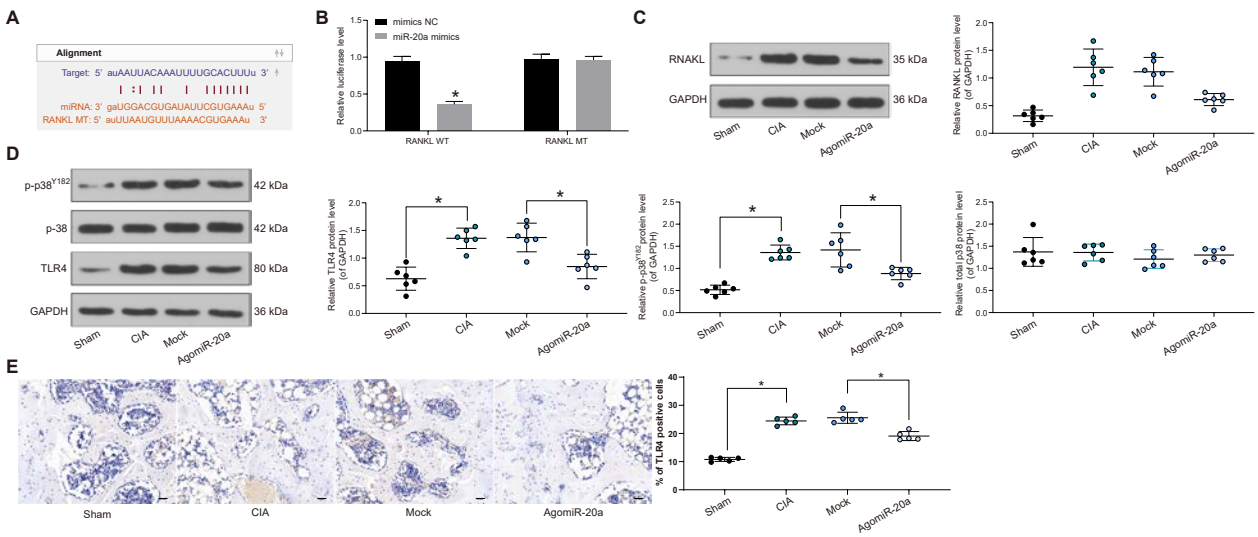


Fig. 5. *miR-20a impairs the induction of the TLR4/p38 pathway by targeting RANKL. **A)** schematic illustration of the predicted miR-20a binding sites in RANKL predicted by StarBase. **B)** The binding between RANKL mRNA and miR-20a determined by dual-luciferase assays. **C)** RANKL protein expression normalized to GAPDH determined by immunoblotting. **D)** The protein expression of p38 and TLR4 as well as the extent of p38 phosphorylation normalized to GAPDH measured by immunoblotting. **E)** The immunohistochemical staining of TLR4 in rats. The data are expressed as the mean ± SD. One-way ANOVA and Tukey's multiple comparison test was used to determine statistical significance, *p < 0.05. Each spot represents for a single mouse in panel C, D and E.*

role through the impairment of RANKL-mediated TLR4/p38 pathway.

This study emphasized a novel role for miR-20a in regulating osteoclastogenesis and bone erosion. Initially, miR-20a was observed to be downregulated in ankle tissues of CIA mice. miRNAs exert substantial roles in mediating multiple biological processes of osteoclast differentiation and function, marking miRNAs as potent biomarkers and targets (18). In line with our findings, miR-20a was found to be reduced in various autoimmune diseases, such as multiple sclerosis (19) and systemic lupus erythematosus (20). miR-20a, belonging to the miRNA-17~92a cluster at 13q31-q32, was established by Gennari et al. to engage in the modulation of bone formation (21). miR-20a was also clarified as a vital inverse mediator of chondrogenic differentiation by repressing autophagy via targeting Atg7 (22). In addition, miR-20a may play a pivotal role in fibroblast-like synoviocytes of adjuvant-induced arthritis by targeting thioredoxin-interacting protein (23). More specifically, decline of miR-20a enhanced cell proliferation, while reducing apoptosis in fibroblast-like synoviocytes, thus playing a critical part in RA (24). Furthermore, breast cancer cell-released exosomal miR-20a-5p facilitated the osteoclast proliferation and differentiation by binding to SRCIN1, thereby potentiating bone metastasis (18). The discordance may be due to the different microenvironments. The inhibitory effect

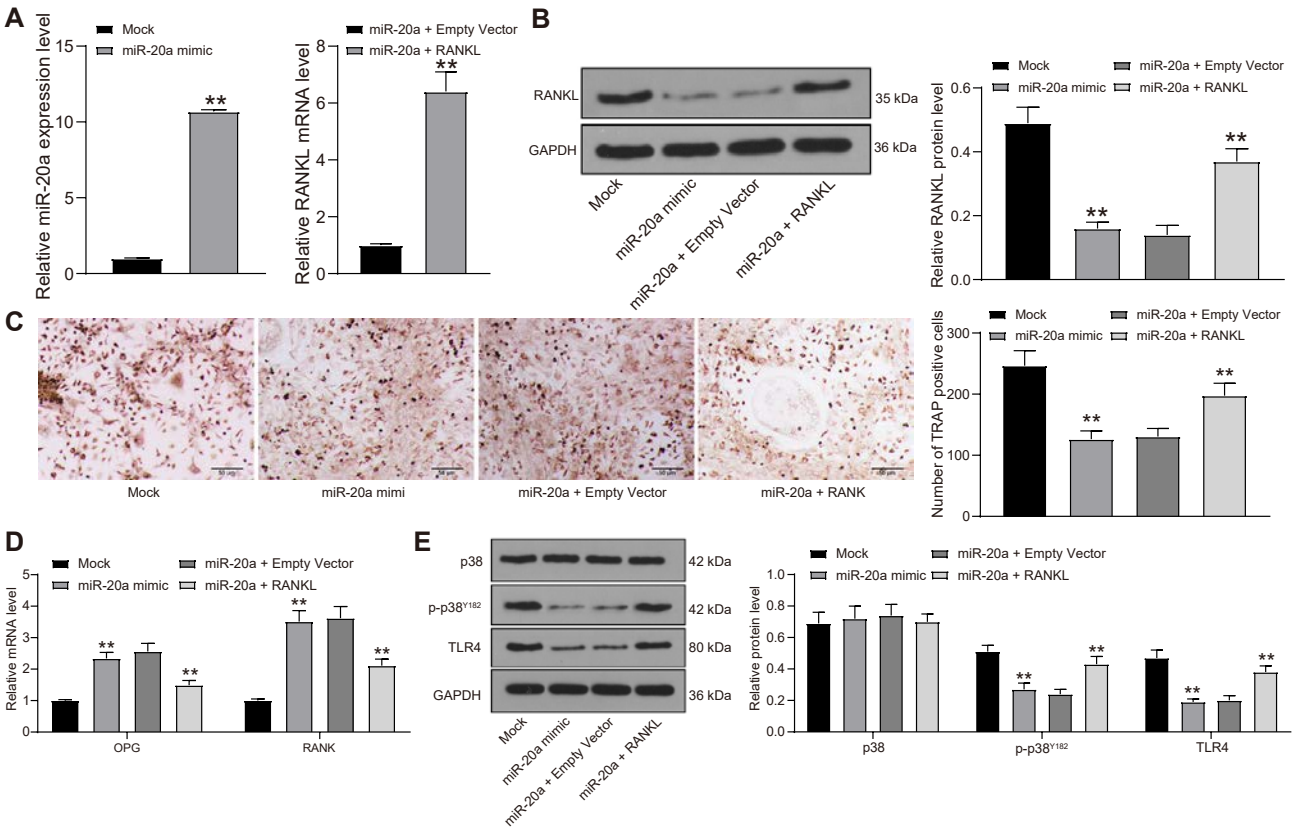


Fig. 6. *miR-20a inhibits RAW264.7 cell differentiation to osteoclasts by targeting RANKL via the TLR4/p38 pathway. RAW264.7 macrophages were transfected with miR-20a mimic alone or with oe-RANKL.* ***A****) RANKL mRNA and miR-20a expression in macrophages measured by RT-qPCR.* ***B****) RANKL protein expression normalized to GAPDH in macrophages determined by immunoblotting.* ***C****) the differentiation ability of RAW264.7 cells into polynuclear osteoclasts determined by TRAP staining.* ***D****) mRNA expression of OPG and RANK in macrophages measured by RT-qPCR.* ***E****) p38 and TLR4 protein expression as well as p38 phosphorylation in macrophages normalized to GAPDH determined by immunoblotting. The statistical differences were assessed using unpaired t-test (panel A), one-way (panel B and C) or two-way ANOVA (panel D and E), and multiple comparison between the groups was performed by using Tukey's post hoc test, **$p < 0.01$.*

of miR-20a on osteoclastogenesis is further verified by the reduced expression and staining intensity of TRAP, an osteoclast marker. These results therefore suggest a protective role of miR-20a in osteoclast-associated bone disorders.

In-silico analysis revealed that the 3'UTR of RANKL contains putative binding sites of miR-20a. Osteoclasts, multinucleated giant cells, have a potency to differentiate from myeloid precursors influenced by the cytokine RANKL (25), indicating the relevance of RANKL to osteoclastogenesis. The majority of studies involving the mechanism of the RANK/RANKL/OPG interaction was conducted in the setting of bone resorption under inflammation exposure, and RANK induced by RANKL promoted the osteoclast differentiation (26). Once primed with RANKL and then stimulated with agonists for TLR4 in the presence of M-CSF, but in the absence of RANKL, the progenitors differentiate to osteoclasts (27). Hyaluronan could suppress RANKL-dependent TLR4 pathway induced by lipopolysaccharide, presenting a substitute target for treating destructed joint bones and cartilages in RA (28). Previously, miR-146a was validated to prevent osteoclast formation evoked by lipopolysaccharides or RANKL alone as well as osteoclastogenesis induced by both lipopolysaccharides and RANKL (29). While the present study provides evidence that miR-20a agomir lowered the expression of RANKL in RA mice. Moreover, miR-20a agomir may also be responsible for the blockage of the TLR4/p38 pathway. TLR4 was closely associated with RA development by modulating osteoclast formation, synovial tissue inflammatory response along with T lymphocyte migration, differentiation and function (30). Similarly, miR-20a hampered the expression patterns of proinflammatory cytokines by targeting TLR4 in lipopolysaccharide-exposed human gingival fibroblasts (31). The negative correlation between miR-20a and TLR4 has also been investigated in human aortic endothelial cells, which may be beneficial to the alleviation of atherosclerosis (32). In turn, deficiency of TLR4 was protective against cholesteatoma-stimulated bone destruction and hindered osteoclast formation by lowering expression of RANKL (33). While the current work provided evidence that miR-20a could enhance the expression of OPG and RANK, yet lower the extent of p38 phosphorylation and TLR4 expression in RAW264.7 cells, which were reversed by RANKL overexpression. Therefore, it could be concluded that miR-20a regulate the process of osteoclastogenesis by interacting with RANKL to block the TLR4/p38 pathway.

Our results demonstrate that miR-20a acted as a negative regulator of osteoclastogenesis through the TLR4/p38 pathway and played a protective role in RA by inhibiting RANKL expression. These data imply that miR-20a may play an anti-arthritic role in the pathophysiology of RA and could act as a novel and additive therapeutic modality for RA and other osteoclast-related diseases, although further studies are needed.

REFERENCES

1. Xiao W, Li S, Pacios S, Wang Y, Graves DT. Bone remodeling under pathological conditions. Front Oral Biol 2016; 18:17-27.
2. Dolati S, Sadreddini S, Rostamzadeh D, Ahmadi M, Jadidi-Niaragh F, Yousefi M. Utilization of nanoparticle technology in rheumatoid arthritis treatment. Biomed Pharmacother 2016; 80:30-41.
3. Maruotti N, Grano M, Colucci S, d'Onofrio F, Cantatore FP. Osteoclastogenesis and arthritis. Clin Exp Med 2011; 11:137-45.
4. Inoue K, Nakano S, Zhao B. Osteoclastic microRNAs and their translational potential in skeletal diseases. Semin Immunopathol 2019; 41:573-82.
5. Vicente R, Noel D, Pers YM, Apparailly F, Jorgensen C. Deregulation and therapeutic potential of microRNAs in arthritic diseases. Nat Rev Rheumatol 2016; 12:211-20.
6. Ji X, Chen X, Yu X. MicroRNAs in Osteoclastogenesis and Function: Potential Therapeutic Targets for Osteoporosis. Int J Mol Sci 2016; 17:349.
7. Philippe L, Alsaleh G, Pichot A, et al. MiR-20a regulates ASK1 expression and TLR4-dependent cytokine release in rheumatoid fibroblast-like synoviocytes. Ann Rheum Dis 2013; 72:1071-9.
8. Sun KT, Chen MY, Tu MG, Wang IK, Chang SS, Li CY. MicroRNA-20a regulates autophagy related

protein-ATG16L1 in hypoxia-induced osteoclast differentiation. Bone 2015; 73:145-53.
9. Gong XY, Zhang Y. Protective effect of miR-20a against hypoxia/reoxygenation treatment on cardiomyocytes cell viability and cell apoptosis by targeting TLR4 and inhibiting p38 MAPK/JNK signaling. In Vitro Cell Dev Biol Anim 2019; 55:793-800.
10. Fan M, Li X, Gao X, et al. LPS Induces Preeclampsia-Like Phenotype in Rats and HTR8/SVneo Cells Dysfunction Through TLR4/p38 MAPK Pathway. Front Physiol 2019; 10:1030.
11. Ji JD, Park-Min KH, Shen Z, Fajardo RJ, Goldring SR, McHugh KP, Ivashkiv LB. Inhibition of RANK expression and osteoclastogenesis by TLRs and IFN-gamma in human osteoclast precursors. J Immunol 2009; 183:7223-33.
12. Kagiya T, Nakamura S. Expression profiling of microRNAs in RAW264.7 cells treated with a combination of tumor necrosis factor alpha and RANKL during osteoclast differentiation. J Periodontal Res 2013; 48:373-85.
13. Brand DD, Latham KA, Rosloniec EF. Collagen-induced arthritis. Nat Protoc 2007; 2:1269-75.
14. Lee SW, Kim JH, Park YB, Lee SK. Bortezomib attenuates murine collagen-induced arthritis. Ann Rheum Dis 2009; 68:1761-7.
15. Sastre D, Baiochi J, de Souza Lima IM, et al. Focused screening reveals functional effects of microRNAs differentially expressed in colorectal cancer. BMC Cancer 2019; 19:1239.
16. Park MC, Kwon YJ, Chung SJ, Park YB, Lee SK. Liver X receptor agonist prevents the evolution of collagen-induced arthritis in mice. Rheumatology (Oxford) 2010; 49:882-90.
17. Ling L, Hu HL, Liu KY, Ram YI, Gao JL, Cao YM. Long noncoding RNA MIRG induces osteoclastogenesis and bone resorption in osteoporosis through negative regulation of miR-1897. Eur Rev Med Pharmacol Sci 2019; 23:10195-203.
18. Guo L, Zhu Y, Li L, Zhou S, Yin G, Yu G, Cui H. Breast cancer cell-derived exosomal miR-20a-5p promotes the proliferation and differentiation of osteoclasts by targeting SRCIN1. Cancer Med 2019; 8:5687-701.
19. Cox MB, Cairns MJ, Gandhi KS, et al. MicroRNAs miR-17 and miR-20a inhibit T cell activation genes and are under-expressed in MS whole blood. PLoS One 2010; 5:e12132.
20. Carlsen AL, Schetter AJ, Nielsen CT, et al. Circulating microRNA expression profiles associated with systemic lupus erythematosus. Arthritis Rheum 2013; 65:1324-34.
21. Gennari L, Bianciardi S, Merlotti D. MicroRNAs in bone diseases. Osteoporos Int 2017; 28:1191-213.
22. Xu R, Wei Y, Yin X, Shi B, Li J. miR-20a suppresses chondrogenic differentiation of ATDC5 cells by regulating Atg7. Sci Rep 2019; 9:9243.
23. Li XF, Shen WW, Sun YY, et al. MicroRNA-20a negatively regulates expression of NLRP3-inflammasome by targeting TXNIP in adjuvant-induced arthritis fibroblast-like synoviocytes. Joint Bone Spine 2016; 83:695-700.
24. Wei XJ, Li XW, Lu JL, et al. MiR-20a regulates fibroblast-like synoviocyte proliferation and apoptosis in rheumatoid arthritis. Eur Rev Med Pharmacol Sci 2017; 21:3886-3893.
25. Charles JF, Aliprantis AO. Osteoclasts: more than 'bone eaters'. Trends Mol Med 2014; 20:449-59.
26. Kichev A, Eede P, Gressens P, Thornton C, Hagberg H. Implicating Receptor Activator of NF-kappaB (RANK)/RANK Ligand Signalling in Microglial Responses to Toll-Like Receptor Stimuli. Dev Neurosci 2017; 39:192-206.
27. Souza PPC, Lerner UH. Finding a Toll on the Route: The Fate of Osteoclast Progenitors After Toll-Like Receptor Activation. Front Immunol 2019; 10:1663.
28. Watanabe T, Takahashi N, Hirabara S, Ishiguro N, Kojima T. Hyaluronan Inhibits Tlr-4-Dependent RANKL Expression in Human Rheumatoid Arthritis Synovial Fibroblasts. PLoS One 2016; 11:e0153142.
29. Gao Y, Wang B, Shen C, Xin W. Overexpression of miR146a blocks the effect of LPS on RANKLinduced osteoclast differentiation. Mol Med Rep 2018; 18:5481-8.
30. Xu N, Wang Y, Zhao S, Jiao T, Xue H, Shan F, Zhang N. Naltrexone (NTX) relieves inflammation in the collagen-induced- arthritis (CIA) rat models through regulating TLR4/NFkappaB signaling pathway. Int Immunopharmacol 2020; 79:106056.
31. Li J, Wang M, Song L, Wang X, Lai W, Jiang S. LncRNA MALAT1 regulates inflammatory cytokine production in lipopolysaccharide-stimulated human

gingival fibroblasts through sponging miR-20a and activating TLR4 pathway. J Periodontal Res 2020; 55:182-90.

32. Chen M, Li W, Zhang Y, Yang J. MicroRNA-20a protects human aortic endothelial cells from Ox-LDL-induced inflammation through targeting TLR4 and TXNIP signaling. Biomed Pharmacother 2018; 103:191-7.
33. Si Y, Chen YB, Chen SJ, et al. TLR4 drives the pathogenesis of acquired cholesteatoma by promoting local inflammation and bone destruction. Sci Rep 2015; 5:16683.

Long non-coding NEAT1 weakens the protective role of sevoflurane on myocardial ischemia/reperfusion injury by mediating the microRNA-140/RhoA axis

PF. Rui, JH. Wang and J. Xu*

Department of Anesthesiology, Liyang People's Hospital of Jiangsu Province, Liyang, Jiangsu, P.R. China

Received October 30, 2020 – Accepted May 19, 2021

The function of long non-coding RNA (lncRNA) nuclear enriched abundant transcript 1 (NEAT1) has been revealed in injury caused by myocardial ischemia/reperfusion (I/R), however, its association with Sevoflurane (Sev), an anesthetic effective for regulating inflammation and oxidative stress, is not yet clear in I/R injury. The aim of this study was to functionally validate and elucidate the mechanism-of-action for Sev-mediated NEAT1 in myocardial I/R injury. Firstly, reduced NEAT1 was revealed in myocardial I/R injured mice treated with Sev. Moreover, restoration of NEAT1 could repress the alleviating role of Sev in cardiac function, infarct size and myocardial apoptosis in mice, while miR-140 was remarkably enhanced in myocardial tissues from mice treated with Sev. Furthermore, miR-140 was suggested and authenticated as a downstream biomolecule of NEAT1 with the help of a bioinformatics tool. Interestingly, miR-140 inhibitor played the same role as NEAT1 overexpression on the cardiac function, infarct size and apoptosis of mice. Finally, it was manifested that RhoA was a putative target of miR-140, which functioned importantly in the Sev/miR-140-mediated myocardial I/R injury. All in all, NEAT1 knockdown contributed to Sev-mediated myocardial I/R injury alleviation via the miR-140/RhoA axis.

Ischemia/reperfusion (I/R) is characterized by deficiency of oxygen supply and the following restoration of blood flow, resulting in irreversible injuries to tissues (1). Acute myocardial infarction is one of the leading causes of death and disability in the world, and the treatment option for easing myocardial injury and reducing myocardial infarction size is timely reperfusion using thrombolytic therapies or primary percutaneous coronary intervention (2). Sevoflurane (Sev) is a volatile anesthetic agent that offers hypnosis, analgesia and akinesia during surgical and procedural interventions (3). The role of Sev during I/R injury has been highlighted in the lung (4), brain (5) and heart (6). Interestingly, LINC00652, a kind of long non-coding RNA (lncRNA), was observed to work with Sev to exert cardioprotective role against myocardial I/R injury (7), hence, we postulated that lncRNAs may engage in the Sev-mediated myocardial I/R injury alleviation.

Noncoding RNAs, a group of RNAs that do not encode proteins, can be divided into lncRNAs, microRNAs (miRNAs) and circular RNAs, and are closely related to cardiovascular disease by regulating cell proliferation, apoptosis and other vital biological events (8). For example, downregulation of nuclear enriched abundant transcript 1 (NEAT1) acted as a protector against the apoptosis of cardiomyocytes under hypoxia/reoxygenation (9). It has been proposed that competing endogenous RNAs (ceRNAs) modulate

Key words: Sevoflurane; long non-coding RNA NEAT1; microRNA-140; RhoA; myocardial ischemia/reperfusion

Corresponding Author:
Dr Jing Xu,
Department of Anesthesiology,
Liyang people's Hospital of Jiangsu Province,
N0. 70, Jianshe West Road, Liyang 213300, Jiangsu, P.R. China
Tel./Fax: +86 15961114205
e-mail: xujing010905@163.com

0393-974X (2021)
Copyright © by BIOLIFE, s.a.s.
This publication and/or article is for individual use only and may not be further reproduced without written permission from the copyright holder.
Unauthorized reproduction may result in financial and other penalties
DISCLOSURE: ALL AUTHORS REPORT NO CONFLICTS OF INTEREST RELEVANT TO THIS ARTICLE.

the distribution of miRNAs on their target mRNAs, thereby exerting a post-transcriptional regulation (10). For instance, NEAT1 enhanced myocardial I/R injury by competing with mitogen-activated protein kinase 6 to regulate miR-495-3p (11). While miR-140, which is predicted as binding miRNA of NEAT1 by a bioinformatics website in the current study, was found to attenuate myocardial I/R injury via inhibiting mitochondria-mediated apoptosis by interacting with YES1 (12). Also lncRNA SNHG1 protected SH-SY5Y cells from injury caused by oxygen glucose deprivation through the miR-140-5p/Bcl-XL axis (13). The additional activity of RhoA was monitored to promote oxidative stress and the progression of cardiovascular diseases (14). More specifically, the protective role of Ginsenoside Rb1 against I/R-induced myocardial injury was achieved by mediating the RhoA signaling pathway (15). In addition, RhoA was found to share binding sites with miR-140 by Starbase in the present study. Based on the aforementioned reports, this experiment was carried out to probe the function of NEAT1 during injury evoked by myocardial I/R in a developed mouse model by regulating the miR-140/RhoA axis with the administration of Sev.

MATERIALS AND METHODS

Mouse treatment

The experiments were carried out under the approval of the Ethics Committee of Liyang People's Hospital of Jiangsu Province on the basis of the Guide for the Care and Use of Laboratory Animals formulated by the National Institutes of Health. Substantial efforts were made to minimize the suffering and numbers of the animals used during the experiment. All mice used in this study were from Beijing Vital River Laboratory Animal Technology Co., Ltd. (Beijing, China). Twenty-seven C57BL/6N male mice (aged 6-8 weeks, weight 15-25 g) were allowed to acclimatize for one week in the animal facility (at a constant temperature of 22℃ with 12 h light/dark cycles) before any intervention was initiated. Mice were allocated into groups of sham (shamed-operated mice), I/R (mice subjected to I/R surgery only), IS (mice inhaled with Sev during the reperfusion of I/R surgery), NEAT1-negative control (NC) (mice injected with mock 48 h before I/R treatment), NEAT1-overexpression (OE, mice injected with NEAT1-OE 48 h before I/R treatment), miR-140 control (mice injected with miR-140 control 48 h before I/R treatment), miR-140 inhibitor (mice injected with miR-140 inhibitor 48 h before I/R treatment), miR-140 inhibitor + dimethylsulfoxide (DMSO, mice injected with miR-140 inhibitor and DMSO 48 h before I/R treatment), miR-140 inhibitor + C3 (mice injected with miR-140 inhibitor and extracellular enzyme C3 48 h before I/R treatment) groups. NEAT1-OE and miR-140 inhibitor fragments and NCs were synthesized by GenePharma (Shanghai, China). The lentiviral vector pLenti6 (Thermo Fisher Scientific Inc., Waltham, MA, USA) was transfected with RNA fragments BLOCK-iT lentiviral RNAi expression system (Thermo Fisher Scientific). The mice were then anesthetized with 1% pentobarbital sodium through an intraperitoneal injection at 60 mg/kg. A longitudinal incision was made between the 2nd, 3rd and 4th ribs to expose the heart. The corresponding transfection solution (10 μL) was slowly injected at the anterior wall of the left ventricle of the mouse. After the injection, the mouse chest was sutured.

Development of a myocardial I/R mouse model

On the day of the I/R experiment, all mice were injected intraperitoneally with atropine at 0.04 mg/kg and with pentobarbital sodium at 60 mg/kg after 5 min. Once the respiratory frequency of mice reached 90 times/min, the mice were connected to an animal breathing apparatus, which was set at the frequency 90-105 times/min with a tidal volume at 1 mL. A longitudinal incision was made between the second and fourth ribs to expose the heart and pericardium. The left anterior descending coronary artery was ligated from the tip of the left auricle. An electrocardiogram (ECG) was applied to assess the ischemic condition. After 30 min, blood flow was restored for reperfusion for 15 min, during which mice inhaled 2.4% Sev continuously, and mice in the sham group inhaled common air. The intercostal and pectoral muscles were sutured to close the chest after heart rhythm stabilization. After the suture, excess gas was extracted with needles from thoracic cavities. When the mice had mild spontaneous respiration, the apparatus was removed. Following, the skin was sutured, the mice were put back into animal rooms with a 0.5 mL saline intraperitoneal injection.

ECG

A small animal ultrasound imaging system was purchased from VisualSonics (Fujifilm VisualSonics, Inc., Toronto, ON, Canada). The left ventricular end-diastolic volume (LVEDV), left ventricular end-systolic volume (LVESV), left ventricular end-diastolic diameter (LVDd) and left ventricular end-systolic diameter (LVDs) were measured to obtain left ventricular ejection fraction (LVEF) and left ventricular fractional shortening (LVFS). LVEF (%) = (LVEDV - LVESV)/(LVEDV) × 100%, LVFS (%) = (LVDd - LVDs)/LVDd × 100%.

Triphenyl tetrazolium chloride (TTC) staining

Slices were cultured in a petri dish containing TTC staining solution (Solabio, China). After a 30-min incubation at 37°C, the stained sections were removed with a pipette, rinsed with 4°C phosphate buffered saline, observed by naked eyes and photographed. The red part represents normal non-ischemic myocardial tissues, the gray part represents ischemic but non-infarct myocardial tissues, and the white part represents myocardial tissues with ischemic infarction. Image-Pro Plus 6.0 software was applied to determine the percentage of myocardial infarction area.

Terminal deoxynucleotidyl transferase (TdT)-mediated dUTP nick-end labeling (TUNEL) staining

The cells in logarithmic growth of each group were plated at 1 × 10^6 cells/mL on the cover glasses in the 6-well plate. Apoptosis was detected using In Situ Cell Death Detection Kit-peroxidase (Roche, Basel, Switzerland). The cell suspension was coated on the cover glasses, reacted with Proteinase K for 15 min and incubated with 50 μL TUNEL solution in a dark chamber for 1 h at 37°C. Following a 10-min treatment with 50 μL diaminobenzidine, the results were recorded using an M-60 microscope (Olympus Optical Co., Ltd., Tokyo, Japan) equipped with BH2 system with attached 35 mm camera (Olympus). The number of TUNEL-positive cells was counted under five randomly-selected high magnification views.

Table I. *Primers for reverse transcription quantitative polymerase chain reaction*

Targets	Primer sequence (5'-3')
NEAT1	Forward: CAAATTCGTGAAGCGTTCCATA
	Reverse: GTGCCGAGTCCGGACGATATTC
miR-140	Forward: TACCACAGGGTAGAACCACGG
	Reverse: TGCTTGGCAATAACAGACCAAC
RhoA	Forward: GATTGGCGCTTTTGGGTACAT
	Reverse: AGCAGCTCTCGTAGCCATTTC
U6	Forward: CTCGCTTCGGCAGCACA
	Reverse: AACGCTTCACGAATTTGCGT
GAPDH	Forward: GGAGCGAGATCCCTCCAAAA
	Reverse: GGCTGTTGTCATACTTCTCATGG

NEAT1: nuclear enriched abundant transcript 1; miR-140: microRNA-140; GAPDH: glyceraldehyde-3-phosphate dehydrogenasea

Microarray analysis

Total RNA was extracted by ice-lysed mouse tissue homogenate in Trizol (Beijing Solabio Life Sciences Co., Ltd., Beijing, China). A total of 0.5 μg total RNA was reversely transcribed into cDNA through PrimeScript™ IV 1st strand cDNA Synthesis Mix (Takara Holdings Inc., Kyoto, Japan). The cDNA was then fragmented and hybridized with a mouse lncRNA expression array V6.0 (Shanghai Biotechnology Corporation), and the array was screened using GeneChip™ Scanner 3000 7G system (Thermo Fisher Scientific Inc., Waltham, MA, USA). Scanning results were subjected to quality assessment and data correction. R language package was used to plot the heatmap using processed data. $p < 0.01$ and $\log_2$ Fold Change| were used as the screening criteria, and the top ten RNAs were selected for analysis.

Reverse transcription quantitative polymerase chain reaction (RT-qPCR)

Total RNA was used for RNA extraction from tissues using Trizol. Totally 5 μg total RNA was collected for reverse transcription and RT-qPCR through the SuperScript™ IV One-Step RT-PCR System. U6 and glyceraldehyde-3-phosphate dehydrogenase (GAPDH) served as the internal normalized references. The primers are displayed in Table I. Relative expression of targets was determined using $2^{-\Delta\Delta Ct}$.

Luciferase reporter assay

HEK293T cells (Cell Bank of Shanghai Institute of Cells, Chinese Academy of Science, Shanghai, China) were grown in Dulbecco's modified Eagle's medium. When the density reached 80%-90%, the cells were detached with 0.25% trypsin and passaged in a 5% CO_2 incubator at 37°C, and the cells in logarithmic growth phase were harvested for further experiments. The targets of NEAT1 and miR-140 were analyzed using StarBase and verified by luciferase reporter assays. The miRNA 3'untranslated region (3'UTR) sequence and the lncRNA and mRNA 3'UTR sequence were inserted into pGL4.18 luciferase reporter vectors (Promega Corporation). HEK293T cell co-transfection was carried out using Lipofectamine 3000 (Invitrogen, Carlsbad, CA, USA). After 24 h, the cells were lysed, and the luciferase activity was assessed by a dual-luciferase reporter assay system (Promega). The rate of firefly luciferase activity to renilla luciferase activity reflects the relative luciferase activity.

Western blot

After 48 h of transfection, the cells were lysed on ice with radio immunoprecipitation assay lysis buffer. The samples were centrifuged at 20,000 g for a period of 10 min at 4°C to collect the supernatant. The bicinchoninic acid kit (Sigma-Aldrich Chemical Company, St Louis, MO, USA) was used to quantify the extracted protein. Equal volumes of proteins (15 μg) were run on 12% sodium dodecyl sulphate-polyacrylamide gel electrophoresis. Afterwards, the proteins were transferred to polyvinylidene fluoride membranes (Millipore, Billerica, MA, USA) and sealed with 5% skim milk for 2 h. Blots were probed with the primary antibody against RhoA (ab187027, Abcam Inc., Cambridge, UK) at 4°C overnight and with the secondary antibody (ab205718, Abcam) for 3 h at room temperature. Lastly, the immunoblot was visualized by Superstar electrochemiluminescence Plus. Gel imaging system (Bio-Rad Laboratories, Hercules, CA, USA) was applied to determine protein expression.

Statistical analysis

Statistical analysis was validated by SPSS 22.0 (IBM Corp. Armonk, NY, USA). All data are expressed as mean ± standard derivation (SD). Statistical significance was determined using unpaired *t*-test and one-way or two-way analysis of variance (ANOVA), as appropriate. If ANOVA was significant, individual differences were assessed using the Tukey's post-test. For all studies, values of $p < 0.05$ were considered statistically significant.

RESULTS

Reduction of myocardial I/R injury is found in mice treated with Sev

To test whether the injury following I/R was successfully induced and to test the relevance of Sev, the biochemical parameters related to cardiac function were measured. The LVEF and LVFS of I/R-treated mice were lower than that of sham-operated mice, and the those of Sev-treated mice were higher than that of the I/R-treated mice without inhalation (Fig. 1A). We later found by heart observation that the myocardial infarction area of Sev-treated mice was significantly smaller than that of mice subjected to I/R alone (Fig. 1B). Subsequently, it was further exhibited that the apoptosis of cardiomyocytes in mice after Sev treatment was significantly reduced

(Fig. 1C), which implied that the I/R model was effectively developed and that Sev treatment could reduce the occurrence of injury caused by myocardial I/R in mice.

Decreased NEAT1 expression was identified in mice with myocardial I/R following Sev treatment

We then performed lncRNA microarray analysis on myocardial tissues of I/R mice treated with Sev or without any other treatment. The microarray analysis results showed that NEAT1 was significantly downregulated after Sev inhalation (Fig. 2A), which was verified by RT-qPCR (Fig. 2B). We then injected NEAT1-NC and NEAT1-OE into the nude mice, and the success of model was established by RT-qPCR analysis of cardiomyocytes (Fig. 2C).

NEAT1 inhibits the role of Sev in myocardial I/R injury

The LVEF and LVFS indices of NEAT1-OE-injected mice were notably decreased compared with the NEAT1-NC-injected mice (Fig. 3A). Meanwhile, NEAT1-OE significantly increased the myocardial infarction area of the heart compared to the NEAT1-NC (Fig. 3B), and overexpression of NEAT1 also resulted in an increased rate of apoptosis in mouse cardiomyocytes (Fig. 3C), from which it can be inferred that NEAT1 could reduce the alleviating role of Sev in injury caused by myocardial I/R.

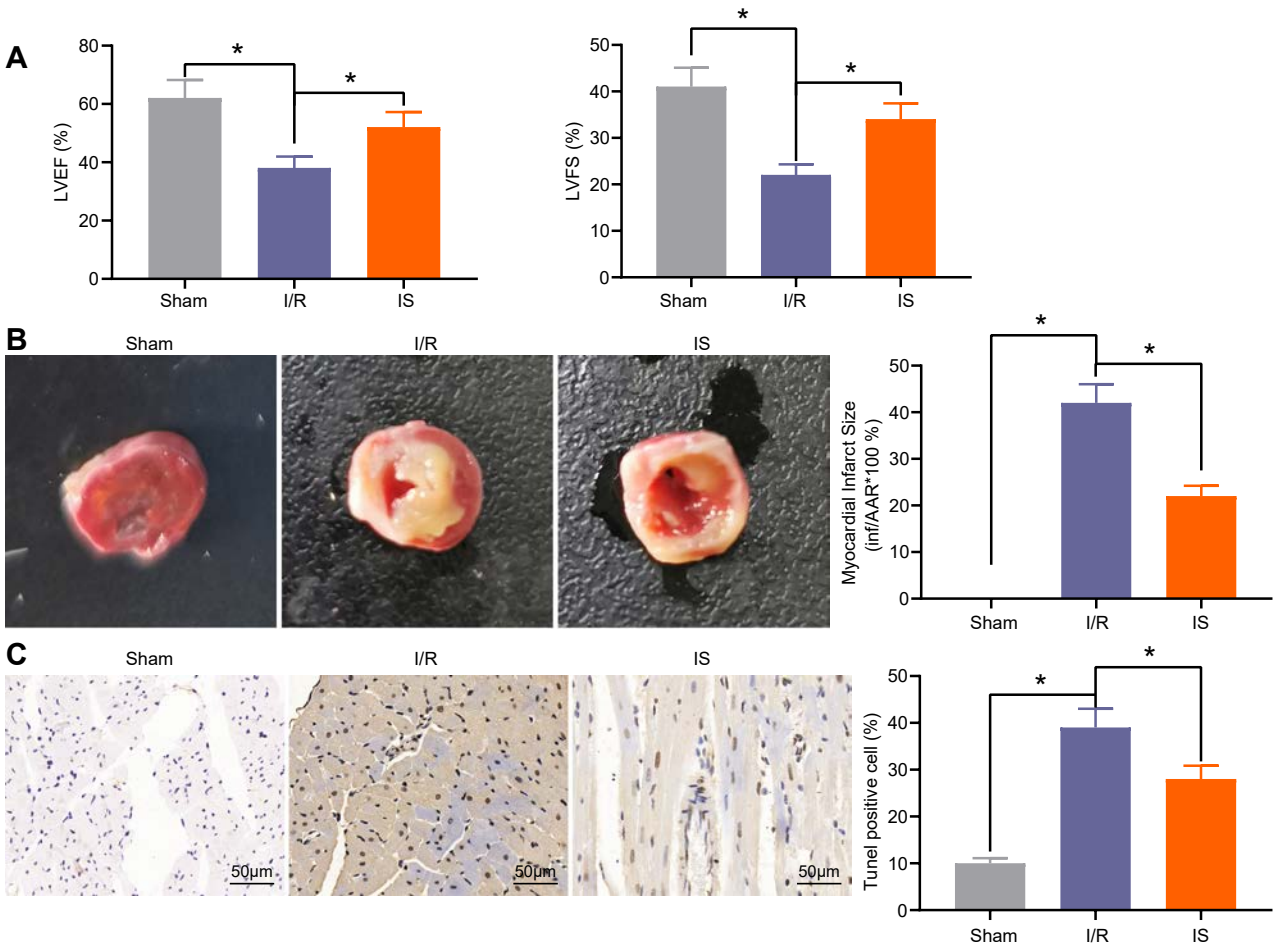


Fig. 1. *Sev acts as a cardio-protector in mice with injury caused by myocardial I/R. **A**) LVEF and LVFS in mice with I/R injury and Sev-treated model evaluated by ECG; **B**) myocardial infarct area in mice tested by TTC staining; **C**) the apoptosis rate of I/R and Sev-treated model assessed by TUNEL staining. *p < 0.05 according to the one-way ANOVA. Results are expressed as mean ± SD (n = 3 per group). The experiment was repeated 3 times.*

miR-140 promotes the role of Sev in myocardial I/R injury

We then performed a miRNA microarray analysis on myocardial tissues of I/R mice treated with Sev or without any other treatment to screen the significantly upregulated miRNAs (Fig. 4A), which was intersected with the binding miRNAs of NEAT1 predicted by StarBase (Fig. 4B). miR-140 was remarkably upregulated in I/R mice treated with Sev and had a targeting relationship with NEAT1. The results of dual-luciferase reporter gene assays showed that in terms of the miR-140 mimic group, the luciferase activity of NEAT1-wild type (WT) was profoundly lower than that of the miR-140 NC group (Fig. 4C). RT-qPCR validated that miR-140 was significantly upregulated in mice subjected to I/R after Sev treatment (Fig. 4D). The expression of miR-140 was then analyzed in mice injected with NEAT1-NC or NEAT1-OE and it was found that the miR-140 expression in NEAT1-OE-injected mice was decreased (Fig. 4E). As a consequence, we administrated miR-140 inhibitor or control into nude mice, which was verified by RT-qPCR (Fig. 4F). miR-140 inhibitor resulted in significantly decreased LVEF and LVFS indices (Fig. 4G). Meanwhile, miR-140 inhibitor led to increased myocardial infarction area in the mouse heart compared with miR-140 control (Fig. 4H). Poor expression of miR-140 also caused increased apoptosis rate in mouse cardiomyocytes (Fig. 4I).

Inhibition of RhoA partially restores the effect of miR-140 on Sev

StarBase website predicted that RhoA was a

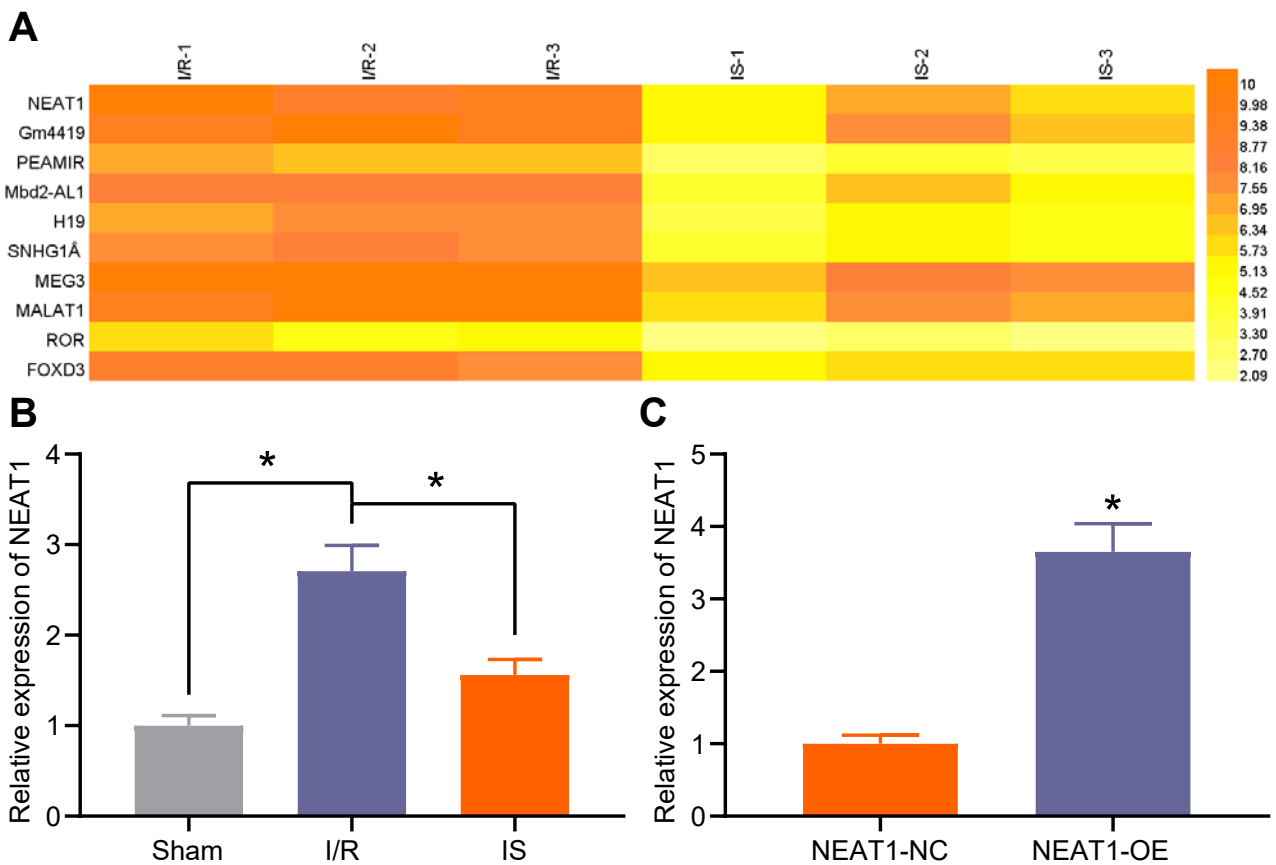


Fig. 2. *NEAT1 is downregulated after Sev treatment in mice with myocardial I/R.* ***A****) differentially expressed lncRNAs between mice subjected to I/R injury with or without Sev treatment screened out by microarray analysis;* ***B****) NEAT1 expression in mice under different treatments evaluated by RT-qPCR;* ***C****) NEAT1 expression in Sev-injected mice administrated with NEAT1-OE or NEAT1-NC. In panel B, *p < 0.05 according to the one-way ANOVA; In panel C, *p < 0.05 according to unpaired t-test. Results are expressed as mean ± SD (n = 3 per group). The experiment was repeated 3 times.*

possible target of miR-140, which was further corroborated by dual-luciferase reporter assays (Fig. 5A). The expression of RhoA in mice injected with NEAT1-NC, NEAT1-OE, miR-140 control or miR-140 inhibitor was analyzed, and its expression was increased in mice with NEAT1-OE and miR-140 inhibitor (Fig. 5B). To further verify the effect of RhoA on I/R injury, we treated mice with RhoA inhibitor Exoenzyme C3 or DMSO in the presence of miR-140 inhibitor, and the success of the delivery was authenticated by Western blot analysis (Fig. 5C). In mice treated with miR-140 inhibitor + C3, the LVEF and LVFS were increased (Fig. 5D), myocardial infarction area was diminished (Fig. 5E) and the apoptosis rate of mouse cardiomyocytes (Fig. 5F) was also decreased significantly relative to the miR-140 inhibitor + DMSO treatment. This proves that the weakening of RhoA activity partially restored the effect of miR-140 on Sev.

DISCUSSION

In spite of the fact that substantial advances have been made in antithrombotic therapy, the mortality of patients with myocardial I/R injury remains high; consequently, there is an urgent need to improve the efficacy of cardioprotective agents to ameliorate myocardial function and limit the total area of infarction during injury caused by I/R (16). Moreover, the emerging relevance of lncRNA to I/R injury of heart caught our attention (17). In view of this, we performed this study to decipher the

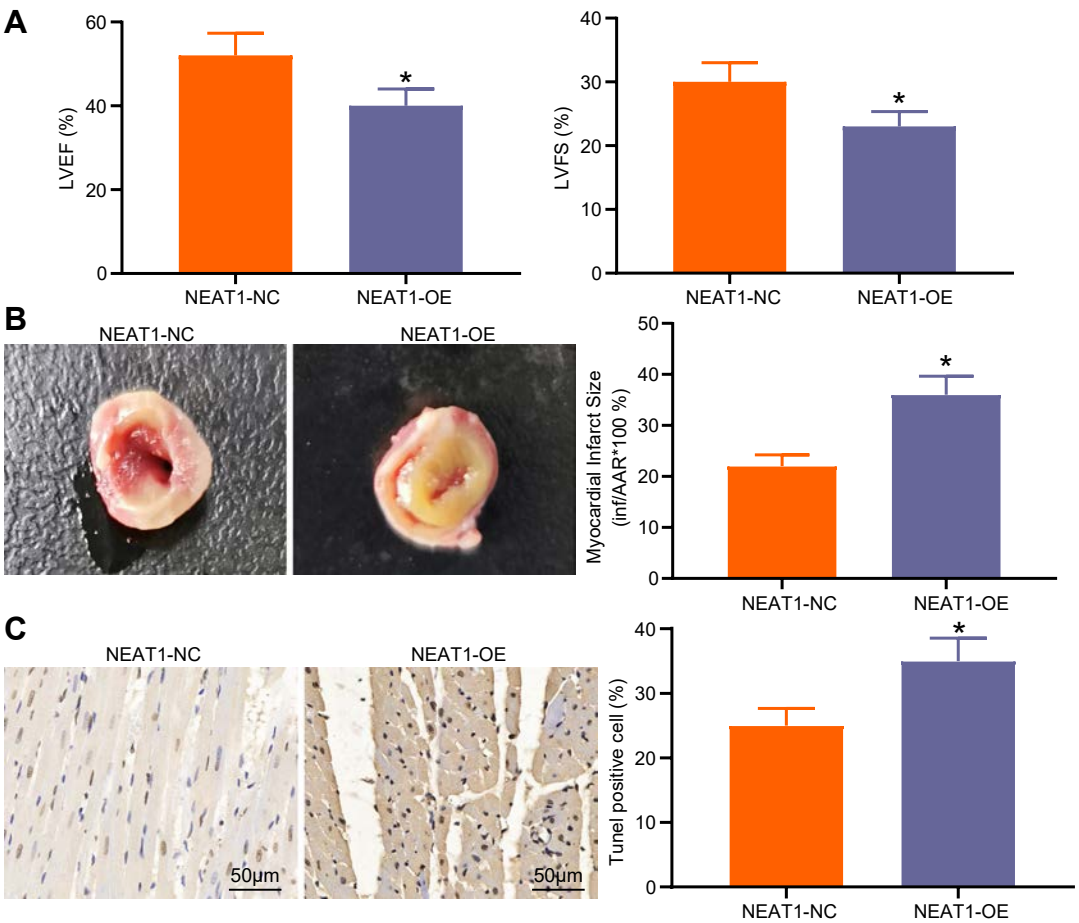


Fig. 3. *NEAT1 upregulation weakens the cardioprotective role of Sev on mice with myocardial I/R injury. A) LVEF and LVFS in mice injected with NEAT1-OE or NEAT1-NC evaluated by ECG; B) myocardial infarct area in mice injected with NEAT1-OE or NEAT1-NC tested by TTC staining; C) the apoptosis rate of injected with NEAT1-OE or NEAT1-NC-treated model assessed by TUNEL staining. *p < 0.05 according to the unpaired t test. Results are expressed as mean ± SD (n = 3 per group). The experiment was repeated 3 times.*

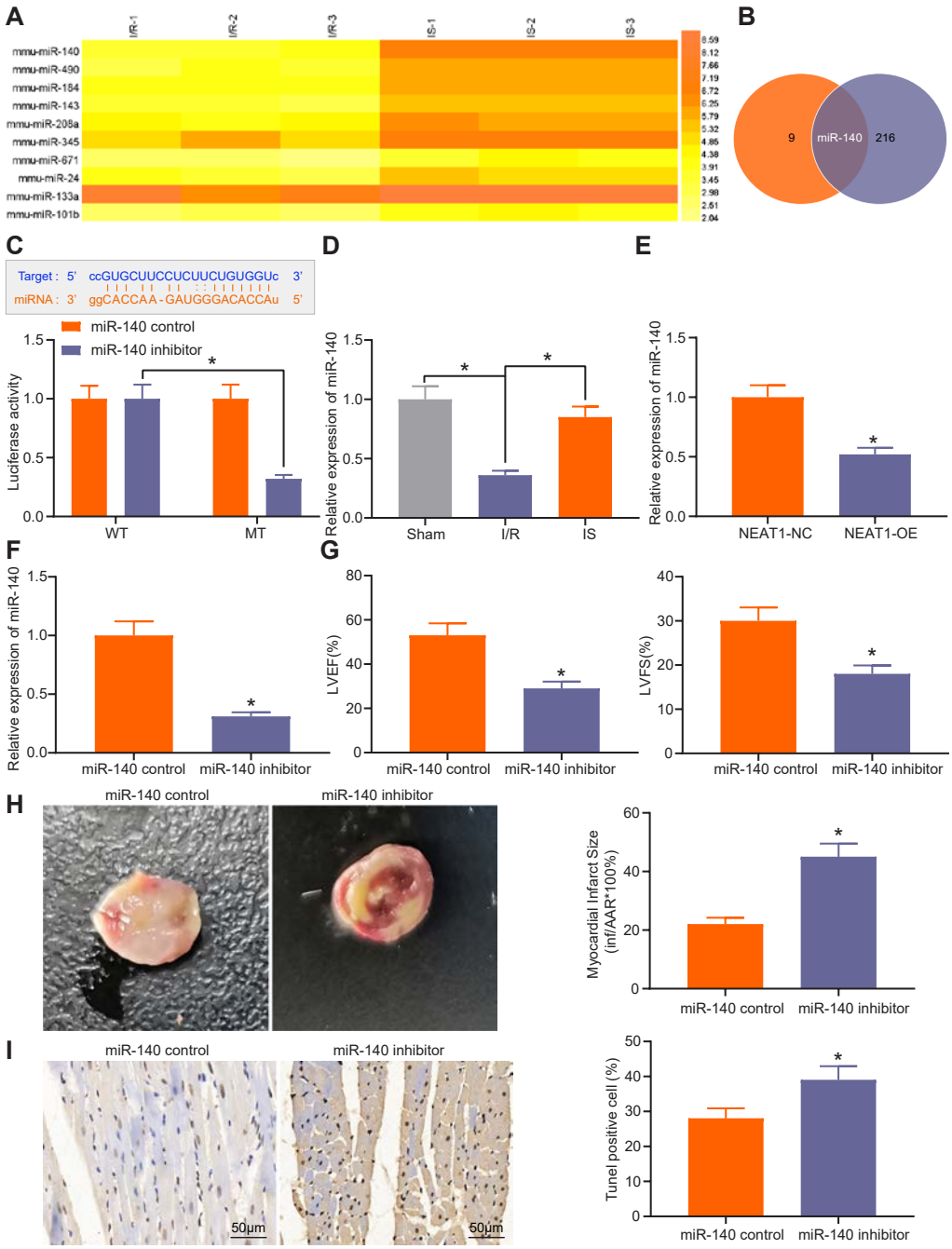


Fig. 4. *miR-140, restored after Sev treatment, is involved in the modulation of Sev-alleviated myocardial I/R injury. **A)** differentially expressed miRNAs between mice subjected to I/R injury with or without Sev treatment screened out by microarray analysis; B) the intersected miRNA in microarray and StarBase prediction results; **C)** the binding relationship between miR-140 and NEAT1 predicted by StarBase and validated by a dualluciferase reporter gene assay; **D)** miR-140 expression in mice under different treatments evaluated by RT-qPCR; **E)** miR-140 expression in Sev-injected mice administrated with NEAT1-OE or NEAT1-NC; **F)** miR-140 expression in Sev-injected mice administrated with miR-140 inhibitor or miR-140 control; **G)** LVEF and LVFS in mice injected with miR-140 inhibitor or miR-140 control evaluated by ECG; **H)** myocardial infarct area in mice injected with miR-140 inhibitor or miR-140 control tested by TTC staining; **I)** the apoptosis rate of injected with miR-140 inhibitor or miR-140 control-treated model assessed by TUNEL staining. In panel C, *p < 0.05 according to the two-way ANOVA; In panel D-I, *p < 0.05 according to unpaired t test. Results are expressed as mean ± SD (n = 3 per group). The experiment was repeated 3 times.*

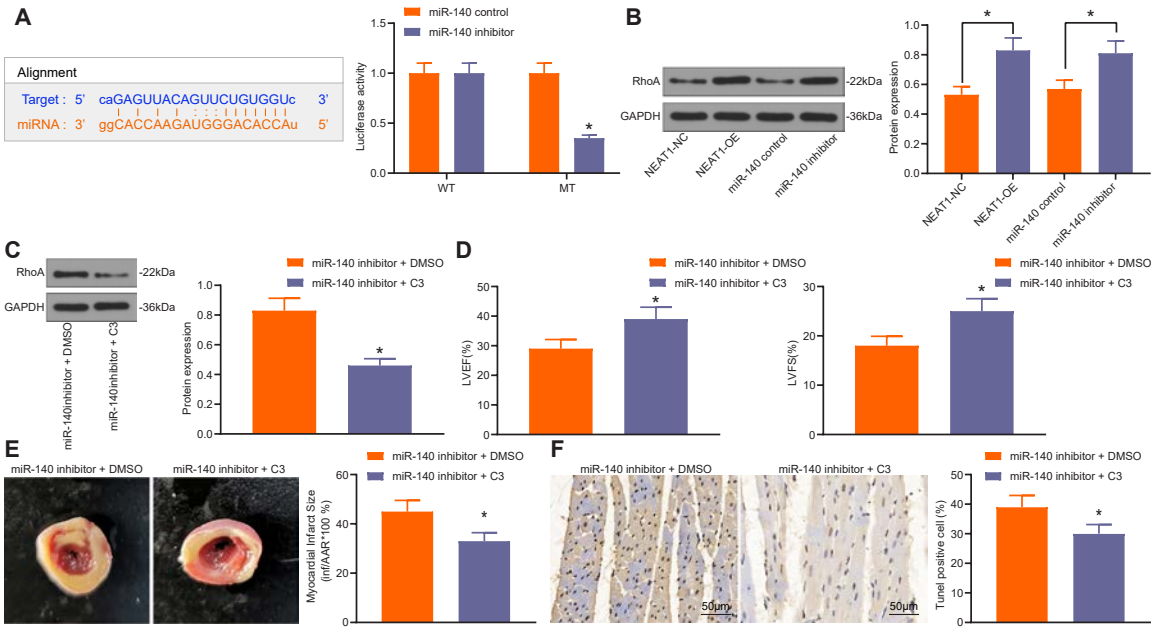


Fig. 5. *RhoA, a target of miR-140, is involved in the modulation of miR-140-dependent myocardial I/R injury. **A**) the binding relationship between miR-140 and RhoA predicted by StarBase and validated by a dualluciferase reporter gene assay; **B**) the protein expression of RhoA in nude mice injected with NEAT1-NC, NEAT1-OE, miR-140 control and miR-140 inhibitor determined by western blot analysis; **C**) the protein expression of RhoA in nude mice injected with miR-140 inhibitor + C3 or miR-140 inhibitor + DMSO determined by western blot analysis; **D**) LVEF and LVFS in mice injected with miR-140 inhibitor + C3 or miR-140 inhibitor + DMSO evaluated by ECG; **E**) myocardial infarct area in mice injected with miR-140 inhibitor + C3 or miR-140 inhibitor + DMSO tested by TTC staining; **F**) the apoptosis rate of injected with miR-140 inhibitor + C3 or miR-140 inhibitor + DMSO-treated model assessed by TUNEL staining. In panel A-C, *p < 0.05 according to the two-way ANOVA; In panel D-F, *p < 0.05 according to unpaired t test. Results are expressed as mean ± SD (n = 3 per group). The experiment was repeated 3 times.*

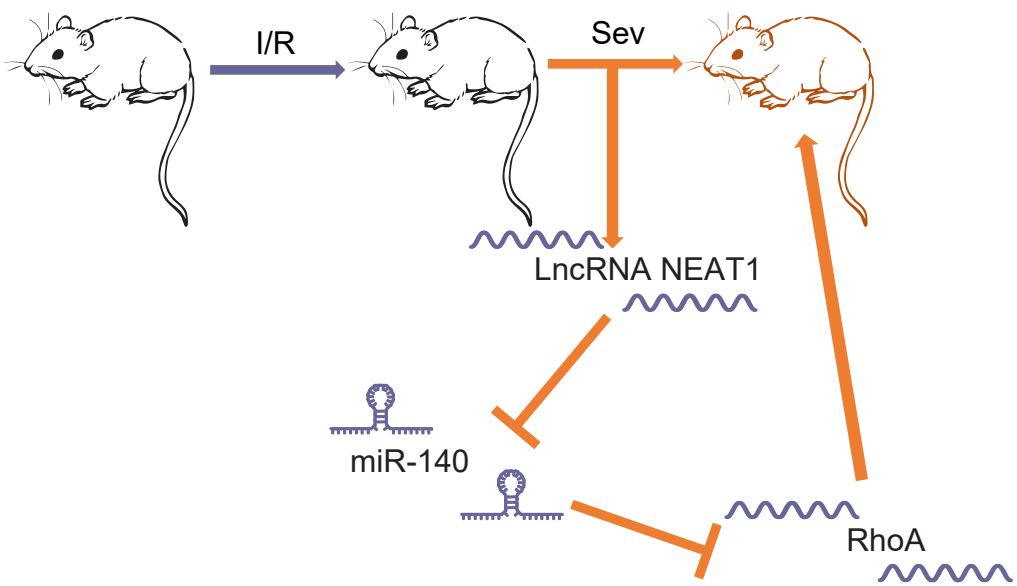


Fig. 6. *A diagram illustrating Sev diminishes injury caused by myocardial I/R via the NEAT1/miR-140/RhoA axis. NEAT1 sponged miR-140 to mediate RhoA expression. Sev treatment mitigated I/R injured mice by downregulating NEAT1 and RhoA, while upregulating miR-140 expression.*

potential mechanism behind myocardial I/R injury, and our obtained data indicate that poor expression of NEAT1 is able to attenuate myocardial I/R injury after Sev treatment in mice by mediating the miR-140/RhoA axis.

Excessive apoptosis is associated with myocardial ischemia, I/R injury and postischemia cardiac remodeling (18), while infarct size is an independent indicator effective in predicting mortality after infarction (19). In the current work, we observed that Sev worked as a cardio-protector against injury induced by myocardial I/R by reducing LVEF, LVFS, myocardial infarct size and apoptosis rate. These observations revealed the beneficial role of Sev on I/R injury, which were largely in line with results of previous studies (20, 21). Moreover, Sev was found to diminish NEAT1, which was enhanced in mice with myocardial I/R, by microarray analysis. NEAT1 has been frequently studied in various cancers as an oncogene, including cervical cancer (22) and colon cancer (23) as well as glioma (24) by regulating cell migration and proliferation along with drug resistance. Additionally, NEAT1 was upregulated in Parkinson's disease and conferred drug-inducible neuroprotection against oxidative stress (25). NEAT1 expression was also enhanced in patients suffering from acute ischemic stroke versus controls, which could predict unsatisfactory recurrence-free survival (26). Furthermore, NEAT1 overexpression repressed the alleviating role of Sev in mice with injury induced by myocardial I/R. Consistently, NEAT1 was overexpressed in cells with myocardial I/R injury relative to normal myocardial cells, and declines in NEAT1 expression contributed to enhanced cell proliferation and inhibited cell apoptosis (27). Furthermore, silencing of NEAT1 promoted LVEF and LVFS to normal levels, implying a protective role of NEAT1 knockdown in diabetic rats with myocardial I/R injuries (28).

The relevance of lncRNA-miRNA-mRNA network to cardiovascular diseases has been highlighted recently (29). After determination of the stimulative role of NEAT1 on myocardial I/R injury, we next sought to find its target miRNA. Through an miRNA microarray analysis of significantly upregulated miRNAs in mice after Sev and Starbase prediction, miR-140 was substantiated as our target. In line with our finding, miR-370 was reduced in mice exhibiting IR injuries, but Sev anesthetic preconditioning promoted the miR-370 expression pattern (30). Previously, circRNA_000203 aggravated cardiac hypertrophy by lowering the expression of miR-140-3p (31). Additionally, miR-140-5p was corroborated as a promising therapeutic target for alleviating brain injury induced by intracerebral hemorrhage (32). Our data presented that, with the treatment of miR-140 inhibitor, the effects of Sev were inhibited. Moreover, Catalpol improved myocardial damage by regulating NEAT1/miR-140-5p in mice with diabetic cardiomyopathy *in vivo* (33). Lastly, we screened out RhoA as a putative target of miR-140. RhoA shares a positive correlation with NEAT1 and an inverse one with miR-140. RhoA activity in myocardium of Sprague-Dawley rats enhanced remarkably compared with that in the sham-operated rats (0.18 ± 0.03) (34). Suppression of RhoA prevented propofol-regulated hippocampal neurotoxicity following cognitive deficits (35). The TLR4/RhoA/ROCK pathway was in blood-brain barrier impairment after cerebral I/R injury (36). Furthermore, Forgione et al. showed that C3 transferase, which could selectively inhibit Rho expression without disturbing other guanine triphosphatases, has the potency to augment neuroprotection and axonal regeneration following spinal cord injury (37). Nevertheless, the cardioprotection role of exoenzyme C3 has been rarely probed. Here, we report that C3 could rescue the inhibitory role of miR-140 inhibitor on Sev-mediated injury alleviation in mice.

Overall, the present study established that NEAT1 positively regulates RhoA expression by binding to miR-140, by which the mechanism of action of the cardioprotection of Sev is weakened against myocardial I/R in the mouse model (Fig. 6). NEAT1 silencing may act as an attractive target for promoting Sev-induced myocardial protection. Further works are warranted to obtain more information about the NEAT1/miR-140/RhoA axis *in vitro*, and to explore new treatment options for myocardial I/R injury.

REFERENCES

1. Lejay A, Fang F, John R, et al. Ischemia reperfusion

injury, ischemic conditioning and diabetes mellitus. J Mol Cell Cardiol 2016; 91:11-22.
2. Hausenloy DJ, Yellon DM. Myocardial ischemia-reperfusion injury: a neglected therapeutic target. J Clin Invest 2013; 123:92-100.
3. Edgington TL, Maani CV. Sevoflurane. StatPearls. Treasure Island (FL) 2020.
4. Rancan L, Huerta L, Cusati G, et al. Sevoflurane prevents liver inflammatory response induced by lung ischemia-reperfusion. Transplantation 2014; 98:1151-7.
5. Wen XR, Fu YY, Liu HZ, et al. Neuroprotection of sevoflurane against ischemia/reperfusion-induced brain injury through inhibiting JNK3/Caspase-3 by enhancing Akt signaling pathway. Mol Neurobiol 2016; 53:1661-71.
6. Zhao J, Wang F, Zhang Y, et al. Sevoflurane preconditioning attenuates myocardial ischemia/reperfusion injury via caveolin-3-dependent cyclooxygenase-2 inhibition. Circulation 2013; 128:S121-9.
7. Zhang SB, Liu TJ, Pu GH, Li BY, Gao XZ, Han XL. Suppression of long non-coding RNA LINC00652 restores sevoflurane-induced cardioprotection against myocardial ischemia-reperfusion injury by targeting GLP-1R through the cAMP/PKA pathway in mice. Cell Physiol Biochem 2018; 49:1476-91.
8. Gao J, Xu W, Wang J, Wang K, Li P. The role and molecular mechanism of non-coding RNAs in pathological cardiac remodeling. Int J Mol Sci 2017; 18.
9. Wu HJ, Tang GM, Shao PY, et al. Long non-coding RNA NEAT1 modulates hypoxia/reoxygenation-induced cardiomyocyte injury via targeting microRNA-520a. Exp Ther Med 2019; 18:2199-206.
10. Kataoka M, Wang DZ. Non-Coding RNAs Including miRNAs and lncRNAs in cardiovascular biology and disease. Cells 2014; 3:883-98.
11. Luo M, Sun Q, Zhao H, Tao J, Yan D. Long noncoding RNA NEAT1 sponges miR-495-3p to enhance myocardial ischemia-reperfusion injury via MAPK6 activation. J Cell Physiol 2020; 235:105-13.
12. Yang S, Li H, Chen L. MicroRNA-140 attenuates myocardial ischemia-reperfusion injury through suppressing mitochondria-mediated apoptosis by targeting YES1. J Cell Biochem 2019; 120:3813-21.
13. Wang DW, Lou XQ, Liu ZL, Zhang N, Pang L. LncRNA SNHG1 protects SH-SY5Y cells from hypoxic injury through miR-140-5p/Bcl-XL axis. Int J Neurosci 2020: 1-10.
14. Shimokawa H, Sunamura S, Satoh K. RhoA/Rho-Kinase in the cardiovascular system. Circ Res 2016; 118:352-66.
15. Cui YC, Pan CS, Yan L, et al. Ginsenoside Rb1 protects against ischemia/reperfusion-induced myocardial injury via energy metabolism regulation mediated by RhoA signaling pathway. Sci Rep 2017; 7:44579.
16. Qi Z, Li S, Su Y, et al. Role of microRNA-145 in protection against myocardial ischemia/reperfusion injury in mice by regulating expression of GZMK with the treatment of sevoflurane. J Cell Physiol 2019.
17. Yu SY, Tang L, Zhou SH. Long noncoding RNAs: new players in ischaemia-reperfusion injury. Heart Lung Circ 2018; 27:322-32.
18. Dong Y, Chen H, Gao J, Liu Y, Li J, Wang J. Molecular machinery and interplay of apoptosis and autophagy in coronary heart disease. J Mol Cell Cardiol 2019; 136:27-41.
19. Sanz-Rosa D, Garcia-Prieto J, Ibanez B. The future: therapy of myocardial protection. Ann N Y Acad Sci 2012; 1254:90-8.
20. Xie D, Zhao J, Guo R, et al. Sevoflurane pre-conditioning ameliorates diabetic myocardial ischemia/reperfusion injury via differential regulation of p38 and ERK. Sci Rep 2020; 10:23.
21. Xie H, Zhang J, Zhu J, Liu LX, Rebecchi M, Hu SM, Wang C. Sevoflurane post-conditioning protects isolated rat hearts against ischemia-reperfusion injury via activation of the ERK1/2 pathway. Acta Pharmacol Sin 2014; 35:1504-13.
22. Xu D, Dong P, Xiong Y, et al. MicroRNA-361-Mediated inhibition of HSP90 expression and EMT in cervical cancer is counteracted by oncogenic lncRNA NEAT1. Cells 2020; 9
23. Zhuang ST, Cai YJ, Liu HP, Qin Y, Wen JF. LncRNA NEAT1/miR-185-5p/IGF2 axis regulates the invasion and migration of colon cancer. Mol Genet Genomic Med 2020; 8:e1125.
24. Mou SJ, Yang PF, Liu YP, Xu N, Jiang WW, Yue WJ. BCLAF1 promotes cell proliferation, invasion and drug-resistance though targeting lncRNA NEAT1 in hepatocellular carcinoma. Life Sci 2020; 242:117177.

25. Simchovitz A, Hanan M, Niederhoffer N, et al. NEAT1 is overexpressed in Parkinson's disease substantia nigra and confers drug-inducible neuroprotection from oxidative stress. FASEB J 2019; 33:11223-34.
26. Li P, Duan S, Fu A. Long noncoding RNA NEAT1 correlates with higher disease risk, worse disease condition, decreased miR-124 and miR-125a and predicts poor recurrence-free survival of acute ischemic stroke. J Clin Lab Anal 2020; 34:e23056.
27. Ren L, Chen S, Liu W, Hou P, Sun W, Yan H. Downregulation of long non-coding RNA nuclear enriched abundant transcript 1 promotes cell proliferation and inhibits cell apoptosis by targeting miR-193a in myocardial ischemia/reperfusion injury. BMC Cardiovasc Disord 2019; 19:192.
28. Ma M, Hui J, Zhang QY, Zhu Y, He Y, Liu XJ. Long non-coding RNA nuclear-enriched abundant transcript 1 inhibition blunts myocardial ischemia reperfusion injury via autophagic flux arrest and apoptosis in streptozotocin-induced diabetic rats. Atherosclerosis 2018; 277:113-22.
29. Huang Y. The novel regulatory role of lncRNA-miRNA-mRNA axis in cardiovascular diseases. J Cell Mol Med 2018; 22:5768-75.
30. Zhao YB, Zhao J, Zhang LJ, et al. MicroRNA-370 protects against myocardial ischemia/reperfusion injury in mice following sevoflurane anesthetic preconditioning through PLIN5-dependent PPAR signaling pathway. Biomed Pharmacother 2019; 113:108697.
31. Li H, Xu JD, Fang XH, et al. Circular RNA circRNA_000203 aggravates cardiac hypertrophy via suppressing miR-26b-5p and miR-140-3p binding to Gata4. Cardiovasc Res 2020; 116:1323-34.
32. Wang S, Cui Y, Xu J, Gao H. miR-140-5p attenuates neuroinflammation and brain injury in rats following intracerebral hemorrhage by targeting TLR4. Inflammation 2019; 42:1869-77.
33. Zou G, Zhong W, Wu F, Wang X, Liu L. Catalpol attenuates cardiomyocyte apoptosis in diabetic cardiomyopathy via Neat1/miR-140-5p/HDAC4 axis. Biochimie 2019; 165:90-9.
34. Luo SY, Chen S, Qin YD, Chen ZW. Urotensin-receptor antagonist SB-710411 Protects Rat Heart against Ischemia-Reperfusion Injury via RhoA/ROCK Pathway. PLoS One 2016; 11:e0146094.
35. Pearn ML, Schilling JM, Jian M, et al. Inhibition of RhoA reduces propofol-mediated growth cone collapse, axonal transport impairment, loss of synaptic connectivity, and behavioural deficits. Br J Anaesth 2018; 120:745-60.
36. Gong P, Li R, Jia HY, Ma Z, Li XY, Dai XR, Luo SY. Anfibatide preserves blood-brain barrier integrity by inhibiting TLR4/RhoA/ROCK pathway after cerebral ischemia/reperfusion injury in rat. J Mol Neurosci 2020; 70:71-83.
37. Forgione N, Fehlings MG. Rho-ROCK inhibition in the treatment of spinal cord injury. World Neurosurg 2014; 82:e535-9.

Anti-cancer effects of baicalein on cervical carcinoma cells through down-regulation of the ERK/p38/MAPK pathway

YH. Luo[1#], L. Zhang[1#], MY. Wang[2], J. Fang[3], JY. Xia[4] and XL. Yu[2*]

[1]Department of Obstetrics and Gynecology, The Traditional Chinese Medicine Hospital of Luzhou, Luzhou, China; [2]Department of Obstetrics and Gynecology, The Affiliated TCM Hospital of South West Medical University, Luzhou, China; [3]Outpatient Department, Liangshan First People's Hospital, Xichang, China; [4]School of Medical Information and Engineering, South West Medical University, Luzhou, China;

Received February 3, 2021 – Accepted May 20,2021

[#]These Authors contributed equally to this work

The objective of this study was to investigate the effects of baicalein on apoptosis of HeLa human cervical cancer (CC) cells and to elucidate the underlying mechanism. HeLa cells were treated with 20, 50, 100, or 200 μmol/L baicalein for 24, 36, and 48 hours, and CCK-8 assays were used to detect cell viability, and flow cytometry was performed to assess apoptosis rate. Reverse-transcription quantitative PCR was used to measure ERK1/2, p38, and JNK mRNA levels in HeLa cells, and western blotting was performed to measure ERK1/2, p38, and JNK protein levels. The CCK-8 assay showed that the OD value of HeLa cells gradually decreased with increasing baicalein concentrations ($P < 0.01$) and treatment time ($P < 0.01$). These results indicated a negative time- and dose-dependent effect of baicalein on HeLa cells. Baicalein treatment of HeLa cells significantly increased apoptosis rate ($P < 0.01$). In HeLa cells treated with 50 or 200 μmol/L baicalein for 24 h, expression levels of ERK1/2 and p38 mRNA were significantly reduced, whereas that of JNK mRNA was increased ($P < 0.01$). The levels of phosphorylated ERK1/2 and p38 were significantly reduced, and the level of JNK protein was increased ($P < 0.01$). Taken together, baicalein appeared to exert anti-cancer effects on HeLa cells through induction of apoptosis and regulation of the ERK/p38/mitogen-activated protein kinase pathway.

Cervical cancer (CC) is one of the most common malignant tumours in the female reproductive system. Human papilloma virus (HPV) infection is one of the main causes of CC, during which HPV DNA is integrated into cervical epithelial cells where it encodes oncoproteins. E6 continuously activates the extracellular signal-regulated kinase 1/2 (ERK1/2) signal pathway and thereby promotes carcinogenesis and inhibits cancer cell apoptosis (1-2). In normal tissues, *ERK1/2* is expressed in the cytoplasm and is not activated during normal cervical epithelial cell proliferation. In CC tissue, *ERK1/2* is expressed in the cytoplasm and nucleus, and ERK1/2 is in an activated state. ERK1/2 is

Key words: baicalein; cervical cancer; HeLa cells; apoptosis; MAPK pathway

**Corresponding Author:*
Dr Xiaolan Yu
Department of Obstetrics and Gynecology,
The Affiliated TCM Hospital of South West Medical University,
Luzhou, Sichuan, 646000, China
Tel/Fax:+86-0830-3161837
e-mail:yuxiaolan129@yeah.net

0393-974X (2021)
Copyright © by BIOLIFE, s.a.s.
This publication and/or article is for individual use only and may not be further reproduced without written permission from the copyright holder.
Unauthorized reproduction may result in financial and other penalties

a protein tyrosine kinase which is activated by phosphorylation, and it can transmit extracellular signals to the nucleus and upregulate the expression of target genes such as c-Jun and c-Fos. The protein products of both these genes may be combined to a transcription factor activator protein 1 (AP-1) in the form of a homodimer or heterodimer, thereby initiating expression of the *myc* gene. myc can then activate a series of cell proliferation signals and jointly induce cell cycle. The expression of protein D1 (cyclin D1) gene leads to abnormal proliferation, differentiation, apoptosis, and metastasis of cancer cells; thus, continuous activation of ERK can inhibit cancer cell apoptosis (3-4). Previous studies showed that treatment of CC with drugs such as cisplatin can promote cancer cell apoptosis by acting on the ERK1/2 and P38 mitogen-activated protein kinase (MAPK) signalling pathways (5-6). The Bcl-2 family plays an important role in regulating cell apoptosis. Phosphorylated ERK1/2 can phosphorylate Bcl-2, activate transcription factors, and interfere with tumour necrosis factor-related apoptosis-inducing ligands to exert anti-apoptotic effects, and induce cancer cell proliferation (7-8). Bax and Bcl-2 are two important members of the Bcl-2 family, and the Bcl-2:Bax ratio determines whether a cell enters apoptosis or not (9, 10). Various traditional Chinese medicines are used to treat CC by regulating the levels of ERK1/2 and Bcl-2 family proteins. Baicalein has shown promising anti-cancer effects, as it can substantially inhibit proliferation and metastasis of cancer cells and promote their apoptosis. However, even though it appears to be effective against CC, the underlying curative effect is unclear (11, 12). The objective of this study was to investigate the effects of baicalein on CC HeLa cells and to elucidate the underlying mechanisms.

MATERIALS AND METHODS

Chemicals

HeLa human CC cells were donated by the Medical Experimental Center of the Affiliated Hospital of Southwest Medical University, and foetal bovine serum (FBS) and Dulbecco's modified Eagle's medium (DMEM) high-glycaemic medium were purchased from Life Science. Baicalein at 99% purity was purchased from Chengdu Must Bio-Technology (Chengdu, China). The baicalein powder was dissolved in sterile dimethyl sulfoxide (DMSO) to produce a 50 mol/L storage solution which was diluted to the respective final concentration before use. Rabbit anti-human GAPDH antibody, horseradish peroxidase-labelled goat anti-mouse IgG (H + L), and horseradish peroxidase-labelled goat anti-rabbit IgG (H + L) were purchased from Biyuntian Biotechnology (Shanghai, China), a DNA marker was purchased from Fermentas (Waltham, MA, USA), and PCR primers for ERK1/2, p-ERK1/2, p38, and JNK were synthesized by Shanghai Shenggong (Shanghai, China). Mouse anti-human ERK1/2 antibody, mouse anti-human p-ERK1/2 antibody, mouse anti-human P38 antibody, mouse anti-human p-P38 antibody, mouse anti-human JNK antibody, mouse anti-human p-JNK antibody, and rabbit anti-human GAPDH antibody were purchased from Cell Signaling Technology (Danvers, MA, USA). A CCK-8 kit was procured from Promega (Madison, WI, USA). An annexin V-fluorescein isothiocyanate/propidium iodide (annexin V-FITC/PI) kit with fluorescein isothiocyanate labelling was purchased from Beyotime Biotechnology Co., Ltd, a K1622 reverse transcription kit was procured from Thermo Fisher Scientific (Waltham, MA, USA), and a TUNEL kit was purchased from Roche (Basel, Switzerland).

Cell culture

HeLa cell culture was performed using DMEM high-glucose culture medium containing 100 mL/L FBS. Cells were cultured in an incubator at 37°C under 50 mL/L CO_2 and were counted during the growth phase of the experiments.

Cell viability assay

A CCK-8 assay was used to detect the proliferation of HeLa cells. To prepare cell suspensions, cells were counted, and suspensions were placed in 96-well plates at 100 µL per well. Baicalein was added at 20, 50, 100, or 200 µmol/L, respectively, and the control treatment received the same doses of DMSO. Each treatment was performed using three technical replicates. Migration of HeLa cells was measured using wound healing assays. HeLa cells (1×10^5 cells/well) were seeded in a 6-well culture plate to produce a confluent monolayer, and the cells were then

wounded using a sterile 200 μL pipette tip. Cells were cultured for 24, 48, or 72 h; 10 μL CCK-8 solution was added and incubated for 1, 2, 3, or 4 h. Absorbance, which is directly proportional to cell proliferation, was measured at 450 nm.

Flow cytometry detection of apoptosis

According to the CCK-8 assay results, HeLa cells were treated with 50 or 200 μmol/L baicalein for 24 h; controls were treated with DMSO. Annexin®-FITC/PI staining and flow cytometry were performed to assess apoptosis rate, according to the manufacturer's instructions. The results were analysed using CellQuest software. The experiment was performed using three replicates.

Reverse-transcription quantitative

PCR (RT-qPCR) Changes in expression levels of ERK1/2, p38, and JNK were assessed using RT-qPCR. HeLa cells were treated with 50 or 200 μmol/L baicalein for 24, 48, and 72 h; controls were treated with DMSO. The medium was subsequently removed, cells were washed twice using phosphate-buffered saline (PBS), and total RNA was isolated using TRIzol reagent, according to the manufacturer's instructions. A reverse-transcription kit K1622 was used to produce first-strand cDNA, and RT-qPCR was used to measure expression of the respective genes. The following PCR primers were used – ERK1/2: forward 5'-AATCACACGGTAGACACTGAAATGCC-3', reverse 5'-CATCATCCCATCTAAAATGTCCCCTG-3'; p38: forward 5'-AGTGTACCTCGTGACGACC-3', reverse 5'-GCCCGCCGAGTGGATATAC-3'; JNK: forward 5'-AGGTGGACAACCAGTTCTACA-3', reverse 5'-GCACAGACTATTCCCTGAGCC-3'; GAPDH: forward 5'-ACCCAGAAGACTGTGGATGG-3', reverse 5'-CACATTGGGGGTAGGAACAC-3'. Relative expression levels were assessed using the $2^{-\triangle\triangle Ct}$ method.

Western blotting

Western blotting was used to detect changes in protein levels of ERK1/2, p38, and JNK in HeLa cells treated with 50 or 200 μmol/L baicalein for 24 h and in controls treated with DMSO. Cells were washed twice with pre-cooled PBS (4°C), and 50 g/L protease inhibitor lysis buffer was added. All steps were performed on ice. After sonication, the solution was centrifuged at 10,000 r/min, and the supernatant was collected; total cell protein was then denatured and stored at -20°C until analysis. For sodium dodecyl sulphate polyacrylamide gel electrophoresis, 5 μL protein with 100 g/L gel was transferred to a 0.2 μmol/L polyvinylidene diflouride membrane with 50 g/L skimmed milk powder and 1 × TBST blocking solution and was incubated for 2 h. The blocking solution was then removed, and the membrane was rinsed twice for 5 min using PBS. Mouse anti-human ERK1/2 antibody (1:15,00), mouse anti-human p-ERK1/2 antibody (1:1,000), mouse anti-human p38 antibody (1:1,500), mouse anti-human p-p38 antibody (1:1,000), mouse anti-human JNK antibody (1:1,500), mouse anti-human p-JNK antibody (1:1,500), mouse anti-human Bcl-2 antibody (1:2,500), mouse anti-human caspase-3 antibody (1:1,000), and rabbit anti-human GAPDH antibody (1:2,000) were added, followed by incubation overnight at 4°C; The membrane was rinsed twice with 1 × TBST for 20 min, and horseradish peroxidase (HRP)-labelled goat anti-mouse IgG (H + L) and HRP-labelled goat anti-rabbit IgG (H + L) (1:2,000) were added, followed by incubation at room temperature for 1 h, rinsing twice with 1 × TBST for 5 min, and gel imaging. Quantity one software was used to perform absorbance analysis and to calculate protein levels. The experiment was conducted using three replicates.

Statistical analyses

All data are expressed as ($\bar{x}\pm s$) deviation. SPSS 23.0 software (IBM, Armonk, NY, USA) was used for analyses. A *t*-test was used to compare two independent samples, and pairwise comparison between multiple samples was performed using one-way analysis of variance. Statistical significance is reported at $P < 0.05$.

RESULTS

Baicalein can inhibit proliferation of HeLa cells

After HeLa cells were treated with 0, 20, 50, 100, or 200 μmol/L baicalein for 24, 48, or 72 hours, cell viability was detected using a CCK-8 assay. The results showed that baicalein significantly inhibited HeLa cell proliferation at concentrations of 50, 100, and 200 μmol/L (Fig. 1 A, B). The cell wound healing assays suggested that in the baicalein treatment at 200 μmol/L, cell migration was significantly reduced, compared with that of the control treatment (Fig. 1 C, D). Baicalein can thus

effectively inhibit proliferation of HeLa cells in a time- and concentration-dependent manner.

Baicalein can promote HeLa cell apoptosis

HeLa cells treated with 50 or 200 μmol/L baicalein for 24 hours showed a significant increase in apoptosis rates ($P < 0.05$), compared with that of the control treatment (Fig. 2 A, B). The results show that baicalein can significantly increase HeLa cell apoptosis.

Baicalein can down-regulate expression of MAPK-related genes

HeLa cells were treated with different concentrations of baicalein and cultured for 24, 48, and 72 hours. RT-qPCR was used to measure expression of the MAPK-related genes p38, ERK, and JNK. p38 and ERK expression was significantly decreased, and JNK expression was significantly increased, compared with that of the control treatment (Fig. 3); thus, baicalein can inhibit expression of MAPK signalling-related downstream genes, and its effect on HeLa cells is closely related to MAPK signalling.

Baicalein inhibited ERK/p38 signalling pathways

Levels of proteins of apoptosis-related signalling pathways were measured (Fig. 4 A, B, E) and found that levels of p38 and ERK proteins in the baicalein treatments were significantly decreased and that of JNK was increased, compared with that of the control treatment (Fig. 4 C, D, F). After baicalein treatment of HeLa cells, levels of pro-apoptosis protein cleavage caspase-3 were reduced, and the level of survival protein Bcl2 was increased, compared with that of

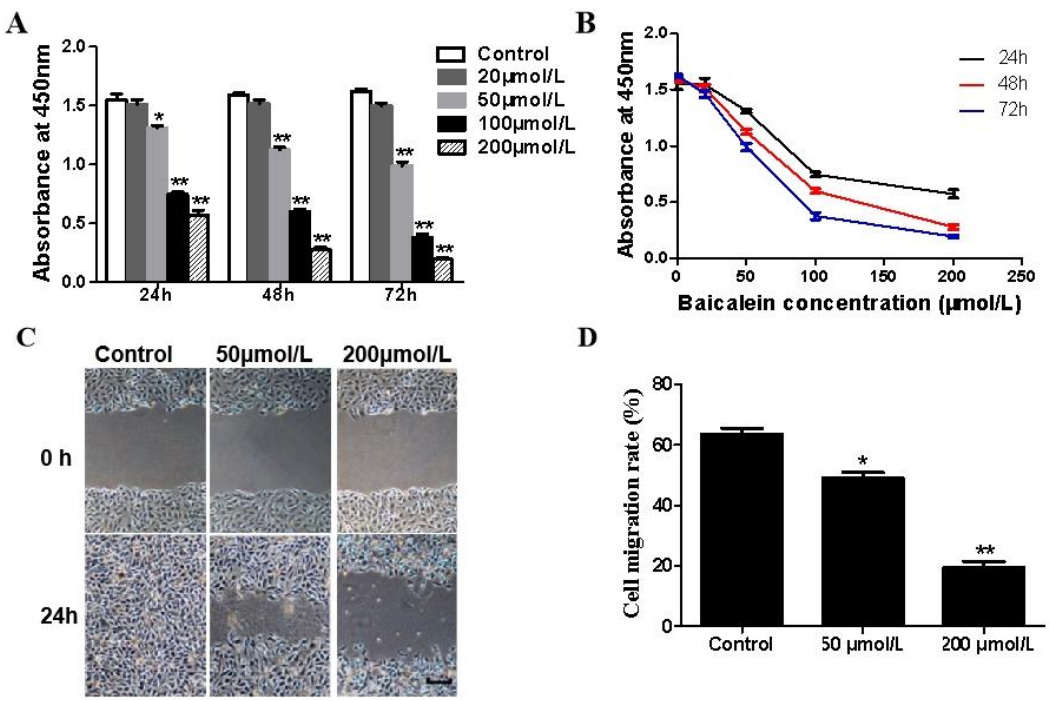


Fig. 1. *Baicalein inhibited proliferation of HeLa cells. **A)** HeLa cells were incubated with baicalein (concentration gradient 0–200 μmol/L). Cell viability was determined using a CCK-8 assay at varying concentrations of baicalein at different timepoints (24, 48, and 72 hours). **B)** CCK-8 assay results were plotted as cellular growth curves. **C)** Cell wound healing assays showed cell migration after treatment of HeLa cells with different concentrations of baicalein (0 [control], 50, and 200 μmol/L) for 0 and 24 hours. **D)** Quantitative statistical analysis of the HeLa cell migration after treatment with different concentrations of baicalein. * $P < 0.05$ vs controls; ** $P < 0.01$ vs controls.*

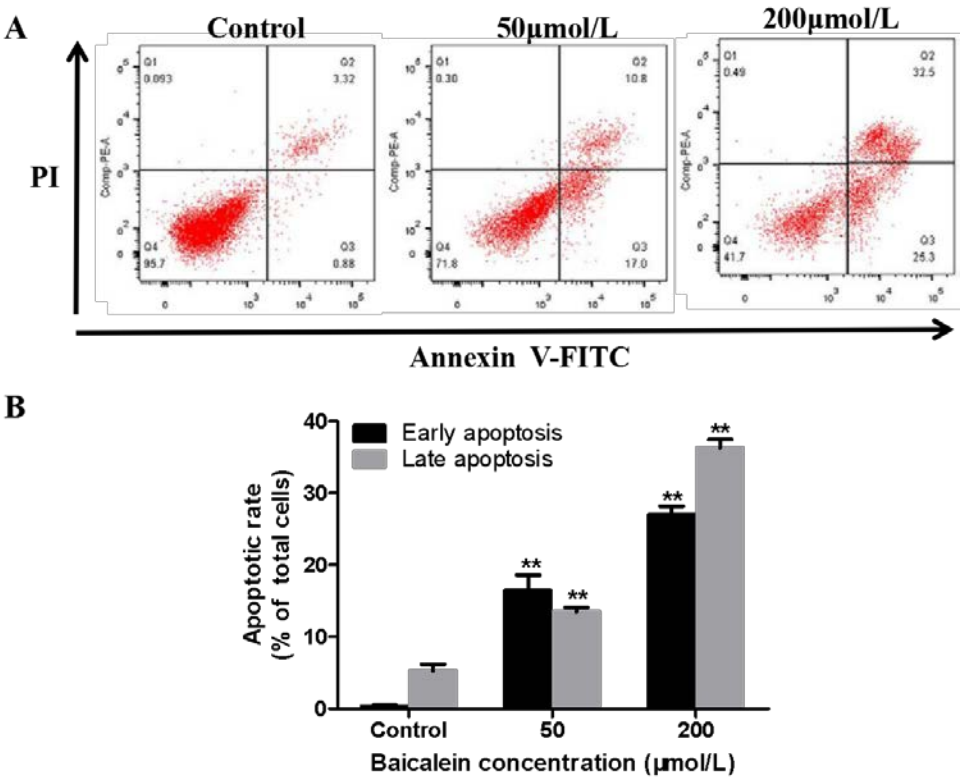


Fig. 2. *Baicalein can induce apoptosis in HELA cells. **A**) A representative image of HeLa cell apoptosis rate detected by flow cytometry. **B**) Semi-quantitative analysis of HeLa cell apoptosis rates: effects of baicalein on early and late apoptosis in HeLa cells. ** P < 0.01 vs controls.*

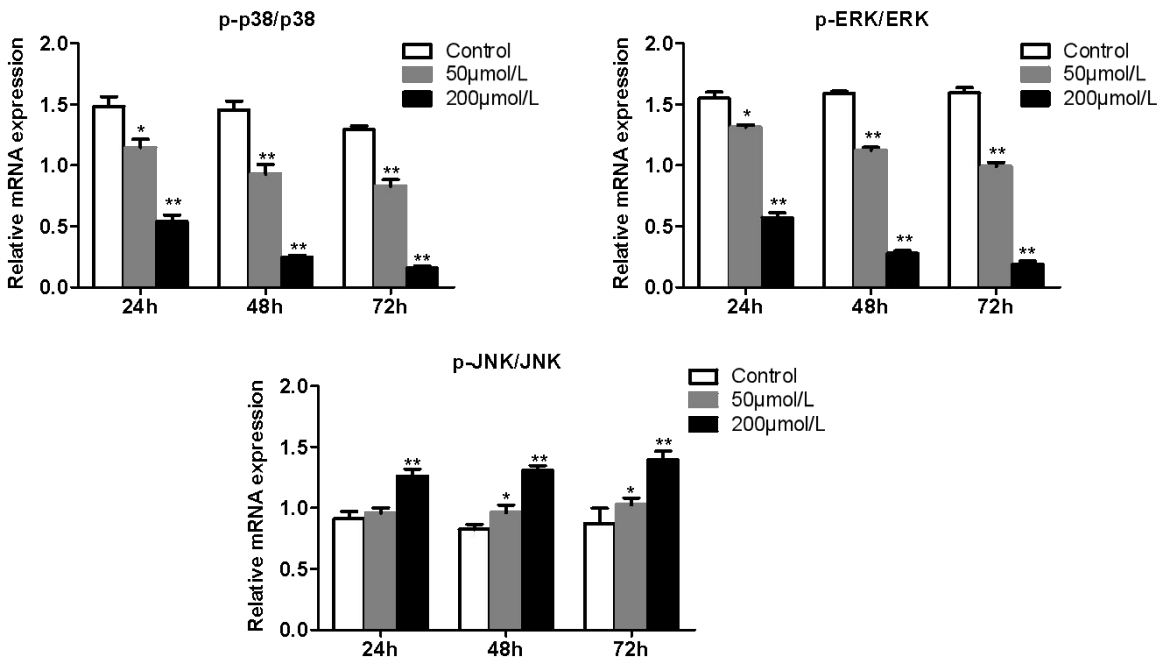


Fig. 3. *RT-qPCR to detect the effect of baicalein on the respective mRNA levels in HeLa cells. HeLa cells were incubated with 0, 50, or 200 μmol/L baicalein for 24, 48, and 72 hours. RT-qPCR was used to detect the mRNA expression of p38, ERK, and JNK.* P < 0.05 vs controls; ** P < 0.01 vs controls.*

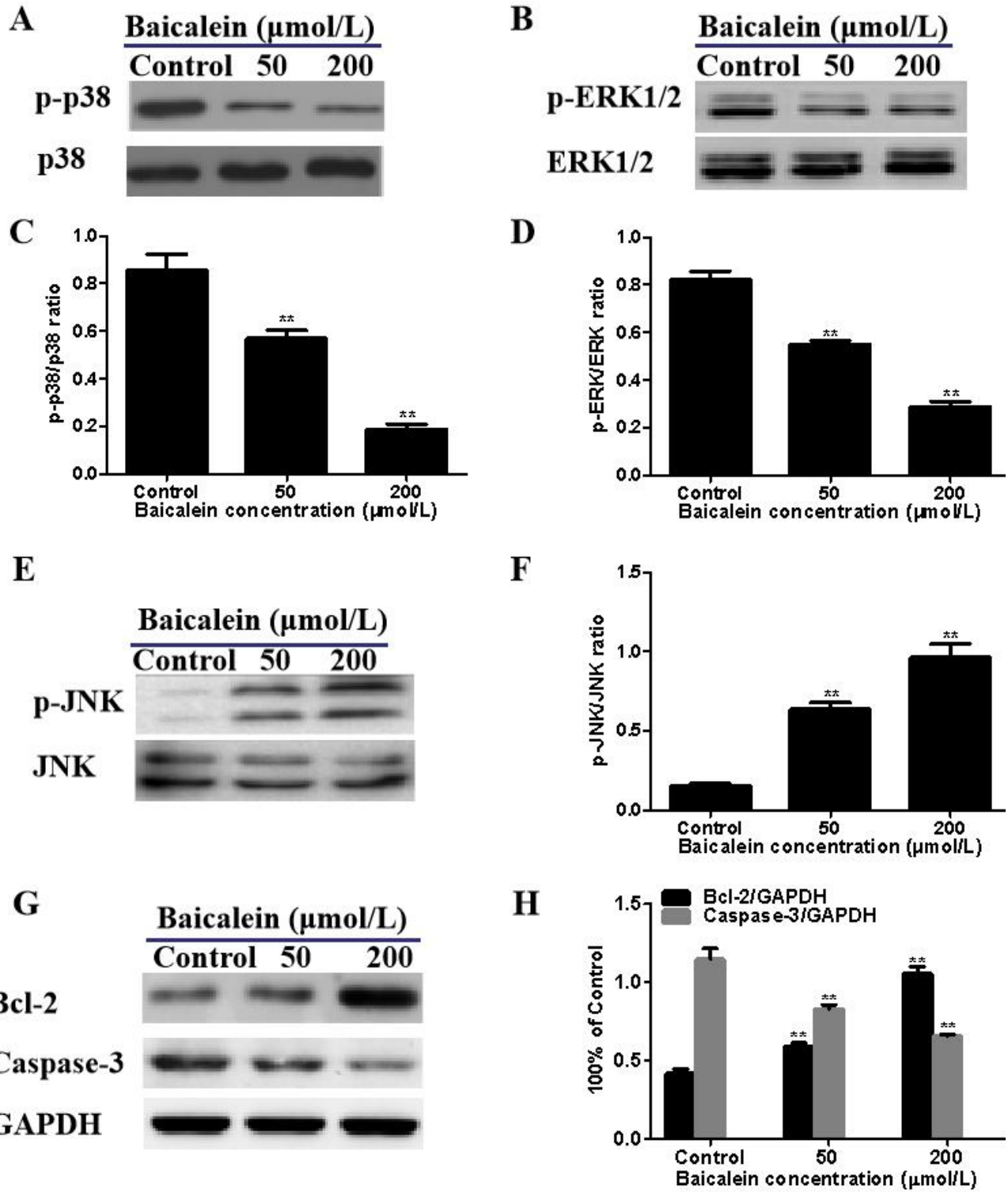


Fig. 4. *Western blot detection of the effect of baicalein on the levels of HeLa cell-related proteins.* ***A, B, E, G****) WB bands of HeLa-cell ERK1/2, p-ERK1/2, p38, p-p38, JNK, p-JNK, Bcl-2, and caspase-3 protein levels.* ***C, D, F, H****) Grey value of the strip indicates the ratios of p-p38/p38, p-ERK/ERK, p-JNK/JNK, Bcl-2/GAPDH, and caspase-3/GAPHD. * P < 0.05 vs controls; ** P < 0.01 vs controls.*

the control (Fig. 4 G, H). The results indicate that baicalein may inhibit HeLa cell growth by inhibiting the p38/ERK/ MAPK signalling pathway.

DISCUSSION

Baicalein belongs to the flavonoids and is an active ingredient extracted from the roots of the traditional Chinese medicinal plant *Scutellaria baicalensis* Georgi. It exerts anti-bacterial, anti-viral, anti-inflammatory, anti-allergic, anti-oxidant and anti-tumour effects. Baicalein can inhibit growth of bladder, prostate, and liver cancer cells (13, 14); however, its effect on CC cells has not been studied so far. Inhibition of tumour cell proliferation and promotion of tumour cell apoptosis are important functions of anti-tumour drugs (15, 16). We found that treatment of HeLa cells with different concentrations of baicalein significantly inhibited cell proliferation in a dose-dependent manner. Annexin®-FITC/PI double-label detection also confirmed that baicalein promoted HeLa cell apoptosis, suggesting that baicalein can inhibit tumour cell growth and promote cell apoptosis. Baicalein has been shown previously to block the cell cycle in leukaemia, osteosarcoma, and other tumour cells (17, 18).

Our results show that baicalein can effectively block the cell cycle process, thereby inhibiting HeLa cell proliferation and promoting apoptosis. Baicalein s a highly effective and specific inhibitor of MAPK1 and 2, which can block MAPK signal transmission and significantly inhibit up-regulation of ERK and p38 mRNA and protein levels, resulting in inhibition of AP-1 transcriptional activity (12, 19, 20). In the current study, baicalein was found to significantly inhibit proliferation of HeLa cells and to promote apoptosis. ERK is the most important member of the MAPK family which includes ERK1 to ERK5. ERK1/2 is mainly involved in regulating cell growth, development, differentiation, apoptosis, metastasis, and other physiological and pathological processes (3-4). ERK1/2 affects the occurrence, development, prevention, and treatment of cancer. Inhibiting expression and activation of ERK1/2 and p38 is thus one option for treating malignant tumours (21-23). After exposing HeLa cells to baicalein, levels of phosphorylated ERK1/2 and p38 were significantly reduced, suggesting that baicalein inhibits the ERK and p38 MAPK signalling pathway by reducing phosphorylation of ERK1/2 and p38, thereby promoting apoptosis.

In summary, baicalein can significantly inhibit HeLa cell proliferation and induce apoptosis in a concentration-dependent manner. Moreover, baicalein can induce HeLa cells apoptosis, and it exerts its effects through induction of apoptosis and regulation of the ERK/p38/MAPK pathway.

ACKNOWLEDGEMENTS

This work was supported by the following project grants: Luzhou Science and Technology Bureau Southwest Medical University Joint Project [2017-LH020], Luzhou Municipal People's Government-Southwest Medical University Science and Technology Strategic Cooperation Project [2019LZXNYDJ53], Project of Sichuan Traditional Chinese Medicine Administration [2018JC029], Sichuan Provincial Department of Science and Technology [2020ZHFP0058] and Liangshan Science and Technology Bureau Project [18YYJS0041].

REFERENCES

1. Maurer K, Luo H, Shen Z, et al. Evaluation of a new solid media specimen transport card for high risk HPV detection and CC prevention. J Clin Virol 2016; 76:14-9.
2. Qureshi R, Arora H, Biswas S, et al. Mutation analysis of EGFR and its correlation with the HPV in Indian CC patients. Tumour Biol 2016; 37(7):9089-98.
3. Branca M, Ciotti M, Santini D, et al. Activation of the ERK/MAP kinase pathway in cervical intraepithelial neoplasia is related to grade of the lesion but not to high-risk human papillomavirus, virus clearance, or prognosis in CC. Am J Clin Pathol 2004; 122(6):902-11.
4. Zhang J, Zhang Y,Liu S, et al. Metadherin confers chemoresistance of CC cells by inducing autophagy and activating ERK/NF-kappaB pathway. Tumour Biol 2013; 34 (4):2433-40.
5. Narayan G, Xie D, Ishdorj G, et al. Epigenetic inactivation of TRAIL decoy receptors at 8p12-

21.3 commonly deleted region confers sensitivity to Apo2L /trail-Cisplatin combination therapy in CC. Genes Chromosomes Cancer 2016; 55(2):177-89.
6. Umayahara K, Takekuma M, Hirashima Y, et al. Phase study of concurrent chemoradiotherapy with weekly cisplatin and paclitaxel in patients with locally advanced uterine CC: The JACCRO GY-01 trial. Gynecol Oncol 2016; 140(2):253-8.
7. Casagrande N, De Paoli M, Celegato M, Borghese C, Mongiat M, Colombatti A, Aldinucci D. Preclinical evaluation of a new liposomal formulation of cisplatin, lipoplatin, to treat cisplatin- resistant CC. Gynecol Oncol 2013; 131(3):744-52.
8. Cetina L, Gonzalez-Enciso A, Cantu D, et al. Brachytherapy vs radical hysterectomy after external beam chemoradiation with gemcitabine plus cisplatin: a randomized, phase study in B2- B CC patients. Ann Oncol 2013; 24(8):2043-7.
9. Tjalma W A, Weyler J J, Bogers J J, et al. The importance of biological factors (bcl-2,bax,p53,PCNA,MI,HPV and angiogenesis) in invasive CC. Eur J Obstet Gynecol Reprod Biol 2001; 97(2):223-30.
10. Zhao LW, Zhong XH, Yang SY, Zhang YZ, Yang NJ. Inotodiol inhabits proliferation and induces apoptosis through modulating expression of cyclin E,p27, bcl-2,and bax in human CC HeLa cells. Asian Pac J Cancer Prev 2014; 15(7):3195- 9.
11. Peng Y, Guo C, Yang Y, Li F, Zhang Y, Jiang B, Li Q. Baicalein induces apoptosis of human CC HeLa cells in vitro. Mol Med Rep 2015;11(3):2129-34.
12. Rose HM, Stuiver M, Thongwichian R, Theillet FX, Feller SM, Selenko P. Quantitative NMR analysis of Erk activity and inhibition by U0126 in a panel of patient- derived colorectal cancer cell lines. Biochim Biophys Acta 2013; 1834(7):1396-401.
13. Guo Z, Hu X, Xing Z, et al. Baicalein inhibits prostate cancer cell growth and metastasis via the caveolin-1/AKT/mTOR pathway. Mol Cell Biochem 2015; 406(1/2):111-9.
14. Li H L, Zhang S, Wang Y,et al. Baicalein induces apoptosis via a mitochondrial-dependent caspase activation pathway in T24 bladder cancer cells Mol Med Rep 2013; 7(1):266-70.
15. Han Z, Zhu S, Han X, Wang Z, Wu S, Zheng R. Baicalein inhibits hepatocellular carcinoma cells through suppressing the expression of CD24. Int Immunopharmacol 2015; 29 2):416-22.
16. Chen XF, Liu Y. microRNA-744 inhibited CC growth and progression through apoptosis induction by regulating Bcl-2. Biomed Pharmacother 2016; 81:379-87.
17. Yu C, Zeng J, Yan Z, Ma Z, Liu S, Huang Z. Baicalein antagonizes acute megakaryoblastic leukemia in vitro and in vivo by inducing cell cycle arrest. Cell Biosci 2016; 6:20.
18. Zhang Y, Song L, Cai L, Wei R, Hu H, Jin W. Effects of baicalein on apoptosis, cell cycle arrest, migration and invasion of osteosarcoma cells. Food Chem Toxicol 2013; 53:325-33.
19. Guo M, Wei H, Hu J, Sun S, Long J, Wang X. U0126 inhibits pancreatic cancer progression via the KRAS signaling pathway in a zebrafish xenotransplantation model. Oncol Rep 2015; 34(2):699-706.
20. Lodi A, Woods S M, Ronen S M. Treatment with the MEK inhibitor U0126 induces decreased hyperpolarized pyruvate to lactate conversion in breast but not prostate cancer cells. NMR Biomed 2013; 26(3):299-306.
21. Dou CY, Cao CJ, Wang Z, et al. EFEMP1 inhibits migration of hepatocellular carcinoma by regulating MMP2 and MMP9 via ERK1/2 activity. Oncol Rep 2016; 35(6):3489-95.
22. Bai L, Mao R, Wang J, et al. ERK1/2 promoted proliferation and inhibited apoptosis of human CC cells and regulated the expression of c-Fos and c-Jun proteins. Med Oncol 2015; 32 (3):57.
23. Aguilar C, Aguilar C, Lopez-Marure R, Jiménez-Sánchez A, Rocha-Zavaleta L.Co-stimulation with stem cell factor and erythropoietin enhances migration of c-Kit expressing CC cells through the sustained activation of ERK1/2. Mol Med Rep 2014; 9(5):1895-902.

Potential role of miR-425, miR-155 and miR-33 in *Streptococcus pneumoniae* pneumonia by using bioinformatics analysis and experimental validation

CG. Chen, BS. Luo and C. Wang

Department of Emergency Medicine, The Second People's Hospital of Wuhu City, Anhui Province, China

Received March 5, 2021 – Accepted May 25, 2021

***Streptococcus pneumoniae* (*S. pneumoniae*) pneumonia is the most common cause of community-acquired pneumonia (CAP). Previous studies have suggested the diagnostic potential of microRNAs (miRNAs) in infectious diseases. In the present study, we aimed to evaluate the potential role of miRNAs in *S. pneumoniae* pneumonia by using bioinformatics analysis and experimental validation. Gene Expression Omnibus (GEO) datasets including GSE97922 and GSE83615 were analyzed for identifying the differentially expressed miRNAs; the miRNA-target genes network was constructed by using miRNet and the targeted genes were subject to Gene Ontology enrichment, Kyoto Encyclopedia of Genes and Genomes and REACTOME pathway analysis; the miRNA and mRNA expression levels were determined by quantitative real-time PCR; protein concentrations were determined by enzyme-linked immunosorbent assay. Our results showed that miR-425, miR-155 and miR-33 were up-regulated in the serum from CAP patients when compared to healthy controls; whereas there was no significant difference in serum miR-222, miR-149, miR-186 and miR-132 expression levels between healthy controls and CAP patients. *In vitro* functional studies showed that lipopolysaccharides (LPS) induced the up-regulation of miR-425, miR-155 and miR-33 in RAW264.7 cells. Mover, miR-425, miR-155 and miR-33 inhibition attenuated LPS-induced inflammatory responses in RAW264.7 cells. In conclusion, our results showed that miR-425, miR-155 and miR-33 were up-regulated in the serum from CAP patients by using bioinformatics analysis and experimental validation; furthermore, miR-425, miR-155 and miR-33 inhibition attenuated LPS-induced inflammatory responses in RAW264.7 cells. Nevertheless, our studies are still at the preliminary stages, and the detailed roles of miR-425, miR-155 and miR-33 in *S. pneumoniae* pneumonia still require further investigation.**

Streptococcus pneumoniae (*S. pneumoniae*) pneumonia is the most common cause of community-acquired pneumonia (CAP) (1, 2). *S. pneumoniae* pneumonia pathology is featured by robust host immune responses that cause lung damage, and is a leading cause of morbidity, leading to hospitalization, admission to intensive care units, long recovery, and a high mortality rate (3, 4). Thus, it is important to decipher molecular mechanisms underlying the pathogenesis and explore effective therapeutic targets for *S. pneumoniae* pneumonia treatment.

MicroRNAs (miRNAs) are small non-coding RNAs that are approximately 21 nucleotides in length (5-7). MiRNAs have important roles in regulating gene expression, both transcriptionally and post-transcriptionally, by targeting the 3' untranslated

Key words: Streptococcus pneumoniae; community-acquired pneumonia; miRNAs; inflammation; RAW264.7 cells

Corresponding Author:
Dr Chen Wang,
Department of Emergency Medicine,
The Second People's Hospital of Wuhu City,
Anhui Province, 241000, China
Tel.: +86 15309636989
e-mail: eywangchen@163.com

0393-974X (2021)
Copyright © by BIOLIFE, s.a.s.
This publication and/or article is for individual use only and may not be further reproduced without written permission from the copyright holder.
Unauthorized reproduction may result in financial and other penalties
DISCLOSURE: ALL AUTHORS REPORT NO CONFLICTS OF INTEREST RELEVANT TO THIS ARTICLE.

regions of the targeted genes. MiRNAs have been reported to involve multiple biological processes including disease progression and inflammatory responses (8, 9). Previous studies have suggested the diagnostic potential of miRNAs in various diseases including infectious diseases. Zhang et al., identified six miRNAs that have good potential to serve as non-invasive biomarkers of pulmonary tuberculosis (10). Berthrams et al., performed miRNA-transcriptome analysis and found that miR-545-3p and miR-519c-3p could be used to discriminate between CAP and chronic obstructive pulmonary disease (11). Recent studies by Wu et al., demonstrated that serum exosomal miRNAs could predict acute respiratory distress syndrome events in patients with severe CAP (12). MiR-155 was found to be essential for *S. pneumoniae* clearance from nasopharynx (13). Further studies showed that miR-302 mimics-based therapy was effective to enhance host recovery from pneumonia caused by *S. pneumoniae* (14). Yet, the diagnostic role of miRNAs in the *S. pneumoniae* pneumonia is not clear.

In the present study, the Gene Expression Omnibus (GEO) datasets including GSE97922 and GSE83615 were downloaded to analyse the differentially expressed miRNAs. Furthermore, miRNA-gene network, Gene Ontology (GO) enrichment and Kyoto Encyclopedia of Genes and Genomes (KEGG) and REACTOME pathways analysis were used to explore the potential regulatory functions of the differentially expressed miRNAs. Further quantitative real-time PCR (qRT-PCR) was performed to analyse the differentially expressed miRNAs in the clinical samples from patients with *S. pneumoniae* pneumonia. Furthermore, *in vitro* studies were also performed to determine the potential miRNAs in regulating inflammatory responses.

MATERIALS AND METHODS

Data collection

Two original microarray datasets comparing gene expression profiles between control and *S. pneumoniae*-infected mice were downloaded from the GEO database. The accession numbers were GSE97922 (4 control mice and 4 *S. pneumoniae*-infected mice) and GSE83615 (4 control mice and 4 *S. pneumoniae*-infected mice). The microarray data of GSE97922 and GSE83615 were based on PGL15547 (Agilent-035430 mouse miRNA array (miRBase release 17 miRNA ID version)) and GPL22070 ((MoGene-2_1-st) Affymetrix Mouse Gene 2.1 ST Array (transcript-level na35ens81)), respectively.

Identification of differentially expressed miRNAs

The differentially expressed miRNAs between control group *S. pneumoniae*-infected group were analyzed by using GEO2R (https://www.ncbi.nlm.nih.gov/geo/geo2r/). The cut-off criterion was set as the $P < 0.05$ and absolute fold change between groups >1.5. Volcano plot for differentially expressed genes in the two datasets was performed by the ggplot2 package in R (version 2.2.1, https://cran.r-project.org/web/packages/ggplot2). The overlapping miRNAs between GSE97922 and GSE83615 were identified as differentially expressed miRNAs through the iGEAK tool (15).

Target genes of potential differentially expressed miRNAs were predicted using miRNet

The miRNA-gene network was constructed from differentially expressed miRNAs using miRNet (http://www.mirnet.ca/), which is an easy-to-use comprehensive tool that integrated data from eleven different miRNA databases (TarBase, miRTarBase, miRecords, miRanda, miR2Disease, HMDD, PhenomiR, SM2miR, PharmacomiR, EpimiR and starBase) (16).

GO and KEGG pathway enrichment analysis

In order to explain the function of differentially expressed miRNAs, biological analyses for GO and KEGG pathway enrichment were performed using Database for Annotation, Visualization and Integrated Discovery (DAVID; http://david.ncifcrf.gov) (version 6.8) and $P<0.05$ was considered statistically significant. DAVID is an analytic tool that provides a comprehensive set of functional annotation information of genes and proteins to users for extracting biological information. GO is a common bioinformatics tool that annotates and analyses biological processes of the genes (17). KEGG is a database resource for understanding high-level functions and biological systems from large-scale molecular datasets generated by high-throughput experimental technologies (18).

Serum samples from patients and healthy controls

A total of 55 patients suspected of CAP were enrolled from January 2015 to June 2019 at the Second People's Hospital of Wuhu City. CAP was defined as the presence of a new infiltrate on a chest radiograph and at least one of the following signs and symptoms: cough, sputum production, dyspnoea, core body temperature > 38.0°C, auscultatory findings of abnormal breathing sounds, and rales along with the identification of *S. pneumoniae* as the etiologic agent by culture (respiratory or blood sample) or with urinary antigen testing. Blood samples from consenting subjects were collected within 24 h of admission to the hospital. A total of 55 healthy controls who underwent routine physical examination in the Second People's Hospital of Wuhu City were also enrolled for blood sample collection. All the studies were approved by the Clinical Research Ethics Committee of the Second People's Hospital of Wuhu City and each enrolled subject signed the written informed consent for the study.

Cell culture

Macrophage RAW 264.7 cells were purchased from the Cell Bank of the Chinese Academy of Sciences (Shanghai, China). The cells were cultured in DMEM medium (Thermo Fisher Scientific, Waltham, USA) supplemented with 10% fetal bovine serum (Sigma-Aldrich, St. Louis, USA) and 1% of penicillin/streptomycin (Sigma-Aldrich) at 37°C in a 5% CO_2 incubator. Cells at passages 3–5 were collected for further experimentation.

Lipopolysaccharides (LPS) treatment and cell transfections

LPS was purchased from Sigma-Aldrich, and the RAW264.7 cells were treated with 1 μg/ml LPS for 24 h before further *in vitro* assays (19). The miR-425 inhibitor, miR-155 inhibitor, miR-33 inhibitor and their respective negative controls were purchased from Ribobio (Guangzhou, China). For cell transfections, RAW264.7 cells were transfected with different miRNA oligonucleotides (50 nM) using the Lipofectamine 2000 reagent (Invitrogen, Carlsbad, USA) by following the manufacturer's protocol.

Quantitative real-time PCR (qRT-PCR)

Total RNA was extracted from serum samples or cells using RNAiso plus Reagent (TaKaRa, Dalian, China). MiRNA reverse transcription primers and qPCR primers were purchased from RiboBio Co. Ltd (Guangzhou, China). Total RNA was reverse-transcribed into cDNA by using the PrimeScript RT Reagent Kit (TaKaRa, Dalian, China). Next, real-time PCR was performed in a Roche LightCycler480 II Real-Time PCR Detection System (Roche, Basel, Switzerland) by using SYBR Premix Ex Taq kit (TaKaRa). The expression level of miRNAs (relative to U6) and mRNA (relative to GAPDH) was analyzed using the $2^{-\Delta\Delta Ct}$ method.

Enzyme-linked immunosorbent assay (ELISA)

The protein concentrations of interleukin 6 (IL-6) and tumor necrosis factor alpha (TNF-α) in cell culture from different groups were measured by using IL-6 Detection ELISA (#M6000B; R&D Systems, Minneapolis, USA) and TNF-α ELISA kit (#MTA00B; R&D Systems), respectively.

Statistical analysis

The GraphPad Prism Software Version 7.0 (GraphPad Software, La Jolla, USA) was used for the statistical analysis. Continuous variables were expressed as the mean ± standard deviation (SD). Significant difference between two groups was analysed using unpaired Student's *t*-test or one-way ANOVA followed by Bonferroni's post hoc test. A *P* value less than 0.05 denoted the presence of a statistically significant difference.

RESULTS

Identification of the differentially expressed miRNAs in GSE97922 and GSE83615 datasets

Based on the screening through the GEO datasets, we found that GSE97922 and GSE83615 included data for the differentially expressed miRNAs between control and *S. pneumoniae*-infected mice. In the GSE79722 dataset, there are 346 differentially expressed miRNAs in neutrophils between phosphate buffered saline (PBS)-treated group and *S. pneumoniae*-infected mice (142 miRNAs were up-regulated and 202 miRNAs were down-regulated; Fig. 1A); in the GSE83615 dataset, there are 47 differentially expressed miRNAs in neutrophils between PBS-treated group and *S. pneumoniae*-infected mice (35 miRNAs were up-regulated and 12 miRNAs were down-regulated) (Fig. 1B). Further analysis revealed that 16 overlapped miRNAs were identified between GSE97922 and GSE83615 datasets (Fig. 1C). The list of 16 miRNAs are shown in Fig. 1D.

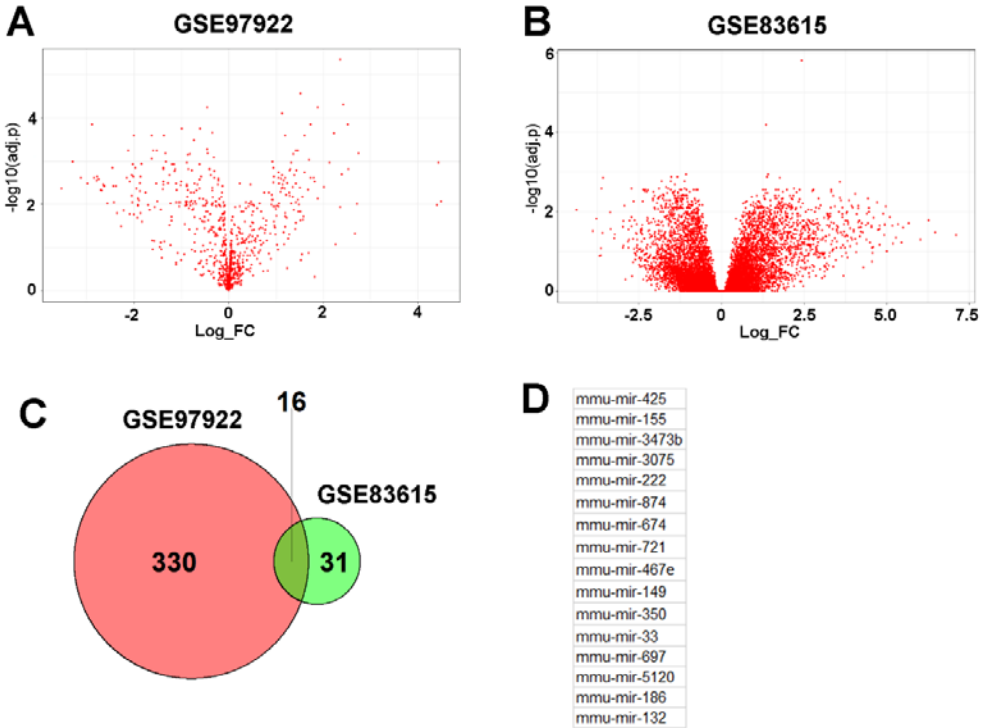


Fig. 1. *Analysis of common differentially expressed miRNAs.* ***A****) Volcano plot of the differentially expressed genes in GSE97922 dataset.* ***B****) Volcano plot of the differentially expressed genes in GSE83615 dataset.* ***C****) Venn diagram shows the common differentially expressed miRNAs between GSE97922 and GSE83615 datasets.* ***D****) The list of the common differentially expressed miRNAs between GSE97922 and GSE83615 datasets.*

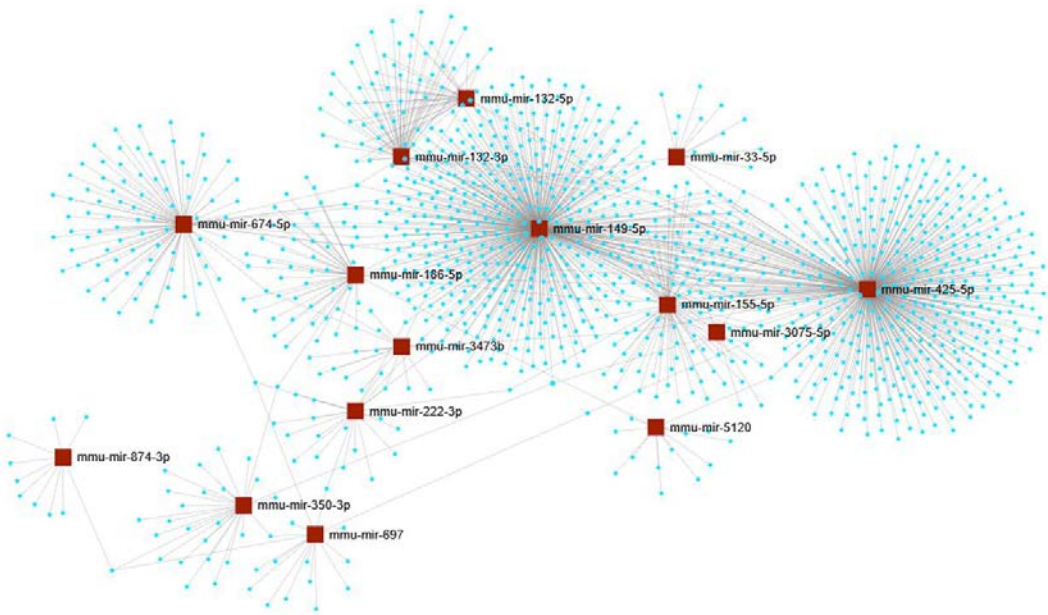


Fig. 2. *MiRNA-targeted genes network constructed by MiRNet.*

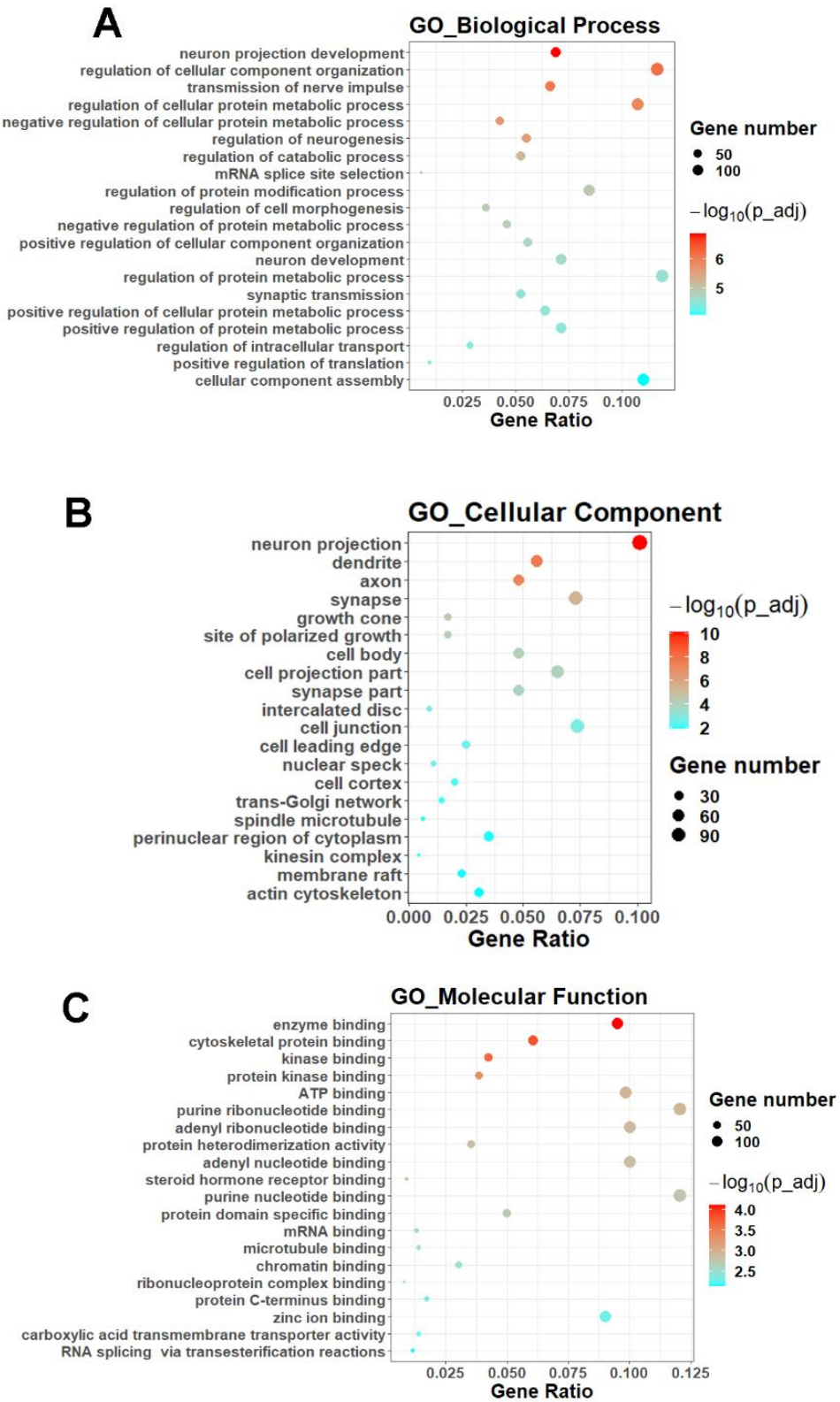


Fig. 3. *GO enrichment analysis of miRNA-targeted genes. The enrichment of these genes in (**A**) Biological Process, (**B**) Cellular Component and (**C**) Molecular Function is shown.*

MiRNA-target gene network analysis

The miRNA-target gene network analysis was performed using the miRNet online web tool and the constructed network are shown in Fig. 2. In the constructed network, there are 1243 nodes, and a total of 1108 genes were targeted by the 16 differentially expressed miRNAs (Fig. 2). Furthermore, the targeted genes were subjected to GO and KEGG pathway enrichment analysis.

GO and KEGG pathway enrichment analysis

The GO enrichment analysis was performed in the miRNA-targeted genes. In the biological process, the genes were significantly enriched in "neuron projection development", "regulation of cellular component organization", transmission of nerve impulse", "regulation of cellular protein metabolic process" and so on (Fig. 3A); in the cellular component, the genes were significantly enriched in "neuron projection", "dendrite", "axon", "synapse" and so on (Fig. 3B); in the molecular function, the genes were significantly enriched in "enzyme binding", "cytoskeletal protein binding", "kinase binding", "protein kinase binding" and so on (Fig. 3C). For the KEGG pathway analysis, the genes were significantly enriched in the "mTOR signaling pathway", "renal cell carcinoma", "Hepatitis B", "ErbB signaling pathway" and so on (Fig. 4A). For the REACTOME pathway, the genes were significantly enriched in "Signaling by SCF-KIT",

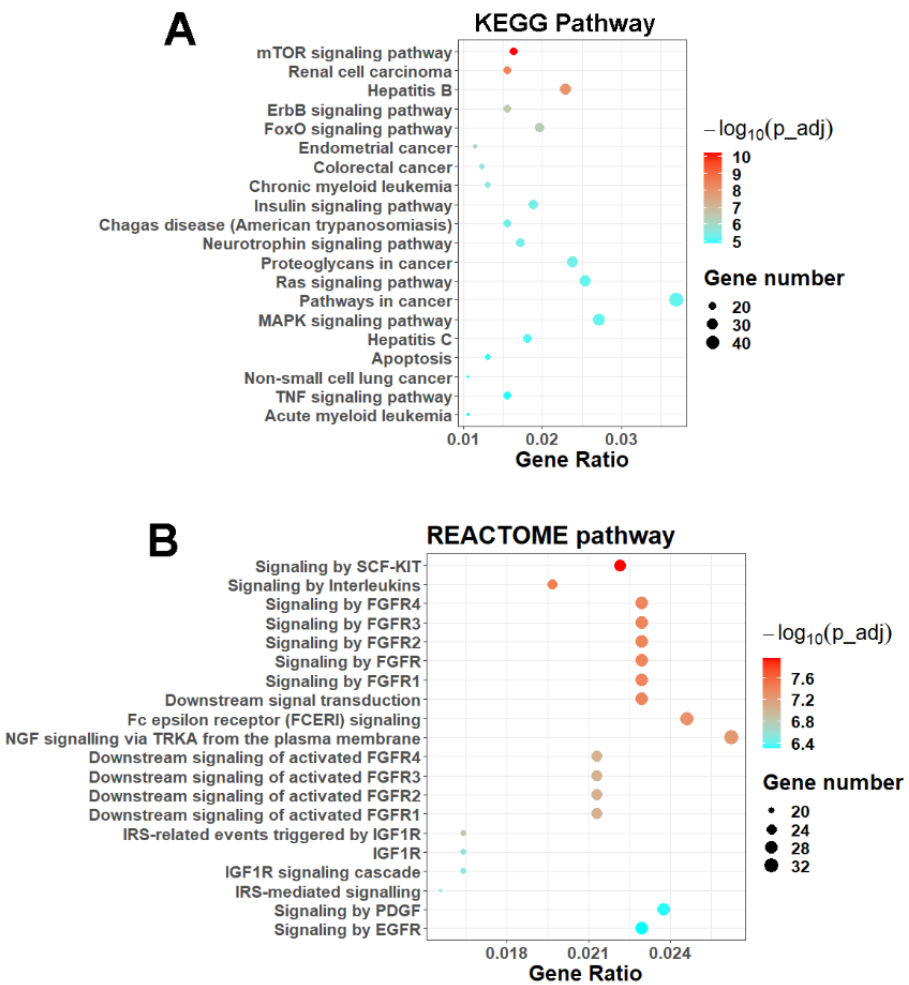


Fig. 4. *KEGG and REACTOME pathway of the miR-targeted genes. The enrichment of these genes in (**A**) KEGG pathway and (**B**) REACTOMNE pathway is shown.*

"Signaling by Interleukins", "Signaling by FGFR4", "Signaling by FGFR3" and so on (Fig. 4B).

Examination of miRNAs in the clinical samples by qRT-PCR

We further examined the expression levels of 7 miRNAs (miR-425, miR-155, miR-222, miR-149, miR-33, miR-186 and miR-132) in the serum from patients with *S. pneumoniae* pneumonia and healthy controls. As shown in Fig. 5, the expression levels of serum miR-425, miR-155 and miR-33 were significantly up-regulated in the patients with *S. pneumoniae* pneumonia when compared to healthy controls; whereas there was no significant difference in the expression levels of serum miR-222, miR-149, miR-186 and miR-132 between patients with *S. pneumoniae* pneumonia and heathy controls.

LPS induced the up-regulation of miR-425, miR-155 and miR-33 in RAW264.7 cells

In order to determine the role of miR-425, miR-155 and miR-33 during infection, we treated RAW264.7 cells with LPS for 24 h. LPS, the major component of the outer membrane of Gram-negative bacteria, is known to be a key pathogenic stimulator in various infectious diseases (20). As expected, LPS treatment significantly increased the mRNA and protein expression levels of IL-6 and TNF-α in RAW264.7 cells (Fig. 6 A-D); furthermore, the up-regulation of miR-425, miR-155 and miR-33 was observed in the RAW264.7 cells after LPS simulation (Fig. 6 E-G).

Effects of miR-425, miR-155 and miR-33 inhibition on the LPS-induced inflammatory responses in RAW264.7 cells

In order to determine whether miR-425, miR-155

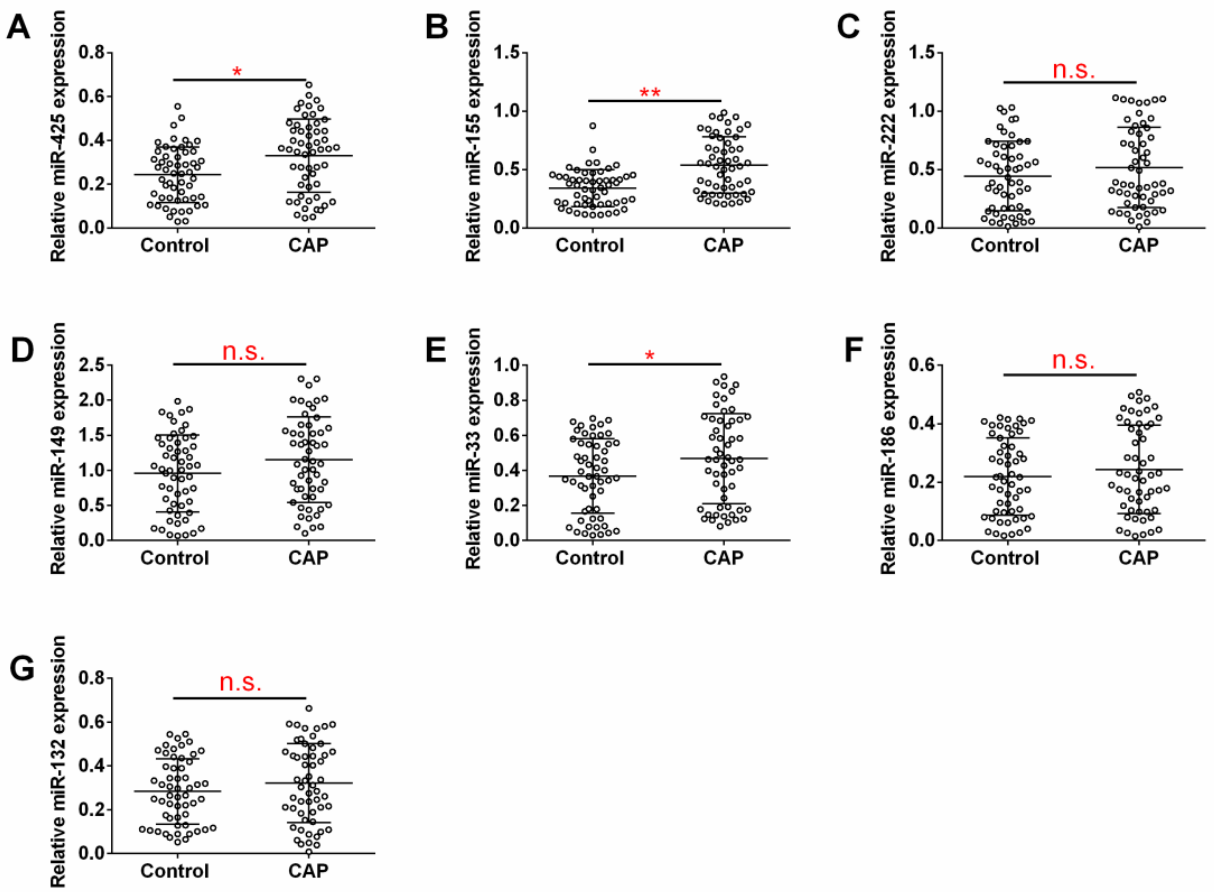


Fig. 5. *The experimental validation of the common differentially expressed miRNAs in the serum from CAP patients and healthy controls. **A)** miR-425, **(B)** miR-155, **(C)** miR-222, (D) miR-149, **(E)** miR-33, **(F)** miR-186 and **(G)* miR-132 in the serum from CAP patients and healthy controls are assessed using qRT-PCR. *P<0.05, **P<0.01; n.s. = non-significant.*

and miR-33 inhibition can attenuate LPS-induced inflammatory responses in RAW264.7 cells, RAW264.7 cells were transfected with miR-425 inhibitor, miR-155 inhibitor or miR-33 inhibitor. MiR-425 inhibitor, miR-155 inhibitor and miR-33 inhibitor transfection down-regulated the expression of miR-425, miR-155 and miR-33 in RAW264.7 cells, respectively (Fig. 7 A-C). Further *in-vitro* studies showed that miR-425 inhibition attenuated the LPS-induced increase in the mRNA and protein expression levels of IL-6 and TNF-α in RAW246.7 cells (Fig. 7 D-G). Consistently, miR-155 inhibition and miR-425 inhibition both partially reversed the increase in mRNA and protein expression levels of IL-6 and TNF-α induced by LPS in RAW246.7 cells (Fig. 7 H-O).

DISCUSSION

S. pneumoniae is the aetiological agent commonly associated with CAP. It can, however, be very difficult to make a definitive microbiological diagnosis. In the present study, we analysed two GEO datasets and identified 16 common differentially expressed miRNAs in the neutrophils from mice infected with *S. pneumoniae*. The miRNA-target genes network was constructed and the targeted genes were subject to GO enrichment, KEGG and REACTOME pathway analysis. Furthermore, we analyzed the 7 miRNAs in the serum from CAP patients and healthy controls. Our results showed that miR-425, miR-155 and miR-33 were up-regulated in in the serum from CAP patients when compared to healthy controls. Repression of miR-425, miR-155 and miR-33 attenuated LPS-induced inflammatory responses in RAW264.7 cells. This study provides some preliminary insights regarding the role of miRNAs in *S. pneumoniae*.

The role of miRNAs in *S. pneumoniae* infection has been deciphered by several lines of evidence. Verschoor et al., showed that miR-155-deficient mice maintained the ability to prevent acute invasive pneumococcal infection, but had significantly higher bacterial burdens following colonization, suggesting that miRNA-155 is required for clearance of *S. pneumoniae* from the nasopharynx (13). Fukuyama et al. showed that nanogel-based pneumococcal surface protein A nasal vaccine induced miR-181a and miR-326-associated Th17 cell responses with neutralizing antibodies against *S. pneumoniae* in macaques (21). Griss et al., found that computational network analysis retrieved miRNA-146a as one putatively important regulator of pneumococci-induced host cell activation

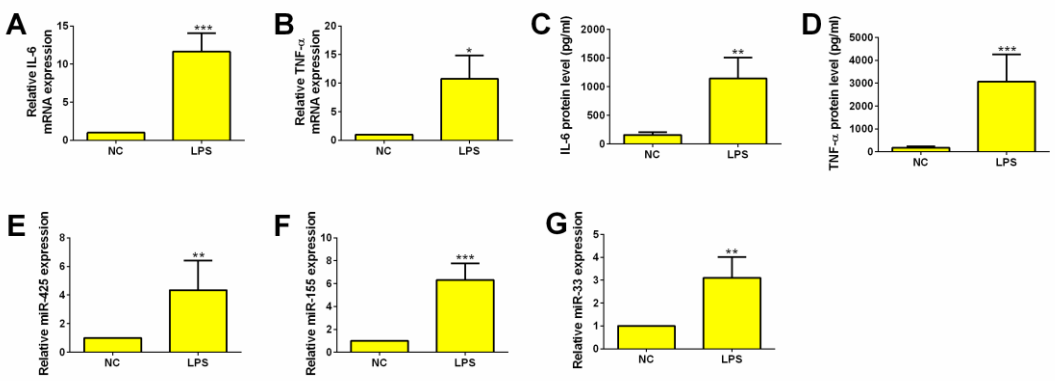


Fig. 6. *LPS induced the up-regulation of miR-425, miR-155 and miR-33 in RAW264.7 cells. RAW264.7 cells were treated with LPS (1 μg/ml) for 24 h, (**A**) IL-6 and (B) TNF-α mRNA expression levels were determined by qRT-PCR; (**C**) IL-6 and (**D**) TNF-α protein levels were determined by ELISA assay; (**E**) miR-425, (**F**) miR-155 and (**G**) miR-33 expression levels were determined by qRT-PCR. N = 3. *P<0.05, **P<0.01 and ***P<0.001.*

and pneumococci recognition induced a negative feedback loop, preventing excessive inflammation via miR-146a and potentially other miRNAs (22). Yao et al., demonstrated that purified *S. pneumoniae* endopeptidase O enhanced particle uptake by macrophages in a miR-155-dependent manner (23). Importantly, Ginsburg et al., found that miRNA host response signatures revealed accurate discrimination between *S. pneumoniae* pneumonia and influenza aetiologies for acute respiratory infections (24). Wang et al., showed that treatment of S. *pneumoniae*-infected mice with miRNA-302 mimics improved lung functions, host recovery and survival, and miRNA-302 mediated its therapeutic effects, not by inhibiting apoptosis and preventing damage, but by promoting proliferation of local epithelial progenitor cells to regenerate alveolar epithelial cells (14). These results suggest that miRNAs may play important roles

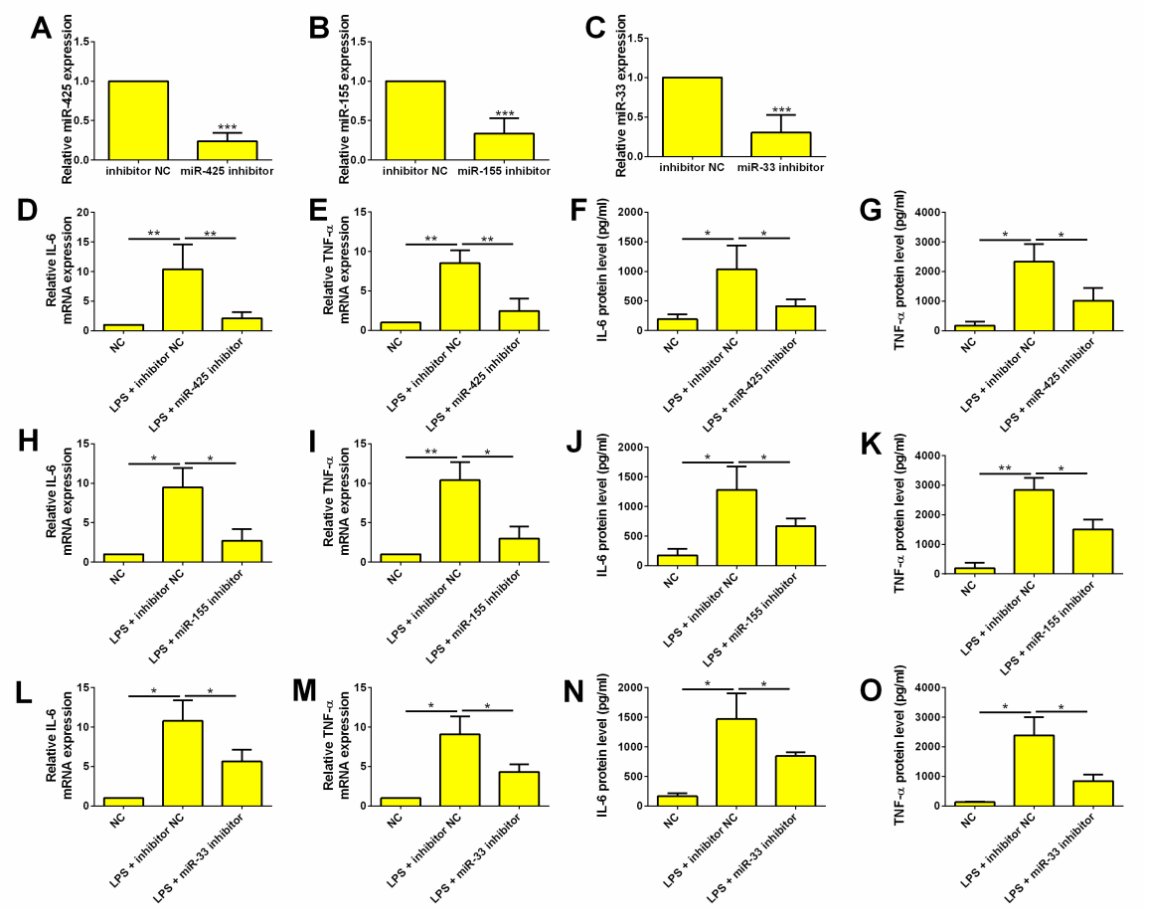


Fig. 7. *Effects of miR-425, miR-155 and miR-33 inhibition on the inflammatory responses in LPS-treated RAW264.7 cells. **A-C**) RAW264.7 cells were transfected with miR-425 inhibitor, miR-155 inhibitor miR-33 inhibitor or their corresponding negative controls, at 24 h after transfection, (A) miR-425, (B) miR-155 and (C) miR-33 expression levels were determined by qRT-PCR. **D-G**) RAW264.7 cells were transfected with miR-425 inhibitor or respective negative control, and after 24 h, RAW264.7 cells were further treated with LPS (1 μg/ml) for 24 h, (D) IL-6 and (E) TNF-α mRNA expression levels were determined by qRT-PCR; (F) IL-6 and (G) TNF-α protein levels were determined by ELISA assay. **H-K**) RAW264.7 cells were transfected with miR-155 inhibitor or respective negative control, and after 24 h, RAW264.7 cells were further treated with LPS (1 μg/ml) for 24 h, (H) IL-6 and (I) TNF-α mRNA expression levels were determined by qRT-PCR; (J) IL-6 and (K) TNF-α protein levels were determined by ELISA assay. **L-O**) RAW264.7 cells were transfected with miR-33 inhibitor or respective negative control, and after 24 h, RAW264.7 cells were further treated with LPS (1 μg/ml) for 24 h, (L) IL-6 and (M) TNF-α mRNA expression levels were determined by qRT-PCR; (N) IL-6 and (O) TNF-α protein levels were determined by ELISA assay. N = 3. *P<0.05, **P<0.01 and ***P<0.001.*

in *S. pneumoniae* infection.

In the present study, we demonstrated that miR-425, miR-155 and miR-33 expression levels were elevated in the serum of CAP patients when compared to healthy controls, and these 3 miRNAs had fair diagnostic potential to discriminate CAP patients from healthy controls. The role of miR-425 has been widely studied in the literature, and miR-425 can function as an oncogene or a tumor suppressor, depending on the cancer type. The role of miR-425 in bacterial infection is unclear. MiR-425 was found to be significantly increased in serum of Tuberculosis (TB) patients, which correlated with the TB infection level (25). In addition, miR-425 was up-regulated in the peripheral blood monocyte-derived macrophage in Bacillus Calmette-Guérin infection (26). Consistently, our data showed the up-regulation of serum miR-425 in the CAP patients, and miR-425 could discriminate CAP patients from healthy controls. Collectively, these data imply that miR-425 could be a potential biomarker for bacterial infection, whereas the diagnostic role of miR-425 in the CPA may still require further detailed examination. MiR-155 has been well-studied in infectious diseases. Cheng et al. found that miR-155 regulated interferon-γ production in natural killer cells via Tim-3 signalling in chronic hepatitis C virus infection (27). Jha et al. demonstrated that miR-155 deficiency exacerbates *Trypanosoma cruzi* infection (28). In addition, miRNA-155 knockout mice were susceptible to *Mycobacterium tuberculosis* infection (29). In *S. pneumoniae* infection, miRNA-155 played an important role in clearing *S. pneumoniae* from the nasopharynx (13). In combination with previous studies, our results imply that miR-155 might exert protective effects again *S. pneumoniae* infection and serve as a potential biomarker for CAP diagnosis. The role of miR-33 has been well documented in cardiovascular diseases, whereas its role in infectious diseases is almost unclear. Ho et al. revealed a cholesterol-miR-33- receptor-interacting protein 140 regulatory pathway that modulated the proinflammatory potential in macrophages in response to an alteration in the intracellular cholesterol status (30). Ouimet et al. demonstrated that *Mycobacterium tuberculosis* induced the miR-33 locus to reprogram autophagy and host lipid metabolism (31). *In vitro* functional studies showed that LPS induced the up-regulation of miR-425, miR-155 and miR-33 in RAW264.7 cells. Mover, miR-425, miR-155 and miR-33 inhibition attenuated LPS-induced inflammatory responses in RAW264.7 cells. Collectively, these data suggest that miR-425, miR-155 and miR-33 may play an important role in CAP.

In the present study, the number of enrolled patients is relatively low, and further studies with a larger cohort are required. Whether these miRNAs are specifically differentially expression in CAP remains elusive, which may require further study. The present study analysed two GEO datasets based on screening, and future studies may consider including more updated datasets to identify more novel miRNAs in *S. pneumoniae* pneumonia. The current study only used LPS to stimulate the murine macrophages, and future studies may use the bacteria strain to infect the human macrophages to further confirm our findings. As miRNAs exerted their biological functions via targeting the 3' untranslated region of the targeted genes, future studies should consider exploring the downstream targets of miR-424, miR-155 and miR-33 to fully decipher the regulatory role of these miRNAs in *S. pneumoniae* pneumonia.

In conclusion, our results showed that miR-425, miR-155 and miR-33 were up-regulated in the serum from CAP patients by using bioinformatics analysis and experimental validation; furthermore, miR-425, miR-155 and miR-33 inhibition attenuated LPS-induced inflammatory responses in RAW264.7 cells. Nevertheless, our research is still at the preliminary stage, and the detailed roles of miR-425, miR-155 and miR-33 in *S. pneumoniae* pneumonia still require further investigation.

REFERENCES

1. Feldman C, Anderson R. The role of streptococcus pneumoniae in community-acquired pneumonia. Semin Respir Crit Care Med 2016; 37:806-18.
2. Rozenbaum MH, Pechlivanoglou P, van der Werf TS, Lo-Ten-Foe JR, Postma MJ, Hak E. The role of Streptococcus pneumoniae in community-acquired pneumonia among adults in Europe: a meta-analysis. Eur J Clin Microbiol Infect Dis 2013; 32:305-16.

3. José RJ, Periselneris JN, Brown JS. Community-acquired pneumonia. Curr Opin Pulm Med 2015; 21:212-18.
4. van der Poll T, Opal SM. Pathogenesis, treatment, and prevention of pneumococcal pneumonia. Lancet 2009; 374:1543-56.
5. Huang W. MicroRNAs: Biomarkers, diagnostics, and therapeutics. Methods Mol Biol 2017; 1617:57-67.
6. Michlewski G, Cáceres JF. Post-transcriptional control of miRNA biogenesis. Rna 2019; 25:1-16.
7. Wang J, Chen J, Sen S. MicroRNA as biomarkers and diagnostics. J Cell Physiol 2016; 231:25-30.
8. Luan X, Zhou X, Naqvi A, Francis M, Foyle D, Nares S, Diekwisch TGH. MicroRNAs and immunity in periodontal health and disease. Int J Oral Sci 2018; 10:24.
9. Tahamtan A, Teymoori-Rad M, Nakstad B, Salimi V. Anti-inflammatory MicroRNAs and their potential for inflammatory diseases treatment. Front Immunol 2018; 9:1377.
10. Zhang X, Guo J, Fan S, et al. Screening and identification of six serum microRNAs as novel potential combination biomarkers for pulmonary tuberculosis diagnosis. PLoS One 2013; 8:e81076.
11. Bertrams W, Griss K, Han M, et al. Transcriptional analysis identifies potential biomarkers and molecular regulators in pneumonia and COPD exacerbation. Sci Rep 2020; 10:241.
12. Wu X, Wu C, Gu W, Ji H,Zhu L. Serum Exosomal MicroRNAs Predict Acute Respiratory Distress Syndrome Events in Patients with Severe Community-Acquired Pneumonia. Biomed Res Int 2019; 2019:3612020.
13. Verschoor CP, Dorrington MG, Novakowski KE, et al. MicroRNA-155 is required for clearance of Streptococcus pneumoniae from the nasopharynx. Infect Immun 2014; 82:4824-33.
14. Wang Y, Li Y, Zhang P, et al. Regenerative therapy based on miRNA-302 mimics for enhancing host recovery from pneumonia caused by Streptococcus pneumoniae. Proc Natl Acad Sci U S A 2019; 116:8493-8.
15. Choi K, Ratner N. iGEAK: an interactive gene expression analysis kit for seamless workflow using the R/shiny platform. BMC Genomics 2019; 20:177.
16. Chang L, Zhou G, Soufan O, Xia J. miRNet 2.0: network-based visual analytics for miRNA functional analysis and systems biology. Nucleic Acids Res 2020; 48:W244-w251.
17. Nota B. Gogadget: an R package for interpretation and visualization of GO enrichment results. Mol Inform 2017; 36(5-6).
18. Yang Q, Wang S, Dai E, et al. Pathway enrichment analysis approach based on topological structure and updated annotation of pathway. Brief Bioinform 2019; 20:168-77.
19. Nemati M, Akseh S, Amiri M, et al. Lactoferrin suppresses LPS-induced expression of HMGB1, microRNA 155, 146, and TLR4/MyD88/NF-κB pathway in RAW264.7 cells. Immunopharmacol Immunotoxicol 2021; 43:153-9.
20. Yücel G, Zhao Z, El-Battrawy I, et al Lipopolysaccharides induced inflammatory responses and electrophysiological dysfunctions in human-induced pluripotent stem cell derived cardiomyocytes. Sci Rep 2017; 7:2935.
21. Fukuyama Y, Yuki Y, Katakai Y, et al. Nanogel-based pneumococcal surface protein A nasal vaccine induces microRNA-associated Th17 cell responses with neutralizing antibodies against Streptococcus pneumoniae in macaques. Mucosal Immunol 2015; 8:1144-53.
22. Griss K, Bertrams W, Sittka-Stark A, et al. MicroRNAs constitute a negative feedback loop in streptococcus pneumoniae-induced macrophage activation. J Infect Dis 2016; 214:288-99.
23. Yao H, Zhang H, Lan K, et al. Purified Streptococcus pneumoniae endopeptidase O (PepO) enhances particle uptake by macrophages in a toll-like receptor 2- and miR-155-Dependent Manner. Infect Immun 2017; 85:e01012-16. doi: 10.1128/IAI.01012-16
24. Poore GD, Ko ER, Valente A, et al. A miRNA Host Response Signature Accurately Discriminates Acute Respiratory Infection Etiologies. Front Microbiol 2018; 9:2957.
25. Alipoor SD, Tabarsi P, Varahram M, et al. Serum Exosomal miRNAs Are Associated with Active Pulmonary Tuberculosis. Dis Markers 2019; 2019:1907426.
26. Alipoor SD, Mortaz E, Tabarsi P, et al. miR-1224 Expression Is Increased in Human Macrophages after Infection with Bacillus Calmette-Guérin (BCG). Iran J Allergy Asthma Immunol 2018; 17:250-7.
27. Cheng YQ, Ren JP, Zhao J, et al. MicroRNA-155

regulates interferon-γ production in natural killer cells via Tim-3 signalling in chronic hepatitis C virus infection. Immunology 2015; 145:485-97.
28. Jha BK, Varikuti S, Seidler GR, Volpedo G, Satoskar AR, McGwire BS. MicroRNA-155 deficiency exacerbates trypanosoma cruzi infection. Infect Immun 2020; 88:e00948-19. doi: 10.1128/IAI.00948-19.
29. Iwai H, Funatogawa K, Matsumura K, et al. MicroRNA-155 knockout mice are susceptible to Mycobacterium tuberculosis infection. Tuberculosis (Edinb) 2015; 95:246-50.
30. Ho PC, Chang KC, Chuang YS, Wei LN. Cholesterol regulation of receptor-interacting protein 140 via microRNA-33 in inflammatory cytokine production. Faseb J 2011; 25:1758-66.
31. Ouimet M, Koster S, Sakowski E, et al. Mycobacterium tuberculosis induces the miR-33 locus to reprogram autophagy and host lipid metabolism. Nat Immunol 2016; 17:677-86.

High cyclic tensile stress disrupts the extracellular matrix in human chondrocyte by F-actin cytoskeletal polymerization and reactive oxygen species production

Y. Li, J. Yang, Q. Feng, S.-Q. Li, Y. Lang, X.-F. Zhang and C. Ye

Department of Orthopaedic Surgery, Fuyang Orthopaedics and Traumatology Affiliated Hospital of Zhejiang Chinese Medical University, Hangzhou, China

Received March 3, 2021 – Accepted May 25, 2021

This study aims to explore the mechanism of cyclic tensile stress (CTS) on human chondrocytes (CHs) relating to the reactive oxygen species (ROS) generation and extracellular matrix (ECM) stability *in vitro*. A well-established CTS model with 5%, 10%, or 20% elongation was performed for CHs stretching. After CTS, the cell viability, total ROS level, main ECM components, matrix metalloproteinase (MMP), tissue inhibitor of metalloproteinase (TIMP), F-actin density, and some anti-oxidative enzymes were analyzed. Additionally, the antioxidant N-acetylcysteine (NAC) and cytochalasin D were used to suppress the ROS production and F-actin polymerization when the CHs underwent CTS, respectively. The treatment of 20% elongation-CST significantly decreased the CH viability and the expressions of collagen II, aggrecan, anti-oxidative enzymes and TIMP3/4, however, it increased the ROS accumulation, F-actin polymerization, and the expression of collagen I and MMP3/13. In contrast, the application of NAC and cytochalasin D could partly rescue the CHs from the injury caused by the high CTS. Therefore, high CTS disrupts the ECM by remodeling the F-actin cytoskeleton and promoting ROS production. Cytochalasin D and NAC are effective in rejecting F-actin cytoskeleton polymerization, and ROS accumulation through a potential synergetic process, which alleviates the ECM injury caused by High CTS.

Osteoarthritis (OA) is a chronic progressive arthritic disease characterized by degenerative changes in articular cartilage and bone hyperplasia around the joints, which is a common cause of joint pain in elderly people (1). Many aspects have been reported to involve the pathogenesis of OA, such as mechanical stress, biochemical stimuli, and genetic mediation (2). Moreover, congenital dysplasia, obesity, loss of muscle strength around joints, and joint trauma also cause the unbalanced mechanical environment of the joint, which aggravates metabolism disorders and damage of extracellular matrix (ECM). All these processes contribute to the regression of chondrocytes (CHs) and the development of OA (3). Type II collagen is the main component of collagen fibers in the ECM. A large number of collagen networks make the cartilage elastic, contributing to withstand specific mechanical forces. After the joint load-bearing surface is damaged, the ECM is redistributed and reconstructed (4). However, the degree of articular cartilage damage is far greater than the ability to repair, so the cartilage is continually damaged because of the ECM degradation**.** In the early stages of the onset of OA, aggrecan (ACAN), another main component of cartilage ECM, is gradually lost, and collagen fibers

Key words: chondrocyte; osteoarthritis; F-actin; reactive oxygen species; extracellular matrix

**Corresponding Author:*
Chun Ye, BM.,
Department of Orthopaedic Surgery,
Fuyang Orthopaedics and Traumatology
Affiliated Hospital of Zhejiang Chinese Medical University,
418 Fengpu Road, Fuchun Street,
Fuyang District, Hangzhou, Zhejiang 311400, China
Tel./Fax: +86 015157100258
e-mail: yechun123@zcmu.edu.cn

0393-974X (2021)
Copyright © by BIOLIFE, s.a.s.
This publication and/or article is for individual use only and may not be further reproduced without written permission from the copyright holder.
Unauthorized reproduction may result in financial and other penalties
DISCLOSURE: ALL AUTHORS REPORT NO CONFLICTS OF INTEREST RELEVANT TO THIS ARTICLE.

express more type I collagen than type II collagen resulting from the degenerated CHs. Meanwhile, the continuous friction caused by external mechanical forces continues to destroy the ECM (5).

Clinical studies have confirmed that the frequency, time, and strength of mechanical force loads are all factors affecting the metabolism of CHs (6). Mechanical stimuli can be converted into biological signals and transmitted to the cell. As a result, the corresponding gene expressions are adjusted to adapt to the changes in the external environment (7). For instance, Smith et al. (8) reported shear stress could increase inflammation, reduce the synthesis of ACAN and type II collagen, and finally induce the occurrence of CH apoptosis; However, the intermittent hydrostatic pressure plays a different role, suggesting that the different forms of mechanical stimulation have different biological effects. Moreover, Gassner et al. (9) confirmed that cyclic tensile stress (CTS) could antagonize the inflammatory effect of IL-1β and up-regulate the expression of ACAN, suggesting that CTS has a protective effect on cartilage. On the contrary, Matsukawa et al. (10) reached an opposing conclusion that CTS promoted NO synthesis in CHs and inhibited ECM synthesis. These controversial studies suggest that the biological effects of mechanical stimulation on CHs are complicated and changeable depending on different strengths and frequencies.

At present, the mechanism of biomechanical conduction of articular CHs is not very clear, but many clinical studies have pointed out that the cytoskeleton has a significant role. Applying different levels of mechanical stress *in vitro* can lead to rearrangement of the CH cytoskeleton, which affects cell proliferation and ECM synthesis (11-13). However, whether the effect of CTS on the ECM stability of CHs is related to cell cytoskeleton remain unknown. Since CTS also affects NO release, we hypothesized whether it might also play a role in the reactive oxygen species (ROS) metabolism. Thus, this study applied cycle stretch to human CHs *in vitro* to observe the changes in ECM, cytoskeleton, and ROS production. These findings underlying force-biosignal transformation may provide a basis for regulating the cytoskeleton to promote articular cartilage remodeling and repair in the treatment of OA.

MATERIALS AND METHODS

Cartilage collection and CH isolation

A total of six knee samples from patients (3 males and 3 females, aged 54-65 years, average 59 years) undergoing amputation of the distal fibula chondrosarcoma were collected for the CH isolation. All patients involved had no history of arthritis. Before the operation, the patients were informed that the collected joint tissue would be used for scientific research, and all signed informed consent. This study was approved by Fuyang Orthopaedics and Traumatology Affiliated Hospital of Zhejiang Chinese Medical University. For the introduction of the CH isolation, the superficial zone of the cartilage from the knee joint was cut into fragments in a flacon tube, and the fragments were digested with 0.25% type XI collagenase (Sigma, St. Louis, MO, USA) for eight h at 37°C. The solution was filtrated and centrifuged to get the CH pellets.

Cyclic stretch

CHs were seeded on a Bioflex 6-well plate with 25 mm loading posts (Flexcell, Hillsborough, NC, USA) at a density of 1.5×10^4 cells per well (Fig. 1A). CHs were cultured under non-stretch conditions until the cell reached at least 70% confluence, and then the Bioflex plate underwent the stretch program of FX-6000T™ Tension System, as previously described (14). CHs in the stretched groups were treated according to a computer-controlled vacuum stretch apparatus with a cycle involving 4 s of stretch (5%, 10%, or 20%) (Fig. 1B) alternating with 4 s of relaxation. CHs were collected after 6 h of cyclic exposure. Meanwhile, CHs under non-stretch conditions were taken as a control group, and were also cultured on the Bioflex 6-well plate in the same medium.

Immunofluorescence of collagen II (IF)

The protein expression of collagen II was determined by IF staining. After treatments, CHs underwent fixation with 4% paraformaldehyde (Beyotime, Shanghai, China) for 15 min and permeabilization with 0.1% Triton-X (Beyotime, Shanghai, China) for 15 min. Then, CHs were washed with phosphate-buffered saline (PBS) and incubated with collagen II primary antibody (dilution of 1:200 in PBS; Abcam, Cambridge, MA, USA; cat#: ab185430) overnight at 4°C. The next day, CHs were incubated with Alexa Fluor488 conjugated secondary

antibody (Invitrogen, St. Louis, MO, USA) for 1 h avoiding the light. The staining fluorescent intensity was detected by an inverted fluorescence microscope to present the expression of the collagen II protein.

F-Actin cytoskeleton analysis

The cytoskeleton of CHs was determined by the intensity of F-actin. After treatments, CHs underwent fixation with 4% paraformaldehyde for 15 min and permeabilization with 0.1% Triton-X for 15 min. CHs were incubated with phalloidin-FITC (dilution of 1:200 in PBS; Abcam, Cambridge, MA, USA; cat#: ab235137) for 1 h in the dark. The staining fluorescent intensity was detected by an inverted fluorescence microscope to present the expression of the F-actin.

Flow cytometry of total ROS analysis

The whole ROS level of CHs under each treatment was determined by ROS Detection Kit (Abcam, Cambridge, MA, USA). The single-CH suspension was prepared and performed on a plate reader according to the manufacturer's instructions. Relative fluorescence units (RFU) were detected by flow cytometry to present 2,7-Dichlorodi-hydrofluorescein diacetate (DCFH-DA).

Real-time polymerase chain reaction (RT-PCR)

The mRNA expressions of aggrecan (ACAN), collagen I, MMP3, MMP13. TIMP3, and TIMP4 were determined by RT-PCR assay. After treatments, the total RNA of CHs was extracted using the TRIzol (Invitrogen, St. Louis, MO, USA) according to the manufacturer's instructions. The RNA was then reverse-transcribed into complementary deoxyribose nucleic acid (cDNA). The RT-PCR analysis was performed using the SYBR Green mix kit (Invitrogen, St. Louis, MO, USA) according to the manufacturer's instructions. The mRNA level of each gene was presented relative to the amount of glyceraldehyde 3-phosphate dehydrogenase (GAPDH) according to the method of $2^{-\Delta\Delta Ct}$. The primers used are listed in Table I.

Cell viability assay

The cell viability under each condition was determined with CASY Cell Counter & Analyzer (OLS OMNI Life Science, Bremen, Germany). After treatments, the CHs were detached from the Bioflex plate with trypsin, and the living cell ratio was measured according to the manufacturer's instructions. Cell viability was shown as a percentage relative to the control group.

Statistical analysis

Statistical analysis was performed and the column diagrams were achieved by GraphPad Prism 6.01 (La Jolla, CA, USA). Data were expressed as mean ± standard deviation (SD). Differences between the two groups

Table I. *Primers for RT-PCR*

Gene name	Forward (5'>3')	Reverse (5'>3')
ACAN	ACTCTGGGTTTTCGTGACTCT	ACACTCAGCGAGTTGTCATGG
Collagen I	GAGGGCCAAGACGAAGACATC	CAGATCACGTCATCGCACAAC
MMP3	AGTCTTCCAATCCTACTGTTGCT	TCCCCGTCACCTCCAATCC
MMP13	ACTGAGAGGCTCCGAGAAATG	GAACCCCGCATCTTGGCTT
TIMP-3	CATGTGCAGTACATCCATACGG	CATCATAGACGCGACCTGTCA
TIMP4	CACTACCATCTGAACTGTGGCTG	GCTTTCGTTCCAACAGCCAGTC
SOD1	GGTGGGCCAAAGGATGAAGAG	CCACAAGCCAAACGACTTCC
CAT	TGGAGCTGGTAACCCAGTAGG	CCTTTGCCTTGGAGTATTTGGTA
GPX1	CAGTCGGTGTATGCCTTCTCG	GAGGGACGCCACATTCTCG
GAPDH	ACAACTTTGGTATCGTGGAAGG	GCCATCACGCCACAGTTTC

were analyzed by using the Student's *t*-test. Comparison between multiple groups was done using a One-way ANOVA test followed by Post Hoc Test (Least Significant Difference). P-value<0.05 to show statistical significance.

RESULTS

High CTS disrupted the ECM of CHs

To determine the effects of CTS on the ECM

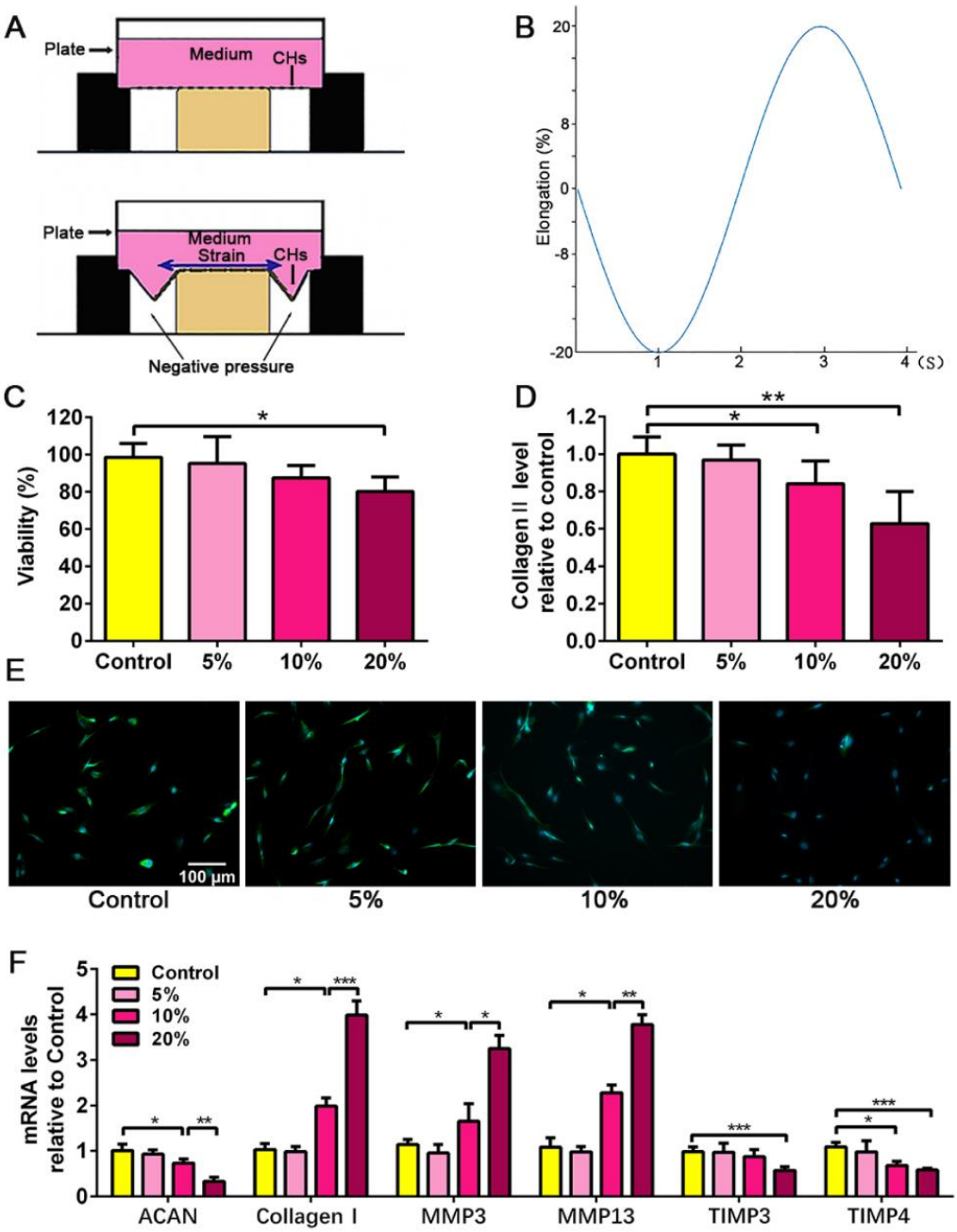


Fig. 1. *High CTS disrupted the ECM of CHs. CHs (1.5×10^4 cells per well) were subjected to the continual cyclical stretch plate for 6 hours. The cells seeded on the plate withaout stretch were defined as Control.* ***A)*** *Schematic diagram of the CH cyclical stretching model. The flexible plate was placed on the Flexcell tension station. Computer-controlled vacuum applied negative pressure under the flexible plate bottom to produce equibiaxial cyclic strain to CHs attached to the plate.* ***B)*** *The cyclical stretching protocol is a sinusoidal wave with a frequency of 0.4 Hz and an amplitude of 5%, 10%, or 20% elongation over 6 h.* ***C)*** *CASY Cell Counter of CH viability.* ***D)*** *Quantification analysis of (****E****) representative images of collagen II IF staining (magnification: 200×).* ***F)*** *RT-PCR analysis of relative mRNA expression. (*P<0.05, **P<0.01, ***P<0.001)*

synthesis of CHs, the CHs were subjected to the continual cyclical stretch plate (Fig. 1A) for 6 hours. During CTS, the bottom membrane of the plate was deformed by the negative pressure to stretch CHs with a sinusoidal wave and a frequency of 0.25 Hz. Three different elongations (5%, 10%, and 20%) were applied to stretch the CHs (Fig. 1B). After 6-h stretching, the CHs on the Bioflex plate were collected with trypsin, and the living cell ratio was measured to uncover the effect of CTS on cell viability. Compared to the control without stretch, the rate of living cells only significantly decreased under the 20% elongation, indicating CTS of 5**%** or 10% did not affect the cell viability, but 20% CTS did (Fig. 1C). As is known, collagen II is the most functional component in ECM synthesized by CHs. After CTS, the expression of collagen II was reduced when the elongation rose to 10% and 20% compared to the control. However, no significant difference was observed between 10% and 20% (Fig. 1D and 1E). In addition to these, the RNA expressions of ACAN, collagen I, catabolic enzymes, and anti-catabolic enzymes during the metabolism of ECM were also analyzed. The result showed that 10% elongation was sufficient to suppress the ACAN and ADAMTS5 expression, but promoted collagen

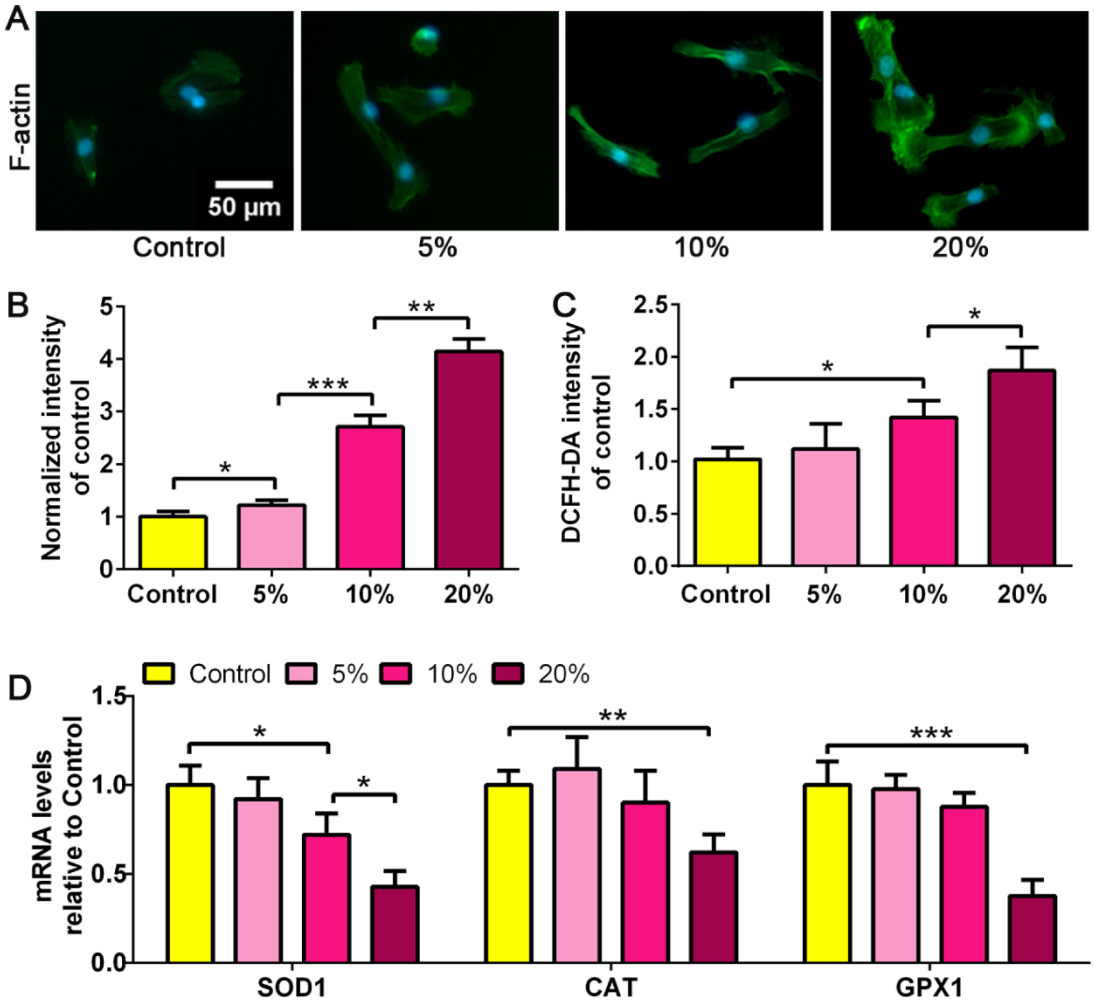


Fig. 2. *High CTS promoted F-actin polymerization and ROS production. CHs (1.5×10^4 cells per well) were subjected to the continual cyclical stretch plate for 6 hours. The cells seeded on the plate without stretch was defined as Control.* ***A****) Representative images of F-actin staining (magnification: 400×) and (****B****) normalized intensity analysis.* ***C****) Flow cytometry of ROS assay.* ***D****) RT-PCR analysis of relative mRNA expression. (*P<0.05, **P<0.01, ***P<0.001)*

I, MMP3, and MMP13 expression, which was more significant under 20% elongation (Fig. 1F).

High CTS promoted F-actin polymerization and ROS production

F-actin density, the DCFH-DA level, and some anti-oxidative enzyme expression were measured to determine how the cytoskeleton and the ROS changed under CST. As shown in Fig. 2 A. B, the density of F-actin was upregulated resulting from the CST, which meant the cytoskeleton of the CHs polymerized after stretching. The polymerization of F-actin was significant even when the elongation was 5%. Furthermore, the ROS production increased starting from the 10% elongation, and its amount was higher under 20% elongation compared to 10% (Fig. 2C). The ROS level was dependent mainly on the balance of the oxidant production and anti-oxidative process. The mRNA expression of SOD1, CAT, and GPX1 was inhibited after high CTS treatment (Fig. 2D).

NAC and cytochalasin D could suppress CTS induced ROS production and F-actin polymerization

Additionally, a widely used antioxidant NAC (Selleck, Houston, TX, USA) and a permeable and potent inhibitor of actin polymerization

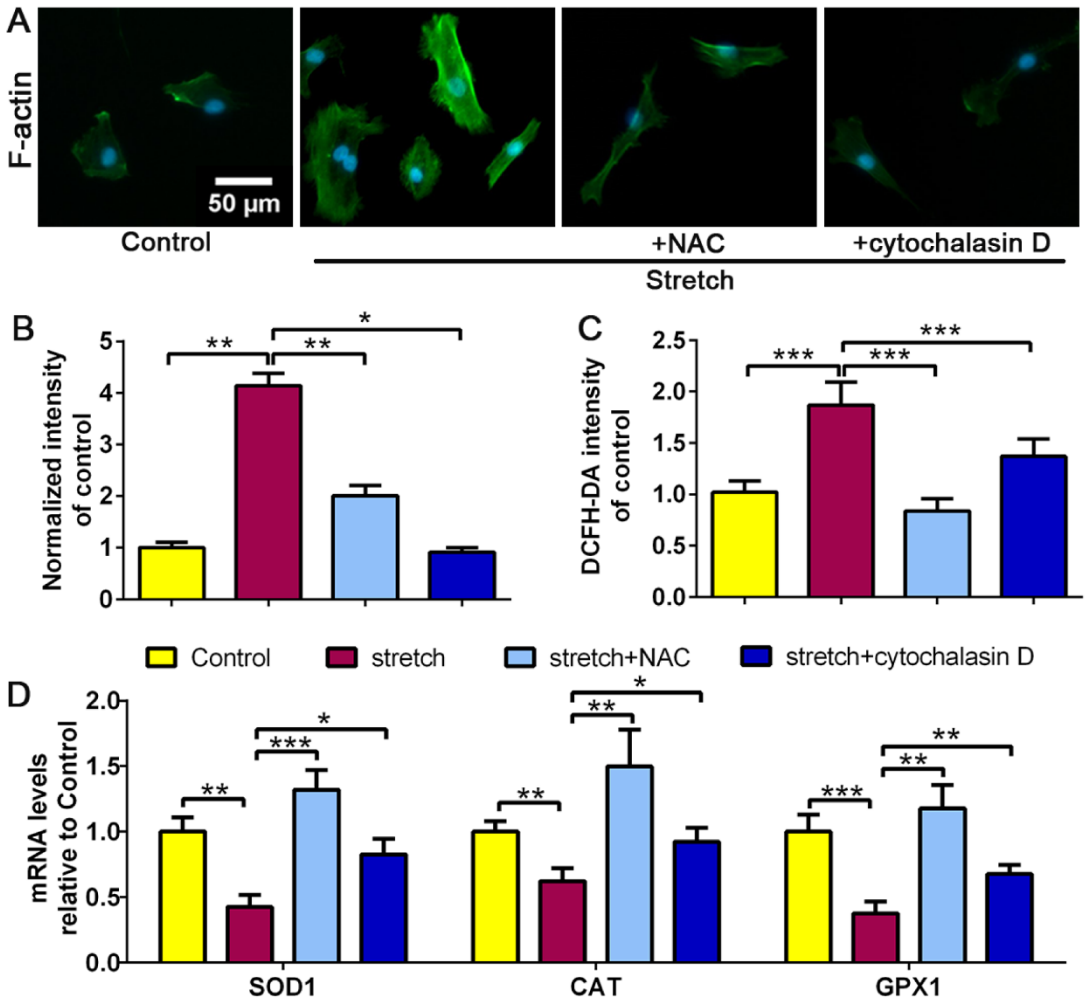


Fig. 3. *NAC and cytochalasin D could suppress CTS induced ROS production and F-actin polymerization. CHs (1.5×10^4 cells per well) were stimulated with NAC (5 mM) or cytochalasin D (2 μM) while stretched under the 20%-elongation for 6 hours.* ***A****) Representative images of F-actin staining (magnification: 400×) and (****B****) normalized intensity analysis.* ***C****) Flow cytometry of ROS assay.* ***D****) RT-PCR analysis of relative mRNA expression. (*P<0.05, **P<0.01, ***P<0.001)*

called cytochalasin D were applied to reverse the ROS activation and cytoskeleton polymerization, respectively. CHs were stimulated with NAC (5 mM) or cytochalasin D (2 μM) while stretched under the 20%-elongation for 6 h (15, 16). The CHs on the Bioflex plate without stretch and drug treatment were grouped as control. As described above, the F-actin was polymerized after stretch compared to the control. However, the NAC treatment was efficient in altering the F-actin polymerization. The cytoskeleton was also disrupted due to the stimulation of cytochalasin D compared to the non-cytochalasin D treated group (Fig. 3 A, B). A highly decreased ROS level was noticed after NAC incubation, and the cytochalasin D also suppressed the ROS during the 20% CTS (Fig. 3C). The mRNA expressions of SOD1, CAT, and GPX1 were also measured, and found to be highly upregulated under NAC treatment and partly protected by cytochalasin D (Fig. 3D). Thus, antioxidant supplements not only inhibited the ROS accumulation, but also alleviated the F-actin polymerization, and the cytochalasin D could also protect the anti-oxidative enzymes and suppress the ROS accumulation.

NAC and cytochalasin D contributed to ECM stability of CHs

Finally, the effects of NAC and cytochalasin D on the viability and ECM stability of CHs were tested. CHs were treated with NAC (5 mM) or

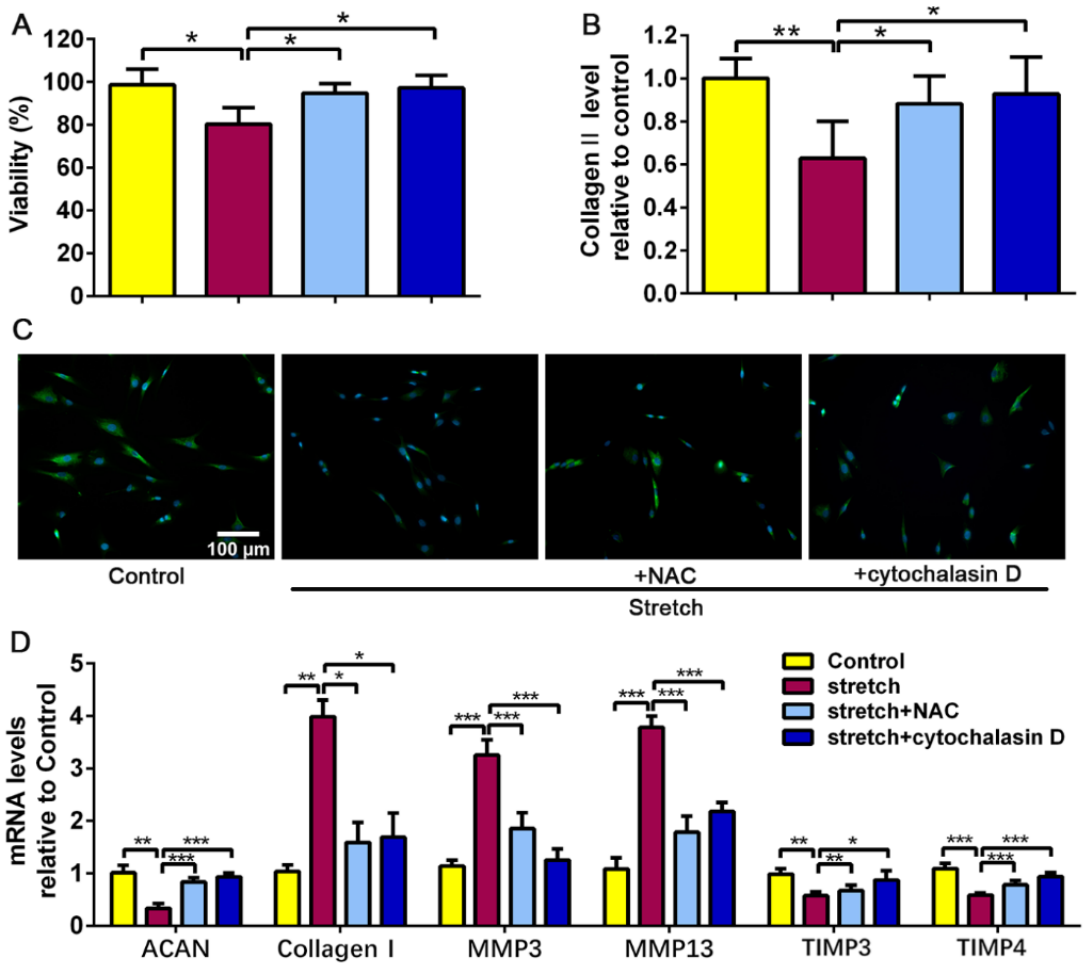


Fig. 4. *NAC and cytochalasin D contributed to the ECM stability of CHs. CHs (1.5×10^4 cells per well) were stimulated with NAC (5 mM) or cytochalasin D (2 μM) while stretched under the 20%-elongation for 6 hours.* ***A****) CASY Cell Counter of CHs viability.* ***B****) Quantification analysis of (****C****) representative images of collagen II IF staining (magnification: 200×).* ***D****) RT-PCR analysis of relative mRNA expression. (*P<0.05, **P<0.01, ***P<0.001)*

cytochalasin D (2 μM) while stretched under the 20%-elongation for 6 h. As shown in Fig. 4A, both NAC and cytochalasin D played a protective role in the CHs viability. Additionally, the application of NAC or cytochalasin D rescued the collagen II expression compared to the CHs stretched without drug treatment (Fig. 4 B, C). The mRNA levels of ACAN, ADAMTS4, and ADAMTS5 under the stimulation of NAC or cytochalasin D were higher than the condition without drug treatment. Furthermore, the collagen I, MMP3, and MMP13 levels were also suppressed due to the presence of NAC and cytochalasin D (Fig. 4D).

DISCUSSION

In this study, the Flexcell system was used to generate negative pressures of different energy through a computer program via stretching the edges of the hydrophilic elastic cell culture membrane. Interestingly, the CST of 5% elongation did not significantly affect CHs viability and ECM stability in the standard culture condition. However, higher CTS (20% elongation, 0.25 Hz, 6 hours) significantly induced CH death, decreased cell viability, and triggered the ROS level, which led to the disordered ECM synthesis. After high CST treatment, the fluorescence of F-actin was enhanced, showing that high CTS could promote the polymerization of CH's cytoskeleton. Meanwhile, the ROS level was enhanced with a reduction of the expression of the anti-oxidative enzymes, which was adverse to CH metabolism. Previous studies have shown CHs cultured in a single layer preferring a differentiated phenotype from spherical to flat. This dedifferentiation progress accompanies elongated cytoskeletal microfilaments, increased F-actin density, decreased collagen II and ACAN expression, and increased collagen I synthesis (17, 18). However, after the addition of cytochalasin D, the dedifferentiated CHs became spherical again. Similarly, the application of cytochalasin D in our study could also destroy the microfilament structure of CHs and reject the high CTS-induced F-actin polymerization, which alleviated the ECM stability. Benya et al. (17) also confirmed that cytochalasin D could enhance the synthesis of collagen II in CHs after cytoskeleton destruction. Furthermore, cytochalasin D in our experiments also showed a function in ROS inhibition, which was the first time noticed in CH metabolism.

Mechanical factors play an essential role in both maintaining the stability of the cartilage environment and causing cartilage damage. Articular CHs experience comprehensive forms of stress, including compressive stress, tensile stress, and shear force. The excess intensity, frequency, and duration of mechanical stimulation lead to disordered CH metabolism, the expression of inflammatory mediators, and the occurrence of apoptosis, which has been confirmed by many studies in the literature. Akagi et al. (19) reported that CST load suppressed bovine CH viability and proteoglycan synthesis. Machida et al. (20) found CTS of 0.5 Hz and 10% elongation could inhibit collagen II and ACAN gene expression by NF-κB activation and MAPK/STAT3 phosphorylation. However, an opposite view held that cyclic stretch powerfully restored the IL-1-induced proteoglycan synthesis reduction in temporomandibular joint CHs by anti-inflammatory stimulus (21). In another study, CST was observed to contribute to the MMP upregulation and ACAN reduction, which are the signals of ECM destruction (22). Articular cartilage is usually under absolute pressure and traction environment in the joint cavity. Appropriate mechanical load is an essential factor in maintaining the integrity of CHs. At the same time, excessive mechanical pressure is also the direct cause of cartilage damage (23, 24).

The cytoskeleton is a channel for the mechanical forces directly transmitting into the cell *in vitro*. The information transmitted by this mechanical signal is extremely fast, and is faster than other methods of communicating information by diffusion of information molecules (25). The microfilament skeleton polymerized by actin subunits is a solid fiber with a diameter of about 4 to 7 nm. There are two forms of cellular actin, including monomeric globules called G-actin and polymeric filaments called F-actin. In the physiological state, the polymerization and depolymerization of F-actin monomers in the cytoskeleton are in a dynamic

equilibrium. The spherical monomers can form a fibrous, highly organized microfilament structure after polymerization (26). Researchers found that the pressure of CHs showed significant changes in the distribution of F-actin, whether normal or OA condition. When the CHs are subjected to excessive mechanical load, it affects the normal remodeling and distribution of the skeleton, leading to a longer time for this remodeling or distribution recovery, and even irreversibility (27). The mechanical integrity of CHs and its influence on downstream activities may be interfered with, to a certain extent, leading to the occurrence of OA (28).

ROS involves the pathological process and contributes to the progress of OA. ROS directly damages CH physiological functions and the typical components of ECM (29). Martin et al. (30) pointed out that CTS can stimulate CHs to produce ROS. The results of this study showed that after 6 hours of 10% CTS on CHs, the expression of ROS increased significantly, suggesting that CTS is an essential cause of reactive oxygen generation. Another example, Yamamoto et al. (31) demonstrated that periodic tensile strain could stimulate osteoblast-like cells HT-3 to produce ROS, and the amount of production was related to the strength of the force, which corresponds to our results. To further confirm the role of ROS in the CTS-induced dysfunction of ECM secretion, NAC was added to eliminate ROS. After cell deacetylation, NAC can generate cysteine-containing reduced sulfhydryl groups to fight the cellular damage of ROS (32). Interestingly, the stimulation of NAC not only decreased the ROS level and upregulated anti-oxidative enzymes after CTS, but also prevented the polymerization of F-actin, helping the stability of ECM. During the treatment of NAC or cytochalasin D, the ECM's decomposing enzyme MMP3/13 was inhibited, and anti-decomposing enzymes TIMP3/4 were up-regulated, which are all necessary for retaining a stable ECM.

In conclusion, our study reveals a novel insight into the disrupted effect of CTS on CH viability and ECM integrity, which is associated with the F-actin cytoskeletal polymerization and ROS production. NAC and cytochalasin D can cooperate to reverse the CTS-induced F-actin polymerization, ROS accumulation, and ECM disorder. These findings provide new ideas for clarifying the role of CTS in the pathogenesis of OA. CHs are cells that can respond sensitively to mechanical stress, but the correlation of their signaling pathways needs to be further explored.

REFERENCES

1. Hunter DJ, Bierma-Zeinstra S. Osteoarthritis. Lancet 2019; 393:1745-59.
2. Guilak F, Nims RJ, Dicks A, Wu CL, Meulenbelt I. Osteoarthritis as a disease of the cartilage pericellular matrix. Matrix Biol 2018; 71-72:40-50.
3. Courties A, Gualillo O, Berenbaum F, Sellam J. Metabolic stress-induced joint inflammation and osteoarthritis. Osteoarthritis Cartilage 2015; 23:1955-65.
4. Moody HR, Afara IO, Singh S, Oloyede A. Potential enhancement of articular cartilage histological grading with collagen integrity. Clin Biomech (Bristol, Avon) 2018; 56:1-10.
5. Vanden BW. Mandibular Cartilage Collagen Network Nanostructure: Insights for Regeneration. Cartilage 2016; 7:274-83.
6. Wang QG, Nguyen B, Thomas CR, Zhang Z, El HA, Kuiper NJ. Molecular profiling of single cells in response to mechanical force: comparison of chondrocytes, chondrons and encapsulated chondrocytes. Biomaterials 2010; 31:1619-25.
7. Dowling EP, Ronan W, McGarry JP. Computational investigation of in situ chondrocyte deformation and actin cytoskeleton remodelling under physiological loading. Acta Biomater 2013; 9:5943-55.
8. Smith RL, Carter DR, Schurman DJ. Pressure and shear differentially alter human articular chondrocyte metabolism: a review. Clin Orthop Relat Res 2004:S89-S95.
9. Gassner R, Buckley MJ, Georgescu H, et al. Cyclic tensile stress exerts antiinflammatory actions on chondrocytes by inhibiting inducible nitric oxide synthase. J Immunol 1999; 163:2187-92.
10. Matsukawa F. Biochemical analysis of extracellular matrix in bovine periodontal ligament. J Osaka Dent Univ 1994; 28:45-55.
11. Madhavan S, Anghelina M, Rath-Deschner B, et al. Biomechanical signals exert sustained attenuation

of proinflammatory gene induction in articular chondrocytes. Osteoarthritis Cartilage 2006; 14:1023-32.
12. Woods A, Wang G, Beier F. Regulation of chondrocyte differentiation by the actin cytoskeleton and adhesive interactions. J Cell Physiol 2007; 213:1-8.
13. Langelier E, Suetterlin R, Hoemann CD, Aebi U, Buschmann MD. The chondrocyte cytoskeleton in mature articular cartilage: structure and distribution of actin, tubulin, and vimentin filaments. J Histochem Cytochem 2000; 48:1307-20.
14. Yuan X, Lin Z, Luo S, Ji G, Yuan C, Wu Y. Effects of different magnitudes of cyclic stretch on Na+-K+-ATPase in skeletal muscle cells in vitro. J Cell Physiol 2007; 212:509-18.
15. Zhang X, Wang YN, Zhu JJ, et al. N-acetylcysteine negatively regulates Notch3 and its malignant signaling. Oncotarget 2016; 24:30855-66.
16. Gold S, Monaghan P, Mertens P, Jackson T. A clathrin independent macropinocytosis-like entry mechanism used by bluetongue virus-1 during infection of BHK cells. PLoS One 2010; 29:e11360.
17. Ingber DE. Tensegrity II. How structural networks influence cellular information processing networks. J Cell Sci 2003; 116:1397-408.
18. Ono S. Mechanism of depolymerization and severing of actin filaments and its significance in cytoskeletal dynamics. Int Rev Cytol 2007; 258:1-82.
19. Akagi M, Nishimura S, Yoshida K, et al. Cyclic tensile stretch load and oxidized low density lipoprotein synergistically induce lectin-like oxidized ldl receptor-1 in cultured bovine chondrocytes, resulting in decreased cell viability and proteoglycan synthesis. J Orthop Res 2006; 24:1782-90.
20. Machida T, Ohta M, Onoguchi A, et al. 5-Hydroxytryptamine induces cyclooxygenase-2 in rat vascular smooth muscle cells: Mechanisms involving Src, PKC and MAPK activation [corrected]. Eur J Pharmacol 2011; 656:19-26.
21. Gassner RJ, Buckley MJ, Studer RK, Evans CH, Agarwal S. Interaction of strain and interleukin-1 in articular cartilage: effects on proteoglycan synthesis in chondrocytes. Int J Oral Maxillofac Surg 2000; 29:389-94.
22. Tetsunaga T, Nishida K, Furumatsu T, et al. Regulation of mechanical stress-induced MMP-13 and ADAMTS-5 expression by RUNX-2 transcriptional factor in SW1353 chondrocyte-like cells. Osteoarthritis Cartilage 2011; 19:222-32.
23. Blain EJ. Involvement of the cytoskeletal elements in articular cartilage homeostasis and pathology. Int J Exp Pathol 2009; 90:1-15.
24. Wong M, Carter DR. Articular cartilage functional histomorphology and mechanobiology: a research perspective. Bone 2003; 33:1-13.
25. Stachowiak MR, Smith MA, Blankman E, et al. A mechanical-biochemical feedback loop regulates remodeling in the actin cytoskeleton. Proc Natl Acad Sci U S A 2014; 111:17528-33.
26. Fioravanti A, Benetti D, Coppola G, Collodel G. Effect of continuous high hydrostatic pressure on the morphology and cytoskeleton of normal and osteoarthritic human chondrocytes cultivated in alginate gels. Clin Exp Rheumatol 2005; 23:847-53.
27. Benya PD, Shaffer JD. Dedifferentiated chondrocytes reexpress the differentiated collagen phenotype when cultured in agarose gels. Cell 1982; 30:215-24.
28. Brown PD, Benya PD. Alterations in chondrocyte cytoskeletal architecture during phenotypic modulation by retinoic acid and dihydrocytochalasin B-induced reexpression. J Cell Biol 1988; 106:171-9.
29. Haklar U, Yuksel M, Velioglu A, Turkmen M, Haklar G, Yalcin AS. Oxygen radicals and nitric oxide levels in chondral or meniscal lesions or both. Clin Orthop Relat Res 2002:135-42.
30. Martin JA, Buckwalter JA. Aging, articular cartilage chondrocyte senescence and osteoarthritis. Biogerontology 2002; 3:257-64.
31. Yamamoto N, Fukuda K, Matsushita T, Matsukawa M, Hara F, Hamanishi C. Cyclic tensile stretch stimulates the release of reactive oxygen species from osteoblast-like cells. Calcif Tissue Int 2005; 76:433-8.
32. Kim RJ, Kang JR, Hah YS, Park HB. N-acetyl cysteine protects cells from chondrocyte death induced by local anesthetics. J Orthop Res 2017; 35:297-303.

Establishment of an immune-related gene prognostic model for head and neck tumors

F. Zhou[#], AX. Chen[#], HY. Lv, DH. Liang and HS. Yu[*]

Department of Radiation Oncology, The Affiliated Hospital of Qingdao University, Qingdao, Shandong, China

Received January 14, 2021 – Accepted May 28, 2021

[#]Co-first authors

This study aimed to screen the key immune-related genes (IRGs) in head and neck squamous cell carcinoma (HNSC) and construct the IRGs-related prognostic model to predict the overall survival (OS) of patients with HNSC. The RNA-seq data and clinical data were downloaded from The Cancer Genome Atlas database, and IRGs were obtained from the Immunology Database and Analysis Portal. Differentially expressed genes (DEGs) between HNSC and normal samples were identified, followed by integration with IRGs to screen differentially expressed IRGs. After univariate and multivariate proportional hazard regression analyses, an IRG-based risk model was constructed. Meanwhile, data chip of GSE65858 as the validation set to assess the predicted performance of established model. Next, univariate and multivariate Cox regression analyses were performed to identify the independent prognostic factor of HNSC, and the Nomogram model was developed to predict patient outcome. Furthermore, the correlation between immune cell infiltration and risk score was analyzed. A total of 65 differently expressed IRGs associated with prognosis of HNSC were screened, and finally a 26-gene IRG signature was identified to construct a prognostic prediction model. The AUC of ROC curve was 0.750. Survival analysis showed that patients in the high-risk group had a worse prognosis. Independent prognostic analysis showed that risk score could be considered as an independent predictor for HNSC prognosis. Nomogram assessment showed that the model had high reliability for predicting the survival of patients with HNSC in 1, 2, 3 years. Ultimately, the abundance of B cells and CD4+ T cell infiltration in HNSC showed negative correlations with risk score. Our IRG-based prognostic risk model may be used to estimate the prognosis of HNSC patients.

The sixth most severe malignancy in the world is head and neck squamous cell carcinoma (HNSC), which contains heterogeneous squamous epithelial neoplasms originating from the oropharynx, oral cavity, hypopharynx, and larynx (1). There were nearly 700,000 new cases of HNSC reported in 2018. It has a high mortality rate of approximately 50% according to global cancer statistics (2). The treatment for HNSC mainly consists of surgery, radiation, and concurrent cisplatin chemotherapy (3). Improved therapies are required for patients with locally advanced disease, recurrence, and metastasis. Recently, targeted therapy and immunotherapy have also been applied in the treatment of HNSC (4). For example, cetuximab, an epidermal growth factor receptor (EGFR)-targeted monoclonal antibody, is

Key words: immune-related genes, immunotherapy, prognostic risk model, Cox regression, HNSC, high-risk genes

**Corresponding Author:*
Hongsheng Yu,
Department of Radiation Oncology,
The Affiliated Hospital of Qingdao University,
No. 16 Jiangsu Rd., Qingdao 266000,
Shandong, China
Tel./Fax: +86 139 6978 6862
e-mail: qdhsyu@126.com

0393-974X (2021)
Copyright © by BIOLIFE, s.a.s.
This publication and/or article is for individual use only and may not be further reproduced without written permission from the copyright holder.
Unauthorized reproduction may result in financial and other penalties
DISCLOSURE: ALL AUTHORS REPORT NO CONFLICTS OF INTEREST RELEVANT TO THIS ARTICLE.

the first FDA-approved targeted therapy for HNSC. However, the application of cetuximab led to an increase in the survival rate by only 2.7 months and a reduction in the relative death risk to 20% (5). Minimal survival benefits from targeted therapy result in more attention on immunotherapy.

Interest in cancer immunotherapy is currently on the rise due to recent clinical successes in immune checkpoint therapy. Immunotherapy with checkpoint inhibition has rapidly become a common therapy for many cancers. Programmed death-ligand 1 (PD-L1) and its receptor PD-1 axis have been shown to have therapeutic value in a wide range of malignancies. Previous studies have reported that anti-PD-1 therapy for advanced HNSC patients achieved significant results (6-9). However, a minority of patients benefit from these agents due to therapy resistance, primarily caused by various tumor cell intrinsic factors (10). The tumor microenvironment (TME) consists of not only malignant cells, but also of a large number of non-malignant cells and the extracellular matrix. Immune cells play crucial roles in protecting non-malignant cells. Various immune cells with different densities located in diverse areas of the tumors may help predict patient prognosis and treatment outcomes (11). Based on a retrospective study, Schneider et al. showed that elevated CD4+ T-lymphocyte infiltration in HNSC patients indicated better treatment outcome, suggesting correlations between immune cell infiltration and prognosis (12). In addition, immune-related genes (IRGs) have been found to be associated with HNSC prognosis (13). Chen et al. demonstrated that elevated levels of intratumoral CXCR5 were correlated with favorable HNSC prognosis, and CXCR5-positive cell infiltration could serve as an independent prognostic factor (14). Gene signatures that comprise different IRGs contribute to the stratification of HNSC patients with different phenotypes, and they affect the prognoses of HNSCs (13, 15).

Accurate prognosis is useful in helping make healthcare decisions for patients with tumors, and recent studies have shown that models are available to predict prognosis (16, 17). In this study, IRGs and clinical information were combined to investigate the potential clinical application of IRGs in the prognostic stratification of HNSC using bioinformatics analysis. An IRG-based prognostic risk model was established, which was demonstrated to have better predictive performance for prognosis in HNSC patients. Our findings present potential targets for immunotherapy in HNSC, and the established risk model may contribute to predicting HNSC patient heterogeneity and prognosis.

MATERIALS AND METHODS

Data acquisition

The RNA-sequencing data and matched clinical data were downloaded from The Cancer Genome Atlas (TCGA) database in December 2019. A total of 44 normal and 501 HNSC samples were included. In addition, IRGs related to HNSC were extracted from the Immunology Database and Analysis Portal database and the immune infiltration data of HNSC patients were procured from the Tumor Immune Estimation Resource.

Screening of differentially expressed IRGs

The Wilcoxon signed-rank test of the Limma package in R was used to analyze the differential expression of genes in HNSC compared to normal ones, and differentially expressed genes (DEGs) were screened with a false discovery rate (FDR) < 0.05 and |log2 fold change (FC)| > 1 as threshold value. Next, the DEGs were integrated with IRGs to obtain the differentially expressed IRGs.

Identification of prognostic-related differentially expressed IRGs

In order to investigate the prognostic value of differentially expressed IRGs, a univariate Cox proportional hazards regression was performed. The overall survival (OS) of each patient was downloaded from the TCGA database, and patients with an OS < 90 days were removed. HR = 1 was set to the cutoff value and genes with $p < 0.05$ were considered as survival-related IRGs. In brief, a gene with HR less than 1 was defined as low-risk gene, and HR more than 1 as a high-risk gene.

Construction of transcription factors (TFs) regulatory network

The Cistrome Data Browser is a public resource that provides information on human and mouse cis-regulations

derived from chromatin propagation analyses of ChIP-seq, DNase-seq, and ATAC-seq. In this study, TFs were downloaded from the Cistrome Data Browser using the Cancer Transcription Factor Targets option. Next, the differential TFs between HNSC and normal samples were screened. In addition, the correlation between differential TF and survival-related IRGs was calculated and the pairs with $|r| > 4$ and $p < 0.01$ were selected. These pairs were visualized by using Cytoscape software (version 3.7.2).

Construction and validation of Cox regression risks model

Based on the survival-related IRGs, multivariate Cox proportional hazards regression was performed to further screen genes that were highly associated with prognosis of HNSC. Genes with $p < 0.05$ were selected for constructing prognostic model. Subsequently, the risk score of this model was evaluated using following formula: Risk score (patient) = $\sum_{i=1}^{n} \mathbf{M}$ where M represents the estimated regression coefficient of the *i*th IRG selected in the multivariate Cox proportional hazards regression analysis.

According to the median value of risk scores, we categorized all patients into high- and low-risk groups. Survival analysis was performed by using the survival package in R to compare the differences in OS rate between the low- and high-risk groups. The IRG-based model was tested using a time-dependent ROC analysis and the ROC curve was plotted using the survival ROC package in R. Model with an area under the ROC curve (AUC) > 0.60 was appropriate for prediction and an AUC > 0.75 was considered to be an outstanding predictive value (18, 19). Next, to evaluable the repeatability and predictive performance of the prognostic model, an independent dataset was selected for validation. After screening the GEO database, only one dataset with number GSE65858 meeting our requirement was identified for subsequent analyses. GSE65858 contained 270 HNSC samples and was analyzed on the GPL10558Illumina HumanHT-12 V4.0 expression beadchip platform. Thus, data from TCGA were used as training set and from GEO were used as validation set. According to the coefficient of each gene obtained from training set, the risk score of patients was calculated in validation set using the same equation, and then classified all patients into high- and low-risk groups based on the median of risk score. Furthermore, the K-M survival curve was plotted to determine the difference between the high- and low-risk groups.

In addition, the univariate and multivariate Cox regression models were used to assess whether risk score could be an independent prognostic factor for HNSC compared to other clinical factors (age, gender, grade, stage, and TMN stage). A factor with $p < 0.05$ was considered as an independent predictor. Based on all independent predictors determined in the multivariate Cox regression analysis, a nomogram model was constructed to predict the 1-, 2-, and 3-year survival probability of HNSC patients. The concordance index was calculated to assess the predictive accuracy of the established nomogram.

Correlation analysis of tumor immune infiltration and risk score

TIMER is an online tool used to analyze tumor-infiltrating immune cells (20). The tumor-infiltrating immune cells in HNSC were investigated using TIMER to estimate the infiltrating abundance of six immune cell types, including neutrophils, dendritic cells, macrophages, B cells, CD8+ T cells, and CD4+ T cells. Based on the IRG-related prognostic model, the correlations between immune cell infiltration and risk score were calculated using the Spearman correlation test.

RESULTS

Differentially expressed IRGs between HNSC and normal samples

After differential expression analysis of 17,788 genes in 44 normal and 501 HNSC samples from the TCGA dataset, a total of 4,784 DEGs were screened with FDR < 0.05 and |log2 FC| > 1, including 1,181 downregulated and 3,603 upregulated genes (Fig. 1 A, B). Then, DEGs and IRGs were integrated, 399 overlapping genes were obtained and considered as differentially expressed IRGs, including 304 upregulated and 95 downregulated IRGs (Fig. 1 C, D). These genes clearly distinguish the disease group from the control group.

Identification of prognosis-related IRGs

Prognosis is essential for clinical management and appropriate decision-making for patients. A univariate Cox proportional hazards model was used to screen the prognostic value of these differential IRGs. Ultimately, 65 IRGs were found to have an

apparent association with the OS of HNSC patients (P <0.05). Forest plots of hazard ratios showed the potential risk for 65 prognosis-related IRGs, of which, 23 IRGs were screened as high-risk genes (HR > 1) and 42 IRGs (HR < 1) were identified as low-risk genes (Fig. 2).

Construction of TF regulatory network

We attained 318 TFs from the Cistrome Data Browser, of which 63 were differentially expressed, including 46 upregulated and 17 downregulated TFs (Fig. 3 A, B). TFs are critical drivers that control gene expression levels, therefore, the correlations between differentially expressed TFs and prognosis-related IRGs were analyzed. A total of 28 TFs showed correlations with 38 prognosis-related IRGs and the TFs-IRG regulatory network is displayed in Fig. 3C. Result indicated that TF FOXP3 was correlated with more prognosis-related IRGs, such as PDCD1, CXCR3, and CCR8, suggesting that FOXP3 might be an important TF. Meanwhile, multiple TFs were correlated with the same IRG NR3C2, indicating that NR3C2 might be a key regulatory target. We also observed that TF ETS1 was interacted with PDGFRB.

Prognostic risk model construction and verification

In the univariate Cox proportional hazards model, 65 IRGs were found to have a significantly independent effect on the OS of HNSC patients. Next, a multivariate Cox proportional hazards analysis was performed to select IRGs that were

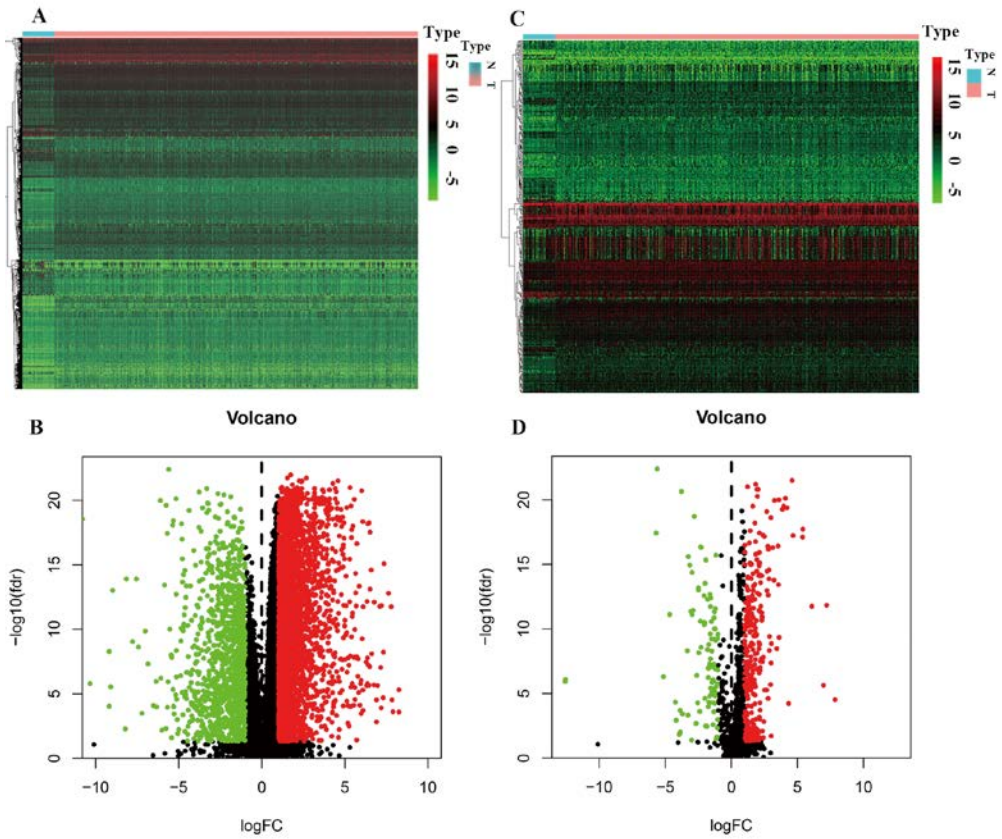


Fig. 1. *Comparison of gene expression profiles between HNSC and normal tissues. Heatmap (**A**) and volcano plot (**B**) of DEGs between two groups. Heatmap (**C**) and volcano plot (**D**) of differentially expressed IRGs between HNSC and normal. The green and red dots represent downregulated and upregulated DEGs or IRGs, respectively. Black dots represent genes or IRGs with no statistical significance.*

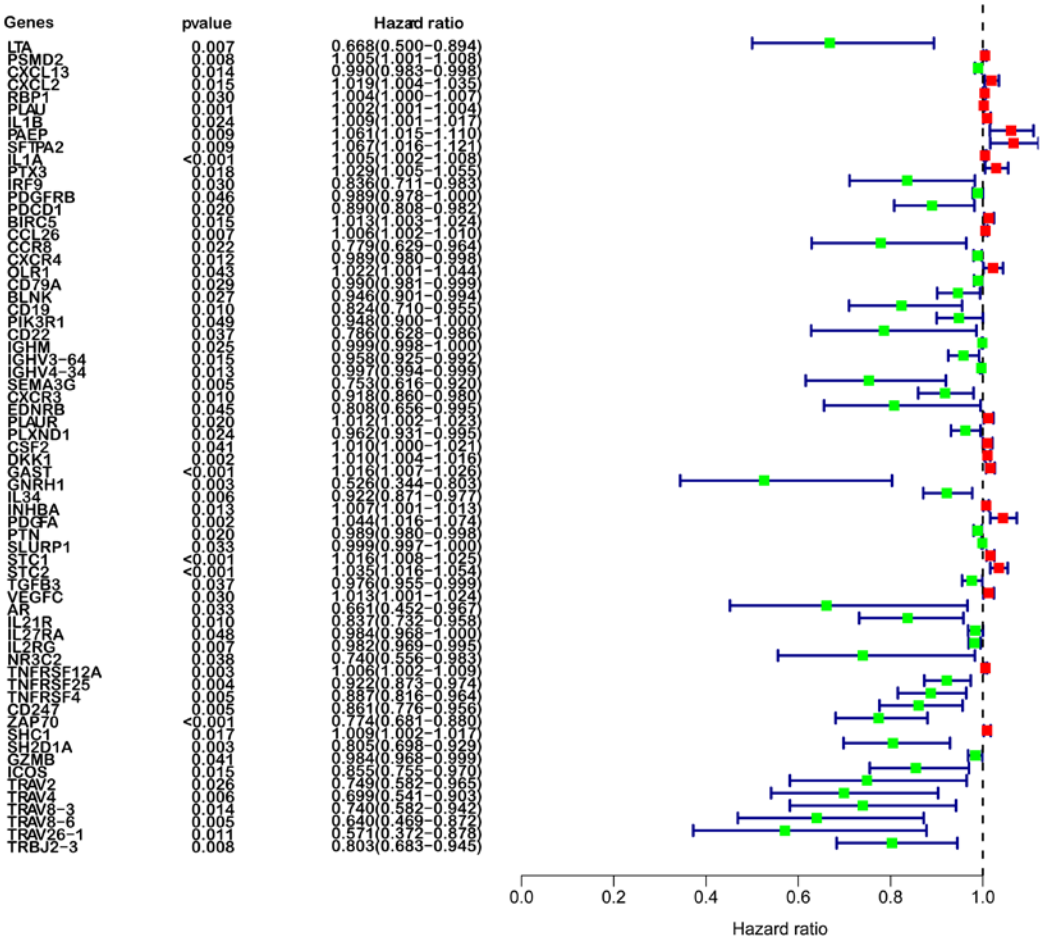


Fig. 2. *Forest plot of the Cox proportional hazards showing the prognostic-related IRGs. p value < 0.05 was considered statistically significant. Green nodes represent genes with low risk (HR < 1) while red nodes represent genes with high risk (HR > 1).*

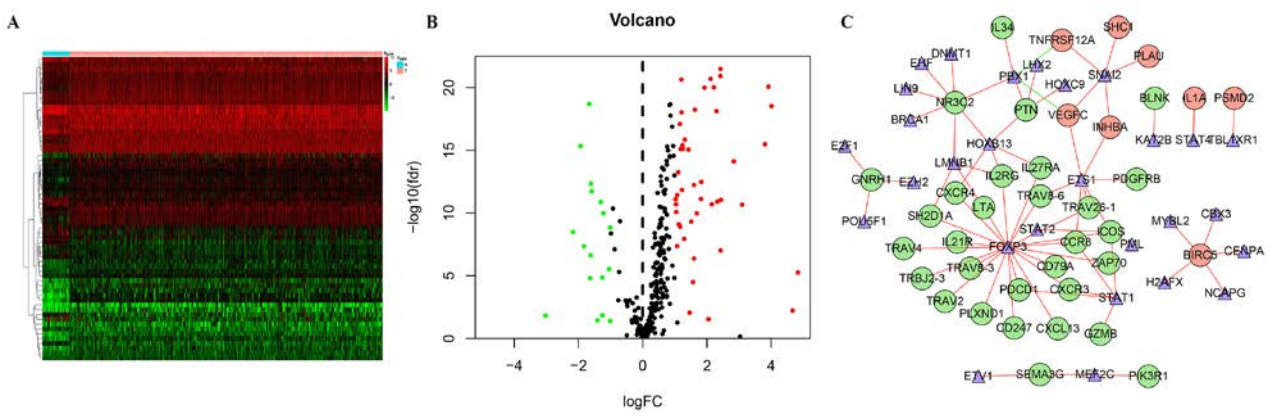


Fig. 3. *TF regulatory network.* ***A)*** *Heatmap of differentially expressed TFs, N: normal, T: tumor. Increasing gene expression is represented by the green to red scale.* ***B)*** *Volcano plot of differentially expressed TFs; the green and red dots represent downregulated and upregulated differentially expressed TFs. The black dots represent TFs with no statistical significance.* ***C)*** *The correlation network of differentially expressed TFs and prognosis-related IRGs. The blue triangle represents TFs, the red circles represent high-risk immune genes, and the green circles represent low-risk immune genes. Red lines indicate a positive regulatory relationship and green lines represent a negatively regulated correlation.*

highly corrected with prognosis of HNSC. Finally, a total of 26 IRGs were obtained to construct the risk model. Based on the expression level of IRGs and the coefficient of multivariate Cox proportional hazards analysis, the risk score was calculated. Next, all sample were divided into high-risk (n = 237) and low-risk (n = 238) groups according to the median risk score. The distribution of risk score and survival states are respectively displayed in Fig. 4 A and 4B. The heatmap showed the gradient changes of the expressions level of the 26 IRGs with risk scores (Fig. 4C). Survival analysis confirmed that patients in the high-risk group showed significantly worse prognosis compared to patients in the low-risk group (Fig. 4D). Meanwhile, a better OS rate was observed after five years for patients in the low-risk group compared to those in the high-risk group (Fig. 4E). Furthermore, ROC curve showed better predictive performance for the prognostic model with an AUC of 0.750 (Fig. 4F). Subsequently, a GEO dataset was used to verify the predicted performance of this model. In the validation set, expression value of four genes was not obtained from the GSE65858, so the remaining 22 genes were utilized to construct a prognostic model. Based on the median value of risk score, 22 genes could distinguish 270 HNSC patients into low- and high-risk groups. K-M survival curve revealed that patients in the high-risk group showed a worse outcome than those in the low-risk group (Fig. 4G), suggesting that these IRGs signature could better predict the prognosis of HNSC patients.

Independent prognostic value of the risk model

To verify whether there was an independent prognostic value for the IRG-based model, the clinical data of patients downloaded from TCGA were analyzed, including gender, pathological stage, age, and histological grade. There were 393 patients with both RNA-seq data and detailed clinical data, 141 and 252 of which were respectively identified as low-risk and high-risk based on risk score. Univariate Cox proportional hazards regression demonstrated that factors including age, pathological stage, N-stage, and risk score had a statistically significant impact on HNSC patient prognosis ($p < 0.05$) (Fig. 5A). Furthermore, N-stage and risk score

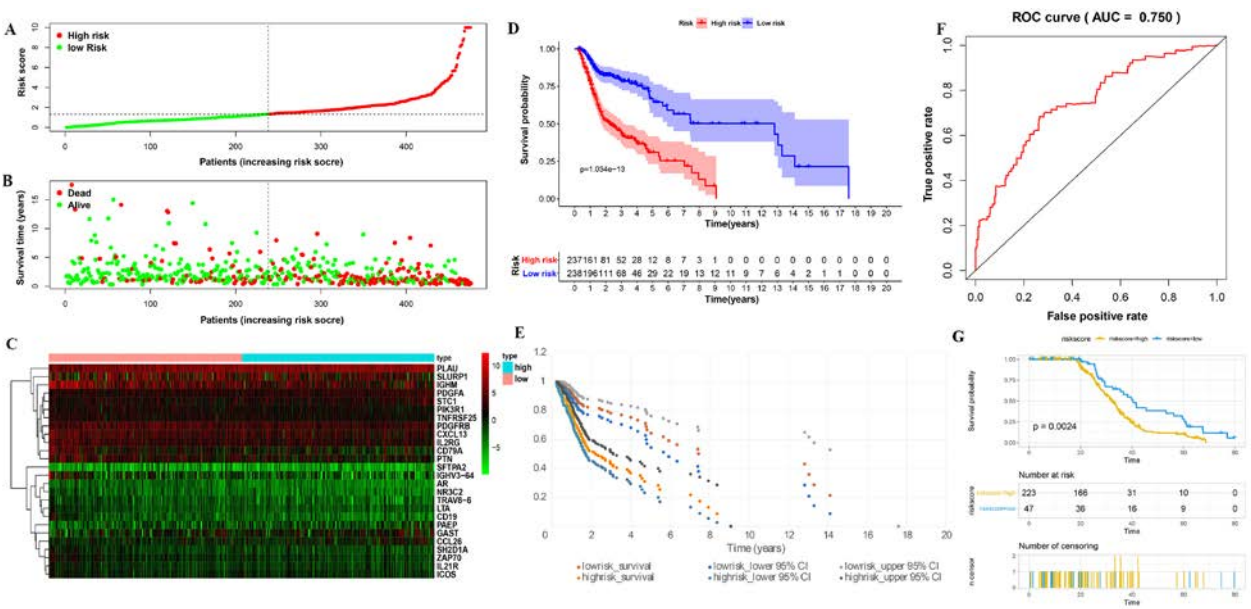


Fig. 4. *Construction of IRG-related prognostic model for HNSC patients. **A**) The distribution of risk score. **B**) The survival status of HNSC patients in high- and low-risk groups. **C**) Heatmap of risk gene expressions in the model. **D**) Kaplan-Meier curve of OS between high- and low-risk groups. **E**) Prognosis analysis for five years of high- and low-risk groups. **F**) Verification of prognostic risk models via a time-dependent ROC curve. **G**) Kaplan–Meier survival curves of overall survival between the high-risk group and low-risk group in the validation data set.*

were identified as independent prognostic factors for the prognosis of HNSC patients in the multivariate Cox regression analysis ($p < 0.05$) (Fig. 5B). These findings indicated that the risk score calculated by IRG-based prognostic model could be utilized to independently predict HNSC patient prognosis.

Moreover, we used the two independent prognostic factors of risk score and T stage to develop the nomogram model (Fig. 6A). For each patient, two lines were drawn up to determine the points. Each factor in the nomogram was assigned a score, and then added the individual scores of all predictors to get the total nomogram score. Combined with the total score, the downward projection of the total score can be used to estimate the 1-, 2-, and 3-year survival. The C-index of the developed nomogram was 0.767; in addition, the calibration plot revealed that the OS probability predicted by nomogram was slightly different from the actual 1-, 2-, and 3-year OS probability (Fig. 6 B-D), especially the 1-year OS probability, suggesting that the nomogram model had good predictive performance and stability.

Correlation analysis of the immune cell and risk score

The correlations between immune cell infiltration and risk score were calculated using the Spearman correlation test, in order to investigate the characteristics of the tumor immune

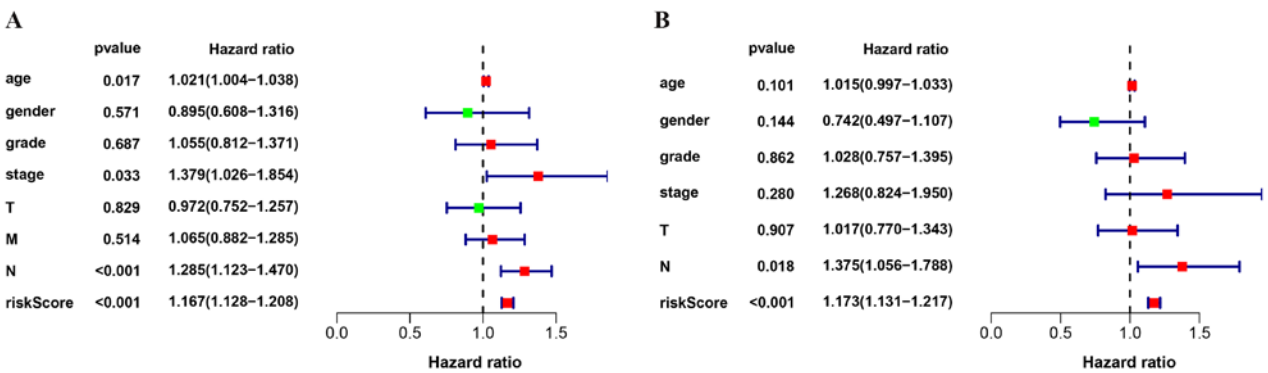


Fig. 5. *Independent prognostic value of the risk model. **A)** Univariate Cox regression analysis. **B)** Multivariate Cox regression analysis. Green nodes represent genes with low risk, while red nodes represent genes with high risk.*

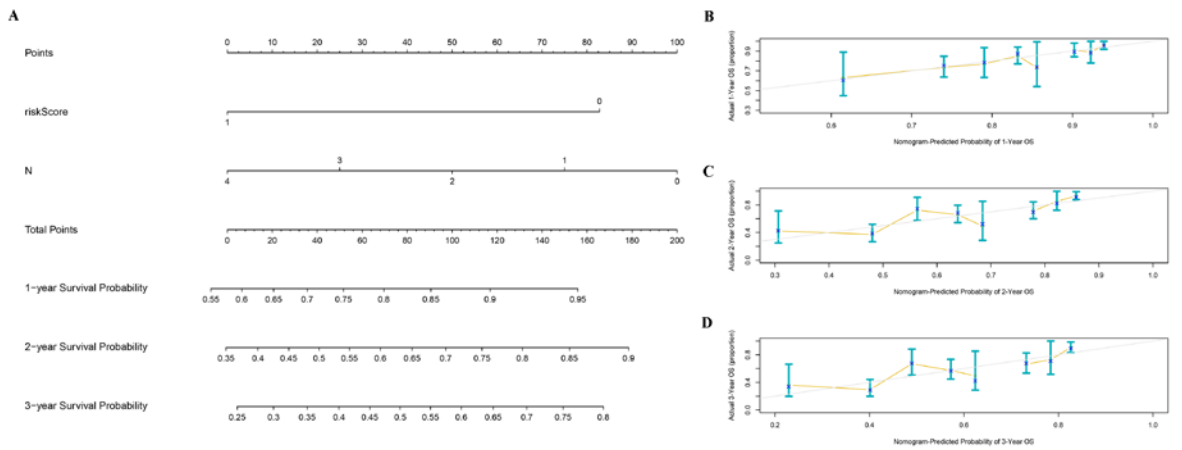


Fig. 6. *Nomogram containing risk score and T stage for predicting HNSC prognosis. **A)** Nomogram to predict the survival probability of 1, 2, and 3 years in HNSC patients. **B)** Calibration curves of the nomogram for the probability of OS at 1 year. **C)** Calibration curves of the nomogram for the probability of OS at 2 years. **D)** Calibration curves of the nomogram for the probability of OS at 3 years.*

microenvironments of HNSC patients. The results showed that there were negative correlations between the risk score and the abundance of B cells (Fig. 7A) and CD4+ T cell infiltration (Fig. 7B).

DISCUSSION

Immunity has been demonstrated to have a significant impact on tumor development and outgrowth, and evading immune control has been considered to be a typical hallmark of tumors (21). IRGs at certain immune checkpoints can be used by tumor cells to escape immune control (22). Chen et al. showed that the IRG prognostic index could be a useful biomarker for distinguishing between immune characteristics and prognosis of HNSC (23). Therefore, the expression of IRGs and their prognostic value in HNSC were investigated in this study. We first identified 399 differentially expressed IRGs, including 304 upregulated and 95 downregulated genes. A total of 65 prognosis-related IRGs were screened, and 26 IRGs were finally identified to be used in the construction of the prognostic model, including PDGFRB, PDGFA, and PLAU. The IRG-based prognostic model revealed a predictive value for the prognosis of HNSC patients. A high-risk score was found to be related to worse prognosis in HNSC patients. In addition, the IRG-based risk model showed correlations among prognosis, tumor stage, and risk score. Ultimately, there were negative correlations between the risk score and the abundance of B cells and CD4+ T cell infiltration in HNSC.

The clinical value of prognostic models has been demonstrated in studies that have contributed to determining healthcare decisions for patients (16, 24). For example, the model established by IRGs and clinical factors could be used to predict the prognosis of HNSC patients with higher predictive performance (25). The 27 IRG-based prognostic gene signatures established by She et al. divided HNSC patients into different immune subtypes and provided an independent predictor of HNSC patient survival (13). The prognostic risk model in our study could consistently and independently predict HNSC patient prognosis.

The platelet-derived growth factor (PDGF)/PDGF receptor (PDGFR) family is crucial for various cellular biological behaviors, including cell proliferation and migration, angiogenesis, and remodeling of extracellular matrix components (26). Their oncogenic alterations have been reported

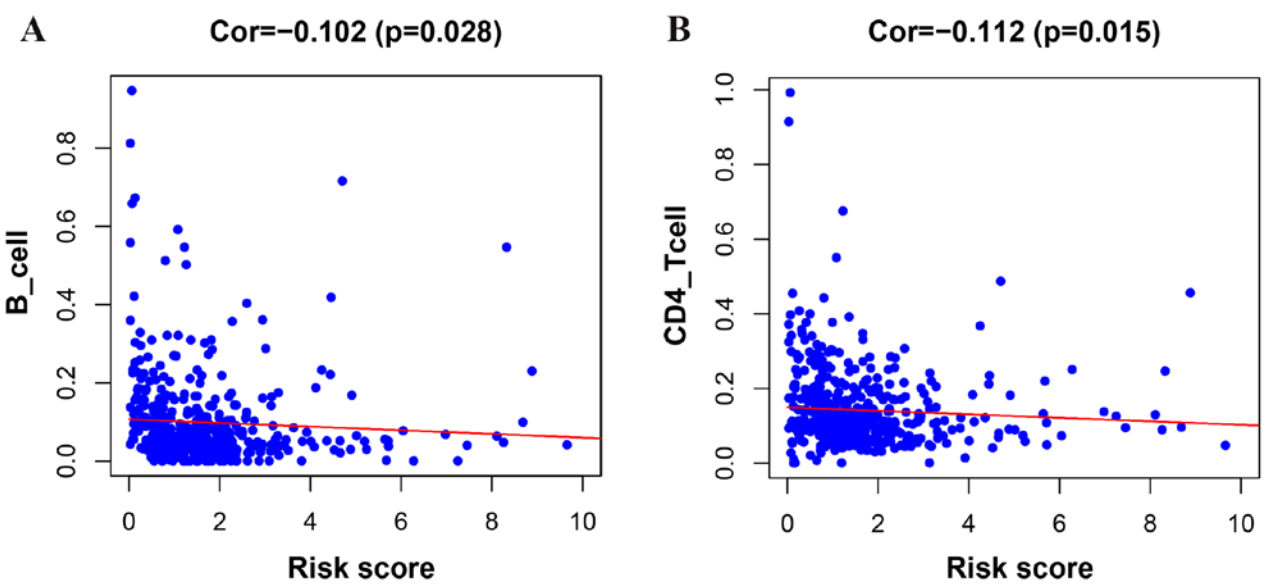


Fig. 7. *Clinical correlation analysis of the prognostic risk model. **A**) Association of the content of B cells and the risk score of the model. **B**) Association of the content of CD4+ T cells and the risk score of the model.*

in various cancers, and more than 10 drugs that interfere with PDGF signaling have been approved in the clinical treatment of several cancers (27, 28). Watts et al. suggested that expression of PDGF-AA in the tumor microenvironment might be correlated with worse prognosis in HNSC patients by mediating the chemotaxis of mesenchymal stromal cells (29). The clinical outcome of HNSC patients could be improved by adding an anti-angiogenic therapy (anti-angiogenic peptides such as PDGF, PDGF-R, and VEGF) in chemotherapy regimens (30). In our study, the TF ETS1 interacted with PDGFRB. Consistent with our results, studies have suggested that EST1 mediates the role of PDGF-induced gene expression (31, 32). For example, Jinnin et al. showed that ETS1 mediated the upregulation of tenascin-C (TN-C) expression by PDGF (33). Yang et al. showed that the abnormal expression of plasminogen activator, urokinase (PLAU) was implicated in the regulation of HNSC initiation and progression. Its expression was also associated with aggressive HNSC, indicating the predictive value of prognosis in HNSC (34). Xu et al. suggested that the two-gene signature consisting of PLAU and SERPINE1 could be independent prognostic factors in HNSC (35).

Local immune activity may play an important role in HNSC and have a positive effect on the response to therapy in HNSC patients (36). Most HNSCs are immune-resistant due to inadequate immune monitoring and the involvement of immunosuppressive mediators in the TME (37). In this study, we found that there were negative correlations between the risk score and the abundance of B cells and CD4+ T cell infiltration in HNSC. Similarly, a previous study demonstrated that tumor T cell infiltration in HNSC was correlated with favorable prognosis, and there was an association between T cell infiltration and improved OS in HNSC (38). Another study also showed that high levels of CD4+ and CD8+ tumor-infiltrating lymphocytes were correlated with improved OS, and tumor-infiltrating lymphocytes were independent prognostic factors in HNSC (39). In addition, it was reported that activated (CD86+), memory, and antigen-presenting (CD86+/CD21-) B cells accounted for the highest percentages of tumor-infiltrating B cells in HNSC (40). Similarly, Hladíková et al. indicated that a high level of tumor-infiltrating B cells indicated a favorable prognosis for patients with oropharyngeal squamous cell carcinoma, a type of HNSC (41).

The current widely-used staging system estimates the risk stratification of HNSC. However, the techniques for assessing high-risk HNSC patients are not currently adequate (42-44). Various algorithms were utilized in this study to develop a risk model showing predictive value for prognosis of HNSC patients by dividing them into high-/low-risk groups. The results identified potential targets for HNSC immunotherapy, and the established risk model may contribute to predict the heterogeneity and prognosis of HNSC patients.

Despite studies having constructed prognostic models for HNSC based on the IRGs, our analysis still has some strengths. Previous studies directly used the IRGs related to the prognosis of HNSC for model construction (13, 45); while in the present analysis, the genes included in the prognostic model were identified from differentially expressed IRGs between HNSC and normal tissues, which could narrow the scope of candidate genes. Moreover, we also established a nomogram model to predict the 1-, 2-, and 3-year survival probability of HNSC patients. In this analysis, 26 IRGs were selected to construct a risk model and these genes provided more novel potential biomarkers for predicting the prognosis of HNSC. However, several limitations should be noted in this analysis. The sample size of HNSC and control was imbalanced, which might affect the selection of DEGs. Furthermore, when predicting whether the risk score could be used as an independent prognostic factor, the clinical information was incomplete, and several key indicators such as HPV status were not considered in this analysis. The specific mechanisms of identified IRGs in the development of HNSC remain unclear. Therefore, in future research, it is necessary to match tumor samples with normal samples when screening for DEGs. In addition, the clinical characteristics of patients need to be considered comprehensively.

In conclusion, a 26-gene IRG signature was identified to construct a prognosis model for HNSC

patients. Patients in the high-risk group had a worse prognosis than those in the low-risk group. Furthermore, we identified negative correlations between the risk score and the abundance of B cells and CD4+ T cell infiltration in HNSC. These IRG genes may become potential prognostic markers and therapeutic targets for patients with HNSC. However, further investigations are required to explore the underlying mechanisms of these IRGs for the prognosis of HNSC.

ACKNOWLEDGEMENTS

This work was supported by the Chinese Society of Clinical Oncology-Program No. Y-HR2018-293, Y-HR2018-294).

We thank The Cancer Genome Atlas, the Cistrome Data Browser, the Immunology Database and Analysis Portal, and the Immune Estimation Resource for sharing large amounts of data.

REFERENCES

1. Solomon B, Young RJ, Rischin D. Head and neck squamous cell carcinoma: Genomics and emerging biomarkers for immunomodulatory cancer treatments. Semin Cancer Biol 2018; 52:228-40.
2. Bray F, Ferlay J, Soerjomataram I, Siegel RL, Torre LA, Jemal A. Global cancer statistics 2018: Globocan estimates of incidence and mortality worldwide for 36 cancers in 185 countries. CA Cancer J Clin 2018; 68:394-424.
3. Colevas AD, Yom SS, Pfister DG, et al. Nccn guidelines insights: Head and neck cancers, version 1.2018. J Natl Compr Canc Netw 2018; 16:479-90
4. Lecerf C, Kamal M, Vacher S, et al. Immune gene expression in head and neck squamous cell carcinoma patients. Eur J Cancer 2019; 121:210-23.
5. Moskovitz J, Moy J, Ferris RL. Immunotherapy for head and neck squamous cell carcinoma. Curr Oncol Rep 2018; 20(2):22.
6. Bauml J, Seiwert TY, Pfister DG, et al. Pembrolizumab for platinum- and cetuximab-refractory head and neck cancer: Results from a single-arm, phase ii study. J Clin Oncol 2017; 35:1542-9.
7. Chow LQM, Haddad R, Gupta S, et al. Antitumor activity of pembrolizumab in biomarker-unselected patients with recurrent and/or metastatic head and neck squamous cell carcinoma: Results from the phase ib keynote-012 expansion cohort. J Clin Oncol 2016; 34:3838-45.
8. Seiwert TY, Burtness B, Mehra R, et al. Safety and clinical activity of pembrolizumab for treatment of recurrent or metastatic squamous cell carcinoma of the head and neck (keynote-012): An open-label, multicentre, phase 1b trial. Lancet Oncol 2016; 17:956-65.
9. Ferris RL, Blumenschein G, Jr., Fayette J, et al. Nivolumab for recurrent squamous-cell carcinoma of the head and neck. N Engl J Med 2016; 375:1856-67.
10. Kalbasi A, Ribas A. Tumour-intrinsic resistance to immune checkpoint blockade. Nat Rev Immunol 2020; 20:25-39.
11. Fridman WH, Pages F, Sautes-Fridman C, Galon J. The immune contexture in human tumours: Impact on clinical outcome. Nat Rev Cancer 2012; 12:298-306.
12. Schneider K, Marbaix E, Bouzin C, Hamoir M, Mahy P, Bol V, Grégoire V. Immune cell infiltration in head and neck squamous cell carcinoma and patient outcome: A retrospective study. Acta Oncol 2018; 57:1165-72.
13. She Y, Kong X, Ge Y, et al. Immune-related gene signature for predicting the prognosis of head and neck squamous cell carcinoma. Cancer Cell Int 2020; 20:22.
14. Chen J, Meng X, Zhou Q, et al. Effect of cxcr5-positive cell infiltration on the immune contexture and patient prognosis in head and neck squamous cell carcinoma. Onco Targets Ther 2020; 13:5869-77.
15. Bai S, Zhang P, Zhang JC, et al. A gene signature associated with prognosis and immune processes in head and neck squamous cell carcinoma. Head Neck 2019; 41:2581-90.
16. Hui D, Maxwell JP, Paiva CE. Dealing with prognostic uncertainty: The role of prognostic models and websites for patients with advanced cancer. Curr Opin Support Palliat Care 2019; 13:360-8.
17. Hui D, Paiva CE, Del Fabbro EG, et al. Prognostication in advanced cancer: Update and directions for future research. Support Care Cancer 2019; 27:1973-84.
18. Han ME, Kim JY, Kim GH, Park SY, Kim YH, Oh SO. Sac3d1: A novel prognostic marker in hepatocellular carcinoma. Sci Rep 2018; 8:15608.
19. Cho SH, Pak K, Jeong DC, Han ME, Oh SO, Kim

YH. The ap2m1 gene expression is a promising biomarker for predicting survival of patients with hepatocellular carcinoma. J Cell Biochem 2019; 120:4140-6.
20. Li T, Fan J, Wang B, et al. Timer: A web server for comprehensive analysis of tumor-infiltrating immune cells. Cancer Res 2017; 77:e108-e10.
21. Schreiber RD, Old LJ, Smyth MJ. Cancer immunoediting: Integrating immunity's roles in cancer suppression and promotion. Science 2011; 331:1565-70.
22. Feng M, Jiang W. Phagocytosis checkpoints as new targets for cancer immunotherapy. Nat Rev Cancer 2019; 19:568-86.
23. Chen Y, Li Z, Sun Y, Zhou GQ. An immune-related gene prognostic index for head and neck squamous cell carcinoma. Clin Cancer Res 2020;
24. Baba Y, Yoshida N, Kinoshita K, et al. Clinical and prognostic features of patients with esophageal cancer and multiple primary cancers: A retrospective single-institution study. Ann Surg 2018; 267:478-83.
25. Yao Y, Yan Z, Lian S, et al. Prognostic value of novel immune-related genomic biomarkers identified in head and neck squamous cell carcinoma. J Immunother Cancer 2020; (2):e000444.
26. Kazlauskas A. Pdgfs and their receptors. Gene 2017; 614:1-7.
27. Roskoski R, Jr. The role of small molecule platelet-derived growth factor receptor (pdgfr) inhibitors in the treatment of neoplastic disorders. Pharmacol Res 2018; 129:65-83.
28. Papadopoulos N, Lennartsson J. The pdgf/pdgfr pathway as a drug target. Mol Aspects Med 2018; 62:75-88.
29. Watts TL, Cui R, Szaniszlo P, Resto VA, Powell DW, Pinchuk IV. Pdgf-aa mediates mesenchymal stromal cell chemotaxis to the head and neck squamous cell carcinoma tumor microenvironment. J Transl Med 2016; 14:337.
30. Schultz JD, Mühlheim K, Erben P, et al. Chemotherapeutic alteration of vegf-/pdgf- and pdgf-rα/β expression by imatinib in hpv-transformed squamous cell carcinoma compared to hpv-negative hnscc in vitro. Oncol Rep 2011; 26:1099-109.
31. Chen J, Cui X, Qian Z, et al. Multi-omics analysis reveals regulators of the response to pdgf-bb treatment in pulmonary artery smooth muscle cells. BMC Genomics 2016; 17:781.
32. Gong J, Han J, He J, et al. Paired related homeobox protein 1 regulates pdgf-induced chemotaxis of hepatic stellate cells in liver fibrosis. Lab Invest 2017; 97:1020-32.
33. Jinnin M, Ihn H, Asano Y, Yamane K, Trojanowska M, Tamaki K. Platelet derived growth factor induced tenascin-c transcription is phosphoinositide 3-kinase/akt-dependent and mediated by ets family transcription factors. J Cell Physiol 2006; 206:718-27.
34. Yang K, Zhang S, Zhang D, et al. Identification of serpine1, plau and acta1 as biomarkers of head and neck squamous cell carcinoma based on integrated bioinformatics analysis. Int J Clin Oncol 2019; 24:1030-41.
35. Xu X, Li M, Hu J, et al. Expression profile analysis identifies a two-gene signature for prediction of head and neck squamous cell carcinoma patient survival. J Cancer Res Ther 2018; 14:1525-34.
36. Oguejiofor K, Hall J, Slater C, et al. Stromal infiltration of cd8 t cells is associated with improved clinical outcome in hpv-positive oropharyngeal squamous carcinoma. Br J Cancer 2015; 113:886-93.
37. Mandal R, Senbabaoglu Y, Desrichard A, et al. The head and neck cancer immune landscape and its immunotherapeutic implications. JCI Insight 2016; 1:e89829.
38. de Ruiter EJ, Ooft ML, Devriese LA, Willems SM. The prognostic role of tumor infiltrating t-lymphocytes in squamous cell carcinoma of the head and neck: A systematic review and meta-analysis. Oncoimmunology 2017; 6:e1356148.
39. Nguyen N, Bellile E, Thomas D, et al. Tumor infiltrating lymphocytes and survival in patients with head and neck squamous cell carcinoma. Head Neck 2016; 38:1074-84.
40. Lechner A, Schlößer HA, Thelen M, et al. Tumor-associated b cells and humoral immune response in head and neck squamous cell carcinoma. Oncoimmunology 2019; 8:1535293.
41. Hladíková K, Koucký V, Bouček J, et al. Tumor-infiltrating b cells affect the progression of oropharyngeal squamous cell carcinoma via cell-to-cell interactions with cd8(+) t cells. J Immunother Cancer 2019; 7:261.
42. Huang L, David O, Cabay RJ, et al. Molecular

classification of lymph node metastases subtypes predict for survival in head and neck cancer. Clin Cancer Res 2019; 25:1795-808.
43. Patel SG, Shah JP. Tnm staging of cancers of the head and neck: Striving for uniformity among diversity. CA Cancer J Clin 2005; 55:242-58; quiz 61-2, 64.
44. Sacco AG, Cohen EE. Current treatment options for recurrent or metastatic head and neck squamous cell carcinoma. J Clin Oncol 2015; 33:3305-13.
45. Yang J, Xie K, Li C. Immune-related genes have prognostic significance in head and neck squamous cell carcinoma. Life Sci 2020; 256:117906.

microRNA-29b mediates Th17/Treg imbalance in chronic obstructive pulmonary disease by targeting IL-22

N. Zhao, MJ. Yu, J. Xu, HY. Wang, B. Liang, L. Ding, YX. Zhang, K. Du and BL. Leng*

Department of Respiratory Medicine, Hangzhou Third Hospital, Hangzhou, Zhejiang, P.R. China

Received January 14, 2021 – Accepted June 4, 2021

Chronic obstructive pulmonary disease (COPD) represents a chronic inflammatory disorder of the airways induced mainly by cigarette smoking. In the current study, cigarette smoke extract (CSE) was used to develop an *in vitro* COPD model using human bronchial epithelium (HBE) cells to expound the possible role of microRNA-29b (miR-29b) in COPD. Firstly, miR-29b and interleukin (IL)-22 expression was assessed in serum of 20 healthy non-smokers, 20 healthy smokers and 20 COPD patients as well as CSE-treated HBE cells. Then, miR-29b and IL-22 expression was altered to evaluate their functions in Th17/Treg ratio. miR-29b inhibited Th17/Treg ratio and levels of IL-22; whereas overexpression of IL-22 reversed these trends. Moreover, rescue experiments found that IL-22 neutralized the repressive effects of miR-29b on Th17/Treg ratio and inflammatory response. Finally, we found that miR-29b blocked the JAK/STAT3 pathway in CSE-treated HBE cells. These data highlighted that miR-29b modulated Th17/Treg imbalance in CSE-induced experimental COPD through inhibition of IL-22-dependent JAK/STAT3 pathway.

As a main public health burden, chronic obstructive pulmonary disease (COPD) is estimated to rank the fifth place worldwide regarding the burden of disease and the third place involving mortality up to 2020 (1). The burden of COPD in China is now larger than that in the developed world, probably because of greater exposure to epidemic risks, an imbalance in economic growth and health-care disparities between rural and urban regions (2). Personal exposure to tobacco smoking, external risk factors, involving secondary and/or tertiary smoking, occupational exposure to dust and toxic fumes, indoor and outdoor air pollution as well as genetic predisposition may elevate the occurrence of COPD (3). Moreover, exposure to cigarette smoke in the long run induces local inflammatory response in the airways that involves both innate immune cells and adaptive immune cells, such as T cells (4). The imbalance between pro-inflammatory and anti-inflammatory responses modulated by the different subgroups of T helper (Th) cells, such as Th17 and regulatory T (Treg) cells, plays a crucial part in the development of this disease (5). Consequently, a further illustration of the relevant mechanism regarding the imbalance between Th17 and Treg cells is of great significance in the management of COPD patients.

MicroRNAs (miRNAs) represent small (~22 nucleotides) non-coding RNAs that typically inhibit gene expression via complementary binding to messenger RNA (mRNA) 3'untranslated region (UTR) and function vitally in cystic idiopathic

Key words: chronic obstructive pulmonary disease; microRNA-29b; Interleukin-22; JAK/STAT3 pathway

*Corresponding Author:
Baolang Leng,
Department of Respiratory Medicine, Hangzhou Third Hospital,
No.38, West Lake Avenue, Hangzhou 310009,
Zhejiang, P.R. China
Tel/Fax: +86-0571-87823137
e-mail: lengbaolang3253@163.com
institutional e-mail: lengbaolang@hzthospital-edu.cn

0393-974X (2021)
Copyright © by BIOLIFE, s.a.s.
This publication and/or article is for individual use only and may not be further reproduced without written permission from the copyright holder.
Unauthorized reproduction may result in financial and other penalties
DISCLOSURE: ALL AUTHORS REPORT NO CONFLICTS OF INTEREST RELEVANT TO THIS ARTICLE.

pulmonary fibrosis, asthma, as well as COPD (6, 7). The presence and stable expression of miRNAs in serum, plasma and urine, and the relevance of their dysregulation in COPD suggest their possible roles as biomarkers and therapeutic targets in the disease (8). Decreased miR-29b expression is linked to airway inflammation in COPD through targeting bromodomain protein 4, and plasma miR-29b has the potency to serve as a biomarker for disease severity in COPD (9), however, its role in the imbalance between Th17 and Treg cells during COPD has rarely been probed. Interestingly, miR-29b was predicted in the present study to directly regulate interleukin (IL)-22 by the TargetScan website (http://www.targetscan.org/vert_72/), a database used for prediction of miRNA targets (10). IL-22 participated in epithelial regeneration and pathology in multiple organs, including the lung, depending on the context and/or cytokine environment, which makes it a promising clinical target (11). In this paper, we aimed to measure the expression and correlation of miR-29b and IL-22 in the context of cigarette smoke extract (CSE)-treated human bronchial epithelium (HBE) cells, and illuminate the molecular mechanisms of this interaction in the ratio of Th17/Treg in peripheral blood mononuclear cells (PBMCs).

MATERIALS AND METHODS

Human tissue samples

Twenty healthy controls (HC), 20 healthy smokers (HS), and 20 COPD patients were included in the study. COPD was diagnosed according to the Global Initiative for Chronic Obstructive Lung Disease criteria. There were no remarkable differences in age, gender, or body mass index among the three groups of participants (Table I). Blood was routinely collected and left to stand for 2 h at 4°C, followed by centrifugation at 1000 g for 5 min to obtain the serum. The RNA in the serum was extracted by Trizol and analyzed by reverse transcriptase quantitative polymerase chain reaction (RT-qPCR) for miR-29b expression. The study protocols were approved by the Institutional Ethics Committee of Hangzhou Third Hospital. Written informed consent was acquired from all volunteers before enrollment.

CSE preparation

CSE was prepared as mentioned previously (12), with minor modifications. Briefly, a research-grade cigarette was bubbled through 100 mL RPMI-1640 medium under constant airflow. Subsequently, the pH value of the medium was adjusted to 7.4 and filtered

Table I. *Basic parameters of clinical participants*

Parameters	Gender	HC (n = 20)	HS (n = 20)	COPD patients (n = 20)	*p* value
Age (years)	Male (n = 10/group)	48.26 ± 5.74	46.26 ± 4.98	49.53 ± 6.25	0.2865
	Female (n = 10/group)	51.38 ± 4.85	50.16 ± 6.24	52.35 ± 4.17	
BMI	Male (n = 10/group)	23.26 ± 1.48	23.49 ± 1.27	22.67 ± 2.05	0.6724
	Female (n = 10/group)	22.15 ± 1.58	21.97 ± 1.18	20.71 ± 1.29	

HC: healthy controls; HS: healthy smokers; COPD: chronic obstructive pulmonary disease; BMI: body mass index . The data were analyzed using two way ANOVA.

using a 0.22-μm filter to remove bacteria and large particles. The obtained solution was 100% CSE and was further diluted to the indicated concentrations.

Cell culture and treatment

HBE cells from ATCC (CRL-2741, Manassas, VA, USA) were grown in RPMI-1640 containing 10% FBS and treated with 1%, 2.5%, 5%, or 10% CSE for a period of 48 h, or with 2.5% CSE for 24, 48, or 72 h. Rux, an inhibitor of the JAK/STAT3 signaling pathway, was from MedChemExpress (HY-50856, Monmouth Junction, NJ, USA). The miR-29b mimic/inhibitor, IL-22 overexpression vector and their respective controls (NC mimic, NC inhibitor, and Vector) used for cell transfection were synthesized by GenePharma Ltd. (Shanghai, China). All transfections were performed using Lipofectamine 2000 (Invitrogen, Carlsbad, CA, USA) according to the manufacturer's protocol. Briefly, 2×10^4 cells were seeded into 96-well plates and grown to 80% confluence. The lipofectamine 2000 reagent and the DNA or RNAi molecules used for transfection were diluted using Opti-MEM Medium (Thermo Fisher Scientific Inc., Waltham, MA, USA), respectively, and each was incubated for 5 min at room temperature. The two solutions were then gently mixed and incubated at room temperature for 20 min. DNA or RNAi molecule-Lipofectamine 2000 complexes were added to each well containing cells and medium. The cells were incubated in a CO_2 incubator at 37°C. After 4-6 h of incubation, the medium was refreshed with RPMI-1640 containing 10% FBS for another 48-h incubation. The cells were subsequently harvested, and the transfection efficiency was detected by RT-qPCR.

RT-qPCR

Trizol one-step method was utilized for total RNA extraction. RT was performed using the KingFisher Cell and Tissue DNA Kit (Fermentas Inc., Hanover, MD, USA), with random primers at 70°C for 5 min, followed by 3-min ice bath, at 37°C for 60 min and 95°C for 10 min. The resulting cDNA was stored temporarily at -20 Cº until use. RT-qPCR was carried out with TaqMan probe, and the reaction system was operated as per the protocol of the kit (Fermentas). Real-time fluorescence PCR (Bio-Rad iQ5, Bio-Rad Laboratories, Hercules, CA, USA) platform was used. The reaction system consisted of 2× Taq MasterMix 5.3 μL, forward primer (5 μM) 1 μL, reverse primer (5 μM) 1 μL, cDNA 1 μL, RNase Free H_2O 11.7 μL. The following thermocycling conditions were used for qPCR: initial denaturation at 95°C for 5 min, followed by 35 cycles of denaturation at 94°C for 45 s, annealing at 56ºC for 45 s, and elongation at 72°C for 45 s. GAPDH and U6 snRNA served as the

Table II. *Primer sequences used in RT qPCR*

Targets	Primer sequences
miR-29b	F: 5'-CGCCTAGCACCATTTGAAATC-3' R: 5'-GTCGTATCCAGTGCAGGGTCCGAGGTATTCGCACTGGATACGACAACACT-3'
U6	F: 5'-CTCGCTTCGGCAGCACA-3' R: 5'-AACGCTTCACGAATTTGCGT-3'
GAPDH	F: 5'- CCACATCGCTCAGACACCAT-3' R: 5'-GCGCCCAATACGACCAAAT-3'
IL-22	F: 5'-CTGCTTCTCGTTGCTCTG-3' R: 5'-CTGACATCTGTGTTGTTA-3'

RT qPCR: reverse transcriptase quantitative polymerase chain reaction; miR 29b: microRNA 29b; IL 22: interleukin 22; F: forward; R: reverse

internal reference to normalize the expression of gene and miRNA respectively. The relative expression levels were calculated by the $2^{-\Delta\Delta Ct}$ method. Primer sequences are displayed in Table II.

Cell counting kit-8 (CCK-8) assay

CCK-8 kit (Sangon Bioengineering Co., Ltd., Shanghai, China) was utilized for cell viability. In brief, CCK-8 solution (10 μL) was added to cells in the 96-well plates and incubated for 60 min. The optical density (OD) value was read at 450 nm with a microplate reader (Bio-Rad).

Enzyme-linked immunosorbent assay (ELISA)

Levels of IL-22 (ab216170), TNF-α (ab181421) and IL-6 (ab46027) were measured in cell supernatants using ELISA kits (Abcam, Cambridge, MA, USA) in line with the manufacturer's instructions, and then measured by Molecular Devices Spectra Max M5 and SoftMax Pro 6.5.1 analytical software at 450 nm.

Western blot

Total protein of cells was extracted using radio immunoprecipitation assay (P0013B, Beyotime, Shanghai, China), and the protein concentration was assessed using a BCA kit (Thermo Fisher Scientific Inc.). An equal volume of protein (40 μg) was subjected to PAGE and transblotted to a polyvinylidene fluoride membrane (Amersham Pharmacia, Piscataway, NJ, USA). After being sealed using 5% skimmed milk powder for 60 min at ambient temperature, the membrane was incubated at 4°C with rabbit monoclonal antibodies against IL-22 (1:2000, ab133545, Abcam), STAT3 (1:1,000, ab68153, Abcam), p-STAT3 (1:1,000, ab76315, Abcam), JAK (1:1,000, ab133666, Abcam), p-JAK (1:1,000, ab138005, Abcam), and GAPDH (1:5,000, ab181602, Abcam) overnight and with HRP-labeled goat anti-rabbit secondary antibody (1:10,000, Jackson Laboratory, Sacramento, CA, USA) for 60 min at ambient temperature. The relative protein expression was analyzed by grayscale scanning of protein bands using Image Pro Plus 6.0 (Media Cybernetics, Bethesda, MD, USA) software after developing the scans in an optical luminometer (GE Healthcare, Chicago, IL, USA).

Flow cytometry

PBMCs were isolated from individual participants through Ficoll density gradient centrifugation. To determine $CD25^+$ forkhead box $p3^+$ ($Foxp3^+$) Tregs (% of $CD3^+$ $CD4^+$), 2×10^6 cells/mL PBMCs were treated with fluorescein isothiocyanate (FITC)-labeled anti-human CD3 and allophycocyanin (APC)-labeled anti-human CD4 for 30 min. After fixation and permeabilization, the cells were treated with Pacific Blue-labeled human antibody against CD25 and phycoerythrin-labeled human antibody against Foxp3 or isotype control (eBioscience, San Diego, CA, USA). To determine $CD4^+$ $IL\text{-}17^+$ Th17 cells (% of $CD3^+$ cells), 2×10^6 cells /mL PBMCs were incubated with PMA (50 ng/mL, Sigma-Aldrich Chemical Company, St Louis, MO, USA) and 500 ng/mL ionomycin (Sigma-Aldrich) in the presence of brefeldin A (2.5 μg/mL; Sigma-Aldrich) and 10% fetal calf serum at room temperature for 4 h. Then, cells were stained with FITC-labeled anti-human CD3 and APC-labeled anti-human CD4 at 4°C for 0.5 h, fixed, permeabilized, and treated with PE-labeled anti-human IL-17A (eBioscience). FACS Canto II (BD Biosciences) and CellQuest software (BD Corporation) were utilized for cell analysis.

Luciferase reporter assay

The target gene and binding sites of miR-29b were predicted using the TargetScan database. Artificially synthesized IL-22 3'UTR full-length gene fragments were inserted into the pMIR-reporter (Promega, Madison, WI, USA), and mutated sites of the seed sequence were synthesized and cloned into the pMIR-reporter reporter plasmid. The sequenced WT and MUT luciferase reporter plasmids were transfected into HEK-293T cells (CRL-11268, ATCC) with miR-29b, respectively. Luciferase activity was tested after 48 h with the help of the Dual-Luciferase Reporter Assay System (Promega).

Data analyses

Data presented in the form of mean ± standard deviation (SD) from at least three experiments were compared by SPSS 22.0 software (IBM, Armonk, NY, USA). Comparison of the differences was analyzed using unpaired *t*-test (two groups) and one-

way or two-way ANOVA followed by Tukey's post hoc test (multiple groups). Statistical significance was assumed at $p < 0.05$.

RESULTS

miR-29b is reduced in COPD patients and in the cellular model

To study the effects of miR-29b on COPD, we measured the miR-29b expression in the serum of COPD patients (Fig. 1A). Serum miR-29b was found to be significantly lower in the HS and COPD groups than that in the HC group. Serum miR-29b was also significantly reduced in the COPD patients compared to the HS group. It was shown that smoking decreased miR-29b in human serum, especially in patients with COPD.

CSE treatment of HBE can mimic COPD *in vitro* (13). Therefore, we treated HBE cells with 1%, 2.5%, 5%, or 10% CSE for a period of 48 h to detect miR-29b expression. First, we tested the effect of CSE on the proliferative capacity of HBE cells. The viability of HBE cells gradually decreased as the CSE concentration increased, and the survival of cells at 2.5% CSE or above concentrations was significantly inhibited (Fig. 1B). RT-qPCR analysis showed that CSE led to a concentration-dependent decrease in miR-29b expression (Fig. 1C). Further analysis using 2.5% CSE demonstrated that miR-29b showed a time-dependent decline from 24 to 72 h (Fig. 1D). Taken together, the results displayed that miR-29b expression was downregulated in both COPD patients and in the cellular model.

miR-29b inhibits IL-22 expression in HBE cells treated with CSE

To detect the effect of miR-29b on CSE-induced inflammation in HBE cells, we first detected the

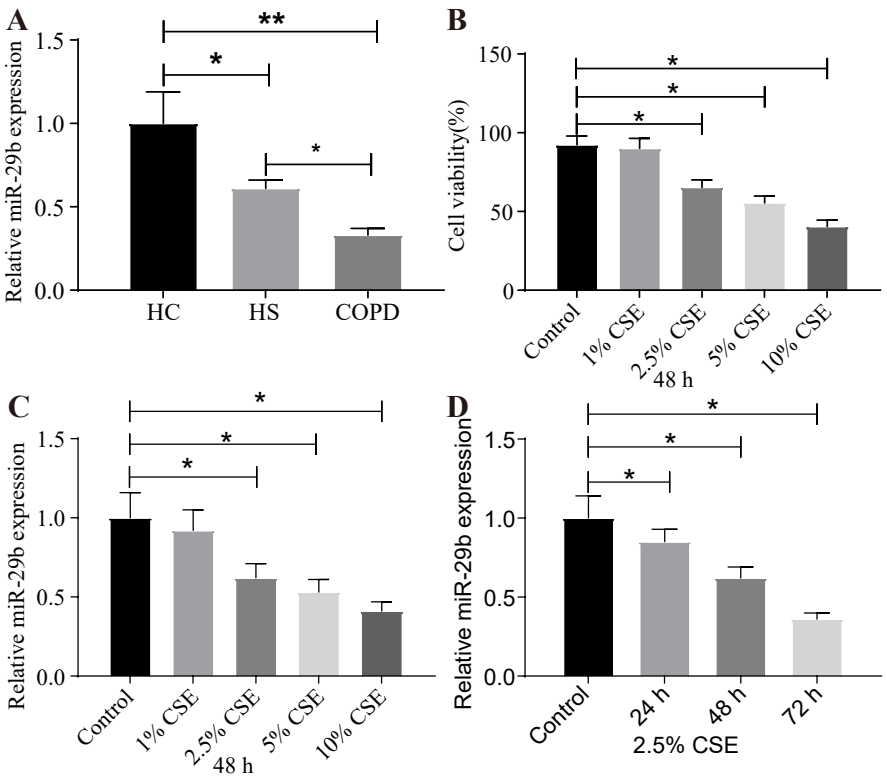


Fig. 1. *miR-29b expression is reduced in both COPD patients and in the cellular model.* ***A)*** *Expression of miR-29b in the serum of HC, HS, and COPD patients analyzed using RT-qPCR;* ***B)*** *HBE cell viability in response to different concentrations of CSE determined using CCK8 assay;* ***C)*** *miR-29b expression determined by RT-qPCR in HBE cells exposed to CSE at the different concentration for 48 h;* ***D)*** *miR-29b expression determined by RT-qPCR after the HBE cells exposed to 2.5% CSE for 24 h, 48 h and 72 h. Data are displayed in the form of mean ± SD from at least three experiments. Analyses were conducted using one-way ANOVA. *$p < 0.05$ and **$p < 0.01$.*

levels of pro-inflammatory factors in the supernatant of CSE-induced HBE cells by ELISA assay. A significant increase in the levels of IL-6, IL-22, and TNF-α was observed in the supernatant of CSE-induced HBE cells compared to the untreated HBE cells (Fig. 2 A-C). Furthermore, we transfected miR-29b mimic/inhibitor into HBE cells prior to CSE stimulation and examined the transfection efficiency by RT-qPCR. Fig. 2D shows that miR-29b mimic/inhibitor transfection was effective.

The ELISA test revealed a significant decline in the pro-inflammatory factor IL-22 in the miR-29b mimic-treated HBE cells, while IL-6 and TNF-α did not change significantly (Fig. 2E). Whereas inhibition of miR-29b resulted in a remarkable increase in the levels of the cellular inflammatory factor IL-22, with insignificant changes in IL-6 and TNF-α levels (Fig. 2E). Further, we subjected cells transfected with miR-29b mimic to 2.5% CSE stimulation for 48 h. It was found that the supernatants of cells delivered with miR-29b mimic and subjected to CSE stimulation showed a significant reduction in IL-22 level when comparing to the cells delivered with miR-NC and subjected to CSE stimulation (Fig. 2F). All in all, miR-29b inhibited IL-22 expression in the COPD cell model.

miR-29b modulates the Th17/Treg ratio

To demonstrate the effect of miR-29b on Th17 cell differentiation, PBMCs were transfected with miR-29b mimic or inhibitor and then exposed to 2.5% CSE for a period of 48 h. Flow cytometry displayed that CSE significantly promoted the proportion of Th17 (IL-17A^{+}CD4^{+}) in CD3^{+} cells (Fig. 3 A, B).

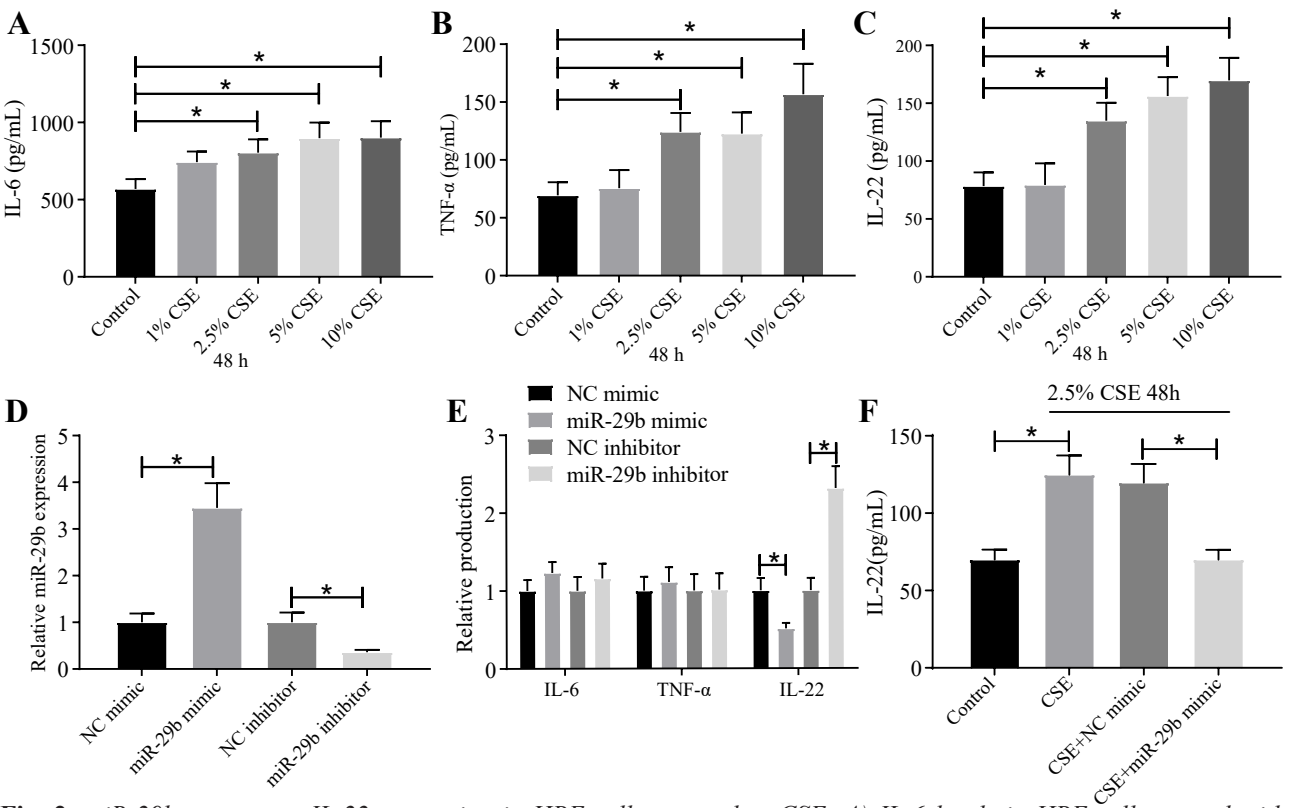


Fig. 2. *miR-29b suppresses IL-22 expression in HBE cells exposed to CSE. **A**) IL-6 levels in HBE cells treated with CSE at the different concentration measured by ELISA; **B**) TNF-α levels in HBE cells treated with CSE at the different concentration measured by ELISA; **C**) IL-22 levels in HBE cells treated with CSE at the different concentration measured by ELISA; **D**) miR-29b expression in response to miR-29b mimic/inhibitor transfection detected by RT-qPCR; **E**) IL-6, TNF-α and IL-22 levels in HBE cells after transfection measured by ELISA; **F**) IL-22 levels in HBE cells after transfection and CSE treatment measured by ELISA. Data are expressed as mean ± SD from three independent experiments. Analyses were conducted using one-way ANOVA. *$p < 0.05$.*

Alternatively, CSE reduced the proportion of Treg cells ($CD25^+FOXP3^+$) in $CD3^+CD4^+$ cells (Fig. 3 A, C), whereas CSE exposure resulted in a significant increase in the ratio of Th17/Treg cells (Fig. 3D). However, overexpression of miR-29b significantly reversed the effects of CSE on Th17, Treg, and Th17/Treg ratio, resulting in reduced Th17 cell frequency, increased Treg cell frequency, and decreased Th17/Treg cell ratio (Fig. 3 A-D). Whereas inhibition of miR-29b showed an augment in Th17 cell frequency, a decline in Treg cell frequency, and a promotion in Th17/Treg cell ratio (Fig. 3 A-D).

miR-29b targets and degrades IL-22 expression

Since miR-29b can inhibit the release of IL-22, we speculated that IL-22 may be a possible target of miR-29b. We therefore studied whether miR-29b can target IL-22 using TargetScan (Fig. 4A). The results suggested that miR-29b has a potential binding site to the IL-22 3'UTR. Next, we verified that miR-29b targeted and bound to the IL-22 mRNA 3'-UTR sequence (Fig. 4B) by dual-luciferase reporter gene assays. Specifically, miR-29b mimic significantly inhibited the luciferase activity of WT-IL-22 containing a binding site to miR-29b, while it had no significant effect on the luciferase activity of MUT-IL-22 with a mutation in the binding site. RT-qPCR revealed that IL-22 level was remarkably enhanced in the serum of the COPD patients compared to the HC and HS (Fig. 4C).

We treated HBE cells with 1%, 2.5%, 5%, or 10% CSE for 48 h to detect the expression of IL-22. RT-qPCR analysis showed that CSE contributed to a concentration-dependent increase in IL-22

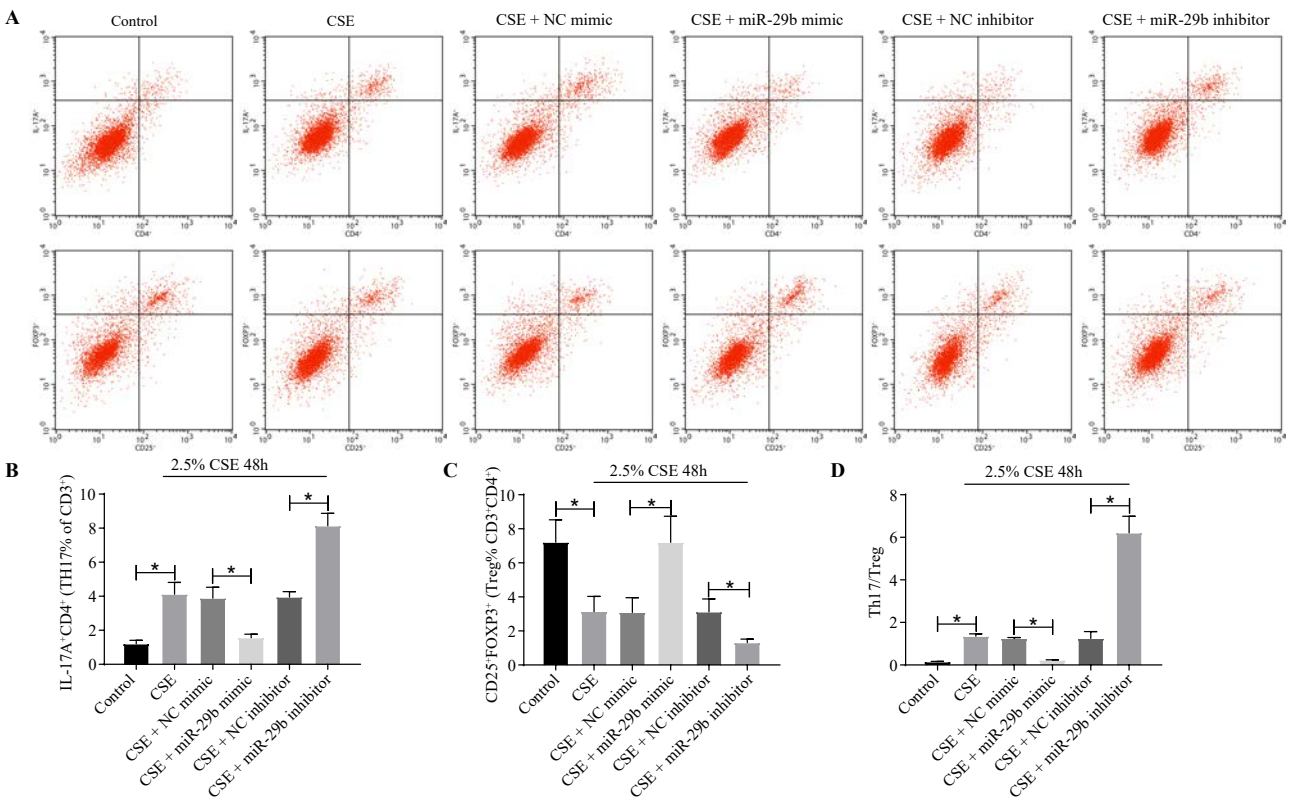


Fig. 3. *miR-29b mediates the Th17/Treg ratio. PBMCs were delivered with miR-29b mimic/inhibitor for 24 h and were exposed to CES for 48 h.* ***a****) flow cytometric analysis of percentage of Th17 and Treg cells in the T cells;* ***b****) frequency of Th17 (IL-17A+CD4+) cells determined using flow cytometry;* ***c****) frequency of Treg (CD25+FOXP3+) cells determined using flow cytometry;* ***d****) the ratio of Th17/Treg cells. data are expressed as mean ± sd from three independent experiments. analyses were conducted using one-way ANOVA. *p < 0.05.*

expression (Fig. 4D). Further analysis showed a time-dependent increase in IL-22 levels from 24 to 72 h (Fig. 4E). Western blot experiments assessed the effect of miR-29b on IL-22 expression. miR-29b mimic significantly suppressed the protein level of IL-22; while miR-29b inhibitor increased the level of IL-22 (Fig. 4F). Taken together, IL-22, expressed highly in both COPD patients and in the cellular model, was targeted and degraded by miR-29b.

miR-29b modulates the Th17/Treg ratio by targeting IL-22

To further investigate whether miR-29b governs the Th17/Treg ratio by targeting IL-22, we performed rescue experiments. The transfection efficiency of IL-22 overexpression was first examined in isolated PBMCs, and Vector-IL-22 successfully promoted the expression of IL-22 (Fig. 5A). We co-transfected miR-29b mimic and pc-DNA 3.1(+)-IL-22 in PBMCs and then exposed them to 2.5% CSE treatment for 48 h. Flow cytometry showed that CSE significantly enhanced the frequency of Th17 cells (IL-17A$^+$CD4$^+$) in CD3$^+$ cells (Fig. 5B, C). Alternatively, CSE diminished the frequency of Treg cells (CD25$^+$FOXP3$^+$) in CD3$^+$CD4$^+$ cells (Fig. 5B, D), whereas CSE exposure contributed to a significant augment in the Th17/Treg ratio (Fig. 5E). In addition, Vector-IL-22 + CSE effectively elevated the number of Th17 cells, reduced the number of Treg cells and promoted the Th17/Treg ratio relative to the Vector + CSE treatment (Fig. 5 B-E). However, under CSE exposure, overexpression of miR-29b significantly reversed the effects of IL-22, resulting in decreased Th17 cell frequency, increased Treg cell frequency, and abated Th17/Treg cell ratio (Fig. 5 B-E).

miR-29b blocks the JAK/STAT3 signaling pathway in CSE-stimulated PBMCs

To further determine the potential mechanism through which miR-29b regulates the Th17/Treg imbalance, we tested the role of miR-29b on the JAK/STAT3 pathway in isolated PBMCs. miR-29b mimic was noted to impair the JAK/STAT3 signaling pathway, as evidenced by significantly reduced extents of JAK and STAT3 phosphorylation.

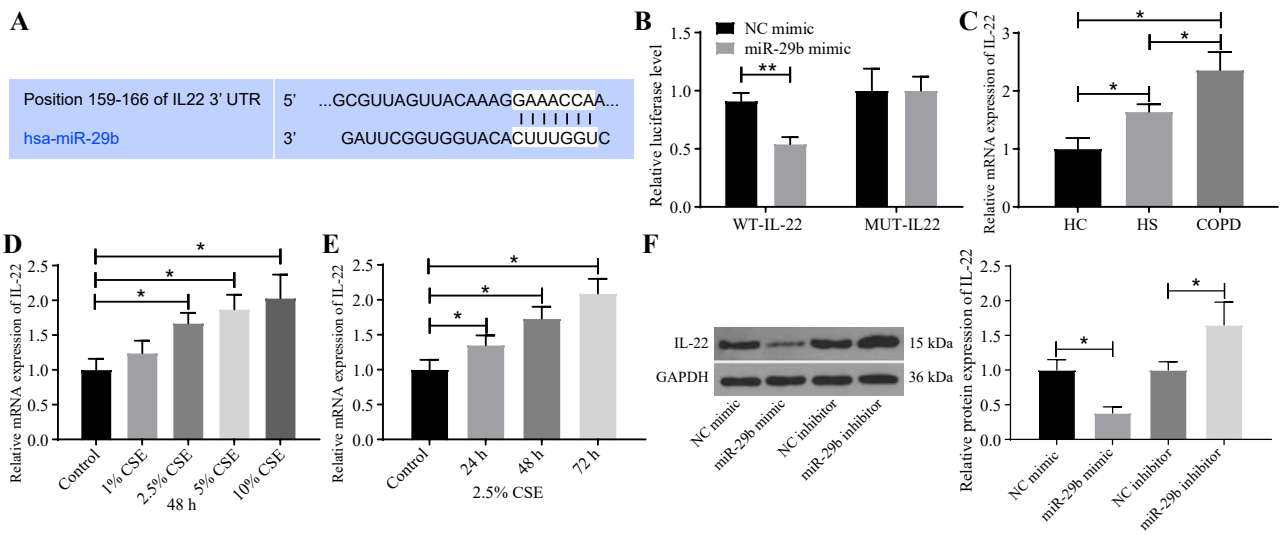


Fig. 4. *miR-29b targets and degrades IL-22. **A**) Potential binding sites of IL-22 3'UTR to miR-29b predicted in TargetScan; **B**) the effects of miR-29b mimic on luciferase activity of WT-IL-22 and MUT-IL-22 reporter vectors assessed by dual-luciferase reporter assay; **C**) IL-22 in the serum of HC, HS, and patients with COPD analyzed using RT-qPCR; **D**) mRNA expression of IL-22 determined by RT-qPCR after the HBE cells were exposed to CSE at the different concentration for 48 h; **E**) mRNA expression of IL-22 determined by RT-qPCR after the HBE cells were exposed to 2.5% CSE for 24 h, 48 h and 72 h; **F**) protein expression of IL-22 in HBE cells after miR-29b inhibitor/mimic assessed by western blot. Data are expressed as mean ± SD from three independent experiments. Analyses were conducted using one-way or two-way ANOVA. *$p < 0.05$ and **$p < 0.01$.*

The extents of JAK or STAT3 phosphorylation were enhanced after suppression of miR-29b (Fig. 6A). Furthermore, CSE activated the JAK/STAT3 signaling pathway in PBMCs (Fig. 6B). Also, the CSE + miR-29b mimic treatment reversed the activating effect of CSE on the JAK/STAT3 signaling pathway and even showed inhibitory effects compared to the CSE + miR-NC treatment (Fig. 6B).

Rux is an inhibitor of the JAK/STAT3 signaling pathway (14). The effect of combined action of Rux and miR-29b inhibitor on JAK/STAT3 phosphorylation was examined by Western blot assay (Fig. 6C). The results showed that Rux significantly inhibited the increase of JAK/STAT3 phosphorylation caused by CSE, and the phosphorylation level of JAK/STAT3 was significantly restored after miR-29b inhibition,

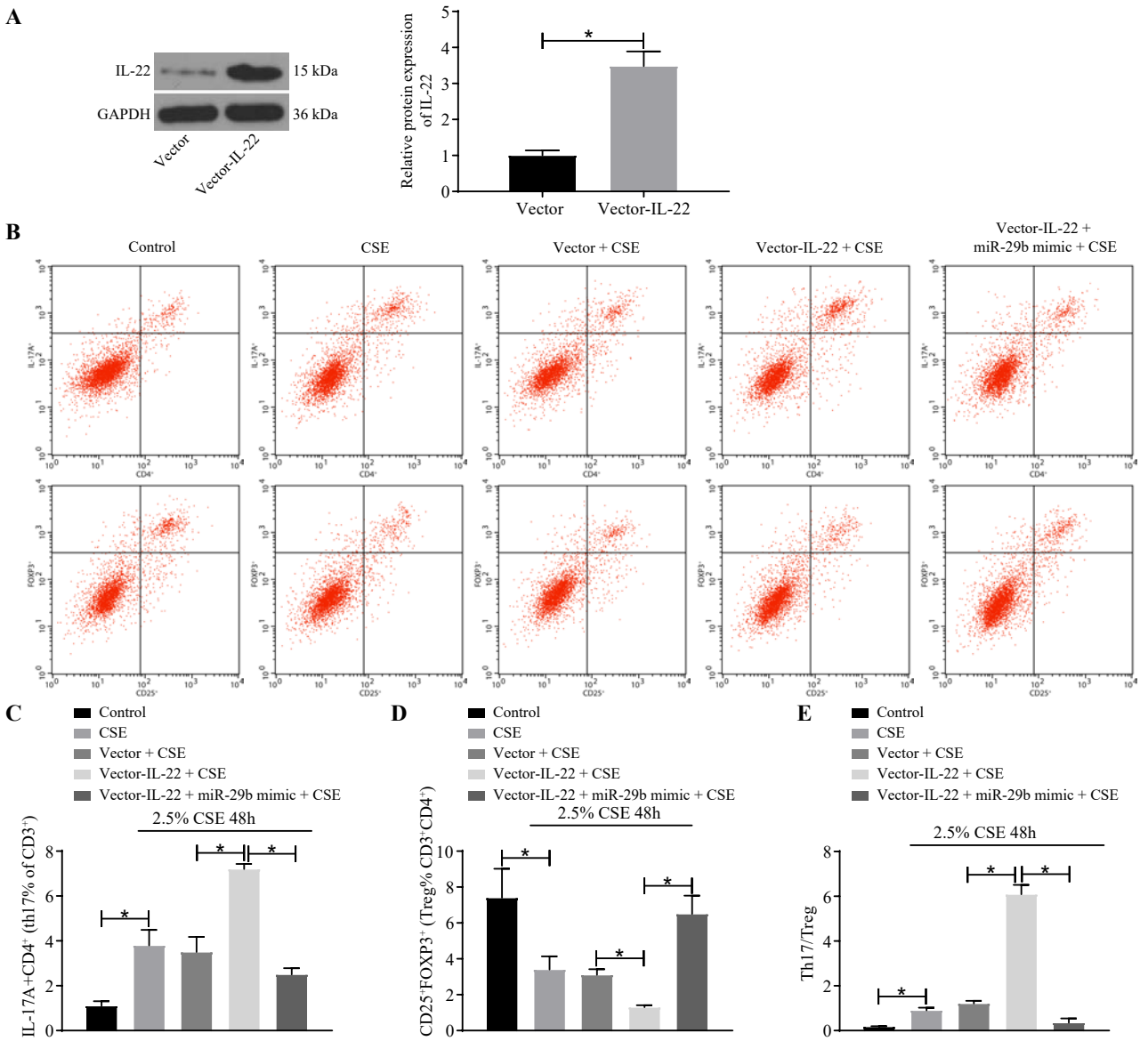


Fig. 5. *miR-29b mediates the Th17/Treg ratio by targeting IL-22. **A)** Protein expression of IL-22 in PBMCs transfected with Vector or Vector-IL-22 determined by Western blot; PBMCs were delivered with pcDNA3.1(+) or pcDNA3.1(+)-IL-22 for 48 h and then were exposed to CSE for 48 h; **B)** flow cytometric analysis of percentage of Th17 and Treg cells in the T cells; **C)** frequency of Th17 (IL-17A$^+$CD4$^+$) cells determined using flow cytometry; **D)** frequency of Treg (CD25$^+$FOXP3$^+$) cells determined using flow cytometry; E) the ratio of Th17/Treg cells. Data are expressed as mean ± SD from three independent experiments. Analyses were conducted using unpaired t test or one-way ANOVA. *p < 0.05.*

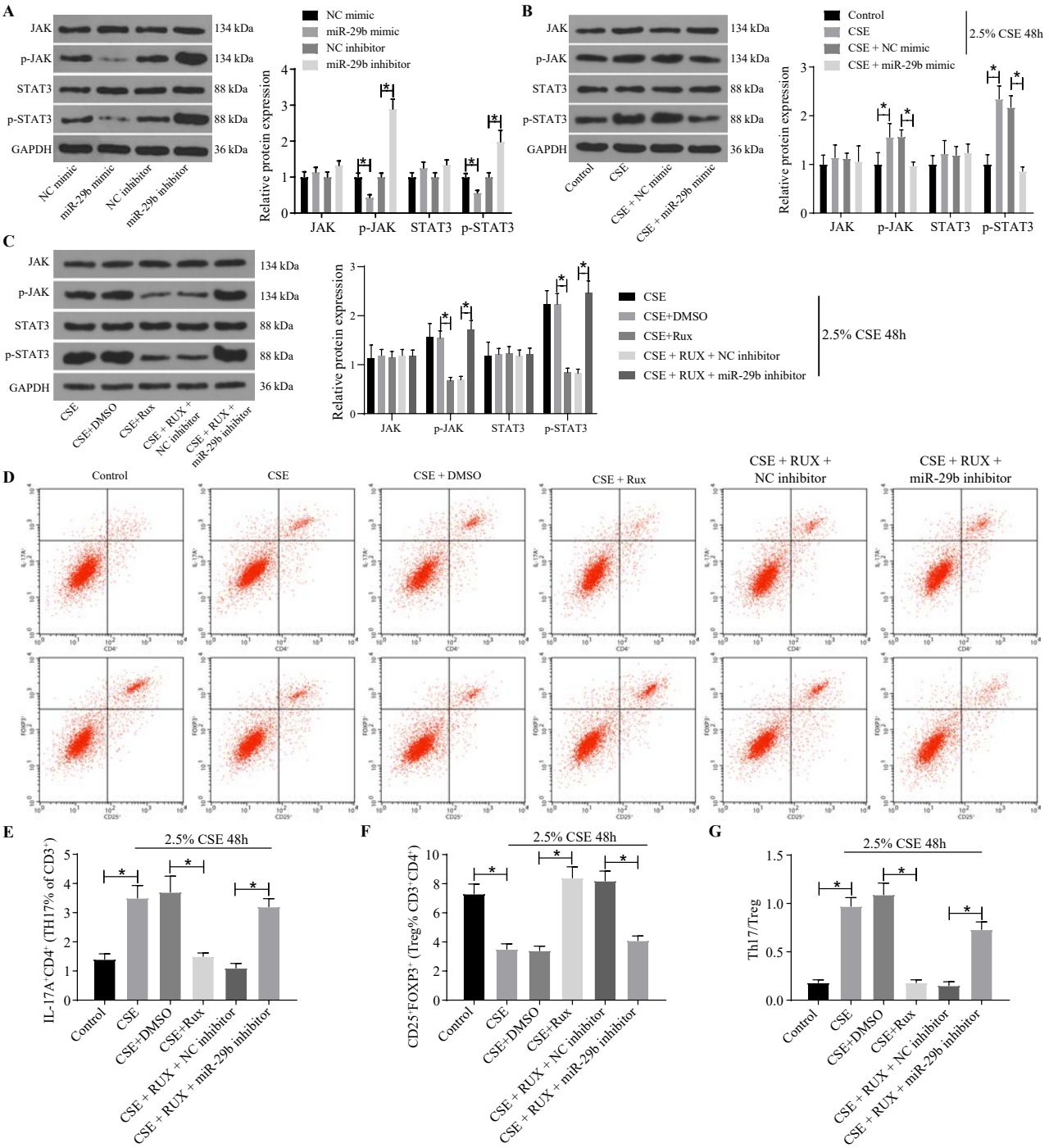


Fig. 6. *miR-29b disrupts the JAK/STAT3 pathway in CSE-stimulated PBMCs.* ***A****) The total protein expression and the extents of JAK and STAT3 phosphorylation in PBMCs in response to miR-29b mimic/inhibitor;* ***B****) the total protein expression and the extents of JAK and STAT3 phosphorylation in PBMCs transfected with miR-29b mimic and exposed to CSE;* ***C****) the total protein expression and the extents of JAK and STAT3 phosphorylation in PBMCs treated with Rux and transfected with miR-29b inhibitor;* ***D****) flow cytometric analysis of percentage of Th17 and Treg cells in the T cells;* ***E****) frequency of Th17 (IL-17A$^+$CD4$^+$) cells determined using flow cytometry;* ***F****) frequency of Treg (CD25$^+$FOXP3$^+$) cells determined using flow cytometry;* ***G****) the ratio of Th17/Treg cells. Data are expressed as mean ± SD from three independent experiments. Analyses were conducted using one-way or two-way ANOVA. *p < 0.05.*

which indicated that miR-29b was involved in JAK/STAT3 phosphorylation and could significantly alleviate the inhibitory effect of Rux on JAK/STAT3 phosphorylation. Using flow cytometry (Fig. 6D), we observed that Rux significantly reduced proportion of Th17 cells (Fig. 6E), augmented the proportion of Treg cells (Fig. 6F), and lowered the Th17/Treg ratio (Fig. 6G). It was found that miR-29b inhibitor reversed the effects of Rux on Th17, Treg and Th17/Treg percentages (Fig. 6D), as manifested by an increase in Th17 cell frequency (Fig. 6E), a decrease in Treg cell frequency (Fig. 6F), and a rise in the Th17/Treg cell ratio (Fig. 6G). These results provided evidence that the JAK/STAT3 signaling pathway was participated in the repressive effect of miR-29b on Th17/Treg imbalance.

DISCUSSION

COPD stands for a major contributor to lung cancer, and around 50-80% of lung cancer patients had pre-existing COPD, with the incidence of lung cancer resulting from COPD rising to 0.8-1.7% (4). Imbalance in Th17/Treg cells is regarded as having a vital role in inflammation and airway remodeling in COPD (15). In the present investigation, using an HBE cell line, miR-29b overexpression attenuated the upregulation of IL-22. In addition, we demonstrated that CSE-induced Th17/Treg imbalance was reduced by miR-29b overexpression in PBMCs, which was reversed by IL-22 upregulation. Moreover, the JAK/STAT3 signaling pathway participated in the modulation of Th17/Treg ratio by miR-29b.

Our observation disclosed that the expression of miR-29b was obviously reduced in COPD patients relative to both HS and HC. Subsequently, we used 1%, 2.5%, 5% or 10% CSE to treat HBE cells for 48 h and used 2.5% CSE to treat HBE cells for 24 h, 48 h and 72 h, respectively. RT-qPCR showed that CSE significantly reduced miR-29b expression in HBE cells in concentration- and time-dependent fashions. In line with our findings, miR-29b expression was reduced in the lung and spleen of murine asthma, and miR-29b reversed the imbalance of Th1/Th2 responses (16). More specifically, lipopolysaccharide-induced COPD resulted in decreased expression of miR-29b in the lung tissues of rats (17). However, its role in mediating the imbalance of Th17/Treg cells remains largely undetermined. Th17 cells release pro-inflammatory cytokines, including IL-22, while $CD25^{+}Foxp3^{+}$ Tregs are able to suppress the inflammation (18). The balance between Th17 and Treg was altered in the COPD animal model, therefore, the Th17/Treg balance is of great importance for immune homeostasis (19). Consistently, we observed that CSE promoted the frequency of Th17 cells, while reduced that of Tregs, thus disturbing the balance of Th17/Treg. By contrast, miR-29b mimic restored the balance by reducing the frequency of Th17 cells and promoting that of Tregs.

Furthermore, we explored the functional effects of miR-29b on HBE cell inflammation cytokines (IL-6, IL-22 and TNF-α). We noted that miR-29b negatively regulated the expression of IL-22, while exerted little impact on the expression of TNF-α and IL-6. It has been previously established that miR-29b was reduced in tumor-associated dendritic cells, and miR-29b targeted various genes related to inflammation (20). Aa a consequence, we postulated that miR-29b could modulate the IL-22 expression through direct targeting; the TargetScan prediction and dual-luciferase reporter gene assay verification corroborated this. Also, the enhancement of IL-22 expression in CSE-exposed cells exhibited time- and concentration-dependent manners. Afterwards, we determined whether IL-22 was involved in the effects of miR-29b on the imbalance of Th17/Treg. IL-22 was found to further disturb the imbalance of Th17/Treg even in the presence of CSE, while miR-29b mimic rescued the pro-inflammatory effects of IL-22 on PBMCs. Starkey et al. proposed that IL-22 played an initiator role in the pathogenesis of CSE-evoked experimental COPD, and neutrophilic airway inflammation was hampered in IL-22-deficit mice compared to wild-type controls (21). In another model of mice under the exposure of 3-d CSE, administration of recombinant IL-22 alone or along with CSE induced airway hyperreactivity, with elevated IL-17A and neutrophils, representing a possible deleterious role (22). Mechanistically, IL-22 mediated its properties through a heterodimeric

transmembrane receptor complex and the following JAK-STAT signaling pathway, including JAK1 and STAT3 (23). Seki et al. also proved that IL-22 attenuated overexpression of PD-L1 in airway epithelial cells through a STAT3-dependent mechanism (24). Therefore, we began to hypothesize that the JAK/STAT3 pathway was also a part of the regulatory axis in Th17/Treg imbalance. Previous studies have identified the targeting relation between miR-29b and STAT3 in different cancers, including lung adenocarcinoma and glioma (25, 26). In our study, miR-29b mimic disrupted the JAK/STAT3 pathway and reversed the simulative role of CSE on the pathway activity. In addition, the repressive effects of Rux, the inhibitor of the JAK/STAT3 pathway on the Th17/Treg imbalance were reversed by miR-29b inhibitor. Meyer et al. revealed that upon exposure to Rux, CD8 T cells were sensitized to dexamethasone-induced apoptosis *in vitro* and significantly reduced tissue immunopathology and manifestations of hemophagocytic lymphohistiocytosis *in vivo* (27).

In conclusion, we exhibited through *in vitro* assays that miR-29b disrupted the Th17/Treg imbalance in COPD. Importantly, we found that miR-29b impaired the JAK/STAT3 pathway by targeting IL-22. Our data suggested that miR-29b is an attractive therapeutic target for CSE-induced Th17/Treg imbalance.

ACKNOWLEDGEMENTS

The authors would like to thank Research Fund of Traditional Chinese Medicine of Zhejiang Provincial (2019ZB103).

REFERENCES

1. Vestbo J, Hurd SS, Agusti AG, et al. Global strategy for the diagnosis, management, and prevention of chronic obstructive pulmonary disease: GOLD executive summary. Am J Respir Crit Care Med 2013; 187:347-65.
2. Fang X, Wang X, Bai C. COPD in China: the burden and importance of proper management. Chest 2011; 139:920-9.
3. Lopez-Campos JL, Tan W, Soriano JB. Global burden of COPD. Respirology 2016; 21:14-23.
4. Ni L, Dong C. Roles of myeloid and lymphoid cells in the pathogenesis of chronic obstructive pulmonary disease. Front Immunol 2018; 9:1431.
5. Ito JT, Cervilha DAB, Lourenco JD, et al. Th17/Treg imbalance in COPD progression: A temporal analysis using a CS-induced model. PLoS One 2019; 14:e0209351.
6. De Smet EG, Mestdagh P, Vandesompele J, Brusselle GG, Bracke KR. Non-coding RNAs in the pathogenesis of COPD. Thorax 2015; 70:782-91.
7. Stolzenburg LR, Harris A. The role of microRNAs in chronic respiratory disease: recent insights. Biol Chem 2018; 399:219-34.
8. Osei ET, Florez-Sampedro L, Timens W, Postma DS, Heijink IH, Brandsma CA. Unravelling the complexity of COPD by microRNAs: it's a small world after all. Eur Respir J 2015; 46:807-18.
9. Tang K, Zhao J, Xie J, Wang J. Decreased miR-29b expression is associated with airway inflammation in chronic obstructive pulmonary disease. Am J Physiol Lung Cell Mol Physiol 2019; 316:L621-L9.
10. Garcia DM, Baek D, Shin C, Bell GW, Grimson A, Bartel DP. Weak seed-pairing stability and high target-site abundance decrease the proficiency of lsy-6 and other microRNAs. Nat Struct Mol Biol 2011; 18:1139-46.
11. Dudakov JA, Hanash AM, van den Brink MR. Interleukin-22: immunobiology and pathology. Annu Rev Immunol 2015; 33:747-85.
12. Ballweg K, Mutze K, Konigshoff M, Eickelberg O, Meiners S. Cigarette smoke extract affects mitochondrial function in alveolar epithelial cells. Am J Physiol Lung Cell Mol Physiol 2014; 307:L895-907.
13. Vlahos R, Bozinovski S. Protocols to Evaluate Cigarette Smoke-Induced Lung Inflammation and Pathology in Mice. Methods Mol Biol 2018; 1725:53-63.
14. Kim JE, Lee YJ, Park HR, Lee DG, Jeong KH, Kang H. The Effect of JAK Inhibitor on the Survival, Anagen Re-Entry, and Hair Follicle Immune Privilege Restoration in Human Dermal Papilla Cells. Int J Mol Sci 2020; 21:5137.
15. Farahani P, Halabian R, Vahedi E, Salimian J. Increased Genes Expression Levels of Cytokines

Related to Th17/Treg Cells in Peripheral Blood Mononuclear Cell Correlate with Clinical Severity in COPD and Mustard Gas-exposed Patients. Iran J Allergy Asthma Immunol 2017; 16:396-403.

16. Yan J, Zhang X, Sun S, et al. miR-29b Reverses T helper 1 cells/T helper 2 cells imbalance and alleviates airway eosinophils recruitment in OVA-induced murine asthma by targeting inducible co-stimulator. Int Arch Allergy Immunol 2019; 180:182-94.
17. Chi Y, Di Q, Han G, Li M, Sun B. Mir-29b mediates the regulation of Nrf2 on airway epithelial remodeling and Th1/Th2 differentiation in COPD rats. Saudi J Biol Sci 2019; 26:1915-21.
18. Wang H, Ying H, Wang S, et al. Imbalance of peripheral blood Th17 and Treg responses in patients with chronic obstructive pulmonary disease. Clin Respir J 2015; 9:330-41.
19. Zheng X, Zhang L, Chen J, Gu Y, Xu J, Ouyang Y. Dendritic cells and Th17/Treg ratio play critical roles in pathogenic process of chronic obstructive pulmonary disease. Biomed Pharmacother 2018; 108:1141-51.
20. Botta C, Cuce M, Pitari MR, et al. MiR-29b antagonizes the pro-inflammatory tumor-promoting activity of multiple myeloma-educated dendritic cells. Leukemia 2018; 32:1003-15.
21. Starkey MR, Plank MW, Casolari P, et al. IL-22 and its receptors are increased in human and experimental COPD and contribute to pathogenesis. Eur Respir J 2019; 54:1800174.
22. Le Rouzic O, Pichavant M, Frealle E, Guillon A, Si-Tahar M, Gosset P. Th17 cytokines: novel potential therapeutic targets for COPD pathogenesis and exacerbations. Eur Respir J 2017; 50:1602434.
23. Wolk K, Witte E, Witte K, Warszawska K, Sabat R. Biology of interleukin-22. Semin Immunopathol 2010; 32:17-31.
24. Seki N, Kan OK, Matsumoto K, et al. Interleukin-22 attenuates double-stranded RNA-induced upregulation of PD-L1 in airway epithelial cells via a STAT3-dependent mechanism. Biochem Biophys Res Commun 2017; 494:242-8.
25. Liu L, Liu L, Lu S. lncRNA H19 promotes viability and epithelial-mesenchymal transition of lung adenocarcinoma cells by targeting miR-29b-3p and modifying STAT3. Int J Oncol 2019; 54:929-41.
26. Xu JX, Yang Y, Zhang X, Luan XP. MicroRNA-29b promotes cell sensitivity to Temozolomide by targeting STAT3 in glioma. Eur Rev Med Pharmacol Sci 2020; 24:1922-31.
27. Meyer LK, Verbist KC, Albeituni S, et al. JAK/STAT pathway inhibition sensitizes CD8 T cells to dexamethasone-induced apoptosis in hyperinflammation. Blood 2020; 136:657-68.

Effect of Interleukin-17 gene on glomerular ultrastructure and podocyte injury in adriamycin nephropathy rat models

XH. Yan, QL. Dong*, G. Jin, YN. Zhu and LP. Zhang

Kidney Disease and Dialysis Center, Shaanxi Provincial People's Hospital, Xian, Shaanxi, China

Received December 23, 2020 – Accepted June 4, 2021

The aim of this study was to investigate the mechanism of interleukin-17 (IL-17) gene in renal tissues of rats suffering from adriamycin (ADM) nephropathy and its effect on the expression level of characteristic proteins, such as Podocalyxin and Nephrin, in podocytes. Sprague-Dawley (SD) rats were randomly divided into a control group (treated with normal saline) and an ADM group (treated with adriamycin). ADM model rats were transfected with lentivirus and divided into a transfection group (transfected with recombinant plasmid IL-17-shRNA) and a negative control group (transfected with plasmid shNC). Coomassie brilliant blue G-250 (CBB) method was adopted to detect the levels of albumin in urine to validate the model. The ultrastructure of rat glomeruli was observed, and the ratio of T helper 17 cells/regulatory T cells (Th17/Treg) was measured by flow cytometry (FCM). The expression levels of IL-17, forkhead box P3 (Foxp3), Nephrin, and Podocalyxin were detected by real-time quantitative PCR (RT-qPCR) and western blot analysis. Results of the study showed that the proteinuria content of the ADM group was significantly higher than that of the control group ($P<0.05$). In the ADM group, the glomerular basement membrane had uneven thickness and incomplete structure, which showed foot process fusion and electron dense accumulation. However, the glomerular basal membrane in the transfected rats was thin and intact, and a small amount of epithelial foot process fusion and electron density accumulation were observed. The percentages of Th17 cells and IL-17 levels in the ADM group were significantly higher than those in the control group, while the percentages of Treg cells, Foxp3, Nephrin, and Podocalyxin levels were significantly lower than those in the control group ($P<0.05$). The percentages of Th17 cells, IL-17, Nephrin, and Podocalyxin in the transfection group were significantly higher than those in the ADM group and the negative control group, while the percentages of Treg cells and Foxp3 were significantly lower than those in the ADM group and the negative control group ($P<0.05$). The results of this study showed that abnormal activation of Th17/IL-17 cells caused podocyte injury and promoted the occurrence and progression of ADM nephropathy. In addition, inhibition of IL-17 gene expression could improve the imbalance of number of Th17 and Treg cells, which may be potentially applied in treatment of patients with primary nephrotic syndrome (PNS).

Primary nephrotic syndrome (PNS) is a relatively common chronic renal immune disease (1) which is characterized by proteinuria, and progresses to chronic kidney failure in severe cases (2). Currently, most patients with PNS are treated with glucocorticoids and immunosuppressants, which

Key words: ADM; IL-17; podocyte; TH17/Treg; Foxp3 level

**Corresponding Author:*
Dr Qianlan Dong,
Kidney Disease and Dialysis Center,
Shaanxi Provincial People's Hospital,
Xian 710068, Shaanxi, China
e-mail: qianlandong@yeah.net

0393-974X (2021)
Copyright © by BIOLIFE, s.a.s.
This publication and/or article is for individual use only and may not be further reproduced without written permission from the copyright holder.
Unauthorized reproduction may result in financial and other penalties
DISCLOSURE: ALL AUTHORS REPORT NO CONFLICTS OF INTEREST RELEVANT TO THIS ARTICLE.

have many side effects and do not offer a cure (3, 4). The pathogenesis and mechanism of PNS remain unclear. Recent studies showed that imbalance of the number of Th17 and regulatory T (Treg) cells was involved in several autoimmune diseases, such as IgA nephropathy and kidney transplantation rejection. It also played an important role in the pathogenesis of these diseases (5, 6). Th17 primarily promotes the immune response and inflammatory response, whereas Treg cells suppress the immune response. Therefore, a complicated balance exists between the proportion of Th17/Treg cells in a normal body state. The Th17 cells mainly secrete cytokines such as interleukin (IL)-17, IL-21, and IL-22, out of which IL-17 is the main effector of Th17 cells with its receptors highly expressed in kidney and spleen tissues (7). Previous studies showed that the expression level of IL-17 in patients with PNSwas significantly increased. A positive correlation was found between the percentage of IL-17+γδT cells and Th17/Treg ratio. Moreover, it may be involved in the pathogenesis of PNS in children by regulating the balance of number of Th17 and Treg cells (8). Therefore, it is of great significance to explore the influence of IL-17 gene on ratio of Th17/Treg cells and the pathogenesis of PNS.

Renal sac epithelial cells, also known as podocytes, are terminally differentiated epithelial cells located in the basal membrane of the glomeruli. The glomerular basement membrane, epithelial cells of renal sacs, and capillary endothelium jointly form the glomerular blood filtration barrier. The podocytes play a central role in the formation of the glomerular filtration barrier (9). Relevant studies showed that the main pathological basis of PNS was injury to podocytes, and the loss of podocyte-specific molecules of Nephrin and Podocalyxin. These factors were also closely related to glomerulosclerosis or minimal lesion nephropathy (10). It was found that the expression levels of Nephrin and Podocalyxin in PNS patients were significantly decreased, the Th17/Treg cell ratio was changed, and the expression level of IL-17 was increased. Therefore, the injury to glomerular podocytes may be related to the abnormal activation of Th17/IL-17 (11). Hence, in this study, a rat model of ADM was established, and the expression level of IL-17 gene was blocked by RNA interference. To study the mechanism of IL-17 gene on ADM neuropathy, the ratio of Th17/Treg cells and the expression levels of IL-17, Foxp3, Nephrin, and Podocalyxin were measured. This study provides theoretical basis for clinical prevention and treatment for primary nephropathic podocytopathy.

MATERIALS AND METHODS

Animals and rat ADM model establishment

Healthy male SD rats (n = 90) aged 4-5 weeks and weighing about 200g were selected and kept in a clean experimental animal room at 20-25°C and relative humidity of 50%±20%. All rats were free to drink and eat and were kept in a 12hlight/dark cycle. All procedures of the experimental animals were approved by the experimental animal management committee, and the experimental methods were conducted in accordance with the "Guidelines for the management and use of laboratory animals".

The rats were randomly divided intoa control group (30 rats) and an ADM group (60 rats). The ADM rat model was constructed by single injection of ADM hydrochloride (6.5mg/kg) (Sigma, USA) through the tail vein. The protein content in urine of the rats was measured using Coomassie brilliant blue G-250 (CBB) method after 2 weeks, 4 weeks, 6 weeks, and 8 weeks of modeling. The proteinuria content greater than 500mg/24h indicated that the modeling was successful.

ADM model rats were transfected by lentivirus

Interference sequence IL-17-shRNA was designed and synthesized based on IL-17 gene information to prepare linearized expression vectors. The linearized vector and IL-17-shRNA gene sequence obtained by T4 DNA ligase were transferred into the competent cells. Monoclones were selected on a plate for plasmid extraction, PCR amplification was conducted, and 2% agar-gel electrophoresis was adopted for amplification product identification. After the PCR analysis, subsequent transfection of 293T cells (Shanghai Baiye Biotechnology Company, China) was carried out. The state of the cell was observed. After 48 h, the supernatant layer was collected and centrifuged at 4,500 g for 5min. The supernatant was filtered and centrifuged for 10 min. The

lower layer was separated, centrifuged for 20 min, and the supernatant was separated and retained. Titer detection and transfection efficiency evaluation were performed before lentivirus plasmid transfection to determine the appropriate virus transfection concentration. The ADM rat models were injected with lentivirus plasmid into the tail vein, and the saline-treated group was set as the control group. Peripheral blood was taken at 1 and 2 weeks after transfection, and the transfection efficiency was observed under a fluorescence microscope.

Ultrastructural characteristics of rat glomeruli

The rats were anesthetized and sacrificed. About 1 m^3 of kidney tissues was extracted, fixed with glutaraldehyde (Shanghai Xinfan Biotechnology Co., Ltd., China) for 2 h, and cleaned with phosphate buffer saline (PBS) (Sigma, United States) for 30 min. Subsequently, 1% osmium acid (Shanghai Standards Biotechnology Co., Ltd., China) was used to fix the tissues again for 90 min, and it was rinsed for 30 min using 0.1 M phosphate rinse solution (Beijing Baiolaibo Technology Co., Ltd., China). Acetone of gradient concentrations (Shanghai Xinfan Biotechnology Co., Ltd., China) (50%, 15 min; 70%, 15 min; 80%, 15 min, 90%, 15 min; and 100%, 40 min) was used for dehydration, acetone and 812 embedding solution (Shanghai Cayou Industrial Co., Ltd., China) were used for embedding at a ratio of 1:1, 1:3, and 1:0. The mixture was left to stand overnight. The tissue slices were prepared by placing them in an oven at 45°C for 24 h followed by another 48 h at 60°C. Lead citrate (Beijing Jimei Biotechnology Co., Ltd., China) and uranium acetate (Shanghai Xinfan Biotechnology Co., Ltd., China) were successively used for dyeing treatment, and the results were observed under a transmission electron microscope.

Flow cytometry (FCM)

Peripheral blood Th17 cells were detected by FCM. 250μL of whole blood was collected after ether anesthesia and diluted to 500 μL using RPMI-1640 medium (Gibco, USA). The tubes were divided into the control tubes and test tubes. In the tubes, a 250 μL diluted full blood sample, 1 μL PMA (Hangzhou Lianke Biotechnology Co., Ltd., China), and 1 μL Monensin (Hangzhou Lianke Biotechnology Co., Ltd., China) were mixed. The tubes were then incubated for 12 h. After centrifugation, the supernatant was discarded for cell lysis. The cells were resuspended with PBS and transferred into an EP (Eppendorf) tube (Shanghai Dingji Biotechnology Co., Ltd., China). The tube was centrifuged at 2,500r/min for 5min before discarding the supernatant. The sample was washed with PBS twice, and 1 μL Anti-Rat CD8a PE (EBI, US) and 1 μL Anti-Rat CD3 FITC (EBI, US) were added, and incubated for 30 min. After washing with PBS, the supernatant was again removed by centrifugation. After fixing, the sample was incubated for 20 min. After washing with PBS, the supernatant was discarded by centrifugation. The intra-prep permeabilization reagent was adopted to treat the cells, after which the sample was incubated for 20 min, centrifuged at 1,000r/min for 5 min, and the supernatant was discarded. 1μL Anti-Rat IL-17A APC (EBI, USA) was added to the test tubes after PBS washing, and 1 μL monoclonal antibody APC-IgG1 (EBI, USA) was added to the control tubes. The samples were incubated at 4°C in a dark environment for 30 min, washed with PBS, centrifuged and then discarded. The cells were resuspended with PBS and detected by FCM.

Detection of peripheral blood Treg cells by FCM was performed as follows. Briefly, 200 μL whole blood was collected after rats were anesthetized with ether, and 100 μL whole blood was added into the labeled control and test tubes. 1 μL Anti-rat CD4 ECD (EBI, USA) and 1 μL Anti-rat CD25 PE (EBI, USA) were added into both tubes. The cells were incubated for 30 min, centrifuged at 1,000r/min for 5 min, and then the supernatant was discarded. The cells were resuspended with PBS and centrifuged again. The cell lysis buffer was added and the tubes were kept still for 5 min. After centrifugation, the supernatant was discarded. After treatment with intra-prep permeabilization reagent, it was incubated for 20 min, then centrifuged and discarded. The tissues were washed with PBS and 1μL Anti-rat Foxp3 Percp cy5 was added into the test tubes (EBI, USA) and 1 μL monoclonal Percp y-IgG2 (EBI, USA) was added into the control tubes. The cells were incubated for 30 min and then washed with PBS. After centrifugation, the supernatant was discarded. The cells were resuspended with PBS and detected by FCM.

RT- fluorescent qPCR

RNA was extracted from the blood samples, and cDNA was obtained by reverse transcription. The fluorescence qPCR instrument (Shanghai Sunshine Biotechnology Co., Ltd., China) was used to detect mRNA expressions of

major effector factors IL-17, transcription factors Foxp3, Nephrin, and Podocalyxin, with GAPDH as the internal reference. Primer design is shown in Table I.

The 50 μL reaction system consisted of 2 × 25μL of RealStar Power SYBR Mixture UNG, 1 μL cDNA, 1 μL upstream primer, 1 μL downstream primer, and 22 μL deionized water.

Western blot

Protein expression levels of Podocalyxin and Nephrin, the characteristic molecules of Podocytes, were measured by JY-ZY5 Western blot transfer electrophoresis apparatus (Beijing Junyi Eastern Electrophoresis Equipment Co., Ltd., China). First, the renal tissue was homogenized and cell lysate was added. After being homogenized, the renal tissue was transferred to a new EP tube, which was placed on ice for half an hour and centrifuged to collect the cell superfluid. Protein concentrations were measured according to the instructions of the bicinchoninic acid (BCA) kit (Sigma, USA). 10% SDS polyacrylamide gel was prepared (Shanghai Hengdailao Biology Co., Ltd., China) and the sample was subjected to electrophoresis. After electrophoresis, the sodium fluoride protein was transferred into polyvinylidene fluoride (PVDF) membrane by wet transfer. The sample was sealed with 5% bovine serum albumin (BSA) at room temperature for 1 h, and the membrane was washed with Tri-buffered saline tween (TBST) for 10 min three times, followed by an overnight incubation with primary antibody at 4°C. The TBST film was washed three times, 10 min each time. Then the film was washed three times at room temperature and was later combined with the secondary antibody for 1 h, and the film was exposed to an anechoic chamber for development and imaging analysis.

Statistical analysis

SPSS 20.0 statistical software was adopted for analysis. The measurement data were expressed as mean ± standard deviation (±s) and were compared by *t*-test between groups; the counting data were expressed as percentage (%), and compared with *chi*-squared test between groups. $P<0.05$ was considered statistically significant.

RESULTS

Proteinuria and IL-17 expression in ADM model rats

The determination of proteinuria in rat urine at 2, 4, 6, and 8 weeks after modeling by CBB method is

Table I. *Fluorescence qPCR primer sequences.*

Primer	**Sequence**
Podocalyxin-F	ATCACCATCGTCTGCATGG
Podocalyxin-R	GCTCCTCTGTGAGTCGTTGTT
Nephrin -F	TGACTCCTAAAGTAATCCTCTCTCCATT
Nephrin-R	CCCAGCTACCCAGGTCAC
Foxp3-F	GAGAAGATACTGGTGTCCGTGG
Foxp3-R	TGAGTTTAGTCCGAAATGAGGC
IL-17-F	GAGAAGATACTGGTGTCCGTGG
IL-17-R	TGAGTTTAGTCCGAAATGAGGC
GAPDH-F	TGGACCTGACCTGCCGTCTAG
GAPDH-R	AGGAGTGGGTGTCGCTGTTGA

shown in Fig.1A. The proteinuria content (mg/24h) in the control group was stable at 2, 4, 6, and 8 weeks, which was 6.22±0.35, 6.39±0.46, 6.42±0.52, and 6.24±0.26, respectively, whereas the proteinuria (mg/24h) of ADM group at 2, 4, 6 and 8 weeks was 67.34±18.21, 375.32±20.37, 518.56±26.42, and 502.10±21.39, respectively. Proteinuria appeared in the rats of the ADM group at the second week of modeling, and it peaked at the sixth week, when it was greater than 500mg/24h, indicating successful modeling. Proteinuria in the ADM group was significantly higher than that in the control group at 2, 4, 6, and 8 weeks after modeling (P<0.05). Fig.1 B, C showed the expression levels of IL-17 in peripheral blood and renal tissues of rats at week 2, 4, 6, and 8 after modeling. The expression levels of IL-17 in peripheral blood and renal tissues of ADM group at 2, 4, 6, and 8 weeks after modeling were significantly higher than those of the control group (P<0.05).

Transfection efficiency of recombinant lentivirus vectors

Fig. 2 A, B shows the expression of 293T cells after 1 week of transfection, and Fig. 2 C, D shows the expression of 293T cells after 2 weeks of transfection. Compared with that at 1 week after transfection, the number of cells labeled with green fluorescent protein increased at 2 weeks after

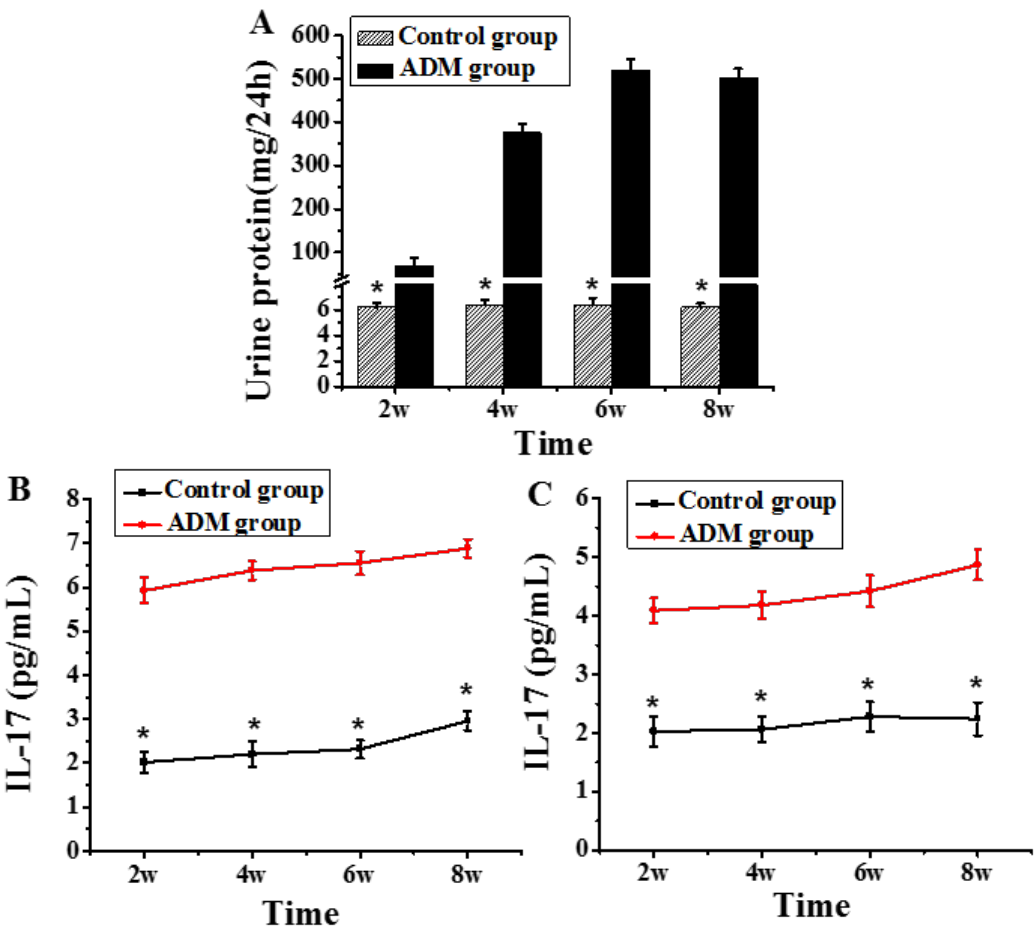


Fig. 1. *Proteinuria content and IL-17 expression at different time points after modeling. **A**) content of proteinuria; **B**) IL-17 levels in peripheral blood; **C**) IL-17 levels in renal tissues. * P<0.05, compared to ADM group.*

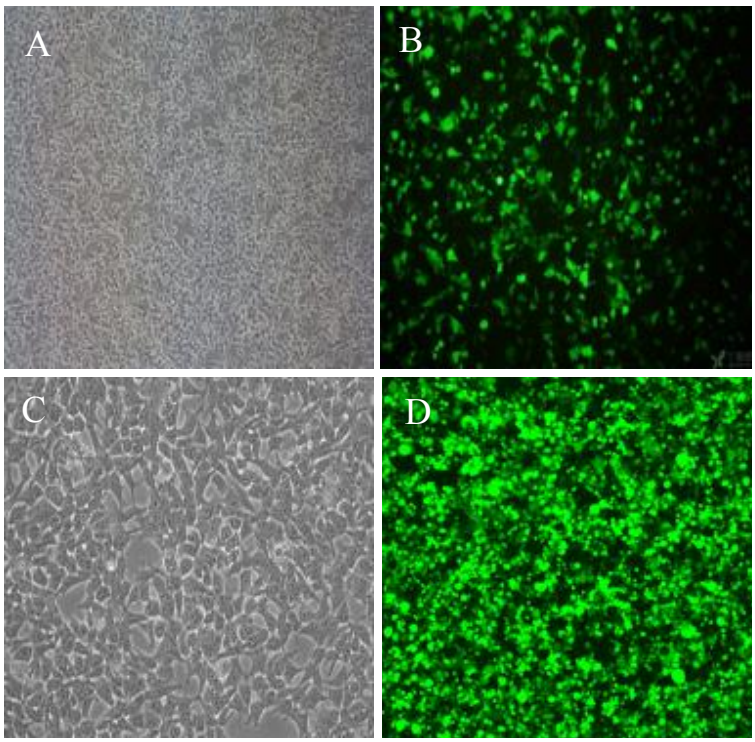


Fig. 2. *Transfection efficiency of ADM model rats with lentivirus-mediated transfection under a fluorescence microscope.* ***A****) white light, 50×, 1 week;* ***B****) fluorescence, ×50, 1 week;* ***C****) white light, ×100, 2 weeks; D: fluorescence, ×5, 2 weeks.*

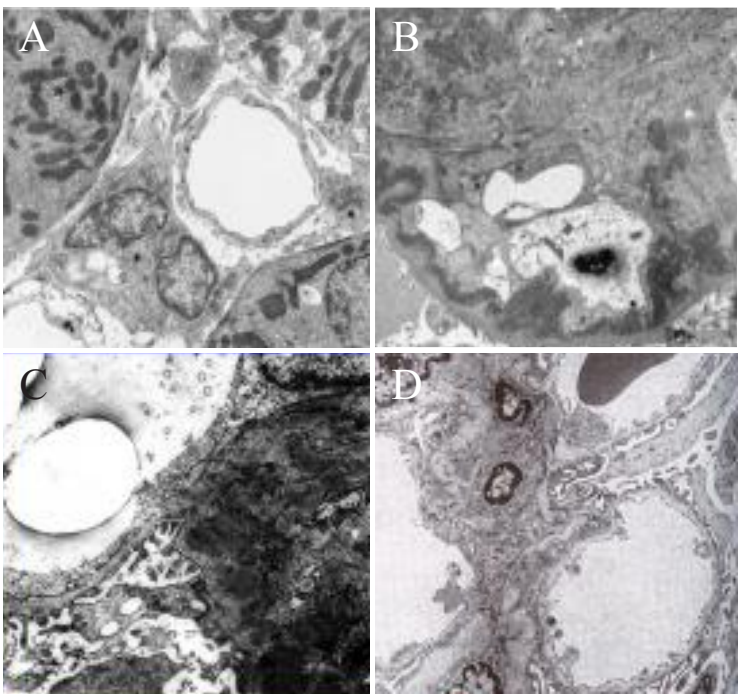


Fig. 3. *Ultrastructure of rat glomeruli, ×10000.* ***A****) control group;* ***B****) ADM group;* ***C****) negative control group;* ***D****) transfection group.*

transfection, which showed enhanced fluorescence, and the transfection efficiency reached over 90%, indicating a successful construction of lentivirus.

Ultrastructural changes of glomeruli

The results of transmission electron microscope scanning of rat glomeruli are shown in Fig. 3. The basal membrane of rat glomeruli of the control group was uniform and complete, normal microvilli of podocytes could be seen, no mesangial matrix hyperplasia was observed, and no electron dense accumulation was found. In the ADM group, the glomerular basement membrane had uneven thickness and incomplete structure, which showed foot process fusion and electron dense accumulation. In the negative control group, the glomerular basement membrane was uneven in thickness, and a large number of foot processes diffused fusion and electron dense accumulation were observed. The glomerular basement membrane of the transfected rats was thin and intact, and a small amount of epithelial foot process fusion and electron density accumulation was observed.

Peripheral blood Th17/Treg cells ratio and the expression levels of IL-17 and Foxp3

The number and proportion of Th17 cells and Treg cells in peripheral blood of rats were measured by FCM, and the results are shown in Fig.4A. The percentage of Th17 cells in the ADM group was significantly higher than that in control group, while the percentage of Treg cells in the ADM group was significantly lower than the control group (P<0.05). The percentage of Th17 cells in the transfection group was significantly higher than that in the ADM group and negative control group, while the percentage of Treg cells was significantly lower than those in the ADM group and negative control group (P<0.05). There was no significant difference in cell percentage between the ADM group and negative control group (P>0.05). The mRNA expression levels of IL-17 and Foxp3 in peripheral blood of rats were measured by fluorescence RT-qPCR and the results are as shown in Fig. 4B. The expression level of IL-17 in the ADM group was significantly higher than that in the control group, while the expression level of Foxp3 was significantly lower than that in

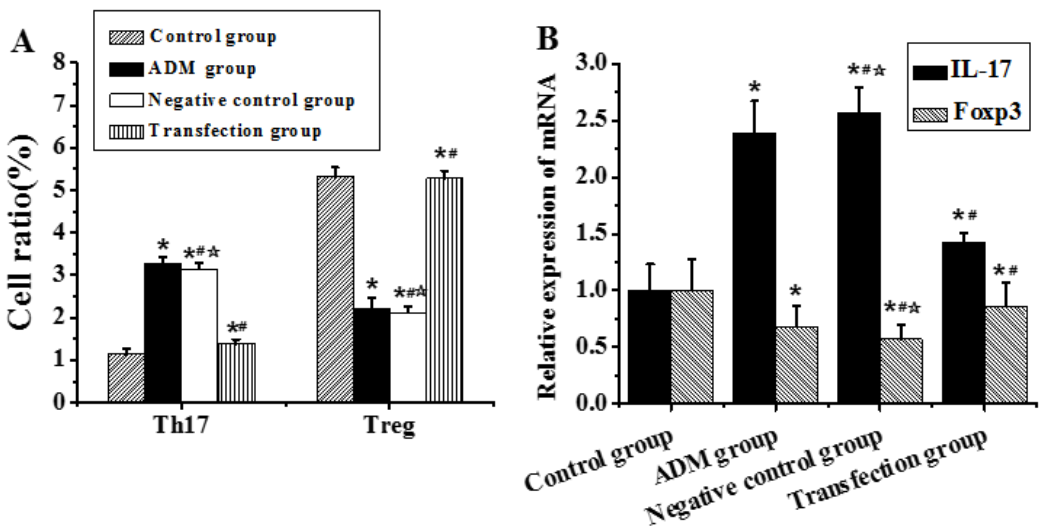


Fig. 4. *Peripheral blood Th17/Treg cell ratio and mRNA expression levels of IL-17 and Foxp3.* ***A****) Th17/Treg cell ratio;* ***B****) mRNA expression levels of IL-17 and Foxp3.*

** P<0.05, compared with the control group; # P<0.05, compared with the ADM group; P<0.05, compared with the transfection group.*

the control group (P<0.05). The expression level of IL-17 in the transfection group was significantly higher than that in the ADM group and negative control group, whereas the expression level of Foxp3 was significantly lower than that in the ADM group and negative control group (P<0.05). There was no significant difference in IL-17 and Foxp3 expression between ADM group and negative control group (P>0.05).

Protein and mRNA expression levels of Nephrin and Podocalyxin

Fig.5A shows the mRNA expression levels of Nephrin and Podocalyxin in rat renal tissues. The expressions of Nephrin and Podocalyxin in the ADM group were significantly lower than those in the control group (P<0.05). The expression levels of Nephrin and Podocalyxin in the transfection group were significantly higher than those of the ADM group and the negative control group (P<0.05). However, there was no significant difference in Nephrin and Podocalyxin expression levels between the ADM group and the negative control group (P>0.05). Comparisons of protein expression levels of Nephrin and Podocalyxin in rat renal tissues are shown in Fig. 5 B, C. The protein expression levels of Nephrin and Podocalyxin in the ADM group were significantly lower than those in control group (P<0.05). The protein expression levels of Nephrin and Podocalyxin in the transfection group were significantly higher than those of the ADM group and the negative control group (P<0.05). However, there was no statistically significant difference in the protein expression levels of Nephrin and Podocalyxin between the ADM group and the negative control group (P>0.05).

DISCUSSION

The most obvious clinical feature of PNS was the production of proteinuria (12). In this study, ADM rat model was prepared by a one-time injection of

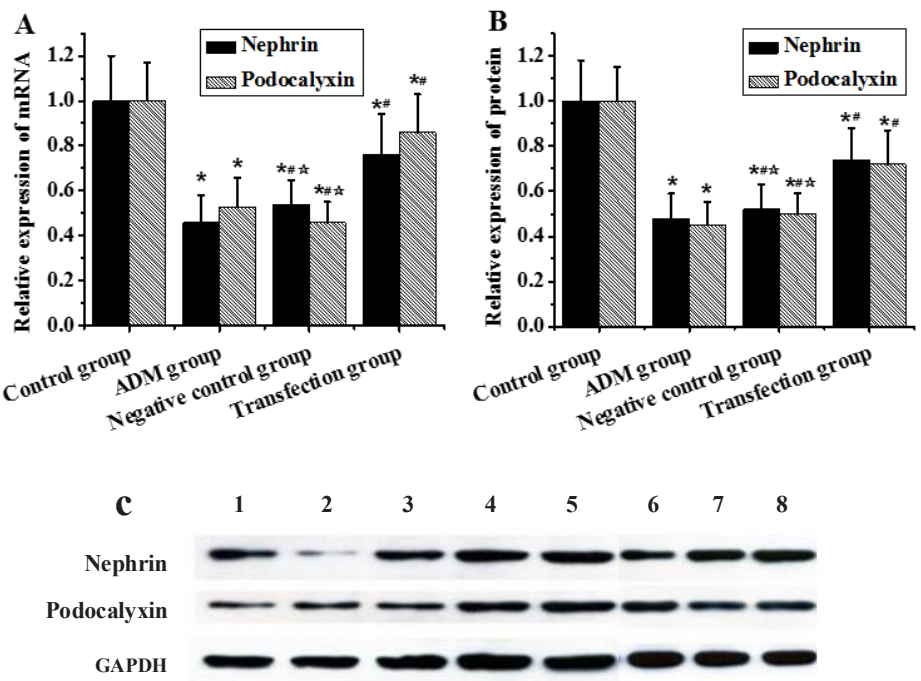


Fig. 5. *mRNA and protein expressions of Nephrin and Podocalyxin in rat renal tissues. **A**) mRNA expression levels of Nephrin and Podocalyxin; **B** and **C**) protein expression levels of Nephrin and Podocalyxin. C) 1, 2: control group. 3, 4: ADM group; 5, 6: negative control group; 7, 8: transfection group. * P<0.05, compared with the control group; # P<0.05, compared with the ADM group; P<0.05, compared with the transfection group.*

ADM hydrochloride into the tail vein. Proteinuria was first observed in the rats at the second week of modelling and peaked at week 6, which was greater than 500mg/24h, indicating that the modeling was successful. Moreover, the protein content of urine in the ADM group at weeks 2, 4, 6, and 8 after modeling was significantly higher than in the control group (P<0.05). In the present study, the glomerular basement membrane of the rats in the control group was uniform in thickness and complete in structure, normal podocyte microvilli could be seen, and no mesangial matrix proliferation nor electron density accumulation were observed. In the ADM group, the glomerular basement membrane had uneven thickness and incomplete structure, indicating foot process fusion and electron dense accumulation. The results showed that the glomerular structure of rats with ADM nephropathy was changed compared with that of the control group. Studies found that the effect of Th17 and Treg cells on immune response were opposite and dependent on each other under normal physiological condition. Under abnormal physiological condition, an imbalance of number of Th17 and Treg cells leads to onset of immune response, eventually resulting in autoimmune diseases (13). IL-17 was the main effector of Th17 cells (14) and Foxp3 was the main transcription factor of Treg cells. Both IL-17 and Foxp3 played a leading role in the pathogenesis of PNS (15). Zhang et al. (16) induced nephropathy in rats by single injection of ADM hydrochloride, and AIN rats developed severe albuminuria, hypoalbuminemia, hyperlipidemia, and podocyte injury. The rats manifested disorder of the cytokine network and decreased Foxp3 level. These observations were in line with the results of this study. The authors showed that the percentages of Th17 cells and IL-17 levels in the ADM group were significantly higher than those in the control group, while the percentages of Treg cells and Foxp3 levels were significantly lower than those in the control group (P<0.05).

Podocytes, as the main components of the glomerular filtration barrier system, would have an impact on the permeability of the glomerular filtration system if damaged, thereby increasing the proteinuria content and causing the occurrence and progression of PNS (17). Podocalyxin and Nephrin were the specific markers of podocytes, which have been commonly used in the detection of podocytic injury (18). It was found in this study that mRNA and protein expression levels of Nephrin and Podocalyxin in rat glomerular in the ADM group were significantly lower than those in control group (P<0.05). It was indicated that ADM could induce podocyte injury in rat nephropathy, and the podocyte-specific molecules, Nephrin and Podocalyxin, were relatively low (19). Subsequently, RNA interference was used to explore the cell, gene, and protein levels from the perspective of molecular biology, and it was found that after RNA interference with IL-17 gene, the percentage of Th17 cells, IL-17 levels, Nephrin, and Podocalyxin levels in the transfected rats group were significantly higher than those in the ADM group and the negative control group, while Treg cell percentages and Foxp3 levels were significantly lower compared to the ADM group and negative control group (P<0.05). It was also indicated that IL-17 secreted by Th17 cells was silenced by RNA interference technology, which could regulate the imbalance of number of Th17 and Treg cells, inhibit the IL-17-mediated podocyte injury, and play an effective role in controlling the progression of PNS.

In conclusion, abnormal activation of Th17/IL-17 could cause podocyte injury and promote the occurrence and progression of ADM nephropathy. Hence, inhibition of IL-17 gene expression could improve the imbalance of number of Th17 and Treg cells, which could potentially act as a novel clinical treatment approach for PNS. However, in this study Th17/Treg and podocyte-related signaling pathways have not been explored. Therefore, further studies are required to confirm these results.

ACKNOWLEDGEMENT

This work was supported by Shaanxi social development fund (No. S2016YFSF0644).

REFERENCES

1. Wang CS, Greenbaum LA. Nephrotic Syndrome. Pediatr Clin North Am 2019; 66(1):73-85.

2. Kopp JB. Global glomerulosclerosis in primary nephrotic syndrome: including age as a variable to predict renal outcomes. Kidney Int 2018; 93(5):1043-4.
3. Yamamoto R, Imai E, Maruyama S, et al. Regional variations in immunosuppressive therapy in patients with primary nephrotic syndrome: the Japan nephrotic syndrome cohort study. Clin Exp Nephrol 2018; 22(6):1266-80.
4. Liu J, Wan Z, Song Q, et al. NR3C1 gene polymorphisms are associated with steroid resistance in patients with primary nephrotic syndrome. Pharmacogenomics 2018; 19(1):45-60.
5. Mortazavi H, Soltani-Zangbar MS, Eghbal-Fard S, et al. Cytokine profile, Treg/Th17 cell frequency changes during different posttransplantational time points in patients undergoing renal transplantation. J Cell Physiol 2019; 234(11):20935-20943.
6. Yang Y, Liu K, Chen Y, Gong Y, Liang Y. Indoleamine 2,3-Dioxygenase (IDO) Regulates Th17/Treg Immunity in Experimental IgA Nephropathy. Folia Biol (Praha) 2019; 65(2):101-8.
7. Mehrotra P, Collett JA, Gunst SJ, Basile DP. Th17 cells contribute to pulmonary fibrosis and inflammation during chronic kidney disease progression after acute ischemia. Am J Physiol Regul Integr Comp Physiol 2018; 314(2):R265-R273.
8. Zhang L, Yan J, Yang B, et al. IL-23 Activated γδ T cells affect Th17 cells and fegulatory T cells by secreting IL-21 in children with primary nephrotic syndrome. Scand J Immunol 2018; 87(1):36-45.
9. Schell C, Sabass B, Helmstaedter M, et al. ARP3 controls the podocyte architecture at the kidney filtration barrier. Dev Cell 2018; 47(6):741-57.
10. Milas O, Gadalean F, Vlad A, et al. Pro-inflammatory cytokines are associated with podocyte damage and proximal tubular dysfunction in the early stage of diabetic kidney disease in type 2 diabetes mellitus patients. J Diabetes Complications 2020; 34(2):107479.
11. Yan J, Li Y, Yang H, Zhang L, Yang B, Wang M, Li Q. Interleukin-17A participates in podocyte injury by inducing IL-1β secretion through ROS-NLRP3 inflammasome-caspase-1 pathway. Scand J Immunol 2018; 87(4):e12645.
12. Singh R, Bhalla K, Nanda S, Gupta A, Mehra S. Correlation of spot urinary protein: Creatinine ratio and quantitative proteinuria in pediatric patients with nephrotic syndrome. J Family Med Prim Care 2019; 8(7):2343-6.
13. Yang XY, Song J, Hou SK, et al. Ulinastatin ameliorates acute kidney injury induced by crush syndrome inflammation by modulating Th17/Treg cells. Int Immunopharmacol 2020; 81:106265.
14. Zhai S, Sun B, Zhang Y, Zhao L, Zhang L. IL-17 aggravates renal injury by promoting podocyte injury in children with primary nephrotic syndrome. Exp Ther Med 2020; 20(1):409-17.
15. Shao XS, Yang XQ, Zhao XD, et al. The prevalence of Th17 cells and FOXP3 regulate T cells (Treg) in children with primary nephrotic syndrome. Pediatr Nephrol 2009; 24(9):1683-90.
16. Zhang Y, Liu W, Li D. Matrine attenuates high glucose-induced podocyte injury by inhibiting HMGB1-associated TLR4-NF-κB signaling. Int J Clin Exp Med 2019; 12(7):8512-21.
17. Yang X, Wu Y, Li Q, Zhang G, Wang M, Yang H, Li Q. CD36 promotes podocyte apoptosis by activating the Pyrin Domain-Containing-3 (NLRP3) inflammasome in primary nephrotic syndrome. Med Sci Monit 2018; 24:6832-9.
18. Kocatürk H, Atasoy N, Bedir F, Karabulut İ, Şebin E, Sarica K. Evaluation of the urinary podocalyxin and nephrin excretion levels to determine a safe time interval between two sessions of SWL for renal stones: a non-randomized exploratory study. Int Urol Nephrol 2019; 51(10):1727-1734.
19. Qiu B, Gao X, Cui WJ, et al. Dexamethasone blocks adriamycin-induced podocytes' mobility via impacting nephrin expression. Sichuan Da Xue Xue Bao Yi Xue Ban 2019; 50(2):197-202.

Maintenance of cellular annexin A1 level is essential for PI3K/AKT/mTOR-mediated proliferation of pancreatic beta cells

ZY. Gu[1,2*], XY. Miao[1,2*], LC. Ma[1,2], JJ. Gao[3], YP. Gong[1,2] and CL. Li[1,2]

[1]Department of Endocrinology, Second Medical Center, Chinese PLA General Hospital, Beijing, China; [2]National Clinical Research Center for Geriatric Diseases, Chinese PLA General Hospital, Beijing, China; [3]Department of Nephrology, the 306th Hospital of Chinese PLA, Beijing, China

Received July 2, 2020 - Accepted March 16, 2021

*These authors contributed equally to this work

Annexin A1 (AnxA1, also known as lipocortin-1), is a calcium-dependent phospholipid binding protein with diverse functions. Previous studies have indicated that AnxA1 is associated with age-related β-cell dysfunction and aging, which lead to decreased β-cell proliferation capacity. However, it has been uncertain whether AnxA1 affects the proliferation of pancreatic beta (β) cells. In the present study, we reduced AnxA1 expression in the MIN6 islet β-cell line using small interfering RNA (AnxA1-siRNA), then measured cell cycle distribution and cellular proliferation. We also measured the expression levels of cell cycle-related proteins such as cyclin D1, cyclin E, and cyclin-dependent kinase 2 (CDK2) by Western blot analysis. We investigated the phosphatidylinositol 3-kinase (PI3K)/ serine/threonine protein kinase B (Akt)/mammalian target of rapamycin (mTOR) signaling pathway to explore the potential mechanism underlying the observed effects. Knockdown of AnxA1 expression using siRNA reduced the rates of MIN6 cell proliferation. The proportions of cells in S and G2/M phases also decreased upon inhibition of AnxA1. Moreover, AnxA1 protein expression in MIN6 cells was positively related to the protein levels of cyclin D1, cyclin E, and CDK2. Activation of the PI3K/Akt/mTOR signaling pathway by AnxA1 may be involved in the signaling cascade to regulate cell proliferation. This study identified a positive correlation between AnxA1 protein and pancreatic β-cell proliferation. AnxA1 protein expression might affect the proliferation of MIN6 cells via regulation of cyclin D1, cyclin E, and CDK2 proteins, as well as the PI3K/Akt/mTOR signaling pathway.

The aging global population is associated with an increase in age-related illnesses, such as diabetes. Islet beta (β)-cell dysfunction is a core component of diabetes that is associated with reductions in β-cell number and insulin secretion ability. A previous study demonstrated that aging is related to reduced β-cell proliferation capacity and enhanced sensitivity to apoptosis (1). Therefore, enhancement of islet β-cell proliferation and prevention of apoptosis will be important in developing new treatments for diabetes.

Annexin A1 (AnxA1, also known as lipocortin-1) reportedly has a diffuse and homogeneous distribution in all pancreatic islet cells. AnxA1 may also be involved in the regulation of β-cell

Key words: Islet beta cell; AnxA1; cell cycle; signaling pathway

Corresponding Author:
Dr Chunlin Li,
Department of Endocrinology,
Second Medical Center & National Clinical Research Center for Geriatric Diseases, Chinese PLA General Hospital,
28 Fuxing Road, Haidian District, Beijing 100853, China
Tel./Fax: +86 010 66876325
e-mail: lichunlin301@163.com

0393-974X (2021)
Copyright © by BIOLIFE, s.a.s.
This publication and/or article is for individual use only and may not be further reproduced without written permission from the copyright holder.
Unauthorized reproduction may result in financial and other penalties
DISCLOSURE: ALL AUTHORS REPORT NO CONFLICTS OF INTEREST RELEVANT TO THIS ARTICLE.

function in rat pancreatic islets (2). Our previous studies demonstrated that AnxA1 expression was dramatically upregulated in the context of age-related β-cell dysfunction in elderly rats, and we proposed that AnxA1 may contribute to age-related β-cell dysfunction and apoptosis (3). However, the relationships of β-cell apoptosis/proliferation with AnxA1 expression have not yet been well-explored.

AnxA1 is a calcium-dependent phospholipid binding protein, which was originally described as a glucocorticoid-inducible protein with anti-inflammatory properties (4, 5). On the basis of recent research, AnxA1 may represent a promising target for metastatic breast cancer and esophageal squamous cell carcinoma therapy (6-8). However, AnxA1 also plays a major regulatory role in diverse systems (e.g., proliferation and differentiation, neutrophil migration, neuroendocrine secretion, and apoptosis) (9-11). Most mechanistic studies indicate that AnxA1 inhibits cytosolic phospholipase 2 activity, as well as arachidonic acid and phospholipid generation (12), which may explain some of its anti-inflammatory and anti-proliferative functions. However, the phosphorylation of AnxA1 may function as a "signal amplifier" promoting the release of intercellular messengers (PGE2), in addition to cell proliferation, chemotaxis, and vascular remodeling (13), therefore, the effects of AnxA1 on cell proliferation differ among cell types.

It is critically important to elucidate the effects of AnxA1 on islet β-cell apoptosis/proliferation and the precise underlying mechanisms involved. In this study, we investigated proliferation and AnxA1 expression in the MIN6 islet β-cell line under various glucose concentrations. Furthermore, using a gene silencing approach with small interfering RNA (siRNA), we determined the role of AnxA1 in regulation of MIN6 cell proliferation and elucidated potential underlying mechanisms.

MATERIALS AND METHODS

Cell culture and treatment

The MIN6 cell line was purchased from the Chinese Academy of Sciences (Shanghai, China), and cultured in Dulbecco's Modified Eagle's Medium (Gibco, Grand Island, NY, USA) supplemented with 15% fetal bovine serum, penicillin (100 IU/mL), and streptomycin (100 μg/mL) at 37°C under 5% CO_2 in a humidified incubator. To determine the effects of glucose on cell proliferation, 40% confluent monolayers of MIN6 cells were cultured in 96-well plates with different concentrations of glucose (5.5, 11.1, 16.7, 25, and 33.3 mM). In some groups, the phosphatidylinositol 3-kinase (PI3K)/protein kinase B (AKT) inhibitor LY294002 was administered at a concentration of 15 nmol/L, and the mammalian target of rapamycin (mTOR) inhibitor rapamycin was administered at a concentration of 20 nmol/L. After 72 h of exposure, cells were collected for the evaluation of proliferation or Western blot analysis.

Cell transfection

MIN6 cells were grown in 25 mM glucose and were transfected with AnxA1-siRNA or scrambled-siRNA (Santa Cruz Biotechnology, USA) using siRNA transfection reagent (Polyplus-transfection, France), in accordance with the manufacturer's protocol. Briefly, cells were seeded in six-well plates at a density of 2×10^5 cells per well. Before transfection, cells were incubated in antibiotic-free medium overnight. AnxA1 or scrambled-siRNA (2.2 μL of 20 μM solution), mixed with Polyplus-transfection reagent, was added to 200 μL of OPTIM-MEM medium and mixed by vortexing, then incubated for 10–15 min at room temperature. The transfection mixture (200 μL) was added dropwise to each well of MIN6 cells for even distribution over the growing cells. After 24 h, the transfection medium was replaced with 2 mL of growth medium, and the cells were grown for an additional period of time. Cells were harvested for analysis at the end of the culture period.

Cell proliferation assay

To assess cell proliferation, the number of living cells was detected using a Cell Counting Kit-8 assay (Beyotime, China). After exposure to different concentrations of glucose for 72 h, the number of viable cells was measured by recording the optical density at 450 nm and generating cell growth curves. Experiments were repeated three times and six replicates per condition were used.

Fluorescence-activated cell sorting analysis

MIN6 cells were seeded in six-well plates at a density

of 2 × 10^5 cells/well, synchronized by incubation in serum-free medium for 12 h, then transfected with siRNA. The cells were washed twice with phosphate-buffered saline, then fixed by suspension in 75% ethanol and incubation at 4°C overnight. The fixed cells were collected by centrifugation, washed with phosphate-buffered saline, treated with RNase (50 μg/mL; Sigma), and stained with propidium iodide (50 μg/mL; Sigma). A fluorescence-activated cell sorting flow cytometer (Becton Dickinson, USA) was used to measure cellular DNA content. The proportions of cells in the G0/G1, S, and G2/M phases were counted using Cell FIT Cell cycle Analysis software (version 2.01.2; Becton Dickinson). Experiments were repeated three times.

Reverse transcription polymerase chain reaction assay

Total RNA was extracted from MIN6 cells and AnxA1 messenger RNA (mRNA) was examined by reverse transcription polymerase chain reaction with 5'-GAAGGGTGCCGGAACTCGCC-3' (sense) and 5'-CCACCACACAGAGCCACCAGG-3' (antisense) primers. β-actin was used as the control, with 5'-CATTGCTGACAGGATGCAGAAG-3' (sense) and 5'-AGAAGCATTTGAGGTGCAC-3' (antisense) primers. Polymerase chain reaction was performed using the following procedure: denaturation at 94°C for 5 min; 40 cycles at 94°C for 45 s, 60°C for 45 s, and 72°C for 45 s; followed by extension at 72°C for 5 min. Polymerase chain reaction products were evaluated by 1% agarose gel electrophoresis mixed with 1 μL/mL ethidium bromide. Images were captured under an ultraviolet lamp.

Western blot analysis

MIN6 cells were washed with phosphate-buffered saline and lysed in RIPA buffer containing 20 μg/mL leupeptin, 10 μg/mL aprotinin, and 1 mM phenylmethylsulfonyl fluoride. Cell lysates were incubated on ice for 30 min, then centrifuged at 12,000 × g at 4°C for 30 min; the supernatants were diluted with sodium dodecyl sulfate sample buffer and heated to 100°C for 5 min. At least 50 μg of protein was separated by sodium dodecyl sulfate polyacrylamide gel electrophoresis, then electrotransferred onto nitrocellulose membranes. Membranes were blocked with casein for 4 h and subsequently incubated with primary antibodies at 4°C overnight. Primary antibodies included anti-AnxA1 (1:250, Abcam, USA), anti-Akt1/2/3 (1:1000, Cell Signaling Technology, USA), anti-phosphorylated-Akt^{473} (1:1000, Cell Signaling Technology), anti-cyclin D1 (1:200, Santa Cruz Biotechnology), anti-cyclin-dependent kinase 2 (CDK2; 1:200, Santa Cruz Biotechnology), anti-cyclin E (1:200, Santa Cruz Biotechnology), anti-mTOR (1:1000, Cell Signaling Technology), and anti-phospho-mTOR (1:400, Cell Signaling Technology). After membranes had been washed with Tris-buffered saline containing 0.1% Tween-20, they were probed with horseradish peroxidase-conjugated secondary antibodies (Zhongshan Golden Bridge Biotechnology, Beijing, China) at a dilution of 1:2,000 in Tris-buffered saline containing 0.1% Tween-20 for 40 min at 37°C. Immunoreactive bands were visualized with an enhanced chemiluminescence kit (Zhongshan Golden Bridge Biotechnology) and captured on X-ray film.

Statistical analysis

All data examined were expressed as means ± standard deviations (SDs). For Western blot analysis, quantitation was carried out by scanning and analysis of band intensity using ImageJ software. Statistical analysis of the data was conducted using SPSS statistical software, version 16.0 (SPSS, Chicago, IL, USA). Comparisons between groups were conducted using analysis of variance; p-values < 0.05 were considered statistically significant.

RESULTS

Glucose induces MIN6 cell proliferation in a dose-dependent manner and is associated with AnxA1 expression

MIN6 cells were incubated with various concentrations of glucose for 72 h. Proliferation was measured using a Cell Counting Kit-8 assay. As shown in Fig. 1A, cell proliferation significantly increased with increasing glucose concentration, up to 25 mM. However, cell proliferation was lower at a glucose concentration of 33.3 mM than at a glucose concentration of 25 mM. To explore the relationship between cell proliferation and AnxA1 expression, we performed Western blot analysis. AnxA1 protein expression in MIN6 cells increased with increasing glucose concentration (Fig. 1B). However, AnxA1 protein expression in MIN6 cells did not

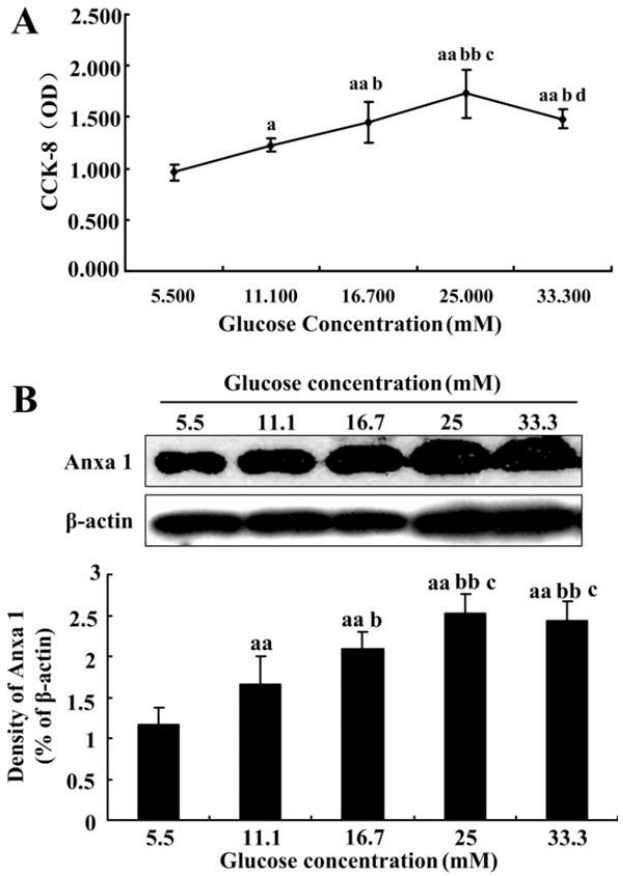


Fig. 1. *Proliferation and AnxA1 expression of MIN6 cells induced under different glucose concentrations. After exposure to various concentrations of glucose for 72 h, (**A**) the proliferation of MIN6 cells was detected using a Cell Counting Kit-8 assay. The experiments were repeated three times, using six replicates per condition. **B**) The ratio of AnxA1 to β-actin expression in MIN6 cells was determined using Western blot assays with specific antibodies (n = 5 per group). Data shown are representative images or expressed as means ± SDs. a = p < 0.05, aa = p < 0.01 compared with 5.5 mM group; b = p < 0.05, bb = p < 0.01 compared with 11.1 mM group; c = p < 0.05 compared with 16.7 mM group; d = p < 0.05 compared with 25 mM group.*

significantly differ between glucose concentrations of 25 mM and 33.3 mM. Changes in AnxA1 protein expression with different concentrations of glucose followed a pattern similar to the changes in MIN6 cell proliferation. Therefore, we speculated that cell proliferation might be related to AnxA1 protein expression in MIN6 cells.

Effects of siRNA transfection on AnxA1 expression and MIN6 cell proliferation

To further investigate whether the proliferation of MIN6 cells was regulated by AnxA1, we carried out siRNA experiments. Reverse transcription polymerase chain reaction and Western blot analysis showed the reduction of AnxA1 mRNA and protein expression levels in MIN6 cells transfected with AnxA1-siRNA, compared with control and scrambled-siRNA groups (Fig. 2 A, B). Moreover, AnxA1-siRNA-transfected MIN6 cells had significantly reduced proliferation rates at 48 h and 72 h post-transfection, compared with control and scrambled-siRNA-transfected cells (Fig. 2C).

AnxA1 regulates the cell cycle and regulatory protein expression in MIN6 cells

The proportions of MIN6 cells in G0/G1, S, and G2/M phases after siRNA transfection were determined by flow cytometry. Compared with the cell cycle distributions of the control and scrambled-siRNA groups, there were significantly lower proportions of AnxA1-siRNA-transfected cells in the S and G2/M phases (Fig. 3A). To further explore whether AnxA1 was involved in regulation of the MIN6 cell cycle, we measured cell cycle regulatory protein expression by Western blot analysis. Compared with the control and scrambled-siRNA-treated cells, AnxA1-siRNA-transfected cells had significantly reduced expression levels of cyclin D1, cyclin E, and CDK2 (Fig. 3 B–E).

The PI3K/Akt/mTOR signaling pathway is involved in AnxA1-mediated MIN6 cell proliferation

The PI3K/Akt/mTOR pathway is an important regulator of mRNA translation that has been associated with increased proliferation, drug resistance, and apoptosis inhibition (14). Treatment of MIN6 cells with AnxA1-siRNA inhibited the PI3K/Akt/mTOR signaling pathway, as indicated by reductions in the active forms of Akt (p-Akt^{473}) and p-mTOR (Fig. 4 A–C). To further explore the mechanisms underlying AnxA1-mediated cell proliferation, MIN6 cells were treated with pharmacological inhibitors of AKT (LY294002) and mTOR (rapamycin). As shown in Fig. 4D, high concentrations of glucose (25 mM)

significantly induced MIN6 cell proliferation, compared with low glucose concentrations (5.5 mM). However, administration of AKT and mTOR inhibitors clearly reversed the glucose-induced MIN6 cell proliferation.

DISCUSSION

In the present study, we used siRNA to alter AnxA1 expression in an islet β-cell line *in vitro*. We found that AnxA1 promoted MIN6 cell proliferation by modulating the cell cycle regulatory protein expression and PI3K/Akt/mTOR signaling pathway activity. Therefore, we presume that AnxA1 is an activator of pancreatic β-cell proliferation.

Our previous studies demonstrated that AnxA1 expression was dramatically upregulated in aging islets in old rats, accompanied by increased islet cell apoptosis (3). We previously proposed that AnxA1 induction in aging islets might be involved in β-cell dysfunction. However, Ohnishi et al. demonstrated that AnxA1 played a regulatory role in glucose-induced insulin secretion in rat pancreatic islets (2). Recently, Rackham et al. demonstrated that AnxA1 is a key modulator of mesenchymal stromal cell-mediated improvements in islet function (15). Therefore, the roles of AnxA1 expression in islet β-cells require further investigation. Previous studies have shown that insulin secretion is defective in both forms of diabetes (types 1 and 2), resulting partly from reduced β-cell mass (16); age also inhibits the proliferation and regenerative capacity of pancreatic β-cells (17). Thus, we explored the effects of AnxA1 on β-cell proliferation. We found

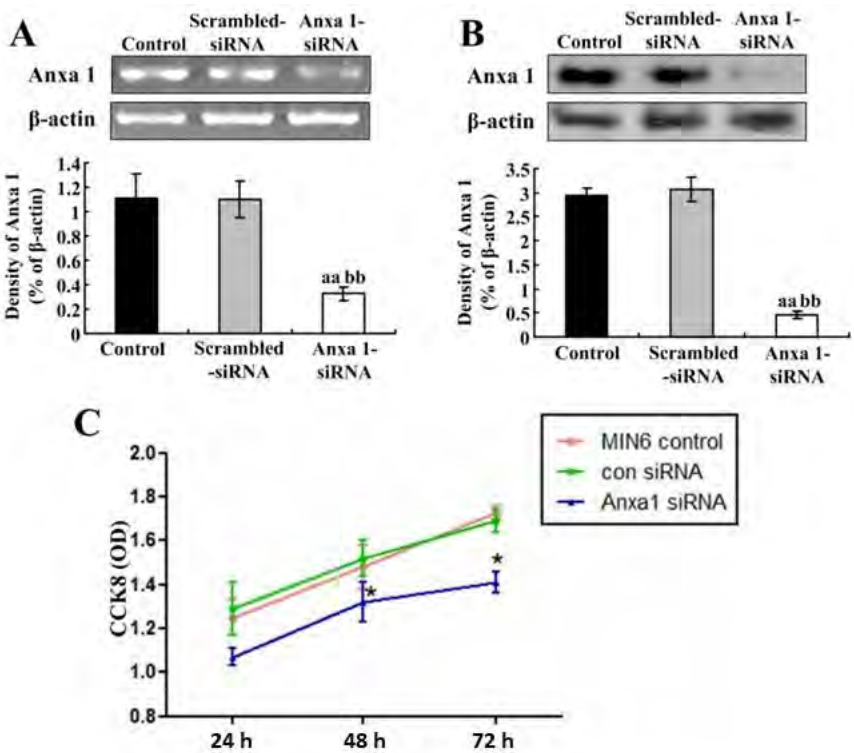


Fig. 2. *Effects of siRNA transfection on AnxA1 expression and cell proliferation in MIN6 cells. After transfection with siRNA for 24 h, the transfection medium was replaced with growth medium (25 mM glucose) for an additional 24, 48, or 72 h. Then, the cells were harvested for AnxA1 mRNA (**A**) and protein (**B**) analysis (n = 5 per group), or measured using a Cell Counting Kit-8 assay. **C**) The experiments were repeated three times, using six replicates per condition. Data shown are representative images or expressed as means ± SDs. a = p < 0.05, aa = p < 0.01 compared with control group; b = p < 0.05, bb = p < 0.01 compared with scrambled-siRNA group.*

that glucose could induce MIN6 β-cell proliferation in a dose-dependent manner with an associated increase in AnxA1 expression, and that this effect was greatest at a glucose concentration of 25 mM (Fig. 1). Moreover, siRNA-mediated inhibition of AnxA1 resulted in significantly reduced MIN6 cell proliferation (Fig. 2C). These results suggested that AnxA1 is involved in the positive regulation of islet β-cell proliferation. The increased AnxA1 expression levels in age-related islets may serve to reduce or prevent aging-induced β-cell apoptosis or death. As described above, we hypothesized that AnxA1 expression may be associated with the induction of islet β-cell proliferation.

The potential mechanism by which AnxA1 activates islet β-cell proliferation requires further investigation. Previous studies revealed the role of AnxA1 in the cell cycle (10, 18). To clarify the role of AnxA1 in islet β-cell proliferation, we calculated the proportions of MIN6 cells in the G0/G1, S, and

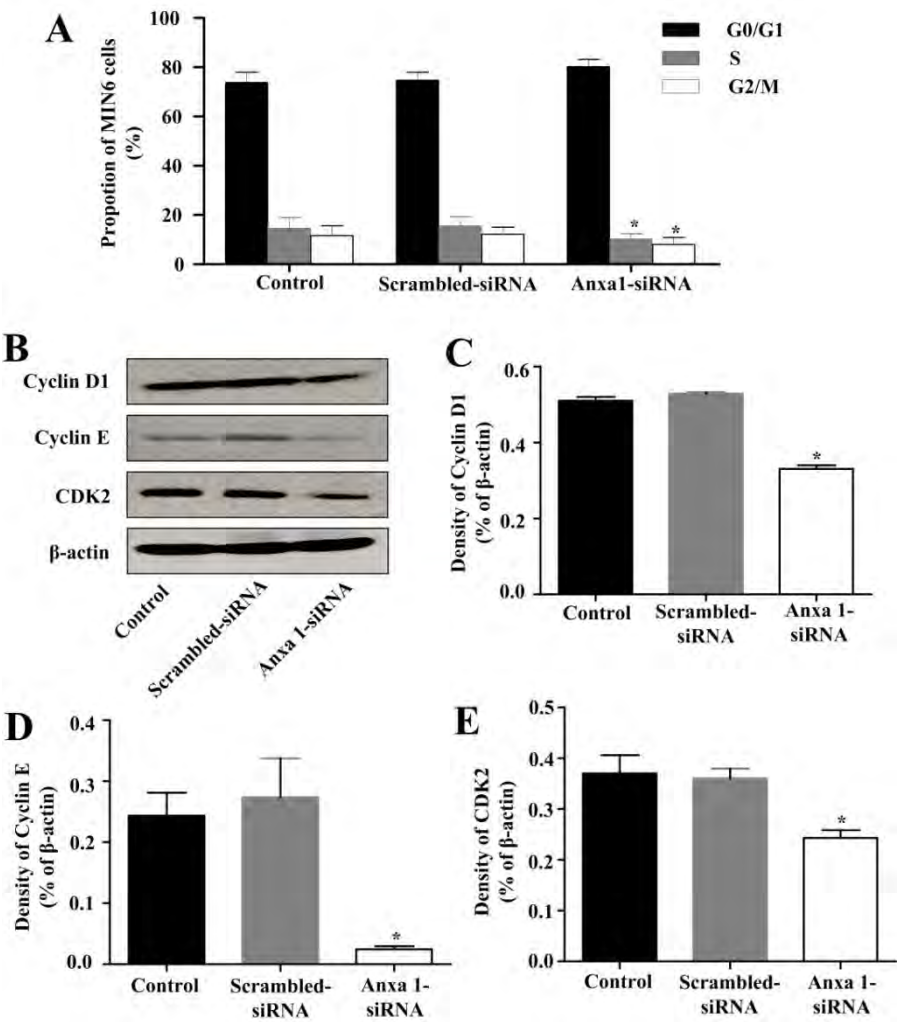


Fig. 3. *Effects of AnxA1-siRNA transfection on the cell cycle and relative protein expression in MIN6 cells. After transfection with siRNA for 24 h, the transfection medium was replaced with growth medium (25 mM glucose) for an additional 24 h.* ***A****) Then, the proportions of MIN6 cells in the G0/G1, S, and G2/M phases after siRNA transfection were determined using flow cytometry.* ***B****) Cells were harvested for cyclin D1, cyclin E, CDK2, and β-actin analyses with specific antibodies. Data shown are representative images or expressed as means ± SDs (n = 5 per group). * = $p < 0.05$ compared with the control or scrambled-siRNA group.*

G2/M phases after siRNA transfection. Compared with the cell cycle distributions in the control and scrambled-siRNA groups, there were significantly lower proportions of AnxA1-siRNA-transfected cells in the S and G2/M phases (Fig. 3A). To further explore whether AnxA1 was involved in regulation of the MIN6 cell cycle, we analyzed the expression patterns of cell cycle regulatory proteins (Fig. 3 B–E). The results showed that AnxA1 can positively regulate the cell cycle: specifically, AnxA1-siRNA-transfected cells exhibited significantly reduced expression levels of cyclin D1, cyclin E, and CDK2. These cell cycle regulatory proteins are expressed mainly in cells in the G1 phase, and are important for inducing DNA synthesis (19). In particular, a lack of cyclin D1 expression might reduce the number of cells entering the S phase, thereby reducing cellular proliferation (20). This effect would be consistent with the finding that inhibition of AnxA1 expression reduced MIN6 cell proliferation. Further research is needed to determine the precise mechanism by which AnxA1 mediates the cell cycle and cell proliferation.

Previous studies demonstrated that the PI3K/Akt pathway is an important regulator of mRNA translation, which is associated with increased proliferation, drug resistance, and apoptosis inhibition (21-23). mTOR, which is modulated by the PI3K/Akt signaling pathway, is also a

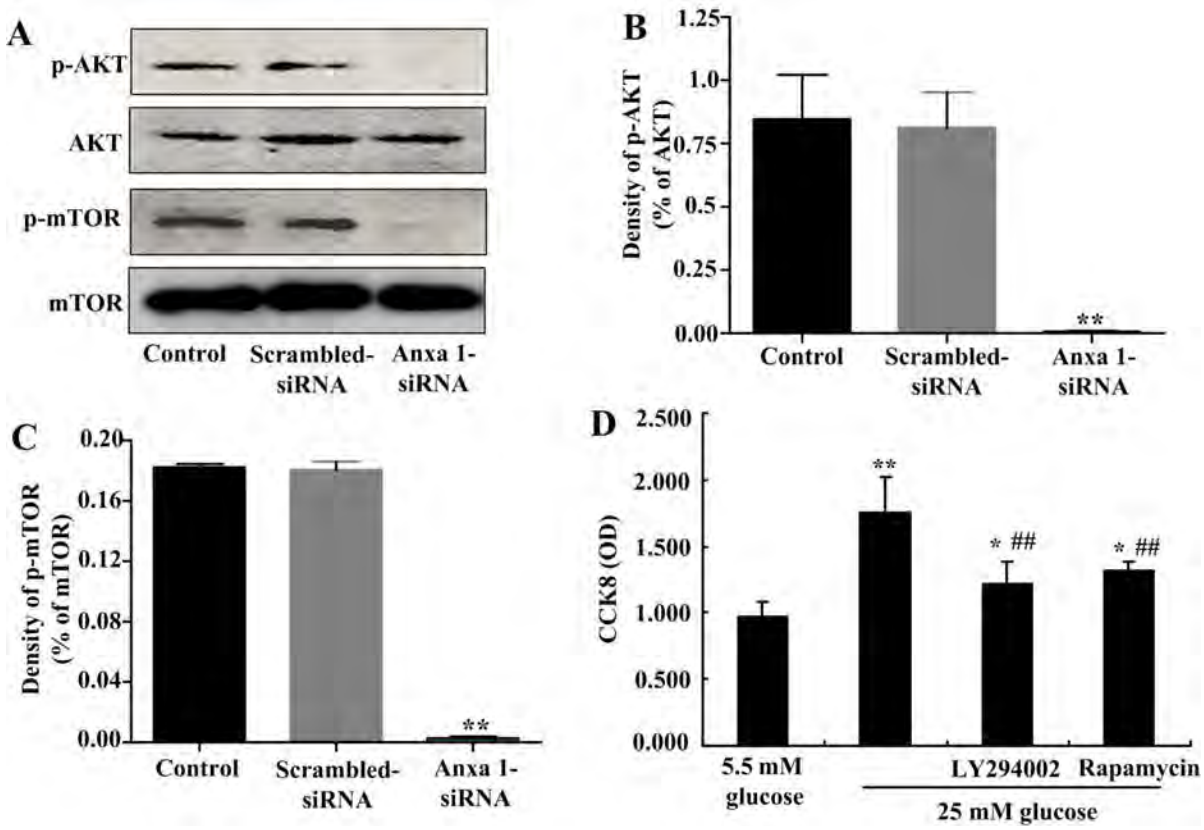


Fig. 4. *Role of PI3K/AKT/mTOR signaling pathway in MIN6 cell proliferation.* ***A, B, C****) After transfection with siRNA for 24 h, the transfection medium was replaced with growth medium (25 mM glucose) for an additional 24 h. Then, the cells were harvested for p-AKT^{473}, AKT, p-mTOR, and mTOR analyses with specific antibodies. Data shown are representative images or expressed as means ± SDs (n = 5 per group). * = p < 0.05 compared with control or scrambled-siRNA group.* ***D****) After exposure to various concentrations of glucose with or without inhibitors for 72 h, the proliferation of MIN6 cells was detected using a Cell Counting Kit-8 assay. The experiments were repeated three times, using six replicates per condition. Data shown are expressed as means ± SDs. * = p < 0.05, ** = p < 0.01 compared with 5.5 mM glucose group; ## = p < 0.01 compared with 25 mM glucose group.*

key regulator of cell growth, including cell cycle progression (24-26). Some studies have indicated that mTOR is essential for the growth and proliferation of early mouse embryos and embryonic stem cells (27, 28). We sought to determine whether the PI3K/Akt/mTOR signaling pathway was involved in AnxA1-mediated cell proliferation. Treatment of MIN6 cells with AnxA1-siRNA inhibited the PI3K/Akt/mTOR signaling pathway, as indicated by reductions in the active forms of Akt (p-Akt^{473}) and p-mTOR (Fig. 4A–C). Moreover, glucose-induced cell proliferation was dramatically reversed by the administration of AKT or mTOR inhibitors (Fig. 4D). Collectively, these results suggested that AnxA1 expression may positively regulate the PI3K/AKT/mTOR signaling pathway, thereby regulating cell cycle regulatory proteins.

The present study found that AnxA1 positively regulates islet β-cell proliferation, possibly via regulation of cyclin D1, cyclin E, and CDK2 proteins, as well as the PI3K/Akt/mTOR signaling pathway. However, these effects were observed only in the MIN6 cell line and thus should be confirmed by further studies using other cell lines and animal models.

REFERENCES

1. Maedler K, Schumann DM, Schulthess F, Oberholzer J, Bosco D, Berney T, Donath MY. Aging correlates with decreased beta-cell proliferative capacity and enhanced sensitivity to apoptosis: a potential role for Fas and pancreatic duodenal homeobox-1. Diabetes 2006; 55:2455-62.
2. Ohnishi M, Tokuda M, Masaki T, et al. Involvement of annexin-I in glucose-induced insulin secretion in rat pancreatic islets. Endocrinology 1995; 136:2421-6.
3. Gu Z, Du Y, Liu Y, et al. Effect of aging on islet beta-cell function and its mechanisms in Wistar rats. Age (Dordr) 2012; 34:1393-403.
4. Lim LH, Solito E, Russo-Marie F, Flower RJ, Perretti M. Promoting detachment of neutrophils adherent to murine postcapillary venules to control inflammation: effect of lipocortin 1. Proc Natl Acad Sci U S A 1998;95:14535-9.
5. Raynal P,Pollard HB. Annexins: the problem of assessing the biological role for a gene family of multifunctional calcium- and phospholipid-binding proteins. Biochim Biophys Acta 1994; 1197:63-93.
6. Bai F, Zhang P, Fu Y, et al. Targeting ANXA1 abrogates Treg-mediated immune suppression in triple-negative breast cancer. J Immunother Cancer 2020; 8.
7. Tang L, Chen Y, Chen H, et al. DCST1-AS1 Promotes TGF-beta-Induced Epithelial-Mesenchymal Transition and Enhances Chemoresistance in Triple-Negative Breast Cancer Cells via ANXA1. Front Oncol 2020; 10:280.
8. Hu C, Peng J, Lv L, Wang X, Zhou Y, Huo J, Liu D. miR-196a regulates the proliferation, invasion and migration of esophageal squamous carcinoma cells by targeting ANXA1. Oncol Lett 2019;17:5201-9.
9. Lim LH,Pervaiz S. Annexin 1: the new face of an old molecule. FASEB J 2007; 21:968-75.
10. Alldridge LC,Bryant CE. Annexin 1 regulates cell proliferation by disruption of cell morphology and inhibition of cyclin D1 expression through sustained activation of the ERK1/2 MAPK signal. Exp Cell Res 2003; 290:93-107.
11. Chatterjee BE, Yona S, Rosignoli G, Young RE, Nourshargh S, Flower RJ, Perretti M. Annexin 1-deficient neutrophils exhibit enhanced transmigration in vivo and increased responsiveness in vitro. J Leukoc Biol 2005; 78:639-46.
12. Flower RJ,Rothwell NJ. Lipocortin-1: cellular mechanisms and clinical relevance. Trends Pharmacol Sci 1994;15:71-6.
13. Skouteris GG,Schroder CH. The hepatocyte growth factor receptor kinase-mediated phosphorylation of lipocortin-1 transduces the proliferating signal of the hepatocyte growth factor. J Biol Chem 1996; 271:27266-73.
14. Ruggero D,Sonenberg N. The Akt of translational control. Oncogene 2005; 24:7426-34.
15. Rackham CL, Vargas AE, Hawkes RG, et al. Annexin A1 is a key modulator of mesenchymal stromal cell-mediated improvements in islet function. Diabetes 2016; 65:129-39.
16. Butler AE, Janson J, Bonner-Weir S, Ritzel R, Rizza RA, Butler PC. Beta-cell deficit and increased beta-cell apoptosis in humans with type 2 diabetes. Diabetes 2003 ;52:102-10.
17. Tschen SI, Dhawan S, Gurlo T, Bhushan A. Age-

dependent decline in beta-cell proliferation restricts the capacity of beta-cell regeneration in mice. Diabetes 2009; 58:1312-20.
18. Raynal P, Pollard HB, Srivastava M. Cell cycle and post-transcriptional regulation of annexin expression in IMR-90 human fibroblasts. Biochem J 1997; 322 (Pt 2):365-71.
19. Musgrove EA. Cyclins: roles in mitogenic signaling and oncogenic transformation. Growth Factors 2006; 24:13-9.
20. Butt AJ, McNeil CM, Musgrove EA, Sutherland RL. Downstream targets of growth factor and oestrogen signalling and endocrine resistance: the potential roles of c-Myc, cyclin D1 and cyclin E. Endocr Relat Cancer 2005; 12 Suppl 1:S47-59.
21. Cantley LC. The phosphoinositide 3-kinase pathway. Science 2002; 296:1655-7.
22. Levine AJ, Feng Z, Mak TW, You H, Jin S. Coordination and communication between the p53 and IGF-1-AKT-TOR signal transduction pathways. Genes Dev 2006; 20:267-75.
23. Davis WJ, Lehmann PZ, Li W. Nuclear PI3K signaling in cell growth and tumorigenesis. Front Cell Dev Biol 2015; 3:24.
24. Dibble CC,Cantley LC. Regulation of mTORC1 by PI3K signaling. Trends Cell Biol 2015; 25:545-55.
25. Zoncu R, Efeyan A, Sabatini DM. mTOR: from growth signal integration to cancer, diabetes and ageing. Nat Rev Mol Cell Biol 2011; 12:21-35.
26. Cuyas E, Corominas-Faja B, Joven J, Menendez JA. Cell cycle regulation by the nutrient-sensing mammalian target of rapamycin (mTOR) pathway. Methods Mol Biol 2014; 1170:113-44.
27. Wen HY, Abbasi S, Kellems RE, Xia Y. mTOR: a placental growth signaling sensor. Placenta 2005; 26 Suppl A:S63-9.
28. Murakami M, Ichisaka T, Maeda M, et al. mTOR is essential for growth and proliferation in early mouse embryos and embryonic stem cells. Mol Cell Biol 2004; 24:6710-8.

CircRNA_103801 accelerates proliferation of osteosarcoma cells by sponging miR-338-3p and regulating HIF-1/Rap1/PI3K-Akt pathway

ZQ. Li[#*], Z. Wang[#], Y. Zhang, C. Lu, QL. Ding, R. Ren, BB. Cheng and LX. Lou

Traumatic Orthopedics, Qinghai University Affiliated Hospital, Xining, China

Received December16, 2020 – Accepted June 14, 2021

This study aimed to investigate the roles of hsa_circRNA_103801 in the progression of osteosarcoma (OS) cells. Quantitative reverse transcription-polymerase chain reaction (RT-qPCR) was used to detect the expression level of circRNA_103801 in OS cells. Cell count kit-8 and Transwell migration and invasion assays were employed to detect the proliferation, migration, and invasion abilities of OS cells. The effects of circRNA_103801 on the apoptosis of OS cells were identified by flow cytometry. The binding relationship between circRNA_103801 and miR-338-3p was verified by bioinformatics analysis. MiR-338-3p level in OS cell lines was detected by RT-qPCR. Additionally, Western blotting was utilized to detect the expression levels of HIF-1, Rap1, PI3K, and Akt in OS cells. The results showed that the expression level of circRNA_103801 was significantly up-regulated in OS patients' tissues. Inhibiting the expression level of circRNA_103801 could attenuate the proliferation, migration, and invasion abilities of OS cells. In addition, the down-regulated expression level of circRNA_103801 could induce cell apoptosis. The results of the luciferase reporter assay suggested that circRNA_103801 could be combined with miR-338-3p, and the RT-qPCR revealed that the miR-338-3p level in OS cells after knockdown of circRNA_103801 was elevated compared with the control group. The results of Western blotting suggested that the expression levels of HIF-1, Rap1, PI3K, and Akt were elevated in OS cells. In conclusion, the circRNA_103801-miR-3388-3p-HIF-1/Rap1/PI3K-Akt pathway could be a therapeutic target of OS.

Osteosarcoma (OS) is one of the most common bone malignancies with a mesenchymal origin, which is common in children and adolescents (1, 2). It is characterized by a high degree of malignancy, strong invasiveness, rapid disease progression, and extremely high mortality rate (3). In recent years, with the development of diagnostic and therapeutic approaches, radical surgery combined with neoadjuvant chemotherapy has widely attracted clinicians' attention, and the prognosis of OS patients has been improved to a certain extent, while the optimal treatment effect has not yet been reported (4, 5). Although clinicians have made great progress in the surgical treatment of OS, the 5-year survival rate of these patients is within 60–70%, and the 5-year survival rate of OS patients with lung metastasis is only 10–20% (6). Therefore, it is highly essential to explore new biomarkers for treating OS.

Circular RNA (circRNA) is a new class of non-coding RNA molecules, widely existing in the cytoplasm of eukaryotic cells. To our knowledge, circRNAs lack a polyadenylated tail, and therefore, are predicted to be less prone to degradation by exonucleases (7). It is noteworthy that circRNA-

Key words: circRNA_103801; miR-3388-3p; osteosarcoma; PI3K-Akt

**Corresponding Author:*
Dr Zeqing Li,
Traumatic Orthopedics,
Qinghai University Affiliated Hospital,
Xining 81000, China
e-mail: li_zeqing@yeah.net

0393-974X (2021)
Copyright © by BIOLIFE, s.a.s.
This publication and/or article is for individual use only and may not be further reproduced without written permission from the copyright holder.
Unauthorized reproduction may result in financial and other penalties
DISCLOSURE: ALL AUTHORS REPORT NO CONFLICTS OF INTEREST RELEVANT TO THIS ARTICLE.

binding proteins play critical roles in regulating synthesis and degradation of circRNAs. Recent studies have shown that in OS, circrna_103801 was found to be associated with HIF-1 and PI3K / Akt pathways, and its binding with miR-370 and miR-877 was predicted by bioinformatics tools (8). MiR-338-3p is a typical multifunctional gene involved in several physiological and pathological processes, such as inflammation, immunity and tumor development. Akt is an ubiquitous mediator of cellular processes, including immune response, inflammatory response, cell proliferation, and cell apoptosis (9). Although the roles of miR-338-3p and Akt in inflammation and tumor growth have not been fully elucidated, the existence of a close relationship between them is noteworthy. Additionally, the roles of circRNA_103801 and miRNA in OS have still remained elusive. Numerous scholars repeatedly reported that circRNAs can serve as noticeable regulators of cancer development and sustained proliferative signaling (10, 11).

The present study aimed to detect the expression level of circRNA_103801 in OS cells, and to assess its effects on the proliferation of OS cell lines. It was also attempted to explore the relationship between circRNA _103801 and the expression of miR-338-3p, and to identify the potential regulatory molecular mechanism.

MATERIALS AND METHODS

Cell culture

MG63 and normal human osteoblast (NHOst) cells were purchased from Shanghai Institute of Biochemistry and Cell Biology (Shanghai, China). Roswell Park Memorial Institute (RPMI)-1640 medium and Dulbecco's modified Eagle's medium (DMEM) were purchased from GIBCO (New York, NY, USA). MG63 cells were cultured in DMEM containing 10% fetal bovine serum (FBS), and NHOst cells were cultured in the RPMI-1640 medium containing 10% FBS in an incubator at 37℃ with 5% CO_2. According to the requirements of the experiment, the cells were inoculated into the required cell culture dish or cell culture plate.

Extraction of total RNA

MG63 and NHOst cell lines were inoculated into a large culture dish. When the fusion degree of cells in the culture dish reached more than 80-90%, RNA could be extracted from the cells. The cells were digested with

Table I. *The sequences of primers used for RT-qPCR.*

Primer	Sequences (5'-3')
circRNA_103801 (forward)	CTGGTGGAAGCAGAGAG
circRNA_103801 (reverse)	CGACCCACTGCTCTTCTC
β-actin (forward)	CGCTCTCTGCTCCTCCTGTTC
β-actin (reverse)	ATCCGTTGACTCCGACCTTCAC

Table II. *The sequences of si_circRNA_103801 and si-NC.*

Primer	Sequences (5'-3')
si_circRNA_103801-1	CACGCTCCTAACCTGTTGATA
si_circRNA_103801-2	CCGCACTCCTACAATAAGGTTG
NC	TTCTCCGAACGTCTCACGTTT

0.25% trypsin and centrifuged (l,000 rpm, 3 min). The cells were washed with 1 mL phosphate-buffered saline (PBS), re-centrifuged twice, and the cell precipitate was transferred to the enzyme-free centrifuge tube. Then, 1 mL of TRIzol lysate was added into the enzyme-free centrifuge tube to dissolve the cell precipitate, and the shaker centrifuge tube was upside down; 200 μL of chloroform was added, and the centrifuge tube was shaken for 15 s and maintained at room temperature for 5 min. Afterwards centrifuge tube was placed into the precooled ultracentrifuge for centrifugation (12,000 rpm, 15 min, 4°C); after centrifugation, the liquid in the centrifuge tube was divided into three layers, in which RNA was located in the upper layer. The upper colorless solution (aqueous phase) was carefully and slowly absorbed with the gun head and transferred to the enzyme-free centrifuge tube for subsequent experiments.

RNA concentration was measured by a NanodropND-1000 spectrophotometer. RNA was reversely transcribed into cDNA using Takara Reverse Transcription Kit (Takara, Tokyo, Japan). Specific primers were designed and synthesized by Invitrogen Inc. (Shanghai branch) using the NCBI Primer blast. β-actin was used as an internal control to normalize gene and protein expressions. The expression of circRNA in MG63 and NHOst cell lines was detected by the quantitative reverse transcription-polymerase chain reaction (RT-qPCR). The Step-One Plus system was used to perform RT-qPCR, and 10 μL reaction system was configured. The corresponding CT value was obtained by a PCR amplification curve. The relative expression levels of genes were compared by calculating the corresponding ΔCT values. The sequences of primers used for RT-qPCR are shown in Table I.

SiRNA transfection by lentivirus

The siRNA sequences of circRNA and negative control (NC) used in the current study were all designed and synthesized by Shanghai Jima Pharmaceutical Technology Co., Ltd (Shanghai, China). MG63 and NHOst cell lines in logarithmic growth phase were selected, digested with trypsin, and centrifuged to obtain the supernatant. The cells were resuspended with medium and inoculated onto a 6-well plate. The cellular density in each well was about 5×10^6 cells/ml. Then, 2 mL of a complete medium was added and incubated for 24 h. After the original medium was aspirated and washed with PBS, the supernatant was added with 5 pg/ml puromycin. At the same time, suspended cell lines (MOI = 100) were also added to the 6-well plate for 24 h. After the original medium was sucked out and cleaned with PBS, the fresh McCoy's 5a medium containing 10% FBS was replaced. After 3-5 days of continuous culture, the stable cell lines of circRNA-knockdown were screened. The culture medium containing puromycin was added into the 6-well plate, and the cells were collected for further experiments. The sequences of primers are presented in Table II.

CCK-8 assay

Cell counting kit-8 (CCK-8) assay was carried out to detect the cell viability. The transfected cells in logarithmic growth phase were digested with 0.25% trypsin solution and centrifuged to obtain the supernatant. The cells were resuspended with medium and counted by a cell counting plate. According to the results of the cell counting, the concentration of suspended cell lines was diluted to about 5,000 cells/100 μl, and then, the diluted suspended cell lines were added into a 96-well plate. The 96-well plate was incubated at 37°C for 24, 48, 72, and 96 h, respectively. After that, 100 μL (10% CCK-8 solution) was added to the 96-well plate. The mentioned plate was placed into an incubator (37°C, 1-4 h). Finally, the SPECTRmaxPLUS34 continuous spectrophotometer was adjusted to 450 nm wavelength, and the absorbance value of each hole was measured and recorded.

Flow cytometry

The transfected cells in logarithmic growth phase were digested with trypsin solution without ethylenediaminetetraacetic acid (EDTA) for 4-5 min. After the adherent cells became round or free, they were transferred to a centrifuge tube for centrifugation (1,000 rpm, 3 min), and washed with PBS to obtain the supernatant. The cells were re-suspended with 500 μL of binding buffer and placed at room temperature for 10 min. Then, 5 μL of Annexin V-FITC solution was added into the centrifuge tube, which was blown and mixed evenly. Afterward, 5 μL of propidium iodide (PI) staining solution was added into the tube, and stored in an ice bath away from the light. They were incubated at room temperature for 5-15 min in the dark. The excitation wavelength was 488 nm, and the emission wavelength was 530 nm.

Transwell assay

After the adherent cells became round or free, the cells were centrifuged in a centrifuge tube at 1,000 rpm for 3 min. After the cells were re-suspended with the original medium, the number of cells was counted by the cell counting plate, and the cell density was adjusted to 3×10^5 cells/ml. After 100 μL of diluted cell suspension was added into the Transwell chamber, and 500 μL of the McCoy's 5A medium with 20% FBS was added into the lower Transwell chamber, the cells were further cultured in an incubator at constant temperature for 24 h. The liquid in the upper Transwell chamber drained, the chamber was taken out, and the cells in the upper chamber were swiped with a cotton swab. The cells were moved into another well and fixed with methanol for 30 min. Next, the polycarbonate film at the bottom was gently cut off with a surgical blade and put onto a clean glass slide. The neutral resin on the polycarbonate film was dropped and the cover glass was covered. Finally, the treated polycarbonate film could be visualized under an inverted microscope and photographed.

Western blot assay

The proteins were loaded onto 4-20% sodium dodecyl sulfate–polyacrylamide gel electrophoresis (SDS-PAGE) according to the protein amount of 30 μg/well. Three compound holes in each group were set up. The power supply was connected according to the positive and negative electrodes, and the power supply was turned on. The voltage value was adjusted to 120 V, and electrophoresis was stopped when the electrophoresis was close to the bottom of the prefabricated rubber. To transfer the output of SDS-PAGE into polyvinylidene fluoride (PVDF) membranes, the glue and the corresponding PVDF membranes were put into methanol for moistening and washing, and then taken out and soaked in the electrokinetic buffer. The glue was taken out, and cut into a proper size. The prefabricated glue, sponge, filter paper and PVDF membranes were used to make the electro-rotary films. The current was 380 mA and the time was set to 100 min. After transferring into PVDF membranes, the membranes were put into 5% skimmed milk powder and sealed for 45 min, washed with pure water, added into primary antibodies (HIF-1, Rap1, PI3K, and Akt), and incubated overnight at 4°C. The PVDF membranes were washed twice with PBST for 15 min each time. The secondary antibody diluted with skimmed milk powder was incubated at room temperature for 1 h, and the membranes were washed twice with PBST for 15 min each time. As for imaging, ECL solutions A and B were mixed at a ratio of 1:1, and the films were taken out. PBST was drained, and ECL light-emitting liquid was added evenly onto the films. The films were covered with a preservative layer, and photographed in a dark room. A scanner was used to import the films into a computer, and Image-J analysis software was used to measure the optical density.

Bioinformatics analysis

The prediction of the interaction between circRNA_103801 and miR-338-3p was undertaken by the starBase database. According to the secondary structure and free energy of RNA, the miRNAs related to circRNAs were detected by the ArrayStar software. The correlation coefficient between circRNA_103801 and miR-338-3p was calculated.

Statistical analysis

SPSS 20.0 (IBM, Armonk, NY, USA) and GraphPad Prism 7.0 (GraphPad Software Inc., San Diego, CA, USA) software were used to analyze the data, and the data were presented as the mean ± standard deviation (SD). The *Chi*-squared test, F-test, and one-way analysis of variance (ANOVA) were used to analyze the data. $P < 0.05$ was considered statistically significant.

RESULTS

Expression of circRNA_103801 was up-regulated in MG63 and NHOst cell lines

The results of RT-qPCR showed that the relative expression level of *circRNA_103801* in MG63 cells was significantly higher than that in NHOst cells ($P < 0.01$, Fig. 1). It was revealed that compared with NC group, the relative expression level of circRNA_103801 in circRNA_103801 siRNA group was significantly reduced ($P < 0.01$, Fig. 2).

Effects of circRNA_103801 on the proliferation, invasion, and migration of MG63 cells

Compared with the blank control group (siRNA-NC), the proliferation activity of MG63 cells in the two target interference groups (siRNA-1 and siRNA-2) was significantly inhibited ($P < 0.001$, Fig. 3). This indicated that circRNA_103801could

maintain the proliferation of OS cells, and knockdown of its expression level could inhibit the proliferation of these cells. The results of Transwell migration and invasion assays showed that there was no significant difference in the number of migrated cells between the down-regulated group and the control group (Fig. 4). This suggested that circRNA_103801 had no significant influence on the metastatic ability of OS cells, and further highlighted the importance of circRNA_103801 in the proliferation of OS cells.

Knockdown of circRNA_103801 induced cell apoptosis

Compared with the control group, the down-regulation of circRNA_103801 significantly increased the apoptosis rate of OS and normal cell lines. The expression levels of apoptosis-related proteins and anti-apoptosis-related proteins were detected by Western blotting. Consistent with the results of flow cytometry, the expression levels of apoptosis-related proteins were significantly up-regulated, and the expression level of Bcl-2 was markedly inhibited after silencing of circRNA_103801 (Fig. 5).

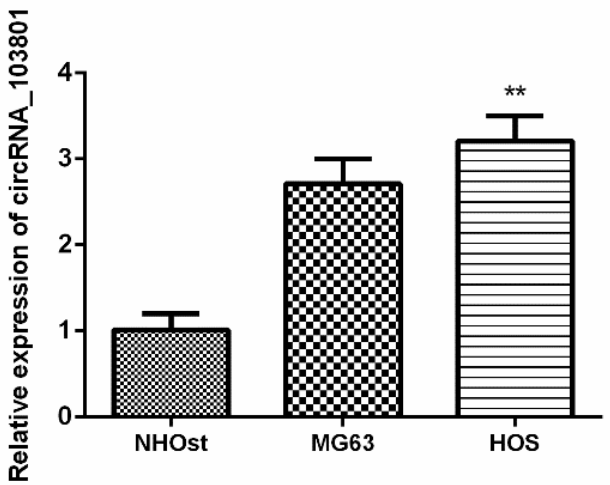


Fig. 1. *Relative expression level of circRNA_103801 in NHOst, MG63, and HOS cells.*

Predicted binding sites of circRNA_103801 with miR-338-3p

The results revealed that the silencing of circRNA_103801 could inhibit the proliferation of OS cells, which might occur by promoting the apoptosis and cell cycle arrest in the G2/M phase. However, the downstream binding site of circRNA_103801 was not detected. In order to further explore the regulatory mechanism of circRNA_103801 in OS cells, starBase was employed to perform analysis and prediction. The predicted results suggested that miR-338-3p could be a downstream target of circRNA_103801, and the potential binding sites between them are illustrated in Fig. 6.

CircRNA_103801 could promote the expression levels of proteins in cells

As shown in Fig. 7, the relative expression levels of HIF-1, Rap1, PI3K, and Akt in cells were elevated by circRNA_103801, which were significantly different from those levels detected in the control group ($P<0.05$).

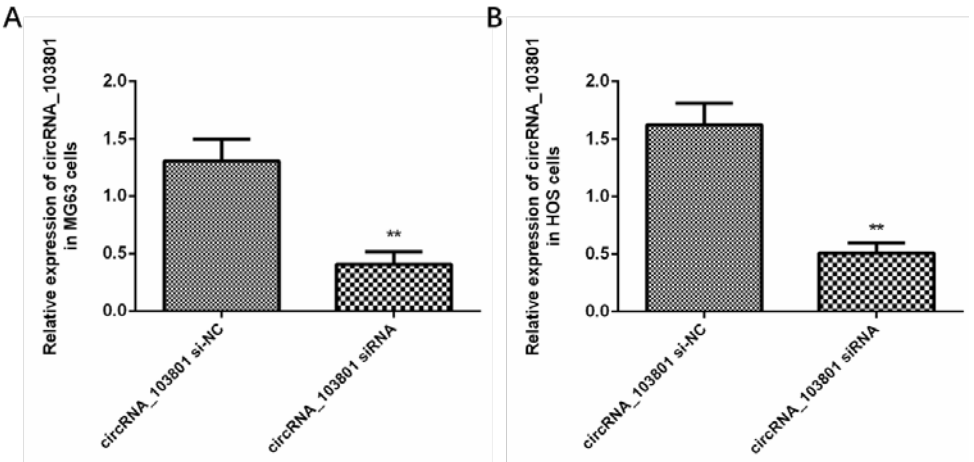


Fig. 2. *Relative expression level of circRNA_103801 in siRNA NC group and circRNA_103801 siRNA group.* ***A****)Relative expression of si_circRNA_103801 in MG63 cells;* ***B****) Relative expression of si_circRNA_103801 in HOS cells.*

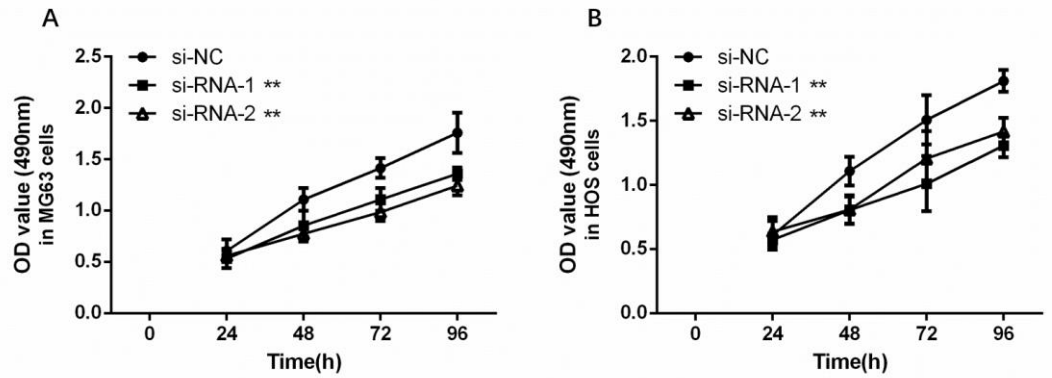


Fig. 3. *Proliferation curve of MG-63 and HOS cells after knockdown of circRNA_103801.* ***A)*** *The proliferation ability of MG63 cells after knocking down circRNA_103801;* ***B)*** *The proliferation ability of HOS cells after knocking down circRNA_103801.*

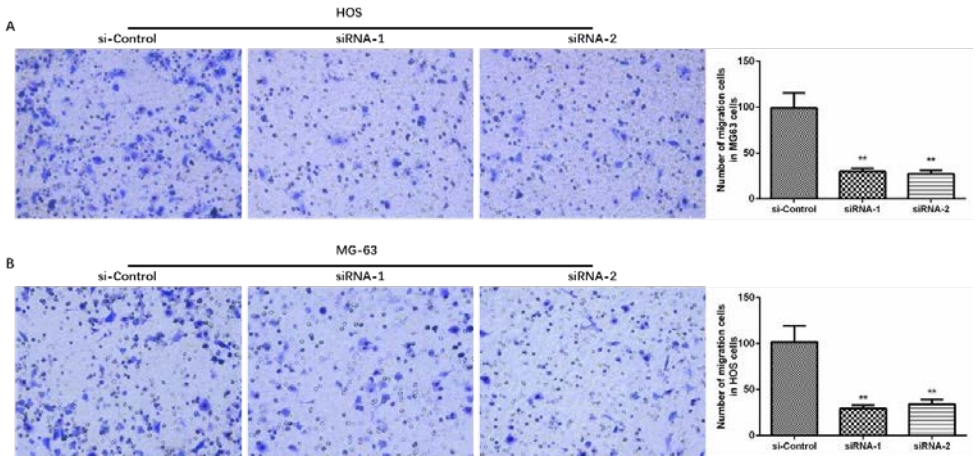


Fig. 4. *Cell invasion of MG-63 and HOS cells after knockdown of circRNA_103801.* ***A)*** *The cell invasion ability of MG63 cells after knocking down circRNA_103801;* ***B)*** *The cell invasion ability of HOS cells after knocking down circRNA_103801.*

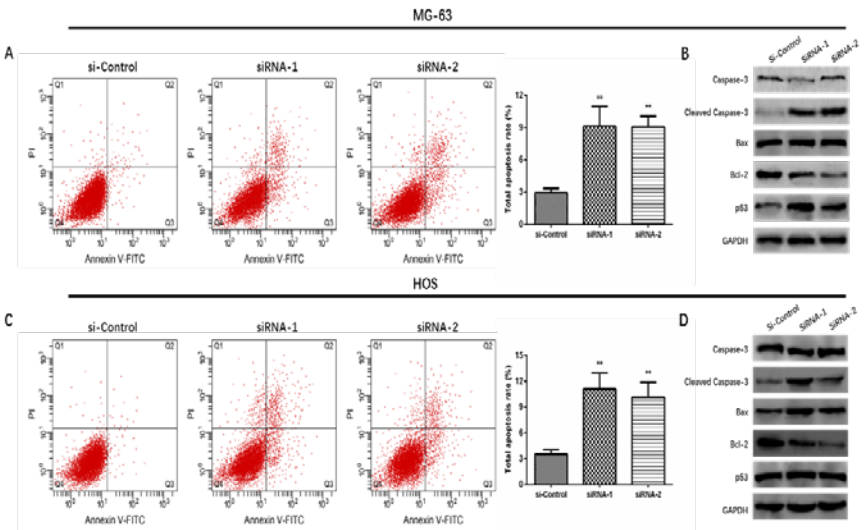


Fig. 5. *Cell apoptosis of MG-63 and HOS cells after knockdown of circRNA_103801.* ***A)*** *The apoptosis ability in MG63 cells after knocking down circRNA_103801;* ***B)*** *The expression of apoptosis proteins in MG63 cells after knocking down circRNA_103801;* ***C)*** *The apoptosis ability in HOS cells after knocking down circRNA_103801;* ***D)*** *The expression of apoptosis proteins in HOS cells after knocking down circRNA_103801.*

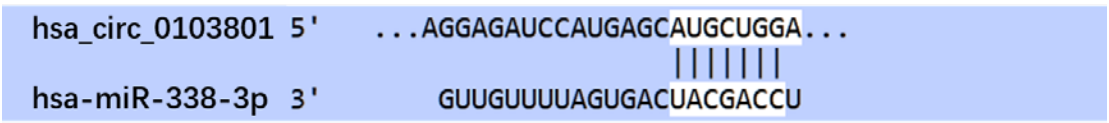


Fig. 6. *Binding sites of circRNA_103801 and miR-338-3P*

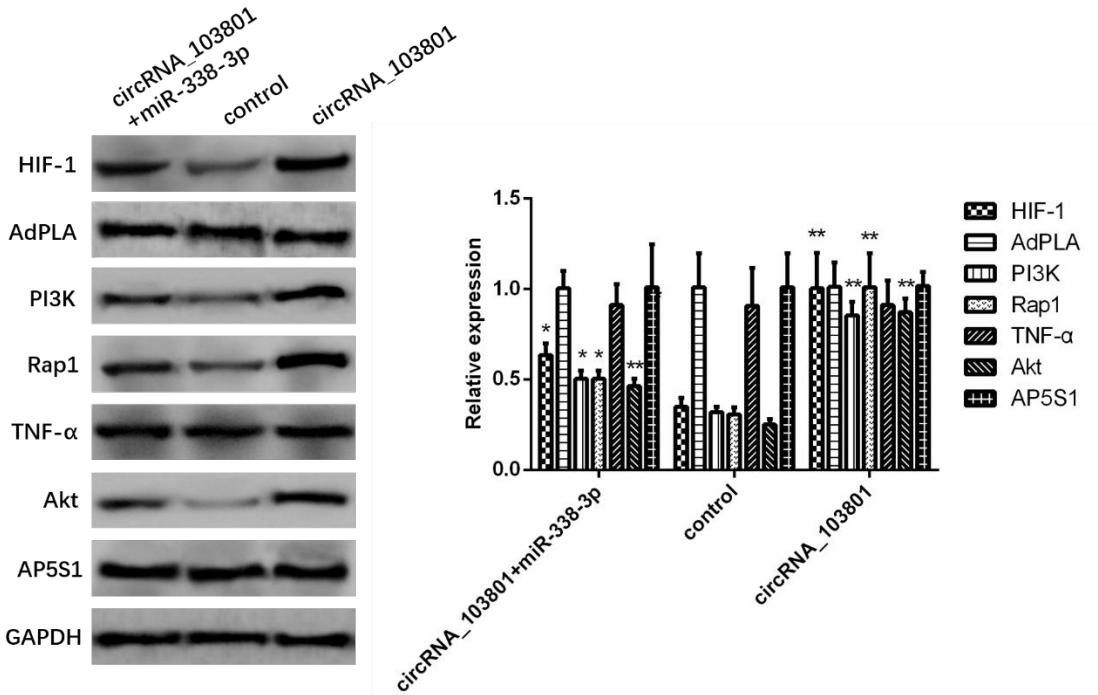


Fig. 7. *The expression levels of HIF-1, AdPLA, PI3K, Rap1, TNF-α, Akt and AP5S1 in circRNA_103801 + miR-338-3p group, control group and circRNA_103801 group.*

DISCUSSION

OS is one of the most common malignant tumors in bone tissues (12, 13). It can be typically transferred into the lung through blood transportation in the early stage, accompanied by a high rate of mortality (14). For patients with OS, the dominant treatment is currently on the basis of surgical resection of lesions, combined with preoperative and postoperative adjuvant treatment (including adjuvant chemotherapy, immunotherapy, targeted therapy) (15-17), extending the survival time of patients with OS to a certain extent, while the effects of treatment of metastatic OS and recurrent OS are not highly optimistic, leading to poor long-term survival of OS patients (18). The 5-year survival rate of OS patients is still at a low level (19), therefore, it is urgent to explore new and effective biomarkers for diagnosis, treatment, and prognosis of OS patients. Cell proliferation, differentiation, and apoptosis are correlated to maintain the balanced growth of normal tissues, however, tumor cells often have apoptosis disorder (20). In order to maintain unlimited proliferation ability, tumor cells often inhibit apoptosis, thereby avoiding their own aging and immune attack. A large number of studies have confirmed that the sponge effect on miRNA is the key mechanism of circRNA, regulating the occurrence and development of diverse diseases. MiRNA is also a kind of small non-coding RNA, which can bind to mRNA through the principle of base complementary pairing, and then degrade mRNA or inhibit the expression of mRNA, thus playing a regulatory role in the regulation of gene transcription and expression.

In conclusion, the circRNA_103801-miR-3388-3p-HIF-1/Rap1/PI3K-Akt pathway could be the therapeutic target of OS.

ACKNOWLEDGEMENT

This study was supported by the National Youth Science Foundation (Grant No. 2018-0302-ZJC-0042).

REFERENCES

1. Harrison DJ, Geller DS, Gill JD, Lewis VO, Gorlick R. Current and future therapeutic approaches for osteosarcoma. Expert Rev Anticancer Ther 2018; 18(1):39-50.
2. Hmada YA, Bernieh A, Morris RW, Lewin J, Allen T. Chondroblastoma-like Osteosarcoma. Arch Pathol Lab Med 2020; 144(1):15-17.
3. Liu X, Wang H, Tao GL, Chu TB, Wang YX, Liu L. LncRNA-TMPO-AS1 promotes apoptosis of osteosarcoma cells by targeting miR-329 and regulating E2F1. Eur Rev Med Pharmacol Sci 2020; 24(21):11006-11015.
4. Su T, Zhang SD, Zhao J. Long non-coding RNA CCAT1 regulates the biological behavior of osteosarcoma cells through the miR-454-3p/ZEB2 axis. Eur Rev Med Pharmacol Sci 2020; 24(21):11016-25.
5. Kimura Y, Tomihara K, Tachinami H, et al. Conventional osteosarcoma of the mandible successfully treated with radical surgery and adjuvant chemotherapy after responding poorly to neoadjuvant chemotherapy: a case report. J Med Case Rep 2017; 11(1):210.
6. Ye CY, Zheng CP, Zhou WJ, Weng SS. MiR-582-5p inhibits the growth and invasion of osteosarcoma cell by targeting NOVA1. Eur Rev Med Pharmacol Sci 2020; 24(21):11026-31.
7. Zhang C, Huang C, Yang P, Li C, Li M. Eldecalcitol induces apoptosis and autophagy in human osteosarcoma MG-63 cells by accumulating ROS to suppress the PI3K/Akt/mTOR signaling pathway. Cell Signal 2020; 78:109841.
8. Liu W, Zhang J, Zou C, et al. Microarray expression profile and functional analysis of circular RNAs in osteosarcoma. Cell Physiol Biochem 2017; 43(3):969-85.
9. Tang F, Wang Y, Hemmings BA, Rüegg C, Xue G. PKB/Akt-dependent regulation of inflammation in cancer. Semin Cancer Biol 2018; 48:62-9.
10. Zhang Y, Li J, Wang Y, Jing J, Li J. The Roles of Circular RNAs in Osteosarcoma. Med Sci Monit 2019; 25:6378-82.
11. Li Z, Li X, Xu D, et al. An update on the roles of circular RNAs in osteosarcoma. Cell Prolif 2021; 54(1):e12936.
12. Biazzo A, De Paolis M. Multidisciplinary approach to osteosarcoma. Acta Orthop Belg. 2016 Dec;82(4):690-8.
13. Brown HK, Tellez-Gabriel M, Heymann D. Cancer stem cells in osteosarcoma. Cancer Lett 2017; 386:189-95.
14. Simpson E, Brown HL. Understanding osteosarcomas. JAAPA 2018; 31(8):15-19.
15. ElKordy MA, ElBaradie TS, ElSebai HI, KhairAlla SM, Amin AAE. Osteosarcoma of the jaw: Challenges in the diagnosis and treatment. J Egypt Natl Canc Inst 2018; 30(1):7-11.
16. Xu M, Wang Z, Yu XC, Lin JH, Hu YC. Guideline for Limb-Salvage Treatment of Osteosarcoma. Orthop Surg 2020; 12(4):1021-9.
17. Wedekind MF, Wagner LM, Cripe TP. Immunotherapy for osteosarcoma: Where do we go from here? Pediatr Blood Cancer 2018; 65(9):e27227.
18. Biazzo A, De Paolis M. Multidisciplinary approach to osteosarcoma. Acta Orthop Belg 2016; 82(4):690-8.
19. Attia A, Siriwardana A, Desai D. Sarcomatoid urothelial carcinoma of the ureter with heterologous elements of chondrosarcoma and osteosarcoma, and concurrent divergent squamous differentiation: A rare case report. Urol Case Rep 2020; 34:101484.
20. Wang S, Li H, Chen S, Wang Z, Yao Y, Chen T, Ye Z, Lin P. Andrographolide induces apoptosis in human osteosarcoma cells via the ROS/JNK pathway. Int J Oncol 2020; 56(6):1417-28.

High dose insulin promotes the proliferation of vascular smooth muscle cells via AP-1/SM-α pathway

Y. Peng[1], P. Cai[1], SF. Zou[2], M. Jia[1], WT. Zhong[1], Y. Wang[3] and XK. Wang[1]

[1]Department of Cardiology, Institute of Field Surgery, Daping Hospital, Army Medical University, Yuzhong District, Chongqing, P.R. China; [2]Department of Cardiac Surgery, Xinqiao Hospital, Army Medical University Shapingba District, Chongqing, P.R. China; [3]Key Laboratory of Basic Pharmacology of Ministry of Education and Joint International Research Laboratory of Ethnomedicine of Ministry of Education, Zunyi Medical University, Honghuagang District, Zunyi, Guizhou, P.R. China

Received April 26, 2021 – Accepted June 16, 2021

Proliferation of vascular smooth muscle cells (VSMCs) participates in multiple cardiovascular disorders, while the mechanism remains unclear. This study aims to investigate the effects of insulin on VSMC. Insulin was used to stimulate rat VSMCs, and the effects on cell cycle and proliferation were subsequently analyzed using flow cytometry. Furthermore, AP-1 and SM-α overexpression vectors were constructed and transfected into VSMCs. AP-1 and SM-α were inhibited by SR11302 and SM-α siRNA, respectively. The mRNA and protein expression levels were subsequently detected using the reverse-transcription quantitative polymerase chain reaction and western blotting, respectively. AP-1 and SM-α gene promoter binding sites were determined using luciferase and chromatin immunoprecipitation assays. As a result, we found that high dose of insulin promoted proliferation of VSMCs and increased the percentage of cells in the S phase by downregulating AP-1. AP-1 was identified to bind to the SM-α gene promoter at locus 2-177 to upregulate SM-α gene expression. Inhibition of AP-1 led to the decrease of SM-α expression. Overexpression of SM-α directly suppressed proliferation of VSMCs, while knocking it down promoted the process. Therefore, this study revealed that insulin downregulated the expression of the SM-α gene by inhibiting AP-1, which in turn facilitated proliferation of VSMCs.

Atherosclerosis, often accompanied with hypertension, hypercholesterolemia or diabetes, is one of the main causes of disease and mortality in the elderly. Insulin resistance and subsequent hyperinsulinemia are independent risk factors for development of atherosclerosis, and further promote the occurrence of restenosis following vascular injury (1). Studies have demonstrated that phenotypic transformation of vascular smooth muscle cells (VSMCs), characterized by increased proliferation, migration and release of inflammatory factors, underlies atherosclerotic plaque formation and vascular remodeling diseases such as restenosis after angioplasty (2). A number of studies have reported that increased proliferation is a common pathogenic mechanism underlying several diseases, including hypertension, atherosclerosis and diabetes mellitus with vascular complications (3, 4), and that proliferation ability of VSMCs was significantly enhanced following treatment with insulin (5). Furthermore, the VSMC differentiation determining

Key words: activator protein 1; insulin; proliferation; smooth muscle alpha-actin; vascular smooth muscle cell

Corresponding Author:
Xukai Wang, M.D.
Department of Cardiology, Institute of Field Surgery,
Daping Hospital, Army Medical University,
No.10 Changjiang Branch Road,
Yuzhong District,
Chongqing, 400042, P.R. China
e-mail: wangxukai@tmmu.edu.cn/wangxuk@163.com

0393-974X (2021)
Copyright © by BIOLIFE, s.a.s.
This publication and/or article is for individual use only and may not be further reproduced without written permission from the copyright holder.
Unauthorized reproduction may result in financial and other penalties
DISCLOSURE: ALL AUTHORS REPORT NO CONFLICTS OF INTEREST RELEVANT TO THIS ARTICLE.

protein, smooth muscle alpha-actin (SM-α), is also a protein marker of contraction. One study showed that insulin could inhibit the expression of SM-α and lead to proliferation and eventual functional abnormalities of VSMCs (6). However, how SM-α directly affects VSMC proliferation needs to be determined.

The cellular transcription factor, activation protein-1 (AP-1), is a heterodimer comprised of c-Jun and c-Fos proteins (7); it binds to a specific region in the SM-α promoter to activate its transcription and induce further downstream responses. However, whether the insulin-induced proliferation of VSMCs and the accompanying downregulation of SM-α gene expression is associated with AP-1 remains unclear. Therefore, the present study aims to investigate the mechanism underlying the downregulation of SM-α gene expression during insulin-induced VSMC proliferation.

MATERIALS AND METHODS

Plasmids, siRNA cells and reagents

The SM-α promoter-specific sequence was obtained from www.ncbi.nlm.nih.gov/nuccore/NM_007392.3. The AP-1 and SM-α overexpression vectors were purchased from Fulengen Co., Ltd (Guangzhou, China). Transformation was performed in *Escherichia coli* XL1-Blue host cells, which were provided by the Department of Genetics, Army Medical University (Chongqing, China). Sprague-Dawley rat VSMCs were purchased from the American Type Culture Collection.

The siRNA oligo sequences 21nt guide (5′→3′) were purchased from Nippon EGT (Japan). The target sequence based on nucleotides of rat SM-α cDNA5'-UGGAUUUGUACCAUUCUUCUG -3' were designed using the online software RNAi Designer(http://sidirect2.rnai.jp/). The control siRNA (luciferase) for the target sequence was 5'-AAGCCATTCTATCCTCTAGAG-3', which already has been confirmed ss not possessing homology to any mammalian gene sequences.

The PrimeScript™ RT reagent kit was purchased from Takara Biotechnology Co., Ltd (Cat. No. RR047A). The Plasmid Mini kit II was purchased from OmegaBio-Tek, Inc (Cat. No. D6945-01/02). Lipofectamine 2000 transfection reagent was purchased from Shanghai Union Technology (China). SR11302 (complete medium supplemented with 10 μmol/l, AP-1 inhibitor) was purchased from APExBIO (USA). DMEM and trypsin solution were purchased from ThermoFisher Scientific, Inc. Fetal bovine serum was purchased from Hari Biotechnology. AP-1 rat monoclonal antibody was purchased from EMD Millipore. SM-α rat monoclonal antibody and horseradish peroxidase-labeled goat anti-rabbit IgG secondary antibody were purchased from OriGene Technologies, Inc. AP-1 and SM-α promoter-specific sequence primers and their segmented primers were synthesized by Sangon Biotech Co., Ltd (Shanghai, China).

Cell culture

VSMCs were cultured in DMEM (Cat. No.11965092, ThermoFisher Scientific) supplemented with 10% fetal bovine serum and 100 U/ml penicillin/streptomycin. Cells were maintained at 37°C in an atmosphere containing 5% CO_2.

Flow cytometry

VSMCs in the blank control and insulin (25, 50, 100, and 125 nmol/l) groups were collected and washed with PBS. Cells were subsequently fixed with 70% ethanol at 4°C overnight. Following centrifugation, the cells were washed with PBS, and incubated with 100 μl ribonuclease at 37°C

Table I. *SM-α gene fragment primer sequences*

Gene	Forward primer (5′ to 3′)	Reverse primer (5′ to 3′)	*PCR size*
Locus 1–1020	AATCCTCCTTGGTTACTTCA	CGGTTTTATCATAGGCATCA	269
Locus 1021-2000	GGTCAGCGATAAACCAACAA	GCTAAGGGCTTGAGATGAGG	253
Locus 1-480	GTGTTTAAGAGCACTGACTG	TCTGAAGTAACCAAGGAGGA	341
Locus 481–1020	CATAAATGTCCCATTCTGCC	GCTGTCTACTCACGCTACCA	253

for 30 min in a water bath. Then, the cells were incubated with 50 μg/ml propidium iodide (500 μl) at 4°C for 30 min. For cell proliferation analysis, BrdU incorporation was analyzed using the APC-BrdU Flow kit (Cat. No. 557892, BD Biosciences). VSMCs were assayed 24 h after the single addition of 10mg/ml BrdU (100μl). Cells were analyzed using a flow cytometer (BD Biosciences).

Transfection

VSMCs in the logarithmic growth phase were inoculated into six-well plates containing serum-free DMEM (Cat. No.11965092 Gibco) and incubated at 37°C for 3 h. Cell transfection was performed by adding the vectors and Lipofectamine 2000 reagent to the cells and incubating at 37°C for 5 h. The transfected cells were harvested and cultured with fresh DMEM supplemented with 10% fetal bovine serum and 100 U/ml penicillin/streptomycin at 37°C for 24 h. Subsequently, the transfected cells were observed by a fluorescence microscope.

Luciferase reporter assay

The primer sequences of the SM-α gene promoter region were designated as locus 1-1020, locus 1021-2000, locus 1-480 and locus 481-1020. The primer sequences were cloned from genomic DNA using PCR and inserted into the luciferase reporter gene (pGL3-basic). The specific primers are presented in Table I. The positive clones were subsequently screened and purified. VSMCs in the logarithmic growth phase were inoculated onto 24-well plates and placed in an incubator at 37°C and 5% CO_2. Cells transfected with SM-α and AP-1 overexpression vectors were used to detect luciferase activity. Luciferase activity was measured in cells transfected with the blank pGL3-basic plasmid, the SM-α plasmid and the SM-α plasmid + AP-1 expression vectors, respectively.

Chromatin-immunoprecipitation (ChIP)

The AP-1 and SM-α promoter binding sites were predicted using the Promoter 2.0 Prediction Server. The sequences of the SM-α promoter were designed and subjected to the ChIP assay using the EZ-Zyme ChIP kit (Cat. No. 17-371; EMD Millipore). Formaldehyde (37%) was added to the media and incubated at room temperature for 10 min. Glycine was subsequently added to the media to quench the unreacted formaldehyde. After 5 min, chromatin and proteins from the formaldehyde cross-linked cells were collected and enzymatically digested. The following antibodies were added to the chromatin: anti-AP-1 (Cat. No. 09-754; 2 μg; EMD Millipore), IgG (Cat. No. 10700; 1 μg; Invitrogen; Thermo Fisher Scientific, Inc.), anti-RNA polymerase (Cat. No. 49-1033; 1 μg; Invitrogen; Thermo Fisher Scientific, Inc.) and were incubated overnight at 4°C. DNA-protein crosslinks were reversed to free DNA, and purified. Gel electrophoresis was used to detect the strip.

Reverse-transcription quantitative PCR (RT-qPCR)

Total RNA was extracted from the VSMCs using TRIzol reagent (Invitrogen; Thermo Fisher Scientific, Inc.), according to the manufacturer's protocol. The RNA was reversely transcribed into cDNA using the PrimeScript™ RT reagent Kit (Takara Biotechnology Co., Ltd) based on the manufacturer's protocol. The qPCR reaction mixture consisted of 2X SYBR Premix Ex TaqTM II, deionized water, a PCR forward primer, a PCR reverse primer and the template cDNA. The primer sequences are presented in Table II. The reaction conditions were as follows: pre-denaturation for 5 min at 95°C, 95°Cfor 10 sec, 58°Cfor 20 sec, and 72°Cfor 30 sec, for a total of 45 cycles. The results were analyzed with SPSS software (version 17.0; IBM Corp.).

Table II. *The primer sequence of genes*

Gene	Forward primer (5′ to 3′)	Reverse primer (5′ to 3′)	*PCR size*
AP-1	CTCAGCAACTTCAACCCG	GCACTTGGAGGCAGCGAT	260
SM-α	CGGGCATCCACGAAACCA	CCGCCGATCCAGACAGAA	200
GAPDH	TCTGCTCCTCCCTGTTC	CACCCCATTTGATGTTAG	327

Western blotting

The cells in all groups were collected and lysed in RIPA lysis buffer (Thermo Fisher Scientific, Inc.). A BCA protein quantitative kit (Cat. No. 23250; Thermo Fisher Scientific, Inc.) was used to determine protein concentration. Proteins were subsequently separated via SDS-PAGE at 95 V for 120 min, followed by an electrophoretic transfer to a polyvinylidene fluoride membrane (EMD Millipore) at 15 V for 50 min. The membrane was blocked with 5% non-fat milk at 4°C for 2 h and incubated with anti-rat primary antibodies against AP-1 (Cat. No. 09-754; 1:2,000; 41 kDa; EMD Millipore), SM-α (Cat. No. ta332577; 1:2,000; 42kDa; OriGene Technologies, Inc.) and β-Tubulin (Cat. No. 2128S; 1:2,000; 55kDa; Cell Signaling Technology) overnight at 4°C. After washing with PBST solution, the membrane was incubated with a goat anti-rabbit IgG secondary antibody (Cat. No. zb-2306; 1:3,000;

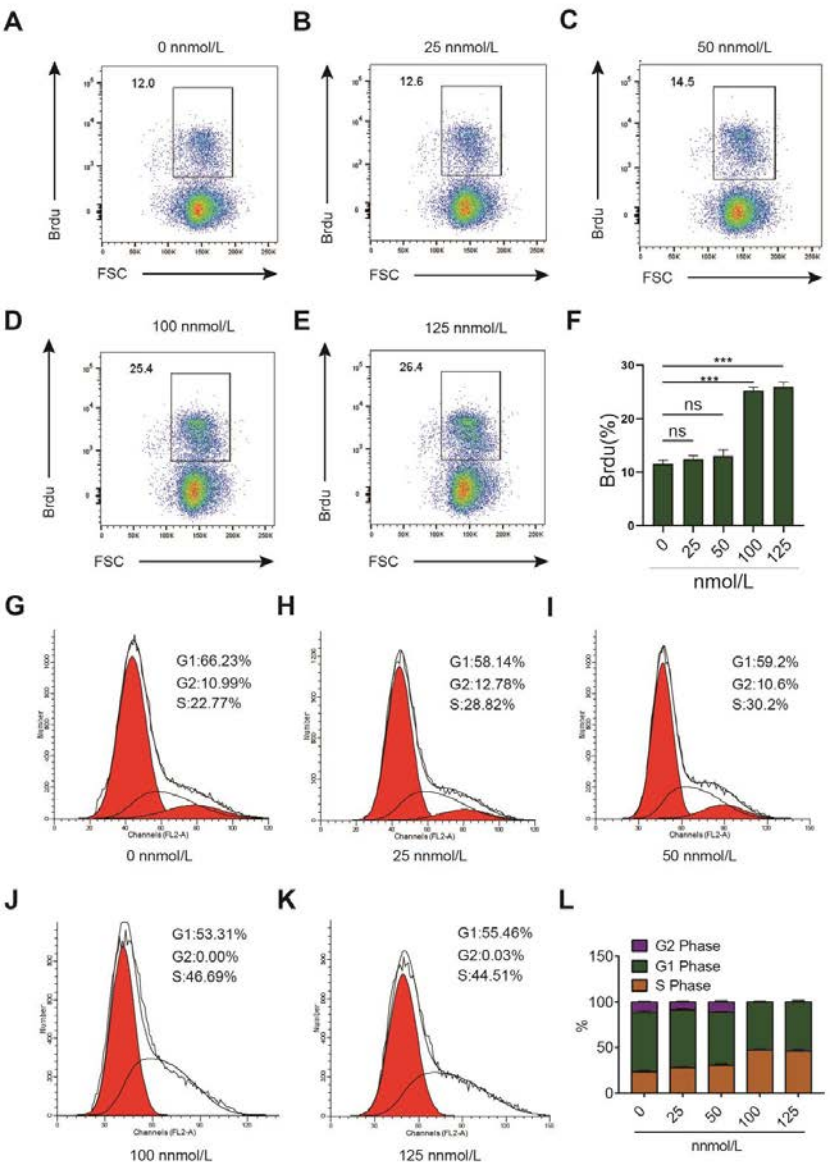


Fig. 1. *High dose of insulin promoted proliferation of VSMCs and increased percentage of cells in the S phase.* ***A-F)*** *VSMCs were treated with increasing concentrations of insulin (0, 25, 50, 100 and 125 nmol/l) and cell proliferation was analyzed by flow cytometry.* ***G-L)*** *The effect of increasing concentrations of insulin (0, 25, 50, 100 and 125 nmol/l) on the VSMC cell cycle was analyzed by flow cytometry. The one-way ANOVA followed by Tukey's post hoc test was used to evaluate statistical significance. Data are presented as the mean ± SEM (n=3). ***P<0.001, ns: not significant.*

OriGene Technologies, Inc.) at room temperature for 1 h. The membrane was washed three times with PBST, incubated with the ECL reagent (Thermo Fisher Scientific, Inc.) and imaged with a Bio-Rad gel imaging system (Bio-Rad). Quantity One software was used to perform densitometry analysis.

Statistical analysis

All statistical analyses were performed using GraphPad Prism software (version 7.0; GraphPad Software, Inc.). Two-tailed unpaired Student's *t*-tests and one-way ANOVA followed by Tukey's multiple comparison post-test were used to compare two or more groups, respectively. $P<0.05$ was considered to indicate a statistically significant difference. All experiments were performed in triplicate.

RESULTS

High dose insulin promotes proliferation of VSMCs and increases percentage of cells in the S phase

Flow cytometry was used to analyze the effect of different concentrations of insulin on the proliferation

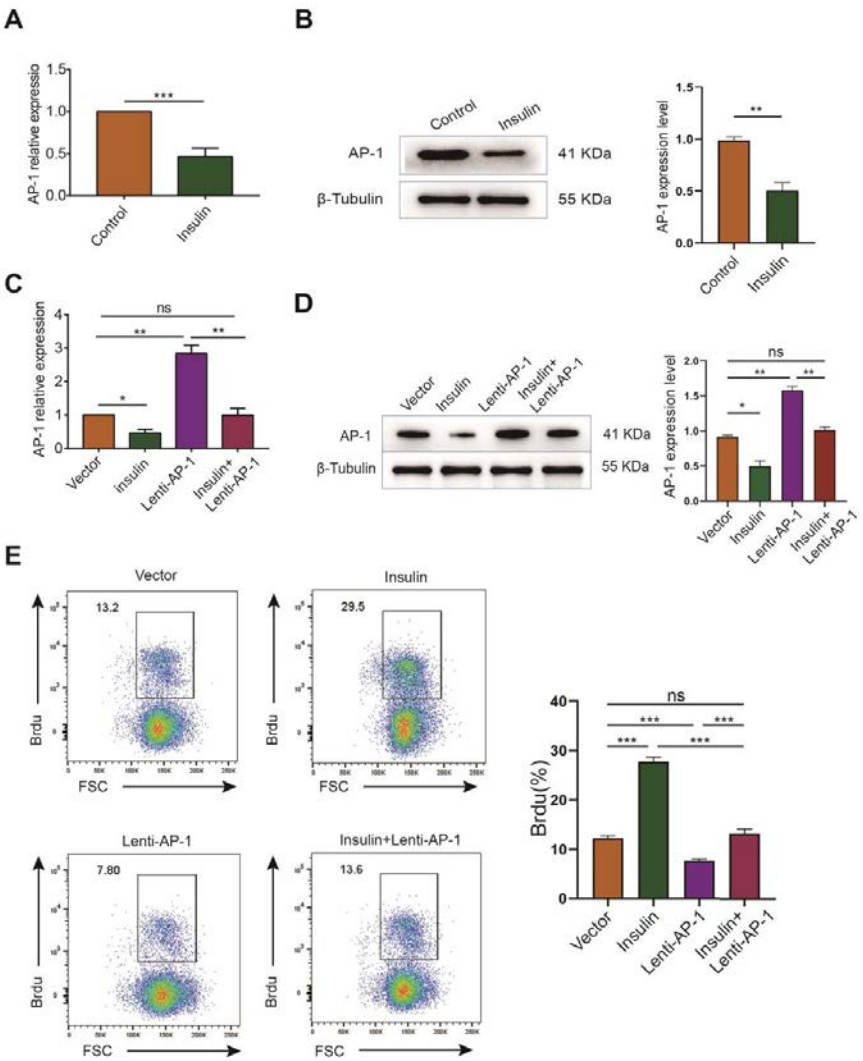
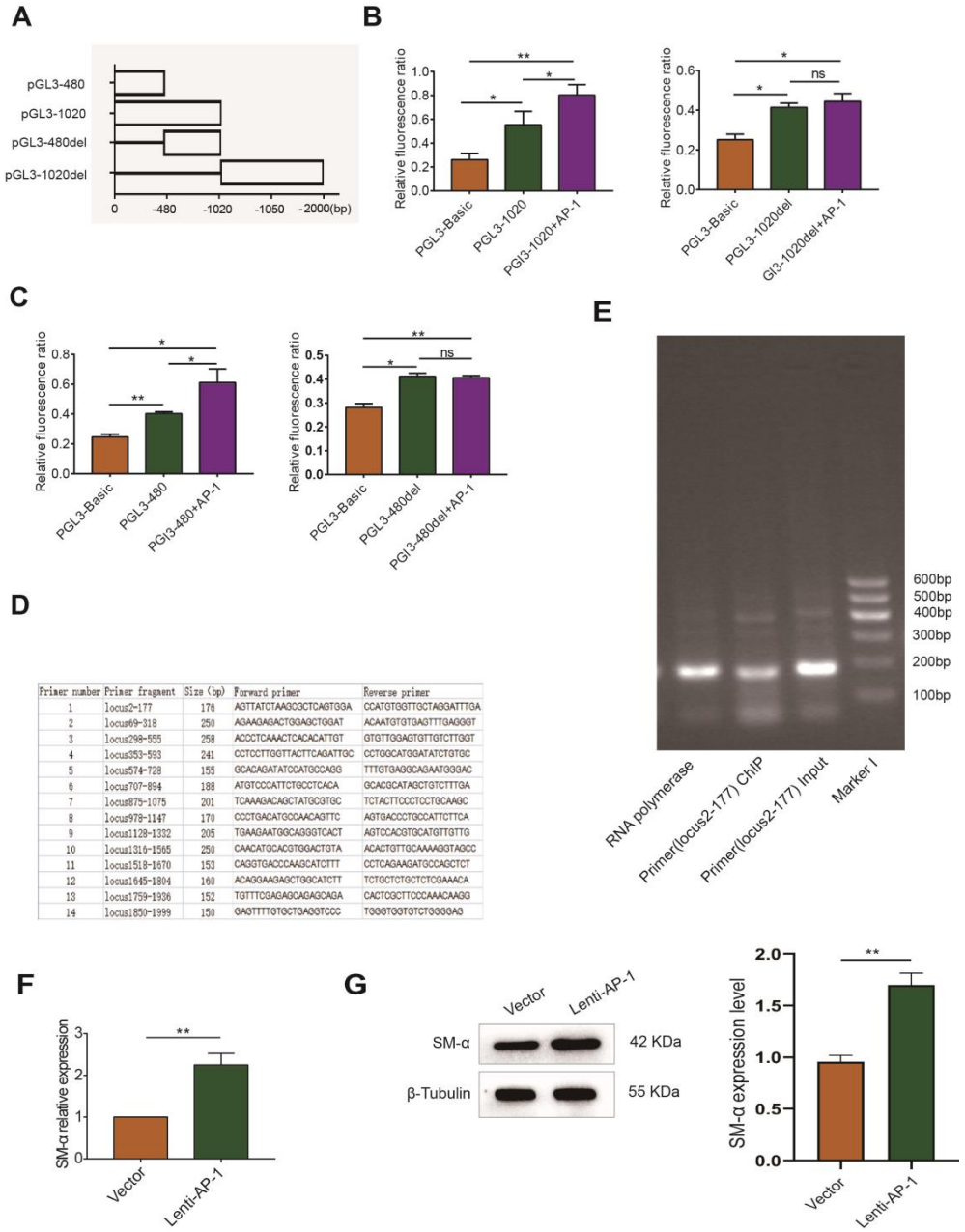


Fig. 2. *AP-1 is downregulated by high dose of insulin and overexpression of AP-1 inhibits VSMC proliferation.* ***A, B****) The expression of AP-1 in VSMCs treated with insulin was analyzed by RT-qPCR and western blotting.* ***C, D****) The expression of AP-1 in VSMCs was analyzed by RT-qPCR and western blotting.* ***E****) The percentage of proliferating VSMCs was analyzed by flow cytometry. The one-way ANOVA followed by Tukey's post hoc test or a two-tailed unpaired Student's t-test was used to evaluate statistical significance. Data are presented as the mean ± SEM (n=3).* $^{*}P<0.05$, $^{**}P<0.01$, $^{***}P<0.001$, *ns: not significant.*

of VSMCs and percentage of cells in the S phase. The results showed that the percentage of proliferating VSMCs increased significantly when treated with 100 and 125 nmol/l insulin (Fig. 1 A-F). Furthermore, the percentage of cells in S phase increased, and then eventually decreased following stimulation with different concentrations of insulin (Fig. 1 G-L). As shown, 100 nmol/l insulin has the maximal effect on the cells, and the percentage of cells in the G2 phase was <1% when treated with 100 and 125 nmol/l insulin (Fig. 1 J-L).



Primer number	Primer fragment	Size (bp)	Forward primer	Reverse primer
1	locus2-177	176	AGTTATCTAAGCGCTCAGTGGA	CCATGTGGTTGCTAGGATTTGA
2	locus69-318	250	AGAAGAGACTGGAGCTGGAT	ACAATGTGTGAGTTTGAGGGT
3	locus299-555	258	ACCCTCAAACTCACACATTGT	GTGTTGGAGTGTTGTCTTGGT
4	locus353-593	241	CCTCCTTGGTTACTTCAGATTGC	CCTGGCATGGATATCTGTGC
5	locus574-728	155	GCACAGATATCCATGCCAGG	TTTGTGAGGCAGAATGGGAC
6	locus707-894	188	ATGTCCCATTCTGCCTCACA	GCACGCATAGCTGTCTTTGA
7	locus875-1075	201	TCAAAGACAGCTATGCGTGC	TCTACTTCCCTCCTGCAAGC
8	locus978-1147	170	CCCTGACATGCCAACAGTTC	AGTGACCCTGCCATTCTTCA
9	locus1128-1332	205	TGAAGAATGGCAGGGTCACT	AGTCCACGTGCATGTTGTTG
10	locus1316-1565	250	CAACATGCACGTGGACTGTA	ACACTGTTGCAAAAGGTAGCC
11	locus1518-1670	153	CAGGTGACCCAAGCATCTTT	CCTCAGAAGATGCCAGCTCT
12	locus1645-1804	160	ACAGGAAGAGCTGGCATCTT	TCTGCTCTGCTCTCGAAACA
13	locus1759-1936	152	TGTTTCGAGAGCAGAGCAGA	CACTCGCTTCCCAAACAAGG
14	locus1850-1999	150	GAGTTTTGTGCTGAGGTCCC	TGGGTGGTGTCTGGGGAG

Fig. 3. *AP-1 binds to SM-α gene promoter at locus 2-177 and upregulates SM-α gene expression.* ***A)*** *The design of the gene primers in the SM-αgene promoter region.* ***B, C)*** *Relative luminescence ratio was analyzed by a luciferase reporter assay.* ***D)*** *The design of primer fragments in the SM-αgene promoter region.* ***E)*** *The gel electrophoresis of the primer by chromatin immunoprecipitation assay-PCR.* ***F, G)*** *The expression of SM-α in VSMCs was analyzed by reverse transcription-quantitative PCR and western blotting. The one-way ANOVA followed by Tukey's post hoc test or a two-tailed unpaired Student's t-test was used to evaluate statistical significance. Data are presented as the mean ± SEM (n=3).* $^{*}P<0.05$, $^{**}P<0.01$, *ns: not significant.*

AP-1 is downregulated by high dose of insulin and overexpression of AP-1 inhibits VSMC proliferation

High dose of insulin promoted the proliferation of VSMCs, however, the underlying mechanism remained unclear. Therefore, in order to investigate whether high dose insulin affected AP-1, 100nmol/l insulin was used to treat VSMCs for 24 h. The RT-qPCR and western blotting revealed that 100nmol/l insulin inhibited the expression of AP-1 (Fig. 2 A, B). Furthermore, VSMCs transfected with the AP-1 overexpression vector were treated with 100nmol/l insulin. The expression of AP-1 was less in the insulin+Lenti-AP-1 group compared with the Lenti-AP-1 only group (Fig. 2 C, D). Additionally, the percentage of proliferating VSMCs was decreased in theinsulin+Lenti-AP-1 group, compared with the insulin only group (Fig. 2E).

AP-1 binds to SM-α gene promoter at locus 2-177 and upregulates SM-α gene expression

As the association between AP-1 and SM-α expression remains unclear in VSMCs, a luciferase reporter assay was used to investigate the binding of AP-1 and the SM-α gene promoter region. Compared with the results in the SM-α overexpression vector group, the relative luminescence intensity of cells in the SM-α + AP-1 overexpression vector group

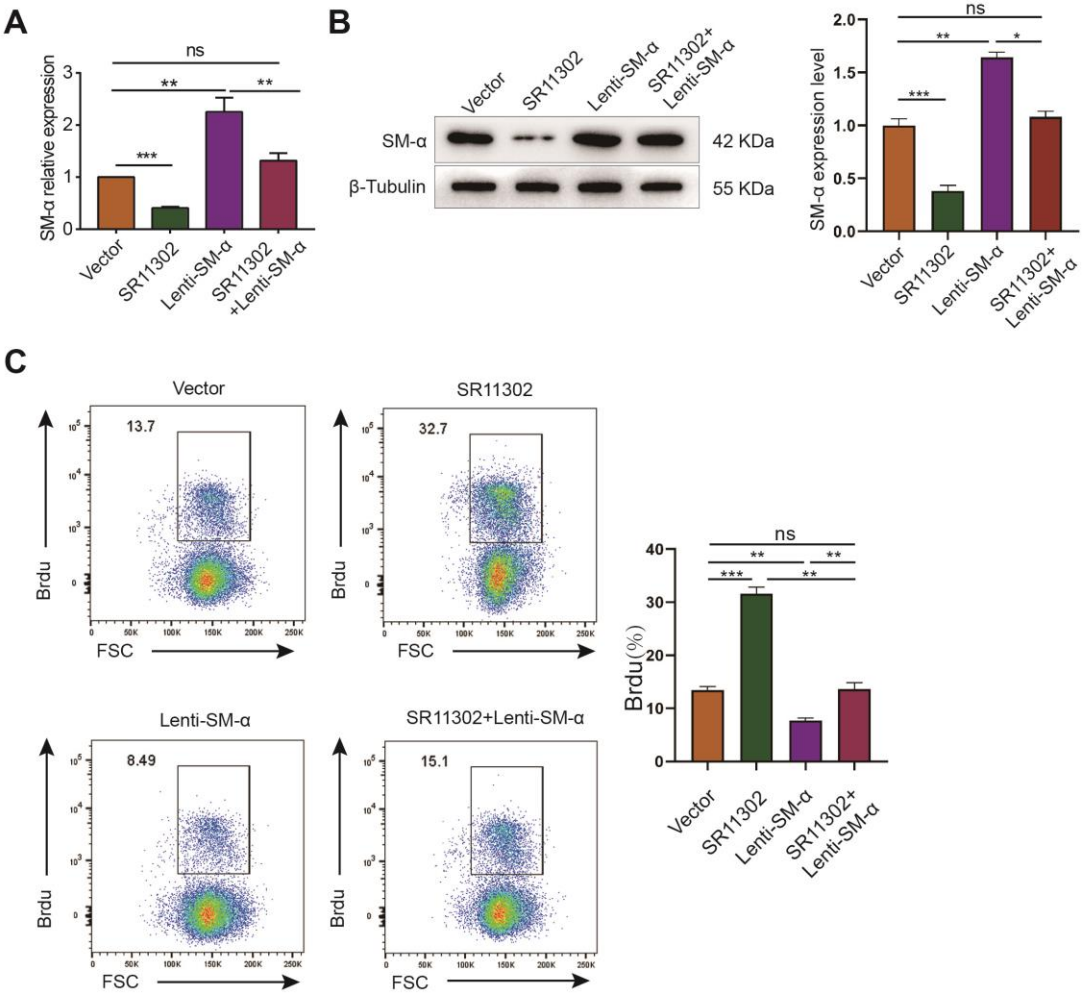


Fig. 4. *Inhibition of AP-1 promotes proliferation of VSMCs and suppresses SM-α expression.* ***A, B****) The expression of SM-α in VSMCs was analyzed by reverse transcription-quantitative and western blotting.* ***C****) The percentage of proliferating VSMCs was analyzed by flow cytometry. The one-way ANOVA followed by Tukey's post hoc test or a two-tailed unpaired Student's t-test was used to evaluate statistical significance. Data are presented as the mean ± SEM (n=3). *P<0.05, **P<0.01, ***P<0.001, ns: not significant.*

significantly increased at locus 1-1020 and locus 1-480 in the SM-α gene promoter region. However, there was no significant change in the relative fluorescence intensity of the cells in the SM-α + AP-1 overexpression vectors group at locus 1021-2000 and locus 481-1020 in the SM-α gene promoter region (Fig. 3 A-C). This highly indicates that the binding site resides in locus 1-480. ChIP assay was used to further validate these results. It was revealed that primer No. 1 expanded the strip (Fig. 3 D, E), suggesting that the accurate binding sites were located at locus 2-177. Then, VSMCs were transfected with the AP-1 overexpression vector, and SM-α gene expression was detected by RT-qPCR and western blotting. As shown in Fig. 3 F, G, the expression of SM-α significantly increased following transfection with the AP-1 overexpression vector compared with the blank control, indicating that AP-1 upregulated SM-α gene expression.

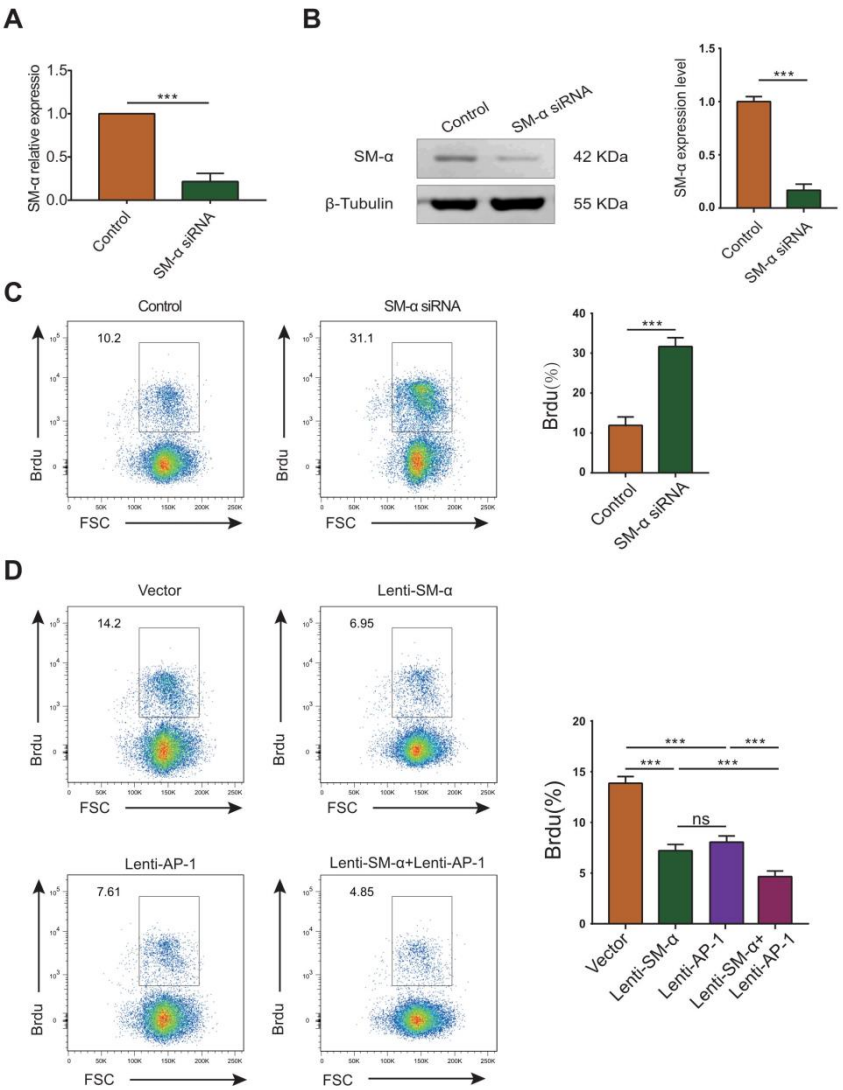


Fig. 5. *Inhibition of SM-α promotes proliferation of VSMCs, while overexpression of SM-α inhibits proliferation of the cells.* ***A, B****) The expression of SM-α in VSMCs was analyzed by reverse transcription-quantitative and western blotting.* ***C, D****) The percentage of proliferating VSMCs was analyzed by flow cytometry. The one-way ANOVA followed by Tukey's post hoc test or a two-tailed unpaired Student's t-test was used to evaluate statistical significance. Data are presented as the mean ± SEM (n=3). *P<0.05, **P<0.01, ***P<0.001, ns: not significant.*

Inhibition of AP-1 promotes proliferation of VSMCs and suppresses SM-α expression

To investigate whether inhibition of AP-1 downregulated SM-α gene expression and promoted the proliferation of VSMCs, VSMCs were treated with 10 μM SR11302 for 1 h and subsequently transfected with the SM-α overexpression vector. The expression of SM-α was lower in the SR11302-treated group compared to that in the vector (blank control) group. Besides, the expression of SM-α was preserved in theSR11302+SM-α overexpression vector group compared to that in the SR11302-treated group (Fig. 4 A, B). Proliferation of VSMCs was mostly suppressed in the SM-α vector group, mildly suppressed in the SR11302+SM-α overexpression vector group compared with that in the SR11302-treated group (Fig. 4C). These results also suggested that elevation of SM-α was more likely to restrain VSMC proliferation than simply being a negative correlation marker for VSMC proliferation.

Inhibition of SM-α promotes proliferation of VSMCs, while overexpression of SM-α inhibits proliferation of the cells

To further confirm whether SM-*α was just negatively correlated with VSMC proliferation or if it directly dictated VSMC proliferation,* we used small interfering RNA (siRNA) to knockdown endogenous SM-α in VSMCs (Fig. 5 A, B). Similar to the effect of SR11302, knockdown of SM-α increased VSMC proliferation independent of AP-1 and insulin (Fig. 5C). We next investigated the SM-α overexpression vector group and found that VSMC proliferation was inhibited compared with the vector (blank control) group. The SM-α+ AP-1 overexpression vectors group had the most suppressive VSMC proliferation (Fig. 5D). These results confirmed that inhibition of SM-α promotes the proliferation of VSMCs, while overexpression of SM-α inhibits proliferation of VSMCs.

DISCUSSION

A number of clinical studies have reported that the prevalence of vascular atherosclerosis in patients with type 2 diabetes mellitus is significantly increased following a high dose of insulin (8, 9). The common pathophysiological mechanism underlying vascular proliferative diseases, such as atherosclerosis, is the abnormal proliferation of VSMCs (10). VSMCs are the main cell types implicated in atherosclerosis development, and unlike other mature cell types, maintain a remarkable plasticity. In mature vessels, differentiated VSMCs control the vascular tone and the blood pressure (11). It has been previously reported that VSMCs exhibited abnormal proliferation in atherosclerotic lesions (12). Moreover, VSMC proliferation was shown to be directly related to insulin level (13). Insulin, a regulator of glucose homeostasis, not only regulates metabolism, but also promotes growth (14). Consequently, there are concerns regarding excessive cell proliferation in patients with diabetes with long-term hyperinsulinemia (15). Under normal conditions, the physiological level of insulin in the body is 4.03-23.46 nmol/l, which is a fasting level, reaching 9.93-124.9 nmol/l two hours after a meal, dropping to 5.06-25 nmol/l after three hours and then returning to fasting levels. However, patients with diabetes are exposed to high levels of insulin as a result of insulin resistance (16). Certain patients with diabetes and accompanying atherosclerosis have insulin levels reaching 50-100nmol/l. Therefore, in the present study, VSMCs were stimulated with different concentrations of insulin (0 nmol/l, 25 nmol/l, 50 nmol/l, 100 nmol/l, 125 nmol/l) for 24 h *in vitro*. Flow cytometry was used to investigate cell proliferation and cell cycle. The results revealed that the percentage of proliferating VSMCs significantly increased at insulin concentrations of 100 and 125 nmol/l. In addition, the percentage of cells in the S phase increased in a concentration-dependent manner and reached a maximum at 100nmol/l insulin, followed by a slight decline. Although the percentage of cells in the S phase decreased following treatment with 125 nmol/l insulin, it still accounted for a large proportion. Therefore, high dose of insulin not only promoted the proliferation of VSMCs, but also exerted effects on VSMCs in the S phase. The results of the present study are consistent with the clinical observation that patients with diabetes are at a significantly higher risk for atherosclerosis following treatment with high doses of insulin (17).

The transcriptional activator AP-1 is a heterodimer

composed of c-Jun and c-Fos proteins (18). AP-1 binds to its receptors and genes through specific conserved sequences to initiate gene expression, thereby controlling several cellular processes, including proliferation, differentiation and apoptosis (19). It has been previously reported that AP-1 is involved in cell proliferation (20). In VSMCs, high expression of AP-1 inhibits the proliferation of VSMCs (21). Another study revealed that AP-1 in normal VSMCs was adequately expressed and its downstream signaling pathways were associated with inhibition of active VSMC restenosis (22). Therefore, in order to investigate whether AP-1 is involved in the VSMC proliferation induced by high dose insulin in the present study, VSMCs were stimulated with high dose insulin for 24 h *in vitro*, and subsequently transfected with an AP-1 overexpression vector. High dose of insulin promoted the proliferation of VSMCs by downregulating AP-1, yet its target genes remain to be clarified.

A previous study revealed that there is a recognition site in the promoter region of the SM-α gene that binds to AP-1 (23). SM-α is a structural protein found in the VSMC cytoskeleton, and plays a key role in cell movement and contraction (24, 25). The expression of SM-α in VSMCs significantly decreases in the presence of blood vessel abnormalities, high blood cholesterol, vascular endothelial injury and other factors that cause the formation of vascular wall plaques (26). Previous studies revealed that the protein expression level of SM-α was decreased in VSMCs that had been stimulated with high dose insulin (27, 28). Moreover, Kee et al. revealed that SM-α was sufficiently expressed in VSMCs under physiological conditions (29), with contrast to limited expression was in proliferating VSMCs. Crawford et al. reported that rats lacking SM-α died shortly after birth due to abnormal VSMC growth and functions (30). However, whether SM-α was negatively correlated with proliferation of VSMCs or it directly affected proliferation of VSMCs remained obscure (31). The present study revealed that AP-1 binds to the SM-α gene promoter at locus 2-177 and upregulates SM-α gene expression. Furthermore, inhibition of AP-1 promoted the proliferation of VSMCs by downregulating SM-α gene expression. These data provided a new understanding of the mechanism by which insulin promotes the abnormal proliferation of VSMCS.

In summary, the present study demonstrated that high dose insulin inhibited the expression of AP-1, resulting in downregulation of SM-α gene expression, which eventually led to abnormal proliferation of VSMCs. However, our study had some limitations. Although the effect of increasing concentrations of insulin on the proliferation of VSMCs was observed *in vitro*, the study remains to be further investigated *in vivo*.

ACKNOWLEDGEMENTS

The authors appreciate the support by the Department of Cardiology, Institute of Field Surgery, Daping Hospital and Department of Cardiac Surgery, Xinqiao Hospital Affiliated to Army Medical University and the Key Laboratory of Basic Pharmacology of the Ministry of Education and Joint International Research Laboratory of Ethnomedicine to the Ministry of Education Affiliated to Zunyi Medical University.

This work was supported by the National Natural Science Foundation of China (No.81370367).

REFERENCES

1. Herman ME, O'Keefe JH, Bell DSH, Schwartz SS. Insulin therapy increases cardiovascular risk in type 2 diabetes. Prog Cardiovasc Dis 2017; 60:422-34.
2. Shiny A, Regin B, Mohan V, Balasubramanyam M. Coordinated augmentation of NFAT and NOD signaling mediates proliferative VSMC phenotype switch under hyperinsulinemia. Atherosclerosis 2016; 246:257-66.
3. Das S, Zhang E, Senapati P, Amaram V, et al. A novel angiotensin II-Induced long noncoding RNA giver regulates oxidative stress, inflammation, and proliferation in vascular smooth muscle cells. Circ Res 2018; 123:1298-312.
4. Buglak NE, Jiang W, Bahnson ESM: Cinnamic aldehyde inhibits vascular smooth muscle cell proliferation and neointimal hyperplasia in Zucker Diabetic Fatty rats. Redox Bio 2018; 19:166-78.
5. Zhang ZW, Guo RW, Lv JL, et al. MicroRNA-99a

inhibits insulin-induced proliferation, migration, dedifferentiation, and rapamycin resistance of vascular smooth muscle cells by inhibiting insulin-like growth factor-1 receptor and mammalian target of rapamycin. Biochem Biophys Res Commun 2017; 486(2):414-42.
6. Ping S, Liu S, Zhou Y, et al. Protein disulfide isomerase-mediated apoptosis and proliferation of vascular smooth muscle cells induced by mechanical stress and advanced glycosylation end products result in diabetic mouse vein graft atherosclerosis. Cell Death Dis 2017; 8:e2818.
7. Ryu NH, Shin JM, Um JY, Park IH, Lee HM. Wogonin inhibits transforming growth factor β1-induced extracellular matrix production via the p38/activator protein 1 signaling pathway in nasal polyp-derived fibroblasts. Am J Rhinol Allergy 2016; 30:128-33.
8. Hua S, Loehr LR, Tanaka H, Heiss G, Coresh J, Selvin E, Matsushita K. Ankle-brachial index and incident diabetes mellitus: the atherosclerosis risk in communities (ARIC) study. Cardiovasc Diabetol 2016; 15:163.
9. He X, Hu X, Ma X, et al. Elevated serum fibroblast growth factor 23 levels as an indicator of lower extremity atherosclerotic disease in Chinese patients with type 2 diabetes mellitus. Cardiovasc Diabetol 2017; 16:77.
10. Gao S, Xu L, Zhang Y, et al. Salusin-α inhibits proliferation and migration of vascular smooth muscle cell via Akt/mTOR signaling. Cell Physiol Biochem 2018; 50:1740-53.
11. Bonetti J, Corti A, Lerouge L, Pompella A, Gaucher C. Phenotypic Modulation of Macrophages and Vascular Smooth Muscle Cells in Atherosclerosis-Nitro-Redox Interconnections. Antioxidants (Basel) 2021; 10(4):516.
12. Bennett MR, Sinha S, Owens GK. Vascular smooth muscle cells in atherosclerosis. Circ Res 2016; 118:692-702.
13. Harith HH, Di Bartolo BA, Cartland SP, Genner S, Kavurma MM. Insulin promotes vascular smooth muscle cell proliferation and apoptosis via differential regulation of tumor necrosis factor-related apoptosis-inducing ligand. J Diabetes 2016; 8:568-78.
14. Yunn NO, Kim J, Kim Y, Leibiger I, Berggren PO, Ryu SH. Mechanistic understanding of insulin receptor modulation:iImplications for the development of anti-diabetic drugs. Pharmacol Ther 2018; 185:86-98.
15. Kvandová M, Majzúnová M, Dovinová I. The role of PPARgamma in cardiovascular diseases. Physiol Res 2016; 65:S343-S363.
16. Petersen MC, Shulman GI. Mechanisms of Insulin Action and Insulin Resistance. Physiol Rev 2018; 98:2133-223.
17. Didangelos T, Kantartzis K. Diabetes and heart failure: is it hyperglycemia or hyperinsulinemia? Curr Vasc Pharmacol 2020; 18:148-57.
18. Janson ND, Jehanathan N, Jung S, Priyathilaka TT, Nam BH, Kim MJ, Lee J. Insight into the molecular function and transcriptional regulation of activator protein 1 (AP-1) components c-Jun/c-Fos ortholog in red lip mullet (Liza haematocheila). Fish Shellfish Immunol 2019; 93:597-611.
19. Lazenka MF, David BG, Lichtman AH, Nestler EJ, Selley DE, Sim-Selley LJ. Delta FosB and AP-1-mediated transcription modulate cannabinoid CB1 receptor signaling and desensitization in striatal and limbic brain regions. Biochem Pharmacol 2014; 91:380-9.
20. Phanstiel DH, Van Bortle K, Spacek D, et al. Static and dynamic DNA loops form AP-1-Bound activation hubs during macrophage development. Mol Cell 2017; 67:1037-48.e6.
21. Zhao J, Imbrie GA, Baur WE, et al. Estrogen receptor-mediated regulation of microRNA inhibits proliferation of vascular smooth muscle cells. Arterioscler Thromb Vasc Biol 2013; 33:257-65.
22. Guo Y, Fan Y, Zhang J, Chang L, Lin JD, Chen YE. Peroxisome proliferator-activated receptor γ coactivator 1β (PGC-1β) protein attenuates vascular lesion formation by inhibition of chromatin loading of minichromosome maintenance complex in smooth muscle cells. J Biol Chem 2013; 88:4625-36.
23. Fang H, Luo X, Wang Y, et al. Correlation between single nucleotide polymorphisms of the ACTA2 gene and coronary artery stenosis in patients with type 2 diabetes mellitus. Exp Ther Med 2014; 7:970-6.
24. Liu Z, Wang Y, Zhu H, Qiu C, Guan G, Wang J, Guo Y. Matrine blocks AGEs- induced HCSMCs phenotypic conversion via suppressing Dll4-Notch pathway. Eur J Pharmacol 2018; 835:126-31.

25. Charles R, Bourmoum M, Claing A. ARF GTPases control phenotypic switching of vascular smooth muscle cells through the regulation of actin function and actin dependent gene expression. Cell Signal 2018; 46:64-75.
26. Sukhanov S, Higashi Y, Shai SY, et al. SM22α (Smooth Muscle Protein 22-α) promoter-driven IGF1R (Insulin-Like Growth Factor 1 Receptor) deficiency promotes atherosclerosis. Arterioscler Thromb Vasc Biol 2018; 38:2306-17.
27. Selig JI, Ouwens DM, Raschke S, et al. Impact of hyperinsulinemia and hyperglycemia on valvular interstitial cells - A link between aortic heart valve degeneration and type 2 diabetes. Biochimica et biophysica acta. Mol Basis Dis 2019; 1865:2526-37.
28. Ackers-Johnson M, Talasila A, Sage AP, et al. Myocardin regulates vascular smooth muscle cell inflammatory activation and disease. Arterioscler Thromb Vasc Biol 2015; 35:817-28.
29. Kee HJ, Kim GR, Cho SN, Kwon JS, Ahn Y, Kook H, Jeong MH. miR-18a-5p MicroRNA increases vascular smooth muscle cell differentiation by downregulating Syndecan4. Korean Circ J 2014; 44:255-63.
30. Crawford K, Flick R, Close L, et al. Mice lacking skeletal muscle actin show reduced muscle strength and growth deficits and die during the neonatal period. Mol cellu Bio 2002; 22:5887-96.
31. Ping S, Li Y, Liu S, et al. simultaneous increases in proliferation and apoptosis of vascular smooth muscle cells accelerate diabetic mouse venous atherosclerosis. PloS One 2015; 10:e0141375.

JOURNAL OF BIOLOGICAL REGULATORS & HOMEOSTATIC AGENTS Vol. 35, no. 3, 1041-1045 (2021)

LETTER TO THE EDITOR

Serum Metalloprotease 3 (MMP-3) biomarker of therapeutic efficacy during treatment of rheumatoid arthritis

G. Di Spigna[1*], FW. Rossi[1,2*], I. Mormile[1], P. Ladogana[1], L. Buonavolontà[1], B. Covelli[1], S. Salzano[3], F. Napolitano[1], A. Giannini[1] and L. Postiglione[1,2]

[1]Department of Translational Medical Sciences, University of Naples Federico II, Naples, Italy; [2]Center for Basic and Clinical Immunology Research (CISI), University of Naples Federico II, Naples, Italy; [3]Institute of Experimental Endocrinology and Oncology "G. Salvatore" (National Research Council), Naples, Italy

Received February 17, 2021 – Accepted May 12, 2021

[*]These authors contributed equally

To the Editor,

In the last three decades, it has been widely acknowledged that serum levels of the Matrix Metalloproteases-3 (MMP-3, stromelysin-1) reflect positively rheumatoid arthritis (RA) disease activity in terms of joint and bone injury, radiological erosion, clinical outcome, and drug responsiveness (1, 2). Physiologically, the balance between the processes of destruction and generation of the extracellular matrix constituents is finely regulated by specific tissue inhibitors of metalloproteases (TIMPs) (3). The key effectors in tissue destruction in patients with RA are metalloproteases, secreted in response to stimulation by pro-inflammatory cytokines (4).

Among the proteases, MMP-3 acts on many substrates of the extracellular matrix and is responsible for activating other metalloproteases, thus playing an essential role in the pathogenesis of the disease (5). *In vitro* and *in vivo* studies indicate that synovial fibroblasts or B cells are great producers of MMP-3, which, in turn, are involved in the joint destruction process. Inflamed synovial fluids are also characterized by high levels of MMP-3, thus confirming its important role in RA pathogenesis. Indeed, according to Ma et al., systemic levels of MMP-3 significantly reflect synovial involvement (6). Several Authors concluded that MMP-3 is a useful diagnostic serum biomarker of RA (7). The excess of MMP-3 in RA patients' joints cannot be balanced by TIMPs; this causes the activation of further MMPs, uncontrolled proteolysis, excessive degradation of the extracellular matrix (8), a progression of the destructive process, and consequent deformation and joint disability (2).

Although many studies have highlighted the potential role of MMP-3 as a marker of bone erosion and disease activity, MMP-3 has not yet gained adequate consideration in clinical practice. This cross-sectional study aimed to evaluate MMP-3 blood levels, as a surrogate marker of activity, in patients affected by RA and treated with different therapeutic regimens, according to the European League Against Rheumatism (EULAR) recommendations (9).

MATERIALS AND METHODS

Levels of MMP-3 were evaluated in serum samples

Key words: MMP-3; rheumatoid arthritis; biomarker; DMARDs; methotrexate

Corresponding Author:
Prof. Loredana Postiglione,
University of Naples Federico II,
Via S. Pansini 5,
80131 Napoli, Italy
Tel: +39 081 7463308
e-mail: loredana.postiglione@unina.it

0393-974X (2021)
Copyright © by BIOLIFE, s.a.s.
This publication and/or article is for individual use only and may not be further reproduced without written permission from the copyright holder.
Unauthorized reproduction may result in financial and other penalties
DISCLOSURE: ALL AUTHORS REPORT NO CONFLICTS OF INTEREST RELEVANT TO THIS ARTICLE.

from 92 patients (F=76; M=16; mean age 49.62±12.43 years) affected by RA, classified according to the ACR/EULAR criteria 2010 (10) and admitted to the Department of Translational Medical Sciences - Autoimmune Diseases Unit of the University of Naples Federico II, and followed up from June 2017 to October 2019. Fifty healthy donors, age and sex-matched, with no immune system diseases, infections, liver or kidney diseases, or cancers, were included as a control group. All patients signed a written informed consensus, and the study was performed following the Helsinki Declaration and according to the Local Ethical Committee (NA 126/15). Changes in treatment with the conventional synthetic disease-modifying antirheumatic drugs (bDMARDs), or methotrexate (MTX), in the previous three months were a reason for exclusion. Patients affected by autoimmune diseases other than RA, hepatic, pulmonary, kidney diseases, acute and chronic infections, or malignancies were also excluded. Exclusion criteria were also non-controlled hypertension (arterial blood pressure ≥140/90 mmHg), hypercholesterolemia, and age <18 years or >70. Disease duration, the number of tender and swelling joints were recorded for all patients; disease activity was evaluated using the Disease Activity Score 28 (DAS28) at a basal time (11). According to the DAS-28 score, patients were classified as having mild (2.6 ≤ DAS28 < 3.2), moderate (3.2 ≤ DAS28 <5.1), or highly active (DAS28 ≥ 5.1) RA.

Patients were divided into groups according to the pharmacological regimen practiced: 30 patients (F=24; M=6) treated with MTX alone (10 mg/week); 10 patients (7=F; 3=M) treated with MTX+Abatacept (750 mg/month administered intravenously); 10 patients (8=F; 2=M) treated with MTX+Tocilizumab (8 mg/kg/month); 12 patients (10=F; 2=M) treated with MTX+Infliximab (3 mg/kg/month). 30 patients (F=27; M=3) affected by early RA (disease duration ≤1 year at the time of diagnosis) (12) were also enrolled and 16 of them (16/30=53%) were receiving corticosteroids (median 5 mg/day prednisone, range 5–10 mg/day) in a stable dose for at least 4 weeks before serum sample collection. Among patients treated with MTX+biological DMARDs (bDMARDs), 5 of them (5/32=15.6%) were treated with corticosteroids (<10 mg/day). Fifty healthy donors were also evaluated as a control group (Table I).

The serum MMP-3 levels obtained at the first observation from patients with early RA were considered as the basal value for all the groups. Serum MMP3 levels of 50 healthy controls and of RA patients were detected by an immunoenzymatic assay. Serum samples were collected in all treated patients at 12 weeks (MTX alone and MTX+ bDMARDs).

Briefly, serum samples were collected from centrifuged venous blood (5 ml) after overnight fasting. Specimens were centrifuged and stored at -80°C until analysis. According to the manufacturer's instructions, the serum level of soluble MMP-3 was measured with a human MMP-3 detection kit (AESKU Diagnostics, Germany). This method can detect in human serum, total MMP-3 in both the pro- and the active form. All measurements were done in duplicate. Serum samples were placed in designated microwells. Plates were then incubated for 30 min at room temperature and washed three times with wash buffer. 100 µL TMB substrate was then added to each well, and plates were incubated for 30 min at room temperature in the dark. 100 µL of stop solution was added to each well, using the same order as the substrate. After 5 minutes of incubation, the absorbance of each microwell was read at 450 nm (optionally 450/620 nm) on a spectrophotometer. The assays were performed blindly, without knowledge of the patient's disease status or activity. The results were expressed in ng/mL.

Serum quantitative MMP-3 concentrations were expressed as means and standard deviation (M±SD). The statistical analysis was carried out using the STATISTICA software (data analysis software system), version 12 (StatSoft, Inc., Tulsa, OK, USA). A one-way ANOVA with NIR post hoc test was performed for comparison involving different groups. Values from groups were compared using a paired Student's t-test. Correlations between parameters were evaluated using Pearson's correlation coefficient. Differences were considered significant when p was <0.05.

RESULTS

The distribution of serum MMP-3 concentrations in healthy controls (N=50) was found to be Gaussian, with M±SD=67.50±23.02 ng/ml, defining as a range of normal reference values 21.46-113.54 ng/ml (M±2SD) (Data not shown). MMP-3 concentrations (ng/mL) in RA patients under different therapeutic regimens (12 weeks) are reported in Fig. 1. The same normal distribution of healthy controls was observed in all patient groups.

Higher values of serum MMP-3 were found in 30 patients affected by early RA (250.12±12.04 ng/ml) and in 30 patients treated with MTX alone (235.35±24.20 ng/ml) in comparison to healthy controls (67.50±23.02 ng/ml) (*p<0.05). Patients treated with a combination of MTX+Abatacept (25.31±8.23 ng/ml), MTX+Tocilizumab (12.35±8.51 ng/ml), or MTX+Infliximab (19.98±15.35 ng/ml), showed significantly lower levels of MMP-3 in comparison to both patients treated with MTX alone and patients with early RA (untreated) (**p<0.001) (Fig. 1).

DAS-28 was evaluated in all patients at baseline and after 12 weeks of treatment. Patients affected by early RA presented a DAS-28 score of 4.49±1.76 (high disease activity), considered as basal value. After 12 weeks of treatment, patients in the MTX-group showed a DAS-28 score of 2.95±0.45 (mild disease activity), and patients treated with combination therapy of MTX+bDMARDs showed a DAS-28 score of 2.35±0.45 (remission/low disease activity).

The decrement of serum MMP-3 at 12 weeks was significant in the bDMARDs group in which we obtained remission (N = 32), but no significant reduction was measured in the MTX group (N = 30) in which we observed a mild disease activity.

Moreover, we assessed the correlations between basal serum MMP-3 and DAS28 score at 12 weeks, and we observed that DAS-28 positively correlated with MMP-3 levels of patients affected by early RA at a basal time (r = 0.7; p<0.02). A slight but not significant was observed between basal DAS-28 and MMP-3 levels in patients treated with all bDMARDs after 12 weeks of treatments. No correlation was observed

Table I. *Demographic characteristic of included patients. Patients were divided groups according to the pharmacological regimen practiced. 50 healthy donors were also evaluated as a control group.*

	Early RA	MTX alone	MTX+ Abatacept	MTX+ Tocilizumab	MTX+ Infliximab	Controls
Number of patients	**30**	**30**	**10**	**10**	**12**	**50**
Age[a]	**49.62±12.43 years**					**47.82±13.15**
Sex (female/male)	**27/3**	**24/6**	**7/3**	**8/2**	**10/2**	**42/8**
Disease duration (months)[a]	6.9± 2.23	39.6±9.82	32.6±4.50	35.8±5.97	37.5±7.06	0
Corticosteroid treatment (range 5–10 mg/ day)	16/30 (53%)	20/30 (66%)	5/32 (15.6%)			0

Patients were divided into groups according to the pharmacological regimen practiced; 50 healthy donors were also evaluated as a control group. [a]The data are presented as the mean ± standard deviation

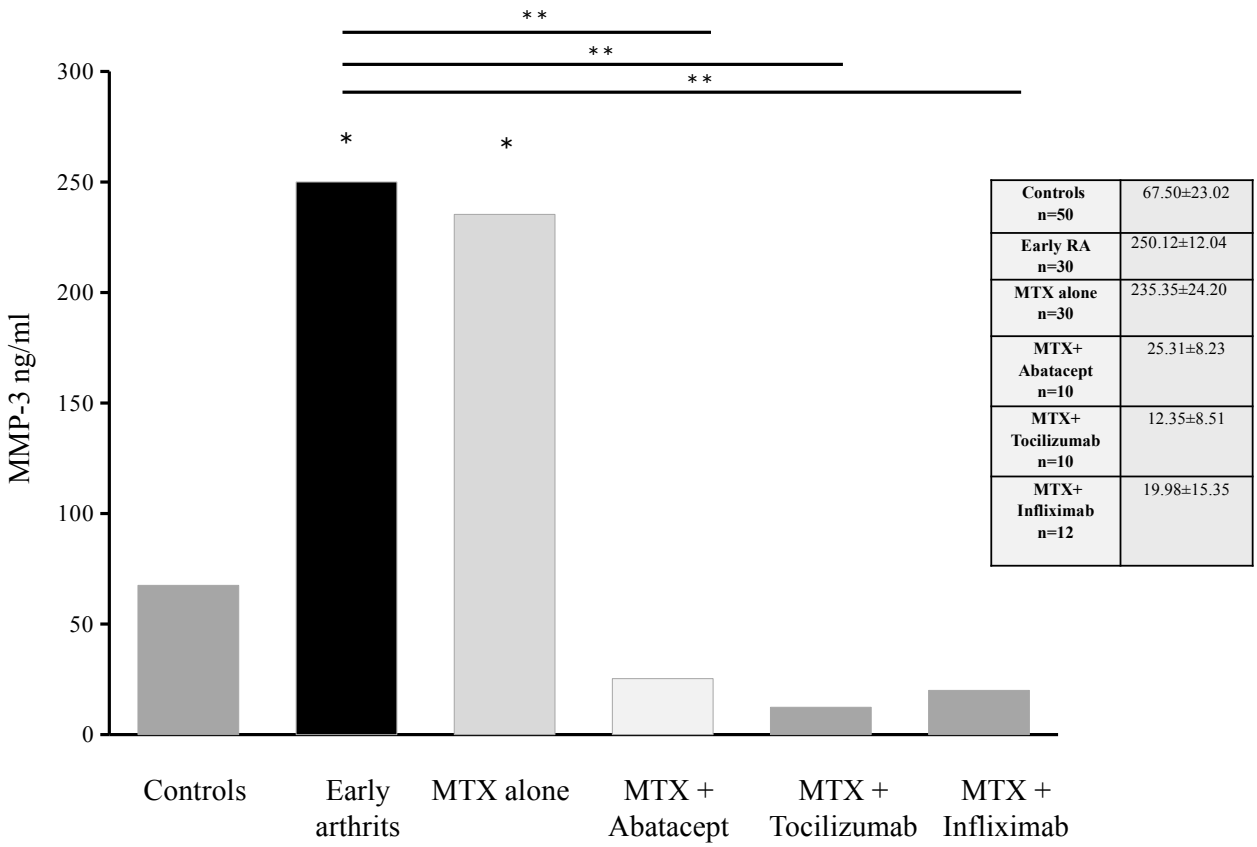


Fig. 1. *Metalloproteases-3 (MMP-3) concentrations in patients with RA. Patients with early RA and patients treated with methotrexate (MTX) alone showed higher values of serum MMP-3 in comparison to controls (*p<0.05); patients treated with a combination of MTX+Abatacept, MTX+Tocilizumab, or MTX+Infliximab, showed significant lower levels of MMP-3 in comparison to patients treated with MTX alone at 12 weeks and in comparison to early RA considered as untreated (**p<0.001). MMP-3 levels were evaluated after 12 weeks of treatment in the biological DMARDs (bDMARDs) group.*

between basal DAS-28 and MMP-3 levels in patients treated with MTX alone at the same time point.

DISCUSSION

The present study showed that the serum values of MMP-3 obtained from patients treated with different biological therapeutic regimens (Abatacept/Etanercept/Infliximab) might be useful in predicting the DAS-28 response of bDMARDs-treated RA patients. DAS-28 correlates positively with MMP-3 levels at a basal time. Although we described a reduction in both DAS-28 and MMP-3 levels in patients treated with bDMARDs at 12 weeks, no significant correlation was observed between the two variables. No correlation was observed between basal DAS-28 and MMP-3 levels in patients treated with MTX after 12 weeks (r=-0.04).

The MMP-3 ratio, calculated as that of the MMP-3 level at 12 weeks to that at baseline, was significantly lower in patients treated with bDMARDs (0.08) than that in the MTX group (0.9) (**p<0.001). This observation suggests that the MMP-3 ratio may be useful as prognostic factor of remission in response to bDMARDs-treated patients.

MMP-3 levels were stratified concerning the therapy performed (MTX alone and MTX+Abatacept/Tocilizumab/Infliximab), and we observed that the levels of MMP-3 in patients after 12 weeks of treatment with bDMARDs were significantly lower

compared with those found in patients with early RA and in patients receiving MTX alone at the same time point (**$p<0.001$).

The results of our study confirmed the concept that metalloproteases can play an important role in the pathogenesis of RA. We also provide data of the effects of different therapeutic regimens on MMP-3 levels after only 12 weeks of treatment, and we hypothesize that this reduction moves in parallel with the reduction of the DAS-28 values. Serum MMP-3 at baseline reflects clinical disease activity of RA and can be considered as an effective and simple marker in evaluating RA patients.

However, further studies and investigations will be carried out to confirm the role of MMP-3 as a prognostic and therapeutic marker in RA; future studies will reveal whether the introduction of this novel biomarker can increase the accuracy of risk models predicting radiographic and clinical progression in RA.

REFERENCES

1. Ma J-D, Wei X-N, Zheng D-H, et al. Continuously elevated serum matrix metalloproteinase-3 for 3~6 months predict one-year radiographic progression in rheumatoid arthritis: a prospective cohort study. Arthritis Res Ther 2015; 14;17:289.
2. Ponikowska M, Świerkot J, Nowak B, Korman L, Wiland P. Autoantibody and metalloproteinase activity in early arthritis. Clinical Rheumatology 2019; 38:827-834.
3. Nagase H, Visse R, Murphy G. Structure and function of matrix metalloproteinases and TIMPs. Cardiovasc Res 2006; 69:562-73.
4. Galis ZS, Muszynski M, Sukhova GK, Simon-Morrissey E, Libby P. Enhanced expression of vascular matrix metalloproteinases induced in vitro by cytokines and in regions of human atherosclerotic lesions. Ann N Y Acad Sci 1995; 17:501-7.
5. Krabben A, Huizinga TW, Mil AH. Biomarkers for radiographic progression in rheumatoid arthritis. Curr Pharm Des 2015; 21:147-69.
6. Ma JD, Zhou JJ, Zheng DH, et al. Serum matrix metalloproteinase-3 as a non- invasive biomarker of histological synovitis for diagnosis of rheumatoid arthritis. Mediators Inflamm 2014; 2014:179284.
7. Lerner A, Neidhöfer S, Reuter S, Matthias T. MMP3 is a reliable marker for disease activity, radiological monitoring, disease outcome predictability, and therapeutic response in rheumatoid arthritis. Best Pract Res Clin Rheumatol 2018; 32:550-62.
8. Tchetverikov I, Lard LR, DeGroot J, et al. Matrix metalloproteinases-3, -8, -9 as markers of disease activity and joint damage progression in early rheumatoid arthritis Ann Rheum Dis 2003; 62:1094-9.
9. Smolen JS, Landewé RBM, Bijlsma JWJ, et al. EULAR recommendations for the management of rheumatoid arthritis with synthetic and biological disease-modifying antirheumatic drugs: 2019 update. Ann Rheum Dis 2020; 79(6):685-99.
10. Aletaha D, Neogi T, Silman AJ, et al. 2010 rheumatoid arthritis classification criteria: An American College of Rheumatology/European league against rheumatism collaborative initiative. Arthritis Rheum 2010; 62:2569-81.
11. Aletaha D, Smolen JS. Joint damage in rheumatoid arthritis progresses in remission according to the Disease Activity Score in 28 joints and is driven by residual swollen joints. Arthritis Rheum 2011; 63:3702-11.
12. Hua C, Daien CI, Combe B, Landewe R. Diagnosis, prognosis and classification of early arthritis: results of a systematic review informing the 2016 update of the EULAR recommendations for the management of early arthritis. RMD Open 2017; 3:1-10.

LETTER TO THE EDITOR

Efficacy of different drug-eluting stents and their influence on inflammation and prognosis in elderly patients with acute myocardial infarction

W-L. Zhang, G-Q. Sun, L-F. Zhang and Z-B. Meng

Department of Cardiology, The Third People's Hospital in Liaocheng, Liaocheng, China

Received December 9, 2020 – Accepted April 14, 2021

To the Editor,

According to the statistics, there are about 500,000 new cases of acute myocardial infarction (AMI) every year in China, and the elderly who are more vulnerable to AMI show an increasing incidence rate (1-3). AMI occurs mainly when long-standing blood flow blocking due to coronary artery occlusion leads to myocardial tissue hypoxemia, inducing plaque growth and rupture in the body, where plaques are formed mainly because platelet adhesion and aggregation block vessels, thereby triggering the disease (4).

The clinical application of drug-eluting stents (DES) marks the milestone of the interventional therapy for heart disease. A DES integrates decrease in cell proliferation, local drug release and metal stent to effectively reduce the incidence of in-stent restenosis, and it is much better than a conventional bare-metal stent regarding incidence of complications (5, 6). Studies have proposed that nonfatal myocardial infarction occurs in more than 50% of AMI patients when conventional bare-metal stents decrease vascular thrombosis. Polymer-free drug-loaded stent is a new stenting method, and rapamycin- and paclitaxel-eluting stents are now two extensively applied approaches clinically. Normally, the efficacy of stent therapy in patients with coronary heart disease can be corroborated, but that in the elderly patients with AMI is rarely researched. Whether paclitaxel-eluting stent will cause postoperative vascular remodeling and thrombosis in patients remains elusive, so this paper observed the efficacy of different drug-eluting stents and their influences on inflammation and prognosis in 78 elderly AMI patients.

MATERIALS AND METHODS

General information

A total of 78 AMI patients aged >60 years, who were admitted to and treated in our hospital from October 2017 to November 2018, were divided into rapamycin group (n=44) and paclitaxel group (n=34) according to their willingness to choose different DES. Rapamycin-eluting stent was used in the rapamycin group, while paclitaxel-eluting stent in paclitaxel group. There was no difference in the general information between the two groups of patients (Table I). This study was approved by the Ethics Committee of The Third People's Hospital in Liaocheng. Signed written informed consent was obtained from all participants before the study.

Inclusion and exclusion criteria

The inclusion criteria were patients conforming to the diagnosis criteria for AMI, those with

Key words: AMI; rapamycin; paclitaxel; IL-6; hs-CRP; prognosis

Corresponding Author:
Wenlong Zhang, BM.
Department of Cardiology,
The Third People's Hospital in Liaocheng,
62 Weiyu Road, Liaocheng, Shandong 252000, China
Tel.: +86 013563028291
e-mail: zhangwl2005@mail.sdu.edu.cn

0393-974X (2021)
Copyright © by BIOLIFE, s.a.s.
This publication and/or article is for individual use only and may not be further reproduced without written permission from the copyright holder.
Unauthorized reproduction may result in financial and other penalties
DISCLOSURE: ALL AUTHORS REPORT NO CONFLICTS OF INTEREST RELEVANT TO THIS ARTICLE.

cardiodynia and chest distress >30 min, those who received coronary angiography within 12 h after onset, and those with stable hemodynamics. Patients were excluded if they suffered from autoimmune diseases, or were allergic to metal stents, had renal dysfunction, or incomplete clinical information.

Treatment methods

Rapamycin-eluting stent (Firebird 2, Beijing Bolong Gansheng Technology Co., Ltd., Beijing, China) was employed in the rapamycin group, whereas paclitaxel-eluting stent (Abbott vascular, USA) was used in the paclitaxel group. According to the Judkins method, coronary arteries were chosen for angiography examination, and then for intracoronary stenting. At 30 min before surgery, 300 mg of aspirin (Bayer) + 300 mg of clopidogrel (Sanofi) were taken orally. Whether thrombus aspiration was performed was based on the angiography results and disease conditions. After surgery, 75 mg of clopidogrel was taken orally for at least 1 year, aspirin was administered for a long period, and angiotensin was given according to the severity of disease. Finally, Siemens software was used for analyses.

Analysis of coronary angiography results

Coronary artery stenosis was mainly evaluated by 2 independent cardiologists based on the results of quantitative coronary arteriography (QCA) of the infarction-related coronary arteries, including left main artery (LM), left anterior descending artery (LDA), and left circumflex artery (LCA) as well as right coronary artery (RCA). The number of coronary artery branches with lesions (single vessel, double vessels and three vessels), the number of stent implantation and also the diameters of the stents were also observed. The decline >50% in the inner diameter of coronary arteries is defined as coronary artery disease or in-stent stenosis.

Determination of inflammatory factors

At 2 days after admission and then 48 h, 7 days and 30 days after surgery, 5 mL of peripheral blood was collected from the patients in both groups, centrifuged and stored at -80°C. The levels of interleukin (IL)-6 and high-sensitivity C-reactive protein (hs-CRP) were measured using ELISA and immunoturbidimetry (Shenzhen Jingmei Biotech Co., Ltd., Shenzhen, China), respectively.

Follow-up and prognosis

After discharge, 1-year follow-up was completed via phone calls and questionnaire, and in the 9th month, coronary angiography was performed to observe the incidence of postoperative cardiac events, including recurrent AMI and targeted vascular remodeling.

Table I. *Baseline information*

Group	n	Sex		Mean age	Myocardial infarction site			Other complicated diseases		
		Male	Female		Anterior wall	Inferior wall	High lateral wall + strictly posterior wall	Diabetes	Hypertension	Hyperlipidemia
Rapamycin group	44	26 (59.09)	18 (40.91)	70.15±5.58	20 (45.45)	19 (43.19)	5 (11.36)	12 (27.27)	8 (18.18)	10 (22.73)
Paclitaxel group	34	18 (52.94)	16 (47.06)	69.48±6.09	16 (47.06)	15 (44.12)	3 (8.82)	9 (26.47)	6 (17.65)	9 (23.53)
χ^2/t		0.447		0.614	0.376			0.825		
P		0.922		0.505	0.761			0.445		

Statistical analysis

Statistical Product and Service Solutions (SPSS) 22.0 software (IBM, Armonk, NY, USA) was adopted to compare the efficacy, CRP and IL-6 levels, and prognosis between the patients in the two groups. *t*-test was performed for measurement data, and enumeration data were expressed as [n (%)] and analyzed using χ^2 test. P<0.05 denoted statistically significant differences.

RESULTS

Comparison between the two groups

There were no obvious differences in infarction-related coronary arteries and the number of coronary artery branches with lesions between the paclitaxel group and the rapamycin group (P>0.05) (Table II).

There were differences in stent diameter and number (P<0.05), but no differences in other factors between the two groups (Table III).

It was found in the 9th month of follow-up that the two groups of patients exhibited similar late lumen loss and postoperative in-stent restenosis (P>0.05) (Table IV).

The patients in the paclitaxel group had a higher level of serum IL-6, but a slightly lower level of hs-CRP than those in the rapamycin group, showing no statistically significant differences (P>0.05). Compared with those before surgery, and at 48 h and 7 h after surgery, the levels of IL-6 and hs-CRP were substantially lowered in the two groups of patients at 30 days after surgery (P<0.05) (Table V-VI).

One-year postoperative follow-up did not reveal a significant difference regarding the number of patients with recurrent AMI, death and vascular remodeling between the two groups (P<0.05) (Table VII).

DISCUSSION

The present study revealed that there were no

Table II. *Coronary angiography results in each group*

Group	n	Infarction-related coronary arteries [n (%)]				Number of coronary artery branches with lesions [n (%)]		
		LM	LAD	LCX	RCA	Single vessel	Double vessels	Three vessels
Rapamycin group	44	2 (4.54)	29 (65.91)	9 (20.45)	4 (9.09)	23 (52.27)	11 (25)	10 (22.73)
Paclitaxel group	34	0 (0.00)	21 (61.76)	7 (20.59)	6 (17.65)	12 (35.29)	10 (29.41)	12 (27.27)
χ^2				2.692			2.445	
P				0.611			0.485	

Table III. *Comparison of stent information between the two groups*

Group	Stent length	Stent diameter	Number of implanted stents	IABP adjuvant therapy	Thrombus aspiration	IIb/IIIa receptor antagonists
	(mm)	(mm)	(piece)	[n, (%)]	[n, (%)]	[n, (%)]
Rapamycin group	36.87±18.45	3.02±0.36	1.44±0.67	5 (11.63)	13 (29.55)	11 (25.00)
Paclitaxel group	38.23±22.27	3.24±0.67*	1.68±0.83*	4 (11.76)	9 (29.41)	8 (23.53)
χ^2	0.773	3.115	3.877	0.231	0.363	0.225
P	0.137	0.046	0.017	0.614	0.125	0.415

**P<0.05 vs Rapamycin group*

Table IV. *Comparisons of coronary angiography results in the 9th month of follow-up*

Group	N	Late lumen loss (mm)	In-stent restenosis (n)
Rapamycin group	44	0.23±0.15	2 (4.54)
Paclitaxel group	34	0.25±0.18	1 (2.94)
χ^2/t		2.972	0.559
P		0.052	0.852

Table V. *Comparison of IL-6 level between the two groups of patients*

Group	n	IL-6			
		Before surgery	At 48 h after surgery	At 7 days after surgery	At 30 days after surgery
Rapamycin group	44	17.64±6.74	35.79±12.25*	24.58±9.45*#	11.76±6.07*#&
Paclitaxel group	34	18.14±5.59	36.94±11.94*	26.81±8.49*#	12.36±5.74*#&
t		0.275	0.515	1.446	0.174
P		0.633	0.349	0.083	0.882

**P<0.05 vs before surgery, #P<0.05 vs at 48 h after surgery, and &P<0.05 vs at 7 days after surgery.*

Table VI. *Comparison of hs-CRP level between the two groups of patients*

Group	n	Hs-CRP			
		Before surgery	At 48 h after surgery	At 7 days after surgery	At 30 days after surgery
Rapamycin group	44	5.75±3.09	11.48±5.03*	7.37±4.48*#	3.54±2.37*#&
Paclitaxel group	34	5.82±2.97	12.61±4.92*	7.73±4.59*#	3.38±2.46*#&
t		0.448	0.889	0.314	0.773
P		0.513	0.225	0.251	0.386

**P<0.05 vs before surgery, #P<0.05 vs at 48 h after surgery, and &P<0.05 vs at 7 days after surgery.*

statistically significant differences in the levels of serum IL-6 and hs-CRP between the two groups of patients, and that compared with those before surgery, 48 h and 7 h after surgery, the levels of IL-6 and hs-CRP were substantially lowered in the two groups of patients at 30 days after surgery. Inflammation drives thrombosis and unstable coronary artery disease. previous studies have corroborated that the expression levels of IL-6 and CRP are raised in AMI patients. CRP is involved in the process of development and progression of arteriosclerosis, which is one of the crucial inducing factors for AMI (7). Postoperative increases in the expression levels of inflammatory factors indicate acute local inflammation in patients, which may be associated with the stimulation of coronary arteries by balloon dilation and stent implantation, release of inflammatory factors due to soft plaque extrusion

Table VII. *Follow-up results in the two groups*

Item	Rapamycin group		Paclitaxel group		χ^2	P
	N	%	N	%		
Death	2	4.54	1	2.94	2.309	0.075
Myocardial infarction	1	2.27	0	0	0.778	0.448
Targeted vascular remodeling	2	4.54	1	2.94	1.997	0.551
Main adverse cardiac events	4	9.09	3	8.82	2.116	0.089
Thrombosis	3	6.82	1	2.92	1.344	0.652

and damage and inflammation-induced restenosis and adverse vascular events (8). Both rapamycin and paclitaxel carried by DES can lower the expression of inflammatory factors, which is directly related to the inhibition of IL-6 expression. In this study, it was found that after 1-year postoperative follow-up, there were few cases of death, myocardial infarction and vascular remodeling, and the patients had a favorable prognosis. According to previous reports, the rate of thrombosis after implantation of rapamycin-eluting stent is 7.8%, and based on the analysis results, the prognosis of the two kinds of DES, namely the incidence of thrombosis and other adverse events may be caused by different pharmacological effects (9-12). In conclusion, either rapamycin-eluting stent or paclitaxel-eluting stent can be safely used in the treatment of elderly AMI patients.

REFERENCES

1. Zhou M, Zou YG, Xue YZ, et al. Long non-coding RNA H19 protects acute myocardial infarction through activating autophagy in mice. Eur Rev Med Pharmacol Sci 2018; 22:5647-51.
2. Krumholz HM, Hennen J, Ridker PM, et al. Use and effectiveness of intravenous heparin therapy for treatment of acute myocardial infarction in the elderly. J Am Coll Cardiol 1998; 31:973-9.
3. Puymirat E, Aissaoui N, Cayla G, et al. Changes in One-Year Mortality in elderly patients admitted with acute myocardial infarction in relation with early management. Am J Med 2017; 130:555-63.
4. Guo TM, Cheng B, Ke L, et al. Prognostic value of neutrophil to lymphocyte ratio for in-hospital mortality in elderly patients with acute myocardial infarction. Curr Med Sci 2018; 38:354-9.
5. Wang H, Peng WJ, Wu P. Use of extracorporeal membrane oxygenation assisted primary to rescue an elderly acute myocardial infarction patient complicated with cardiac arrest. Zhonghua Xin Xue Guan Bing Za Zhi 2018; 46:224-5.
6. Krumholz HM, Hennen J, Ridker PM et al. Use and effectiveness of intravenous heparin therapy for treatment of acute myocardial infarction in the elderly. J Am Coll Cardiol 1998; 31:973-9.
7. Zhang Y, Shao T, Yao L, Yue H, Zhang Z. Effects of tirofiban on stent thrombosis, Hs-CRP, IL-6 and sICAM-1 after PCI of acute myocardial infarction. Exp Ther Med 2018; 16:3383-8.
8. Hu T, Lin S, Du R et al. Design, preparation and performance of a novel drug-eluting stent with multiple layer coatings. Biomater Sci 2017; 5:1845-57.
9. Xiu WJ, Yang HT, Zheng YY, Ma YT, Xie X. Drug-eluting balloons versus second-generation drug-eluting stents for treating in-stent restenosis in coronary heart disease after PCI: A Meta-Analysis. Cardiol Res Pract 2018; 2018:7658145
10. Liang M, Tan HC, Low AF. Three-year follow-up optical coherence tomography of under-expanded drug-eluting stent in-stent restenosis treated with ABSORB bioresorbable vascular scaffold following ultra-high pressure pre-dilatation. J Cardiol Cases 2018; 17:4-8.
11. Bundhun PK, Yanamala CM, Huang WQ. Comparing

Stent Thrombosis associated with Zotarolimus Eluting Stents versus Everolimus Eluting Stents at 1 year follow up: a systematic review and meta-analysis of 6 randomized controlled trials. BMC Cardiovasc Disord 2017; 17:84.

12. Muller-Hulsbeck S, Keirse K, Zeller T, Schroe H, Diaz-Cartelle J. Long-term results from the MAJESTIC trial of the eluvia paclitaxel-eluting stent for femoropopliteal treatment: 3-year follow-up. Cardiovasc Intervent Radiol 2017; 40:1832-8.

LETTER TO THE EDITOR

Pidotimod as add-on therapy in patients with pollen-induced allergic rhinitis and asthma and associated respiratory infections

M. Marogna[1] and G Ciprandi[2]

[1] U.O.C. Pneumologia, Azienda Ospedaliera Fondazione Macchi, Varese, Italy; [2]Allergy Clinic, Casa di Cura Villa Montallegro, Genoa, Italy

Received February 25, 2021 – Accepted May 13, 2021

To the Editor,

Type 2 allergic inflammation results in generating nasal obstruction, in fact, eosinophil count in nasal mucosa closely correlates with nasal airflow, so that the more intense the allergic inflammation, the greater the nasal obstruction (1). Type 2 inflammation also surrounds the entire respiratory tract. Consistently, uncontrolled AR can worsen asthma by different pathophysiologic mechanisms (2). As a result, the term "united airways disease" has been coined to highlight the close association between the upper and lower respiratory tract (3). AR is also the leading risk factor for asthma onset.

On the other hand, the type 2 polarization implicates a type 1 disequilibrium characterized by impaired interferon production. Deficient interferon release allows increased susceptibility to respiratory infection (4). Consequently, treating AR could be an efficient way to improve asthma and predisposition to infections. In this regard, there is evidence that second-generation antihistamines could favorably reduce nasal symptoms, including nasal congestion, and hamper inflammation (5). Cetirizine exerts an additional anti-allergic activity as it affects nasal inflammation (6), however, antihistaminic therapy is unlikely to succeed in abolishing allergic reactions. Therefore, there is growing interest in investigating agents able to modulate the immune response. Pidotimod, a synthetic thymic dipeptide, could be an ideal candidate in this context, as it modulates the innate and adaptative immunity increasing type 1 and decreasing type 2 response (7). A recent meta-analysis demonstrated that pidotimod significantly reduced the risk of recurrent infections (8). A mechanistic study supported these outcomes demonstrating that pidotimod polarized the immune response toward a physiologic type 1 response suppressing type 2 cytokines (9).

Based on this background, we tested the hypothesis that pidotimod, used as add-on therapy, could improve respiratory symptoms, dampen allergic inflammation, and prevent respiratory infections in AR patients continuously treated with cetirizine.

MATERIALS AND METHODS

This pilot study included a group of patients with pollen-induced AR. The study involved a randomized, controlled open design. The inclusion criteria were documented diagnosis or AR, sensitization only to *Graminaee* and *Betulaceae* pollens, history of recurrent respiratory infections, concomitant intermittent asthma exacerbated by pollen exposure, and adulthood. Exclusion

Key words: allergic rhinitis; asthma; pollen allergy; respiratory infection; pidotimod

Corresponding Author:
Dr Giorgio Ciprandi,
Allergy Clinic,
Casa di Cura Villa Montallegro,
Genoa, Italy
e-mail: gio.cip@libero.it

0393-974X (2021)
Copyright © by BIOLIFE, s.a.s.
This publication and/or article is for individual use only and may not be further reproduced without written permission from the copyright holder.
Unauthorized reproduction may result in financial and other penalties
DISCLOSURE: ALL AUTHORS REPORT NO CONFLICTS OF INTEREST RELEVANT TO THIS ARTICLE.

criteria were perennial AR, uncontrolled and intrinsic asthma, comorbidity, and concomitant medications able to interfere with the interpretation of the results. AR diagnosis was considered if there was a documented sensitization, assessed by skin prick test and/or measurement of serum allergen-specific IgE, and demonstrated a cause/effect relationship between exposure to sensitizing allergen and symptom occurrence. Asthma was diagnosed using the global initiative for asthma (GINA) criteria (www.ginasthma.com). Patients gave informed written consent, and the study was conducted following the good clinical practice methodology.

Patients were randomly (ratio 1:1) assigned into two groups: Group A (control group) and Group B (active group). All patients took cetirizine one tablet (10 mg) daily from March to June. Patients assigned to Group B also took pidotimod one sachet (800 mg) for ten consecutive days monthly from March to May. The patients were evaluated at the beginning and the end of the cetirizine treatment. The considered parameters included assessing respiratory symptom severity, symptomatic use of rescue medications, nasal eosinophils, lung function, antibiotic use, and days with respiratory infections. Nasal symptoms included nasal itching, sneezing, watery rhinorrhea, and congestion. Ocular symptoms consisted of conjunctival itching, lacrimation, and redness. Symptoms were scored using a four-point scale. A total symptom score (TSS) was calculated, summing nasal and ocular symptoms. Asthma symptoms were cough, wheezing, and breathlessness measured as well as upper respiratory symptoms. As the hazelnut pollens were present from the end of January, the patients were already symptomatic at the beginning of cetirizine treatment.

The asthma control test (ACT) questionnaire was administered to all patients. The ACT questionnaire consisted of 5 questions with five possible responses, exploring the patient's perception of his/her asthma control (22). The result could range between 0 and 25, where 25 was the optimal asthma control.

Nasal eosinophils were counted by nasal cytology, a well-standardized methodology. Intranasal corticosteroids were suspended ten days before the examination. Data are expressed as a mean of 10 fields and as a percentage of eosinophils on inflammatory cells. A pulmonary function test was performed assessing spirometry, as stated by the European Respiratory Society (24). Forced expiratory volume in one second (FEV_1) was measured and expressed as the percent of predicted. Symptomatic use (such as on-demand) of intranasal corticosteroid (budesonide 100 mcg, one puff per nostril, twice a day) and inhaled salbutamol (100 mcg, one puff) were recorded and considered as days of use. Antibiotics for respiratory infections were used following the best standard practice and were calculated as days of use. Work or school absence was calculated as days. The data were recorded in the previous year and compared with the treatment period.

The statistical analysis was performed using the χ^2 test, Pearson test, and *t*-test with Satterthwaite corrections. Moreover, the analysis of the covariance (ANCOVA) was performed.

RESULTS

The study population included 90 patients, however six patients dropped out as they did not return to the follow-up visit, therefore 84 patients completed the study: 41 (17 females, mean age 31.2 years, age range 18-57) in Group A and 43 (19 females, mean age 28.3 years, age range 19-58) in Group B. The findings were analyzed by intragroup and intergroup comparison as reported in Table I. Table I also reports the variations (expressed as percentage) between the two observations.

Intragroup analysis

Group A. TSS and asthma symptoms significantly ($p<0.0001$) decreased after treatment (mean decrease -28.5% and -51.5%, respectively). FEV_1 significantly ($p<0.0001$) increased (+6.5%) as well as ACT score (+13.6%). The number of nasal eosinophils significantly ($p<0.0001$) decreased (-8.5%). The symptomatic use of intranasal budesonide and inhaled salbutamol significantly ($p<0.0001$) decreased (-21.9% and -35.8%, respectively) as well as the days with antibiotics ($p=0.0003$; -21.1%). The work/school absence days significantly decreased ($p<0.0001$; -32.9%).

Group B. TSS and asthma symptoms significantly ($p<0.0001$) decreased after treatment (mean decrease -54.9% and -79.2%, respectively). FEV_1 significantly ($p<0.0001$) increased (+21.8%) as well as ACT score ($p<0.0001$; 33.3%). The number of nasal eosinophils

Table I. *Clinical data of Group A and Group B before and after treatments.*

		Pre	Post	Intragroup	Var. %	Intergroup
Parameter	**Group**	**Mean±SE**	**Mean±SE**	**analysis**	**Mean±SE**	**analysis**
TSS	***A***	7.2±0.2	5.0 ±0.3	P<0.0001	-28.5±3.7	P<0.0001
	B	7.7±0.3	3.3±0.3	P<0.0001	-54.9±4.5	
Asthma symptoms	***A***	6.1±0.3	2.8 ±0.2	P<0.0001	-51.5±3.3	P<0.0001
	B	5.2±0.3	0.9±0.2	P<0.0001	-79.2±4.7	
FEV_1 (% of predicted)	***A***	90.2±0.8	96.0 ±1.1	P<0.0001	6.5±1.0	P<0.0001
	B	85.7±0.5	104.3±1.6	P<0.0001	21.8±2.0	
ACT	***A***	18.1±0.4	20.4 ±0.4	P<0.0001	13.6±2.1	P<0.0001
	B	17.5±0.3	23.0±0.4	P<0.0001	33.3±3.4	
Nasal eosinophils	***A***	20.0±0.8	16.0 ±0.8	P<0.0001	-28.5±3.7	P<0.0001
	B	23.2±0.8	10.4±0.9	P<0.0001	-54.9±4.5	
Intranasal CS (days)	***A***	15.1±0.6	11.2 ±0.8	P<0.0001	-21.9±6.5	P<0.0001
	B	17.0±0.6	5.2±0.7	P<0.0001	-67.2±4.8	
Salbutamol (days)	***A***	11.4±0.6	7.4 ±0.7	P<0.0001	-35.8±4.8	P<0.0001
	B	12.3±0.5	3.1±0.9	P<0.0001	-76.7±5.4	
Antibiotics (days)	***A***	6.9±0.4	5.0 ±0.4	P=0.0003	-21.1±7.4	P<0.0001
	B	7,1±0.4	1.4±1.7	P<0.0001	-78.0±5.1	
Work/ school absence (days)	***A***	10.2±0.5	6.4 ±0.5	P<0.0001	-32.9±5.9	P<0.0001
	B	10.9±0.4	1.2±0.2	P<0.0001	-89.1±2.2	

significantly (p<0.0001) decreased (-54.9%). The symptomatic use of intranasal budesonide and inhaled salbutamol significantly (p<0.0001) decreased (-67.2% and -76.7%, respectively) as well as the days with antibiotics (p<0.0001; -78%). The work/school absence days significantly decreased (p<0.0001; -89.1%).

The comparison between groups showed significant differences, as reported in Figs. 1-3. TSS decreased more significantly (p<0.0001) in Group B than in Group A. Moreover, asthma symptoms were significantly (p<0.0001) lower in group B than in Group A. Mean FEV_1 values were significantly (p<0.0001) higher in Group B. Mean ACT score was significantly (<0.0001) higher in Group B. Nasal eosinophils were significantly (p<0.0001) lower in Group B. The symptomatic use of intranasal budesonide and inhaled salbutamol was significantly

(p<0.0001 for both) lower in Group B as well as use of antibiotics (p<0.0001) in Group B. The work/school absences were significantly (p<0.0001) lower in Group B. The treatments were safe and well tolerated in all patients.

DISCUSSION

A very recent study demonstrated that pidotimod could shorten the recovery time, prevent secondary infections, and abbreviate their duration in children and adolescents with infectious mononucleosis (10). Moreover, another study documented that pidotimod significantly improved nasal obstruction in children with AR (1). These outcomes supported the idea that pidotimod can modulate the innate and adaptive immune response of both types 1 and 2.

The current study consequently explored the possibility that pidotimod, used as add-on therapy to cetirizine, could relieve nasal and bronchial symptoms, improve lung function, reduce type 2 nasal inflammation, prevent respiratory infections, save the use of symptomatic medications, such as intranasal corticosteroids and bronchodilators, and

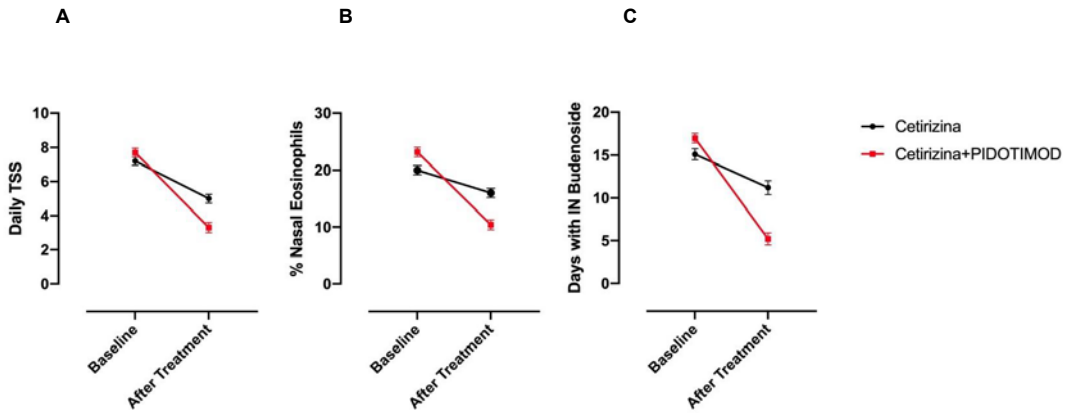


Fig. 1. ***A)*** *daily nasal symptoms;* ***B)*** *nasal eosinophil count;* ***C)*** *mean days of symptomatic use of intranasal budesonide. Data are reported for patients treated with cetirizine (in black) and cetirizine plus pidotimod (in red); at baseline and after treatment.*

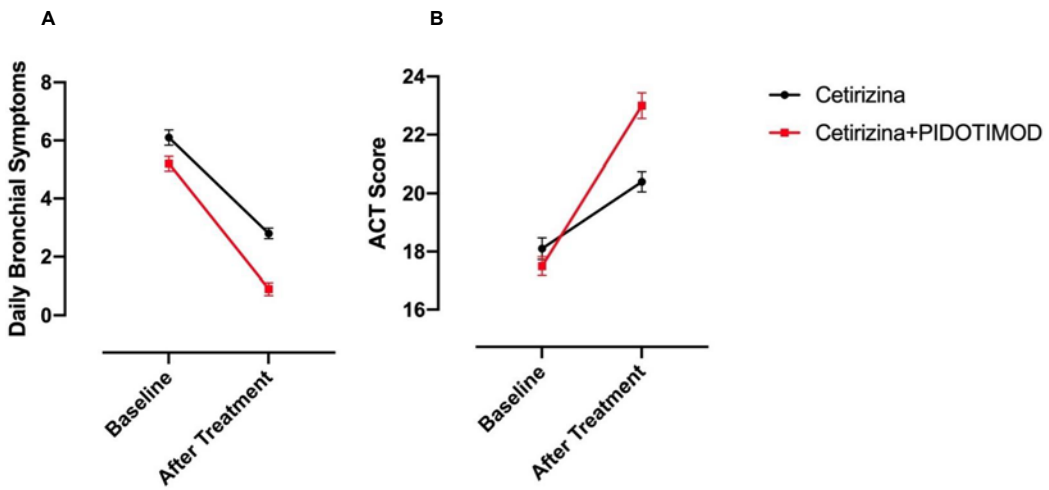


Fig. 2. *A) daily bronchial symptoms; B) ACT scores; Data are reported for patients treated with cetirizine (in black) and cetirizine plus pidotimod (in red); at baseline and after treatment.*

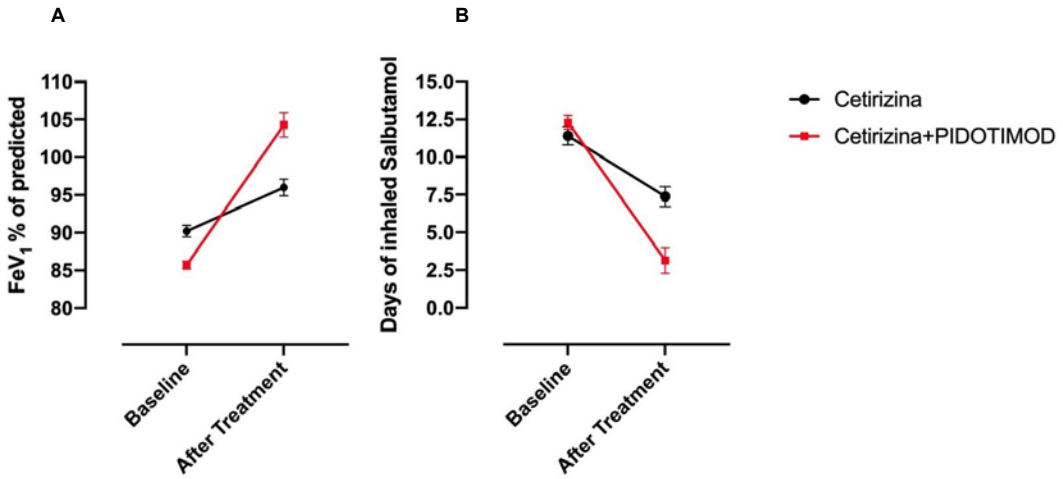


Fig. 3. ***A)*** *FEV_1 values expressed as % of predicted.* ***B)*** *Mean of days with salbutamol use. Data are reported for patients treated with cetirizine (in black) and cetirizine plus pidotimod (in red); at baseline and after treatment.*

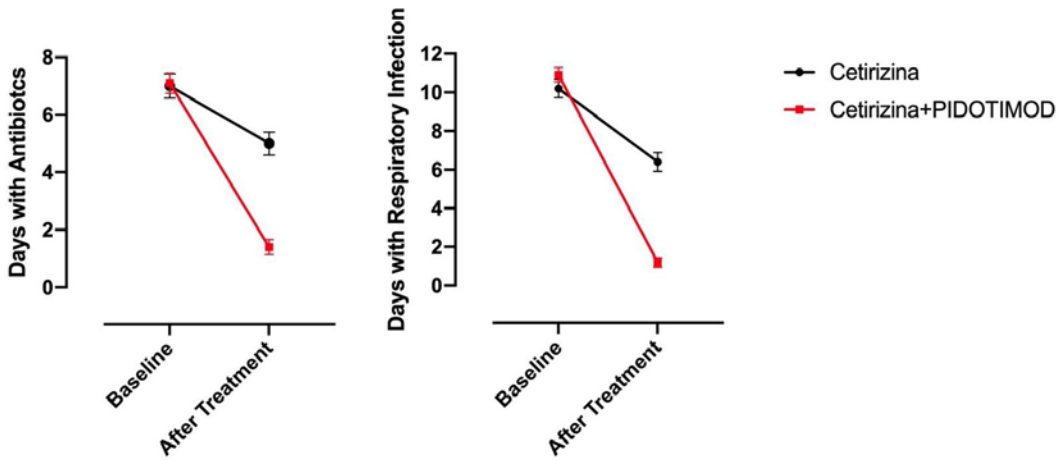


Fig. 4. ***A)*** *Mean days with antibiotic use.* ***B)*** *Mean days with respiratory infections. Data are reported for patients treated with cetirizine (in black) and cetirizine plus pidotimod (in red); at baseline and after treatment.*

antibiotics for infections, and ultimately reduce work/school absences.

The outcomes demonstrated that cetirizine *per se* improved all these aspects, confirming the well-known anti-allergic activity. However, the pidotimod addition provided a significant further improvement of all the variables. Consequently, this study was consistent with previous studies showing a reinforcement of type 1 immunity and mitigation of type 2 response. In particular, add-on pidotimod significantly reduced the use of symptomatic medications for rhinitis and asthma as well as respiratory infections, including the use of antibiotics and loss of work/school days. Notably, add-on pidotimod contributed to a relevant inhibition of type 2 nasal inflammation, therefore, these findings confirmed the well-known concept that controlled AR could significantly affect asthma course (12).

The present study has some limitations, including the open design, the lack of mediator assessment, and the very limited number of recruited patients. As a consequence, the findings need to be confirmed by

studies conducted with rigorous methodology.

In conclusion, the recent experience confirmed pidotimod's ability to enhance type 1 immunity and modulate type 2 response. Moreover, pidotimod was safe and well-tolerated.

REFERENCES

1. Ciprandi G, Cirillo I, Vizzaccaro A, Milanese M, Tosca MA. Nasal obstruction in patients with seasonal allergic rhinitis: relationships between allergic inflammation and nasal airflow. Int Arch Allergy Immunol 2004; 134:34-40.
2. Yii ACA, Tay TR, Choo XN, Koh MSY, Tee AKH, Wang D-Y. Precision medicine in united airways disease: A "treatable traits" approach. Allergy 2018; 73(10):1964-78.
3. Wise SK, Lin SY, Toskala E, Orlandi RR, Akdis CA, Alt JA, et al. International Consensus Statement on Allergy and Rhinology: Allergic Rhinitis. Int Forum Allergy Rhinol 2018; 8(2):108-352.
4. Cirillo I, Marseglia GL, Klersy C, Ciprandi G. Allergic patients have more numerous and prolonged respiratory infections than nonallergic subjects. Allergy 2007; 62(9):1087-90.
5. Ciprandi G, Cosentino C, Milanese M, Mondino C. Fexofenadine reduces nasal congestion in perennial allergic rhinitis. Allergy 2001; 56(11):1068-70.
6. Ciprandi G, Tosca MA, Ricca V, et al. Cetirizine treatment of rhinitis in children with pollen allergy: evidence of its antiallergic activity. Clin Exp Allergy 1997; 27(10):1160-6
7. Esposito S, Jones MH, Feleszko W, et al. Prevention of new respiratory episodes in children with recurrent respiratory infections: an expert consensus statement from the World Association of Infectious Diseases and Immunological Disorders (WAidid). Microorganisms 2020; 8:1810.
8. Niu H, Wang R, Jia YT, Cai Y. Pidotimod, an immunostimulant in pediatric recurrent respiratory tract infections: a meta-analysis of randomized controlled trials. Int Immunopharmacol 2019; 67:35-45.
9. Zhou Y, Dai Y. Comparison of effects of Pidotimod and spleen amino-peptide on clinical symptoms and Th1/Th2 cytokines in children with RRI. Chin J Bioch Pharm 2012; 33:64-9.
10. La Mantia I, Varricchio A, Andaloro C, Ciprandi G. Pidotimod in children with infectious mononucleosis: a preliminary randomized controlled study. J Biol Regulat Homeostat Agents 2020; 34(4):1597-9.
11. Brindisi G, Zicari AM, Schiavi L, et al. Efficacy of pidotimod use in treating allergic rhinitis in a pediatric population. Ital J Pediatr 2020; 46:93.
12. De Vittori V, Pacilio A, Indinnimeo L, et al. When asthma and rhinitis coexist, could rhinitis reduce asthma control in children? Allergy Asthma Proc 2019; 40(3):e8-e13.

LETTER TO THE EDITOR

Diagnostic value and correlation of miRNA-499 and miR-18A in patients with acute myocardial infarction

Q. Liu[1], J-Y. Zhao[2], H-Y. Liu[3], T-T. Li[4], Y-X. Guo[5] and Y-H. Liu[6]

[1]Department of Cardiovascular Medicine, People's Hospital of Rizhao Lanshan, Rizhao, China; [2]Department of Cardiology, Jiyang People's Hospital, Jinan, China; Disinfection Supply Center ,Qingdao Central Hospital, Qingdao University, Qingdao, China; Operation Room, Zhangqiu District People's Hospital, Jinan, China; [5]Department of Respiratory, Zhangqiu District People's Hospital, Jinan, China; [6]Department of Cardiology, Zhangqiu District People's Hospital, Jinan, China

Received December 16, 2020 – Accepted March 16, 2021

To the Editor,

Acute myocardial infarction (AMI), a myocardial perfusion disorder, is a major cause of morbidity and mortality worldwide (1). Clinically, the diagnosis of AMI is mainly judged by the patient's obvious symptoms, abnormal electrocardiogram and changes in related enzyme indexes during blood testing. However, such diagnosis methods are not quite comprehensive. Some cases are misjudged, and the patients are unable to receive correct and effective treatment in time, which may endanger life and affect the prognosis (2).

Certain microRNAs can serve as potential diagnostic biomarkers and therapeutic targets, such as miR-499 and miR-19a (3, 4). It has been reported that miR-499 is highly expressed in a series of cardiovascular diseases (5). MiR-18a, as a member of the miR-17-92 family (6), can inhibit autophagy brain-derived neurotrophic factor (BDNF) up-regulation and Akt/mTOR axis inactivation of cardiomyocytes in aging AMI rats while promoting aging, which can be considered as an active biomarker for the potential treatment of AMI (7), however, there are few reports on the correlation of miR-499 and miR-18a with AMI.

MATERIALS AND METHODS

A total of 121 patients with AMI treated in the People's Hospital of Rizhao Lanshan from January 2015 to March 2016 were selected as the research subjects, including 69 males and 52 females, aged (64.05±6.55) years. All patients met the WHO diagnostic criteria for AMI: typical chest pain lasting more than 30 minutes; ECG abnormalities such as ST segment lifting more than 0.2 mm; markers of myocardial necrosis, cTn and creatine kinase (CK) more than two times higher than normal; admission to hospital within 24 hours after the initial onset of symptoms; complete clinical case data. Exclusion criteria were: previous history of heart disease; hematological disease; history of malignant tumors; liver insufficiency and renal failure; non-cooperation with treatment. According to Killip grading, the patients were divided into subgroups I (n=29), II (n=31), III (n=30) and IV (n=31). In addition, 75 healthy volunteers (no history of cardiovascular disease), consisting of 42 males and 33 females. aged (63.95±6.21) years, who underwent physical examination during the same period in our hospital were selected as the control group. There were no statistically significant differences in gender and age between the two groups (p>0.05), suggesting comparability. The patients

Key words: acute myocardial infarction; miR-499; miR-18a; diagnostic value; correlation

Corresponding Author:
Dr Yihong Liu,
Department of Cardiology,
Zhangqiu District People's Hospital,
No.1920 Huiquan Road,
Jinan 250200, China
e-mail: iuewc8@163.com

0393-974X (2021)
Copyright © by BIOLIFE, s.a.s.
This publication and/or article is for individual use only and may not be further reproduced without written permission from the copyright holder.
Unauthorized reproduction may result in financial and other penalties
DISCLOSURE: ALL AUTHORS REPORT NO CONFLICTS OF INTEREST RELEVANT TO THIS ARTICLE.

and healthy subjects who participated in the study were fully informed about the study and signed informed consent. At the same time, the hospital ethics committee approved the study. Patients were followed-up for 3 years by telephone or door-to-door visits to understand the physical condition and life/death situation after treatment. The survival time was calculated on a monthly basis.

Blood sample collection and index detection

Fasting venous blood of 5-10 mL was collected from all participants in the early morning and centrifuged at 1000 rpm for 10 min to collect the serum. Total cholesterol (TC), triacylglycerol (TG), high density lipoprotein cholesterol (HDL-C), low-density lipoprotein cholesterol (LDL-C), pro-BNP, and left ventricular ejection fraction (LVEF) in the serum were determined by a biochemical analyzer.

Total RNA extraction and qPCR quantification

Plasma (200 μL) was added to 1000 μL QIAzol lysate (QIGEN, Germany) to separate the total serum, which was then left standing at room temperature for 15 min. miRNeasy serum/plasma kit (QIGEN, Germany) was then employed to extract the total serum RNA, the concentration and purity of which at 260-280nm were detected by ultraviolet spectrophotometer, and those with OD260/OD280>1.8 were used for follow-up qPCR detection. PrimeScript miRNA cDNA Synthesis Kit (Takara, Japan) was used to reverse cDNA, and ABI 7500 Real-Time PCR System (ApplieBiosystems, USA) was used to perform qPCR amplification. Primers of miR-499 and miR-18a (Table I) were designed and synthesized by Shanghai Sangon Biotechlogy Co., Ltd. qPCR parameters were 95℃ for 30 s, 90℃ for 5 s, 65℃ for 30 s, totaling 40 cycles. With U6 was as the internal reference, $2^{-\Delta\Delta Ct}$ method was used for standardization.

Statistical analysis

The above index data was input into SPSS20.0 software package (Asia Analytics Formerly SPSS China) for statistical analysis, and GraphPad Prism 6 (GraphPad Software, San Diego, USA) was applied for mapping. The measurement data were expressed as mean ± SD. The comparison methods of the inter-group data were independent sample *t*-test, Log rank test, and one-way analysis of variance, and the post hoc comparison was performed by LSD-*t* test. The counting data were represented by n, and χ^2 test was used for comparison between groups. The diagnostic value of serum miR-449 and miR-18a in patients with AMI was evaluated using ROC. Kaplan-Meier algorithm was adopted to analyze survival, and Cox univariate regression was used to analyze the risk factors of AMI patients. All data were double-tailed. With 95% as its confidence interval, a statistically significant difference was assumed at $p<0.05$.

RESULTS

General information

There were no significant differences in gender, age or BMI between the two groups ($p>0.05$). The contents of TG and Pro-BNP in the research group were statistically higher than those in the control group ($p<0.01$), and the contents of HDL-C and LVEF in the research group were notably lower than those in the control group ($p<0.01$) (Table II).

Comparison of the relative expression levels of miR-499 and miR-18a

In this study, peripheral blood samples of 121 AMI patients and 75 healthy subjects were taken, and miRNA expression levels were quantified by qPCR. It was found that both miR-499 (t=19.3158, $p<0.001$)

Table I. *Primer sequences*

	Upstream primer (5'→3')	Downstream primer (5 '→3')
miR-499	GGTCCAGACTGGGGTCCCAGC	GCATGCCGCAGTGGTTAGGGA
miR-18a	GCTGAGCTAAGGTGCATCTAG	TCAACTGGTGTCGTGGAGT
U6	GCTTCGGCACATATACTAAAAT	CGCTTCACGAATTTGCGTGTCAT

and miR-18a (t=21.1137, p<0.001) were abnormally up-regulated in peripheral blood of AMI patients.

Clinical value of miR-499 and miR-18a

In order to understand the clinical value of miR-499 and miR-18a in AMI, the relationship between miR-499 and miR-18a and the general data of AMI patients was statistically analyzed. The results suggested that miR-499 and miR-18a were not corelated with gender, BMI, TC, TG, HDL-C and LDL-C. BMI, TC, TG, HDL-C and LDL-C. miR-499 and miR-18a were found to be related to age, Killip grading, Pro-BNP and LVEF (Tables 3 * ROMAN and IV)

MiR-499 + miR-18a was a potential marker for MI diagnosis

In order to determine whether miR-499 or miR-18a can be used as a marker for AMI diagnosis, this section constructed ROC curves of miR-499 and miR-18a in the diagnosis of AMI patients. The diagnosis of miR-499, miR-18a, and miR-499 + miR-18a in 121 patients with MI (Fig. 1) showed that the AUC value of AMI diagnosed by miR-499 was 0.9018 (95%CI: 0.8597-0.9439), the AUC value of AMI diagnosed by miR-18a was 0.9225 (95%CI: 0.8840-0.9611), and the AUC value of AMI diagnosed by miR-499+miR-18a was 0.9380 (95%CI: 0.9044-0.9715), indicating that miR-499 + miR-18a had better diagnostic value, (p<0.001).

Analysis of the relative expression levels of miR-499 and miR-18a on the prognosis of AMI patients

The patients were sorted according to the relative expression of miR-499 and miR-18a. Patients above the median values of miR-499 (2.093) and miR-18a (2.354) were included in the high expression group, while those under the median values were assigned into the low expression group. Over time, the 3-year survival rate in the high-expression group was remarkably lower than that in the low-expression group. (Fig. 2)

Table II. *General information*

	Research group (n=121)	Control group (n=75)	χ^2/t	p
Gender [n(%)]			0.3988	0.528
Male	69 (57.02)	52 (69.33)		
Female	42 (42.98)	38 (30.67)		
Age (years old)	64.05±6.55	63.95±6.21	0.1060	0.9157
BMI (kg/m^2)	23.04±2.16	22.45±2.09	1.882	0.0614
Killip grading			0.531	0.466
Grade I	29 (23.97)	—		
Grade II	31 (25.62)	—		
Grade III	30 (24.79)	—		
Grade IV	31 (25.62)	—		
TC (mmol/L)	4.36±0.62	4.45±0.57	1.0182	0.3098
TG (mmol/L)	1.76±0.75	1.09±0.37	7.207	<0.001
HDL-C (mmol/L)	0.72±0.19	1.08±0.28	10.7181	<0.001
LDL-C (mmol/L)	2.83±0.62	2.74±0.42	1.1088	0.2689
SBP (mmHg)	130.84±20.36	126.54±3.24	1.8131	0.0714
DBP (mmHg)	76.51±14.25	75.16±2.08	0.8143	0.4165
Pro-BNP (ng/L)	7654±1023.61	76.4±9.56	64.0459	<0.001
LVEF	44.1±4.13	65.3±6.12	28.9453	<0.001

Table III. *Correlation between general information and miR-499 (n=121)*

	n(%)/mean±SD	miR-499	t/r	*p*
Gender [n(%)]			1.112	0.2684
Male	69 (57.02)	1.95±0.29		
Female	42 (42.98)	1.89±0.25		
Age (years old)			3.712	**<0.0001**
≤60	44	1.83±0.22		
>60	67	2.05±0.35		
BMI (kg/m^2)	23.04±2.16	2.13±0.45	-0.1323	0.1480
Killip grading				
Grade I	29 (23.97)	1.10±0.16	15.9308	**<0.0001**
Grade II	31 (25.62)	1.97±0.25	8.7345	**<0.0001**
Grade III	30 (24.79)	2.74±0.42	8.6270	**<0.0001**
Grade IV	31 (25.62)	3.94±0.64		
TC (mmol/L)	4.36±0.62	2.13±0.45	0.1082	0.2375
TG (mmol/L)	1.76±0.75	2.13±0.45	0.1155	0.2069
HDL-C (mmol/L)	0.72±0.19	2.13±0.45	0.1101	0.2294
LDL-C (mmol/L)	2.83±0.62	2.13±0.45	0.1316	0.1503
Pro-BNP (ng/L)	7654±1023.61	2.13±0.45	0.6694	**<0.0001**
LVEF	44.1±4.13	2.13±0.45	-0.6225	**<0.0001**

Table IV. *Correlation between general information and miR-18a (n=121)*

	n(%)/mean±SD	miR-18a	t/r	*p*
Gender [n(%)]			1.210	0.2289
Male	69 (57.02)	2.09±0.31		
Female	42 (42.98)	2.02±0.27		
Age (years old)			3.5902	**<0.0001**
≤60	44	1.89±0.23		
>60	67	2.10±0.34		
BMI (kg/m^2)	23.04±2.16	2.46±0.48	-0.1475	0.1063
Killip grading				
Grade I	29 (23.97)	1.12±0.18	15.0558	**<0.0001**
Grade II	31 (25.62)	2.09±0.30	11.1151	**<0.0001**
Grade III	30 (24.79)	3.11±0.41	7.5639	**<0.0001**
Grade IV	31 (25.62)	4.12±0.61		
TC (mmol/L)	4.36±0.62	2.46±0.48	0.1438	0.1155
TG (mmol/L)	1.76±0.75	2.46±0.48	0.1093	0.2328
HDL-C (mmol/L)	0.72±0.19	2.46±0.48	0.1013	0.2688
LDL-C (mmol/L)	2.83±0.62	2.46±0.48	0.1098	0.2305
Pro-BNP (ng/L)	7654±1023.61	2.46±0.48	0.5000	**<0.0001**
LVEF	44.1±4.13	2.46±0.48	-0.8829	**<0.0001**

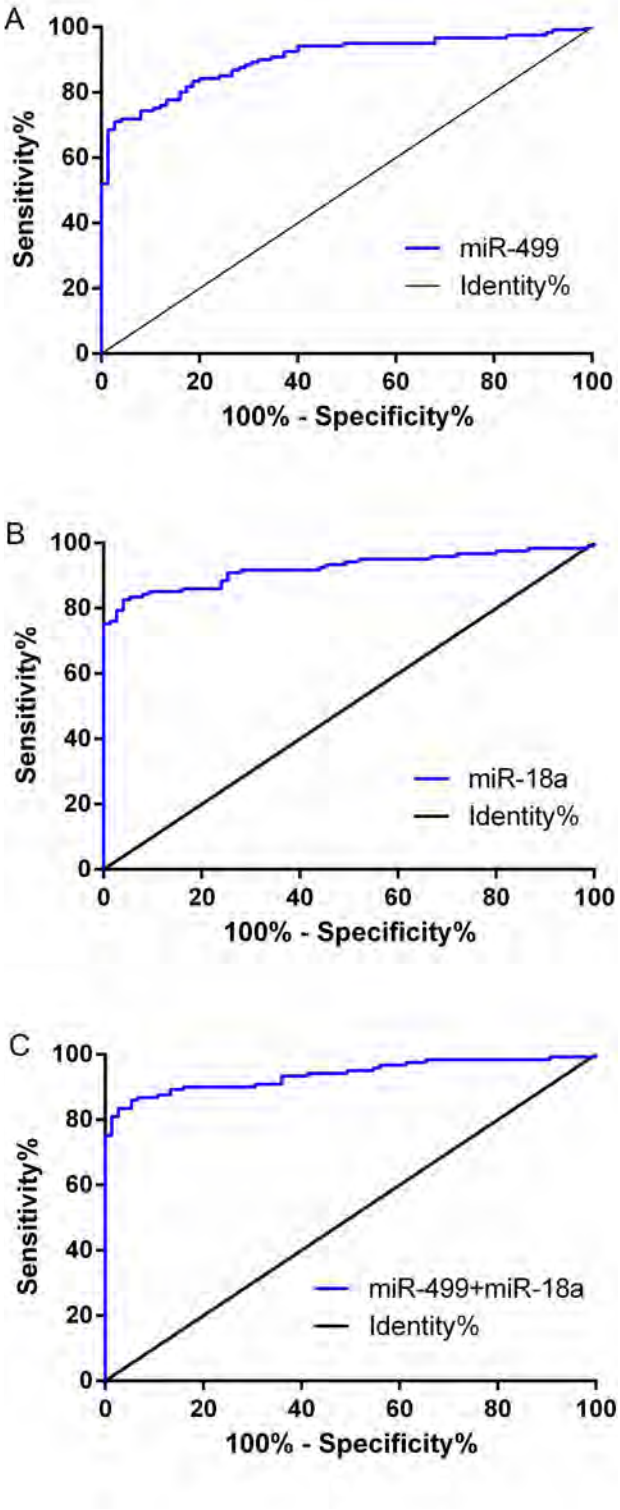


Fig. 1. *miR-499 and miR-18a for AMI diagnosis. **A**) ROC curve of AMI diagnosed by miR-499; **B**) ROC curve of AMI diagnosed by miR-18a; **C**) ROC curve of AMI diagnosed by miR-499 + miR-18a.*

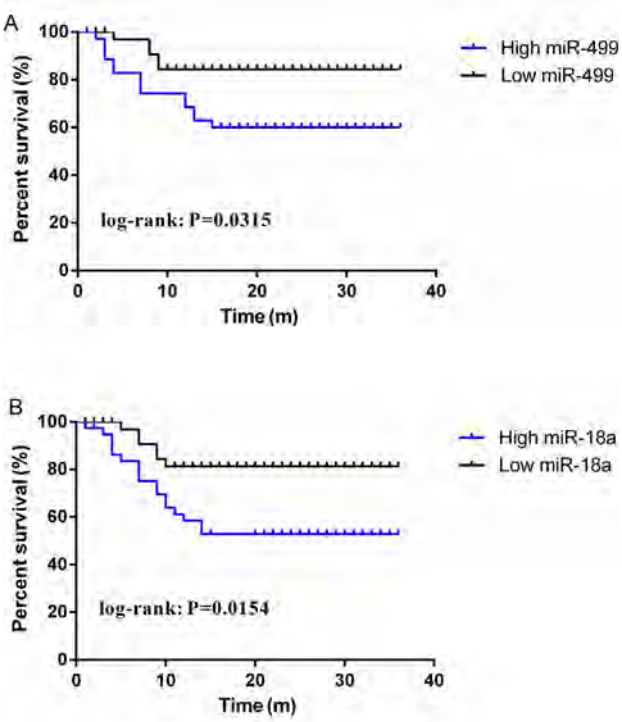


Fig. 2. *Effects of miR-499 and miR-18a on 3-year survival of AMI patients. **A**) miR-499 relative expression and AMI survival analysis; **B**) miR-18a relative expression and AMI survival analysis.*

MiR-499 and miR-18a for COX risk analysis

COX univariate analysis (Table V) showed that high miR-499 (p=0.013), high miR-18a (p=0.039), Pro-BNP (p=0.034), and LVEF (p=0.019) were independent risk factors for 3-year survival of AMI patients.

DISCUSSION

The results showed that miR-499 and miR-18a were highly expressed in AMI patients, and were related to age, Killip grading, Pro-BNP and LVEF. Moreover, the survival of the high-expression groups of miR-499 and miR-18a was statistically worse than that of the corresponding low-expression groups, and the high miR-499 and miR-18a expressions were risk factors for AMI. MiR-499 is exceedingly lowly expressed in healthy people, increases after MIR, and its level is higher in patients with AMI than those with unstable angina (8). In addition, miR-499

Table V. *COX univariate risk analysis*

	HR	*p*	95%CI	SE
miR-499 (high *vs* low)	1.830	**0.013**	1.137-3.215	0.275
miR-18a (high *vs* low)	1.585	**0.039**	1.012-2.756	0.268
Gender (male *vs* female)	1.581	0.076	0.953-2.622	0.427
Age (≤60 *vs* >60)	1.475	0.043	1.024-2.348	0.236
TC (mmol/L)	0.791	0.225	0.531-1.208	0.241
TG (mmol/L)	0.971	0.175	0.624-1.412	0.249
HDL-C (mmol/L)	1.264	0.184	0.841-1.969	0.267
LDL-C (mmol/L)	1.364	0.097	0.742-2.036	0.349
Pro-BNP (ng/L)	1.579	**0.034**	1.002-2.621	0.262
LVEF	1.707	**0.019**	1.042-2.842	0.266

can inhibit the downstream NF-kB/TNF-α signaling pathway by targeting PDCD4 to promote endothelial cell inflammation (9). Research has revealed that miR-18a can regulate neuronal plasticity and development by targeting brain, and has become a therapeutic target for neurodevelopment and psychiatric-related diseases (10). It is suggested that the high expression of the miR-499 and miR-18a in AMI may be the human body's stress response to AMI damage and reflect the degree of AMI damage.

The results demonstrated that miR-499+miR-18a presented the highest AUC value (0.9380) in the diagnosis of AMI, indicating that their combined diagnosis has promising potential value in AMI. According to Wang et al. (11) and Lin et al. (12), miR-499 and miR-18a can act as biomarkers for the diagnosis of cardiovascular diseases. The results of this paper further show that miR-499+miR-18a is of potential value in the diagnosis of AMI.

REFERENCES

1. Members WG, Mozaffarian D, Benjamin EJ, et al. Heart Disease and Stroke Statistics-2016 Update: A Report from the American Heart Association. Circulation 2016; 133:e38.
2. Gilson J, Khalighi K, Elmi F, Krishnamurthy M, Talebian A, Toor RS. Lyme disease presenting with facial palsy and myocarditis mimicking myocardial infarction. J Community Hosp Intern Med Perspect 2017; 7:363365.
3. Zhong J, He Y, Chen W, Shui X, Chen C, Lei W. Circulating microRNA-19a as a Potential Novel Biomarker for Diagnosis of Acute Myocardial Infarction. Int J Mol Sci 2014; 15:20355-64.
4. Zhao CH, Cheng GC, He RL, Hong Y, Wan QL, Wang ZZ, Pan ZY. Analysis and clinical significance of microRNA-499 expression levels in serum of patients with acute myocardial infarction. Genet Mol

Res 2015; 14:4027-34.
5. Shi Y, Han Y, Niu L, Li J, Chen Y. MiR-499 inhibited hypoxia/reoxygenation induced cardiomyocytes injury by targeting SOX6. Biotechnol Lett 2019; 41:837-47.
6. Zhou Y, Wu R, Su H, Li K, Chen C, Xie R. miR-18a increases insulin sensitivity by inhibiting PTEN. Aging (Albany NY) 2020; 13:1357-68.
7. Bin L, Deguang F, Jing X. Cardioprotective effects of microRNA-18a on acute myocardial infarction by promoting cardiomyocyte autophagy and suppressing cellular senescence via brain derived neurotrophic factor. Cell Biosci 2019; 9:38.
8. Chen X, Zhang L, Su T, et al. Kinetics of plasma microRNA-499 expression in acute myocardial infarction. J Thorac Dis 2015; 7:890-96.
9. Zhang YH, He K, Shi G. Effects of MicroRNA-499 on the inflammatory damage of endothelial cells during coronary artery disease via the targeting of PDCD4 through the NF-Kβ/TNF-α signaling pathway. Cell Physiol Biochem 2017; 44:110-24.
10. Vaghi V, Polacchini A, Baj G, Pinheiro VL, Vicario A, Tongiorgi E. Pharmacological profile of Brain-Derived Neurotrophic Factor (BDNF) splice variants translation using a novel drug screening assay: a ″Quantitative Code″. J Biol Chem 2014; 289:27702-13.
11. Wang Q, Ma J, Jiang Z, Wu F, Ping J, Ming L. Identification of microRNAs as diagnostic biomarkers for acute myocardial infarction in Asian populations: a systematic review and meta-analysis. Medicine 2017; 96:7173.
12. Bin L, Deguang F, Jing X. Cardioprotective effects of microRNA-18a on acute myocardial infarction by promoting cardiomyocyte autophagy and suppressing cellular senescence via brain derived neurotrophic factor. Cell Biosci 2019; 9:38.

LETTER TO THE EDITOR

High resolution computerized tomography quantitative evaluation of the correlation between central airway and pulmonary function grading in chronic obstructive pulmonary disease

J. Pu*, MJ. Zhou*, JW. Shao, ST. Xiang, Q. He, W. Su, SZ. He, CW. Mao, RG. Ruan and BL. Song

Department of Radiology, The Second People's Hospital of Yunnan Province, & the Fourth Affiliated Hospital, Kunming Medical University, Kunming, China

Received August 5, 2020 – Accepted March 18, 2021

*These authors contributed equally to this study

To the Editor,

Chronic obstructive pulmonary disease (COPD) is a disease that can be prevented and treated. Its incidence has a high morbidity and mortality rate and causes heavy social and economic burden (1). Furthermore, it is presently the fourth leading cause of death (2). At present, the gold standard for the clinical diagnosis of COPD is the pulmonary function test (PFT) (3). However, PFT examination requires the close cooperation of patients, which are limited by the patient's health status and disease classification, and affects the accuracy of the results (4). Furthermore, PFT cannot help to analyze the cause of airflow limitation (5).

In recent years, with the continuous development of imaging technology and post-processing software, high resolution computerized tomography (HRCT) can accurately and quantitatively analyze the early airway, lung tissue and blood vessel changes in COPD (6). Hence, HRCT has the advantages of early diagnosis, quantitative analysis and prognosis evaluation of COPD. Furthermore, HRCT is more precise than PFT. HRCT can detect early changes in COPD, analyze the causes of airflow limitation, and guide and assist the clinical diagnosis and treatment. To date, there have been many studies on small airway changes in COPD (7), but few on central airway changes in COPD, and the correlation between central airway and pulmonary function in COPD has rarely been reported.

The present study aims to evaluate the correlation between central airway parameters and pulmonary function grading, in order to provide new ideas for the evaluation of COPD.

MATERIALS AND METHODS

Clinical data were gathered from January 2018 to January 2019 for patients with COPD in the Respiratory Department of the Fourth Affiliated Hospital of Kunming Medical University. The diagnostic criteria were established based on the diagnostic and staging criteria of COPD published by the National Institute of Cardiopulmonary Hematology (NHLBL) and the World Health Organization (WHO) in the 2017 edition of Chronic Obstructive Pulmonary Disease (GOLD). The present study was approved by the ethics committee of our hospital, and all patients provided a signed informed consent.

The inclusion criteria were: patients who were diagnosed with COPD and who completed the chest

Key words: chronic obstructive pulmonary disease; high resolution ct; airway; pulmonary function; quantitative analysis

Corresponding Author:
Qian He,
Department of Radiology,
The Second People's Hospital of Yunnan Province,
& the Fourth Affiliated Hospital of Kunming Medical University,
No.176 of Qingnian street, Wuhua District, Kunming 650000, China
Tel.: +86 0871 65156650 3143 - Fax: +86 0871 65156650 3142
e-mail: qianhe529@163.com

0393-974X (2021)
Copyright © by BIOLIFE, s.a.s.
This publication and/or article is for individual use only and may not be further reproduced without written permission from the copyright holder.
Unauthorized reproduction may result in financial and other penalties
DISCLOSURE: ALL AUTHORS REPORT NO CONFLICTS OF INTEREST RELEVANT TO THIS ARTICLE.

computed tomography (CT) examination within two days after the pulmonary function examination. Exclusion criteria were: COPD patients with bronchiectasis; COPD patients with bronchial asthma; COPD patients with a large area (more than one lung lobe) of infection, tracheal intubation, tracheotomy and central airway neoplasms; patients who were unable to cooperate with the expiratory and end-inspiratory breath-holding during scanning; patients with a CT image quality affected by respiration or patients whose CT images were unable to be measured.

Pulmonary function tests were performed using the master SCREEN series pulmonary function tester of JAEGER (Germany). Before the test, the pulmonary function was routinely calibrated and measured by professionals, according to routine operation. The examination included forced vital capacity (FVC), forced expiratory volume in one second (FEV1), forced expiratory volume in the first second (FEVl/FVC), percentage of forced expiratory volume in the first second (FEVl/FVC), and percentage of forced expiratory volume in 1 second (FEV1) accounts for the predicted value.

CT examinations

The CT scanning was performed using CT scanning equipment of Toshiba "Aquilion ONE" 320 slice CT scanners. Before the examination, breath-holding training was carried out for each patient to achieve the best state of maximum inspiratory end and maximum expiratory end. The subjects lay in a supine position, with their hands held high on the top of their head. The scanning ranged from the apex of the lungs to the bottom of the lungs. These patients were examined at the end of inspiration and expiration, respectively. Specific scanning parameters were as follows: spiral scanning, the matrix was 512×512, the pitch was 1.484, the acquisition layer thickness was 5 mm. Inspiratory end using conventional scanning: 120 KV, AEC. Reference image settings: layer thickness was 5 mm, SD = 10. Spherical tube rotation time was 0.5 s/circle. Low-dose breath scanning: 100 KV, AEC. Reference image settings: layer thickness was 5 mm, SD = 2 0; tube rotation time was 0.5 s/lap.

CT image reconstruction parameters: slice thickness was 1.0 mm, spacing was 0.8 mm, and reconstruction function was Fc56 (high resolution). The data of the end-inspiratory and end-expiratory HRCT scans were transmitted to the Aquilion ONE 320 row Vitrea post-processing workstations for data analysis (Figs. 1 and 2).

Manual measurement was performed for the end-inspiratory central trachea volume (Tin), the end-expiratory central trachea volume (Tex), and the end-inspiratory central trachea diameter (Din), and the end-expiratory central trachea diameter (Dex). A width of window (WW) of 400 and a window level (WL) of 40 were used to measure the wall thickness. The airway tubes were measured by selecting a WW of 1,500 and a WL of -650. The magnification was ×300, the position was at the lower edge of the aortic arch, and the diameter of the inner airway was chosen for measurement. Vitrea post-processing software was used to automatically measure the airway volume, which requires the manual tailoring of the surrounding airway, in order to obtain the central airway volume (volume of the central airway trachea at the end of inspiration, Vin) and the expiratory central airway volume (volume of the central airway trachea at the end of expiration, Vex). The volume change of the expiratory-inspiratory phase (Vin-Vex) was calculated based on the bifurcation of each segment of bronchi. Multiplier reformation (MPR) was used to observe and measure the trachea, the left and right main bronchi, the right upper lobe, middle lobe and inferior lobe bronchi, and the left upper lobe and inferior lobe bronchi. The length of the central airway(s) was calculated, and a WW of 1,500 and a WL of -650 were selected for measurement. The ratio of the central airway volume change between the inspiratory phase and expiratory phase to the central airway length (Vin-VexSR) was calculated. The above measurements were measured by two attending physicians who were blinded to the measurements, and the average value was computed. When there were differences, consultations were carried out to reach a consensus. Since the airway volume is influenced by height and weight, there were individual differences. In the present study, the principal airway volume was calibrated by measuring the length of the central airway, and evaluated by Vin-VexSR.

Statistical analysis

SPSS 20.0 software (IBM, Chicago, USA) was used to conduct the statistical analysis. Continuous variables were expressed as mean ± standard deviation (SD). Discontinuous variables were expressed in percentage (%). For multiple comparisons, each value was compared by one-way ANOVA, followed by Dunnett's test, when

each datum conformed to the normal distribution, while non-normally distributed continuous data were compared using non-parametric tests. Counting data were analyzed by *chi*-squared test. A *P*-value of <0.05 was considered statistically significant.

RESULTS

In the present study, a total of 56 COPD patients participated of whom 35 were male and 21 were female, age range within 42-89 (68.26±9.47) years. There was no correlation among gender, age and pulmonary function grade (Table I).

The pulmonary function examination results for the 56 patients were as follows: grade I, 15 cases (26.8%), and FEV1% was 98.47±7.74; grade II, 16 cases (28.6%), and FEV1% was 56.56±10.24; grade III, 16 cases (28.6%), and FEV1% was 40.63±6.19; grade IV, nine cases (16.1%), and FEV1% was 26.67±2.06.

Relationship between CT quantitative parameters and pulmonary function grading

The correlation between CT quantitative parameters and pulmonary function grading was positively correlated with Tin, Tex, Din and Vin-Vex, and negatively correlated with Dex, Vin-VexRS. The differences in Tin, Tex, Din, Dex, Vin, Vex, Vin-Vex and Vin-VexSR among the different pulmonary function grades were statistically significant (P<0.01). Using ANOVA, the F-values were 10.66, 70142, 6.023, 7.344, 14.20, 31.87, 8.745 and 9.12, respectively (Table II).

DISCUSSION

COPD is a chronic airway inflammatory disease. With the progression of the disease, the large airway cartilage can be destroyed or lead to cartilage atrophy. Impulse Oscillation Oscillation (IOS) is

Table I. *Clinical data and pulmonary function classification of 56 COPD patients*

General information	Pulmonary function test				F Value	P Value
	Class I (n=15)	Class II (n=16)	Class III (n=16)	Class IV (n=9)		
Age	67±8.97	69.28±5.24	71.3±8.92	68.39±9.11	0.552	0.427
Gender						0.791
Male	8	11	10	6		
Female	7	5	6	3		

Table II. *Correlation between different pulmonary function grades and central airway parameters in 56 cases of COPD*

Airway parameters	Pulmonary function classification				F Value	P Value
	Grade I	Grade II	Grade III	Grade IV		
Tin	1.00±0.30	1.17±0.31	1.39±0.31	1.74±0.47	10.66	<0.01
Tex	1.24±0.34	1.31±0.38	1.76±0.62	2.06±0.64	7.142	<0.01
Din	18.00±2.69	17.80±3.38	19.76±2.99	22.46±2.06	6.023	0.01
Dex	19.75±3.31	17.13±3.59	15.97±2.45	14.01±2.79	7.344	<0.01
Vin	49.34±6.16	42.86±6.49	34.65±9.48	34.32±3.64	14.20	<0.01
Vex	45.74±5.96	36.03±7.28	25.39±8.12	20.02±7.50	31.87	<0.01
Vin-Vex	3.61±3.13	7.60±7.29	9.25±2.80	14.30±5.98	8.745	<0.01
Vin-VexSR	0.11±0.10	0.25±0.25	0.31±0.09	0.27±0.19	9.12	<0.01

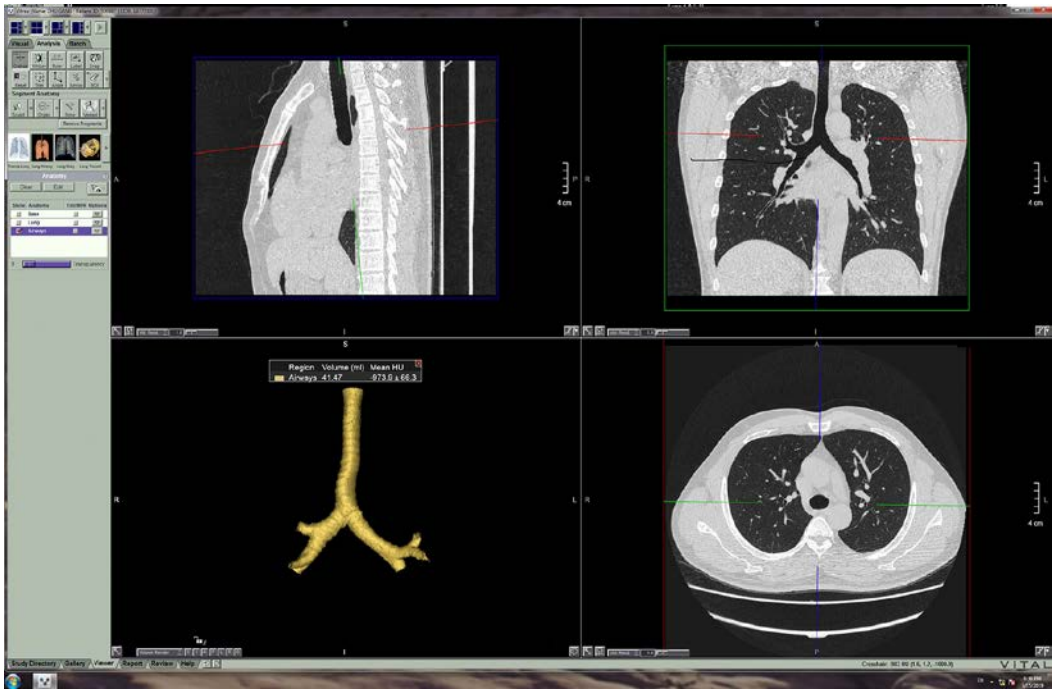


Fig. 1. *Vitrea post-processing workstation interface*

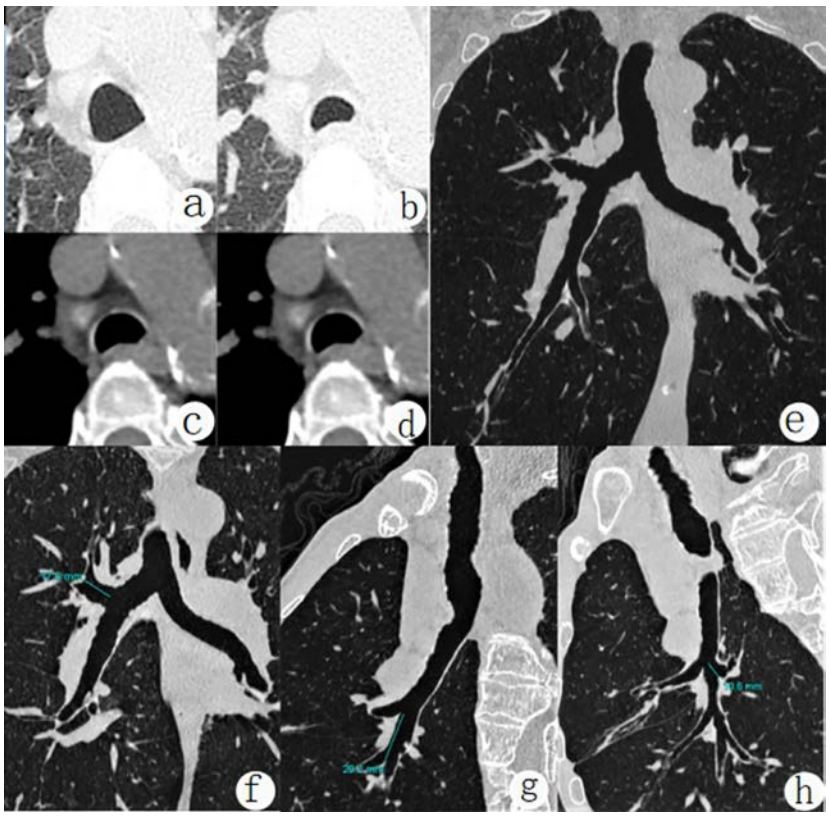


Fig. 2. *Measurement of airway parameters by multiplanar reconstruction.* ***a, b****) The anterior and posterior diameters of inspiratory and expiratory tracheas were measured by lung window.* ***c, d****) Mediastinal window was used to measure the wall thickness of inspiratory and expiratory phases.* ***e-h****) The length of the trachea, left and right main bronchus and lobar bronchus were measured by multiplier reconstruction.*

a new technique for lung function measurement developed in recent years. Based on the principle of forced oscillation, the frequency spectrum of resting breathing under pulse oscillation is analyzed. The central airway parameters can reflect airway deformation and collapse, and provide a new evaluation method for central airway remodeling, which is in agreement with the study conducted by Nakano et al. (8). The results of the present study show that the correlation between pulmonary function classification and central airway volume is higher than that between central airway diameter, which is due to the different position of the central airway wall damage and collapse. The differences in Tin, Tex, Din, Dex, Vin, Vex, Vin-Vex and Vin-VexSR among the different pulmonary function grades were statistically significant (P<0.01). For the side wall, the measurement of the airway diameter in the present study was to choose the front-back diameter. That is, only when a membrane and front wall collapse occurs can a diameter change occur, while the front wall, side wall and back membrane of the airway can change in volume when a collapse occurs in one of these. Hence, the measurement of central airway volume is better than central airway diameter measurement. Moreover, the sensitivity of the inner airway parameters at the end of inspiration was higher than that at the end of inspiration. The change in airway volume increased with the severity of the disease. This indicates that with the aggravation of the disease, the collapse of the airway wall was aggravated. At the end of expiration, the airway volume is reduced. Supporting this, airway collapse has been proven to the maximum extent. Baroni, Leong and other studies (9-10) also recommend the measurement of the degree of airway collapse at the end of expiration. Excessive dynamic Airway Collapse (EDAC) refers to the scenario where posterior wall of the trachea-bronchus is obviously invaginated during tidal exhalation. Its clinical manifestations are indistinguishable from other common obstructive airway diseases, but the principles of treatment are different. The diagnosis requires appropriate imaging. Long-term sequelae include recurrent lower respiratory tract infections and even chronic respiratory failure (11). Tracheobronchomalacia is a condition characterized by flaccidity of the tracheal support cartilage which leads to tracheal collapse and further damage to the bronchi.

In conclusion, there is a correlation between changes in central airway wall thickness, diameter, volume and end-inspiratory volume, and pulmonary function classification. End-expiratory central airway volume in central airway parameters is the most sensitive index to reflect the pulmonary function classification.

REFERENCES

1. Miravitlles M, Ribera A. Understanding the impact of symptoms on the burden of COPD. Respir Res 2017; 18:67.
2. Tan WC, Bourbeau J, Aaron SD, et al. Global initiative for chronic obstructive lung disease 2017 classification and lung function decline in chronic obstructive pulmonary disease. Am J Respir Crit Care Med 2018;197:670-3.
3. Schermer TR, Jacobs JE, Chavannes NH, et al. Validity of spirometric testing in a general practice population of patients with chronic obstructive pulmonary disease (COPD). Thorax 2003; 58:861-6.
4. Starobin D, Kramer MR, Yarmolovsky A, et al. Assessment of functional capacity in patients with chronic obstructive pulmonary disease: correlation between cardiopulmonary exercise, 6 minute walk and 15 step exercise oximetry test. Isr Med Assoc J 2006; 8:460-3.
5. Şerifoğlu İ, Ulubay G. The methods other than spirometry in the early diagnosis of COPD. Tuberk Toraks 2019; 67:63-70.
6. Ostridge K, Gove K, Paas KHW, et al. Using novel computed tomography analysis to describe the contribution and distribution of emphysema and small airways disease in chronic obstructive pulmonary disease. Ann Am Thorac Soc 2019; 16:990-7.
7. Zhao D, Zhou Y, Jiang C, et al. Small airway disease: A different phenotype of early stage COPD associated with biomass smoke exposure. Respirology 2018; 23:198-205.
8. Nakano Y, Muro S, Sakai H, et al. Computed tomographic measurements of airway dimensions

and emphysema in smokers: correlation with lung function. Am J Respir Crit Care Med 2000; 162(3 Pt 1):1102-8.

9. Baroni RH, Feller-Kopman D, Nishino M, et al. Tracheobronchomalacia: comparison between end-expiratory and dynamic expiratory CT for evaluation of central airway collapse. Radiology 2005; 235:635-41.
10. Leong P, Tran A, Rangaswamy J, et al. Expiratory central airway collapse in stable COPD and during exacerbations. Respir Res 2017; 18:163.
11. Weinstein DJ, Hull JE, Ritchie BL, Hayes JA, Morris MJ. Exercise-associated excessive dynamic airway collapse in military personnel. Ann Am Thorac Soc. 2016; 13(9):1476-82.

LETTER TO THE EDITOR

Conservative treatment of partial rotator cuff tears, comparison between infiltrative treatment with corticosteroids, medium molecular weight hyaluronic acid and high molecular weight hyaluronic acid: a prospective study

N. Setaro and A. Gigante

Department of Clinical and Molecular Science, School of Medicine, Università Politecnica delle Marche, Ancona, Italy

Received March 16, 2021 - Accepted May 18, 2021

To the Editor,

Rotator cuff disease is the main cause of shoulder pain and disability. The causes arise from a multivariate etiology, often due to age-related chronic degeneration in which the decrease in collagen synthesis plays a role, and increased expression and metabolism of free radicals imbalance in favor of catabolic activity (1)the shoulder joint is thought to age more by its tendons than by its cartilages, the incidence of rotator cuff tears being considered to increase with age. The purpose of this work was to assess the natural history of the shoulder joint based on a clinical and radiological study of 200 patients aged 70 to 101 years.\nThe cohort was composed of 48 men (34%. It is important to remember that during life, the rotator cuff is exposed to a series of forces, represented by elongation, compression and subacromial microtrauma responsible for the progressive weakening and degeneration of the tendon fibers and their consequent rupture (2). Classically, the diagnosis is clinical with predominantly nocturnal pain, joint stiffness, instability and loss of strength during flexion, abduction and extra-rotation. Furthermore, a rotator cuff injury can alter the balance and stability of the shoulder joint, leading to the onset of eccentric arthrosis in the medium to long term. Also for this reason the correct treatment of these injuries is of considerable importance. Clinical diagnosis can be confirmed by ultrasound or Magnetic Resonance Imaging (MRI) (gold standard). The first management in the treatment of rotator cuff tears is conservative and includes: oral anti-inflammatory drugs, topical agents, injections of intra-articular substances, physical therapies and joint rehabilitation exercises (3, 4). In the literature there are numerous publications on the use of injections of steroids and local anesthetics, administered alone or in combination with other therapies. However, there are far fewer studies on the effectiveness of hyaluronic acid (HA) injection treatment in rotator cuff disorders. To our knowledge, no studies in the literature have compared the results obtained from treatment with intra-articular injections of corticosteroids and those obtained with intra-articular injections of HA in a uniform group of patients with partial rotator cuff tear. Furthermore, in this study, the results obtained by injecting two different types of hyaluronic acid that differed in their molecular weight were compared. The aim of the present study was to compare three different possibilities of infiltrative treatment in rotator cuff tendinopathy, evaluating the results obtained from

Key words: shoulder; rotator cuff ; partial tears; tendinopathy; hyaluronic acid; orthopedic; conservative treatment; molecular weight; corticosteroids; infiltative treatment

Corresponding Author:
Nicola Setaro, MD
Department of Clinical and Molecular Sciences,
Università Politecnica delle Marche,
Via Tronto 10/ 60126, Ancona, Italy
Tel.: +39 071 5963346 - Fax: +39 071 5963341
e-mail: nicola.setaro@libero.it

0393-974X (2021)
Copyright © by BIOLIFE, s.a.s.
This publication and/or article is for individual use only and may not be further reproduced without written permission from the copyright holder.
Unauthorized reproduction may result in financial and other penalties
DISCLOSURE: ALL AUTHORS REPORT NO CONFLICTS OF INTEREST RELEVANT TO THIS ARTICLE.

each treatment in terms of safety, pain reduction, and improvement of shoulder function.

MATERIALS AND METHODS

Study design and patients

This is a prospective, open label, non-randomized and uncontrolled study. All patients with shoulder pain and functional impotence were evaluated between March 2017 and September 2020 at our university hospital. Each patient underwent careful clinical evaluation, X-rays (to rule out fractures, calcifications, or other disorders) and MRI to frame the type of injury and classify it. Modified Neer's classification was used to classify lesions. Only patients who showed evidence of partial rotator cuff tear (Neer grade II) on MRI were recruited for the study. All other patients suffering from shoulder pain and functional impotence due to other causes were excluded. In detail, the exclusion criteria from the study were: age under 30 and over 80 years, shoulder instability anterior, posterior, multidirectional, Superior Labrum From Anterior to Posterior (SLAP) lesions, rheumatoid arthritis, amyloidosis, chondrocalcinosis, gout, rheumatological diseases, shoulder trauma within the last year, adhesive capsulitis/calcific tendonitis, previous subacromial injection therapies (any drug), diabetes, major depressive syndrome, grade I lesions according to Neer's classification (Bursitis, acute/chronic tendonitis without tear), Neer's grade III lesions (Complete tear without glenohumeral osteoarthritis), Neer's grade IV lesions (Cuff tear arthropathy). The total number of patients recruited was 60, of which 34 were females and 26 were males. The mean age of the patients corresponded to 57±15.8 years. Thirty-nine patients had shoulder injury of the dominant limb, while twenty-one had shoulder injury of the contralateral limb. Each patient who participated in the study read and signed an informed consent. Subsequently each patient filled in pre-treatment self-assessment questionnaires such as Visual analogue scale (VAS), Oxford shoulder score (OSS) and Constant-Murley score (CMS). Patients were then divided into three uniform groups for age, sex and pretreatment symptoms in order to reduce the biases as much as possible. Each group consisted of twenty patients. At this point each patient underwent an infiltrative cycle by three subacromial intra-articular injections (one every 7 days). Patients in the first group (group A) underwent intra-articular injections of Depo-Medrol® 40mg; the patients of the second group (group B) underwent intra-articular injections of Condronil® IALDUE; while the patients of the third group (group C) underwent intra-articular injections of Fluicondrial® H 40. Depo-Medrol® contains 40 mg of methylprednisolone acetate particularly indicated among other things for the treatment of bursitis, synovitis and tenosynovitis. Condronil® IALDUE is a sterile, injectable, biodegradable and isotonic gel, for intra-articular use, consisting of a medium molecular weight hyaluronic acid (1000-1500 kDalton), produced by streptococcus equi bacteria, formulated at a concentration of 20mg/ml in a physiological buffer. Each vial contains 40 mg of active ingredient. Fluicondrial® H 40 is a sterile injectable, biodegradable and isotonic gel, for intra-articular use, and consists of a high molecular weight hyaluronic acid (2500-3500 kDalton), produced by Streptococcus Equi bacteria, formulated at a concentration of 20 mg/ml. Each vial contains 40 mg of active ingredient. After each injection, patients were advised to apply ice for 20 minutes 3 times a day for 3 days. The use of other painkilling and anti-inflammatory drugs was banned to avoid that these could alter the results of the study. Furthermore, any physiotherapy exercise was not recommended, on the contrary it was recommended to avoid functional loads on the affected shoulder.

The primary endpoint of the study was to assess pain relief 15 days (day 30 from the first injection) and 30 days after the cycle of three injections, compared to baseline. The secondary endpoint was to evaluate the maintenance of pain relief at 60 and 120 days after the end of the infiltrative cycle. As additional endpoints, the global assessment of patients and range of motion (ROM) were evaluated through questionnaires and functional tests, respectively. Furthermore, the change in the signal of the lesion on MRI at 180 days after treatment was evaluated by comparing it with that of pretreatment MRI.

Infiltrative technique and follow-up

Intra-articular injections were performed without anesthesia, on a sterile field, with a 21G needle. The injections were administered in the subacromial space (posterior way), approximately 1 cm below the inferior posterolateral margin of the acromion. The needle was oriented in the direction of the coracoid process. To

achieve greater precision of the procedure, a 10-12 MHz ultrasound guide was used. No further rehabilitative protocol was prescribed during the entire study. The procedure thus performed usually allows the patient to get up and leave a few minutes after the treatment.

Each patient underwent a clinical evaluation before treatment, then 15, 30, 60 and 120 days after the infiltrative cycle. At each follow-up, patients underwent clinical evaluation of the affected shoulder and had to complete three different questionnaires. The first questionnaire was the VAS scale in which patients had to indicate a pain level in the affected shoulder from 1 to 10. The second questionnaire was Oxford Shoulder Score, a specific questionnaire developed for patients with degenerative or inflammatory shoulder diseases. In 2009, the scoring method for the OSS was modified so that each of the 12 items is scored from 0 (worst/most severe) to 4 (best/fewest symptoms). The total score therefore ranges from 0 to 48, with a lower score indicating a greater degree of disability. The questions deal with pain and possible handicaps in private and in professional life. In this study, the modified version of the Oxford Shoulder Score was used (5, 6). This questionnaire reports on the overall assessment of the patient. The third questionnaire was the Constant-Murley Score. This score is calculated from the answers to eight questions, five of which are based on objective assessments and three on subjective assessments. The maximum score is 100, which corresponds to one optimal state of health (7). Note that for both the Constant-Murley score and the OSS, the patient was questioned about his health during the previous 2 weeks; normally these ratings are used to investigate health in the previous 4 weeks. Pretreatment and at follow-up at 30 and 120 days from the end of the infiltrative cycle, the range of motion in abduction of the affected shoulder was assessed. In addition, 180 days after the end of the infiltrative cycle, patients underwent a new MRI to assess whether the lesion signal had changed.

Statistical analysis

All the following data are presented as the mean, standard deviation (±SD), minimum and maximum, and lower and upper confidence limits ($p<0.05$). VAS pain reduction, Constant-Murley Score evolution and Oxford Shoulder Score evolution, evaluated at day 15, 30, 60 and 120, were analysed within each cuff tear grade by means of Student's *t*-test for paired data. For each effectiveness variable the comparisons between cuff tear grades were carried out by means of an analysis of covariance for repeated measures model, considering the baseline value of the efficacy variable as covariate.

RESULTS

Of the 60 patients recruited for the study, all completed follow-up. The results of the VAS score, pre-treatment and after 15, 30, 60 and 120 days from the treatment are shown in Table I. The variations in VAS scores across the three different treatments are represented in Fig. 1. The OSS results, pretreatment, after 15, 30, 60 and 120 days from the treatment are reported in Table II. The variations in OSS results across the three different treatments are represented in Fig. 2. The CMS results, pretreatment, after 15, 30, 60 and 120 days from the treatment are reported in Table III. The variations in CMS results across the three different treatments are represented in Fig. 3.

The short-term result was the evaluation of the effectiveness of the three treatments 15 days after the conclusion of the infiltrative cycle (30th day after the first injection) and 30 days after the conclusion of the infiltrative cycle (45th day after the first injection). The patients included in group A (group treated with corticosteroids) reported a decrease in mean VAS from 7.45±1.37 preinjection to 6.28±1.68 at 15 days to 6.04±1.49 at 30 days; the mean Oxford shoulder score increased from 27.73±4.53 preinjection to 31.68±4.25 at 15 days to 31.95±4.39 at 30 days, whereas the mean Constant-Murley score increased from 53.60±8.7 to 59.42±6.73 at 15 days to 59.75±7.20 at 30 days. The patients included in group B (group treated with medium molecular weight hyaluronic acid) reported a decrease in mean VAS from 7.84±1.31 preinjection to 6.14±1.34 at 15 days to 5.19±1.38 at 30 days, the mean Oxford shoulder score increased from 28.69±4.27 preinjection to 32.28±4.15 at 15 days to 38.15±5.20 at 30 days, whereas the mean Constant-Murley score increased from 50.20±7.83 to 60.20±6.00 at 15 days to 64.28±7.40 at 30 days. The patients included in group C (group treated with hight molecular weight hyaluronic acid) reported a decrease in mean VAS

Table I. *Clinical outcomes measured by the VAS score in terms of pain reduction; pre-treatment and after 15, 30, 60 and 120 days of follow-up.*

VAS	PRE	Day 15	Day 30	Day 60	Day 120
Group A	7.45±1.37	6.28±1.68	6.04±1.49	7.75±1.15	8.40±1.19
Group B	7.84±1.31	6.14±1.34	5.19±1.38	4.82±1.28	4.10±1.54
Group C	7.69±1.34	6.25±1.53	5.24±1.76	5.19±1.82	4.91±1.72

Table II. *Evaluation of the overall condition of patients as measured by OSS; pre-treatment and after 15, 30, 60 and 120 days of follow-up.*

OSS	PRE	Day 15	Day 30	Day 60	Day 120
Group A	27.73±4.53	31.68±4.25	31.95±4.39	28.10±4.61	25.83±4.58
Group B	28.69±3.39	32.38±3.63	38.15±5.20	43.10±3.63	46.20±3.39
Group C	28.50±4.05	31.70±5.75	37.80±4.82	41.70±4.78	44.73±5.25

Table III. *Functional conditions of the shoulder joint assessed through the CMS; pretratment and after 3, 6, 12 and 24 months of follow-up.*

CMS	PRE	Day 15	Day 30	Day 60	Day 120
Group A	53.60±8.7	59.42±6.73	59.75±7.20	54.37±6.72	48.42±7.94
Group B	50.20±7.83	60.20±6.00	64.28±7.40	78.39±5.75	86.69±6.37
Group C	51.50±6.84	59.40±6.55	61.14±6.82	70.53±6.28	74.57±6.89

from 7.69±1.34 preinjection to 6.25±1.53 at 15 days to 5.24±1.76 at 30 days, the mean Oxford shoulder score increased from 28.50±4.05 preinjection to 31.70±5.75 at 15 days to 37.80±4.82 at 30 days, whereas the mean Constant-Murley score increased from 51.50±6.84 to 59.40±6.75 at 15 days to 61.14±6.82 at 30 days.

The middle-term results were the evaluation of the effectiveness of the three treatments 60 days after the cycle conclusion (75th day after the first injection). Patients in group A had a mean VAS score of 7.75±1.15 worse than pretreatment. The mean Oxford shoulder score was 28.10±4.61, whereas the mean Constant-Murley score was 54.37±6.72; both of these scores were better than pretreatment, but worse than those found in the previous follow-up. The mean VAS, OSS and CMS scores of the patients in group B were respectively 4.82±1.28, 43.10±3.63 and 78.39±5.75. In patients of group C these scores were respectively 5.19±1.82, 41.70±4.78 and 70.53±6.28. Both patients in group B and patients in group C continued to show progressive improvement in mean VAS score, mean OSS, and mean CMS at 60 days of follow-up.

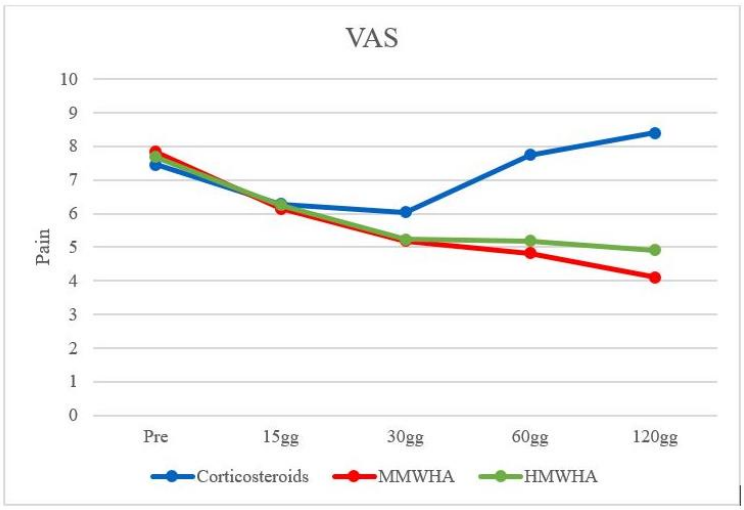


Fig. 1. *Mean VAS score decreases significantly in all three groups up to 30 days after the end of treatment. It subsequently increases in the group treated with corticosteroids, while it continues to decrease significantly in the groups treated with hyaluronic acid; curca decreases more in the group treated with MMWHA.*

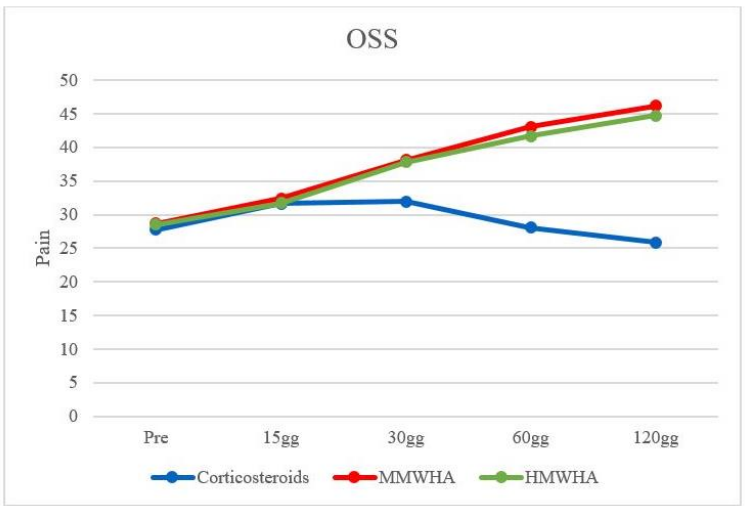


Fig. 2. *Mean OSS increases significantly in all three groups up to 30 days after the end of treatment. It subsequently decreases in the group treated with corticosteroids, while it continues to increase significantly in the groups treated with hyaluronic acid; the curve grows more in the group treated with MMWHA.*

The long-term results were the evaluation of the effectiveness of the three treatments 120 days after the infiltrative cycle conclusion. In patients in group A the mean VAS score was 8.40±1.19 higher than all other measurements including pretreatment. The mean OSS was 25.83±4.58, whereas the mean CMS was 48.42±7.94. These two scores were worse than in previous follow-ups and pretreatment. Group B patients showed the following mean scores: 4.10±1.54 (VAS), 46.20±3.39 (OSS) and 86.69±6.37 (CMS). Group C patients showed the following mean scores: 4.91±1.72 (VAS), 44.73±5.25 (OSS) and 74.57±6.89 (CMS). Both group B and group C continued to show better average results in all scores with respect to both pretreatment and previous follow-ups. Furthermore, 180 days after treatment, all patients underwent a follow-up MRI. The intensity of the lesion signal appeared reduced in

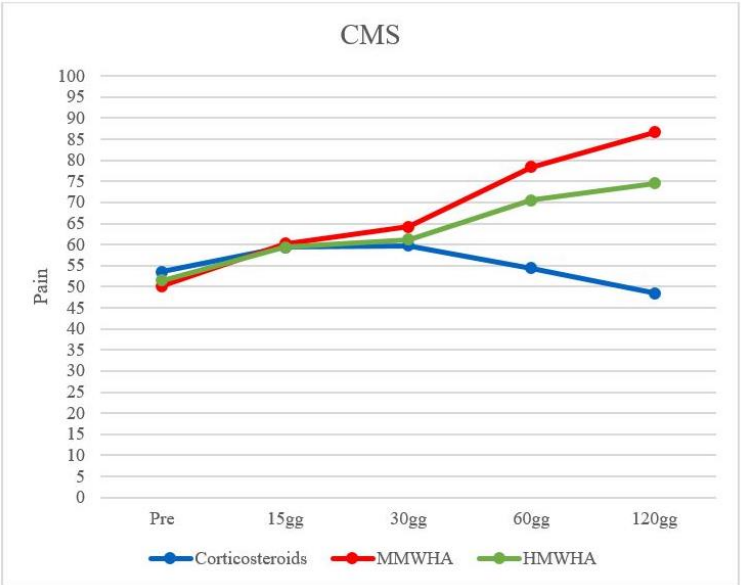


Fig. 3. *Mean CMS increases significantly in all three groups up to 30 days after the end of treatment. It subsequently decreases in the group treated with corticosteroids, while it continues to increase significantly in the groups treated with hyaluronic acid; the curve grows more in the group treated with MMWHA.*

20 patients, of whom only 1 belonged to group A. It appeared identical to pretreatment in 28 patients, of whom 10 belonged to group A. It appeared increased in 12 patients including 9 belonging to group A.

Range of motion assesment

In the pretreatment, the range of motion in abduction in the three groups was 59.4±14.7° in group A, 60.0±12.1° in group B and 59.8±12.5° in group C, respectively. After 30 days from the end of the infiltrative cycle, group A showed a ROM of 110.5±4.9°, group B showed a ROM of 165.8±5.7°, while group C showed a ROM of 165.4±5.3°. At the 120-day follow-up the ROM results in abduction were 58.3±7.3° in group A, 168.5±4.8° in group B and 166.3±4.2° in group C, respectively. ROM data are shown in Table IV.

DISCUSSION

The results of the present study provided new information on the management of conservative treatment of partial rotator cuff tears. In 2015 Nakamura et al. conducted a study on the effects of corticosteroids and hyaluronic acid in rotator cuff tears *in vitro* and in rats, showing that, unlike HA, corticosteroids caused cell death and inhibited the proliferation of tendon fibroblasts, which led to a delay in healing of the tendons and consequent decrease in biomechanical strength in the rat model (8)and the surgical sites were injected with CS or HA. The rotator cuff tendons were subjected to biomechanical testing, microscopic and immunohistochemical analysis of proliferating cell nuclear antigen (PCNA. Honda et al. demonstrated that HA accelerated tendon-to-bone healing in the rotator cuff repair model, improving biomechanical strength and increasing chondroid formation and tendon maturity at the tendon-bone interface (9)its effect on tendon-to-bone healing remains unknown.\ nPURPOSE: To examine the effect of HA on the chondrogenesis of mesenchymal stem cells (MSCs. Regarding the effect of subacromial injections of hyaluronic acid in rotator cuff tears in humans, scientific evidence demonstrates the clinical efficacy of this treatment in patients with partial rotator cuff tears (10). In the current prospective study, the results were estimated with both subjective (VAS

Table IV. *Range of motion assesment. After 30 days from the end of treatment, all three groups showed a statistically significant improvement in abduction's ROM compared to pretreatment. After 120 days from the end of treatment, only the groups treated with hyaluronic acid showed a significant improvement in abduction's ROM compared to pretreatment.*

ROM	PRE	Day 30	ROM Significance *(p < 0.05)*	Day 120	ROM Significance *(p < 0.05)*
Group A	59.4±14.7°	110.5±4.9°	*(p < 0.01)*	58.3±7.3°	*(p > 0.05)*
Group B	60.0±12.1°	165.8±5.7°	*(p < 0.01)*	168.5±4.8°	*(p < 0.01)*
Group C	59.8±12.5°	165.4±5.3°	*(p < 0.01)*	166.3±4.2°	*(p < 0.01)*

and OSS) and objective (Constant-Murley) and ROM evaluation of the affected shoulder versus the healthy shoulder. We observed pain relief and functional improvement in all patient subgroups during the first month of therapy. However, while at the 15-day follow-up there was no significant difference in the efficacy of the three treatments, already at the 30-day follow-up significantly better results were seen in patients treated with medium molecular weight hyaluronic acid (MMWHA) and high molecular weight hyaluronic acid (HMWHA) than in those treated with corticosteroids. At the 60-day follow-up, patients treated with corticosteroids showed similar mean clinical results to those seen before the infiltrative treatment, while at the 120-day follow-up there was a significant worsening of both pain symptoms and function compared to to pretreatment. In contrast, both types of hyaluronic acid showed consistent improvement in both painful symptoms and shoulder function for up to 120 days of follow-up; the MMWHA-treated group showed statistically better mean clinical results than HMWHA-treated patients at 60 and 120 days of follow-up. The best medium-long term results obtained in group B patients are probably related to the greater viscoinductive properties recognized of medium molecular weight hyaluronates (1000 kDa - 2500 kDa) (11)therefore, tolerability is a key factor in treatment choice. Hyaluronic acid (HA. The hyaluronic acid groups showed significantly better ROM in abduction than the corticosteroid group. The data regarding the variation of the signal on the MRI demonstrates that there is no clear correlation between clinical improvement and MRI signal; this is in agreement with other studies in the literature (12). However, it shows that in most cases the reduction of the lesion signal is observed in groups B and C, i.e., in patients treated with hyaluronic acid. The results of the present study showed greater efficacy in terms of pain reduction and functional recovery of the shoulder joint for patients treated with intra-articular injections of medium molecular weight hyaluronic acid. It should be, however, emphasized that the drugs were not injected into the degenerated tendon, but nearby and/or into the joint space. Therefore it can be hypothesized that the changes in the synovial fluid may exert a positive effect on the tendon itself, but it cannot be excluded that the clinical improvement may be due to the effects primarily related to hyaluronic acid. Further studies are needed to determine the true effects of hyaluronic acid on the repair of rotator cuff tendon tears.

REFERENCES

1. Nové-Josserand L, Walch G, Adeleine P, Courpron P. Effect of age on the natural history of the shoulder: A clinical and radiological study in the elderly. Rev Chir Orthopédique Réparatrice Appar Mot 2001; 91:508-14.
2. Rolf O, Ochs K, Böhm TD, Baumann B, Kirschner S, Gohlke F. [Rotator cuff tear--an occupational disease? An epidemiological analysis]. Z Orthop Ihre Grenzgeb 2006; 144(5):519-23.
3. Burbank KM, Stevenson JH, Czarnecki GR, Dorfman J. Chronic shoulder pain: part II. Treatment. Am Fam

Physician 2008; 77(4):493-7.
4. Smidt N, de Vet HCW, Bouter LM, Dekker J, Arendzen JH, de Bie RA, et al. Effectiveness of exercise therapy: a best-evidence summary of systematic reviews. Aust J Physiother 2005; 51(2):71-85.
5. Dawson J, Fitzpatrick R, Carr A, Murray D. Questionnaire on the perceptions of patients about total hip replacement. J Bone Joint Surg Br 1996; 78(2):185-90.
6. Dawson J, Rogers K, Fitzpatrick R, Carr A. The Oxford shoulder score revisited. Arch Orthop Trauma Surg 2009; 129(1):119-23.
7. Constant CR, Murley AH. A clinical method of functional assessment of the shoulder. Clin Orthop 1987; (214):160-4.
8. Nakamura H, Gotoh M, Kanazawa T, Ohta K, Nakamura K, Honda H, et al. Effects of corticosteroids and hyaluronic acid on torn rotator cuff tendons in vitro and in rats. J Orthop Res Off Publ Orthop Res Soc 2015; 33(10):1523-30.
9. Honda H, Gotoh M, Kanazawa T, Ohzono H, Nakamura H, Ohta K, et al. Hyaluronic Acid Accelerates Tendon-to-Bone Healing After Rotator Cuff Repair. Am J Sports Med 2017; 45(14):3322-30.
10. Gigante A, Cecconi S, Enea D, Cesari E, Valeri G, Busilacchi A. Effect of Subacromial Injections of Hyaluronan on Different Grades of Rotator Cuff Lesion: A Prospective Study. Eur J Inflamm 2013; 11(3):777-87.
11. Chevalier X, Migliore A. Safety and Tolerability of Intra-Articular Hyaluronic Acid Injection (Sinovial®) in Experimental and Clinical Practice. Eur J Inflamm 2013; 11(3):573-80.
12. Crim J, Burks R, Manaster BJ, Hanrahan C, Hung M, Greis P. Temporal evolution of MRI findings after arthroscopic rotator cuff repair. AJR Am J Roentgenol 2010; 195(6):1361-6.

LETTER TO THE EDITOR

A 12-year follow-up study of mucoepidermoid carcinoma-associated membranous nephropathy

WX. Xie*, MF. Chen, L. Gao and ZK. Feng

Department of Stomatology, Tongcheng People's Hospital, Anhui Province Tongcheng, China

Received July 13, 2020 - Accepted March 9, 2021

To the Editor,

Malignant tumors can cause nephritis and nephrotic syndrome. The incidence of cancer in nephrotic syndrome ranges within 11-13% (1, 2), and its main pathological type is membranous nephropathy (3). Lung cancer is the most common membranous nephropathy-associated malignant tumor, followed by gastric, intestinal, prostate, and breast cancers (4, 5). Mucoepidermoid carcinoma-associated membranous nephropathy has rarely been reported. This study analyzes the diagnosis and treatment of a patient with a mouth floor mucoepidermoid carcinoma-associated membranous nephropathy who was admitted to the Department of Stomatology in 2007 and the results of the 12-year follow-up. The study was conducted in accordance with the Declaration of Helsinki and approved by the ethics committee of Tongcheng People's Hospital, and written informed consent was obtained from the patient.

The patient was a 59-year-old man who had a 30-year history of drinking and smoking but had no other systemic diseases. In January 2007, he sought medical advice due to fatigue and edema of the lower limbs after experiencing an upper respiratory tract infection and was diagnosed with nephrotic syndrome. The patient was treated with cyclophosphamide and methylprednisolone for five months but the condition was not significantly alleviated. His urine protein was 6.97 g/24h and the urinary sediment red blood cell was 40,000/ml. The patient's renal tubular functions were: NAG enzyme 29.3 U/g; Cr; Ccr 79.86 ml/min; Alb 16.4 g/l: GLO 19.5 g/L; BUN 24.7 mg/dl; Scr 0.8 mg/dl; UA 311 μmol/L; TG 0.57 mmol/L; Chol 7.31 mmol/L; ferritin 390.88 ng/ml; CA12-5 67.6 IU/ml; Immunization: complement C3 0.715 g/L; C4 0.118 g/L; CD4 555/μl; CD8 346/μl; CD3 915/μl; CD20 135/μl; CD19 130/μl. The pathological diagnosis of the renal biopsy was membranous nephropathy, CKD2 stage (Fig. 1). The patient was treated with an oral administration of Tripterygium wilfordii polyglycoside, lotensin, diovan, and Xinshenyan capsules, and the edema of both the lower limbs was markedly alleviated but hypoproteinemia and proteinuria were not effectively controlled. On October 2007, the patient underwent a local biopsy because of his experience with salivation when speaking. A painless mass the size of a broad bean was found on the right floor of the mouth and the mass grew rapidly and affected the patient's eating and pronunciation. The pathological diagnosis was an epithelial malignant tumor, and the possibility of adenogenic and mucoepidermoid carcinoma needed to be excluded. Since hypoproteinemia could not be effectively corrected, the patient was not treated with the surgical resection of the mass.

On December 10, 2007, the patient was admitted to our department. Admission examination results

Key words: membranous nephropathy; mucoepidermoid carcinoma; surgical treatment; long-term prognosis; malignant tumor

Corresponding Author:
Dr Wang-Xiang Xie,
Department of Stomatology, Tongcheng People's Hospital,
No. 44 of Tongcheng West Street, Tongcheng, 231400,
Anhui Provine, China
Tel.: +86 556 6197000 - Fax: +86 556 6197424
e-mail: xiewx92176@163.com

0393-974X (2021)
Copyright © by BIOLIFE, s.a.s.
This publication and/or article is for individual use only and may not be further reproduced without written permission from the copyright holder.
Unauthorized reproduction may result in financial and other penalties
DISCLOSURE: ALL AUTHORS REPORT NO CONFLICTS OF INTEREST RELEVANT TO THIS ARTICLE.

were: BP was 126/70 mmHg, edema appeared in both lower limbs, on the right floor of the mouth there was a mass of 4×3 cm which had a hard texture, smooth surface, and clear boundary. The mass could be moved by pushing, the tongue was raised by the mass, and the patient's tongue extension was limited. The right submandibular and cervical lymph nodes could not be touched. The patient's total protein was 37.5 g/L, albumin was 17.5 g/L, globulin was 20.0 g/L, urinary occult blood was ++, and urinary protein was ++. The patient continued to receive treatment with an oral administration of tripterygium wilfordii polyglycoside, lotensin, diovan, and Xinshenyan capsules for membranous nephropathy and received a large dose of albumin and plasma alternately to correct hypoproteinemia. Pre-operative preparations including multidisciplinary consultation were actively carried out, the possible perioperative problems were discussed, and the corresponding emergency measures were provided. On December 21, the patient's albumin level increased to 26.3 g/L. On December 22, the patient underwent "right suprahyoid dissection + enlarged resection of right mouth floor mass" under general anesthesia. During the operation, SpO_2 decreased to 62%, the reason was considered to be due to a stress pulmonary edema and the patient was treated with a large dose of hormone immediately as shock treatment. As a result, the SpO_2 was corrected in time and the operation was successfully completed.

After the operation, the patient continued with drug treatment for membranous nephropathy and took antibiotics to prevent infection and took albumin and plasma alternately. On December 25, 2007, the patient's albumin level was 33.3 g/L. On December 27, 2007, the patient's albumin level was 31.7 g/L. Thereafter, the administration of albumin and plasma were discontinued. On January 1, 2008, a stitch was removed and the incision healed well. On January 2, 2008, the patient's albumin level was 29.8 g/L, his lower limb edema subsided, and he was discharged safely. After discharge, the patient continued to receive drug treatment for membranous nephropathy. The postoperative pathological reports were as follows: (floor of mouth) differentiated cancer, some areas had lymphoepithelial carcinoma, some areas had epidermoid cells, and differentiated mucoepidermoid carcinoma could not be excluded. No lymph node metastasis was found (Fig. 2).

Clinical follow-up

After discharge, the patient was re-examined in the Department of Endocrinology or the Department of Nephrology in our hospital. On March 5, 2008,

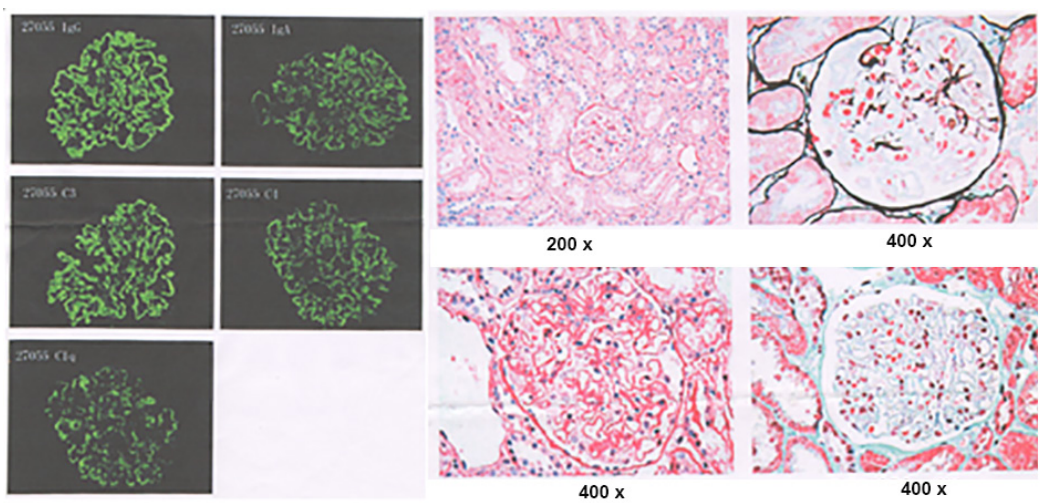


Fig. 1. *Needle biopsy of kidney in 2007.*

the patient's total protein was 49.8 g/L, albumin was 30.6 g/L, globulin was 19.2g/L, and urinary protein was 3.37. On May 28, 2008, the patient's total protein was 67.8 g/L, albumin was 42.7g/L, and urinary protein was 0.49.The patient continued to be treated with diovan + Xinshenyan Capsule + Yishenpill; On June 30, 2008, the patient's total protein was 66.0g/L, albumin was 42.1g/L, and globulin was 23.9g/L. On December 16, 2008, the patient's total protein was 67.7 g/L, albumin was 42.7 g/L, globulin was 25.0 g/L, and urinary protein was 0.59 g/24h, the patient continued to receive drug treatment for membranous nephropathy. On December 22, 2009, the patient's total protein was 72.4 g/L, albumin was 48.6 g/L, globulin was 23.8 g/L, and urinary protein was 0.25 g/24h, the patient stopped drug treatment for membranous nephropathy. On October 9, 2011, his total protein was 68.3 g/L, albumin was 45.8 g/L, and globulin was 22.5 g/L, no abnormalities were found in the routine urine test.

On September 2014, a painless mass was found in the patient's anterior gingiva of the mandible. Since no discomfort was found, the patient did not visit a doctor and receive treatment. In October 2017, the patient visited our department again because of self-awareness of the enlargement of the mass, which affected the activity of the tongue and the patient was admitted. Admission examination results: 31-47 teeth deletion, partial alveolar bone defect, at the lingual side against the 32nd and 33rd teeth, a mass with a size of 12.0×1.5 cm was touched, the mass had a hard texture and clear boundary, smooth surface, and was immobilized. The bilateral submandibular and cervical lymph nodes could not

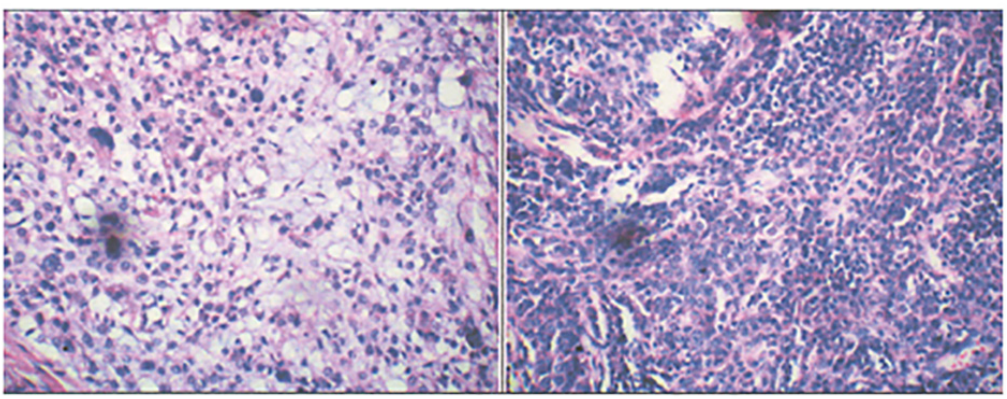


Fig. 2. *Postoperative pathology in 2007.*

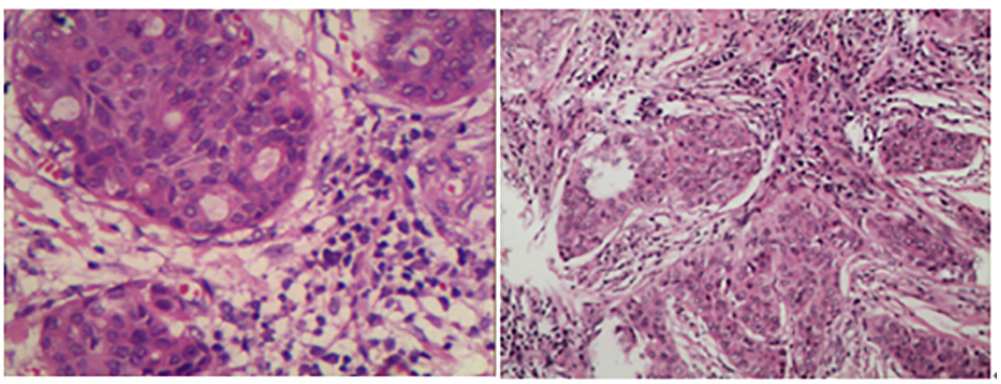


Fig. 3. *Postoperative pathology of tumor recurrence in 2017.*

be touched. Positron emission tomography (PET)/computed tomography (CT) revealed that there was a soft tissue swelling at the lower gingiva on the left floor of the mouth, which invaded towards the right and lowered to the mandible bone, and the FDG metabolism was significantly increased. It was considered as a malignant lesion (the possibility of recurrence of the tumor was high). No metastases with an abnormal increase in FDG metabolism were found in the rest of the patient's body. Total protein was 58.7 g/L, albumin was 38.9 g/L, globulin was 19.8 g/L, and no abnormalities were found in the rest of the biochemical examinations. The routine urine test was negative (-). Diagnosis: tumors on the floor of the mouth (recurrence of malignant tumors on the floor of the mouth). After admission, positive preoperative examination and preoperative preparation were performed. On October 22, the patient underwent an extended resection of the tumors on the floor of the mouth (partial mandibular resection) under general anesthesia (Fig. 3). After the operation, the patient prophylactically took antibiotics. At 12 days after surgery, the stitches were removed and the incision healed well. After 20 months, post-operative re-examination was performed, no recurrence of the tumors was found, no signs such as lower limb edema were found, and no significant abnormalities were found in the rest of the biochemical examinations.

At present, there are few reports on renal damage associated with oral and maxillofacial malignant tumors, and renal damage associated with mucoepidermoid carcinoma of the floor of the mouth is rarer (6-10). In the present case, malignant tumors on the floor of the mouth were not detected until 10 months after the diagnosis of nephrotic syndrome. After admission, the patient was treated for membranous nephropathy and additionally injected with large doses of albumin and plasma to correct hypoproteinemia. The enlarged resection of tumors on the floor of the mouth was successfully completed with multidisciplinary cooperation. At two years after the operation, all biochemical indexes were normal. The patient discontinued the drugs for membranous nephropathy. However, the tumor recurred seven years later. From the discovery of the first tumor, the patient had been followed-up for nearly 20 months, the biochemical indexes were stable and normal, and membranous nephropathy did not recur. The tumor was found 10 months after receiving the nephrotic syndrome diagnosis and the simple drug treatment did not present an excellent effect on membranous nephropathy. After the resection of the tumor, proteinuria gradually subsided and the plasma albumin level gradually returned to a normal range.

The first complete surgical excision of mucoepidermoid carcinoma-associated membranous nephropathy is therefore the key to the treatment of tumors and membranous nephropathy and the preoperative application of albumin and plasma to correct hypoproteinemia is a prerequisite for complete surgery.

REFERENCES

1. Myoga H, Akimoto T, Mato N, et al. Nephrotic syndrome and a retroperitoneal mass: a case report of a patient with recurrent invasive thymoma. Intern Med 2017; 56:3317-22.
2. Daanen RA, Maas RJH, Koornstra RHT, et al. Nivolumab-associated nephrotic syndrome in a patient with renal cell carcinoma: a case report. J Immunother 2017; 40:345-48.
3. Nagayama I, Akimoto T, Ono Y, Ueda Y, Nagata D. Remission of nephrotic syndrome after surgical intervention for bronchogenic carcinoma: the 10-year follow-up of a patient with membranous nephropathy. Int Med Case Rep J 2018; 11:167-71.
4. Daanen RA, Maas RJH, Koornstra RHT, Steenbergen EJ, van Herpen CML, Willemsen AECAB. Nivolumab-associated nephrotic syndrome in a patient with renal cell carcinoma: a case report. J Immunother 2017; 40:345-8.
5. Bouatou Y, Koessler T, Oniszczuk J, et al. Nephrotic syndrome in small cell lung cancer and induction of C-Mip in podocytes. Am J Kidney Dis 2017; 69:477-80.
6. Lee JC, Yamauchi H, Hopper J Jr. The association of cancer and the nephrotic syndrome. Ann Intern Med 1966; 64:41-51.
7. Brandwein-Gensler M, Ivanov K, Wallace

DI, et al. Mucoepidermoid carcinoma: a clinicopathologic study of 80 patients with special reference to histological grading. Am J Surg Pathol 2001; 25:835-45.
8. Singh H, Yadav AK, Chand S, Singh A, Shukla B. Central mucoepidermoid carcinoma: Case report with review of literature. Natl J Maxillofac Surg 2019; 10:109-13.
9. Cipriani NA, Lusardi JJ, McElherne J, et al. Mucoepidermoid carcinoma: a comparison of histologic grading systems and relationship to MAML2 rearrangement and prognosis. Am J Surg Pathol 2019;43:885-97.
10. Abt NB, Lawler ME, Zacharias J, Lahey ET. Primary intraosseous mucoepidermoid carcinoma of the mandible: radiographic evolution and clinicopathological features. BMJ Case Rep 2019; 12(4). pii: e224612.

LETTER TO THE EDITOR

Predictors of responsiveness to biostimulation treatments (PEMFs and/or shockwaves) in patients with complex regional pain syndrome type I of the ankle

A. Notarnicola[1,2], I. Covelli[1,2], L. Moretti[1], S. Setti[3], F. De Terlizzi[3] and B. Moretti[1,2]

[1]Orthopedics Section, Department of Basic Medical Sciences, Neuroscience and Sensory Organs, Faculty of Medicine and Surgery, University of Study of Bari, General Hospital, Bari, Italy; [2] Course of Motor and Sports Sciences, Department of Medical Sciences of Basis, Neurosciences and Organs of Sense, Faculty of Medicine and Surgery, University of Study of Bari, Bari, Italy; [3]IGEA SpA - Clinical Biophysics - Carpi (Mo), Italy

Received March 8, 2021 – Accepted May 12, 2021

To the Editor,

Complex regional pain syndrome type 1 (CRPS-1) is defined as a clinical picture of local pain, allodynia and hyperalgesia following injury (1). CRPS-1 treatment guidelines recommend a multidisciplinary approach, including sympathetic blocks to reduce pain, drug treatment to control inflammation, as well as rehabilitation, physical and occupational therapy to promote the functional and trophic recovery of the area (2). The 2013 Cochrane review concludes that there is low quality evidence for many treatments, such as bisphosphonates, calcitonin, ketamine and mirror therapy, as well as for rehabilitation and for physical and occupational therapy (3). Despite these conclusions, a number of guidelines were drawn up in 2006 (4). The guidelines published by the region of Tuscany, updated in 2019, and the 2015 guidelines issued by the Society of Hand Surgery (5) propose biophysical stimulation using pulsed electromagnetic fields (PEMFs) among the physiotherapy treatments for CRPS-1 and for the initial phase of reflex sympathetic algodystrophy (the entire document in PDF format is available on the Tuscany Region website at the following link: http://www.regione.toscana.it/pubblicazioni). PEMFs exert a significant anti-inflammatory effect, linked to the increase in binding density of the membrane adenosine receptors (A_{2A}, A_3), with subsequent inhibition of inflammatory cytokine release (IL-1β, IL-6, IL-8, PGE2) (5). At bone level, the action of the PEMFs also ensures the recruitment and proliferation of osteoblasts, the stimulation of growth factor synthesis (TGF-β1, BMP-2,-4,-7), and the mineralization of the extracellular matrix, promoting the differentiation of the mesenchymal stem cells into osteoblasts and increasing osteoclast apoptosis with inhibition of the bone absorption process associated with CRPS-1 (6).

Recent clinical experience supports the use of extracorporeal shock wave therapy (ESWT) to treat CRPS (7). The shockwaves are acoustic impulses below the audible range for humans, which quickly reach a high-pressure peak (100 MPa in 10 microseconds), triggering the synthesis of nitric oxide (8). The clinical improvements observed following ESWT treatment in CRPS-1 may be correlated to its revascularizing, analgesic and osteogenetic effects (9).

The indications for CRPS-1 treatment using biostimulation methods such as ESWT and PEMFs are still unclear. The objective of this study,

Key words: Complex regional pain syndrome (CRPS); pulsed electromagnetic fields (PEMFs); extracorporeal shockwave therapy (ESWT)

Corresponding Author:
Angela Notarnicola, M.D. Ph.D.,
Orthopedics Section, Department of Medical Sciences of Basis,
Neurosciences and Organs of Sense, Faculty of Medicine and Surgery,
University of Study of Bari, General Hospital, Bari,
Piazza Giulio Cesare n.11, 70124, Bari, Italy
Tel./fax.: +39 0805592938
e-mail: angelanotarnicola@yahoo.it

0393-974X (2021)
Copyright © by BIOLIFE, s.a.s.
This publication and/or article is for individual use only and may not be further reproduced without written permission from the copyright holder.
Unauthorized reproduction may result in financial and other penalties

conducted in a group of patients with CRPS-1 of the ankle, was to explore the clinical response to these two types of biostimulation, administered alone or sequentially, and to examine whether the results may be influenced by certain clinical and epidemiological characteristics.

MATERIALS AND METHODS

This is a retrospective study which examined the data gathered at the shockwave clinic of the Orthopedics and Traumatology unit of the Policlinico of Bari between January 2018 and December 2019 from patients with a diagnosis of CRPS-1, who came to our unit during the previous three years and who underwent a biostimulation treatment with PEMFs (I-ONE® Therapy, IGEA SpA), extracorporeal shock wave therapy (ESWT), or a PEMF treatment followed by one using ESWT. Due to its retrospective nature, the Ethics Committee was informed of the trial. The subjects gave informed and signed consent to participate in the study. All patients who came to our facility for an appointment or treatment for CRPS-1 of the ankle were entered into the clinic's administrative database. The clinical and imaging data which had allowed our clinicians to formulate a diagnosis of CRPS-1 were retrieved from the database, together with the patients' medical files. All of this information (clinical and treatment data) was reviewed by a researcher who had not previously been involved in the clinical management of the patients, and a new database was created to hold the reviewed data.

Patients were included when: i) the clinical data confirmed that all reported signs and symptoms formed part of the Budapest 2007 criteria (now also known as the new International Association for the Study of Pain [IASP] criteria for CRPS, consisting of four symptoms and two or more signs), were monitored and verified at the patient's visit (10); ii) clinical details were available on the onset and duration of the pain, together with any aspects typical of the disease, as well as epidemiological and demographic data (weight, height, age, gender); iii) the previous treatments involving antiresorptive bisphosphonates and rehabilitation, and the methods used to administer PEMFs and/or ESWT and their administration dosage per treatment cycle were well defined; iv) any association between drug treatment and PEMFs and/or ESWT was clear; v) it had been possible to arrange at least three follow-up visits at the three time points for clinical monitoring purposes (T0, prior to beginning treatment; T1, end of each treatment; T2, three months after each treatment). The exclusion criteria were as follows: a history of neurological disorders (e.g. stroke, neurodegenerative disease or traumatic brain injury); nerve damage (CRPS type 2), confirmed by nerve conduction tests, and similar disease states without a confirmed diagnosis of CRPS-1, such as regional migratory osteoporosis, post-traumatic bone marrow edema, postarthroscopic bone marrow edema, etc.; the specific and absolute contraindications of both instrumental therapies (presence of cardiac pacemaker, tumor, coagulopathy, severe unstable heart disease, pregnancy or breastfeeding.).

The clinical subtype, whether "hot" or "cold", was defined at baseline, by measuring the temperature difference between the affected and the contralateral limb using an infrared digital thermometer (Vibeey). In addition, pain was monitored using the VAS scale, while the American Orthopedic Foot and Ankle Society score (AOFAS) was administered to monitor disability and limb function. In accordance with our clinical practice, we prescribed the passage from one treatment (PEMFs) to the next (ESWT) in those patients in whom the VAS score did not change by at least 2 points between T0 and T2.

PEMF treatment

Patients allocated to the PEMF group were instructed to use PEMFs (I-ONE® therapy, IGEA, Carpi, Italy) for 4 h per day, not necessarily consecutively, for 30 days. If the VAS score of the patients didn't change by at least 2 points at T1, the treatment was prolonged for another 30 days. The device consists of a signal generator system, which produces a pulsed signal of 1.5 mT peak magnetic field intensity and a frequency of 75 Hz, and a coil which is placed on the joint. The therapy was managed at home, and the patient had the option of wearing the battery-operated device during the day or at night, and was instructed to suspend treatment in the event of side effects, such as skin irritation or a burning sensation.

Shockwave (SW) administration procedure

ESWT was administered on a day hospital basis using a Minilith SL1 electromagnetic device (Storz Medical, Tägerwilen, Swiss) under Aloka SSD 900 in-line ultrasound guidance (Aloka Co., Ltd. Tokyo, Japan), over

three sessions at seven-day intervals. The device emitted 4000 impulses with an energy flow density (EFD) of between 0.05 and 0.25 mJ/mm^2. No local anesthesia was necessary, in accordance with the ISMST guidelines (11).

Statistical analysis

Data on continuous variables is reported as mean, standard deviation, median and range in the descriptive analysis, and as mean and standard deviation only in the comparative analysis between groups. Categorical variables have been reported as absolute numbers and percentages. Comparison between the 3 groups was performed using ANOVA for continuous variables, and a 2x3 contingency table and chi square test for categorical variables. Comparison of repeated measurements on the same group at baseline vs follow-up values was performed using a paired Student t-test. Predictive factors for successful PEMF therapy were identified by comparing the values identified as being "with benefit" (reduction of pain, $VAS_{end\ of\ treatment}$-$VAS_{baseline}$ <0) with those "without benefit" (no reduction of pain, $VAS_{end\ of\ treatment}$-$VAS_{baseline}$ ≥0) recorded in the different groups. Comparisons of continuous variables were performed using a heteroscedastic unpaired Student t-test, and using contingency tables and a *chi*-squared test for categorical variables. P-values of <0.05 were considered statistically significant. Statistical analyses were performed using NCSS statistical software (Hintze, J. 2013, NCSS 9; NCSS, LLC. Kaysville, Utah, USA, www.ncss.com) and InStat GraphPad.

RESULTS

The data of 29 patients was collected in the present study. Of these patients, 15 underwent PEMF followed by ESWT, 7 were treated using PEMF only, and 7 underwent ESWT therapy only. As a result, 22 were treated with PEMF, and 22 with ESWT. The shockwave treatment was administered at a mean EDF value of 0.12 +/- 0.03 mJ/mm^2 (range 0.08-0.19 mJ/mm^2), and descriptive statistics of the entire patient group are given in Table I.

The mean duration of PEMF therapy was 27±7 days, while the mean energy density flux (ml/mm^2) for ESWT therapy was 0.12±0.03. A lack of response to bisphosphonate therapy was defined as no reduction in pain levels during this type of treatment. The patient cohort was divided into 3 subgroups according to treatment: 7 patients underwent PEMF only, 7 patients underwent ESWT only, and 15 were treated sequentially, undergoing PEMF as the initial therapy followed by ESWT (Table II).

Time since onset of symptoms was very different between the groups: the longest time since symptom onset was observed in the group which received both

Table I. *Descriptive statistics of the entire patient group at T0.*

	YES	NO	MEAN	ST.DEV.	MEDIAN	MIN	MAX
Age			55	12	54	23	76
Weight			78	21	75	44	165
Height			163	21	165	63	184
Time Since Onset (Months)			22	24	11	1	72
Sex (Males)	12 (41%)	17 (59%)					
Smoke	3 (10%)	26 (90%)					
Alcool	3 (10%)	26 (90%)					
Sensation (Warm)	11 (38%)	18 (62%)					
Previous Treatment Bisfosfonates	15 (52%)	14 (48%)					
Pemf Therapy	22 (76%)	7 (24%)					
Eswt Therapy	22 (76%)	7 (24%)					

treatments. This dual treatment group also had the highest percentage of patients previously treated with bisphosphonates. VAS and AOFAS scores differed significantly between the groups at baseline, therefore the scores were analyzed separately for each group and only the differences were compared.

In all cases, a significant reduction in VAS was observed at follow up with respect to each baseline

Table II. *Descriptive characteristics of the patients in the three groups.*

	PEMF		**ESWT**		**PEMF+ESWT**		
Number Of Patients	N=7		N=7		N=15		
	MEAN	ST.DEV.	MEAN	ST.DEV.	MEAN	ST.DEV.	P value
Age (Years)	53	11	57	18	56	9	0.8071
Weight (Kg)	76	12	77	6	80	28	0.9057
Height (Cm)	172	8	165	8	159	28	0.4137
Time Since Onset (Months)	6	4	18	22	32	27	0.0509
Duration Pemf (Days)	30	0	-	-	25	8	N/D
Energy Eswt (Mj/Mm2)	-	-	0.11	0.02	0.12	0.04	0.5420
	YES	NO	YES	NO	YES	NO	P value
Sex [Males, N.(%)]	4 (57%)	3 (43%)	2 (29%)	5 (71%)	6 (40%)	9 (60%)	0.5482
Smoke [n.(%)]	1 (14%)	6 (86%)	1 (14%)	6 (86%)	2 (13%)	13 (87%)	0.9972
Alcool [n. (%)]	0 (0%)	7 (100%)	1 (14%)	6 (86%)	2 (13%)	13 (87%)	0.5859
Sensation (Warm) [n. (%)]	3 (43%)	4 (57%)	2 (29%)	5 (71%)	6 (40%)	9 (60%)	0.8353
Non-Responders To Bisf. Th. [n. (%)]	2 (29%)	5 (71%)	2 (29%)	5 (71%)	11 (73%)	4 (27%)	0.0547

Table III. *Comparison between patients with benefits versus patients without benefits.*

	PEMF with benefit		**PEMF without benefit**		
	N=14		N=8		
	mean	St.dev.	mean	St.dev.	p value
Age (Years)	53.7	9.0	55.1	10.7	0.379
Weight (Kg)	78.1	12.7	68.8	16.6	0.096
Height (Cm)	170.5	7.7	163.5	10.7	0.064
Vas At Baseline	8.1	1.6	9.0	1.8	0.177
Aofas At Baseline	53	17	44	22	0.162
Bmi (Kg/M2)	26.7	3.3	25.5	4.4	0.246
Time Onset (Months)	13	16	35	32	**0.050**
	YES	NO	YES	NO	
Males [N. (%)]	8 (53%)	7 (47%)	3 (37%)	5 (63%)	0.235
Smoking Status [n. (%)]	1 (7%)	14 (93%	2 (25%)	6 (75%)	0.107
Alcool [N. (%)]	0 (0%)	15 (100%)	2 (25%)	6 (75%)	**0.025**
Previous Bisfosfonates Th[n. (%)]	7 (47%)	8 (53%)	7 (88%)	1 (12%)	**0.028**
Warm Sensation [n. (%)]	6 (43%)	9 (57%)	3 (37%)	5 (63%)	0.403

value ($p<0.05$), with the PEMF group showing the greatest reduction ($p<0.0001$) (Figure 1a). A significant increase in AOFAS score was also observed in all groups compared to their baseline values ($p<0.05$) (Figure 1b).

To ensure a comparison between homogeneous groups, we focused our attention on the patient groups who underwent one therapy only. Given that the VAS and AOFAS scores differed significantly between the groups at baseline, the variations in these scores were calculated from baseline to end of therapy and 3 months later, and only the variations were considered in the statistical analysis.

The reduction in the VAS score was significantly higher in the PEMF group compared to the ESWT group at the end of treatment ($p=0.0009$), and slightly higher three months later ($p=0.0540$) (Figure 2a), while the increase in the AOFAS score did not differ significantly between groups (p=n.s.) (Figures 2b, 3 and 4).

Predictive factors of successful PEMF therapy

To determine the patients who might benefit from PEMF treatment, we analyzed the groups of 7+15 patients who underwent PEMF as a first or only therapy. We analyzed pain values after the PEMF treatment only (T2). PEMF treatment was

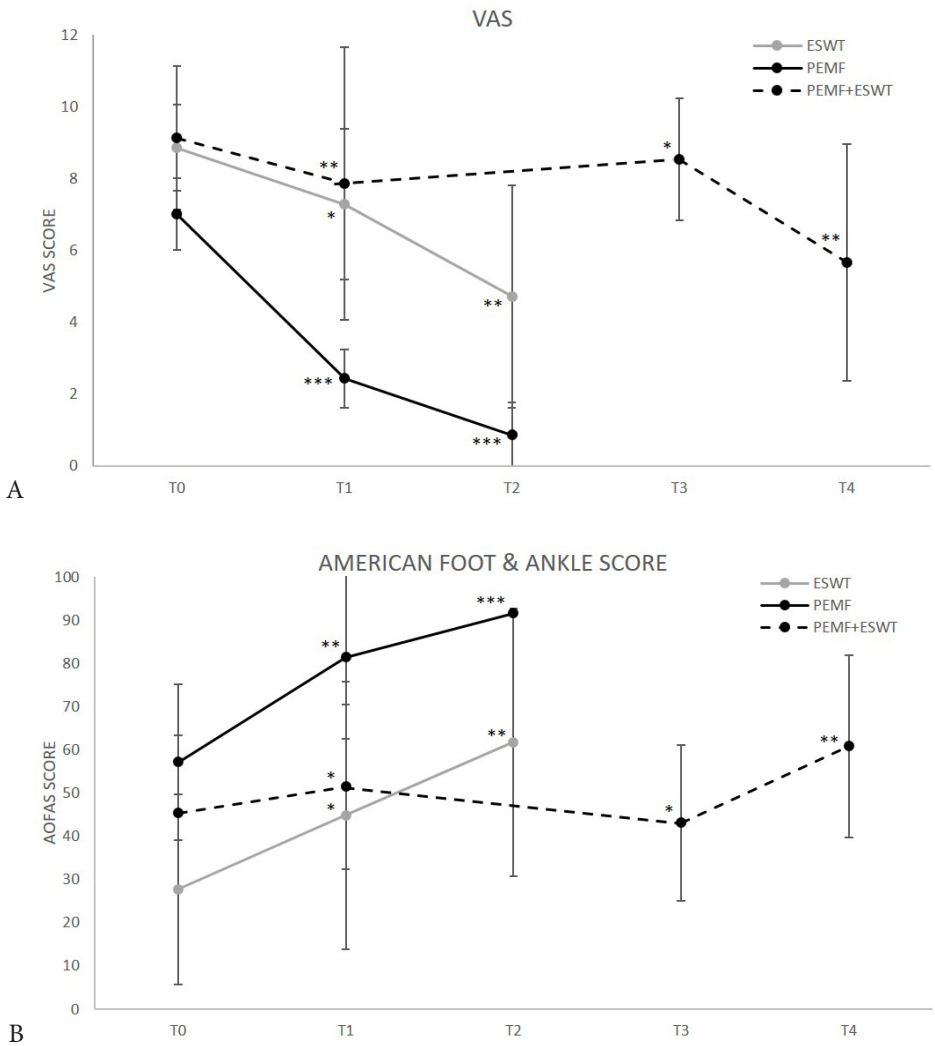


Fig. 1. a) *Mean VAS values at each time in the 3 groups;* ***b)*** *mean AOFAS score values at each time in the 3 groups. ***p<0.0005, **p<0.005, *p<0.05, p value versus baseline in each group. T0 baseline, T1 end of therapy, T2 three months later, T3 end of 2nd therapy, T4 three months later.*

beneficial when pain (measured using the VAS score) was reduced between baseline and the end of PEMF treatment (T2). We identified 14 patients for whom PEMF therapy was beneficial (reduction in VAS score) and 8 patients who responded poorly to treatment (Table III). We investigated all possible predictive factors to determine those which differed significantly between the two groups. Time since onset, heavy alcohol use and unsuccessful previous bisphosphonate treatment were significant predictors of benefit from PEMF therapy.

DISCUSSION

Our data showed that the two biostimulation treatments led to a remission in pain symptoms and a functional recovery in patients suffering from CRPS-1 of the ankle within three months. In particular,

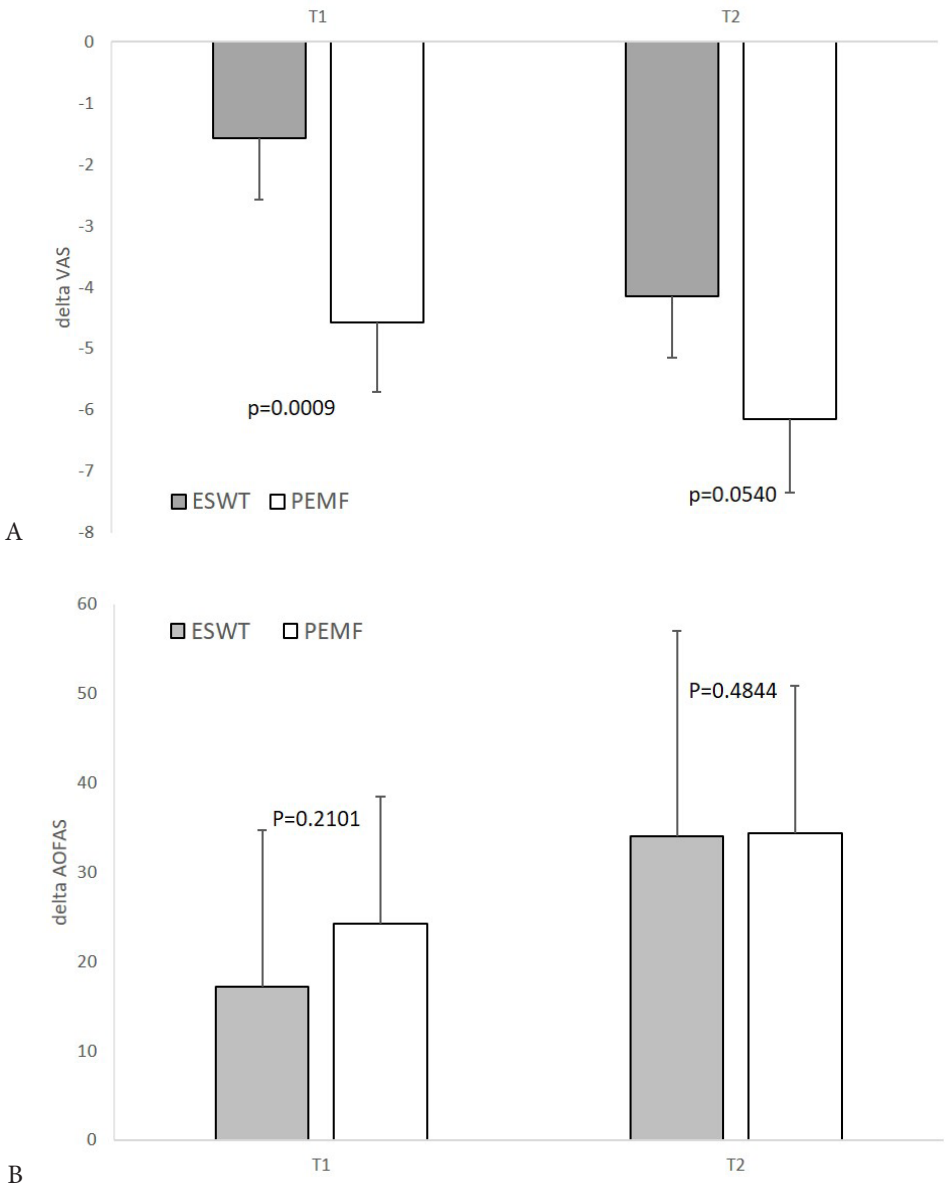


Fig. 2. ***a)*** *Reduction in VAS in PEMF and in ESWT group, at the end of therapy (T1) and three months later (T2);* ***b)*** *reduction in AOFAS in PEMF and in ESWT group, at the end of therapy (T1) and three months later (T2).*

patients treated with PEMFs tended to show a more marked remission by the end of treatment (T1, one month after end of treatment), while the shockwave treatment led to a more evident improvement after 3 months (T2). In the sequential treatment involving PEMFs followed by ESWT, reserved for patients who did not respond to the first treatment (presumably due to a more chronic situation)), administration of ESWT led to clinical and functional improvement. Our assessment times, with two short-term follow ups, suggest an association between the benefits experienced and the effects of treatment. According to the literature, spontaneous recovery from CRPS is not expected for at least 6-13 months (12). To date, no study has evaluated the possible prognostic factors for ESWT and PEMFs as treatment in CRPS patients. Our study showed that a longer time interval between the onset of symptoms and beginning PEMF treatment,

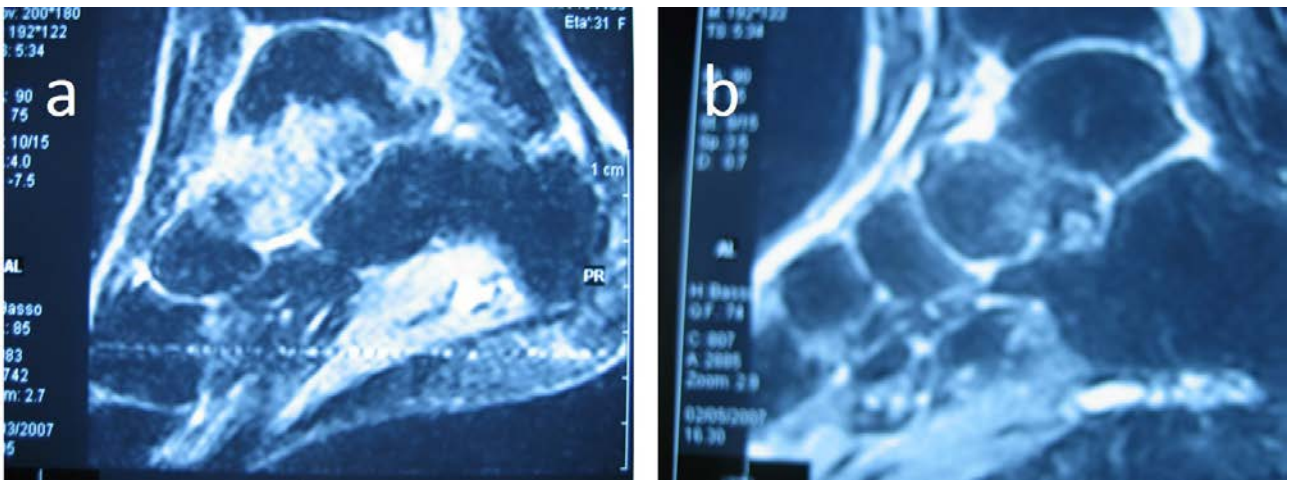


Fig. 3. ***a****) MRI showing intraspongious edema of the astragalus in a patient affected by CRPS-I of the ankle at T0.* ***b****) MRI showing reduction of the intraspongious edema in the same patient at three months after PEMFs (T2).*

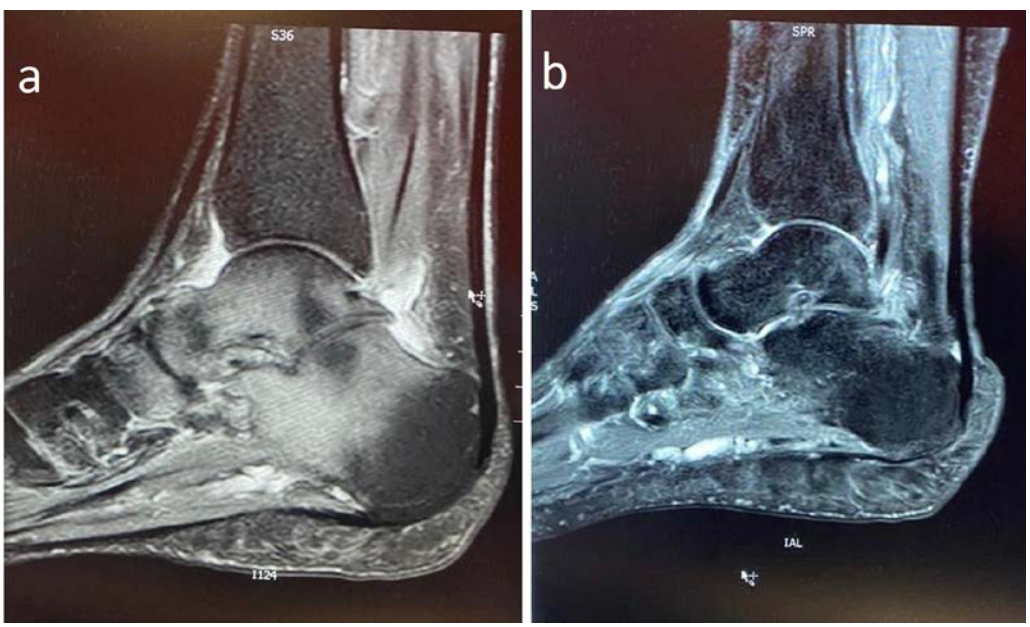


Fig. 4. ***a****) MRI showing intraspongious edema of the astragalus and the heel in a patient affected by CRPS-I of the ankle before treatment (T0).* ***b****) MRI showing reduction of the intraspongious edema in the same patient at T2 after PEMFs and ESWT.*

alcohol use and failure of previous drug treatment with bisphosphonates may be predictive of a failure of treatment with PEMFs also. The strength of this study is the fact that this is the first to investigate the clinical effects of CEMPs in CRPS compared with a control group treated with SW therapy. The weakness is the retrospective design of the study.

Our results suggest that treatment with PEMFs may be less effective in cases where the clinical picture clearly does not respond to an anti-inflammatory stimulus, for reasons associated with time (in cases of chronic disease, with a greater degenerative and ischemic component), biological characteristics (patients who have already failed to respond to bisphosphonates) or vascular or tissue metabolism changes (due to prolonged alcohol use). It therefore seems reasonable to assume that PEMF treatment for CRPS-1 should be initiated as soon as possible, in order to act on the inflammatory component of the condition.

The present study has a number of limitations. Firstly, its retrospective nature meant we were unable to assess all confounding factors which may have affected the results. Secondly, previous factors predictive of biostimulation treatment failure, associated disease and psychological factors were not considered because these are not accurately reported in individual patient histories, and further epidemiological studies are needed to address these limitations. Thirdly, there is a lack of follow up at longer time intervals that would permit an analysis of the long-term effects of treatment. Fourthly, the statistical analysis has not deepened with a statistical regression study, due to the small size of the sample. Lastly, the number of enrolled patients was very small, and the study was preliminary in nature.

If PEMFs and ESWT are shown to be beneficial, these therapies should be developed as the recommended methods to reduce pain and other CRPS-1 symptoms, and we hope that this study will offer increased insight into our limited understanding of this debilitating condition and its neuropsychological components.

CONFLICT OF INTEREST: S. Setti and F. De Terlizzi are employed by IGEA SpA.

REFERENCES

1. Merskey H, Bogduk N. Classification of chronic pain: descriptions of chronic pain syndromes and definitions of pain terms. In. Edited by Press I. Seattle: IASP Press 1994; 40-43.
2. Harden RN, Oaklander AL, Burton AW. Complex regional pain syndrome: practical diagnostic and treatment guidelines, 4th edition. Pain Med 2013; 14:180-229.
3. O'Connell NE, Wand BM, McAuley J, et al. Interventions for treating pain and disability in adults with complex regional pain syndrome. Cochrane Database Syst Rev 2013; 4:CD009416.
4. Dworkin RH, O'Connor AB, Kent J, et al. Interventional management of neuropathic pain: NeuPSIG recommendations. Pain 2013; 154:2249-61.
5. Atzei A, Martini L, Rosati M, Cannavò F, Marzella L, Merello A, Odella S, Braidotti F, Tognon S. Sindrome da Dolore Regionale Complesso – CRPS. Chirurgia della Mano 2015; 52:3.
6. Pagani S, Veronesi F, Aldini NN, Fini M. Complex Regional Pain Syndrome Type I, a Debilitating and Poorly Understood Syndrome. Possible Role for Pulsed Electromagnetic Fields: A Narrative Review. Pain Physician 2017; 20(6):E807-E822.
7. Notarnicola A, Moretti L, Tafuri S, Panella A, Filipponi M, Casalino A, Panella M, Moretti B. Shockwave therapy in the management of complex regional pain syndrome in medial femoral condyle of the knee. Ultrasound Med Biol 2010; 36(6):874-9.
8. D Agostino MC, Frairia R, Romeo P, et al. Extracorporeal shockwaves as regenerative therapy in orthopedic traumatology: a narrative review from basic research to clinical practice J Biol Regul Homeost Agents 2016; 30(2):323-32.
9. Moretti B, Iannone F, Notarnicola A, Lapadula G, Moretti L, Patella V, Garofalo R. Extracorporeal shock waves down-regulate the expression of interleukin-10 and tumor necrosis factor-alpha in osteoarthritic chondrocytes. BMC Musculoskelet Disord 2008; 9:16.
10. Harden R, Bruehl S, Perez R, et al. Validation of proposed diagnostic criteria (The "Budapest Criteria") for complex regional pain syndrome. Pain 2010; 150(2):268-74.
11. Tiele R. New guidelines for ESWT. Newslett ISMST 2009; 5:20. Available at: http://www.ismst.com/pdf/

ISMST_Newsletter_2009-03_No5.pdf
12. Bean DJ, Johnson MH, Kydd RR. The outcome of complex regional pain syndrome type 1: a systematic review. J. Pain 2014; 15:677-90.

JOURNAL OF BIOLOGICAL REGULATORS & HOMEOSTATIC AGENTS Vol. 35, no. 3, 1097-1101 (2021)

LETTER TO THE EDITOR

Acute uncomplicated cystitis management in clinical practice: a nationwide survey

S.E. Aragona[1], G. Ciprandi[2] and Study Group on Urinary Infections[*]

*[1]Center of Regenerative Medicine, Humanitas Mater Domini, Castellanza (VA), Italy; [2]Allergy Clinic, Casa di Cura Villa Montallegro, Genoa, Italy; *Study Group on Urinary Infections members: L. Vasciaveo, M. Cantelmi, G. Ciavolino, F. Ciarrocchi, G. Amendola, G. Micalizzi, E. Pastore, C. Salvaggio, M. Farina, R. Marino, V. Soro, F. Mastrorosa, B. Pinzello, U. Polizzotti, V. Minnella, V. Iannone*

Received March 25, 2021 – Accepted May 13, 2021

To the Editor,

Urinary tract infections (UTIs) are the most common bacterial infections in women, with one-half of all women experiencing at least one UTI in their lifetime (1). However, these data are underestimated; in fact, about 50% of UTI do not come to medical attention. Over 65 years of age, UTI incidence tends to increase due to functional and anatomical problems (2).

Most UTIs in women are acute uncomplicated cystitis, mainly caused by *Escherichia coli* (86%), but also by *Staphylococcus saprophyticus* (4%), *Klebsiella* species (3%), *Proteus* species (3%), *Enterobacter* species (1.4%), *Citrobacter* species (0.8%), or *Enterococcus* species (0.5%) as recently pointed out (3). Although acute uncomplicated cystitis (AUC) may not be considered a severe condition, the patients' quality of life is often significantly affected. AUC results in an estimated six days of discomfort, leading to approximately 7 million office visits per year with associated costs of $1.6 billion in the U.S. (4). The symptoms cause missing work or school, and up to one-half of patients reports avoiding sexual activity for an average of one week.

The main factors that predispose to cystitis are age, female sex, diabetes, pregnancy, vesicoureteral reflux, urinary stasis, kidney malformations, high frequency of sexual intercourse, and intrauterine use contraceptive devices, as well as functional disorders of the gut. Bacteria invade the bladder, migrating from the rectum as well as colonizing from the perineum and vagina. Once inside, bacteria adhere through *fimbriae* and *pili*, so starting the infection. History is the most important tool for diagnosing acute uncomplicated cystitis, and a focused physical examination and urinalysis should support it. Classic AUC identifiers include fever, dysuria, such as burning and/or pain during micturition, pollakiuria, urinary urgency, and sometimes hematuria. The new onset of pollakiuria and dysuria, with the absence of vaginal discharge or irritation, has a positive predictive value of 90% for AUC (5). As a result, AUC remains one of the most common indications for prescribing antibiotics, but there is no single, best agent for treatment. Usually, fosfomycin, nitrofurantoin, or trimethoprim are first-line therapies.

On the other hand, identifying a specific microbiota in the urinary tract may have important implications in the maintenance of health and/or the development of cystitis. Namely, the use of broad-spectrum antibiotics can negatively affect beneficial microbes

Key words: acute uncomplicated cystitis; survey; clinical practice; Lactobacilli; d-mannose; vitamin D; quercetin; bearberry; nettle

Corresponding Author:
Dr Giorgio Ciprandi,
Casa di Cura Villa Montallegro,
Genoa, Italy
e-mail: gio.cip@libero.it

0393-974X (2021)
Copyright © by BIOLIFE, s.a.s.
This publication and/or article is for individual use only and may not be further reproduced without written permission from the copyright holder.
Unauthorized reproduction may result in financial and other penalties
DISCLOSURE: ALL AUTHORS REPORT NO CONFLICTS OF INTEREST RELEVANT TO THIS ARTICLE.

in the host and consequential selective overgrowth of pathogenic bacteria. Long-term use of antibiotics leads to bacterial resistance in up to 50% of cases for specific antimicrobials. Moreover, bacterial biofilms reduce antibiotic effectiveness. Thus, probiotics, mainly Lactobacilli, have emerged as an alternative or adjuvant therapy to prevent and treat AUC (6). The lactic acid produced by Lactobacilli decreases pH, leading to an unfavorable microenvironment for the majority of pathogenic bacteria. Lactobacillus species produce additional antibacterial metabolites, including hydrogen peroxide and bacteriocin (6).

In this regard, *Lactobacillus acidophilus* was effective in preventing and treating cystitis in menopausal women (7). Likewise, *Lactobacillus rhamnosus* reduced urinary infections in children (8). D-mannose, a simple sugar, hinders bacteria adhesion to the urothelium and is effective in AUC management (9). Vitamin D supplementation is also useful in AUC treatment as its deficiency has been associated with increased risk for infection; vitamin D also exerts immune-modulatory activity (10). Quercetin is a flavonoid with antimicrobial, anti-inflammatory, and anti-oxidative activities; thus, it effectively reduces bladder edema, and inflammatory infiltrate during ACU (11). Bearberry (*Arctostaphylos uva-ursi*) has antiseptic and anti-inflammatory activities, demonstrated in women with AUC (12). Nettle (*Urtica dioica*) has antimicrobial, anti-oxidant, and diuretic activities (13).

A new nutraceutical containing all these components (Cistiduo®, Aurora Biofarma, Milan, Italy) has been recently launched based on this background. Therefore, a nationwide survey investigated the attitude of managing AUC by a group of Italian gynecologists, using this nutraceutical as add-on therapy.

MATERIALS AND METHODS

The survey was conducted in gynecological primary care clinics distributed across Italy, ensuring extensive and complete national coverage during 2020. Gynecologists recruited all consecutive outpatients with AUC. The inclusion criteria were to have AUC, adulthood, and ongoing antibiotic treatment. Exclusion criteria were to have comorbidities and concomitant medications able to interfere with the interpretations of the results. All participants signed informed consent. The procedure was conducted in a real-world setting.

The patients were subdivided into two groups. Group A (active group) was treated with an oral antibiotic for one week associated with Cistiduo®: one sachet in the morning and one in the evening for seven days, then once a day for additional seven days. Group B (control group) took oral antibiotics alone. Patients were evaluated immediately before treatment (T0) and after treatment (T1).

Cistiduo® contains d-mannose 800 mg, nettle dry extract 100 mg, quercetin 85 mg, bearberry dry extract 50 mg, vitamin D3 200 IU, *Lactobacillus acidophilus* 10^9 CFU/g, and *Lactobacillus rhamnosus* $0.5x10^9$ CFU/g. Notably, Cistiduo® has an innovative packaging, as the sachet is internally divided into two separate compartments, which inhibit the interaction of the components until taking it.

The evaluated parameters included: fever (expressed as % of patients with fever), burning and pain during micturition (assessed by a visual analogic scale: 0=no symptom, 10=very severe symptom), pollakiuria (scored as absent, mild. moderate, and severe), and hematuria (expressed as % of patients having it).

Statistical analysis was performed using the GraphPad Prism software (version 8.0.1 for Windows; GraphPad Software®, San Diego, CA, USA). For all tests, the accepted minimum significance limit was 0.05.

RESULTS

The current survey included 96 patients (mean age 49±14 years) with ACU: 73 in Group A and 23 in Group B. The considered parameters were not statistically different between groups at baseline, so the two groups were homogeneous. At T1, the percentage of patients with fever decreased from 31.5% to 1.4% in Group A, and from 34.8% to 0% in Group B, without any statistical intergroup difference.

VAS for burning decreased from 8 (6-9) to 1(1-1) in Group A, and from 8 (7-9) to 2 (1-2) in Group

B; the intergroup comparison showed a significant difference ($p<0.001$) as reported in Fig. 1. VAS for pain decreased from 7 (5-8) to 1 (1-1) in Group A, and from 7 (6-9) to 2 (1-2) in Group B; there was a significant intergroup difference ($p<0.001$) as reported in Fig. 2.

Pollakiuria was mild in 23.3%, moderate in 32.9%, and severe in 41.1% of patients in Group A at baseline; pollakiuria became absent in 89% and mild in 11% at the end of the treatment. Group B patients had mild pollakiuria in 17.4%, moderate in 43.5%, and severe in 39.1% at baseline. At the end of the study, 65.2% had no pollakiuria, 30.4% mild, and 4.4% moderate.

The intergroup analysis showed a significant difference ($p=0.013$), as reported in Fig. 3. Hematuria was reported only by two patients in Group A, both at T0 and T1. The nutraceutical was safe and well-tolerated by all patients.

DISCUSSION

AUC is a widespread disease in women, so that almost all women experience urinary symptoms due to infection at some time during their lifetime. Anatomic and behavioral factors promote urinary infections. Intestinal bacteria, mainly *Escherichia coli*, colonize the bladder when pro-infective factors overthrow defensive mechanisms.

AUC is usually a benign and self-resolving disease, but gynecologists commonly prescribe a short course of oral antibiotics to quickly resolve infection. However, antibiotics may be scarcely effective, mainly due to antibiotic resistance. This issue represents a current emergence as new antibiotics are very few. Another factor affecting antibiotic effectiveness is characterized by bacterial biofilms that protect bacteria from antibiotics. Moreover, intestinal and urogenital dysbiosis exert an important pathogenic role in AUC. As a consequence, the use of probiotics has been proposed for some years. In particular, Lactobacilli are the ideal candidate because they constitute the major component of local microbiota and produce substances able to kill bacteria. Furthermore, Lactobacilli produce a large amount of lactic acid, which decreases local pH, thus creating an unfavorable environment for pathogens proliferation.

Previous studies demonstrated that *L acidophilus* and *L rhamnosus* were effective in treating AUC (7, 8). d-mannose also exerts positive effects in hindering pathogens, acting as prebiotic and inhibiting bacterial adhesion. Vitamin D is an important pleiotropic hormone that reinforces the immune response to pathogens. There is growing interest in herbal medications as there is a traditional millenarian medicine based on their active ingredients; quercetin and dry extracts of uva-

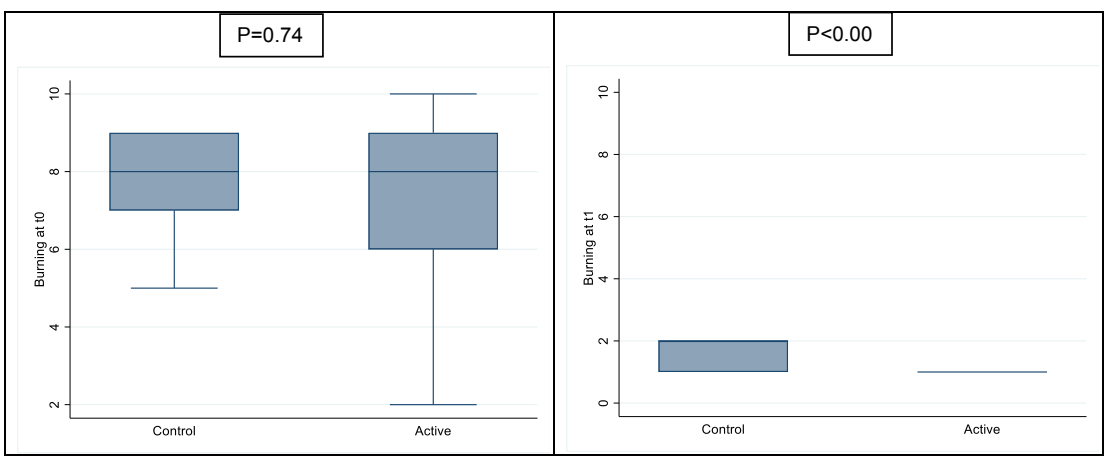


Fig. 1. *Severity of burning during micturition at baseline and after treatment in controls and actively-treated patients.*

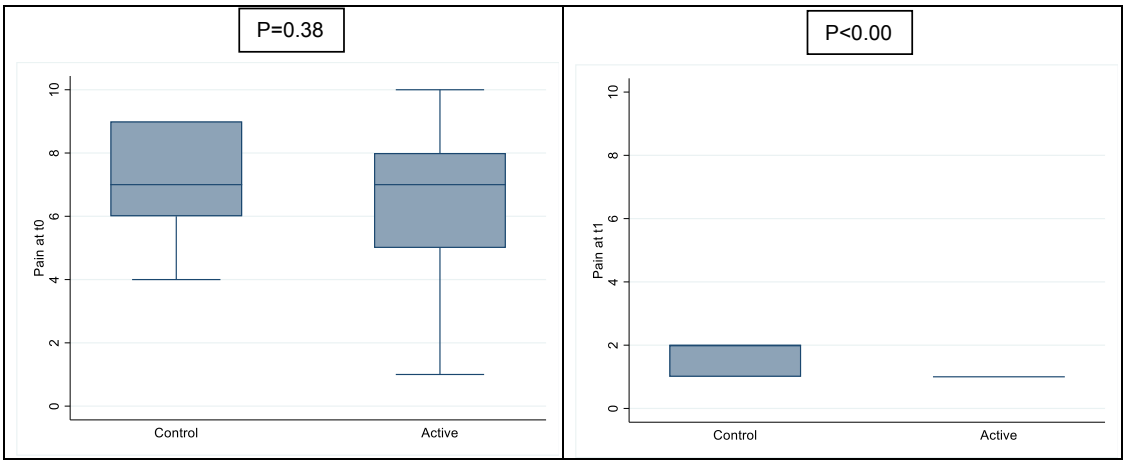


Fig. 2. *Severity of pain during micturition at baseline and after treatment in controls and actively-treated patients.*

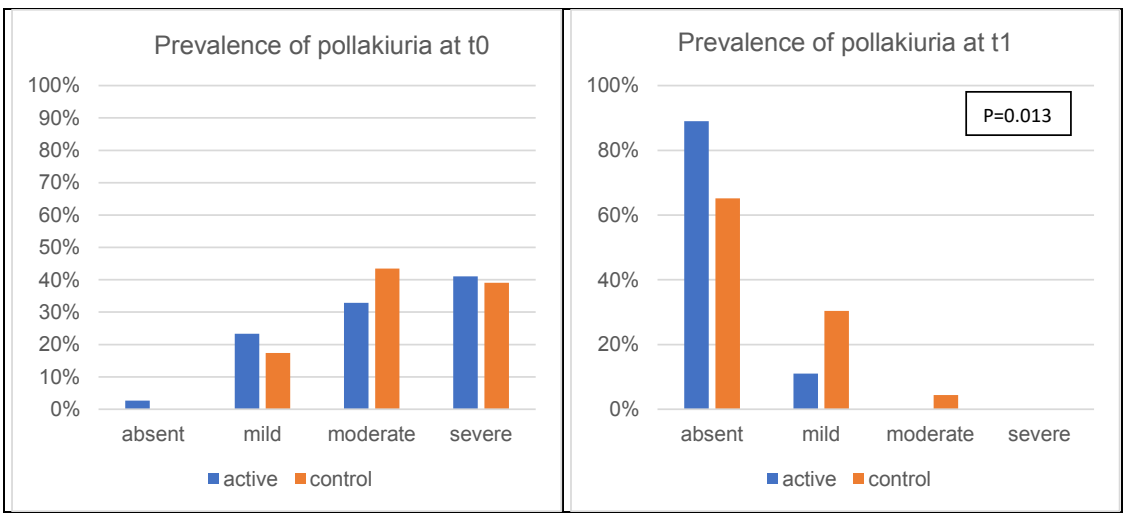


Fig. 3. *Percentages distribution of patients with absent, mild, moderate, and severe pollakiuria at baseline and after treatment in controls and actively-treated patients.*

ursi and nettle are components with evidence-based effectiveness.

Consequently, the nutraceutical Cistiduo®, containing these components, could be a promising food supplement useful as add-on therapy in patients with AUC. For this reason, the current survey explored its effectiveness in clinical practice. A large panel of Italian gynecologists contributed to this initiative. The outcomes provided documentation that a 14-day course with the nutraceutical, added to a one-week antibiotic course, significantly reduced the perception of burning and painful micturition and improved pollakiuria. The multicomponent composition could explain its positive efficacy as it may act on several aspects involved in the infectious and inflammatory reactions present in AUC.

On the other hand, the present survey has some limitations, including the open design, the lack of objective parameters, including biomarkers, mainly concerning interleukin-8, pathogen documentation, and biofilm documentation. However, the study was conducted in a real-life setting, such as the

primary care clinics. Thus, it was based only on patient-reported outcomes (PRO), which are well-known validated tools to evaluate data and provide clinically-relevant results. As a result, the findings of the current survey may reflect what happens in daily practice, so the findings document outcomes occurring in the real-world. Moreover, the patient distribution was not homogeneous and no statistical sample size calculation was carried out a priori due to the exploratory nature of the study, however the real-life nature of this study legitimized this limitation. Of course, further rigorous studies should be conducted to confirm these preliminary results.

In conclusion, the present survey showed a multicomponent nutraceutical, containing Lactobacilli, d-mannose, vitamin D3, quercetin, nettle, and uva-ursi, could be a promising add-on strategy in AUC management.

REFERENCES

1. Colgan R, Williams M. Diagnosis and treatment of acute uncomplicated cystitis. Am Fam Physician 2011; 84:771-6.
2. Gupta K, Hooton TM, Naber KG, et al. International clinical practice guidelines for the treatment of acute uncomplicated cystitis and pyelonephritis in women: a 2010 update by the Infectious Disease Society of America and the European Society for Microbiology and Infectious Diseases. Clin Infect Dis 2011; 52(5):e103-e120.
3. Bonkat G, Bartoletti R, Bruvere F, et al. Urological infections guidelines by the European Association of Urology. https://uroweb.org/guideline/urological-infections accessed on 26 February 2021.
4. Douglas-Moore JL, Goddard J. Current best practice in the management of cystitis and pelvic pain. Ther Adv Urol 2018; 10:17-22.
5. Lala V, Minter DA. Acute cystitis. StatPearls November 2020. https://www.statpearls.com
6. Aragon IM, Herrera-Imbroda B, Queipo-Ortuno MI, et al. The urinary tract microbiome in health and disease. Eur Urol Focus 2018; 4(1):128-38.
7. Mainini G, Passaro M, Schiattarella A, et al. Prevention and treatment of cystitis during menopausal: efficacy of a nutraceutical containing D-mannose, inulin, cranberry, bearberry, Olea europea, Orthosiphon and Lactobacillus acidophilus. Menopause Rev 2020; 19(3):130-4.
8. Daniel M, Szymanik-Grzelak H, Turczyn A, et al. Lactobacillus rhamnosus PL1 and Lactobacillus plantarum PM1 versus placebo as a prophylaxis for recurrence urinary tract infections in children: a study protocol for a randomized controlled trial. BMC Urol 2020; 20:168.
9. Domenici L, Monti M, Bracchi C, et al. D-mannose: a promising support for acute urinary tract infections in women. A pilot study. Eur Rev Med Pharmacol Sci 2016; 20:2920-5.
10. Haghdoost S, Pazandeh F, Darvish S, et al. Association of serum vitamin D levels and urinary tract infection in pregnant women: a case control study. Eur J Obstetr Gynecol Reprod Biol 2019; 243:51-6.
11. Wang BL, Gao X, Men K, et al. Treating acute cystitis with biodegradable micelle-encapsulated quercetin. Int J Nanomed 2012; 7:2239-47.
12. Moore M, Trill J, Simpson C, et al. Uva-ursi extract and ibuprofen as alternative treatments for uncomplicated urinary tract infection in women (ATAFUTI): a factorial randomized trial. Clin Microb Infect 2019; 25:973-80.
13. Uncini Manganelli RE, Zaccaro L, Tomei PE. Antiviral acitivity in vitro of Urtica dioica L., Parietaria diffusa M. et K. and Sambucus nigra L. J Ethnopharmacol 2005; 98:323-7

LETTER TO THE EDITOR

Inhibition of the TLR9-dependent p38 MAPK signaling pathway improves the pathogenesis of primary Sjögren's syndrome in the NOD/Ltj mouse

N. Cao[1,2,3*], H. Shi[1,2,3*], C. Chen[1,2,3*], L. Zheng[1,2,3*] and C. Yu[1,2,3]

[1]Department of Oral a nd Maxillofacial Surgery, College of Stomatology, the Ninth People's Hospital, Shanghai Jiao Tong University School of Medicine, Shanghai, China; [2]National Clinical Research Center of Oral Disease, Shanghai, China; [3]Shanghai Key Laboratory of Stomatology & Shanghai Research Institute of Stomatology, Shanghai, China

Received March 23, 2021 – Accepted May 14, 2021

*First co-authors

To the Editor,

Primary Sjögren's syndrome (pSS) is a systemic autoimmune disease characterized by reduced activity of the exocrine glands (principally the salivary and lacrimal glands) due to chronic lymphocytic infiltration. pSS is characterized by the production of both organ-specific and -nonspecific autoantibodies, of which anti-SSA/Ro and anti-SSB/La antibodies are typical . Both the etiology and pathogenesis of pSS remain unclear, although genetic, hormonal, and environmental factors may play significant roles. Toll-like receptors (TLRs) play significant roles in the innate and adaptive immune responses to autoimmune diseases . Activation of TLR9 signaling may trigger high-level interferon (IFN)-α/β production, contributing to pSS pathogenesis . Inhibitors of mitogen-activated protein kinase (MAPK) signaling pathways (located downstream of TLR9) alleviate the clinical symptoms of systemic lupus erythematosus (SLE) and rheumatoid arthritis (RA) . Therefore, inhibition of p38 MAPK pathway can be used to treat pSS.

Overexpression of TLRs 7 and 9 has been found to significantly activate the p38 MAPK pathway in pSS patients . Moreover, the NOD mouse model was ideal for exploring the utility of TLR9 or p38 MAPK inhibitors in treating pSS. The TLR9-dependent p38 MAPK signaling pathway plays a major role in pSS pathogenesis . To further confirm this, we used TLR9/p38 MAPK inhibitors ODN2088, VX-702, and HQ to inhibit these signaling pathways in NOD/Ltj mice, and observed their clinical manifestations, histopathologies, and the expression levels of signature autoantibodies. Our goal was to derive novel treatments for pSS.

MATERIALS AND METHODS

Mice

NOD/Ltj (female) and Balb/c (female) mice were purchased from the Shanghai Laboratory Animal Center, Chinese Academy of Sciences, and maintained under specific pathogen-free conditions. Mice were divided into the following five groups (n = 5 per group): Group 1:

Key words: Primary Sjögren's syndrome; NOD; TLR9; p38 MAPK; inhibitor

Corresponding Author:
Dr Chuangqi Yu,
Department of Oral and Maxillofacial Surgery,
Ninth People's Hospital,
Shanghai Jiao Tong University School of Medicine,
Shanghai key laboratory of Stomatology,
639 Zhizaoju Road, Shanghai 200011, China
Tel.: +86 021 63138341 5388 - Fax: +86-021 53072423
e-mail: yucq1508@sh9hospital.org

0393-974X (2021)
Copyright © by BIOLIFE, s.a.s.
This publication and/or article is for individual use only and may not be further reproduced without written permission from the copyright holder.
Unauthorized reproduction may result in financial and other penalties
DISCLOSURE: ALL AUTHORS REPORT NO CONFLICTS OF INTEREST RELEVANT TO THIS ARTICLE.

NOD/Ltj mice treated with the TLR9 inhibitor ODN2088 (InvivoGen, San Diego, CA, USA); Group 2: NOD/Ltj mice treated with the p38 MAPK inhibitor VX-702 (Selleck Chemicals LLC; Houston, TX, USA); Group 3: NOD/Ltj mice treated with the TLR9 inhibitor HQ; Group 4: untreated NOD/Ltj mice (positive control); and Group 5: untreated Balb/c mice (negative control). ODN2088 was delivered via weekly intraperitoneal injection (1 mg/mL in 200 μL). VX-702 and HQ were administered via daily intragastric gavage at 5 mg/kg in 200 μL. Therapy commenced in week 5 and persisted for 5 weeks; all mice were then sacrificed. All animal experiments adhered to the dictates of the guidelines for the care and use of laboratory animals and were approved by the Committee of Ethics, Faculty of Medicine, Shanghai Jiao Tong University.

Measurement of stimulated salivary flow

After stimulation of salivary secretion by injecting 0.5 μg/g body weight saline solution of pilocarpine (Sigma-Aldrich, St. Louis, MO, USA) into the femoral artery, saliva was collected on small, pre-weighed cotton balls inserted into the mouth for 5 min. Salivary flow was assessed by weighing the balls.

Sample collection and isolation of peripheral blood mononuclear cells (PBMCs)

PBMCs were isolated using a Lympholyte-Mammal kit (Cedarlane, Burlington, NC, USA) according to the manufacturer's instructions and washed twice in sterile phosphate-buffered saline (PBS). Submandibular glands (SMGs) were dissected, cleared of adipose tissue and lymph nodes, and fixed in 20% (v/v) buffered formalin.

Flow cytometry

PBMCs were collected using a Lympholyte-Mammal kit (Cedarlane) according to the manufacturer's protocol. After washing twice with sterile PBS, PBMCs were resuspended in 0.2-mL aliquots of PBS; aliquots containing 1×10^6 cells/mL were incubated with interleukin (IL)-1 and tumor necrosis factor (TNF)-α (both 50 ng/mL) (Peprotech EC, London, UK) for 12 min at 37°C; 40% (v/v) formaldehyde was added to a final concentration of 3% (v/v), and incubation continued for a further 10 min at 37°C followed by cooling on ice for 1 min. Cells were further permeabilized via slow addition of 774 μL of chilled 100% ethanol on ice over 30 min, and the suspensions gently vortexed and the cells counted (to ensure that each tube contained 1×10^6 cells). Incubation buffer (3 mL of 0.5 g bovine serum albumin/100 mL 1× PBS) was added to each tube, followed by centrifugation, cell washing, resuspension in 0.4 mL PBS, and flow cytometry.

Histopathology

SMGs were collected in 20% (v/v) buffered formalin, fixed, and paraffin-embedded, then sliced to a thickness of approximately 4 μm, subjected to routine hematoxylin and eosin (HE) staining, and examined under a light microscope. Inflammation was semi-quantified by the number of inflammatory cell infiltrates (foci) with at least 50 mononuclear cells per 4 mm^2 salivary gland tissue.

Immunohistochemistry

Immunohistochemical staining was used to detect TLR9-positive and p-p38 MAPK-positive SMG cells, as previously described, employing a monoclonal rabbit anti-p-p38 MAPK antibody (Cell Signaling Technology, Beverly, MA, USA) and a polyclonal rabbit anti-TLR9 antibody (Santa Cruz Biotechnology, Santa Cruz, CA, USA). Sections incubated in PBS alone served as negative controls. A brown color reflected immunoreactivity. The TLR9 and p-p38 MAPK-positivities of lymphocytes and acinar epithelial cells were scored as follows: 0, no positivity; 1, a ratio of positive lymphocytes: all lymphocytes or positive acinar epithelial cells: all acinar epithelial cells of 1–30%; 2, one or both of these ratios 31–50%; and 3, one or both of these ratios >50%. Two observers independently graded all samples.

Detection of autoantibodies and apoptosis

Anti-SSA/Ro and anti-SSB/La autoantibodies were quantitated using a commercial enzyme-linked immunosorbent assay (ELISA) kit (Alpha Diagnostic International Inc., San Antonio, TX, USA) according to the manufacturer's instructions. Plasma was used at a dilution of 1:100 and absorbance read at 450 nm. Antibody concentrations were calculated using immunoglobulin standards provided with the kit.

A TUNEL kit was used to detect epithelial cell apoptosis in SMG sections from NOD and Balb/c mice according to the manufacturer's instructions (Roche Diagnostics, Nutley, NJ, USA). Sections were rinsed twice with xylene

(10 min each time), rehydrated in a series of ethanol baths (absolute ethanol for 5 min followed by 90, 70, and 50% [v/v] ethanol, each for 2 min), washed in PBS for 2 min, incubated in proteinase K (without DNase; 20 µg/mL, 10 mM Tris, pH 7.4) for 15 min at room temperature, rinsed three times in PBS, immersed in a sodium citrate/Triton X-100 solution to induce cell permeabilization, incubated in TdT enzyme solution with a nucleotide cocktail, rinsed in PBS, and incubated in Converter-POD. The sections were then subjected to nuclear counterstaining with 3,3'-diaminobenzidine (DAB), counterstained with hematoxylin (a brown color reflected immunoreactivity), and observed under a fluorescence microscope.

Statistical analysis

Between-group data (means with standard deviations) were compared using Student's *t*-test. A *p*-value <0.05 was considered to reflect statistical significance.

RESULTS

Increased salivary secretion by NOD/Ltj mice treated with ODN2088.

Compared to untreated NOD/Ltj mice, salivary secretion by NOD/Ltj mice treated with ODN2088 increased significantly, but not to the level of control Balb/c mice ($P = 0.0220$). However, salivary

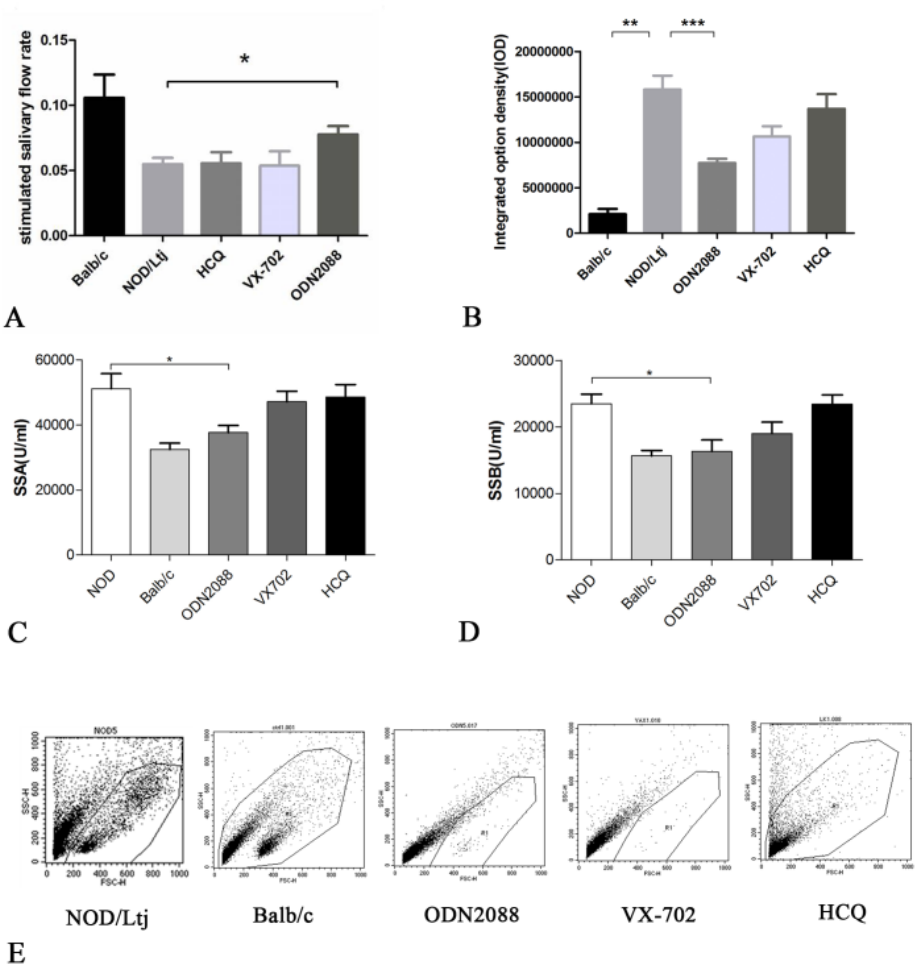


Fig. 1. *The stimulated salivary flow rate, SS-associated autoantibodies, flow cytometry of PBMCs and Tunel assay for epithelial cell apoptosis of submandibular gland in Balb/c and NOD/Ltj mouse.* ***A)*** *The stimulated salivary flow rate in Balb/c and NOD/Ltj mouse.* ***B)*** *Tunel assay for epithelial cell apoptosis of submandibular gland in NOD mice and Balb/c mice.* ***C)*** *Titers of anti-SSA/Ro autoantibodies detected by ELISA in NOD mice and Balb/c mice.* ***D)*** *Titers of anti-SSB/La autoantibodies detected by ELISA in NOD mice and Balb/c mice.E, IL-1 and TNF-α stimulated PBMCs derived from NOD and Balb/c mouse were analysis by flow cytometry. * 0.05> p>0.01; ** 0.01> p >0.001; *** p < 0.0001.*

secretion did not differ among NOD/Ltj mice administered VX-702, HQ, or no treatment. Thus, ODN2088 significantly improved the salivary flow of NOD/Ltj mice (Fig. 1A).

Decreased PBMC levels in the three treatment groups.

IL-1- and TNF-alpha-stimulated PBMCs from NOD and Balb/c mice were subjected to flow cytometry. PBMC numbers were extremely low in NOD mice given any of the three drugs, but the numbers in both control groups were normal (Fig. 1E).

Changes in plasma autoantibody levels

Peripheral blood plasma from NOD and Balb/c mice was subjected to ELISA. The titers of anti-SSA/Ro and anti-SSB/La antibodies in NOD mice treated with ODN2088 were the lowest among all treatment groups (Fig. 1 C and D), although statistical significance was not attained. However, the titers trended lower in all three treatment groups compared to the controls.

Epithelial cell apoptosis in SMGs

Epithelial cell apoptosis in SMGs was assessed using TUNEL assay. Apoptosis was significantly reduced in NOD mice treated with ODN2088, and less so in mice treated with VX-702 or HQ. However, a significant difference was only observed between NOD mice treated with ODN2088 and untreated NOD mice (Fig. 1B).

Histopathological changes in salivary glands.

Periductal inflammatory cell foci were observed

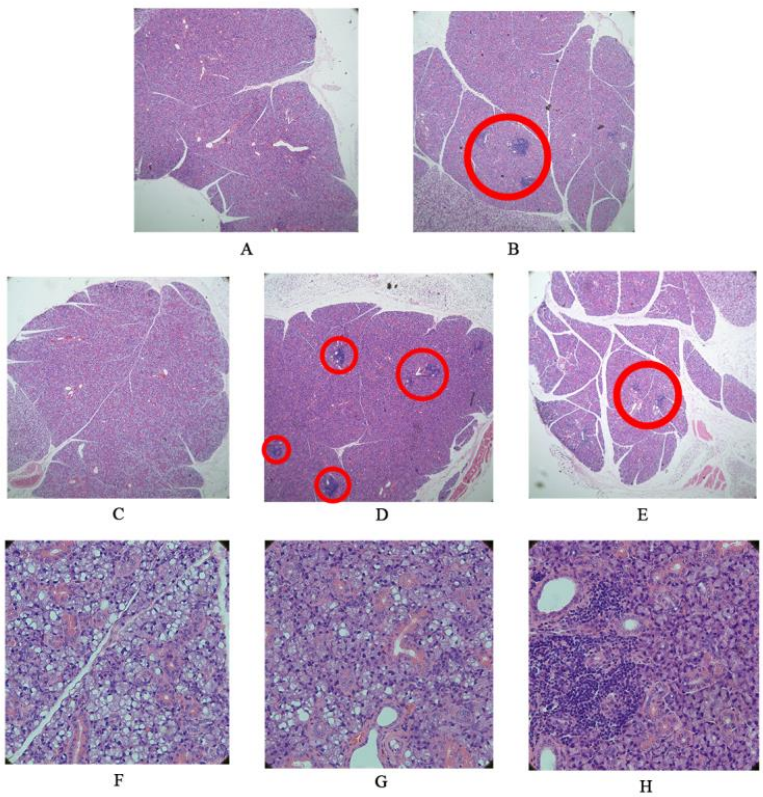


Fig. 2. *HE staining of submandibular glands of NOD and Balb/C mice.* ***A)*** *No lymphocytes foci can be observed in Balb/c mouse(50× magnification).* ***B)*** *Typical lymphocytes foci can be observed in NOD mouse (50× magnification).* ***C)*** *No lymphocytes foci can be observed in NOD mouse received VX-702 (50× magnification).* ***D)*** *Typical lymphocytes foci can be observed in NOD mouse received hydroxychloroquine (50× magnification).* ***E)*** *Typical lymphocytes foci can be observed in NOD mouse received ODN2088 (50 ×magnification).* ***F, G)*** *Vacuolar degeneration of acinar cells can be observed in the NOD mice received VX-702 and the NOD mice received ODN2088 (200 ×magnification).* ***H)*** *No vacuolar degeneration of acinar cells can be observed in NOD mice received hydroxychloroquine (200× magnification).*

in the SMGs of all NOD mice treated with HQ (3–5 foci), 20% of mice treated with ODN2088 (2 foci in one gland), and all untreated mice (3–5 foci). No foci were found in NOD mice treated with VX-702, or any Balb/c mice (Fig. 2). However, vacuolar degeneration of acinar cells was observed in NOD mice treated with VX-702 or ODN2088, but not HQ. No degeneration was apparent in untreated NOD or Balb/c mice (Fig. 2).

TLR9- and phospho-p38 MAPK-positive cells in SMGs.

Immunohistochemistry was used to measure TLR9 and p-p38 MAPK expression levels in the SMGs of NOD and control mice. TLR9 was evident in the acinar epithelial cells and infiltrating lymphocytes of all NOD mice (score = 2; Fig. 3). The experimental and control mice did not differ significantly in this context. p-p38 MAPK staining was evident in lymphocytes

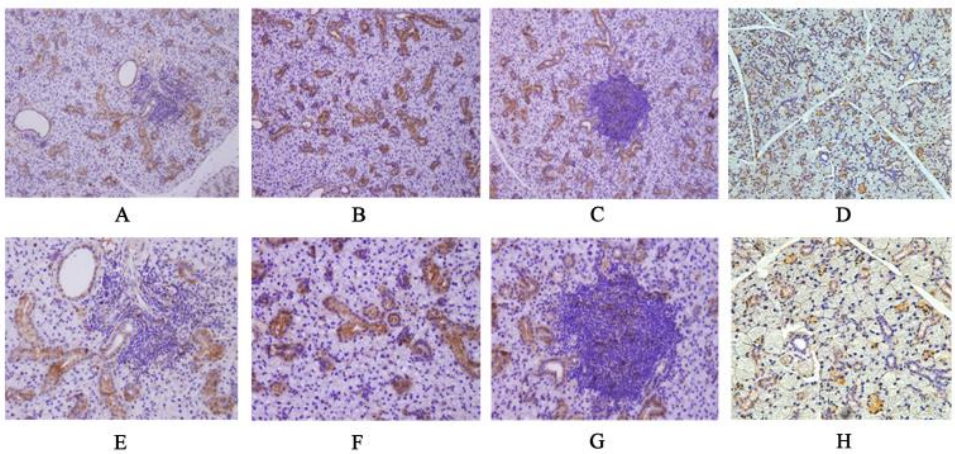


Fig. 3. *Immunohistochemical staining for TLR9 in submandibular gland of NOD mouse received ODN2088, VX-702, hydroxychloroquine and NOD mouse without any treatment.* ***A, E****) Glandular epithelium cells and infiltrating lymphocytes in NOD mouse were positively stained (200× magnification, 400× magnification).* ***B, F****) Glandular epithelium cells in NOD mouse received VX-702 were positively stained (200× magnification, 400× magnification).* ***C, G****) Glandular epithelium cells and infiltrating lymphocytes in NOD mouse received hydroxychloroquine were positively stained (200× magnification, 400 × magnification).* ***D, H****) Glandular epithelium cells in NOD mouse received ODN2088 were positively stained (200× magnification, 400× magnification).*

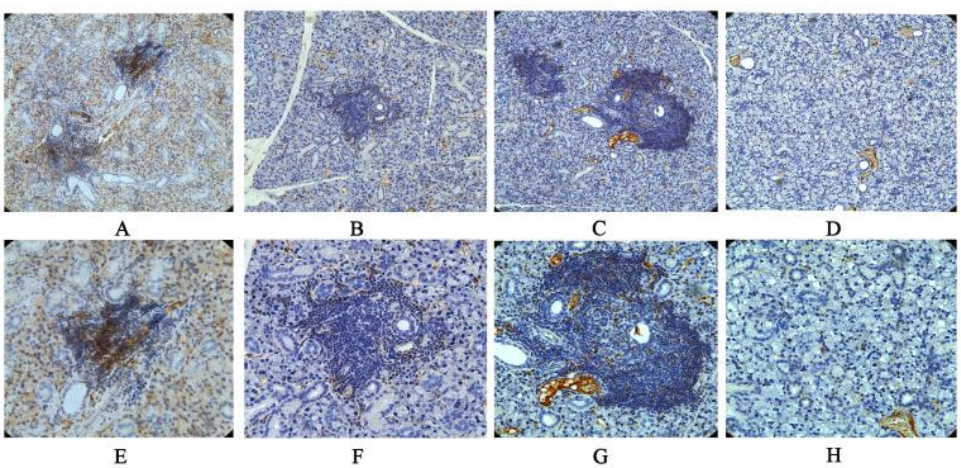


Fig. 4. *Immunohistochemistry for p-p38 MAPK in submandibular gland of NOD mouse received ODN2088, VX-702, hydroxychloroquine and NOD mouse without any treatment.* ***A, E****) Infiltrating lymphocytes in NOD mouse were positive (200× magnification, 400× magnification).* ***B, F****) Infiltrating lymphocytes in NOD mouse received ODN2088 were positive in part (200× magnification, 400× magnification).* ***C, G****) A little of infiltrating lymphocytes in NOD mouse received hydroxychloroquine were positive (200× magnification, 400× magnification).* ***D, H****) Few infiltrating lymphocytes in NOD mouse received VX-702 were positive (200× magnification, 400× magnification).*

infiltrating the SMGs and in a few adjacent ductal or acinar epithelial cells [scores: untreated NOD mice, 2; NOD mice treated with ODN2088 or HQ, 1; NOD mice treated with VX-702, 0; (Fig. 4)].

DISCUSSION

To further confirm the importance of the TLR9-dependent p38 MAPK pathway in the pSS context, we inhibited the TLR9/p38MAPK pathway in NOD/Ltj mice using various inhibitors (ODN2088, HQ, and VX-702) and observed the effects of such treatments on the histopathological features of disease and the expression levels of signature autoantibodies. We found that ODN2088 was the best inhibitor tested, significantly improving the stimulated salivary flow of NOD/Ltj mice, reducing lymphocyte infiltration in SMGs, and the plasma anti-SSA/Ro and anti-SSB/La titers. VX-702 ameliorated only lymphocytic infiltration into SMGs. HQ (which is widely used to treat pSS) had almost no effect.

Our results therefore suggest that blocking only TLR9 improved the clinical and pathological symptoms of NOD/Ltj mice. TLR9-dependent p38 MAPK signaling pathway plays an important role in pSS pathogenesis . The route of administration may affect inhibitor action. ODN2088 was administered via weekly intraperitoneal injection, but VX-702 and HQ were administered intragastrically on a daily basis. Drugs administered intraperitoneally act much more rapidly than those given intragastrically. We observed two phenomena that we cannot explain. Firstly, vacuolar degeneration of acinar cells was observed in NOD mice treated with VX-702 or ODN2088. Secondly, PBMC numbers were extremely low in NOD mice treated with any of the three inhibitors, in contrast to previous reports.

Overall, inhibition of the TLR9-dependent p38 MAPK signaling pathway alleviates the clinical symptoms of pSS to some extent, constituting a novel therapy for pSS.

ACKNOWLEDGEMENTS

This work was supported by National Natural Science Foundation of China (Grant No. 81671004, 81771089, 81800990), Natural Science Foundation of Shanghai (Grant No. 16ZR1419000), Shanghai Jiao Tong University Biomedical Engineering cross research foundation (YG2015MS03), Shanghai Summit & Plateau Disciplines

REFERENCES

1. Feltsan T, Stanko P, Mracna J. Sjogren s syndrome in present. Bratisl Lek Listy 2012; 113(8):514-6.
2. Spachidou MP, Bourazopoulou E, Maratheftis CI, Kapsogeorgou EK, Moutsopoulos HM, Tzioufas AG, Manoussakis MN. Expression of functional Toll-like receptors by salivary gland epithelial cells: increased mRNA expression in cells derived from patients with primary Sjogren's syndrome. Clin Exp Immunol 2007; 147(3):497-503.
3. Mavragani CP, Crow MK. Activation of the type I interferon pathway in primary Sjogren's syndrome. J Autoimmun 2010; 35(3):225-31.
4. Gupta GK, Agrawal DK. CpG oligodeoxynucleotides as TLR9 agonists: therapeutic application in allergy and asthma. BioDrugs 2010; 24(4):225-35.
5. Zheng L, Zhang Z, Yu C, Yang C. Expression of Toll-like receptors 7, 8, and 9 in primary Sjogren's syndrome. Oral Surg Oral Med Oral Pathol Oral Radiol Endod 2010; 109(6):844-50.
6. Zheng L, Zhang Z, Yu C, Tu L, Zhong L, Yang C. Association between IFN-alpha and primary Sjogren's syndrome. Oral Surg Oral Med Oral Pathol Oral Radiol Endod 2009; 107(1):e12-8.
7. Willeke P, Schotte H, Schluter B, et al. Interleukin 1beta and tumour necrosis factor alpha secreting cells are increased in the peripheral blood of patients with primary Sjogren's syndrome. Ann Rheum Dis 2003; 62(4):359-62.
8. Shi H, Yu CQ, Xie LS, Wang ZJ, Zhang P, Zheng LY. Activation of TLR9-dependent p38MAPK pathway in the pathogenesis of primary Sjogren's syndrome in NOD/Ltj mouse. J Oral Pathol Med 2014; 43(10):785-91.
9. Li P, Noriyoshi O, Yang Z, Susumu S, Yasufumi M, Xiao W. p38 mitogen-activated protein kinase and nuclear factor-kappaB facilitate CD40-mediated salivary epithelial cell death. J Rheumatol 2012; 39(6):1256-64.

LETTER TO THE EDITOR

MiR-203 inhibits cell proliferation, invasion, and migration of ovarian cancer through regulating RGS17

SL. Wang[1], XW. Dong[2], F. Zhao[2] and CX. Li[2]

[1]The Fifth Department of Oncology, the Fourth People's Hospital of Zibo, Zibo, China;
[2]Gynecology department of Zibo Central Hospital, Zibo, China

Received May 22, 2020 – Accepted September 24, 2020

To the Editor,

Ovarian cancer (OC) is the fifth leading cause of cancer-related deaths in women worldwide. Long noncoding RNA (lncRNA) has been found to be a key regulator in various biological processes. MicroRNA (miRNA) is a small non coding RNA, which plays a role in regulating the expression of genes in a variety of biological processes (1). Increasing evidence suggests that miRNAs play an important role in controlling the invasion and metastasis of cancer cells (2-4). MiR-203 inhibits ovarian tumor metastasis by targeting RGS17 and weakening TGFβ pathway (5). The key regulatory point of G protein activity is the inactivation of G protein by GTP hydrolysis, through which GTPase activating protein (GAP) is significantly enhanced in cells. The G-protein modulator signal transduction (RGS) protein is a highly diverse heterotrimeric G-protein. Previous studies have shown that RGS protein inhibited LPA-stimulated growth signals in ovarian cancer cells (6, 7), and more than ten RGS transcripts were identified in ovarian cancer cells, many of which were differential expression of cell lines in normal ovarian cells and OC cells.

However, bioinformatics and functional analysis showed that miR-203 could target RGS17 gene. In this study, we investigated the interaction of miR-203-RGS17 and inhibited the progression of ovarian cancer. It was found that the expression of miR-203 significantly increased to inhibit the migration and invasion of OC cells by RGS17. In addition, we identified miR-203 as a regulator to inhibit RGS17 expression in OC.

MATERIALS AND METHODS

Cell culture and transfection

OC cell lines SKOV3 and OVCAR3 were obtained from American Type Culture Collection and cultured in Dulbecco's modified Eagle's medium (DMEM) supplemented with 10% FBS (Hyclone, USA), 100U/ml penicillin and 100μg/ml streptomycin (Invitrogen, USA). HEK293T cells were cultured in DMEM medium containing 10% FBS, 100 U/ml penicillin, 100μg/ml streptomycin, 1% glutamine.

HEK293T cells were seeded into 96-well plates at a density of about 1×10^6 cells/well. DMEM medium was added to each well and incubated for another 24 h. After the cells adhered to the wall, they were transfected. MiR-203 mimic or overexpression of RGS17 vector was transfected into cells according to the instructions of lipofectaminetm2000 (Invitrogen, USA). The related indexes were detected 48 h later. Three groups were established: NC group (negative control), miR-203 mimic (SKOV3 and OVCAR cells

Key words: invasion and migration; ovarian cancer; miR-203; proliferation; RGS17

Corresponding Author:
Dr Caixia Li,
Gynecology Department
of Zibo Central Hospital,
54 Gongqingtuan Western Road
Zhangdian District, Zibo 255000, China
e-mail: yuanjacx816840@163.com

0393-974X (2021)
Copyright © by BIOLIFE, s.a.s.
This publication and/or article is for individual use only and may not be further reproduced without written permission from the copyright holder.
Unauthorized reproduction may result in financial and other penalties
DISCLOSURE: ALL AUTHORS REPORT NO CONFLICTS OF INTEREST RELEVANT TO THIS ARTICLE.

transfected with miR-203 mimic) and miR-203 mimic + RGS17 (SKOV3 and OVCAR cells transfected with miR-203 mimic and RGS17).

MTT determination

The MTT assay kit was used to check cell proliferation according to the manufacturer's instructions. Ovarian cancer cells were cultured (8000 cells/well) ina 96-well plate. At different time points, 10 µl MTT reagent (10 mg/ml) was added to each pore and incubated for about 4 h. The reaction was terminated by the addition of 100 µl cracking reagent and incubated in the dark at 22°C for 2 h. The absorbance was measured at 570nm on Bio-Rad.

Cell migration assay

The chamber system was used to measure the migration. These cells were inserted into 24-well plates and 30 µl of 3×10^4 cells in serum-free DMEM were added to the upper chamber. DMEM (supplemented with 10% FBS) was added to the inferior chamber of each well and the cells were incubated for 24 h. The cells in the lower side of the membrane were fixed with methanol and stained with 0.1% crystal violet. The migrating cells were counted in at least three different areas.

Real time quantitative PCR analysis

Trizol reagent (Invitrogen, USA) was used to extract total RNA from tissues and cells. The extracted RNA was reverse transcribed into complementary DNA (cDNA). RT-qPCR was performed with fluorescent RT-qPCR instrument. The specific reaction conditions were as follows: pre-denaturation at 95°C for 10 min, denaturation at 95°C for 30 min. After renaturation for 30 s at 55°C, it was extended for 2 min at 72°C for a total of 35 cycles. The relative expression of miR-203 and RGS17 were quantified by the $2^{-\Delta\Delta CT}$ method. The primer sequences used in this study were as follows: RGS17, foward: 5'-CCA GGA ACC CCT CCT TAC TC-3', reverse: 5'-TGT GTC CGA AGG ACT AGG GA-3'; miR-203, forward: 5'-AGG GGT GTA ACA TCC TCG ACT G-3', reverse: 5'-AGT GTC GTG GAG TTT GCG TGT CAT-3'; U6: forward: 5'-GCA ACG GCA GCA CAT ATA CTA AAA T-3', reverse: 5'-CGC TTC AGA ATT TGC GTG TCA T-3',GAPDH, forward: 5'-CGC TCT CTG CTC CTC CTG TTC-3', reverse: 5'-ATC CGT TGA CTC CGA CCT TCA C-3'.

Western blotting

The protein was extracted from cells by using protein lysates. The concentration of the extracted protein was quantified by the analysis of bicinchoninic acid (BCA) assay kit (Pierce, Rockford, IL, USA). The extracted protein was transferred to PVDF membrane. The membrane was then incubated overnight at 4°C with rabbit anti-human RGS17 primary antibody (Abcam, USA) and 3-phosphoglyceraldehyde dehydrogenase (GAPDH) (Proteintech, USA). After washing with tris buffer salt water and Tween-20 (TBST), the membrane was incubated with the second antibody of Goat anti-rabbit immunoglobulin G (IgG) labeled with horseradish peroxidase for 1 h at 37°C. After washing, enhanced chemiluminescence (ECL) was used for developing color (Thermo Fisher, USA).

Statistical analysis

Student's *t*-test was used for statistical analysis. The results are expressed as the mean ± standard deviation (SD). $P < 0.05$ was considered statistically significant for all statistical analysis.

RESULTS

Expression of miR-203 and RGS17 were detected in ovarian cancer

To study the role and mechanism of miR-203 and RGS17 in ovarian cancer, RT- qPCR was used to analyze the expression of miR-203 and RGS17 in SKOV3 and OVCAR cell lines. As expected, miR-203 was negatively correlated with RGS17 and significantly decreased in OC cell lines compared with normal IOSE144 cells (Fig. 1A), whereas RGS17 was up-regulated in OC cell lines (Fig. 1B). There was a specific regulatory relationship between miR-203 and RGS17 mRNA.

MiR-203 inhibited tumorigenicity and metastasis in vitro

In order to identify the effect of miR-203 on ovarian cancer cell proliferation, migration, and invasion, both SKOV3 and OVCAR3 cells were transfected with the miR-203 overexpression mimic vector. After 48 h of transfection, expression level of miR-203 was detected by RT-qPCR. The results showed that the expression of miR-203

was significantly increased in both SKOV3 and OVCAR3 cells compared with the control group (Fig. 1A). Cell proliferation was then determined to use a cell-counting kit, with 2 $\times 10^3$ cells used as the initial concentration. After culturing for different times (1, 2, 3 and 4 days), cell proliferation was detected by measuring the absorbance at 450 nm. Expression of miR-203 significantly suppressed cell proliferation at 2 days in both SKOV3 and OVCAR3 cells. However, there was no significant difference after transfection with the NC vector compared with the control group (Fig. 1 B, C). To determine the effect of miR-203 on metastasis, Transwell migration and invasion assays were carried out using SKOV3 and OVCAR3 cells transfected with the miR-203 mimic, NC, or their respective controls. The miR-203-transfected OC cells showed significantly lower migration and invasion than the control or NC groups (Fig. 1 F-I). Together, these results showed that miR-203 inhibited OC cell proliferation, migration, and invasion *in vitro*.

RGS-17 overexpression reversed miR-203-induced cell proliferation, migration, and invasion inhibition

Previous studies have shown that RGS17 expression played an important role in the

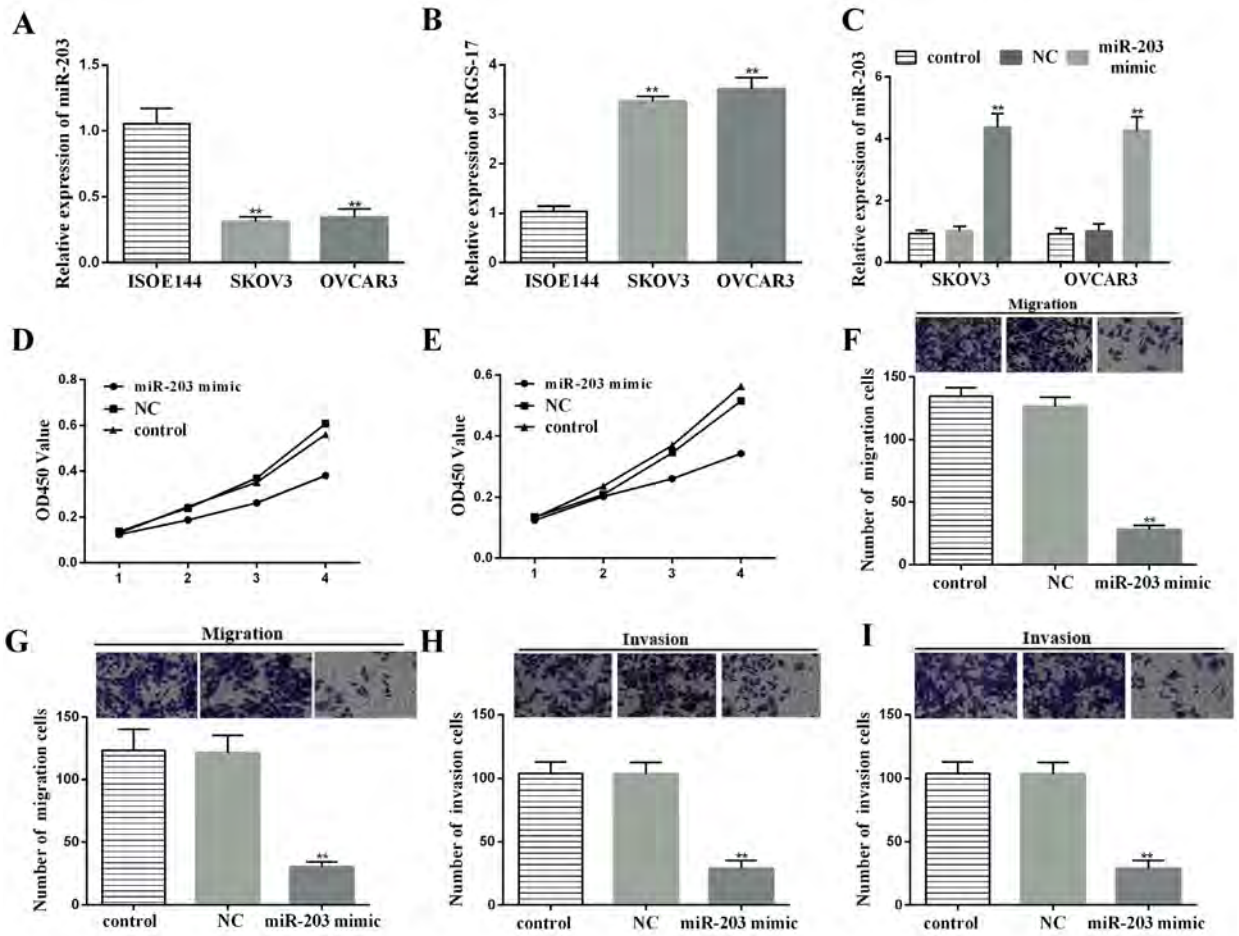


Fig. 1. *Overexpression of miR-203 significantly inhibited cell proliferation, migration and invasion.* ***A, B****) MiR-203 and RGS17 expressions were measured by RT-qPCR in SKOV3 and OVCAR cells.* ***C****) RT-qPCR was performed to measure the expression level of miR-203 in SKOV3 and OVCAR cells after transfection with miR-203 mimic or corresponding negative control (NC).* ***D, E****) Overexpression of miR-203 significantly inhibited the proliferation of SKOV3 and OVCAR cells.* ***F - I****) After transfection with miR-203, cell migration and invasion in SKOV3 and OVCAR cells were measured by Transwell assay mimic or NC. *P < 0.05, **P < 0.01, relative to the control.*

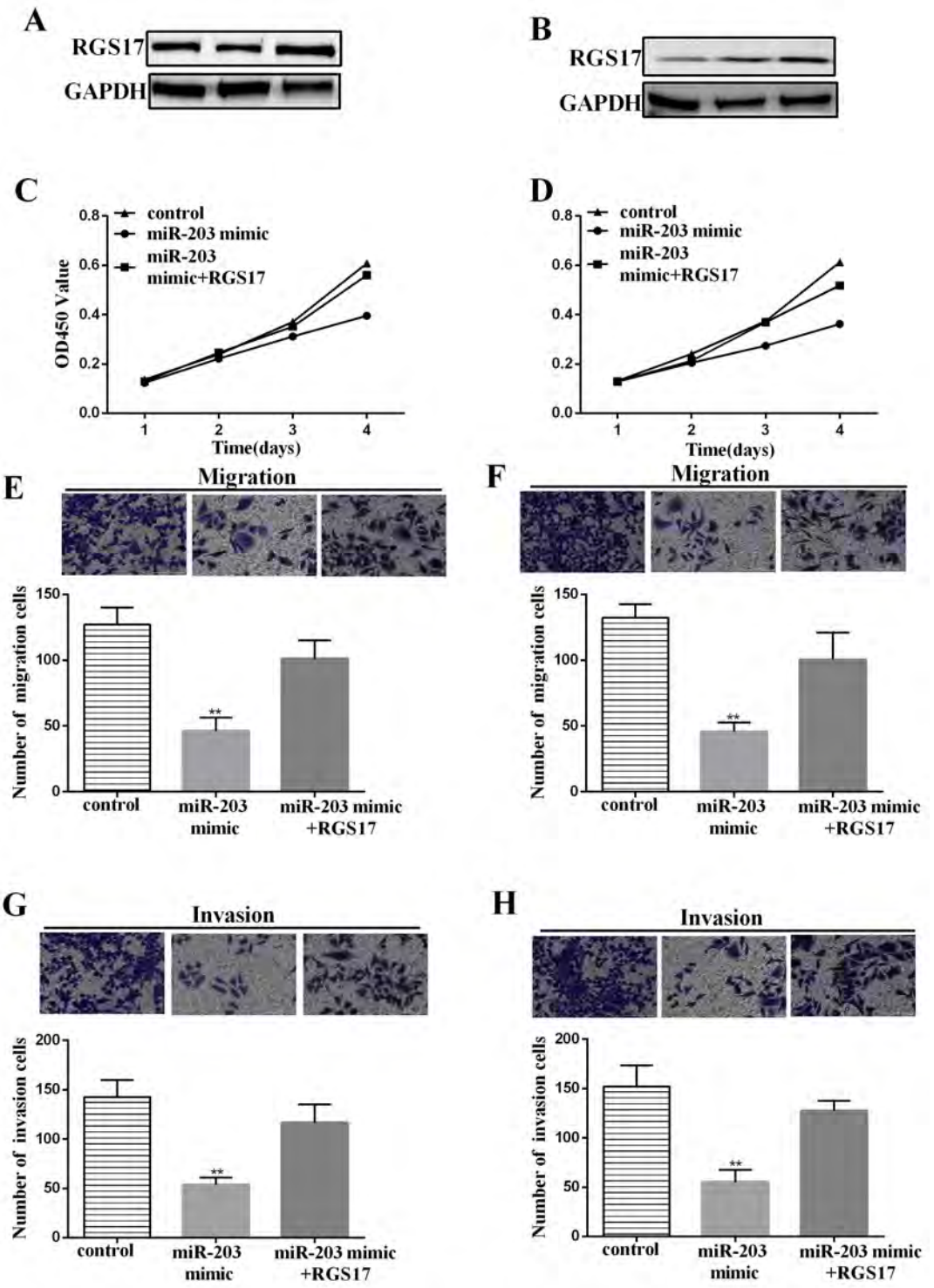


Fig 2. *RGS17 expression reduced miR-203 induced cell proliferation, migration and invasion.* ***A, B****) Western blot analysis was performed to measure the expression of RGS17 in SKOV3 and OVCAR cells after transfection with RGS17 overexpression vector or corresponding negative control (NC) vector.* ***C, D****) The ectopic expression of RGS17 significantly reversed the inhibition of SKOV3 and OVCAR cell proliferation induced by miR-203 mimic or miR-203 mimic + RGS17.* ***E, F****) Cell migration determination in SKOV3 and OVCAR cells with Transwell assay.* ***G, H****) Cell invasion in SKOV3 and OVCAR cells were measured by Transwell assay.*

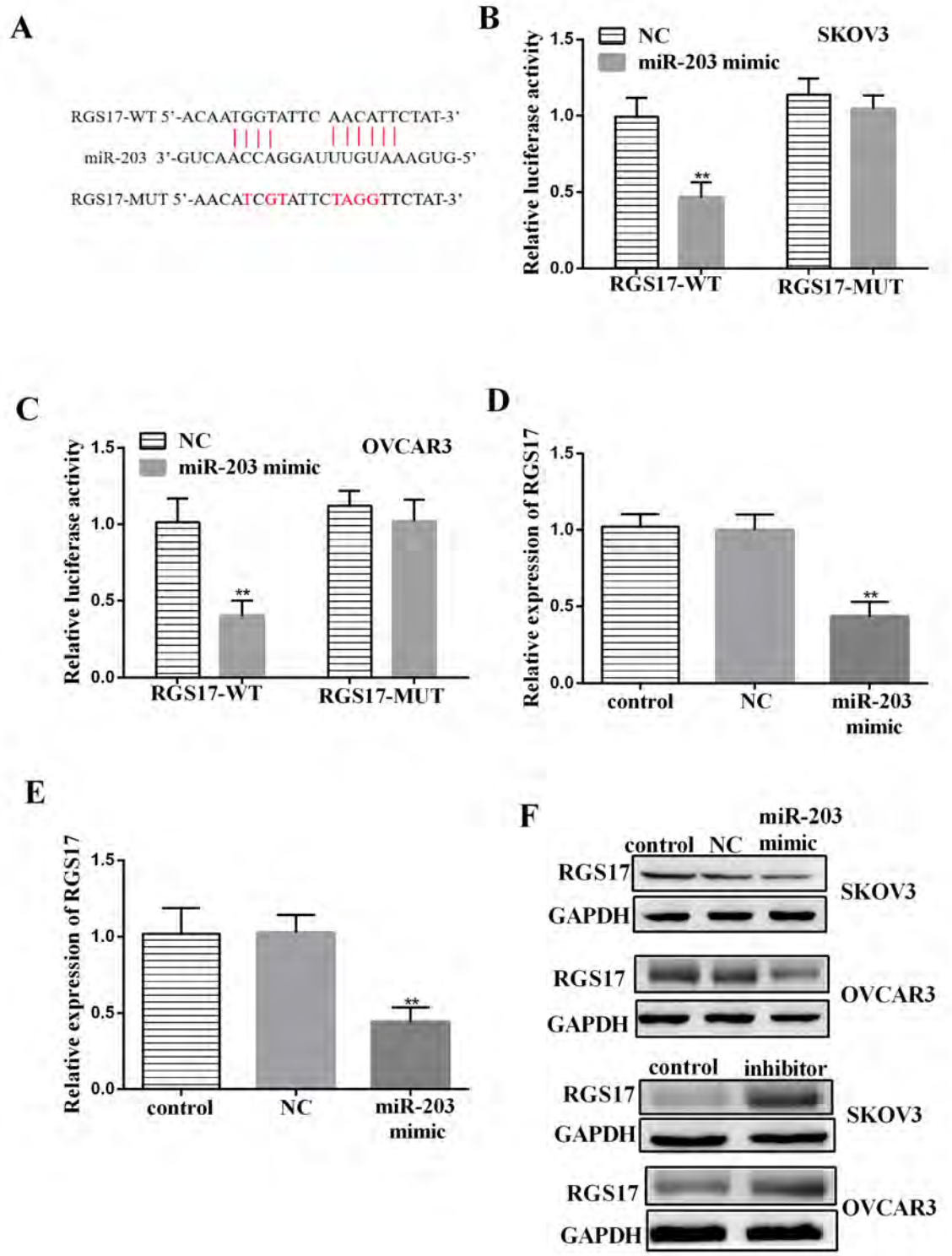


Fig 3. *RGS17 is a potential target of miR-203.* ***A)*** *The predicted binding sites between miR-203 and RGS17, as well as the mutant sites in the mutant-RGS17 luciferase vector.* ***B, C)*** *Luciferase reporter assays were used to detect luciferase activity of SKOV3 and OVCAR cells transfected with WT-RGS17 or MUT-RGS17.* ***D, E)*** *RT-PCR analysis was performed to measure the expression of RGS17 in SKOV3 and OVCAR cells transfected with miR-203 mimic.* ***F)*** *Western blot analysis was performed to measure the expression of RGS17 protein expression in SKOV3 and OVCAR cells after miR-203 analog transfection.*

maintenance of tumor cell proliferation. To determine whether RGS17 was involved in the suppression of miR-203-mediated tumor cell proliferation, RGS17 overexpression vectors were constructed and successfully transfected into SKOV3 and OVCAR cells. Western blotting showed that the expression of RGS17 was significantly increased in both SKOV3 and OVCAR cells (Fig. 2 A, B). Previous studies reported that the expression of miR-203 significantly inhibited proliferation of both SKOV3 and OVCAR cells. However, RGS17 overexpression reversed miR-203-induced proliferation inhibition in both SKOV3 and OVCAR cells (Fig. 2 C, D). Transwell migration and invasion assays were carried out on SKOV3 and OVCAR cells. It was shown that RGS17-transfected OC cells significantly reversed the miR-203-induced migration and invasiveness inhibition (Fig. 2 E-H). Taken together, the results showed that the antitumor effect of miR-203 on OC cells was decreased after overexpression of RGS17.

RGS-17 was the direct target of miR-203

To determine the possible interaction between miR-203 and RGS17, we first carried out a bioinformatics screen for its possible target genes, using an online 3'-UTR binding site prediction database. A mutated version of the RGS17 3'-UTR was constructed (Fig. 3A). This mutated construct was fused to the luciferase coding region and co-transfected into HEK293T cells along with miR-203 mimic. The relative luciferase activity showed that when the wild-type RGS17 3'-UTR was co-transfected with miR-203 mimic, RGS17 expression was significantly decreased ($P< 0.01$) compared with co-transfection with the control miRNA. However, this effect was not observed after mutant 3'-UTR of RGS17, indicating that miR-203 can suppress RGS17 expression by targeting 3'-UTR of RGS17 (Fig. 3 B, C). Western blotting and RT-qPCR analysis further confirmed that miR-203 expression significantly inhibited RGS17 expression in both protein and mRNA level *in vitro* (Fig. 3 D-F). Our results also showed that inhibiting miR-203 expression with miR-203 inhibitor treatment significantly promoted RGS17 expression in both SKOV3 and OVCAR cells.

DISCUSSION

Recently, miR-203 has been reported to be dysfunctional in a variety of cancer types. The down-regulation of miR-203 has been found in lung cancer, gastric cancer and glioblastoma (8-10). It is reported that the expression of miR-203 is up-regulated in ovarian cancer tissues (11), indicating that the expression pattern of miR-203 depends on the type of cancer. MiR-203 has been shown to be a predictor of chemotherapy response (12), therefore, it may be of great clinical significance to study the potential mechanism of miR-203 in different types of cancer. Our results have shown that the expression level of miR-203 in OC cells was lower than that in normal cells. In contrast to miR-203, RGS17 expression induces tumorigenesis. In the present study, the results showed that miR-203 expression in OC cells was significantly lower than that in normal cells, but RGS17 expression in OC cells was significantly increased. We also found that the expression of miR-203 significantly inhibited the proliferation of OC cells and reduced cell migration and invasion. However, overexpression of RGS17 reversed miR-203 induced an antitumor effect. The double fluorescein test further confirmed that miR-203 was integrated into the 3'-UTR of RGS17 and down-regulated the expression of RGS17 after transcription. We have also shown that miR-203 can inhibit cell proliferation, invasion and migration of OC by reducing RGS17. However, the exact regulatory mechanism of RGS17 in promoting cell proliferation, invasion and migration of OC is still unknown, therefore needs further study. In conclusion, this study shows that miR-203 inhibits cell proliferation, invasion and migration in OC by targeting RGS17. Therefore, miR-203 may be a new diagnosis and treatment option for OC patients.

REFERENCES

1. Bartel DP. MicroRNAs: genomics, biogenesis, mechanism, and function. Cell 2004; 116:281-97.
2. Nicoloso MS, Spizzo R, Shimizu M, Rossi S,Calin GA. MicroRNAs--the micro steering wheel of tumour metastases. Nat Rev Cancer 2009; 9:293-302.

3. Sheervalilou R, Shirvaliloo S, Fekri Aval S, Khamaneh AM, Sharifi A, Ansarin K , Zarghami N. A new insight on reciprocal relationship between microRNA expression and epigenetic modifications in human lung cancer. Tumour Biol 2017; 39:1010428317695032.
4. Li Z, Yu X, Shen J, Law PT, Chan MT, Wu WK. MicroRNA expression and its implications for diagnosis and therapy of gallbladder cancer. Oncotarget 2015; 6:13914-21.
5. Wang B, Li X, Zhao G, et al. miR-203 inhibits ovarian tumor metastasis by targeting BIRC5 and attenuating the TGFbeta pathway. J Exp Clin Cancer Res 2018; 37:235.
6. Berman DM, Gilman AG. Mammalian RGS proteins: barbarians at the gate. J Biol Chem 1998; 273:1269-72.
7. Hurst JH, Henkel PA, Brown AL, Hooks SB. Endogenous RGS proteins attenuate Galpha(i)-mediated lysophosphatidic acid signaling pathways in ovarian cancer cells. Cell Signal 2008; 20:381-89.
8. Liao H, Bai Y, Qiu S, et al. MiR-203 downregulation is responsible for chemoresistance in human glioblastoma by promoting epithelial-mesenchymal transition via SNAI2. Oncotarget 2015; 6:8914-28.
9. Wang N, Liang H, Zhou Y, et al. miR-203 suppresses the proliferation and migration and promotes the apoptosis of lung cancer cells by targeting SRC. PLoS One 2014; 9:e105570.
10. Zhou X, Xu G, Yin C, Jin W, Zhang G. Down-regulation of miR-203 induced by Helicobacter pylori infection promotes the proliferation and invasion of gastric cancer by targeting CASK. Oncotarget 2014; 5:11631-40.
11. Wang S, Zhao X, Wang J, et al. Upregulation of microRNA-203 is associated with advanced tumor progression and poor prognosis in epithelial ovarian cancer. Med Oncol 2013; 30:681.
12. Zhou Y, Wan G, Spizzo R, et al. miR-203 induces oxaliplatin resistance in colorectal cancer cells by negatively regulating ATM kinase. Mol Oncol 2014; 8:83-92.

LETTER TO THE EDITOR

Long non-coding RNA MIAT increases malignancy of prostate cancer cells through the microRNA-203/glutaminase axis

XL. Hu, J. Ding and XM. Zhang*

Department of Oncology, The Affiliated Changzhou No.2 People's Hospital of Nanjing Medical University, Changzhou, Jiangsu, P.R. China

Received November 13, 2021 – Accepted May 19, 2021

To the Editor,

Prostate cancer (PCa) is the second most common neoplastic disease and the sixth leading cause of cancer mortality in males with an estimated 1,276,106 new cases and 358,989 deaths in 2018 worldwide (1). It remains a great health problem since there is no curable strategy for the management of this disease. Considering the large coverage and high morbidity and mortality rates, finding novel biomarkers for PCa prediction and treatment is still an important issue for researchers in this field.

Aberrant expression of long non-coding RNAs (lncRNAs), a major subtype of the ncRNAs over 200 nucleotides in length, is implicated in development and progression of cancers (2). One of the well-known mechanisms by which lncRNA functions is that they can mediate the expression of mRNAs through competitively binding to the shared microRNA (miRNA) response elements, termed competitive endogenous RNA (ceRNA) (3). The lncRNA myocardial infarction-associated transcript (MIAT), initially separated as a candidate gene for myocardial infarction, has been noted as an oncogene in neuroendocrine PCa (4); however, the exact roles of MIAT in PCa development and the potential molecules are largely unknown. Intriguingly, predictions on a Bioinformatics System StarBase (http://starbase.sysu.edu.cn/) suggested that MIAT could bind to miR-203, while glutaminase (GLS) is one of the mRNA targets of miR-203, and downregulation of miR-203 has been reported to be correlated with PCa pathogenesis (5). GLS converts glutamine into glutamate and plays a key role in promoting cell metabolism for cancer cell growth including PCa (6). Therefore, we hypothesized that lncRNA MIAT possibly upregulates GLS through competitively binding to miR-203, thereby promoting PCa progression. To this end, altered expression of these transcripts was introduced in cells to validate their interactions and functions in PCa development.

MATERIALS AND METHODS

Clinical samples

Thirty-four PCa patients admitted to The Affiliated Changzhou No.2 People's Hospital of Nanjing Medical University between July 2016 and September 2018 were enrolled in the study. The age of the patients ranged from 45 to 83 years with a mean age of 64.81±10.39 years. The patients had not undergone chemotherapy or radiotherapy prior to surgery, nor had they received PCa treatment in the three months before surgery. Patients with other malignancies, diabetes, or cardiovascular diseases were excluded. The tumor tissues and the adjacent normal tissues (over 3 cm away from the lesion sites) were collected during surgery and instantly stored in liquid nitrogen until further use.

This study was approved by the Ethics Committee of The

Key words: prostate cancer; LncRNA MIAT; miR-203; glutaminase; proliferation; Wnt/β-catenin

*Corresponding Author:
Dr Xianming Zhang,
Department of Oncology,
The Affiliated Changzhou No.2 People's Hospital
of Nanjing Medical University, No. 68, Gehuzhong Road,
Wujin District, Changzhou 213003, Jiangsu, P.R. China
Tel./Fax: 0519-88104931
e-mail: Zhangxianming432@163.com

0393-974X (2021)
Copyright © by BIOLIFE, s.a.s.
This publication and/or article is for individual use only and may not be further reproduced without written permission from the copyright holder.
Unauthorized reproduction may result in financial and other penalties
DISCLOSURE: ALL AUTHORS REPORT NO CONFLICTS OF INTEREST RELEVANT TO THIS ARTICLE.

Affiliated Changzhou No.2 People's Hospital of Nanjing Medical University and was performed in compliance with the Declaration of Helsinki. Signed informed consent was received from each eligible participant.

RT-qPCR

Total RNA was collected using the TRIzol reagent and reversely transcribed to cDNA using a KingFisher Cell and Tissue DNA Kit (Fermentas Inc., Hanover, MD, USA). Next, the real-time qPCR system (Fermentas) was conducted according to the manufacturer's protocol. Table I lists the primer sequences. The reaction was conducted on a real-time qPCR Kit (iQ5, Bio-Rad, Inc., Hercules, CA, USA). GAPDH was set as the internal control for lncRNA and mRNAs, while U6 was used for miRNA. Relative gene expression was determined using the $2^{-\Delta\Delta Ct}$ method.

Cell culture and treatment

Human PCa cell lines PC-3, LNCap, Vcap and DU145 and prostatic epithelial cell line (RWPE-1) were acquired from ATCC (Manassas, VA, USA). The cells were cultivated in RPMI-1640 supplemented with 10% fetal bovine serum and 5,000 U/mL penicillin-streptomycin (Gibco, Thermo Fisher Scientific Inc., Waltham, MA, USA) at 37°C with 5% CO_2. The cells were harvested once they reached 80% confluence.

miR-203 mimic, pcDNA-3.1 (+)-lncRNA MIAT, pcDNA-3.1 (+)-GLS and the corresponding mimic control empty vectors were synthetized by GenePharma Co., Ltd. (Shanghai, China). The cells were sorted in 6-well plates and cultured in complete RPMI-1640 for 24 h. Once reaching a 70% confluence, the cells were transfected with miR-203 mimic or pcDNA vectors using a Lipofectamine 2000 kit (Invitrogen, Thermo Fisher). The medium was renewed 6 h later, and the cells were harvested for further use after a 48-h incubation.

5-ethynyl-2'-deoxyuridine (EdU) labeling assay

A BeyoClick™ EdU-488 kit (Beyotime Biotechnology Co., Ltd., Shanghai, China) was used to measure cell proliferation according to the manufacturer's instructions. The EdU solution (diluted in culture medium at 1:1000) was loaded into the culture plates for 2 h of warm incubation. The cells were fixed in 4% paraformaldehyde, incubated in glycocoll solution for 8 min, and the rinsed in phosphate-buffered saline (PBS) containing 0.5% TritonX-100. Thereafter, the cells were cultured with Apollo® staining reaction solution for 30 min, and further stained with Hoechst 33342 reaction solution at room temperature for 20 min. The labeling was captured under a fluorescence microscope (Nikon Inverted Microscope TE2000, Instruments Inc., Tokyo, Japan) at a 400× magnification with 3 fields of view selected. The cells stained in red at a 550 nm excitation channel were proliferative cells, while those stained in purple at a 350 nm excitation channel were total cells. Cell proliferation

Table I. *Primer sequences for RT-qPCR*

Gene	Primer sequence (5'-3')
miR-203	F: GGGGTGAAATGTTTAGGAC
	R: CAGTGCGTGTCGTGGAGT
lncRNA MIAT	F: CTGAGCCAGCTTCACTGGAA
	R: TCGTCACATAGGCAGTGTT
GLS	F: TGCAGAGGGTCATGTTGAAG
	R: CATCCATGGGAGTGTTATTCC
U6	F: GCTTCGGCAGCACATATACTAAAAT
	R: CGCTTCACGAATTTGCGTGTCAT
GAPDH	F: GTCTCCTCTGACTTCAACAGCG
	R: ACCACCCTGTTGCTGTAGCCAA

RT-qPCR; reverse transcription-quantitative polymerase chain reaction; GLS; glutaminase; GAPDH; glyceraldehyde-3-phosphate dehydrogenase

rate was evaluated as follows: Proliferation rate (%) = proliferative cells/total cells ×100%.

Cell Counting Kit-8 (CCK-8) method

Growth of cells was further determined using a CCK-8 kit (Sangon Biotech Co., Ltd., Shanghai, China) according to the manufacturer's instructions. In brief, cells well seeded onto 96-well plates. At 0, 24, 48, and 72 h, respectively, each well was loaded with 10 μL CCK-8 solution for another 1 h of incubation. After that, the optical density of each well at 450 nm was determined using a microplate reader (Bio-Rad Laboratories, Hercules, CA, USA).

Transwell assays

For migration, each apical chamber was loaded with 100 μL cell suspension in serum-free medium (containing 2. 5 × 10^5 cells), while each basolateral chamber was filled with 750 μL 10% fetal bovine serum-supplemented medium. Cell invasion was determined in a similar manner with additional precoating of 80 μL Matrigel (356234, BD Biosciences, Franklin Lakes, NJ, USA) on the apical chambers before cell loading. After 24 h of incubation at 37°C, cells on the inner membrane of the apical chamber were discarded, and the cells that migrated or invaded to the lower membranes were fixed and stained with 0.1% crystal violet for 40 min. The number of cells was counted under the fluorescence scope with five fields selected.

Western blot analysis

Total protein from cells was extracted using radio-immunoprecipitation assay cell lysis buffer, and the concentration was determined using a BCA kit (Thermo Fisher). Then, 40 μg total protein was run on SDS-PAGE and transferred on PVDF membranes (Amersham, Arlington Heights, IL, USA). The membranes were blocked by 5% non-fat milk for 1 h, and then co-cultured with the antibodies to GLS (1:2,000, ab113509, Abcam Inc., Cambridge, MA, USA), β-catenin (1:4,000, ab6302, Abcam), p-β-catenin (1:2,000, ab32403, Abcam) and GAPDH (1:5,000, ab181602, Abcam) at 4°C overnight, and then with horseradish peroxidase-labeled secondary antibody goat anti-rabbit (1:10,000, Jackson, USA) at 37°C for 1 h. The protein bands were developed using an ECL reagent (GE Healthcare, Chicago, Illinois, United States), and the gray value of the protein bands was analyzed using Image Pro Plus 6.0 (Media Cybernetics, USA) to evaluate relative protein expression.

Dual-luciferase reporter gene assay

Binding relationship between miR-203 and lncRNA MIAT or GLS mRNA was first predicted on StarBase (http://starbase.sysu.edu.cn/). Then the GLS 3'UTR or full-length gene fragment of MIAT was synthetized and inserted into the pMIR-reporter (Promega, Madison, WI, USA) to construct wild-type (WT) vectors, and the corresponding mutant-type (MUT) vectors were constructed using the mutant binding sequences. Well-constructed WT or MUT pMIR-reporter vectors were co-transfected with either miR-203 mimic or negative control (NC) mimic into HEK-293T cells. Forty-eight hours later, the relative luciferase activity was detected using the Dual-Luciferase-Reporter Assay System (Promega). Three independent experiments were performed.

RNA pull-down assay

Cells were administrated with 50 nM biotin-labeled WT-bio-miR-203 and MUT-bio-203 (Genecreate Bioengineering Co., Ltd., Wuhan, Hubei, China). Forty-eight hours later, the cells were cultured in specific lysis buffer (Ambion, Aystin, Texas, USA) for 10 min. The lysates were then cultured with M-280 streptavidin beads (S3762, Sigma-Aldrich Chemical Company, St Louis, MO, USA) precoated with RNase-free BSA and yeast tRNA (TRNABAK-RO, Sigma) at 4°C overnight. Thereafter, the complex was successively washed in PBS, low salt buffer and high salt buffer. The RNA pulled-down was purified by TRIzol, and the abundance of lncRNA MIAT was measured by RT-qPCR.

Fluorescence in situ hybridization (FISH) assay

Cells were seeded in 24-well plates at 6 × 10^4 per well. Once reaching a 60-70% confluence, the cells were fixed in 4% paraformaldehyde containing 0.5% Triton X-100 for 10 min. After that, each well was blocked with 20 μL Dig Easy Hyb (BREA-106, Biocreative Co., Ltd., Beijing, China) at 37°C for 30 min and then filled with Stellaris RNA FISH (Biosearch Technologies, CA, USA) containing probes of lncRNA MIAT overnight. The slides werethen quenched using anti-fluorescence quenching (BIH0252, BioRike Biotechnology Co., Ltd., Fujian, China) and photographed under a fluorescence microscope.

Statistical analysis

SPSS 22.0 system (IBM Corp. Armonk, NY, USA) was utilized for data analysis. Data were exhibited as mean ± standard deviation (SD) from three individual experiments. Differences were compared by *t*-test (between two groups), or by one-way or two-way analysis of variance (ANOVA) followed by Tukey's post hoc test (over two groups). Pearson's correlation test was used to evaluate the correlation between variables. $p < 0.05$ represents statistical significance.

RESULTS

Silencing of lncRNA MIAT reduces proliferation and metastasis of PCa cells

We first determined the lncRNA MIAT expression in 34 pairs of PCa tissues and the adjacent tissues. The RT-qPCR identified a high expression profile of MIAT in the cancer tissues compared to the normal ones (Fig. 1A).

Expression of lncRNA MIAT in PCa cell lines (LNCap, PC-3, VCap and DU145) and in RWPE-1 cells was determined. Higher expression of MIAT was found in the PCa cell lines than that in RWPE-1 cells, especially in the PC-3 cell line (Fig. 1B). Therefore, the PC-3 cells were used for the following experiments, and another PCa cell line DU145 was also included for validation experiments.

Artificial downregulation of lncRNA MIAT was introduced in PC-3 and DU145 cells using siRNA, and the transfection efficiency was determined by RT-qPCR (Fig. 1C). Thereafter, the CCK-8 and EdU labeling assay results suggested that the viability of PC-3 and DU145 cells was reduced following MIAT downregulation (Fig. 1 D, E). In addition, the Transwell assays showed that the migration and invasion of PC-3 and DU145 was increased by si-lncRNA MIAT (Fig. 1F). These results showed that downregulation of lncRNA MIAT suppresses proliferation and metastasis of PCa cells.

LncRNA MIAT sponges miR-203

The putative binding sites between lncRNA MIAT and miR-203 were first predicted on StarBase. The subsequent FISH assay identified a cytoplasm-localization of lncRNA MIAT in PC-3 and DU145 cells (Fig. 2A). Furthermore, the RT-qPCR results found a poor expression profile of miR-203 in 34 pairs of PCa tissues compared to the adjacent tissues (Fig. 2B).

To further validate the binding relationship between miR-203 and lncRNA MIAT, miR-203 mimic was first administrated into PC-3 and DU-145 cells, after which the miR-203 expression was increased (Fig. 2C). The luciferase assay results showed that the luciferase activity in cells co-transfected with miR-203 mimic and WT-lncRNA MIAT was notably decreased, while that in cells co-transfected with MUT-lncRNA MIAT or NC mimic showed no changes (Fig. 2D). In addition, the RT-qPCR results showed that miR-203 inhibited lncRNA MIAT expression in PC-3 and DU145 cell lines (Fig. 2E). In addition, the binding relationship between these two transcripts was further validated by an RNA-pull down assay, where an enrichment of lncRNA MIAT was found in the compound pulled down by Bio-probe-miR-203 (Fig. 2F).

LncRNA MIAT sponges miR-203 to increase GLS mRNA expression

Still, the binding site between miR-203 and GLS mRNA was first predicted on StarBase. As aforementioned, GLS has been suggested to be linked to PCa progression. Likewise, the binding relationship between miR-203 and GLS was validated through the dual luciferase assay, which found a decline in the luciferase activity in cells co-transfected with WT-GLS-3'-UTR and miR-203 mimic (Fig. 3A). Next, the RT-qPCR results identified an increase in the mRNA expression of GLS in the tumor tissues from 34 PCa patients in relation to the normal tissues (Fig. 3B). In addition, the mRNA and protein expression of GLS in PC-3 and DU145 cells was suppressed by miR-203 mimic (Fig. 3 C, D). To further confirm their interactions with lncRNA MIAT, we found that downregulation of lncRNA MIAT in PC-3 and cells led to an increase in miR-203 expression (Fig. 3E) while a decline in mRNA and protein expression of GLS (Fig. 3 E, F). These findings suggest that lncRNA MIAT sponges miR-203 to increase GLS expression.

lncRNA MIAT/miR-203/GLS axis modulates the Wnt/β-catenin signaling to affect PCa progression

To further identify the involvement of the above molecules in the MIAT-mediated events, rescue

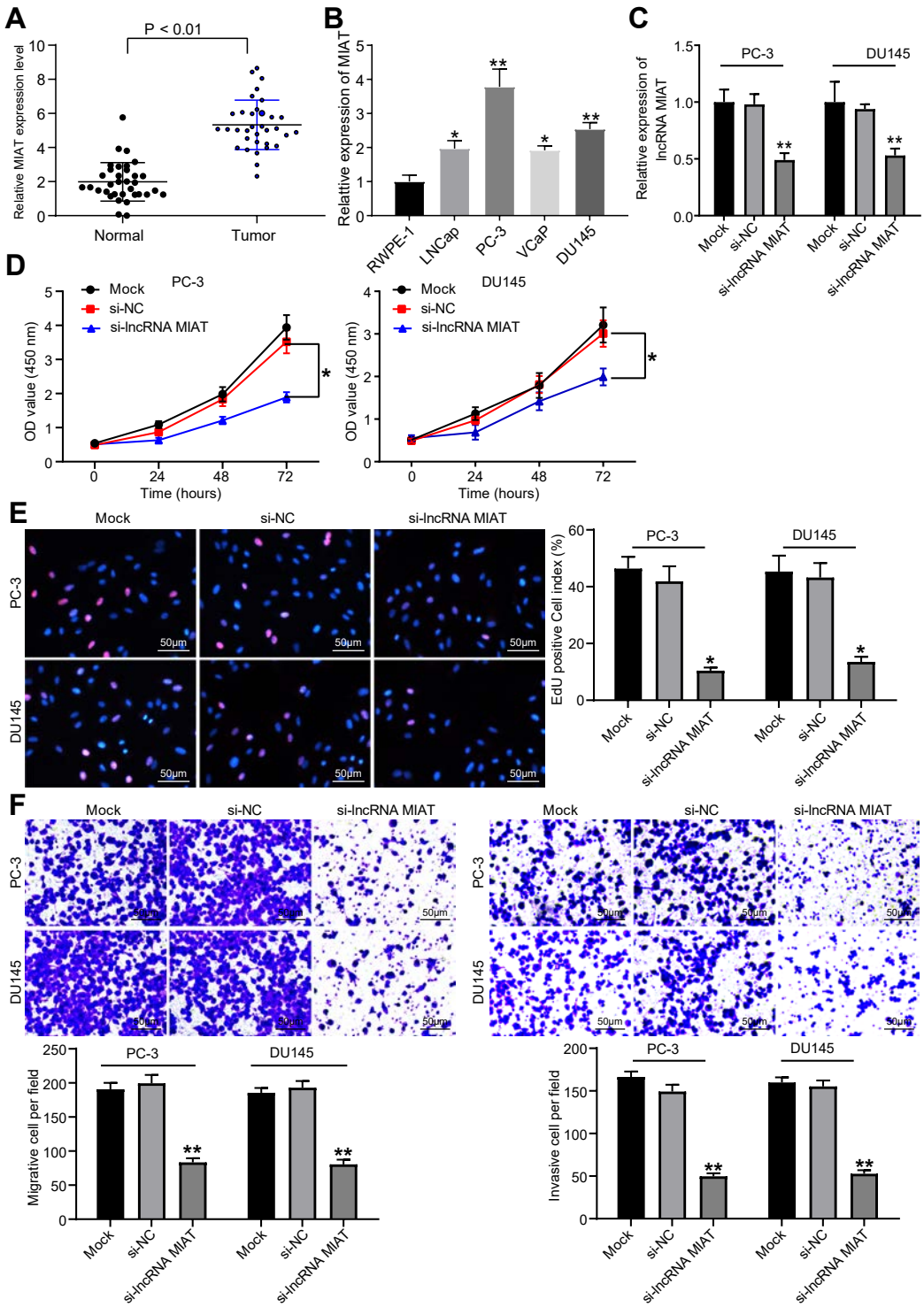


Fig. 1. *Silencing of lncRNA MIAT inhibits proliferation and metastasis of PCa cells. **A**) expression of lncRNA MIAT in 34 pairs of PCa tissues and normal tissues determined by RT-qPCR; **B**) expression of lncRNA MIAT in PCa cell lines (LNCap, PC-3, VCap and DU145) and in normal prostatic epithelial cell (RWPE-1) measured by RT-qPCR; **C**) lncRNA MIAT expression in PC-3 and DU145 cells after si-lncRNA MIAT transfection evaluated by RT-qPCR; **D, E**) viability and proliferation of PC-3 and DU145 cells determined by CCK-8 (D) and EdU labeling (E) assays; **F**) migration and invasion abilities of PC-3 and DU145 cells determined by Transwell assays. Data were compared by paired t-test (A), one-way ANOVA (B), or two-way ANOVA (C, D, E and F). *p < 0.05.*

experiments were performed. Overexpression of lncRNA MIAT or GLS was introduced in PC-3 and DU-145 cells (Fig. 4A). The CCK-8 and EdU labeling assays suggested that miR-203 mimic inhibited proliferation of PC-3 and DU-145 cells, while overexpression of lncRNA MIAT or GLS blocked the inhibitory effect of miR-203 mimic on PCa cell growth (Fig. 4 B, C). Likewise, the Transwell assay results suggested that the migratory and invasive potentials of PC-3 and DU145 cells were suppressed by miR-203 but recovered by the further overexpression of lncRNA MIAT of GLS (Fig. 4D).

lncRNA MIAT has been reported as a positive regulator of the Wnt/β-catenin pathway (7). We thus speculated that there might be a similar interaction between MIAT and this signaling in PCa. Therefore, total level and the phosphorylation of β-catenin in PC-3 and DU145 cells were evaluated (Fig. 4E). According to the Western blot analysis, after lncRNA MIAT inhibition or miR-203 overexpression, the phosphorylation of β-catenin in cells was increased, though the total level of β-catenin showed no changes. Moreover, either overexpression MIAT or GLS recovered the β-catenin phosphorylation that was inhibited by miR-203 mimic. These results collectively indicate that the lncRNA MIAT/miR-203/GLS axis mediates the Wnt/β-catenin pathway.

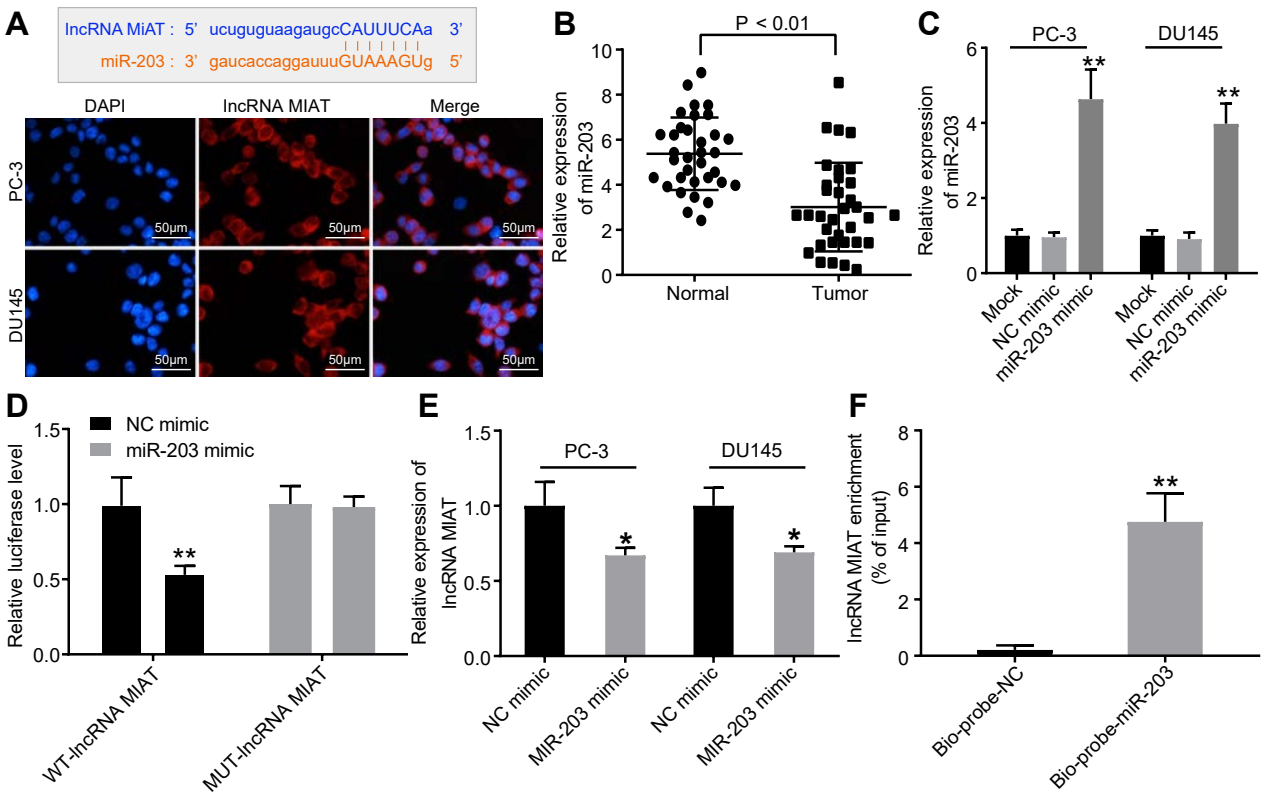


Fig. 2. *LncRNA MIAT sponges miR-203. **A**) putative binding site between lncRNA MIAT and miR-203 predicted on StarBase (http://starbase.sysu.edu.cn/), and subcellular localization of lncRNA MIAT in PC-3 and DU145 cells determined by a FISH assay; **B**) miR-203 expression in 34 pairs of PCa tissues and the adjacent normal ones detected by RT-qPCR; **C**) miR-203 expression in PC-3 and DU145 cells after miR-203 mimic transfection determined by RT-qPCR; **D**) binding relationship between lncRNA MIAT and miR-203 validated through a dual luciferase reporter gene assay; **E**) lncRNA MIAT expression in PC-3 and DU145 cells after miR-203 mimic transfection measured by RT-qPCR; **F**) binding relationship between lncRNA MIAT and miR-203 further validated using an RNA-pull down assay. Data were compared by paired t test (A), unpaired t test (F), two-way ANOVA (C and D) and one-way ANOVA (E). *p < 0.05, **p < 0.01.*

DISCUSSION

PCa remains a huge health concern in males. Although more than half of PCa cases are diagnosed as a localized type with low risk and a 5-year survival rate of nearly 100%, the patients diagnosed as aggressive types with distant metastatic potential have a significant reduction in survival rate to 31% (8). Discovering biomarkers implicated in PCa progression has aroused wide interest and has been one of the major topics in today's cancer management. In this paper, we identified a novel ceRNA network involving lncRNA MIAT/miR-203/GLS that triggers PCa cell proliferation and metastasis through activating the Wnt/β-catenin pathway.

LncRNAs play versatile functions in tumor growth, invasion and metastasis, therefore are closely linked to cancer progression with no exception for PCa. LncRNA MIAT was noted as a potential biomarker and therapeutic target for neuroendocrine PCa due to its selective upregulation in neuroendocrine PCa cells (4). Here, we first explored the expression of this

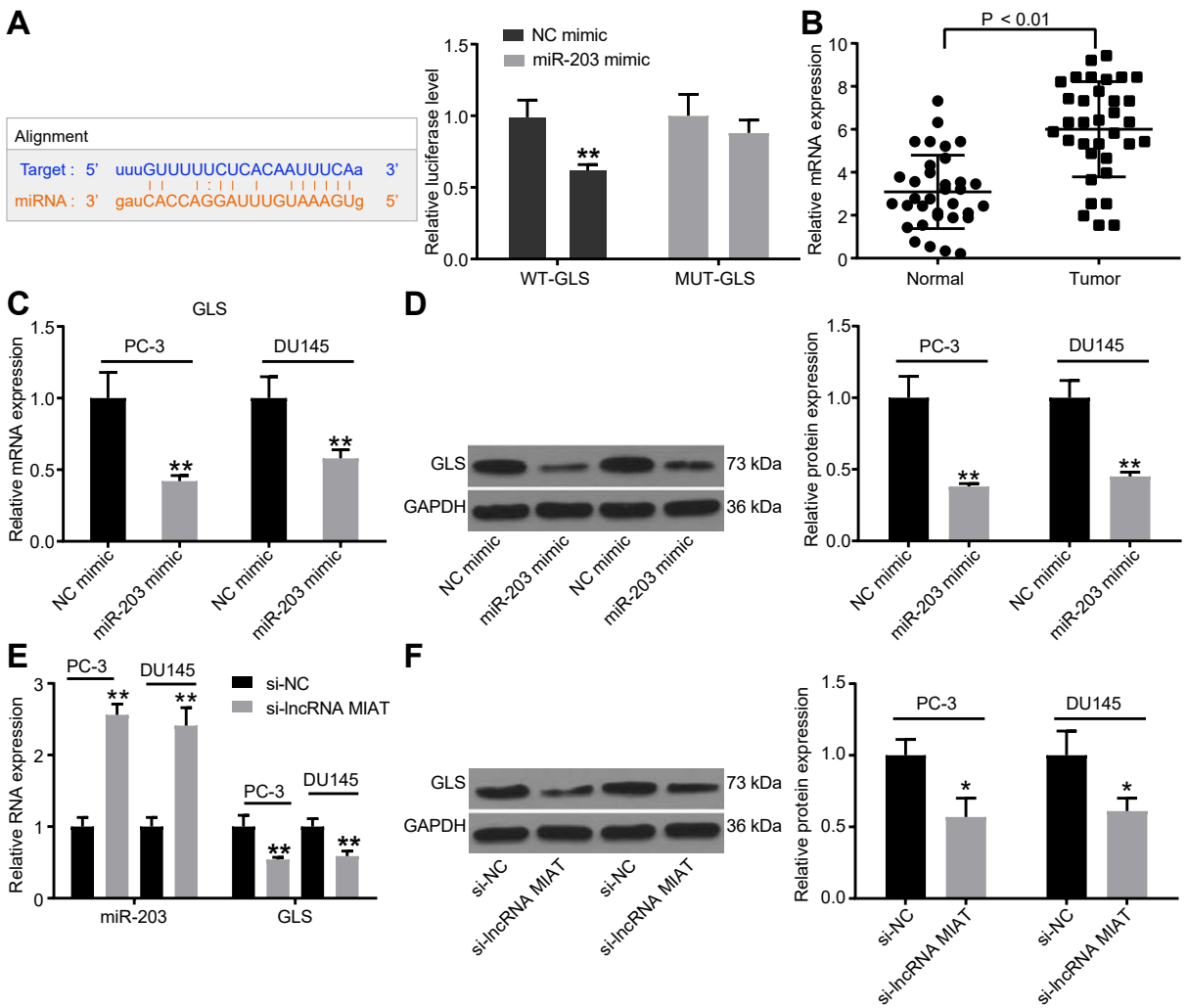


Fig. 3. *LncRNA MIAT sponges miR-203 to increase GLS mRNA expression.* ***A)*** *binding sites between miR-203 and GLS predicted on StarBase (http://starbase.sysu.edu.cn/);* ***B)*** *mRNA expression of GLS in cancer and normal tissues detected by RT-qPCR;* ***C, D)****, mRNA (C) and protein (D) expression of GLS in PC-3 and DU145 cells after miR-203 mimic transfection determined by RT-qPCR and western blot analysis, respectively;* ***E)*** *expression of miR-203 and GLS mRNA in cells after si-lncRNA MIAT transfection measured by RT-qPCR;* ***F)*** *protein level of GLS in cells after si-lncRNA MIAT transfection determined by western blot analysis. Data were analyzed by paired t test (B), or two-way ANOVA (A, C, D, E and F). *p < 0.05, **p < 0.01.*

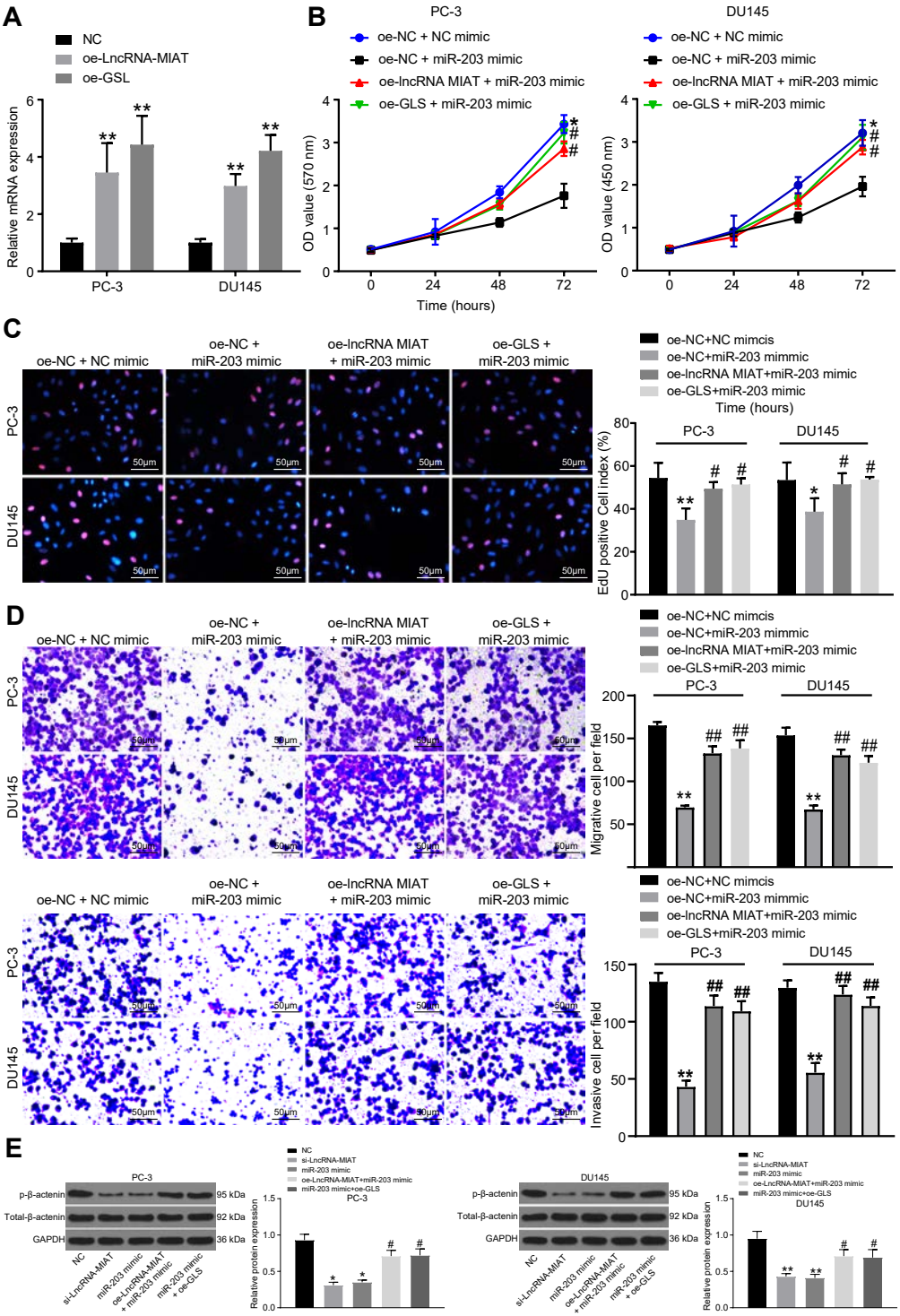


Fig. 4. *The lncRNA MIAT/miR-203/GLS axis modulates the Wnt/β-catenin signaling to affect PCa progression.* ***A)*** *expression of lncRNA MIAT and GLS in PC-3 and DU145 cells after overexpressing vector transfection measured by RT-qPCR;* ***B, C)*** *viability and proliferation of PC-3 and DU145 cells measured by CCK-8 (B) and EdU labeling (C) assays;* ***D)*** *migration and invasion abilities of PC-3 and DU145 cells evaluated by Transwell assays;* ***E)*** *Total β-catenin and phosphorylated β-catenin in PC-3 and DU145 cells after different treatments determined by western blot analysis. Data were compared by two-way ANOVA (A, B, C and D) or one-way ANOVA (E). *p < 0.05 vs oe-NC + NC mimic or vs NC; #p < 0.05 vs oe-NC + miR-203 mimic or vs miR-203 mimic.*

lncRNA in PCa tissues and cell lines. Importantly, an abundance of lncRNA MIAT was found either in cancer tissue samples or in cancer cell lines as compared to the normal ones. Then, downregulation of MIAT was introduced in two typical PC cell lines, PC-3 and DU-145, after which we witnessed a decline in cell proliferation, migration and invasion. The similar oncogenic function of MIAT has been well-recognized in many malignancies to date. Here, we report a similar oncogenic effect of MIAT in PCa by triggering proliferation and invasiveness of cancer cells.

miR-203 was first found as a possible miRNA sponge for lncRNA MIAT on the StarBase System, and GLS was suggested as a putative target for miR-203. Then the binding relationships between miR-203 and lncRNA MIAT or GLS were validated by RNA-pull down (for MIAT and miR-203 only) and through luciferase assays. As expected, miR-203 expression was negatively while GLS expression was positively correlated with lncRNA MIAT expression in PCa tissue samples and cell lines, further validating that lncRNA MIAT enforces GLS expression through sequestering miR-203. miR-203 has been documented as a tumor suppressor in many cancer types including PCa (9). These are in in line with our findings that administration of miR-203 mimic suppressed PCa cell proliferation, migration and invasion. However, either lncRNA MIAT or GLS upregulation abrogated the cancer suppressing roles of miR-203. GLS exerts oncogenic properties through triggering glutamine metabolism, a hall mark of cancer. Dysregulation of GLS and glutamine synthetase are crucial events that are closely linked to metabolic and oxidative stress and apoptosis of cancer cells and anabolic adaptation of tumors (10). In PCa, GLS was also found to promote glucose uptake and glutaminolysis and consequently increase the invasiveness of cells through the suppression of thioredoxin-interacting protein (TXNIP) (11). Here, we validated that up-regulation of GLS is at least partially responsible for lncRNA MIAT-mediated events.

As aforementioned, lncRNA MIAT has been identified as a positive regulator of the Wnt/β-catenin pathway (7). This signaling is a widely-recognized cancer trigger by mediating the tumor-immune cycle in most of the nodes, and it is frequently activated and correlated with metastasis and aggressiveness of PCa (12). As expected, we identified that miR-203 inhibited the phosphorylation of β-catenin in PCa cells, while this inhibition was blocked by lncRNA MIAT or GLS overexpression again, indicating that activation of Wnt/β-catenin is possibly involved in the role of the lncRNA MIAT/miR-203/GLS axis in PCa.

To sum up, this study demonstrated a novel ceRNA network in PCa progression. Suppression of lncRNA MIAT inhibits PCa cell growth and malignancy through miR-203 upregulation and the following GLS downregulation and Wnt/β-catenin inactivation. However, the major limitation of this research is that all major experiments were performed on cell models. We would like the validate these results in animal models in our future studies. We also hope more research will be conducted in this field to validate our findings and to provide more ideas in PCa treatment.

REFERENCES

1. Bray F, Ferlay J, Soerjomataram I, Siegel RL, Torre LA, Jemal A. Global cancer statistics 2018: GLOBOCAN estimates of incidence and mortality worldwide for 36 cancers in 185 countries. CA Cancer J Clin 2018; 68:394-424.
2. Lorenzi L, Avila Cobos F, Decock A, et al. Long noncoding RNA expression profiling in cancer: challenges and opportunities. Genes Chromosomes Cancer 2019; 58:191-9.
3. Karreth FA, Pandolfi PP. ceRNA cross-talk in cancer: when ce-bling rivalries go awry. Cancer Discov 2013; 3:1113-21.
4. Crea F, Venalainen E, Ci X, et al. The role of epigenetics and long noncoding RNA MIAT in neuroendocrine prostate cancer. Epigenomics 2016; 8:721-31.
5. Chen LZ, Ding Z, Zhang Y, He ST, Wang XH. MiR-203 over-expression promotes prostate cancer cell apoptosis and reduces ADM resistance. Eur Rev Med Pharmacol Sci 2018; 22:3734-41.
6. Zhang J, Mao S, Guo Y, Wu Y, Yao X, Huang Y. Inhibition of GLS suppresses proliferation and promotes apoptosis in prostate cancer. Biosci Rep 2019; 39(6):BSR20181826.
7. Zhong W, Xu Z, Wen S, Xie T, Wang F, Wang

Q, Chen J. Long non-coding RNA myocardial infarction associated transcript promotes epithelial-mesenchymal transition and is an independent risk factor for poor prognosis of tongue squamous cell carcinoma. J Oral Pathol Med 2019; 48:720-7.
8. Surasi DSS, Chapin B, Tang C, Ravizzini G, Bathala TK. Imaging and management of prostate cancer. Semin Ultrasound CT MR 2020; 41:207-21.
9. Zhang LS, Ma HG, Sun FH, Zhao WC, Li G. MiR-203 inhibits the malignant behavior of prostate cancer cells by targeting RGS17. Eur Rev Med Pharmacol Sci 2019; 23:5667-74.
10. Mates JM, Campos-Sandoval JA, Santos-Jimenez JL, Marquez J. Dysregulation of glutaminase and glutamine synthetase in cancer. Cancer Lett 2019; 467:29-39.
11. Zacharias NM, McCullough C, Shanmugavelandy S, et al. Metabolic differences in glutamine utilization lead to metabolic vulnerabilities in prostate cancer. Sci Rep 2017; 7:16159.
12. Jung SJ, Oh S, Lee GT, et al. Clinical significance of Wnt/beta-Catenin signalling and androgen receptor expression in prostate cancer. World J Mens Health 2013; 31:36-46.

LETTER TO THE EDITOR

Screening of hub genes for prognosis of gastric cancer based on bioinformatics

D-Y. Han[1], Y-F. Zhang[1], Z-M. Wang[2], Y-C. Chang[1] and X-S. Wang[2]*

[1]Clinical Laboratory, Henan University of Science and Technology Affiliated First Hospital, Luoyang, Henan, China; [2]Henan Key Laboratory of Cancer Epigenetics of Cancer Hospital, Henan University of Science and Technology Affiliated First Hospital, Luoyang, Henan, China

Received November 16, 2020 – Accepted May 19,2021

To the Editor,

Gastric cancer (GC) is one of the most common malignancies and is the second leading cause of death worldwide (1). As a classic example of gene-environment interaction, the pathogenesis of GC could be affected by abnormal gene expression, which plays an important role in its development. Several genetic and epigenetic alterations can mediate the transition of cancer from one stage to another, including mutations in oncogenes, tumor suppressor genes, cell cycle and mismatch repair genes (2). The biomarkers and therapeutic targets recently found in GC have made a great contribution to improve the diagnosis and treatment. Many gene expression profiling studies on GC carcinogenesis have shown hundreds of differentially expressed genes (DEGs), such as SERPINH1, NPY, and PTGDR, involved in different pathways, biological processes, and molecular functions. However, in terms of the biological complexity, poor prognosis and high reoccurrence of GC, it remains urgently necessary to identify novel diagnostic and prognostic biomarkers (3). In this study, the genes as effective biomarkers for diagnosis and prognosis of GC were identified by the bioinformatics analysis including Gene Ontology (GO), Kyoto encyclopedia of genes and genomes (KEGG) enrichment analysis, protein-protein interaction (PPI) network, and Kaplan-Meier plot, hoping to provide an important theoretical basis for the further discovery of new therapeutic targets for this disease.

MATERIALS AND METHODS

Gene expression profile data

Gene Expression Omnibus (GEO) database (http://www.nc bi.nlm.nih.gov/geo/) is a gene expression database established and maintained by the national biotechnology information center (NCBI). It contains high-throughput gene expression data submitted by institutions around the world. This study employed a gene expression profile data-set (GSE54129) obtained from the GEO database. GSE54129 Platform annotation information was GPL570 (HG-U133_Plus_2) Affymetrix Human Genome U133 Plus 2.0 Array. The GSE54129 profile consisted of 111 GC samples and 21 corresponding paired normal tissues (4).

Identification of the DEGs in profile

R language limma package (3.40.2 version) was used to screen gene expression microarray data of tumor and normal tissue samples with "False discovery rate (FDR) < 0.05 and log2FC ≥ 2 or ≤ -2" as the screening of threshold. Visualized volcano plot of the DEGs were implemented by R language under the ggplot2 package (3.1.1) .

Key words: gastric cancer; differentially expressed genes; enrichment analysis; protein-protein interaction; survival analysis

**Corresponding Author:*
Dr. Xinshuai Wang,
Henan Key Laboratory of Cancer Epigenetics of Cancer Hospital,
Henan University of Science and Technology Affiliated First Hospital,
No.24 jinghua Road, Jianxi District, Luoyang,
Henan 471003, P R China
Tel./Fax: +86 0379 64830725
e-mail: wangxiaoshuai5066@hotmail.com

0393-974X (2021)
Copyright © by BIOLIFE, s.a.s.
This publication and/or article is for individual use only and may not be further reproduced without written permission from the copyright holder.
Unauthorized reproduction may result in financial and other penalties
DISCLOSURE: ALL AUTHORS REPORT NO CONFLICTS OF INTEREST RELEVANT TO THIS ARTICLE.

Enrichment analysis of the DEGs

GO analysis, including molecular function (MF), cellular component (CC) and biological process (BP) domains, is a tool widely used for annotating specific genes and gene products, and can also assemble biological features for high-throughput genome and transcriptome data. KEGG is a database resource used to understand high-level functions and utilities of a biological system from molecular-level information by genome sequencing and other high-throughput experimental technologies. In this study, GO function enrichment analysis and KEGG pathway enrichment analysis were performed on DEGs, and the data obtained were visualized through ggplot2 package and pathview package (version 1.24.0).

PPI network and modules analysis of the DEGs

The online resource Search Tool for the Retrieval of Interacting Genes (STRING, https://string-db.org/cgi/input.pl) can be used to construct relationships for hub proteins. In order to identify the key genes, the screened DEGs were uploaded to the STRING database (version 10.5), then the network graph data obtained from the STRING database was uploaded to Cytoscape software (version 3.7.2). Two topological features, degree and betweenness, were calculated to identify candidate hub nodes. Combined score > 0.4 (5) and MCODE >2 (6) were used as the screening thresholds to obtain the corresponding functional module network graph. In order to further analyze the key genes, MCODE score > 10 was selected to obtain one functional module network graph. Degree >21 was selected according to the degree of connectivity and MCODE score to screen the hub genes.

Survival analysis and expression level of hub genes

The Kaplan-Meier plot (http://kmplot.com/analysis/) can evaluate the survival of cancer patients using the gene expression data. The prognosis of GC database for survival analysis were downloaded from TCGA reference data of 111 patients with GC. Hub genes were uploaded to the Kaplan-Meier plot to analyze the correlation between the hub genes and the survival time of GC patients. The online resource Gene Expression Profiling Interactive Analysis (GEPIA, http://gepia.cancer-pku.cn/index.html), originated from The Cancer Genome Atlas (TCGA) database, was used to analyze gene expression levels in tumor and normal tissues. The expression values of genes associated with GC prognosis in 619 samples were obtained from the TCGA database, and divided into two groups, including a tumor group (n=408) and a normal group (n=211). Then, the hub genes between the two groups were analyzed by GEPIA.

Statistical analysis

Generally, $P < 0.05$ was considered statistically significant. FDR method was used to adjust the P value for multiple tests, and $FDR < 0.05$ was used as the threshold for screening DEGs. Hypergeometric distribution method was used for enrichment analysis.

RESULTS

Differential expression analysis

In the present study, R language correlation functions were used to analyze GSE54129 data (21 normal sample tissues and 111 GC sample tissues) from GEO database with a total of 54675 gene expression microarray data. Through preliminary data cleaning, 20183 differential gene expression matrices (up-regulated or down-regulated genes) were obtained. Taking "FDR < 0.05 and log2FC ≥ 2 or ≤ -2" as the threshold, a total of 469 DEGs were obtained, including 229 up-regulated genes and 240 down-regulated genes (Fig. 1). The top 10 up-regulated genes were BANF1, PCGF1, TRAPPC1, SNX27, AP2M1, SPTAN1, EGR1, RAP2A, PKM, FKBP1A, and top 10 down-regulated genes were VSTM2A, ANKHD1, NCKAP5, PCAT18, SALL1, LOC101929340, NUMB, SPINK7, ADH7,CYP2C19 (Table I).

Functional enrichment analysis of DEGs

To further understand the functional role of the screened DEGs in GC, the GO and KEGG pathway enrichment were analyzed by the Cluster Profiler package. The functional analysis revealed that in the MF group, the screened DEGs were particularly concentrated in the structural composition of extracellular matrix, glycosaminoglycan binding, heparin binding, sulfide compounds, extracellular matrix structural constituent conferring tensile strength and other molecular functions (Fig. 2). In the CC group, these genes were found to be enriched

Table I. *Top 10 up-regulated and top 10 down-regulated genes*

Gene		logFC	P.Value	adj.P.Val
Up-regulated genes	BANF1	3.21285372	9.9E-91	2E-86
	PCGF1	2.651727558	2.54E-75	2.56E-71
	TRAPPC1	3.002785964	1.03E-73	6.91E-70
	SNX27	2.733349721	1.3E-68	6.54E-65
	AP2M1	2.085950927	8.41E-62	3.39E-58
	SPTAN1	3.141938948	2.58E-60	8.69E-57
	EGR1	5.86266568	1.54E-59	4.43E-56
	RAP2A	2.953540563	1.8E-59	4.53E-56
	PKM	3.882183515	1.27E-57	2.84E-54
	FKBP1A	2.21744815	2.26E-57	4.23E-54
Down-regulated genes	VSTM2A	-2.077791154	3.92E-55	6.08E-52
	ANKHD1	-2.13407034	4.5E-52	5.68E-49
	NCKAP5	-2.209762288	1.91E-49	1.75E-46
	PCAT18	-2.507059551	1.85E-46	1.44E-43
	SALL1	-2.347951901	6.14E-44	3.75E-41
	LOC101929340	-2.099668915	4.36E-40	1.8E-37
	NUMB	-2.060539009	3.18E-39	1.2E-36
	SPINK7	-2.297882324	3.17E-38	1.08E-35
	ADH7	-3.196598063	6.64E-38	2.24E-35
	CYP2C19	-2.163345302	1.33E-37	4.33E-35

mainly in the components related to extracellular matrix, collagen-containing extracellular matrix, endoplasmic reticulum, extracellular matrix components, basement membrane and others (Fig. 2). In the BP group, the significant enrichment of these genes were mainly enriched in the process corresponding to extracellular structures, extracellular matrix, leukocyte migration, vascular system development regulation and others (Fig. 2). Moreover, according to KEGG pathway enrichment analysis, the DEGs mainly participated in diverse metabolism-associated signaling pathways, such as Chemical carcinogenesis, Metabolism of xenobiotics by cytochrome P450, Drug metabolism-cytochrome P450, ECM-receptor interaction (Table II).

PPI network and module analysis

In this study, 469 DEGs were uploaded to the STRING database (version 10.5), Cytoscape (version 3.7.2) and MCODE plugin for the visualized analysis of differential gene PPI network. After importing the PPI network of 469 DEGs, eleven modules were presented in the results, however, the first module was chosen according to the score and the degree of closeness of relevance. In total, 25 nodes and 198 edges were formed in the PPI network that was generated using Cytoscape software (Fig. 3), and 4 potential key genes, which respectively were FN1, TIMP1, FBN1 and MMP2, were chosen as the hub genes.

Survival curve and expression level of hub genes

The prognoses of GC database for survival analysis were downloaded from TCGA reference data of 111 patients with GC. According to the median expression value of Kaplan-Meier plot, the patients were divided into a high-expression group and a low-expression group. With $P<0.05$ as the significance level, it was found that the expressions of FN1, TIMP1, FBN1 and MMP2 were closely related to the survival prognosis of patients (Fig. 4). The survival rates of the four genes in the high expression group were decreased compared with those of the low expression group, so it could be speculated that FN1, TIMP1, FBN1 and MMP2 were the oncogenes. Compared with normal tissues, the expression levels of FN1, TIMP1 and FBN1 in GC tissues were significantly higher ($P<0.05$). Although the expression level of MMP2 in GC tissues was higher than that in normal tissues, there was no statistical significance (Fig. 5). These findings were in accordance with the results obtained from the survival analysis.

Table II. *KEGG pathway enrichment analysis of DEGs in normal and GC tissues*

ID	Path	pvalue	FDR	Count
hsa05204	Chemical carcinogenesis	6.12E-10	1.46E-07	16
hsa00980	Metabolism of xenobiotics by cytochrome P450	1.36E-07	1.62E-05	13
hsa00982	Drug metabolism - cytochrome P450	5.60E-07	4.46E-05	12
hsa04512	ECM-receptor interaction	5.06E-06	0.000302	12
hsa04510	Focal adhesion	3.63E-05	0.001451	17

FDR: false discovery rate

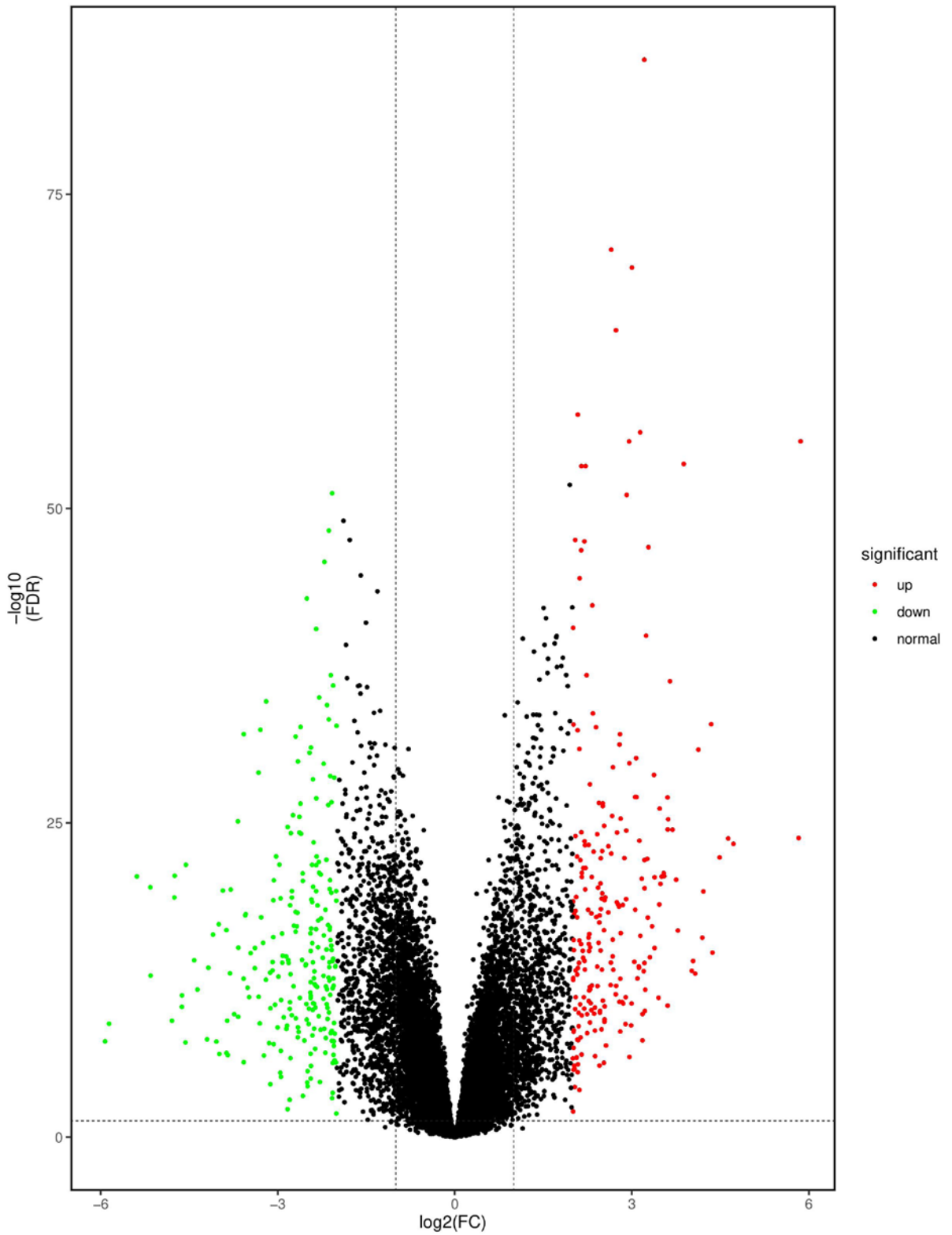


Fig. 1. *Volcano map of 469 DEGs. The red dots represent 229 up-regulated genes, the green dots represent 240 down-regulated genes.*

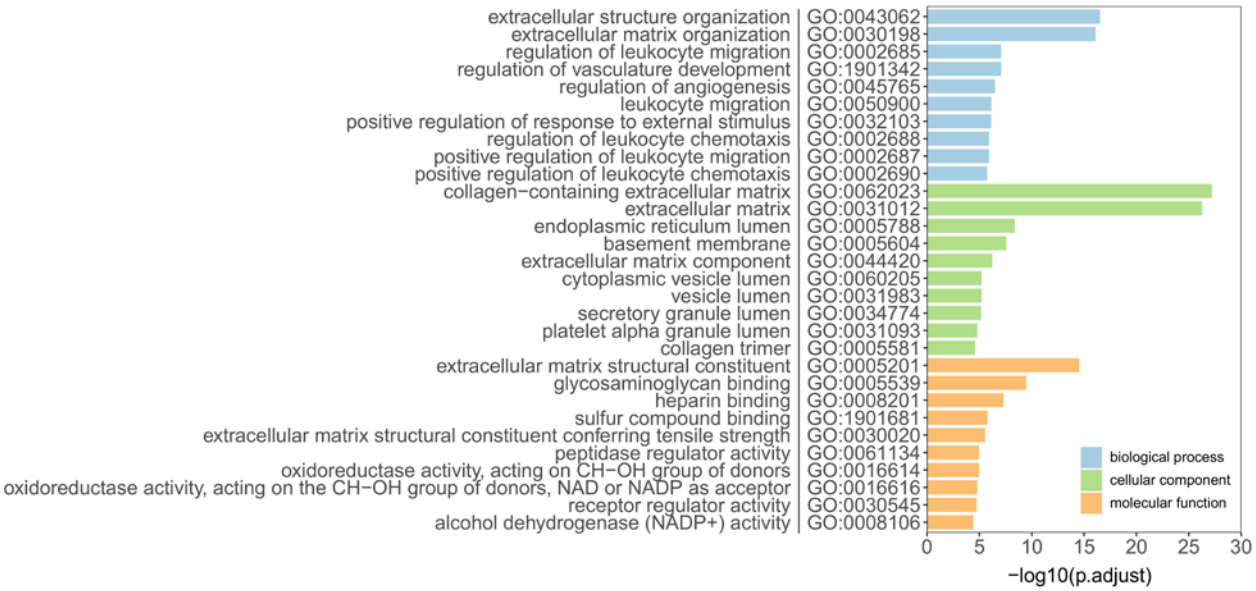


Fig. 2. *Visual histogram of GO analysis of DEGs in normal and GC tissue. The yellow bars represent the molecular function, the green bars represent the cellular component, the blue bars represent the biological process.*

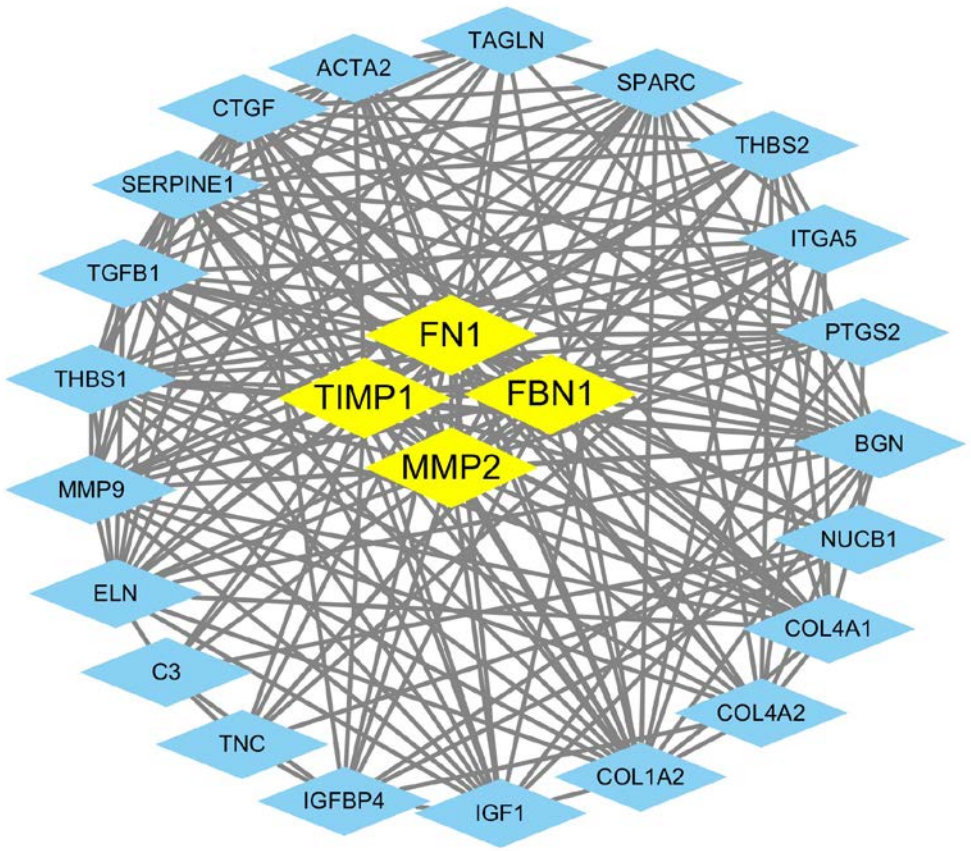


Fig. 3. *The PPI network of the 469 DEGs in GC. The blue rhombi indicate genes with lowered expression and yellow rhombi indicate overexpressed genes. Lines represent interaction of the protein with other proteins in the network.*

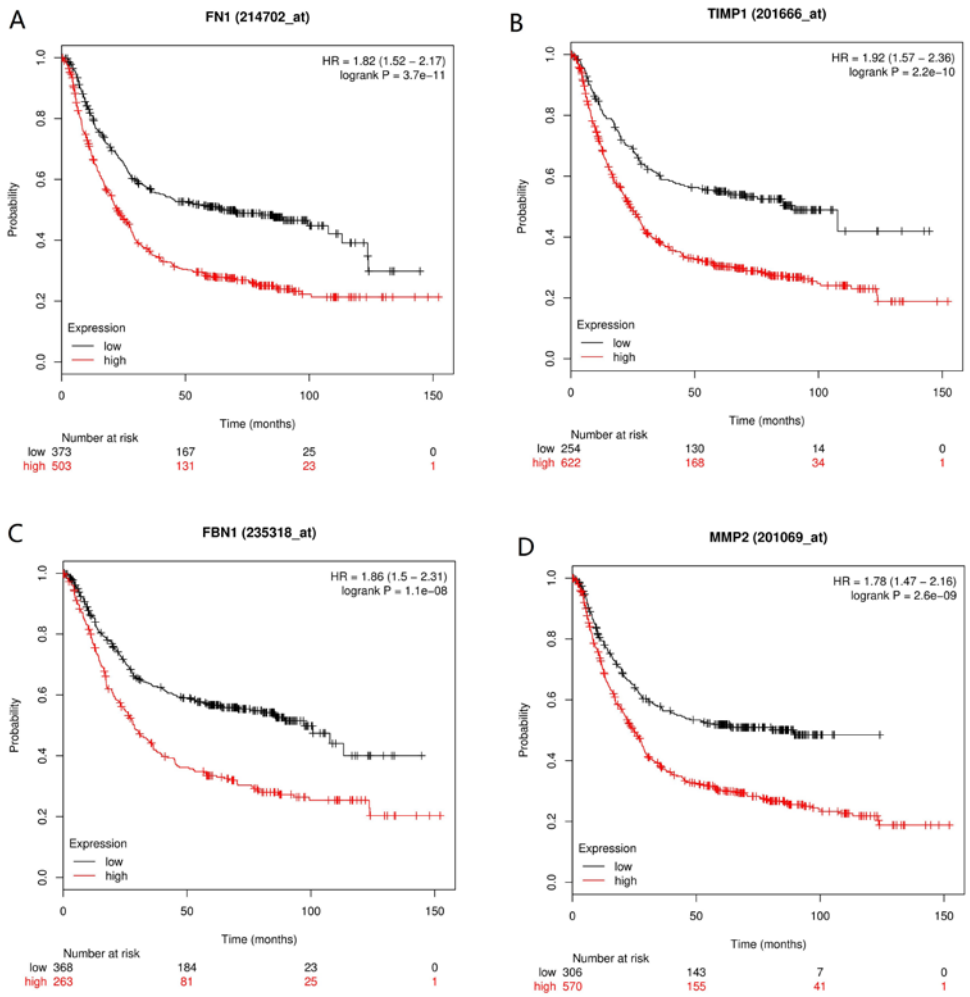


Fig. 4. *Kaplan-Meier survival curves of the four genes in 111 patients with GC. Higher FN1 (**A**), TIMP1 (**B**), FBN1 (**C**) and MMP2 (**D**) expression is associated with poorer prognosis with P=3.7e-11, 2.2e-10, 1.1e-08 and 2.6e-09, respectively.*

DISCUSSION

In this study, 469 DEGs were screened between GC and normal tissue. These DEGs, mainly located in the extracellular matrix and basement membrane, were proved to be associated with development and progression of cancer (7).

FN1, TIMP1, FBN1 and MMP2 were chosen as the hub genes in the PPI network, and their high expression would result in poor survival prognosis of patients. FN1 is involved in the occurrence and development of a variety of tumors and is up-regulated in a variety of cancer types. Soikkeli showed that the protein and mRNA levels of FN1 gene in GC tissues increased, and the protein expression of FN1 was positively correlated with tumor size (8). TIMP1 appears to be more diverse and complex in tumor development and proliferation (9), and its levels are higher in the most aggressive tumors. FBN1 has been shown to promote tumor growth, which would increase cell apoptosis *in vitro* and decrease tumor growth *in vivo* after silencing, suggesting its association with poor prognosis (10). The over-expression of MMP2 can promote the invasion of GC cells (11), meanwhile, MMP2 can degrade collagen and promote the metastasis of cancer cells (12). These previous studies are consistent with our results, suggesting the four genes are likely related to the progression of GC. Moreover, TIMP1 and FBN1 were firstly identified to be related to the progression

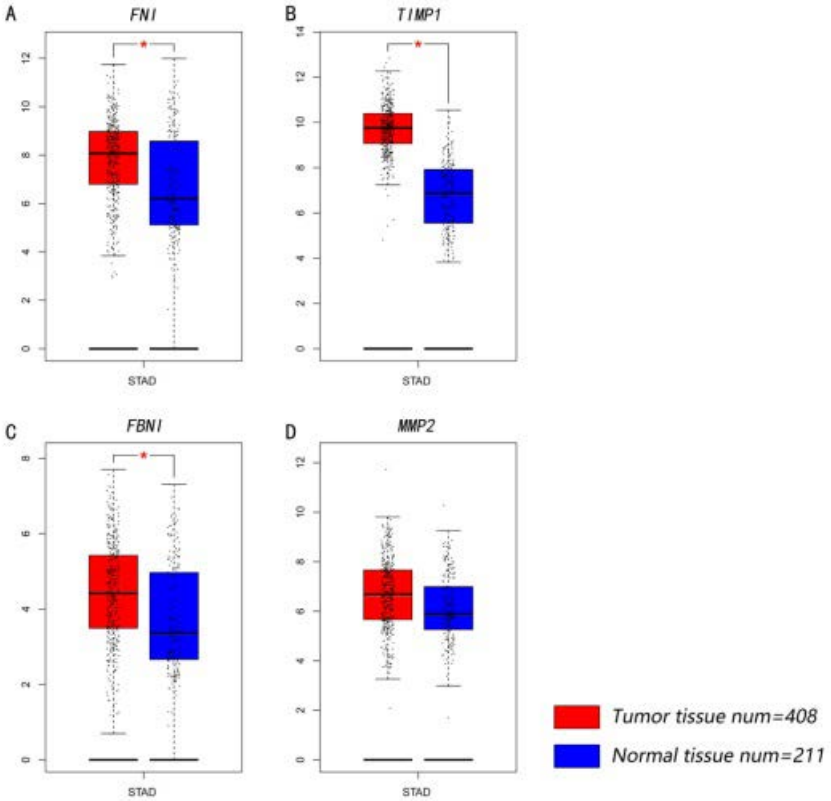


Fig. 5. *Expression analysis of FN1, TIMP1, FBN1 and MMP2 gene in GC and normal tissues. The expression levels of FN1 (**A**), TIMP1 (**B**) and FBN1 (**C**) in GC tissues are significantly higher than those in normal tissues (P<0.05). There is no statistically significant difference between the expression level of MMP2 (**D**) in GC tissues and normal tissues (P>0.05). * significant difference between GC and normal tissues.*

of GC after information retrieval about GSE54129. Although there are several limitations to this study, such as the lack of experimental validations, our results provide an important bioinformatics basis and relevant theoretical basis for future research of GC.

In summary, FN1, TIMP1, FBN1 and MMP2 were identified as hub genes related to the progression of GC and can be prognostic biomarkers for therapeutic targets.

REFERENCES

1. Ferlay J, Shin H-R, Bray F, Forman D, Mathers C, Parkin DM. Estimates of worldwide burden of cancer in 2008: GLOBOCAN 2008. Int J Cancer 2010; 127(12):2893-917.
2. Smith MG, Hold GL, Tahara E, El-Omar EM. Cellular and molecular aspects of gastric cancer. World J Gastroenterol 2006; 12(19):2979-90.
3. Kang M-H, Choi H, Oshima M, et al. Estrogen-related receptor gamma functions as a tumor suppressor in gastric cancer. Nat Commun 2018; 9(1):1920.
4. Hippo Y, Taniguchi H, Tsutsumi S, et al. Global gene expression analysis of gastric cancer by oligonucleotide microarrays. Cancer Res 2002; 62(1):233-40.
5. Cao L, Chen Y, Zhang M, et al. Identification of hub genes and potential molecular mechanisms in gastric cancer by integrated bioinformatics analysis. Peer J 2018; 6:e5180.
6. Li L, Zhu Z, Zhao Y, et al. FN1, SPARC, and SERPINE1 are highly expressed and significantly related to a poor prognosis of gastric adenocarcinoma revealed by microarray and bioinformatics. Sci Rep 2019; 9(1):7827.
7. Brown Y, Hua S, Tanwar PS. Extracellular matrix-mediated regulation of cancer stem cells and

chemoresistance. Int J Biochem Cell Biol 2019; 109:90-104.
8. Soikkeli J, Podlasz P, Yin M, et al. Metastatic outgrowth encompasses COL-I, FN1, and POSTN up-regulation and assembly to fibrillar networks regulating cell adhesion, migration, and growth. Am J Pathol 2010; 177(1):387-403.
9. Gong Y, Chippada-Venkata UD, Galsky MD, Huang J, Oh WK. Elevated circulating tissue inhibitor of metalloproteinase 1 (TIMP-1) levels are associated with neuroendocrine differentiation in castration resistant prostate cancer. Prostate 2015; 75(6):616-27.
10. Ma X, Wei J, Zhang L, et al. miR-486-5p inhibits cell growth of papillary thyroid carcinoma by targeting fibrillin-1. Biomed Pharmacother 2016; 80:220-6.
11. Bae IH, Park MJ, Yoon SH, Kang SW, Lee SS, Choi KM, Um HD. Bcl-w promotes gastric cancer cell invasion by inducing matrix metalloproteinase-2 expression via phosphoinositide 3-kinase, Akt, and Sp1. Cancer Res 2006; 66(10):4991-5.
12. Mook OR, Frederiks WM, Noorden CJFV. The role of gelatinases in colorectal cancer progression and metastasis. Biochim Biophys Acta 2004; 1705(2):69-89.

LETTER TO THE EDITOR

Activated Th9 cells in diabetic coronary heart disease

HY. Chen[1#], Y. Bao[1#], JJ. Zou[1#], XL. Cong[2#], XX. Zhang[1], JY. Zheng[1], XF. Chen[1] and YQ. Shi[1*]

[1]Department of Endocrinology, Changzheng Hospital, Naval Medical University, Shanghai, China;
[2]Department of Cardiology, Changzheng Hospital, Naval Medical University, Shanghai, China

Received December 7, 2020 – Accepted May 19, 2021

#These authors contributed equally to this work

To the Editor,

Diabetes mellitus (DM), especially its predominant form, type 2 diabetes mellitus (T2DM), is a major risk factor for coronary heart disease (CHD) [also known as coronary artery disease (CAD)] (1, 2). Diabetic CHD (DM-CHD) represents the leading cause of morbidity and mortality in diabetic patients (3). DM-induced hyperglycaemia induces endothelial dysfunction and cardiovascular damage and accelerates the process of atherosclerosis, the leading cause of CHD (4). The synergistic interaction between DM and CHD occurs via metabolic inflammation (meta-inflammation).

Meta-inflammation is due to dysfunction of the immune system. T helper cells (Th cells) play an important role in the immune system. Upon antigen-specific stimulation, naïve $CD4^+$ T cells have the potential to differentiate into various T helper (Th) cell subsets, including Th1, Th2, Th17, T regulatory (Treg), and the recently discovered Th9 and Th22 cells (5). Interleukin (IL)-9-producing Th cells (Th9) are a subset of $CD4^+$ T cells associated with various inflammatory diseases. The signature cytokine for Th9 cells is IL-9. PU.1 (also known as SPI1) is the key transcription factor through which Th9 cells regulate IL-9 production. Recent evidence indicates that Th9 cells and IL-9 participate in the occurrence and progression of tumours, autoimmune diseases, and inflammatory diseases (6). However, studies evaluating the association of Th9 cells with metabolic disorders, including DM-CHD, are limited.

This study therefore aimed to analyse the proportion of Th9 cells and the changes in Th9-related cytokines, including IL-9 and PU.1, in DM-CHD patients and DM-CHD experimental rats.

MATERIALS AND METHODS

Human blood collection

DM-CHD patients (n=18) and healthy control (HC) individuals (n=12) who underwent physical examinations during the same period were enrolled from the Department of Endocrinology, Changzheng Hospital. Coronary angiography (CAG) and an oral glucose tolerance test (OGTT) were performed to identify the presence of CHD and/or T2DM. The diagnosis of T2DM is based on the T2DM diagnostic criteria proposed by the WHO in 1999. The diagnosis of coronary heart disease is based on coronary angiography with 1 or more stenoses ≥50%. Patients with severe heart failure, acute and chronic infectious diseases, malignant tumours, and autoimmune diseases were excluded from this study.

This study was approved by the Research Ethics Committee of Changzheng Hospital, and written informed consent was obtained from each participant. Peripheral venous blood (2-3 mL) was drawn in the morning from all

Key words: diabetic coronary heart disease; Th9; IL-9; PU.1

Corresponding Author:
Dr Yongquan Shi,
Department of Endocrinology, Changzheng Hospital,
Naval Medical University, 415 Fengyang Road,
Huangpu District, Shanghai, 200003, China
Tel.: +86 021 81885373 - Fax: +86 63586228
e-mail: young.stone@smmu.edu.cn

0393-974X (2021)
Copyright © by BIOLIFE, s.a.s.
This publication and/or article is for individual use only and may not be further reproduced without written permission from the copyright holder.
Unauthorized reproduction may result in financial and other penalties
DISCLOSURE: ALL AUTHORS REPORT NO CONFLICTS OF INTEREST RELEVANT TO THIS ARTICLE.

participants after they fasted for more than 8 hours. Blood samples were collected into collection tubes containing 0.2 mL sodium heparin. Peripheral blood mononuclear cells (PBMCs) were isolated using a Ficoll (Solarbio Life Sciences, Beijing, China) density gradient for flow cytometry analysis and quantitative real-time PCR (qRT-PCR). The sera were separated by centrifugation at 3000 r/min for 15 min and stored at -80°C until further use.

Establishment of a rat model of DM-CHD

Ten male SD rats (8 weeks old, weighing 210-230 g) and ten Zucker Diabetic Fatty (ZDF) rats (8 weeks old, weighing 330-350 g, a model of T2DM) were raised under controlled temperatures (25±1°C) and humidity (50-70%), with 12 h light/dark cycles and *ad libitum* access to food and water. All experiments took place in Changzheng Hospital. All animal procedures were approved by the Animal Care and Use Committee of Changzheng Hospital (no. 2016SL039). After 7 days of adaptive feeding, ZDF rats were fed a high-fat diet containing 6.5% crude fat and 23.5% crude protein (Purina #5008). Three weeks later, the blood glucose of each rat was measured, and the rats with random blood glucose exceeding 16.8 mmol/L were considered DM rats. The DM rats received a daily subcutaneous injection of isoprenaline hydrochloride (ISO; Shanghai Hefeng Pharmaceutical Co., Ltd., Shanghai, China) at a dose of 1 mg/mL for 10 consecutive days. Age-matched SD rats served as the control rats and were fed a normal diet.

Measurement of serum lipid parameters

The human/rat serum levels of total cholesterol (TC), triglycerides (TG), low-density lipoprotein cholesterol (LDL-C), and high-density lipoprotein cholesterol (HDL-C) were determined by an automatic biochemical analyser.

RNA extraction and qRT-PCR

Total RNA was extracted from human/rat PBMCs or rat heart tissues with TRIzol reagent (Invitrogen, Thermo Fisher Scientific, Inc., Waltham, MA, USA). The RNA was converted into cDNA using a Reverse Transcription Kit (Takara, Dalian, China), after which cRNA was synthesized from the total RNA using the SYBR Premix Dimmer Eraser kit (Takara) according to the manufacturer's instructions. The relative mRNA levels of IL-9 and PU.1 were calculated by the $2^{-\Delta\Delta Ct}$ method and normalized to the internal control β-actin.

Detection of the Th9 proportion by flow cytometry

The proportion of Th9 cells ($IL\text{-}9^+$ $CD4^+$ T cells) to $CD4^+$ T cells in peripheral blood samples was detected using flow cytometry. Briefly, PBMCs were isolated, resuspended in RPMI 1640 medium containing 10% foetal bovine serum (FBS), and adjusted to a density of $5 \cdot 10^6$/mL. Following 4 h of incubation at 37°C in 5% CO_2 under the stimulation of phorbol ester (PMA, 50 μg/L), ionomycin (1 mg/L) and brefeldin A (BFA, 0.4 μmol/L), PBMCs were incubated with FITC-conjugated anti-CD4 antibody at 4°C in the dark for 20 min. After that, the cells were fixed and permeabilized with BD Cytofix/Cytoperm Fixation/Permeabilization Solution Kit and then incubated with PE-conjugated anti-IL-9 antibody at 4°C in the dark for 30 min. Thereafter, the cells were washed with PBS twice and analysed with a BD FACSCalibur flow cytometer (BD Bioscience, San Jose, CA, USA).

Enzyme-linked immunosorbent assay (ELISA)

The human/rat serum levels of IL-9 were measured using an ELISA kit (LifeSpan Biosciences, Seattle, WA, USA) according to the manufacturer's instructions. For the determination of oxidative stress parameters, the rat serum levels of superoxide dismutase (SOD) and malondialdehyde (MDA) were measured with commercial ELISA kits (Nanjing JianCheng Bioengineering Institute, Nanjing, China) according to the manufacturer's instructions.

Western blot

Total protein from rat heart tissues was extracted using radioimmunoprecipitation assay lysis buffer (Beyotime, Beijing, China). The protein concentrations were determined by BCA assay. Then, equal amounts of protein from the cell lysates were separated with 10% sodium dodecyl sulfate-polyacrylamide gel electrophoresis (SDS-PAGE) and transferred to polyvinylidene fluoride (PVDF) membranes (Millipore Corp., Billerica, MA, USA). The membranes were blocked with 5% skim milk and then incubated with the following primary antibodies against IL-9 (1:1000; #AF4134; R&D Systems, Minneapolis, MN, USA), PU.1 (1:1000; #sc-390405; Santa Cruz Biotechnology, Dallas, TX, USA), and β-actin (1:1000; #sc-47778; Santa Cruz Biotechnology) overnight at 4°C, followed by horseradish peroxidase (HRP)-conjugated

secondary antibodies (1:2000; Santa Cruz Biotechnology) at room temperature for 2 h. The bands were visualized using an enhanced chemiluminescence reagent and quantified using ImageJ software.

Statistical analysis

All statistical analyses were performed using GraphPad Prism 7. Student's *t*-test was used to compare normally distributed data between the two groups. Oneway analysis of variance (ANOVA) was used to analyse differences among multiple groups. Correlations between TC, TG, HDL-C, LDL-C, and IL-9 levels were evaluated by Pearson correlation tests. The values are presented as the mean ± standard deviation (SD) from three independent experiments. $p<0.05$ was considered statistically significant.

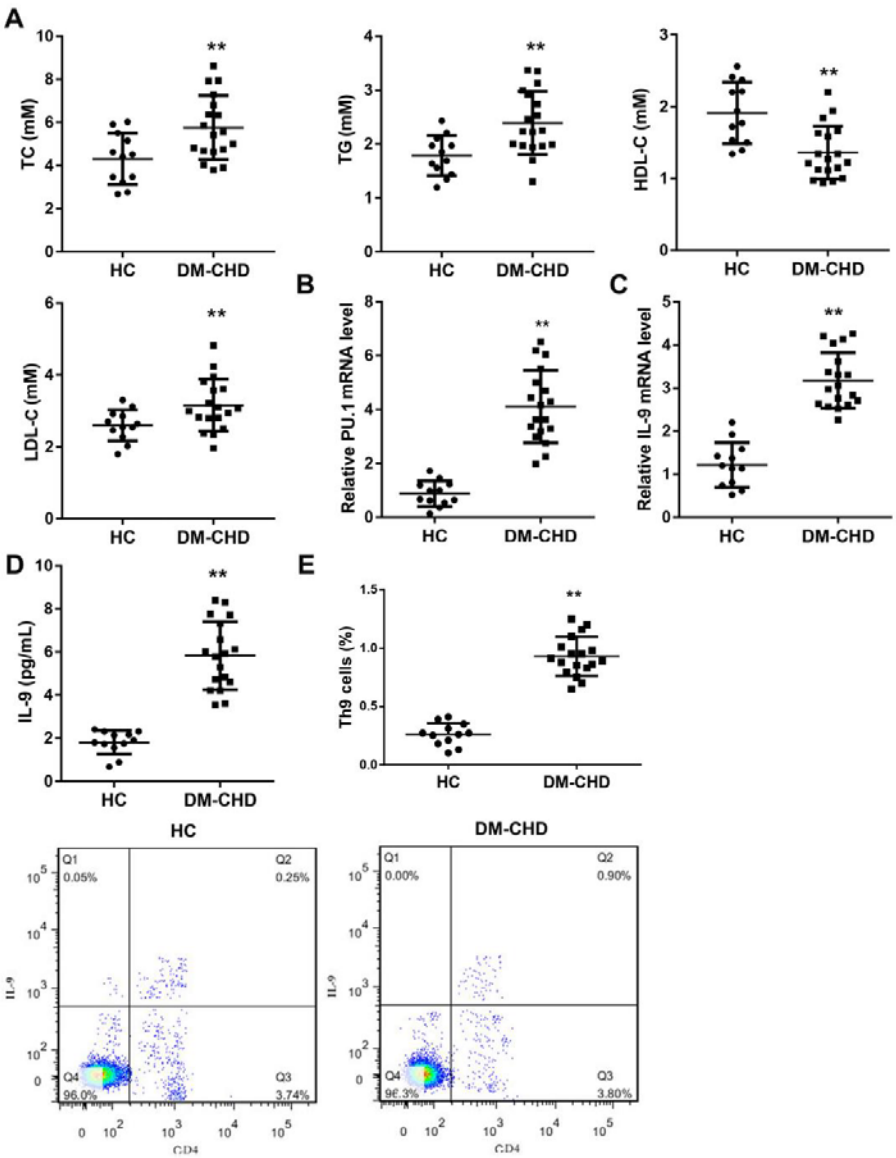


Fig. 1. *DM-CHD patients showed dyslipidaemia and activated Th9 cells. Peripheral venous blood was drawn from DM-CHD patients (n=18) and healthy control individuals (HC, n=12), and PBMCs and sera were prepared.* ***A)*** *The serum levels of lipid parameters (TC, TG, LDL-C, and HDL-C) were determined by an automatic biochemical analyser. The mRNA levels of PU.1* ***(B)*** *and IL-9* ***(C)*** *in PBMCs were examined using qRT-PCR.* ***D)*** *The serum levels of IL-9 were measured using ELISA.* ***E)*** *The proportion of Th9 cells (IL-9$^+$ CD4$^+$ T cells) to CD4$^+$ T cells was detected using flow cytometry.* $^{**}p<0.01$ *vs HC.*

RESULTS

DM-CHD patients showed dyslipidaemia and increased Th9 cells

Table I presents the clinical characteristics of the study participants. The serum levels of TC, TG, and LDL-C were higher, whereas the levels of HDL-C were lower in most DM-CHD patients compared to HC individuals (Fig. 1A), indicating dyslipidaemia in the DM-CHD patients. Furthermore, the mRNA levels of Th9-specific transcription factor PU.1 (Fig. 1B) and Th9-related cytokine IL-9 (Fig. 1C) in the PBMCs were significantly higher in most DM-CHD patients than in HC individuals. Moreover, the ELISA analysis results showed upregulated serum levels of IL-9 in most DM-CHD patients (Fig. 1D). In addition, the proportion of Th9 cells (IL-9$^+$ CD4$^+$ T cells) was markedly higher in the DM-CHD group than in the HC group (Fig. 1E).

Table I. *Demographic and clinicopathologic information*

	HC	DM-CHD
Number	12	18
Age	56.4±12.6	63.7±11.5
Sex		
Male	7 (58.3%)	11 (61.1%)
Female	5 (41.7%)	7 (38.9%)
Body weight (kg)	60.37±7.64	65.56±10.12
Medical history (year)	0	5.16±2.33
Coronary stenosis score	0.98±0.73	96.69±45.74*
Glucose levels (mmol/L)		
Fasting blood glucose	4.80±0.58	9.65±2.46*
Glycosylated hemoglobin	4.80±0.52	7.43±1.38*
Glycosylated serum protein	1.75±0.44	2.88±1.01*
Risk factors		
High blood pressure	2 (16.7%)	14 (77.8%) *
Systolic pressure (mmgH)	123.45±14.38	127.25±18.66
Diastolic pressure (mmgH)	74.46±6.61	78.63±9.88
Dyslipidemia		
Triglyceride (mmol/L)	1.22±0.31	2.44±1.14*
Cholesterol (mmol/L)	1.92±1.12	4.51±1.25*
LDL (mmol/L)	2.31±0.88	2.66±1.06
HDL (mmol/L)	1.46±0.38	1.49±0.48
hs-CRP (mg/L)	1.39±0.42	4.65±1.65*
Renal function		
Urea nitrogen (μmol/L)	5.39±0.74	5.76±1.66
Creatinine (μmol/L)	75.96±8.92	94.24±18.32*
Uric acid (μmol/L)	295.62±67.60	327.68±69.80

*$p<0.05$, DM-CHD vs HC

The correlation between TC, TG, HDL-C, LDL-C, and IL-9

The results of the Pearson correlation analyses indicated that in DM-CHD patients, the serum level of IL-9 was positively and significantly correlated with the serum levels of TC, TG, and LDL-C (Table II, r=0.739, 0.800, and 0.619, respectively; p≤0.001, ≤0.001, and 0.006, respectively). In contrast, the serum level of IL-9 was negatively and significantly correlated with the serum levels of HDL-C (r=-0.664; p=0.003).

Table II. *Correlation between TC, TG, HDL-C, LDL-C and IL-9*

IL-9 (pg/mL)	r value	p value
TC	0.739	0
TG	0.800	0
HDL-C	-0.664	0.003
LDL-C	0.619	0.006

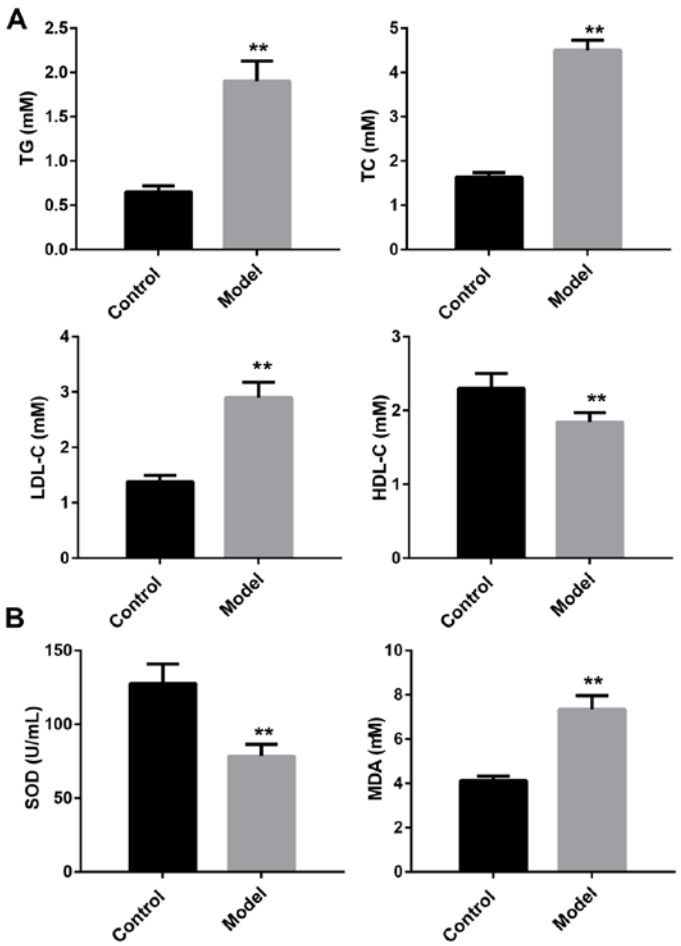


Fig. 2. *Levels of TC, TG, LDL-C, HDL-C, SOD, and MDA in control and DM-CHD model rats. The ZDF rat model of DM-CHD was prepared by high-fat diet feeding combined with injection of ISO for 10 consecutive days (model group, n=10). SD rats served as the control rats and were fed a normal diet (control group, n=10).* ***A)*** *The serum levels of lipid parameters (TC, TG, LDL-C, and HDL-C) were determined by an automatic biochemical analyser.* ***B)*** *The serum levels of lipid peroxidation indexes (SOD and MDA) were measured using ELISA.* $^{**}p<0.01$ *vs Control.*

DM-CHD rats showed dyslipidaemia and elevated oxidative stress

Next, the rat model of DM-CHD was produced by high-fat diet feeding of ZDF rats combined with the injection of ISO for 10 consecutive days, with SD rats fed a normal diet used as the control rats. Compared with the control group, the serum levels of TC, TG, and LDL-C were significantly higher, whereas the levels of HDL-C were lower in the DM-CHD model group (Fig. 2A). These results in rats showed lipid changes consistent with the human data. Furthermore, the serum levels of antioxidant SOD were notably lower, whereas the levels of prooxidant MDA were higher in the DM-CHD model group than in the control group (Fig. 2B).

DM-CHD rats showed increased Th9 cells

Finally, the percentage of Th9 cells and the

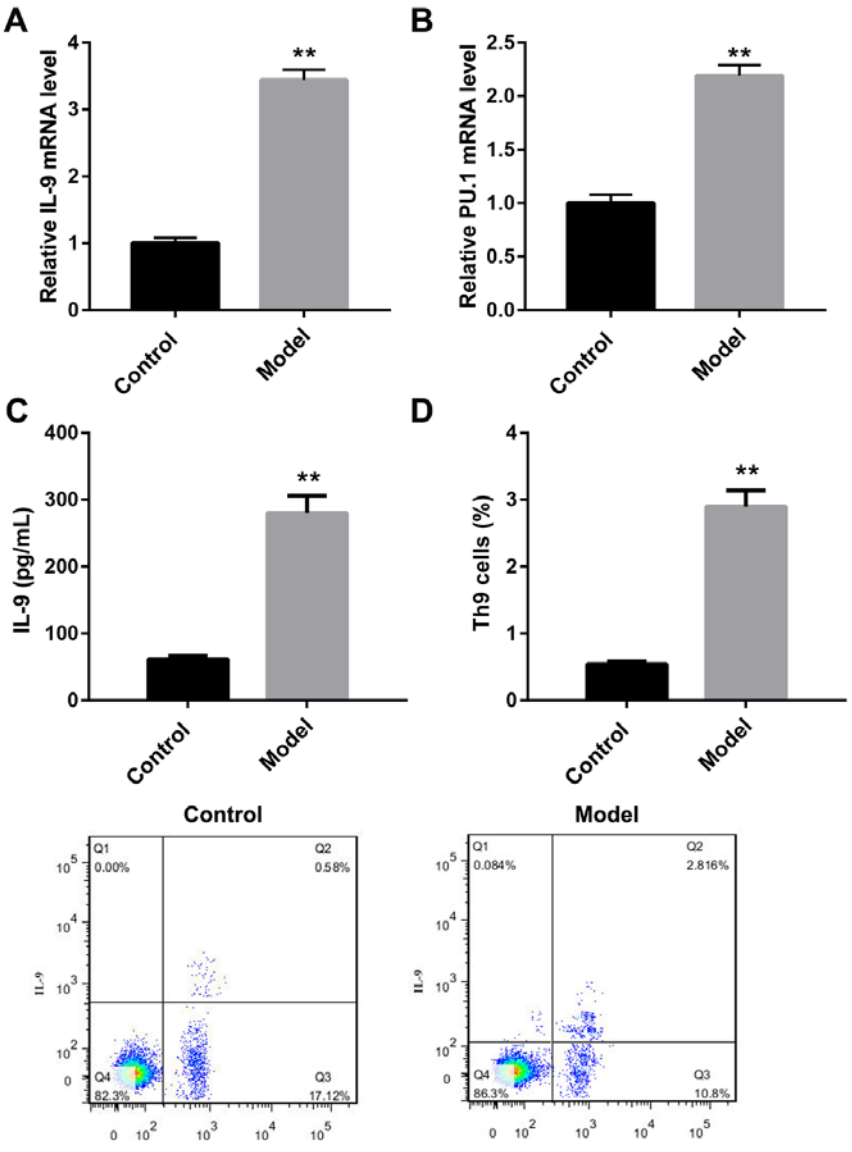


Fig. 3. *Activated Th9 cells in peripheral blood from DM-CHD model rats. The ZDF rat model of DM-CHD was prepared by high-fat diet feeding combined with injection of ISO for 10 consecutive days (model group, n=10). SD rats served as the control rats and were fed a normal diet (control group, n=10). The mRNA levels of IL-9* ***(A)*** *and PU.1* ***(B)*** *in rat PBMCs were examined using qRT-PCR.* ***(C)*** *The serum levels of IL-9 were measured using ELISA.* ***(D)*** *The proportion of Th9 cells (IL-9$^+$ CD4$^+$ T cells) to CD4$^+$ T cells was detected using flow cytometry. $^{**}p<0.01$ vs Control.*

expression of Th9-related cytokines in the DM-CHD model rats were examined. The mRNA levels of the Th9-related cytokine IL-9 (Fig. 3A) and Th9-specific transcription factor PU.1 (Fig. 3B) in PBMCs were significantly higher in DM-CHD model rats than in control rats. Moreover, ELISA analysis showed upregulated serum levels of IL-9 in DM-CHD model rats (Fig. 3C). In addition, the proportion of Th9 cells (IL-9$^+$ CD4$^+$ T cells) was markedly higher in the DM-CHD rats than in the control rats (Fig. 3D).

In addition, the mRNA and protein levels of IL-9 (Fig. 4A and C) and PU.1 (Fig. 4B and C) in rat heart tissues were significantly higher in DM-CHD model rats than in control rats. These data indicated that DM-CHD rats showed increased Th9 cells, which was consistent with the human data.

DISCUSSION

Dyslipidaemia is one of the most important factors

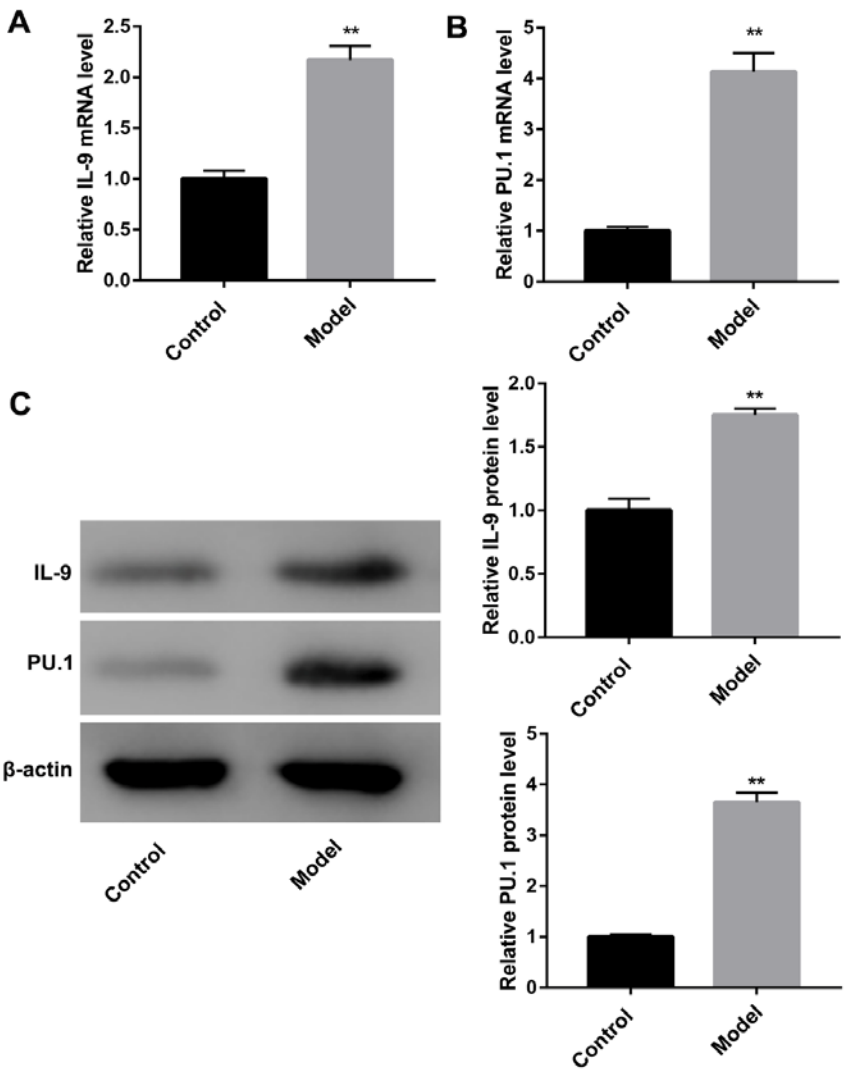


Fig. 4. *Activated Th9 cells in heart tissues from DM-CHD model rats. The ZDF rat model of DM-CHD was prepared by high-fat diet feeding combined with injection of ISO for 10 consecutive days (model group, n=10). SD rats served as the control rats and were fed a normal diet (control group, n=10). The mRNA levels of IL-9* ***(A)*** *and PU.1* ***(B)*** *in rat heart tissues were examined using qRT-PCR.* ***(C)*** *The protein levels of IL-9 and PU.1 in rat heart tissues were measured using western blots.* $^{**}p<0.01$ *vs Control.*

for CHD, particularly under diabetic conditions (7). In the present study, DM-CHD patients and DM-CHD model rats showed higher serum levels of TC, TG, and LDL-C but lower levels of HDL-C, which was in line with previous studies (8). Oxidative stress is a key pathogenic mechanism implicated in DM-CHD (9). The results of this study showed increased serum levels of prooxidant MDA but decreased antioxidant SOD in DM-CHD model rats. It was speculated that the enhancement of oxidative stress stimulates the expression of the signature cytokine interleukin (IL)-9. The synergistic interaction between DM and CHD occurs via meta-inflammation due to dysfunction of the immune system. Th9 cells, a recently discovered subset of helper T cells, are characterized by high secretion levels of IL-9(10). Thus, Th9 cells may be involved in meta-inflammation and thus in metabolic disorders. A previous study showed that plasma IL-9 levels were significantly higher ($p=0.002$) in T2DM patients than in control individuals (11) and that PU.1 expression was significantly increased in patients with acute coronary syndromes (12). Intriguingly, the results of this study showed an increased proportion of Th9 cells, increased Th9-related cytokine (IL-9), and increased mRNA levels of key transcription factor (PU.1) in peripheral blood from DM-CHD patients and DM-CHD model rats. In addition, the serum levels of IL-9 in DM-CHD patients were positively and significantly correlated with serum levels of TC, TG, and LDL-C but negatively correlated with serum levels of HDL-C. In conclusion, these results indicated that increased Th9 cells are closely related to dyslipidaemia in DM-CHD.

ACKNOWLEDGEMENTS

The research was funded by the National Natural Science Foundation of China (Grant No. 81700717) and National Key Research and Development Project (No. 2018YFC1314100).

REFERENCES

1. Ali MK, Narayan KMV, Tandon N. Diabetes & coronary heart disease: current perspectives. Indian J Med Res 2010; 132(5):584-97.
2. Naito R, Miyauchi K. Coronary artery disease and type 2 diabetes mellitus. Int Heart J 2017; 58(4) 475-80.
3. Hammoud T, Tanguay JF, Bourassa MG. Management of coronary artery disease: therapeutic options in patients with diabetes. J Am Coll Cardiol 2000; 36(2):355-65.
4. Aravindhan V, Madhumitha H. Metainflammation in diabetic coronary artery disease: emerging role of innate and adaptive immune responses. J Diabetes Res 2016; 6264149.
5. Ye J, Wang Y, Wang Z, et al. Circulating Th1, Th2, Th9, Th17, Th22, and Treg levels in aortic dissection patients. Mediat Inflamm 2018; 2018:5697149.
6. Elyaman W and Khoury SJ. Th9 cells in the pathogenesis of EAE and multiple sclerosis. Semin Immunopathol 2016; 39(1):1-9.
7. Lee JS, Chang PY, Zhang Y, et al. Triglyceride and HDL-C dyslipidemia and risks of coronary heart disease and ischemic stroke by glycemic dysregulation status: the strong heart study. Diabetes Care 2017; 40(4):529-37.
8. Cai G, Shi G, Xue S, et al. The atherogenic index of plasma is a strong and independent predictor for coronary artery disease in the Chinese Han population. Medicine (Baltimore) 2017; 96(37):e8058.
9. Tibaut M, Petrovič D. Oxidative stress genes, antioxidants and coronary artery disease in type 2 diabetes mellitus. Cardiovasc Hematol Agents Med Chem 2016; 14(1):23-38.
10. Zhao P, Xiao X, Ghobrial RM, et al. IL-9 and Th9 cells: progress and challenges. Int Immunol 2013; 25(10):547-51.
11. Hang H, Yuan S, Yang Q, et al. Multiplex bead array assay of plasma cytokines in type 2 diabetes mellitus with diabetic retinopathy. Mol Vis 2014; 20:1137-45.
12. Lin YZ, Wu BW, Lu ZD, et al. Circulating Th22 and Th9 Levels in Patients with Acute Coronary Syndrome. Mediat Inflamm 2013; 2013:635672.

JOURNAL OF BIOLOGICAL REGULATORS & HOMEOSTATIC AGENTS Vol. 35, no. 3, 1145-1149 (2021)

LETTER TO THE EDITOR

Latex allergy: advantages of molecular diagnostics during coronavirus

M. De Amici[1], F. Barocci[2], A. Licari[3,4], S. Caimmi[3], A. Marseglia[3], G. Testa[3], C. Torre[5] and G.L. Marseglia[3,4]

[1]Immuno-Allergology Laboratory of Clinical Chemistry and Pediatric Clinic, Foundation IRCCS Policlinic San Matteo, Pavia, Italy; [2]Medicine Unit Laboratory, ASST Rhodense Garbagnate Milanese, Rho, Italy; [3]Pediatric Clinic, Fondazione IRCCS Policlinico San Matteo, Pavia, Italy; [4]Department of Clinical, Surgical, Diagnostic and Pediatric Sciences, University of Pavia, Pavia, Italy; [5]Laboratory of Clinical Chemistry, Fondazione IRCCS Policlinico San Matteo, Pavia, Italy

Received January 11, 2021 – Accepted May 21, 2021

To the Editor,

Although in 1927 Stern described for the first time the allergic reactions to natural rubber latex (NRL), only in recent decades a significant effort has been made to reduce the incidence of latex allergy. Latex is a whitish milky secretion containing many substances of which about only 2% are proteins. Most are removed when the latex is processed, only a small fraction remains in the finished product which is involved in the onset of allergic reactions. Some commercial firms have carried out intense research to reduce the protein content (through double or triple centrifugation). Latex is present in much of the healthcare equipment used, such as catheters, balloons, nasogastric tubes, gloves, urinary catheters, endotracheal tubes, ventilation tubes. During latex processing chemical antioxidants are added which can also cause type IV hypersensitivity reactions. Since 1979 IgE-mediated allergy to NRL has been recognized as a major health problem, with vast economic implications, especially in patients who are candidates to surgical operations (1). Latex allergy caused by gloves worn or aerosol particle inhalation has also become frequent among healthcare professionals.

The coronavirus disease pandemic 2019 (COVID-19) has led to an increase in the use of latex aids, therefore, in allergic conditions, a correct diagnostic evaluation is advantageous. In fact, in relation to the pandemic, there has been a notable increase in the use of latex gloves in both work and private environments, as it is the material that maintains integrity longer during use, for example, compared to vinyl ones which break more easily and do not mould to the hand. The use of latex gloves helps prevent infections only through correct use - they must be appropriately disposed of and changed every time after use [according to the instructions of the Istituto Superiore di Sanità (ISS)]. The need for Personal Protective Equipment (PPE) can create problems for latex allergic individuals and is also a risk for others who may unintentionally develop a latex allergy from repeated use of this type of glove.

In the 1980s, there was an increased demand for latex gloves to protect healthcare workers resulting in a latex allergy epidemic with various symptoms, from contact dermatitis, itchy, watery eyes and nose, asthma and anaphylaxis. Therefore, it is essential not to forget what was learned in the 1980s and 1990s

Key words: latex; molecular diagnostics; COVID-19

Corresponding Author:
Dr Fiorella Barocci,
Medicine Unit Laboratory,
ASST Rhodense - Garbagnate Milanese,
Rho (Milan), Italy
Tel.: +39 3385065564
e-mail: fiorellabarocci@yahoo.it

0393-974X (2021)
Copyright © by BIOLIFE, s.a.s.
This publication and/or article is for individual use only and may not be further reproduced without written permission from the copyright holder.
Unauthorized reproduction may result in financial and other penalties
DISCLOSURE: ALL AUTHORS REPORT NO CONFLICTS OF INTEREST RELEVANT TO THIS ARTICLE.

regarding the potential development of latex allergy and prevent exposure to already allergic individuals.

According to the publications in "The Journal of The European Academy of Dermatology and Venereology" the dermatologists of Lecco Hospital found that a large number of patients hospitalized with ongoing COVID-19 infection, but also asymptomatic ones, who had skin lesions of the extremities (hands, feet): red spots, swelling and itching/burning sensation. Therefore, it is essential to distinguish COVID-19-related cutaneous manifestations from other closely resembling skin lesions, including -allergic skin reactions to latex.

Latex allergy may outbreak as an immuno-mediated mechanism associated with clinical symptoms, including immediate reactions via immunoglobulins and/or the delayed reactions mediated by lymphocytes. These are also known as allergic contact dermatitis and are caused by sensitization to rubber products induced by additives such as thiurams, carbamates, mercaptans, diphenyl guanidine, and antioxidants, which prevent deterioration of the rubber. The IgE-mediated allergy is caused by direct contact of the products in latex with the skin or by inhalation of airborne latex particles. The protein part of the latex stimulates the production of specific IgE (sIgE) with their corresponding antibody response and it is possible to relate awareness of latex reaction to the development of symptoms such as rhinitis, conjunctivitis and/or allergic asthma (1), however, in addition, anaphylactic reactions are also possible (2). The allergenic sources for the population at risk are surgical and domestic gloves, catheters, condoms,

Table I. *The two main allergens of latex*

Major Allergen	**Characteristics**
Hev b 1 (14,6KdA)	An insoluble allergenic latex specific protein insoluble in water and located on the surface of the rubber particles of larger size
Hev b 3 (24kDa)	An insoluble allergenic protein located on the surface of the rubber particles of smaller dimensions. HEV b 1 and HEV B 3 are strongly associated with latex allergy in subjects exposed to repeated surgical operations

Table II. *Major allergens of latex with important cross-reactive properties towards foods*

Major Allergen	**Characteristics**
Hev b 5 (16 kDa)	A powerful heat stable allergenic. The protein is homologous to protein fractions identified in kiwi and potato. The IgE positivity specifications are prevalent in HCW patients
Hev b 6.02 (5 kDa)	A small allergenic protein (hevein) cross-reacting with avocado, chestnut, banana, kiwi. Despite the considerable cross-reactivity between these allergens, no correlation was found between latex-fruit syndrome and hevein sensitization or hevein-like domains. Specific IgE are significantly prevailing in HCW.

accessories for the cleaning of washable rubber, hemostatic laces, pacifiers for children and balloons and toys. These are just some examples of articles that may contain latex proteins capable of causing IgE-mediated allergy.

Hepner and Castells published an extensive list of latex-containing products used in operating theaters, in post-anesthesia, in the care unit, in addition to those presently available in the community, together with alternative latex-free products. The exposure to natural rubber latex may be either direct by skin or mucous membrane contact, or by inhalation. Children with spina bifida (SB), health care workers (HCWs), subjects with a history of several surgical procedures, non-HCWs with exposure to latex such as chemical and pharmaceutical products, food chain workers, cleaners, workers in greenhouses, hairdressers, workers in the food industry and 'rubber industry', and subjects with food allergy and atopy, belong to a group with a high risk of developing an allergy to NRL3. To date, characterized and standardized allergenic extracts have been used to determine specific IgE; however, molecular biology has finally provided more accurate tools and bypassed the problem of standardization of the complex and heterogeneous extracted NRL.

The most common worldwide serum testing detects bound IgE using an enzymatic reagent in an *in-vitro* assay. Serological diagnostics has evolved with the identification and use of the individual antigenic components. The use of recombinant allergens allows to identify the allergenic profile of each patient which allows the clinician to make accurate assessments. The individual molecular components must be used when the latex (k82) has a concentration >1KUA/l. Without specialist request, it is preferred, on the advice of clinical allergologists, to have cut-off > 1 KUA/l "recommended" to execute recombinants. Otherwise a cut-off > 0.1 KUA/l remains valid (3). Therefore, the Component Resolved Diagnosis (CRD) provides for the use of the following molecular components in allergological diagnostics *in vitro*: (k215) Hev b 1, (k217) Hev b 3, (k218) Hev b 5, (k219) Hev b 6.01 , (k220) Hev b 6.02, (k222) Hev b 9, (k224) Hev b 11 e (k221) Hev b 8 (profilin). One or more profiles may be created according to the characteristics of the sample (child, HCW, preoperative) or provide text reflex without distinction of the origin.

Recently 15 different allergenic latex components have been well characterized for their biological function, physiological role and, above all, for their allergenic potential (www.allergen.org) and have been officially recognized and nominated by WHO/IUIS (Subcommittee on the nomenclature of allergens). Modern research has led to the purification of natural and recombinant allergenic proteins from NRL, referred to as Hev b 1, 2, 3, 5, 6, and 15, identified as main allergens of *Hevea brasiliensis* (4, 5). The proteins of the rubber particles comprise the two main allergens Hev b 1 and Hev b 3, both strongly associated with latex allergy in SB patients (6) (Table I). Other proteins are also found in the latex, which play major allergens but with important cross-reactive properties towards foods (Table II).

Table III. *Latex proteins and cross-reactivity*

Major Allergen	**Characteristics**
Hev b 8 (15 kDa)	An allergenic protein aspecific latex also present in all eukaryotic cells. It is equipped with a high level of similarity with the other profilins, however it contains certain uncommon epitopes. Hev b 8 is an important mediator of cross-reactivity between pollen and common fruits, or exotic or tropical fruits. In view of the panallergenic nature of profilin, recognition of IgE anti Hev b 8 should not be taken as proof of primary sensitisation to latex.
Hev b 11 (32 kDa)	An allergenic protein that shows a strong similarity with other molecules of the same family present in fruits such as chestnuts, avocado and banana.

Latex fruit syndrome Hev b 2 (β-1,3-glucanase) PR-2 are enzymes widely spread in the plant kingdom and common epitopes have been identified in the 1-3 β-glucanase of tomato, potato, pepper, banana, latex, Ole e 9 and birch and ash pollen (Palomares, CEA 2005), but also in avocado, chestnut, banana, kiwi, fig (Breiteneder et al. JACI 2000). IgE directed against the protein part of Hev b 2 are found in subjects with food allergy, while those directed against the carbohydrate part of Hev b 2 are found in subjects without food allergy (Breiteneder H, personal communication)

Finally, like profilin Hev b 8, two smaller molecules can create immunological interferences, being ubiquitous proteins in higher organisms as highly cross-reactive panallergens in the plant world. A significant percentage of patients allergic to pollen is sensitized to profilin, giving rise to cross-reactivity serological tests with latex and various common fruits (kiwi, banana) or tropical or exotic fruits (avocado, pineapple) (Table III).

Molecular diagnostics uses the most important latex components by determining allergen sensitization profiles in the different groups of latex allergic patients (7, 8) (Fig. 1). The evaluation of the distribution of latex allergens inside and outside the gloves showed a higher concentration of Hev b 5 and Hev b 6.02 on the inside, while Hev b 1 and Hev b 3 on the outside, confirming a close relationship between the different localization of allergens. This implicates a different sensitization pathway according to the different groups of the population at risk and the resulting selectivity of the IgE specific response (9).

Molecular-specific diagnosis of latex is an important tool to obtain a precise assessment in patients with medical risk, allowing an appropriate strategy of intervention and/or avoidance, significantly reducing the risks and healthcare costs. Serum IgE_tests that use highly purified allergens or recombinant involve less risks for the patient, unlike the prick tests where the patient has a high risk of anaphylaxis. Furthermore, prick tests may be influenced by the assumption of interfering with essential drugs or may not be feasible to people with

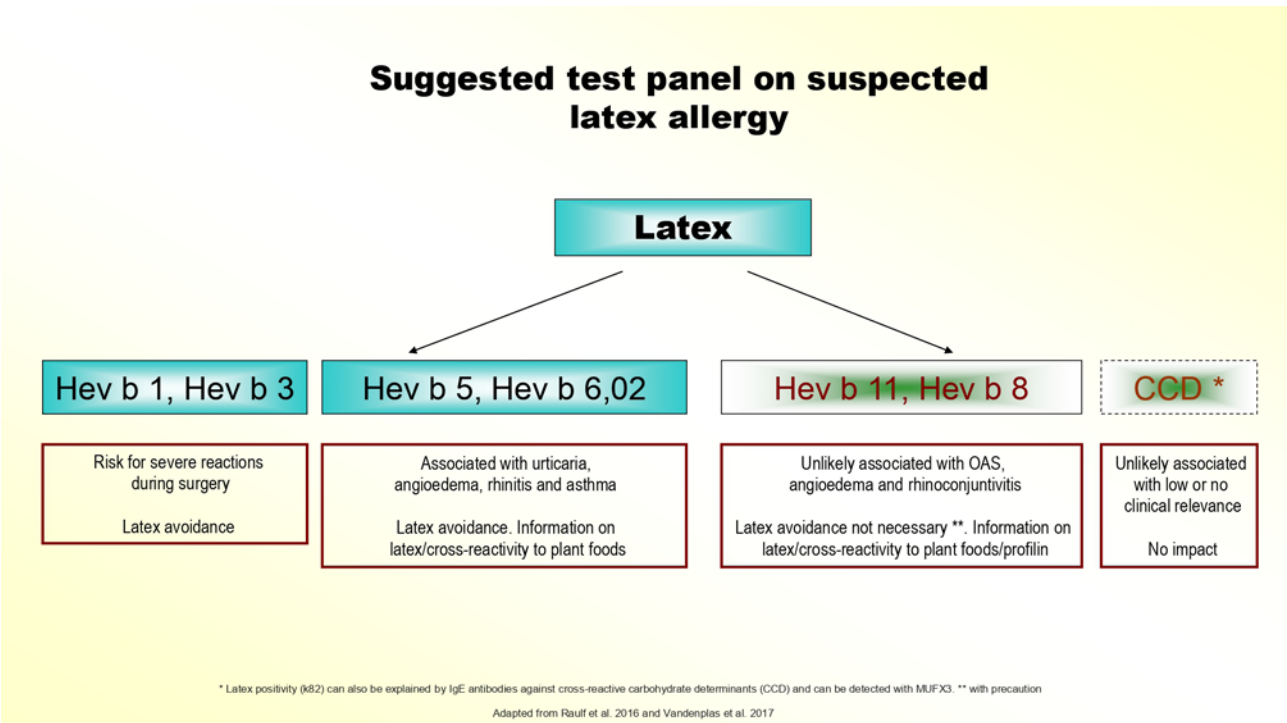


Fig. 1. *The most important latex components*

skin conditions unsuitable for skin tests. Moreover, the development of screening test with multiple or multiplex allergens tests identifies multiple specific IgEs, even for latex recombinants, requiring a small blood volume and making these tests more useful in childhood (10).

In clinical practice the central role of CRD in latex sensitization is currently to distinguish between true allergic disease and a mono-sensitization to profilin. The absence of a clear correlation between specific allergenic proteins and clinical pictures of latex allergy makes CRD of little use in this regard. The preventive identification of subjects predisposed to latex-fruit syndrome based on sensitivity to specific molecules will be more useful in the future.

Undoubtedly, a more accurate diagnosis based on molecular components can better define the patient's sensitization profile, and consequently set up an immunotherapy tailored to the individual patient (patient-tailored immunotherapy) (11).

Precision medicine (PM) represents a potentially more significant relevance in an emerging coronavirus pandemic in order to allow the selection of specific preventive measures. Applying PM premises in an emerging coronavirus pandemic acquires potentially more significant relevance to allow the selection of specific preventive measures and biomarkers that will be useful in disease management (12).

ACKNOWLEDGEMENTS

The Authors would like to thank Prof. Onorario Dr. Luigi Nespoli Varese Insubria University for the scientific review, and Dr Francesco Laureti for the scientific contribution.

REFERENCES

1. Vandenplas O, Raulf M. Occupational latex allergy: the current state of affairs. Curr Allergy Asthma Rep 2017; 17:14
2. Panesar SS, Javad S, de Silva D, et al. The epidemiology of anaphylaxis in Europe: a systematic review. Allergy 2013; 68:1353-61
3. Bernardini R, Novembre E, Lombardi E, et al. Risk factors for latex allergy in patients with spina bifida and latex sensitization. Clin Exp Allergy 1999; 29(5).
4. Kurup VP, Sussman GL, Yeang HY et al. Specific IgE response to purified and recombinant allergens in latex allergy. Clin Mol Allergy 2005; 3:11.
5. Raulf-Heimsoth M, Rihs HP, Rozynek P. et al. Quantitative analysis of immunoglobulin E reactivity profiles in patients allergic or sensitized to natural rubber latex (Hevea brasiliensis). Clin Exp Allergy 2007; 37:1657-67
6. Scala E, Alessandri C, Palazzo P, et al. IgE recognition patterns of profilin, PR-10, and tropomyosin panallergens tested in 3,113 allergic patients by allergen microarray-based technology. PLoS One 2011; 6:e24912.
7. Vandenplas O, Raulf M. Occupational latex allergy: the current state of affairs. Curr Allergy Asthma Rep 2017; 17:14.
8. Raulf M. EAACI Molecular Allergology User's Guide. Pediatr Allergy Immunol 2016; 27:1-250.
9. Peixinho C, Tavares-Ratado P, Tomás MR, et al. Latexallergy: new insights to explain different sensitization profiles in different risk groups. Br J Dermatol.2008; 159:132-6
10. Ansotegui IJ, Melioli G, Canonica GW, et al. IgE allergy diagnostics and other relevant tests in allergy, a World Allergy Organization position paper. World Allergy Organization Journal (2020).
11. Valenta R, Twaroch T, Swoboda I. Component-resol-ved diagnosis to optimize allergen-specificimmunothera-py in the Mediterranean area. J Investig Allergol ClinImmunol. 2007; 17:36-4.
12. Crisci CD, Ardusso LRF, Mossuz A, Müller L. A Precision medicine approach to SARS-CoV-2 pandemic management Curr Treat Options Allergy 2020; 8:1-19. doi: 10.1007/s40521-020-00258-8.

LETTER TO THE EDITOR

Hypertonic saline with xylitol and hyaluronate may shorten the viral shedding duration in asymptomatic COVID-19 positive subjects: a pilot study

G. Ciprandi[1], I. La Mantia[2], F.P. Brunese[3], Al. Varricchio[4] and At. Varricchio[5]

[1]Allergy Clinic, Casa di Cura Villa Montallegro, Genoa, Italy; [2]ENT Department, University of Catania, Catania, Italy; [3]Primary Care Paediatrics, ASL Caserta, Italy; [4]ENT Department, Ospedale Santobono, Naples, Italy; [5]UOSD Video-Endoscopia delle VAS, P.O. San Gennaro – ASL Napoli 1-centro, Naples, Italy

Received March 16. 2021 – Accepted May 27, 2021

To the Editor,

Coronavirus disease 19 (COVID-19) is a new pandemic that has affected more than 80 million people. COVID-19 is caused by a new coronavirus strain, acute respiratory syndrome coronavirus-2 (SARS-CoV-2). COVID-19 may range from asymptomatic to severe acute respiratory syndrome and coagulative disorder, causing the death of up to 3% of patients (1). However, significant differences exist between countries concerning the incidence, spread, severity, and mortality rates (2).

The World Health Organization defined diagnostic criteria and measures to mitigate and contain the outbreak worldwide. In particular, real-time reverse transcription-polymerase chain reaction (RT-PCR) is the gold standard to confirm COVID-19. Usually, molecular testing requires the collection of a specimen using a nasal swab. Moreover, negative molecular testing also establishes recovery after at least three symptomless days (3). In the general population, screening epidemic outbreaks could reveal asymptomatic COVID-19 carriers in many tested subjects. It is easy to find asymptomatic subjects in the contacts of COVID-19 patients, mainly cohabitants. The health agencies established specific rules to contain the pandemic spread, including isolation for confirmed COVID-19 patients and quarantine for their cohabitants or contacts. Return to the community is possible only after negative RT-PCR testing.

The shedding of viral RNA from respiratory droplets appears to outlast symptoms, and a rapid decline does not always follow seroconversion in viral load. Even asymptomatic COVID-19 may experience a long wait before achieving negative testing. The duration of viral shedding depends on various factors, including the host's ability to clear the virus, viral load, the integrity of the immune system, and therapeutical intervention (4). Moreover, there are discordant outcomes from the relevant studies, i.e., one study reported shedding duration up to 37.8 days after the initial diagnosis (5), and another found immunocompromised patients may prolong viral shedding for two months and more (6).

There is still no specific treatment for COVID-19. The Italian Agency for Drugs (AIFA) released Guide Lines to manage COVID-19 at home (7). This document establishes that symptomless positive subjects do not require any treatment apart from active observation over time. However, as viral

Key words: viral shedding; symptomless COVID-19; aerosolization; topical antibiotics; hyaluronic acid; hypertonic saline; xylitol

Corresponding Author:
Dr Giorgio Ciprandi,
Allergy Clinic,
Casa di Cura Villa Montallegro,
Genoa, Italy
e-mail: gio.cip@libero.it

0393-974X (2021)
Copyright © by BIOLIFE, s.a.s.
This publication and/or article is for individual use only and may not be further reproduced without written permission from the copyright holder.
Unauthorized reproduction may result in financial and other penalties
DISCLOSURE: ALL AUTHORS REPORT NO CONFLICTS OF INTEREST RELEVANT TO THIS ARTICLE.

shedding may persist for a long time, they should observe quarantine also for weeks if not for some months. This fact results in severe social and economic problems.

It has been reported that nasal saline irrigation might be a safe and beneficial remedy in patients with mild COVID-19 (8). Nasal irrigation with hypertonic saline (HS) for the common cold reduced illness duration by 22%, use of symptomatic medications by 36%, and spread into the family by 35%, as well as viral load, as NaCl has an antiviral effect (9). We previously reported that nasal nebulization of a medical device with hypertonic saline (3%) solution, high-molecular-weight sodium hyaluronate 0.2%, and xylitol 5% improved smell dysfunction in COVID-19 patients (10).

As many cohabitants of COVID-19 patients may continue to be positive to RT-PCR testing for an extended period, the current study explored the possibility of shortening the duration of viral shedding in asymptomatic COVID-19 subjects.

MATERIALS AND METHODS

The current study included 172 subjects (80 males and 92 females, aged between 18 and 75 years) with asymptomatic COVID-19 as cohabitants of COVID-19 patients. Inclusion criteria were: adulthood, SARS-CoV-2 infection confirmed by positive molecular testing by nasal swab, the complete absence of symptoms, to be a member of a family with one COVID-19 patient. Exclusion criteria were symptomatic COVID-19, concomitant comorbidity, or current treatment able to interfere with interpretation of the results. The study was performed according to the Helsinki Conference ethical rules, and the internal review board approved the procedure. Each subject signed informed consent.

For nebulization therapy, a medical device was used: a 5 mL solution containing hypertonic saline (3%), high-molecular-weight sodium hyaluronate 0.2%, and xylitol 5% (Aluneb iper, Sakura Italia, Lonato del Garda, Italy). The inhaled therapy was performed using the nasal douche Rinowash (Airliquide Medical System, Italy) that was connected to an aerosol nebulizer with a pneumatic compressor (1.5 bar per 5 L/min) Nebula (Air Liquide Medical Systems, Italy). This nasal device allows the nebulization of particles with a median aerodynamic diameter > 10 microns over a nebulization time of 60-90 seconds for each application. The nebulization therapy was administered twice a day for seven days and started after at least a second positive molecular testing performed one week after the first. Patients were advised to manage the device following hygienic measures to avoid contamination. In addition, the device includes a containment chamber of the liquid returning from the nasal cavities. The nasal swab for molecular testing was repeated after seven days. A group of asymptomatic COVID-19 subjects refused any treatment and served as controls.

RESULTS

The study globally included 172 subjects. Sixteen COVID-19 patients had one cohabitant relative with asymptomatic COVID-19, 24 patients had two positive relatives, and 36 patients had three family members positive for RT-PCR testing. All subjects were positive at the second testing, i.e., on the 14th day. Seventy-two subjects performed therapy from the 7th to the 14th day. All of them were negative at the nasal swab testing performed on the fourteenth day. Sixty-three subjects performed therapy from the 14th to the 21st day. All of them were negative at the nasal swab testing performed on the 21st day. Thirty-seven subjects did not use any medication and were negative on the 28th day. All treated patients completed the therapy. The treatment was safe and well-tolerated in all treated subjects.

DISCUSSION

COVID-19 pandemic affected many people also through healthy carriers. Asymptomatic COVID-19 subjects are contagious as well as symptomatic patients. Moreover, viral shedding can persist for an extended period also in asymptomatic subjects. Nasal irrigation with saline solution is currently the only method that has been recommended in mild COVID-19. At present, only one ongoing study investigated the efficacy and safety of nasal irrigation in outpatients with mild COVID-19 (11). The study compared HS with HS plus 1% surfactant or no intervention. The interim analysis demonstrated that nasal irrigation significantly shortened symptom

duration, mainly concerning nasal congestion and headache. The authors also hypothesized that HS and surfactant could reduce viral shedding.

Subjects positive to the molecular test but without symptoms should be submitted to quarantine and repeat a nasal swab after 14 days. The Italian legislation established only observation for these subjects. The practical problem may occur when a positive test persists for an extended period, causing relevant inconvenience.

The current experience showed that a 7-day course using a medical device containing HS, hyaluronate, and xylitol shortly cleared viral shedding in asymptomatic COVID-19. The intriguing outcome was the rapid viral clearance achieved by the treated participants. Untreated subjects became negative to RT-PCR only after 28 days, whereas treated subjects achieve negativity after one course of topical therapy one or two weeks earlier.

Hypertonic saline solution has many well-known advantages on upper airways, removing secretion and reducing nasal congestion, opening and cleaning the nose, and improving viral clearance, as it has antiviral activity. Hyaluronic acid (HA) has many activities, including activation of innate immunity against viral pathogens, resolution of the inflammatory cascade, moistening respiratory mucosa, and cytoprotection of the epithelial barrier (12). Xylitol exerts an antiviral activity, modulates the immune system, and has decongestant and fluidifying upper airway activity (13). Therefore, these three components provide beneficial effects of this medical device. Moreover, the Rhinowash nasal device contributed to a quick and effective administration of the product. The current outcomes suggest that therapy with a medical device containing HS, HA, and xylitol could shorten viral shedding in asymptomatic COVID-19 subjects.

On the other hand, the current experience has some limitations, including the open study design, the lack of placebo control. This study was preliminary and cannot be considered proof of actual effectiveness in COVID-19 patients. Consequently, further studies should be conducted to answer these unmet needs.

In conclusion, the current experience seemed to suggest that a medical device with HS, HA, and xylitol adequately nebulized into the nose by a specific nasal douche could shorten the time of viral shedding in asymptomatic subjects positive to RT-PCR for RNA of SARS-CoV-2.

REFERENCES

1. Johns Hopkins Coronavirus Resource Center. https://coronavirus.jhu.edu/(2020).
2. Kamps BS, Hoffmann C. COVID refernce 2020.5. https://www.CovidReference.com
3. WHO - Country & Technical Guidance - Coronavirus disease (COVID-19) https://www.who.int/emergencies/diseases/novel-coronavirus-2019/technical-guidance
4. Qu Y-M, Kang E-M, Cong H-Y. Positive result of Sars-Cov-2 in sputum from a cured patient with COVID-19. Travel Med Infect Dis 2020; 34:101619.
5. Agarwal V, Venkatakrishnan AJ, Puranik A, et al. Long-term SARS-CoV-2 RNA shedding and its temporal association to IgG seropositivity. Cell Death Discovery 2020; 6:138.
6. Nakajima Y, Ogai A, Furukawa K, et al. Prolonged viral shedding of SARS-CoV-2 in an immunocompromised patient. J Infect Chemother 2021: 27(2):387-9.
7. AIFA - Farmaci utilizzabili per il trattamento della malattia COVID-19 https://www.aifa.gov.it/aggiornamento-sui-farmaci-utilizzabili-per-il-trattamento-della malattia-covid19
8. Farrell NF, Klatt-Cromwell C, Schneider JS. Benefits and safety of nasal saline irrigations in a pandemic-washing COVID-19 away. JAMA Otolaryngol 2020; 146(9):787-8.
9. Ramalingam S, Graham C, Dove J, et al. A pilot, open-labeled, randomized controlled trial of hypertonic saline nasal irrigation and gargling for the common cold. Sci Rep 2019; 9:1015
10. Varricchio A, La Mantia I, Brunese FP, Ciprandi G. Smell recovery in patients with COVID-19: an experience with nebulized nasal treatment. J Biol Reg Hom Ag 2021; 35(2).
11. Kimura KS, Freeman MH, Wessinger BC, et al. Interim analysis of an open-label randomized controlled trial evaluating nasal irrigations in non-hospitalized patients with coronavirus disease 2019. Int Forum Allergy Rhinol 2020; 10(12):1325-28.

12. Jiang D, Liang J, Noble PW. Hyaluronan as an immune regulator in human disease. Physiol Rev 2011; 91(1):221-64.

13. Salli K, Lehtinen MJ, Tiihonen K, et al. Xylitol's health benefits beyond dental health: a comprehensive review. Nutrients 2019; 11(8):1813.

LETTER TO THE EDITOR

Viral shedding in symptomatic patients with mild COVID-19: an experience with nebulized nasal treatment

At. Varricchio[1], I. La Mantia[2], F.P. Brunese[3], Al. Varricchio[4] and G. Ciprandi[5]

[1]UOSD Video-Endoscopia delle VAS, P.O. San Gennaro - ASL Napoli 1-centro, Naples, Italy; [2]ENT Department, University of Catania, Catania, Italy; [3]Primary Care Paediatrics, ASL Caserta, Italy; [4]ENT Department, Ospedale Santobono, Naples, Italy; [5]Allergy Clinic, Casa di Cura Villa Montallegro, Genoa, Italy

Received March 16, 2021 – Accepted May 27, 2021

To the Editor,

A new coronavirus strain, severe acute respiratory syndrome coronavirus-2 (SARS-CoV-2), has caused the most critical pandemic in the last century. Namely, coronavirus disease 19 (COVID-19) has implicated more than 100 million confirmed cases of COVID-19, including almost 3 million deaths, reported to The World Health Organization (WHO). COVID-19 may range from asymptomatic appearance to severe acute respiratory syndrome and coagulative disorder, causing the deaths of up to 3% of patients (1). However, significant differences exist among countries concerning the spread, severity, and mortality rates (2). The WHO defined diagnostic criteria and measures to mitigate and contain the outbreak worldwide. In particular, molecular testing (RT-PCR) by nasal swab is the gold standard to confirm COVID-19.

Negative molecular testing also establishes recovery after at least three symptomless days (3). However, the duration of viral shedding depends on several factors, including the host's ability to clear the virus, viral load, the integrity of the immune system, and therapeutical intervention (4). Moreover, there are discordant outcomes from the studies published to date. Agarwal and colleagues retrospectively evaluated 851 COVID-19 patients, reporting a shedding duration up to 37.8 days after the initial diagnosis (5). Positive molecular testing can persist even for a long time; for example, an immunocompromised patient prolonged viral shedding for two months (6).

There is still no specific treatment for symptomatic cases. The Italian Agency for Drugs (AIFA) released Guide Lines for treating COVID-19 at home (7). However, there is no mention of the topical treatment of upper respiratory tract infection. In this regard, nasal saline irrigation might be a safe and beneficial remedy in patients with mild COVID-19 (8). This consideration is derived from a study which demonstrated that nasal irrigation with hypertonic saline (HS) for the common cold reduced illness duration by 22%, use of symptomatic medications by 36%, spread into the family by 35%, and viral load, as NaCl has an antiviral effect (9). Thus, a galenic preparation, containing isotonic thiamphenicol 125 mg diluted in 4 mL in a medical device with saline solution, high-molecular-weight sodium hyaluronate at 0.2%, and xylitol 5%, administered by the nasal douche Rhinowash, reduced symptom perception, spotting, neutrophil, and bacteria count in children with acute rhinopharyngitis (10). More recently, we

Key words: viral shedding; mild COVID-19; aerosolization; topical antibiotics; hyaluronic acid; hypertonic saline; xylitol

Corresponding Author:
Dr Giorgio Ciprandi,
Allergy Clinic,
Casa di Cura Villa Montallegro,
Genoa, Italy
e-mail: gio.cip@libero.it

0393-974X (2021)
Copyright © by BIOLIFE, s.a.s.
This publication and/or article is for individual use only and may not be further reproduced without written permission from the copyright holder.
Unauthorized reproduction may result in financial and other penalties
DISCLOSURE: ALL AUTHORS REPORT NO CONFLICTS OF INTEREST RELEVANT TO THIS ARTICLE.

reported that the nebulization of the same medical device restored the olfaction in COVID-19 patients (11). Based on this background, the current study explored the possibility of shortening the duration of viral shedding in patients with mild COVID-19.

MATERIALS AND METHODS

The current study included 76 patients (40 males and 36 females, aged between 31 and 65 years) with mild COVID-19, confirmed by nasal swab positive molecular testing. The inclusion criteria were: adulthood, COVID-19 diagnosis documented by molecular test, and mild symptoms, including fever lower than 37.5°C, dry cough, malaise, and smell and taste impairment, lasting no more than three days. Exclusion criteria were severe COVID-19, requiring hospitalization and pharmacological treatment, concomitant comorbidity, or current treatment which could interfere with the results. The study was carried outaccording to the Declaration of Helsinki, and the internal review board approved the procedure. Each patient signed informed consent for participation.

Nebulization therapy used a galenic preparation, including tobramycin 0.45% and lincomycin 0.75% diluted in 5 mL of a medical device, containing hypertonic saline (3%), high-molecular-weight sodium hyaluronate 0.2%, and xylitol 5% (Aluneb iper, Sakura Italia, Lonato del Garda, Italy), manufactured by Laboratori Farmaceutici Orlandi (Marcianise, Italy). The inhaled therapy was performed using the nasal douche Rinowash (Airliquide Medical System, Italy) connected to an aerosol nebulizer with a pneumatic compressor (1.5 bar per 5 L/min) Nebula (Air Liquide Medical Systems, Italy). This nasal device allows the nebulization of particles with a median aerodynamic diameter > 10 microns over a nebulization time of 60-90 seconds for each application. The nebulization therapy was administered twice a day for seven days. The patients were advised to manage the device following hygiene measures to avoid contamination. In addition, the device includes a containment chamber of the liquid returning from the nasal cavities. The nasal swab for molecular testing was repeated after ten days. As each patient had at least one cohabitant positive to the molecular test but symptomless, these subjects were considered controls, as they did not take any medication and repeated, as established by the national rules, the nasal swab after two weeks.

RESULTS

All patients completed the seven-day treatment. At the end of the treatment, all patients were symptomless. The molecular testing, performed on the tenth day, showed that all patients had a negative result. The treatment was safe and well-tolerated in all patients. All cohabitants still had positive molecular testing after 14 days.

DISCUSSION

At present, the Italian Agency for Drugs recommends a “wait and see” strategy for mild COVID-19. However, patients with mild COVID-19 often turn to doctors to have symptomatic treatment to resolve respiratory complaints and become negative to nasal swabs quickly.

The current experience showed that a 7-day course of galenic preparation with two antibiotics (tobramycin and lincomycin) diluted in a medical device containing HS, hyaluronate, and xylitol, shortly cleared viral shedding. On the contrary, all symptomless cohabitants persisted in positive molecular testing at the second nasal swab. At present, only one ongoing study investigated the efficacy and safety of nasal irrigation in outpatients with COVID-19 (12). The study compared HS with HS together with 1% surfactant or no intervention. The interim analysis demonstrated that nasal irrigation significantly shortened symptom duration, mainly concerning nasal congestion and headache. The authors also hypothesized that HS and surfactant could reduce viral shedding.

Topical antibiotic therapy may have advantages as it allows for very low dosage, abating adverse events and resistance, arriving directly at the target organ, and dissolving the biofilm. Even though COVID-19 is a viral disease, topical antibiotics could reduce pathogenic factors promoting viral growth, including post-viral dysbiosis and consequent bacterial super-infection, common during viral infection. Hypertonic saline solution has many well-known advantages on upper airways, removing secretion and reducing nasal congestion, opening and cleaning the nose, and improving viral clearance,

and has additional antiviral activity. Hyaluronic acid (HA) has many activities, including activation of innate immunity against viral pathogens, resolution of the inflammatory cascade, moistening respiratory mucosa, and cytoprotection of the epithelial barrier (13). Xylitol exerts an antiviral activity, modulates the immune system, and has decongestant and fluidifying upper airway activity (14). Therefore, these three components provide added beneficial effects to this medical device. Moreover, the Rhinowash nasal device contributed to a quick and effective administration of the galenic preparation.

The current outcomes could suggest that a galenic preparation with topical vancomycin and lincomycin and a medical device containing HS, HA, and xylitol, nebulized by a nasal douche, could shorten viral shedding in mild COVID-19 patients in comparison with untreated cohabitants who had persistent positive molecular testing.

On the other hand, the current experience has some limitations, including the open study design, the lack of adequate control. This study was preliminary and cannot be considered proof of actual effectiveness in COVID-19 patients. Consequently, further studies should be conducted to answer these unmet needs.

In conclusion, the current experience seemed to suggest that a galenic preparation with topical antibiotics, HS, HA, and xylitol adequately nebulized into the nose by a specific nasal device could shorten the time of viral shedding in patients with mild COVID-19.

REFERENCES

1. Johns Hopkins Coronavirus Resource Center. https://coronavirus.jhu.edu/(2020).
2. Kamps BS, Hoffmann C. COVID refernce 2020.5. https://www.CovidReference.com
3. WHO - Country & Technical Guidance - Coronavirus disease (COVID-19) https://www.who.int/emergencies/diseases/novel-coronavirus-2019/technical-guidance
4. Qu Y-M, Kang E-M, Cong H-Y. Positive result of Sars-Cov-2 in sputum from a cured patient with COVID-19. Travel Med Infect Dis 2020; 34:101619.
5. Agarwal V, Venkatakrishnan AJ, Puranik A, et al. Long-term SARS-CoV-2 RNA shedding and its temporal association to IgG seropositivity. Cell Death Discovery 2020; 6:138.
6. Nakajima Y, Ogai A, Furukawa K, et al. Prolonged viral shedding of SARS-CoV-2 in an immunocompromised patient. J Infect Chemother 2021: 27(2):387-9.
7. AIFA - Farmaci utilizzabili per il trattamento della malattia COVID-19 https://www.aifa.gov.it/aggiornamento-sui-farmaci-utilizzabili-per-il-trattamento-della malattia-covid19
8. Farrell NF, Klatt-Cromwell C, Schneider JS. Benefits and safety of nasal saline irrigations in a pandemic-washing COVID-19 away. JAMA Otolaryngol 2020; 146(9):787-8.
9. Ramalingam S, Graham C, Dove J, et al. A pilot, open-labeled, randomized controlled trial of hypertonic saline nasal irrigation and gargling for the common cold. Sci Rep 2019; 9:1015.
10. Varricchio A, Capasso M, Avvisati F, et al. Inhaled hyaluronic acid as ancillary treatment in children with bacterial acute rhinopharyngitis. J Biol Reg Hom Agents 2014; 28(3):537543.
11. Varricchio A, La Mantia I, Brunese FP, Ciprandi G. Smell recovery in patients with COVID-19: an experience with nebulized nasal treatment. J Biol Reg Hom Agents 2021; 35(2).
12. Kimura KS, Freeman MH, Wessinger BC, et al. Interim analysis of an open-label randomized controlled trial evaluating nasal irrigations in non-hospitalized patients with coronavirus disease 2019. Int Forum Allergy Rhinol 2020; 10(12):1325-8.
13. Jiang D, Liang J, Noble PW. Hyaluronan as an immune regulator in human disease. Physiol Rev 2011; 91(1):221-64.
14. Salli K, Lehtinen MJ, Tiihonen K, et al. Xylitol's health benefits beyond dental health: a comprehensive review. Nutrients 2019; 11(8):1813.

LETTER TO THE EDITOR

Immunoregulatory role of circulating endothelial vWF positive cells in patients after acute myocardial infarction

G. Laskarin[1*], M. Rakić[2*], V. Sotošek[3], D. Travica Samsa[2], V. Peršić[2,4], T. Kehler[2], D. Gobić[5], L. Zaputović[5] and D. Rukavina[1,6]

[1]Department of Physiology and Immunology, Faculty of Medicine, University of Rijeka, Rijeka, Croatia; [2]Department of Cardiology, Hospital for Medical Rehabilitation of Hearth and Lung Diseases and Rheumatism "Thalassotherapia-Opatija", Opatija, Croatia; [3]Department of Anaesthesiology, Resuscitation, Emergency and Intensive Care Medicine, Faculty of Medicine, University of Rijeka, Rijeka, Croatia; [4]Department of Medical Rehabilitation, Faculty of Medicine, University of Rijeka, Croatia; [5]Department of Internal Medicine, Faculty of Medicine, University of Rijeka, Rijeka, Rijeka, Croatia; [6]Department of Biomedical Sciences in Rijeka, Croatian Academy of Sciences and Arts, Rijeka, Croatia

Received February 17, 2021 – Accepted May 28, 2021

*These Authors contributed equally to the study.

To the Editor,

The frequency of circulating endothelial cells which express pan-endothelial marker von Willebrand factor (vWF) increases with both endothelial dysfunction and acute myocardial infarction (AMI) (1). Increases in circulating vWF^+ cells correlate with poor clinical outcomes and death in AMI, suggesting that they participate in the pathogenesis of AMI (1, 2). We previously hypothesized that increased vWF^+ cells in the circulation of patients with AMI could act as antigen presenting cells, leading to a direct interaction with NK and T cells and resulting in cytokine secretion, thus enhancing systemic inflammatory reaction and causing additional endothelial damage by cytotoxic potential of lymphocytes (2). This is mostly seen in patients with non-ST-segment elevation myocardial infarction (NSTEMI) who are treated conservatively, as prolonged myocardial ischemia could sustain a local and systemic inflammatory reaction (3, 4). In patients with ST-segment elevation myocardial infarction (STEMI) treated with primary percutaneous coronary intervention (PCI) of the single arterial stenosis responsible for infarct, the inflammation is quenched, whereas it fluctuates for a month in patients with NSTEMI without PCI (2). Under inflammatory conditions, vWF^+ endothelial cells could take on the proinflammatory antigen-presenting phenotype, resembling $CD14^+$ monocytes (2). In patients with AMI, the injured endothelium expresses and secretes interleukin (IL)-15, which is important for T and natural killer (NK) cell proliferation, chemotaxis and binding to endothelial cells, perforin (P) expression, and cytotoxicity (5). P is a cytotoxic mediator constitutively stored in NK cells and induced in T cells, and is released from

Key words: acute myocardial infarction; NK cells; perforin; T cells; von Willebrand factor positive cells

Corresponding Author:
Vlatka Sotosek, M.D., Ph.D.
Anaesthesiology, Resuscitation, Emergency and Intensive Care Medicine, Faculty of Medicine, University of Rijeka, B. Branchetta 20
51000 Rijeka, Croatia
Tel.: + 385 51 65 11 85 - Fax: + 385 51 67 56 99
e-mail: vlatkast@medri.uniri.hr

0393-974X (2021)
Copyright © by BIOLIFE, s.a.s.
This publication and/or article is for individual use only and may not be further reproduced without written permission from the copyright holder.
Unauthorized reproduction may result in financial and other penalties
DISCLOSURE: ALL AUTHORS REPORT NO CONFLICTS OF INTEREST RELEVANT TO THIS ARTICLE.

granules after stimulation to kill targets (6). It is a critical mechanism for the elimination of injured cells (6). However, the dynamics of vWF^+ cells in the circulation and their possible immune functions after AMI are not completely understood. This study investigated the dynamic characteristics and possible interaction of circulating vWF^+ cells with T and/or NK cells in comparison to $CD14^+$ cells in patients with AMI in terms of perforin expression *in vitro*.

MATERIALS AND METHODS

Patients

Patients with AMI who were admitted to the Clinical Hospital Center Rijeka, Croatia, and Special Hospital Thalassotherapia-Opatija, Opatija, Croatia, were enrolled in a prospective study from October 2013 to May 2016. They were treated according to the then current guidelines of the European Cardiac Society (3, 4). All patients with AMI received anti-ischemic therapy (beta-blocker, an angiotensin-converting enzyme inhibitor, statin, acetylsalicylic acid, and clopidogrel). Given the type of AMI and the administration of percutaneous coronary intervention (PCI), patients with AMI were divided into three groups: a) patients with STEMI treated with primary PCI and implantation of one stent in the culprit lesion; b) patients with NSTEMI treated with PCI and implantation of one or two stents in the culprit lesions within the first 24 h; and c) patients with NSTEMI treated conservatively without PCI. Venous peripheral blood (10 mL) samples were taken from all patients with AMI on day one, before PCI (if applied), and on days 7 and 28 during early inpatient cardiac rehabilitation. Blood samples were taken once from healthy subjects who underwent a clinical examination and routine laboratory analyses as part of a preventive medical program. Clinical and laboratory characteristics of patients with AMI and healthy controls are shown in Table I. The exclusion criteria for healthy subjects and patients included generative age in women; chronological age above 80 years for all subjects; unstable angina pectoris; uncontrolled arrhythmia (heart rate >130/min); significant valvular deficiency (Gradus III or IV); congestive heart failure (concentration of N-terminal pro-brain natriuretic protein >150 pg/mL); significant peripheral vascular disease; uncontrolled endocrine disease (plasma glucose >11mmol/L or concentration of thyrotropin-*releasing hormone* >4.20 mU/L); uncontrolled hypertension (systolic blood pressure >180 mmHg or diastolic >100 mmHg); infectious and autoimmune disease; injury to organs and blood transfusions. The Ethics Committees of two hospitals and the Faculty of Medicine, University of Rijeka approved the study according to the "Ethical principles for medical research involving human subjects" in the Declaration of Helsinki outlined by the World Medical Association. All subjects provided written consent for participation in the study.

Routine laboratory analyses

Hematological analysis was performed using an automatic analyzer (Hematology analyzer XS-1000i, Sysmex, Kobe, Japan). Biochemical analysis was determined by a photometric method using Dimension Xpand, (Siemens Healthcare Diagnostics, Newark, DE, USA). Cardiac troponin I (cTn I) was analyzed by the one-step enzyme immunoassay based on the "sandwich" principle with two cTn I-specific monoclonal antibodies in the serum samples using analyzer Dimension RXL (Siemens Healthcare, Diagnostics, New York, DE, USA).

Separation of peripheral blood mononuclear cells

Peripheral blood mononuclear cells (PBMCs) were extracted from 10 ml blood sample by gradient density centrifugation (Lymphoprep, Axis-Shield PoC AS, Oslo, Norway), and centrifuged at 600 × g for 20 min (option without brake). The PBMCs were collected with a Pasteur pipette (Hirschmann Laborgerate GmbH, Eberstadt, Germany) from the interface of the Lymphoprep, resuspended in 10 ml Roswell Park Memorial (RPMI) 1640 media (GIBCO, Gaithersburg, MD, USA) and washed (10 min, 350 x g). The cell-pellet was resuspended in 1 ml of RPMI tissue culture medium [RPMI 1640 supplemented with L-glutamate, (2 mM), penicillin 5 U/L), streptomycin sulfate, (0.05 g/L), 10% fetal calf serum (FCS); all from, Kemika, Zagreb, Croatia] and the cells counted in a Neubauer chamber with Trypan blue stain (Serva, Heidelberg, Germany) using a light microscope (Carl Zeiss, Jena, Germany). Cell viability was always >95%.

Flow cytometry

Labeling of cell markers was performed in isolated PBMCs (2×10^5/sample) from patients with AMI on days 1, 7, and 28, and healthy subjects. Antibodies were obtained

Table I. *Demographic, clinical and laboratory characteristics of patients with acute myocardial infarction*

	Value / number of patients (N)			
	Healthy Control (N28)	**STEMI with PCI (N16)**	**NSTEMI without PCI (N15)**	**NSTEMI with PCI (N17)**
Clinical characteristics				
Male / Female	13/15	12/4	6/9	7/10
Fatal outcome	0/0	0/0	0/2	1/0
Diabetes	0	7	3	3
Arterial hypertension	0	16	15	17
Hyperlipoproteinemia	0	16	8	15
Oral hypoglycemic drugs	0	3	2	3
Insulin therapy	0	1	1	0
Anti-ishemic therapy	0	16	15	17
Coronary culprit lesion (PCI)		LAD (8×), D1 (1×), RCA(6×), OM1(1×)		LAD(11×), D1(1×), D2(1×), RCA(5×), LCX(2×), OM1(1×)
	Value / median (percentile 25th, percentile 75th)			
Age Male (years)	60 (58, 64)	62 (54,71)	62 (54, 70)	60 (55, 69)
Age Female (years)	68 (60, 70)	67 (59, 75)	70 (62, 76)	71 (64, 70)
Body mass index (kg/m2)	25 (22, 27) [a,b] *p = 0.002*	29 (26, 31)	28 (25, 31)	28 (26, 32)
Systolic pressure (mm Hg)	126 (119,130) [a,b] *p = 0.002*	130 (115, 140)	130 (120, 148)	130 (120, 140)
Diastolic pressure (mm Hg)	78 (70, 80) [a, b, c] *p = 0.002*	70 (65, 80)	70 (65, 80)	70 (65, 75)
Laboratory characteristics				
hs CRP (mg/L)	2.85 (1.5, 4.1) [a]*p = 0.0001,* [b,c]*p = 0.001*	13.3 (6.8, 31.1)	15,8 (10.7, 18.9)	11.8 (5.4, 20.4)
CTn I (ng/L)	0.02 (0.01, 0.03) [a,b,c] *p = 0.0006*	33.2 (13, 74.2)	6.3 (2.7, 16.6)	4.1 (1.3, 10)
NT pro-BNP	14 (10.7, 20) [a,b,c] *p = 0.0004*	67 (48, 123)	66 (40, 87)	58 (35, 81)
Erythrocytes ($\times 10^{12}$/L)	4.8 (4.5, 5)	4.4 (4.2, 4.6)	4.2 (4, 4.4)	4.15 (4, 4.6)
Leukocytes ($\times 10^9$ /L)	6.2 (5.3, 7.1) [a] *p = 0.002*	11.8 (10, 13.7)	7.65 (6.5, 8.7)	7.3 (5.4, 8.1)
Thrombocytes ($\times 10^9$ /L)	278 (249, 310) [a] *p =0.002*	188 (135, 197)	302 (173, 305)	228 (172, 256)
AST (IU/L)	18 (14, 19) [a] *p = 0.0000*	77 (40, 137)	19 (16, 25)	15 (13, 53)
ALT (IU/L)	20 (17, 23) [a] *p = 0.0001*	49.4 (35, 60)	19 (14, 21)	28 (18, 83)
Urate (μmol/L)	314 (264, 384) [a] *p =0.001*	428 (406, 454)	345 (286, 414)	314 (264, 344)
Creatinine (μmol/L)	87 (85, 92)	86 (63.5, 121)	90 (82, 110)	82.5 (76, 118)
Glucose (mmol/L)	5.6 (5.3, 5.9)	8 (6.7, 8.9)	8.7 (7.7, 9.1)	5.5 (5, 7.7)
LDL cholesterol (mmol/L)	3,2 (1.9, 3.8)	3.9 (3.4, 4.1)	2.2 (1.7, 2.9)	2.2 (1.9, 2.7)
HDL cholesterol (mmol/L)	1.8 (1.6-2.3) [a] *p = 0.0006*	1.3 (1-1.4)	0.8 (0.7-1.4)	1 (0.8, 1.3)
Triglicerides (mmol/L)	0.9 (0.6, 1.1) [a] *p= 0.0001*	2 (1.9, 3.1)	0.9 (0.9-1.2)	1.1 (1, 1.3)

*ALT: alanine transaminase; AST: aspartate transaminase; D1: the first diagonal artery; D2: the second diagonal artery; ESR: erythrocyte sedimentation rate; HDL: high density lipoprotein; hsCRP: high sensitive C: reactive protein; CTn I: cardiac troponin I; LAD: left anterior descending artery; LCX: the left circumflex artery; LDL: low density lipoprotein; NT proBNP: N-terminal pro brain natriuretic peptide; OM1: the first obtuse marginal artery; RCA: right coronary artery. *a (control vs STEMI with PCI); b (control vs NSTEMI with PCI); c (control vs NSTEMI without PCI).*

from BD Biosciences (San Jose, USA), and used at 20 μL/10^6 cells for 30 min at 4°C, unless otherwise indicated. All washes (2 × 5 min at 400 × g) were performed in fluorescence-activated cell sorter (FACS) buffer [NaCl (140 mM), KH_2PO_4 (1.9 mM), Na_2HPO_4 (16.5 mM), KCl (3.75 mM) (all from Kemika), Na_2EDTA (0.96 mM, Fluka, Buchs, Switzerland), NaN_3 (1.5 mM, Difco, Detroit, Michigan, USA)], except in intracellular antigen labeling, when saponin buffer [0.1% saponin (Sigma, Poole, Dorset, USA), 2% fetal calf serum in phosphate-buffered saline (PBS: $NaHPO_4 \times 12H_2O$ 33.9 mM, NaCl 136.8 mM, KH2PO4 3 mM of distilled water, all from Kemika) 0.05% bovine serum albumin (Sigma, Poole, Dorset, USA)] was used. Samples were initially incubated with 10% heat-inactivated fetal calf serum (Gibco) for 20 min at room temperature (RT) to block Fc receptor binding and washed. The pellet was resuspended, and the cells indirectly labeled with vWF monoclonal antibody (mAb) (mouse IgG1, 3E2D10, Abcam, Cambridge, UK, dilution 1:100) or CD14 mAb (mouse IgG2a, M5E2, dilution 1:100) followed by incubation with secondary goat anti-mouse (GAM) polyclonal antibodies conjugated with fluorescein isothiocyanate (FITC). In some samples, HLA DR, CD80, or CD86 were labeled by the addition of phycoerythrin (PE)-conjugated anti-HLA-DR mAb (mouse IgG2a, G46-6), anti-CD80 mAb (mouse IgG1, L307.4), or anti-CD86 mAb (mouse IgG1, FUN-1), respectively. During magnetic separation, cell fractions were single labeled using unconjugated antibodies directed toward vWF, CD14 or CD1a, (mouse IgG1, OKT-6, Department of Immunology and Inflammation, Clinical Institute Humanitas, Rozzano, Italy, dilution 1:100), PE-conjugated CD56 mAb (mouse IgG1, B159) and FITC conjugated CD3 (mouse IgG1, UCHT1). Detection of IL-15 was performed in permeabilized and pre-labeled vWF^+ cells, according to the principle of the method described earlier (7). Briefly, freshly isolated PBMCs (10⁶/mL) were incubated with phorbol-myristate-acetate (PMA, 10 ng/mL), ionomycin (1 μM), and monensin (3 μM) (all from Sigma-Aldrich Chemie, Steinheim, Germany) for 5 h at 37°C, in a humidified atmosphere containing 5% CO_2. Then, non-specific binding was blocked, and the cells were labeled using anti-vWF mAb and GAM-FITC. Next, the cells were fixed in 4% paraformaldehyde (Kemika, Zagreb, Croatia), pH 7.4 for 10 min at RT, washed, and permeabilized in 100 uL saponin buffer for 20 min at RT. PE-conjugated IL-15 mAb (mouse IgG1, 34559, R&D Systems, Minneapolis, USA, 20 μL/10^6 cells) was added into cell samples. After two washes in saponin buffer, the cells were resuspended in 1 mL of FACS buffer to restore membrane integrity, washed in FACS buffer, and resuspended in 200 μL of 2% paraformaldehyde. P was detected in CD3/CD56 labeled cells after coculture with purified vWF^+ cells, $CD14^+$ or $CD14^-$ cells at cell ratios 2.5 and 5:1, or after culture in medium only for 18 h at 37°C in a humidified atmosphere with 5% CO_2. P was labeled intracellularly using unconjugated anti-P mAb (mouse IgG2b, δG9, Department of Physiology and Immunology, Medical Faculty University of Rijeka, Rijeka Croatia, 3μg/10^6 cells) and GAM FITC in fixed and permeabilized cells. Then surface CD3 and CD56 was labeled directly using FITC-conjugated CD3 mAb (mouse IgG1, UCHT-1) and PE-conjugated CD56 mAb (mouse IgG1, B159). We used unconjugated mouse IgG1 (MOPC-31C, dilution 1:100), FITC or PE-conjugated mouse IgG1 (MOPC-21), unconjugated or PE-conjugated mouse IgG2a (clone 155-178), and unconjugated mouse IgG2b (clone 27-35) as the control, according to the isotype of specific mAb used. All labeled cell samples were acquired immediately by FACS Calibur flow cytometry and CellQuestPro Software (Becton Dickinson, New Jersey, USA). The viability of vWF^+ and $CD14^+$ cells was assessed with propidium iodide (PI; 0.5 μg/mL/10^6 cells, Sigma-Aldrich Chemie, Daisenhofen, Germany) and flow cytometry.

Enrichment of peripheral blood cell-subpopulations

PBMC cells were cultured overnight (18 h) in tissue culture Petri dishes 100 × 20 mm (TPP, Trasadingen, Switzerland) at 37°C, in a humidified 5% CO_2 incubator to obtain non-adherent and adherent cells (fractions). The non-adherent cells were lymphocytes, which consisted of T and NK cells. They were used for the positive separation of $CD56^+$ cells. For this purpose, non-adherent cells were collected and filtered through 100 μm nylon mesh to remove possible clumps. Subsequently, the cells were resuspended in 80 μL of ice-cold FACS buffer and 20 uL of microbeads-conjugated anti-CD56 mAb (mouse IgG1, Miltenyi Biotec, Bergisch Gladbach, Germany, 20 μL/10^7 cells). Following a 15-min incubation at 4°C, the cells were centrifuged at 400 × g for 10 min, resuspended in 500 μL of FACS buffer, applied onto the large column, and placed in the magnetic field of Vario-MACS separator

(both from Miltenyi Biotec). After the cells ran through, the column was washed with 3 mL of FACS buffer four times, then removed from the magnetic field. The $CD56^+$ cells were flushed out using the same medium, whereas CD56 negative cells were collected separately and were used as a source of enriched and functionally untouched $CD3^+$ cells, however with the possible impurity of $CD56^+$ cells. The adherent fraction contained cells with adhesive properties ($CD14^+$ monocytes, $CD1a^+$ dendritic cells, and vWF^+ endothelial cells), which were collected by a pipette and filtered through 100 μm nylon mesh, then pelleted, and used for the separation of vWF^+ cells. The adherent cells were incubated with anti-vWF mAb (1 μg per 10^6 of total cells) for 30 min in the presence of FACS buffer (60 μL) and blocking reagent (20 μL, Miltenyi Biotec) to reduce non-specific antibody binding. Then, the cells were washed and resuspended in 60 μL of ice-cold FACS buffer. Secondary polyclonal goat anti-mouse IgG MicroBeads (Miltenyi Biotec, 20 μL/10^6 cells) were added, and cells were incubated for 15 min, at 4°C. The following steps of vWF^+ cell isolation were identical to the isolation procedure of $CD56^+$ cells. $CD14^+$ cells were purified from vWF^- fraction using unconjugated anti-CD14 mAb (mouse IgG2a, M5E2, BD Bioscience, dilution 1:100/10^6 cells). Enriched vWF^+, $CD14^+$ and $CD14^-$ fractions were tested for the presence of $CD14^+$ monocytes and $CD1a^+$ dendritic cells with strong antigen-presenting properties.

Statistical analyses

Statistical analyses were performed using the data analysis software system TIBCO Statistica, Version 13.4.0.14 (Palo Alto, CA, USA). The Kruskal-Wallis non-parametric test was used to calculate the differences between groups. A P-value of <0.05 for the differences between the groups was determined to be significant, using the non-parametric Kruskal-Wallis test. The Mann-Whitney U-test evaluated differences between two groups of interest with significance levels adjusted to several mutual comparisons.

RESULTS

Dynamic changes of vWF^+ and $CD14^+$ cells in patients with AMI

In all patients with AMI, the percentage of vWF^+ cells was higher on days 1, 7, and 28 after AMI when compared to the healthy controls, which was 1.64% (1.3%; 2.2%), [median (25th; 75th percentiles)] (Fig. 1 A-C). In STEMI patients treated with primary PCI, the percentage of vWF^+ cells was the highest on day 7 (approximately 5%) and statistically significantly differed from that on days 1 and 28 after acute coronary event (Fig. 1A). In NSTEMI patients without PCI, vWF^+ cells were approximately 15% on day 1 and around 12% on day 28 (Fig. 1B). Both values were statistically significantly higher when compared to day 7 (4%, Fig. 1B). In NSTEMI patients treated with primary PCI, the percentage of vWF^+ cells was 15% on day 1 before the intervention, and then 18% and 12% on days 7 and 28, respectively (Fig. 1C). In these patients, vWF^+ cells were highest on day 7, and it was significantly higher than on day 1 and day 28 (Fig. 1C).

In STEMI patients treated with primary PCI, the frequency of $CD14^+$ cells increased significantly on day 1 after AMI, whereas the highest percentage of $CD14^+$ cells was found on day 7 in these patients (Fig. 1D) and NSTEMI patients without PCI (Fig. 1E). The percentage of $CD14^+$ cells on day 7 were higher than that of day 28 and of healthy controls in both groups (Fig. 1D and 1E). Additionally, in NSTEMI patients without PCI, the percentage of $CD14^+$ cells on day 7 was higher than that of day 1 as the proportion of $CD14^+$ cells on day 1 remained almost unchanged compared to that of the controls (Fig. 1E).

Phenotype of vWF^+ cells and $CD14^+$ cells in patients with AMI

Dynamic changes in HLA-DR, CD80, CD86, and IL-15 expression (Fig. 1 F-I) and viability of vWF^+ cells (Fig. 1J) were observed during the month after AMI. The frequency of HLA-DR expressing vWF^+ cells statistically increased on days 1 and 7 compared to the controls and day 28 (Fig. 1F), whereas CD80 expression decreased (Fig. 1G). CD86 expression remained statistically unchanged on days 1 and 7 and significantly decreased on day 28 (Fig. 1H). IL-15 expression in vWF^+ cells dropped on day 7 after AMI, and was statistically marginally lower compared to day 28 ($P = 0.029$, Fig. I). A significantly higher percentage was found of killed vWF^+ cells in the circulation on

day 1 and 28 after AMI than in the control group. At the same time, they dropped on day 7 and became marginally significant toward day 1 (P = 0.02) and day 28 (P = 0.05, Fig. J). Further, we compared the phenotype of vWF$^+$ and CD14$^+$ cells in NSTEMI patients on day 1 after AMI before PCI, as their number was the highest at that time-point. The percentage of HLA-DR$^+$ cells did not differ between vWF$^+$ cells and CD14$^+$ cells (Fig. 1K). The frequency of vWF$^+$ cells expressing CD80 was negligible (Fig. 1L), whereas CD86 was expressed in 40% -75% of vWF$^+$ cells (Fig. 1M). Both were statistically significantly lower when compared to CD14$^+$ cells. IL-15 was significantly lower in vWF$^+$ cells than in CD14$^+$ cells (Fig. 1N). Percentages of killed CD14$^+$ cells did not significantly differ one month after AMI (Fig. 1O).

Enrichment of vWF$^+$ cells, CD14$^+$ cells and CD3$^+$ lymphocytes

We showed the placement of vWF$^+$ events within an oval fence (set up on a "back gating" principle) in dot plots specified by size or FSC (X-axis) and

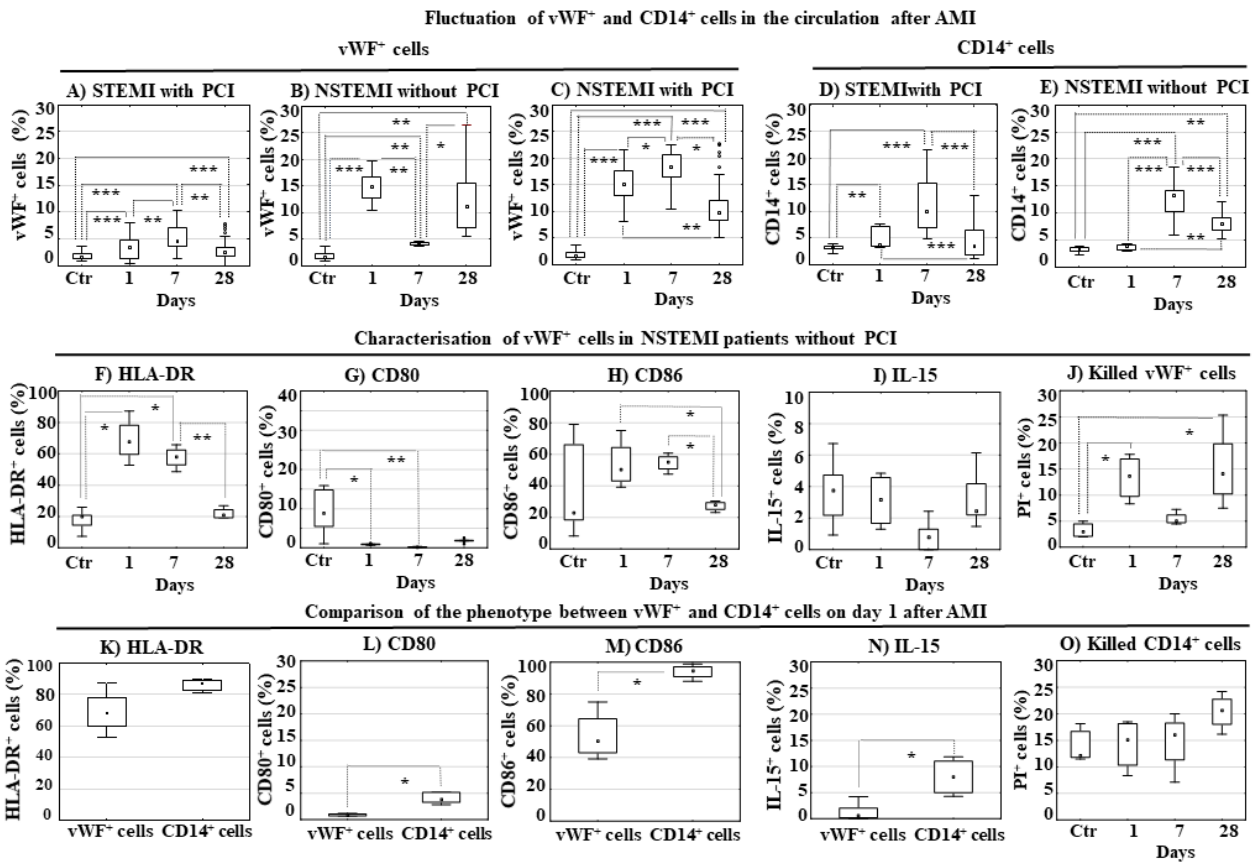


Fig. 1. *Fluctuation of vWF$^+$ and CD14$^+$ cells in the circulation after acute myocardial infarction (AMI). The proportion of circulating vWF$^+$ cells (**A, B, C**) and CD14$^+$ cells (**D, E**) in patients with ST-elevation myocardial infarction (STEMI) and primary percutaneous coronary intervention (PCI) (A, D), patients with non - ST- elevation myocardial infarction (NSTEMI) without PCI (B, E) and patients with NSTEMI and PCI (C) on day 1, day 7 and day 28 are compared with the controls (Ctr). Graphs show 8-32 experiments per group in the upper row, and the levels of statistical significance are *P<0.012, **P<0.005, ***P<0.0001. Dynamic changes in HLA-DR (**F**), CD80 (**G**), CD86 (**H**) and IL-15 (**I**) expression, as well as killed vWF$^+$ cells (**J**) in NSTEMI patients without PCI (middle row). Comparison of HLA-DR (**K**), CD80 (**L**), CD86 (**M**) and interleukin (IL)-15 (**N**) between vWF$^+$ and CD14$^+$ cells in NSTEMI patients without PCI on day 1 and fluctuation of killed CD14$^+$ cells (**O**) in NSTEMI patients without PCI (lower row). Graphs show 4-6 experiments per group in the middle and lower row, and the levels of statistical significance are *P=0.04; **P=0.03, ***P=0.01. Bars represent median (▫), 25% - 75% (□), non-outlier range (I).*

FITC fluorescence (Y-axis) for adherent cells (Fig. 2A) and non-adherent cells (Fig. 2B). In the dot plot shown, the adherent cells contained 13.2% of vWF^+ cells compared to the control labeling of 0.2% (Fig. 2A), whereas vWF^+ cells accounted for only 0.7% in the non-adherent cells compared with control (0.3%) (Fig. 2B). A higher frequency of vWF^+ cells in adherent [13% (10.1%; 15.2%)] than in non-adherent fraction ($P < 0.05$) derived from six independent experiments determined further separation of vWF^+ cells from the adherent cell fraction. In the sample shown, enrichment of vWF^+ cells was 78.71% after positive magnetic separation (Fig. 2C) and was in accordance with the median of 72.2% (70.5%; 77.9%) in the six experiments performed. The enriched vWF^+ subpopulation did not contain $CD1a^+$ cells, whereas $CD14^+$ cells were represented with 2.9% in the histogram shown (Fig. 2C). $CD14^+$ cells were selected by positive magnetic separation from vWF negative fraction to the enrichment of 82.42% (Fig. 2D). The median enrichment of $CD14^+$ cells was 80% (78%; 81.2%). We did not find $CD14^+$ cells in the $CD14^-$ adherent fraction (Fig. 2D). $CD14^+$ and $CD14^-$ fraction did not contain $CD1a^+$ cells (Fig. 2D), therefore the $CD14^-$ fraction served as a control in T cell coculture experiments.

$CD56^+$ cells were separated from the non-adherent cells to a degree of purification of 97.06% (Fig. 2E), which corresponds to 96.33% (95%; 97.7%) of purity in five experiments performed. Functionally intact $CD3^+$ T cells remained in the non-adherent fraction of PBMCs after removing $CD56^+$ cells by positive magnetic separation (Fig. 2E). They were enriched to 69% in the shown sample and corresponded to

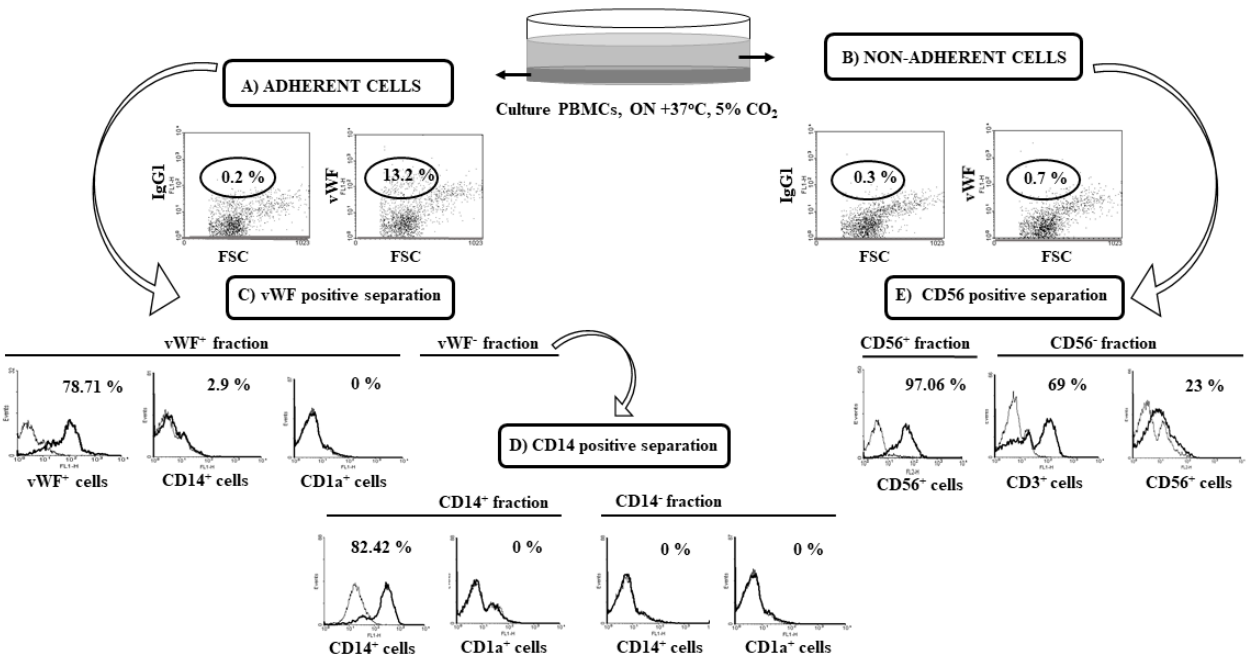


Fig. 2. *Enrichment strategy for subpopulations from peripheral blood mononuclear cells (PBMCs) in NSTEMI patients without PCI treatment on the first day after acute myocardial infarction. The location and proportion of vWF^+ cells concerning isotype-matched controls are shown in sample dot plots in numbers within an oval fence (set up on a "back gating" principle) in adherent cells (**A**) and non-adherent cells (**B**). The thick curve laid above the thin curve in histograms illustrate the enrichment of vWF^+ cells and admixture of $CD14^+$ and $CD1a^+$ cells in adherent vWF^+ cell fraction (**C**); the enrichment of $CD14^+$ cells and the admixture of $CD1a^+$ cells in adherent $CD14^+$ fraction, and the percentage of $CD14^+$, $CD1a^+$ cells in adherent $CD14^-$ fraction (**D**); the purification of $CD56^+$ cells in non-adherent $CD56^+$ fraction, and the enrichment of $CD3^+$ cells and admixture of $CD56^+$ cells in the non-adherent $CD56^-$ cell fraction (**E**). The numbers above the histograms indicate the difference in the percentage of labeled events with specific antibodies (thick histogram curve) and isotype control (thin histogram curve).*

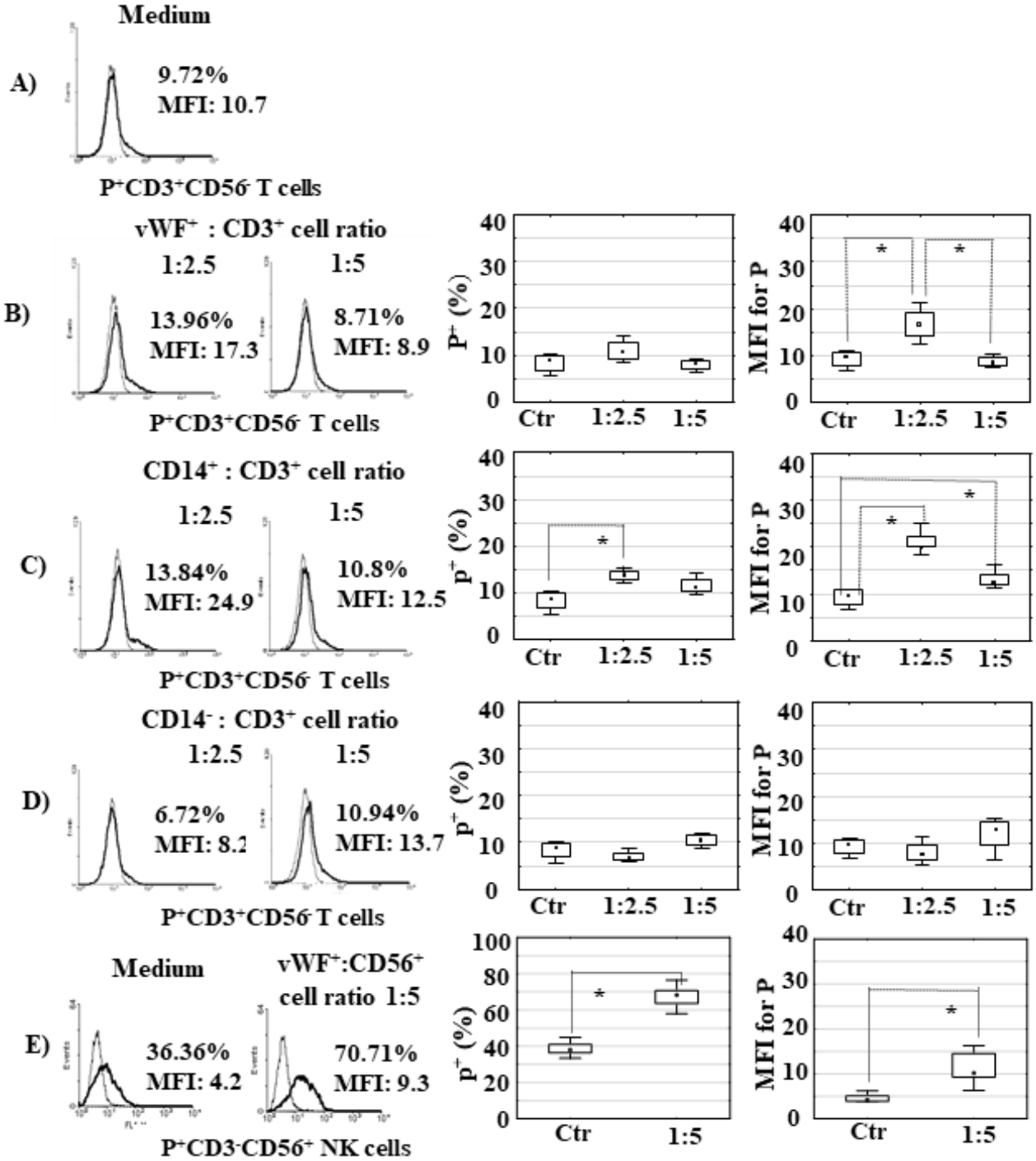


Fig. 3. *Perforin (P) expression in $CD3^+CD56^-$ T cells and $CD3^-CD56^+$ NK cells in NSTEMI patients before PCI on the first day after acute myocardial infarction. Histograms and bars show the percentage of P^+ T cells and mean fluorescence intensity (MFI) for P in T cells cultured in medium only (**A**) or cocultured with vWF^+ cells (**B**), $CD14^+$ cells (**C**), and $CD14^-$ cells (**D**) at ratios 2.5:1 and 5:1 after 18 h. Percentage and MFI for P in NK cells cultured in medium only or cocultured with vWF^+ cells at ratio 5:1 after 18 h is illustrated in histograms and shown in the charts (**E**). The numbers above the histograms indicate the difference in the percentage of P^+ cells (thick histogram curve) and isotype IgG2b controls (thin histogram curve), while bars represent the median (25^{th}; 75^{th} percentiles) of 3-5 experiments performed in each group. The level of statistical significance is *P = 0.019.*

the median of 68% (56%; 69%) in four experiments performed. These cells contained $CD56^+$ cells in 23% in the shown histogram (Fig. 2E).

Effect of vWF^+ and $CD14^+$ cells on the maintenance of perforin in cultured T and NK cells

Fig. 3 shows the expression of P in $CD3^+CD56^-$ T cells after an 18- h coculture with vWF^+ cells, $CD14^+$ or $CD14^-$ cells, as well as in $CD3^-CD56^+$ NK cells after the coculture with vWF^+ cells in NSTEMI patients on day 1 after AMI before PCI. In the shown histogram sample, 9.72% of unstimulated T cells expressed P with mean fluorescence intensity, MFI 10.7 after an 18-h culture in medium only (Fig. 3A). It corresponds to a median of 8.96% (6.83%; 9.96%) in three experiments. Histograms in Fig. 3B illustrate P expression in T cells after coculture with vWF^+ cells at a ratio 1:2.5 (13.96%, MFI 17.3) and a ratio 1:5 (8.71%, MFI 8.9). The median percentage of P^+ T cells cocultured with vWF^+ cells did not significantly change, whereas MFI for P significantly increased in the T cells cocultured with vWF^+ cells at the ratio of 2.5:1 when compared to the ratio of 5:1 or T cells cultured in medium only (Fig. 3B).

Fig. 3C shows P regulation by $CD14^+$ cells. Histograms illustrate the percentage and MFI for P in T cells after the coculture with $CD14^+$ cells at ratio 1:2.5 (13.84%, MFI 24.9) and the ratio 1:5 (10.8%, MFI 12.5), when compared to isotype control. Bars proved that $CD14^+$ cells significantly increased the frequency of P^+ T cells at cell ratio 1:2.5 and MFI for P in both tested ratios compared to unstimulated T cells (Fig. 3C). P expression and MFI for P in T cells did not change after coculture with $CD14^-$ cells (Fig. 3D).

In Fig. 3E, histograms illustrate P expression in $CD3^-CD56^+$ NK cells after an18-h coculture with vWF^+ cells at cell ratio 5:1 (70.71%, MFI 9.3), when compared to NK cells cultured in medium only (36.36%, MFI 4.2). These differences in the percentage and the MFI were statistically significant, as shown in the chart (Fig. 3E**).**

DISCUSSION

We found a higher proportion of circulating vWF^+ cells in NSTEMI patients treated conservatively and before PCI implementation than in STEMI patients on day 1 after the AMI, which confirmed the greater inflammatory response in NSTEMI patients, as previously shown (8). The early peak of the circulating vWF^+ cells in NSTEMI patients appeared simultaneously as the largest increase in the frequency of $CD3^-CD56^+$ NK cells, their cytotoxic $CD56^{dim+}$ subset, P^+ NK cells, and P^+ T cells (8), suggesting the early interaction of circulating vWF^+ cells and lymphocytes. HLA-DR and CD86 expression in circulating vWF^+ cells on days 1 and 7 enable their antigen-presenting capacities to T cells, as shown for $CD14^+$ monocytes (9), while monocytes peak later in the circulation, after the NSTEMI and STEMI. In NSTEMI patients, early circulating vWF^+ cells with negligible CD14 expression increased MFI for P in autologous $CD3^+CD56^-$ T cells at 1:2.5 cell ratio in a direct contact after 18 h. Enriched $CD14^+$ cells more efficiently enhanced frequency and MFI for P on the first day after NSTEMI in a dose-dependent manner, due to the higher expression of CD80 and CD86 costimulatory molecules. However, vWF^+ cells enhanced P in $CD3^-CD56^+$ NK cells, possibly due to the sustained production of IL-15, a strong proinflammatory activator (5). Upregulation of cytotoxic mediator P may enable cytotoxic effectors to destroy circulating vWF^+ cells, as cytotoxic effector cells promote rupture of vulnerable atherosclerotic lesions which are covered with vWF^+ endothelial cells, involving NKG2D/MICA/B endothelial cell recognition mechanism (10). It matches the increased frequency of killed vWF^+ cells on day 1 and statistically marginally decreased number of circulating vWF^+ cells on day 7 in NSTEMI patients. A drop in circulating vWF^+ cells may temporarily reduce the systemic cellular immune response, which mirrors the subsequent decrease in NK cells, P^+ NK cells, and their P^+CD56^{dim+} subset on day 14 (8). However, circulating vWF^+ cell regrowth in NSTEMI patients treated conservatively on day 28, concomitantly with the enhanced degree of inflammation, is a characteristic of multivessel chronic coronary artery disease (11). In contrast, the frequency of vWF^+ cells in NSTEMI patients treated with PCI decreased gradually. Their dynamic resembles the dynamic in STEMI patients, where

primary PCI removed the culprit stenosis and the acute ischemic inflammation. However, an explicit increase in the count of circulating vWF^+ cells appeared on day 1, possibly due to PCI (12). It seems that circulatory vWF^+ cells fine-tune T and NK cell functions early after AMI. In order to reach a final conclusion, it is necessary to expand the research and try to remove the weaknesses of this investigation, for example, related to the purification of cellular subpopulations.

ACKNOWLEDGEMENTS

This work was supported by the Special Hospital for Medical Rehabilitation of Heart and Lung Diseases and Rheumatism "Thalassotherapia-Opatija", Opatija, Croatia and the grant from the Croatian Ministry of Science No. 062-620402-0376 and No. 062-620402-0377, University of Rijeka, Rijeka, Croatia grants No. Uni-ri-biomed-18-110 and No. Uni-ri-biomed-18-160. We thank Editage (www.editage.com) for English language editing.

REFERENCES

1. Wu MD, Atkinson TM, Lindner JR. Platelets and von Willebrand factor in atherogenesis. Blood 2017; 129(11):1415-19.
2. Rakic M, Persic V, Kehler T, et.al. Possible role of circulating endothelial cells in patients after acute myocardial infarction. Med Hypotheses 2018; 117:42-6.
3. Hamm CW, Bassand JP, Agewall S et al. ESC Guidelines for the management of acute coronary syndromes in patients presenting without persistent ST-segment elevation: The Task Force for the management of acute coronary syndromes (ACS) in patients presenting without persistent ST-segment elevation of the European Society of Cardiology (ESC). Eur Heart J 2011; 32(23):2999-3054.
4. Roffi M, Patrono C, Collet JP et al. 2015 ESC Guidelines for the management of acute coronary syndromes in patients presenting without persistent ST-segment elevation: Task Force for the Management of Acute Coronary Syndromes in Patients Presenting without Persistent ST-Segment Elevation of the European Society of Cardiology (ESC). Eur Heart J 2016; 37(3):267-315.
5. Guo L, Liu MF, Huang JN, Li JM, Jiang J, Wang JA. Role of interleukin-15 in cardiovascular diseases. J Cell Mol Med 2020;24(13):7094-01.
6. Xu J, Yang N, Xie T, Yang G, Chang L, Yan D, Li T. Summary and comparison of the perforin in teleosts and mammals: a review. Scand J Immunol 2021; e13047.
7. Laskarin G, Medancic SS, Redzovic A, Duric D, Rukavina D. Specific decidual CD14(+) cells hamper cognate NK cell proliferation and cytolytic mediator expression after mucin 1 treatment in vitro. J Reprod Immunol 2012; 95(1-2):36-45.
8. Laskarin G, Persic V, Ruzic A et al. Perforin-Mediated Cytotoxicity in non-ST Elevation Myocardial Infarction. Scand J Immunol 2011; 74(2):195-204.
9. Sprangers S, de Vries TJ, Everts V. Monocyte Heterogeneity: Consequences for Monocyte-Derived Immune Cells. J Immunol Res 2016; 2016:1475435.
10. Bonaccorsi I, Spinelli D, Cantoni C, et al. Symptomatic Carotid Atherosclerotic Plaques Are Associated With Increased Infiltration of Natural Killer (NK) Cells and Higher Serum Levels of NK Activating Receptor Ligands. Front Immunol 2019; 10:1503.
11. Di Stefano R, Di Bello V, Barsotti MC, et al. Inflammatory markers and cardiac function in acute coronary syndrome: difference in ST-segment elevation myocardial infarction (STEMI) and in non-STEMI models. Biomed Pharmacother 2009; 63(10):773-80.
12. Vargová K, Toth-Zsamboki E, Beres BJ, et al. Circulating endothelial cell count, plasma vWF and soluble ICAM-1 levels following primary or elective percutaneous coronary intervention. Atherosclerosis 2008; 198(2):366-72.

JOURNAL OF BIOLOGICAL REGULATORS & HOMEOSTATIC AGENTS Vol. 35, no. 3, 1169-1176 (2021)

LETTER TO THE EDITOR

ARA290 inhibits high glucose-induced apoptosis of NRK-52E cells

L.-J. Zhao[1,#], X.-L. Sun[1,#], J. Qiu[1], B.-L. Xiao[1], X.-Y. Fan[1], T. Wang[1] and C.-L. Li[2,*]

[1]Hemodialysis Center, Yantai Yuhuangding Hospital Affiliated to Qingdao University, Yantai, China; [2]Department of Endocrinology, Yantai Yuhuangding Hospital Affiliated to Qingdao University, Yantai, China

Received January 29, 2021 – Accepted June 4, 2021

#These Authors contributed equally to this work

To the Editor,

Erythropoietin (EPO) is a glycoprotein hormone mainly synthesized and secreted by adult kidney fibroblasts. It is mediated by EPO receptor (EPOR), which inhibits apoptosis of erythroid colonies and maintains its development for mature red blood cells (1). Because of its erythropoiesis, EPO has been widely used in the clinical treatment of renal and tumor chemotherapy-related anemia (2). Because EPOR was previously thought to exist only in erythroid cells, its role was limited to the hematopoietic system. However, recent studies have found that some non-hematopoietic cells of the body also express EPOR, such as vascular endothelial cells, cardiomyocytes, and the administration of exogenous EPO or EPO derivatives can exert non-hematological protective effects on the above-mentioned tissue cells through the anti-apoptotic mechanism (3, 4).

Diabetic nephropathy (DN) is a major complication and cause of death in diabetes. Therefore, the prevention and treatment of DN is a severe challenge faced by the nephrology community in the world. A large number of studies have confirmed that apoptosis of renal tubular epithelial cells (RTEC) plays an important role in the occurrence and development of DN under high glucose environment (5). It has been reported that renal intrinsic cells such as RTEC also express EPOR (6), but whether EPO and its derivatives can inhibit RTEC apoptosis in DN and its possible mechanism is rarely reported.

MAPK (mitogen-activated protein kinase) and p53 are the main signaling pathways that regulate apoptosis (7). The MAPK family consists of three members: JNK, ERK and p38. Activation of JNK and p38 is related to apoptosis, and ERK is involved in cell proliferation (8, 9). P53, a key molecule regulating apoptosis, can induce apoptosis by upregulating proteins encoding apoptosis such as Bax; and Bax can inhibit Bcl-2 expression by interacting with Bcl-2, thereby causing apoptosis (10).

MATERIALS AND METHODS

Cell culture

Rat NRK-52E cells (Cell Culture Center, Shanghai, China) were cultured at 37°C in an incubator, using 5% fetal bovine serum (FBS, Gibco, Rockville, MD, USA), 100 U/mL penicillin (Gibco, Rockville, MD, USA), 100 μg/mL (Gibco, Rockville, MD, USA) streptomycin in Dulbecco's Modified Eagle Medium (DMEM, Gibco,

Key words: ARA290; diabetic nephropathy; apoptosis; NRK-52E cells; Bax-inhibiting peptides, MAPK signaling pathway

*Corresponding Author:
Chaolin Li, MD.
Department of Endocrinology, Yantai Yuhuangding Hospital Affiliated to Qingdao University, NO 20, Yuhuangding East Road, Yantai, Shandong 264000, China
Tel./Fax: +86 018553546162
e-mail: lichaolin66@mail.sdufe.edu.cn

0393-974X (2021)
Copyright © by BIOLIFE, s.a.s.
This publication and/or article is for individual use only and may not be further reproduced without written permission from the copyright holder.
Unauthorized reproduction may result in financial and other penalties
DISCLOSURE: ALL AUTHORS REPORT NO CONFLICTS OF INTEREST RELEVANT TO THIS ARTICLE.

Rockville, MD, USA). When the cells had grown to 80-90%, they were digested with trypsin (Gibco, Rockville, MD, USA) and passed.

Cell Counting Kit-8 (CCK-8) Assay

According to the experimental grouping, cells were treated with the corresponding reagents: high glucose, ARA290 (ARAIM Pharmaceuticals, Ossining, USA) and BIP (Bax-inhibiting peptides) (Med Chem Express, Beijing, China). After culturing for 6 h, 12 h, 18 h, and 24 h, respectively, 10 μL of CCK-8 solution (Jian Cheng, Nanjing, China) was added to all wells, and the cells were incubated for 2 h. The microplate reader (Thermo Fisher Scientific, Waltham, MA, USA) measured the 450 nm light absorption value and the cell viability was calculated.

Quantitative real-time polymerase chain reaction (qRT-PCR)

Each treatment group was washed with pre-cooled phosphate buffered saline (PBS) and total RNA was extracted (Thermo Fisher Scientific, Waltham, MA, USA). Reverse transcription and polymerase chain reaction were carried out, and the reaction conditions were: pre-deformation, 95°C, 1 min, 95°C, 15 s, 58°C, 20 s, 72°C, 45 s, 40 cycles. The dissolution curve was 60°C - 95°C, and the temperature was raised by 1°C every 20 s. Using glyceraldheyde 3-phosphate dehydrogenase (GAPDH) (Thermo Fisher Scientific, Waltham, MA, USA) as an internal reference, and the quantitative analysis was performed based on the quantitative amount of the target gene ($2^{-\Delta\Delta Ct}$). All the primers are listed in Table 1.

Western blot

After the cells were treated, the cellular protein was extracted 24 h after the drug treatment, and the protein concentration was determined using the bicinchoninic acid (BCA) kit (Jian Cheng, Nanjing, China). 20 ~ 80 μg protein was used for sodium dodecyl sulphate-polyacrylamide gel electrophoresis (SDS-PAGE) separation, and then transferred to polyvinylidene difluoride (PVDF) membrane (Millipore, Billerica, MA, USA). The PVDF membrane was blocked with skimmed milk powder for 2 h, then the PVDF membrane was rinsed with tris buffered saline-tween (TBST) once and incubated overnight at 4°C with the diluted primary antibody (p53, P-p53, 1:1000, Abcam, Cambridge, MA, USA, Rabbit; p38, P-p38, 1:1000, Abcam, Cambridge, MA, USA, Rabbit; Bax, Bcl-2, 1:1000, Abcam, Cambridge, MA, USA, Mouse; Caspase3, 1:1000, Abcam, Cambridge, MA, USA, Mouse; JNK, p-JNK, 1:1000, Abcam, Cambridge, MA, USA, Rabbit; ERK, p-ERK, 1:2000, Abcam, Cambridge, MA, USA, Rabbit; GAPDH, Abcam, Cambridge, MA, USA, 1:5000, Abcam, Cambridge, MA, USA, Rabbit). The next day, the PVDF membrane was blocked with HRP-labeled

Table I. *Real time PCR primers*

Gene name	Forward (5'>3')	Reverse (5'>3')
P53	CTCTCCCCCGCAAAAGAAAAA	CGGAACATCTCGAAGCGTTTA
P38	TGACCCTTATGACCAGTCCTTT	GTCAGGCTCTTCCACTCATCTAT
Caspase3	ATGGAGAACAACAAAACCTCAGT	TTGCTCCCATGTATGGTCTTTAC
Bax	TGAAGACAGGGGCCTTTTTG	AATTCGCCGGAGACACTCG
Bcl-2	GTCGCTACCGTCGTGACTTC	CAGACATGCACCTACCCAGC
JNK	AGCAGAAGCAAACGTGACAAC	GCTGCACACACTATTCCTTGAG
ERK	GGTTGTTCCCAAATGCTGACT	CAACTTCAATCCTCTTGTGAGGG
GAPDH	ACAACTTTGGTATCGTGGAAGG	GCCATCACGCCACAGTTTC

RT-PCR: quantitative reverse-transcription polymerase chain reaction

secondary antibody at room temperature for 2 h, then added with electrochemiluminescence (ECL) developer solution (Corning, Corning, NY, USA) and exposed, and Image Lab™ Software image processing software was used to analyze the target band.

Immunofluorescence

After fixing the cells of each group with 4% paraformaldehyde for 15 min, the cell membrane was permeated with 0.5% Triton X-100 (Jian Cheng, Nanjing, China), and then goat serum was added to the slide for blocking for 30 mins. After removing the blocking solution, the diluted primary antibody 8-OHdG was added (Abcam, Cambridge, MA, USA, Rabbit, 1:3000), and incubated overnight at 4°C; the following day, the fluorescent secondary antibody and 4',6-diamidino-2-phenylindole (DAPI) (Jian Cheng, Nanjing, China) were added sequentially in the dark, and the slides were sealed at room temperature with a solution containing anti-fluorescence quenching agent. Finally, the images were collected and observed under a Zeiss microscope (Thermo Fisher Scientific, Waltham, MA, USA).

Terminal deoxynucleotidyl transferase (TdT)-mediated dUTP nick end labeling (TUNEL) staining

2×10^5 cells of log phase-proliferated NRK-52E cells were inoculated into 24-well plates, and cells of different treatment groups were stained with TUNEL kit (Elabscience, Wuhan, China) in the dark. After DAPI staining, the results were observed under a fluorescence microscope and recorded.

Detection of apoptosis by flow cytometry

The NRK-52E cells were collected first and then were made into a single cell suspension according to the kit instructions (Thermo Fisher Scientific, Waltham, MA, USA). Next, FITC (fluorescein isothiocyanate) and propidium iodide (PI) were added in the dark chamber. Then flow cytometry (Becton Dickinson, Heidelberg, Germany) was used to detect the apoptosis level.

Statistical analysis

All data were processed using Statistical Product and Service Solutions (SPSS) 21.0 statistical software (IBM, Armonk, NY, USA). The experimental data were expressed as mean ± standard deviation. The statistical results of the experiment were analyzed by SPSS 21 statistical software and the corresponding conclusions were obtained ($P<0.05$ is significant difference, $P<0.01$ is very significant).

RESULTS

Effects of high glucose on NRK-52E cells

Firstly, 0, 5, 15, 25 mmol/L high glucose were selected to culture NRK-52E cells, and detect cell activity by CCK-8 assay (Fig. 1A). The results indicated that when the concentration of high glucose was higher than 5 mmol/L, the cell viability was reduced. At the same time, we collected four groups of cell proteins and total RNA, and detected p53 and P-p53 protein expression (Fig. 1B). It was found that the expression of p53 and P-p53 increased with the increase of glucose concentration. qRT-PCR detection of p38 mRNA and p53 mRNA revealed that p53 mRNA increased after high glucose culture, but p38 mRNA did not increase obviously (Fig. 1C). Secondly, in order to verify the apoptosis rate of each group of cells (Fig. 1D), we found by flow cytometry that when the concentration of high glucose was less than 5 mmol/L, the apoptosis rate did not increase significantly, and when the concentration was higher than 15 mmol/L, the apoptosis rate increased obviously.

Effect of ARA290 on NRK-52E cells

In order to study whether ARA290 has an effect on NRK-52E cells under physiological conditions, we first used the CCK-8 assay to detect the effect of ARA290 at different concentrations on the viability of NRK-52E cells (Fig. 1E). The results indicated that when the concentration of ARA290 was 5-10 nmol/mL, it can promote the increase of cell viability, and when the concentration was greater than 10 nmol/mL, the cell viability decreased. At the same time, we collected four groups of cell proteins and total RNA, and detected p53 and P-p53 protein expression (Fig. 1F). The results showed that the expression of p53 and p-p53 increased after NRK-52E cells were cultured with 15 nmol/mL ARA290, while the expression of p53 and P-p53 in the first three groups was not significant. qRT-PCR detection

of p38 mRNA and p53 mRNA revealed that when the concentration of ARA290 was 5 to 10 nmol/mL, p53 mRNA did not change significantly, and when it was greater than 10 nmol/mL, p53 mRNA expression increased (Fig. 1G). On the contrary, p38 mRNA expression did not change significantly. In order to verify the apoptosis rate of each group of cells (Fig. 1H), we found by flow cytometry that when the concentration of ARA290 was 5 to 10 nmol/mL, the apoptosis rate was low and there was no significant difference. When the concentration was higher than 10 nmol/mL, the apoptosis rate increased.

Effects of ARA290 on NRK-52E cell apoptosis in high glucose environment

In order to detect the anti-apoptotic effect of ARA290 on NRK-52E cells in 25 mmol/L high glucose culture, we tested the apoptosis rate of each group by TUNEL staining (Fig. 2A) and flow cytometry (Fig. 2B). As a result, it was found that the apoptosis rate of the HG group increased obviously. But in the 10 nmol/mL ARA290 group, ARA290 effectively inhibited apoptosis induced by high glucose. At the same time, in order to clarify the mechanism of high glucose damage to NRK-52E cells, we detected the DNA damage index 8-OHdG by immunofluorescence staining (Fig. 2C), and found that the expression of 8-OHdG in the nucleus of the 25 mmol/L glucose group was obviously increased, while 8-OHdG in the ARA290 group was obviously reduced. In addition, we collected total protein from each group and detected p53, P-p53, Bax, Bcl-2 and

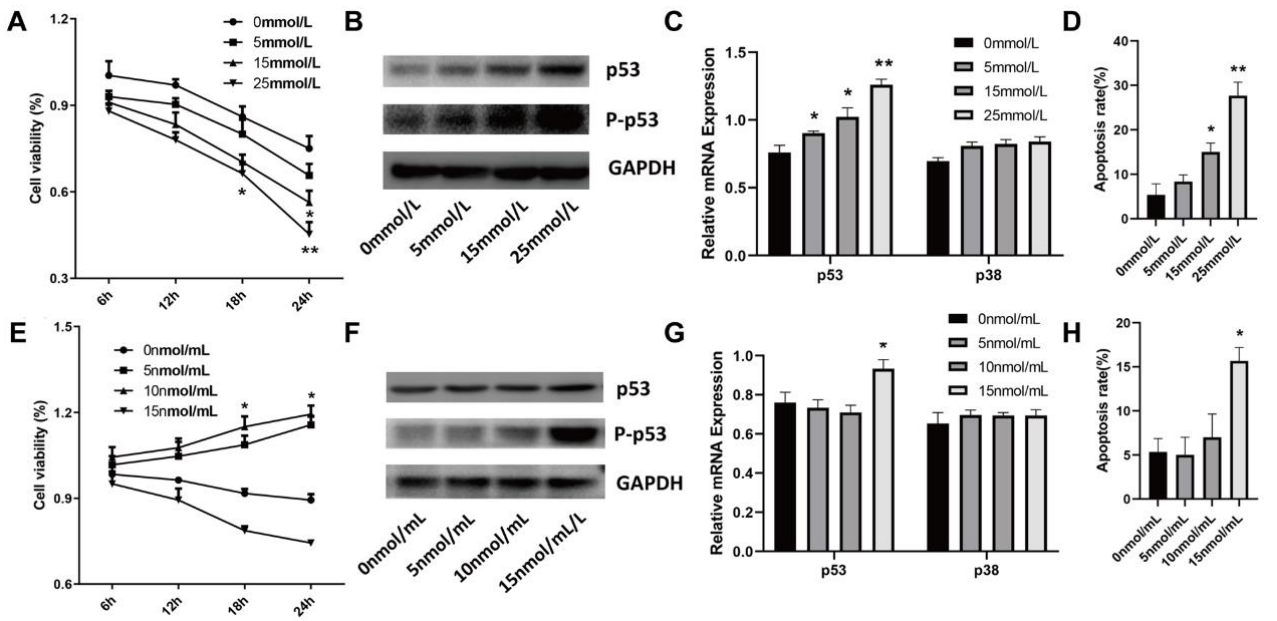


Fig. 1. *Effects of high glucose and ARA290 on NRK-52E cells.* ***A)*** *CCK-8 assay was used to detect the effect of different glucose concentrations on the activity of NRK-52E cells.* ***B)*** *WB detection (0 mmol/L glucose, 5 mmol/L glucose, 15 mmol/L glucose, 25 mmol/L glucose) group p53 and P-p53 expression.* ***C)*** *qRT-PCR detection (0 mmol/L glucose, 5 mmol/L glucose, 15 mmol/L glucose, 25 mmol/L glucose) group expression of p38 and p53.* ***D)*** *Flow cytometry detection (0 mmol/L glucose, 5 mmol/L glucose, 15 mmol/L glucose, 25 mmol/L glucose) group NRK-52E cell apoptosis rate. * indicates statistical difference from the 0 mmol/L glucose group P<0.05; ** indicates statistical difference from the 0 mmol/L glucose group P<0.01;* ***E)*** *CCK-8 assay was used to detect the effect of different ARA290 concentrations on the activity of NRK-52E cells.* ***F)*** *WB detection (0 nmol/mL ARA290, 5 nmol/mL ARA290, 10 nmol/mL ARA290, 15 nmol/mL ARA290) expression of p53 and P-p53 in the group.* ***G)*** *qRT-PCR detection (0 nmol/mL ARA290, 5 nmol/mL ARA290, 10 nmol/mL ARA290, 15 nmol/mL ARA290) group expression of p38 and p53.* ***H)*** *Flow cytometry detection (0 nmol/mL ARA290, 5 nmol/mL ARA290, 10 nmol/mL ARA290, 15 nmol/mL ARA290) group of NRK-52E cells apoptosis rate. * indicates statistical difference from the 0 nmol/mL ARA290 group P<0.05.*

Caspase3 expression by western blot (WB) (Fig. 2D). The results indicated that the expression of p53, P-p53, Bax and Caspase3 in the HG group was obviously increased, but the expression of Bcl-2 was obviously suppressed. In the ARA290 group, the expression of p53, P-p53, Bax and Caspase3 was obviously reduced, and 10 nmol/mL ARA290 intervention promoted the increase of Bcl-2 expression. At the same time, we found that the Bax / Bcl-2 ratio was obviously increased in the ARA290 group. And p53, Bax, Bcl-2 and Caspase3 were detected by qRT-PCR with similar results (Fig. 2E).

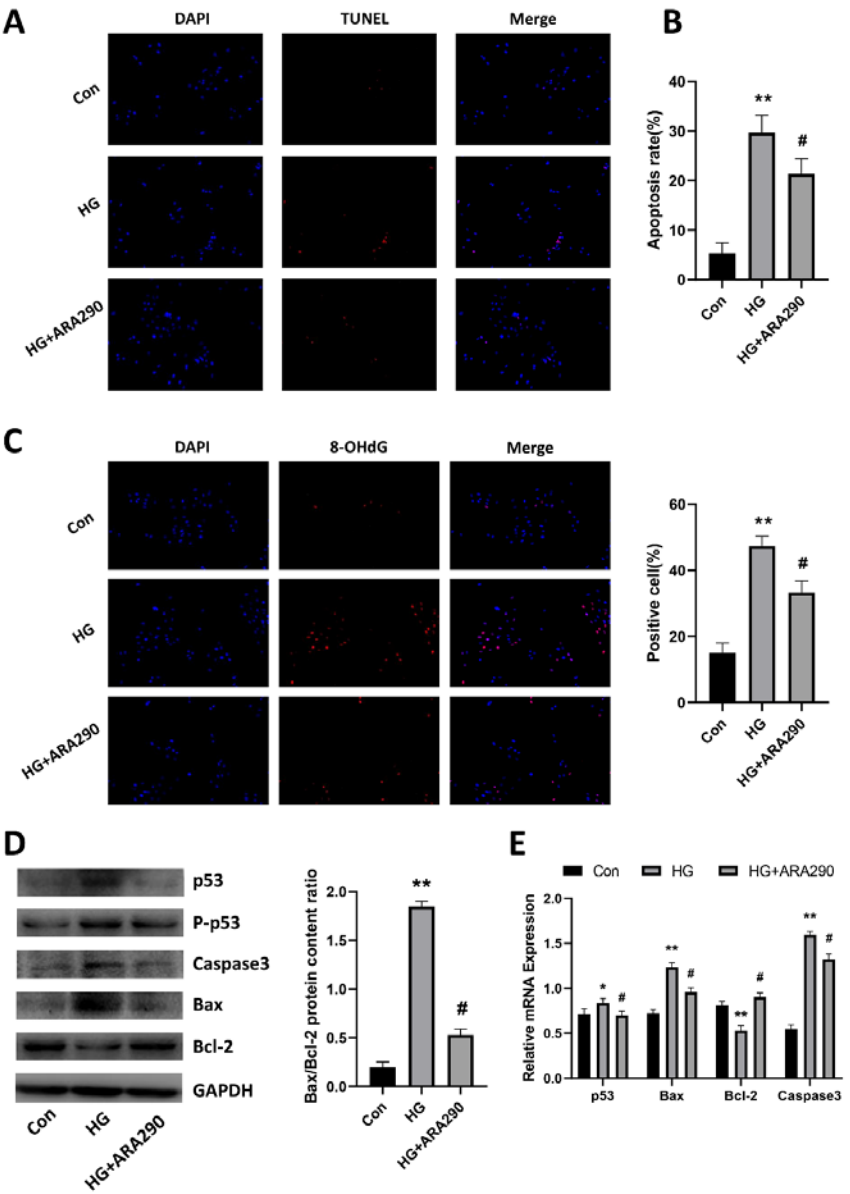


Fig. 2. *Effects of ARA290 on NRK-52E cell apoptosis in high glucose environment.* ***A****) TUNEL staining (magnification: 200×).* ***B****) Flow cytometry was used to detect the apoptosis rate of NRK-52E cells.* ***C****) The expression of 8-OhdG was detected by immunofluorescence staining (magnification: 200×), and the positive cell ratio was analyzed.* ***D****) WB detected p53, P-p53, Caspase3, Bax, Bcl-2 expression, and protein bands were used to analyze the expression ratio of Bax/Bcl-2.* ***E****) qRT-PCR was used to detect the expression of p53, Bax, Bcl-2, and Caspase3 mRNA. * indicates statistical difference from the Con group P<0.05; ** indicates statistical difference from the Con group P<0.01; # indicates statistical difference from the HG group P<0.05.*

BIP can increase the anti-apoptosis effect of ARA290 induced by high glucose

In order to further clarify the role of Bax in the reduction of high glucose-induced apoptosis in NRK-52E cells, we used BIP to intervene in NRK-52E cells. Firstly, 25 mmol/L high glucose and different concentrations of BIP were incubated with NRK-52E cells, and the cell activity was measured after 24 h of incubation. As a result, it was found that BIP at different concentrations could inhibit the decrease in the activity of NRK-52E cells after high glucose treatment, and was most significant

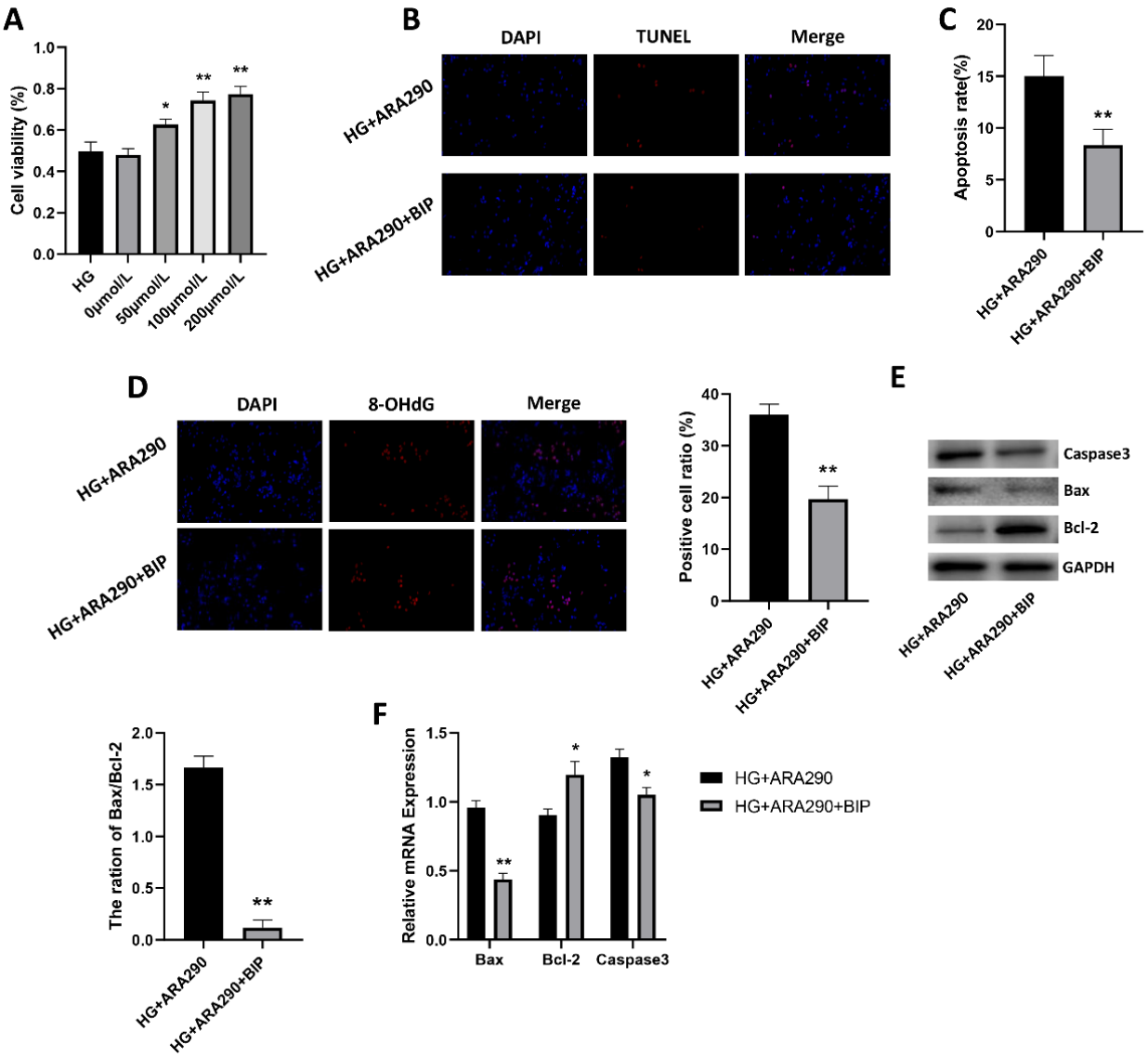


Fig. 3. *BIP can increase the anti-apoptosis effect of ARA290 induced by high glucose. **A**) CCK-8 assay was used to detect the effect of different BIP concentrations on the activity of NRK-52E cells. **B**) TUNEL staining (magnification: 200×). **C**) Flow cytometry was used to detect the apoptosis rate of NRK-52E cells. **D**) The expression of 8-OhdG was detected by immunofluorescence staining (magnification: 200×), and the positive cell ratio was analyzed. **E**) WB detected Caspase3, Bax, Bcl-2 expression, and protein bands were used to analyze the expression ratio of Bax/Bcl-2. **F**) qRT-PCR was used to detect the expression of Bax, Bcl-2, and Caspase3 mRNA. * indicates statistical difference from the HG+ARA290 group P<0.05; ** indicates statistical difference from the HG+ARA290 group P<0.01.*

at 200 μmol/L (Fig. 3A). Therefore, we selected this concentration for the follow-up study. TUNEL staining found that compared with the HG+ARA290 group, the NRK-52E cell apoptosis rate was lower in the HG+ARA290+BIP group (Fig. 3B). At the same time, flow cytometry detected similar rates of apoptosis in both groups. (Fig. 3C). In addition, immunofluorescence staining to detect the expression level of 8-OHdG found that compared with the HG+ARA290 group, the expression level of 8-OHdG was lower in the HG+ARA290+BIP group (Fig. 3D). At the same time, WB was used to detect the expression of Bax, Bcl-2, and Caspase3. It was found that after BIP intervention, it can enhance the expression of anti-apoptotic protein of ARA290 and reduce the expression of apoptosis-related protein of NRK-52E cells. In addition, the Bax/Bcl-2 ratio in the HG+ARA290+BIP group was obviously reduced (Fig. 3E). In addition, qRT-PCR also obtained similar results as WB (Fig. 3F).

Effects of ARA290 on MAPK signaling pathway in NRK-52E cells

Compared with the control group, the expression levels of p-JNK and p-ERK in the HG group were obviously increased, but the expression of p-p38 was not, and the expressions of JNK, ERK, and p38 were not obviously changed. At the same time, compared with the 25 mmol/L HG group, the expression levels of p-JNK and p-ERK in the ARA290 group were obviously reduced, while the expressions of JNK, ERK and p38 were not obviously changed (Fig. 4A). At the same time, we also confirmed by qRT-PCR detection that JNK mRNA, ERK mRNA and p38 mRNA were not significantly different in each group (Fig. 4B).

DISCUSSION

ARA290 is the latest EPO-derived peptide. It mimics the spiral B structure of EPO, has the same tissue protection effect as EPO, and has no hematopoietic activity (11). In accordance with previous studies (12), we determined the intervention concentration of ARA290 and found that 10 nmol/mL ARA290 can inhibit the increase of Bax / Bcl-2 ratio induced by 25 mmol/L glucose and reduce the apoptosis of NRK-52E cells.

In the present study, we found that the apoptosis of NRK-52E cells in the model group increased

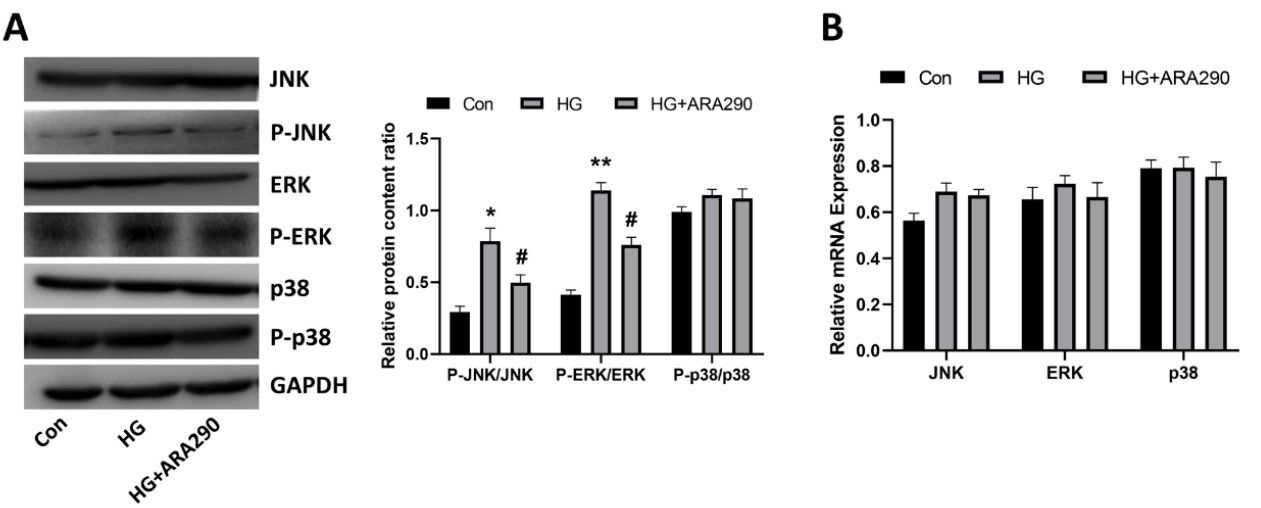


Fig. 4. *Effects of ARA290 on MAPK signaling pathway in NRK-52E cells.* ***A****) WB detected JNK, P-JNK. ERK, P-ERK, p38, P-p38 expression, gray value analysis.* ***B****) qRT-PCR was used to detect the expression of JNK, ERK and p38 mRNA. * indicates statistical difference from the Con group P<0.05; ** indicates statistical difference from the Con group P<0.01, # indicates statistical difference from the HG group P<0.05.*

obviously compared with the normal control group, and the expression of the key execution enzyme Caspase-3 also increased obviously. After treatment with 10 nmol/mL ARA290, apoptosis of NRK-52E cells was inhibited and Caspase-3 expression was reduced. This confirms that ARA290 can inhibit the apoptosis of NRK-52E cells caused by high glucose environment. To further clarify that Bax regulates high glucose-induced apoptosis and the anti-apoptotic effect of ARA290, we used 200 μmol/L BIP to intervene in NRK-52E cells. The results found that BIP can effectively inhibit the high glucose-induced increase in Bax expression. In addition, BIP can further enhance the anti-apoptotic effect of ARA290, inhibit the increase of Caspas3 expression, promote the increase of Bcl-2 expression, and inhibit the up-regulation of 8-OHdG expression, thereby further reducing the high glucose-induced apoptosis of NRK-52E cells.

In this research, the expression of MAPK pathway-related molecules in NRK-52E cells cultured in 25 mmol/L glucose was tested. The results showed that the expression of p-JNK and p-ERK in the model group was obviously increased. After 10 nmol/mL ARA290 intervention, the expression of p-JNK and p-ERK decreased obviously. Therefore, this study speculated that the apoptosis of NRK-52E cells promoted by high glucose environment may be related to the activation of MAPK pathway, but its role is not dependent on p38 pathway. At the same time, ARA290 inhibited apoptosis of NRK-52E cells through MAPK pathway and was not dependent on p38 pathway.

In conclusion, the protective effect of ARA290 on NRK-52E cell apoptosis under high glucose environment may be related to the regulation of MAPK pathway and down-regulating the Bax / Bcl-2 ratio. However, its specific approach is still unclear and needs further exploration and research.

REFERENCES

1. Spivak JL. Erythropoietin. Blood Rev 1989; 3:130-5.
2. Erslev AJ. Erythropoietin and anemia of cancer. Eur J Haematol 2000; 64:353-8.
3. Banaei S, Ahmadiasl N, Alihemmati A. Combination Anti-Apoptotic Effect of Erythropoietin and Melatonin on Ischemia Reperfusion-Induced Renal Injury in Rats. Acta Med Iran 2016; 54:624-30.
4. Vazquez-Mellado MJ, Aguilar C, Rocha-Zavaleta L. Erythropoietin protects neuroblastoma cells against etoposide and vincristine by activating ERK and AKT pathways but has no effect in kidney cells. Life Sci 2015; 137:142-9.
5. Lin CY, Lin TY, Lee MC, Chen SC, Chang JS. Hyperglycemia: GDNF-EGR1 pathway target renal epithelial cell migration and apoptosis in diabetic renal embryopathy. Plos One 2013; 8: e56731.
6. Breggia AC, Wojchowski DM, Himmelfarb J. JAK2/Y343/STAT5 signaling axis is required for erythropoietin-mediated protection against ischemic injury in primary renal tubular epithelial cells. Am J Physiol Renal Physiol 2008; 295:F1689-F1695.
7. Sun Y, Liu WZ, Liu T, Feng X, Yang N, Zhou HF. Signaling pathway of MAPK/ERK in cell proliferation, differentiation, migration, senescence and apoptosis. J Recept Signal Transduct Res 2015; 35:600-4.
8. Wagner EF, Nebreda AR. Signal integration by JNK and p38 MAPK pathways in cancer development. Nat Rev Cancer 2009; 9:537-549.
9. Kim EK, Choi EJ. Pathological roles of MAPK signaling pathways in human diseases. Biochim Biophys Acta 2010; 1802:396-405.
10. Lu Z, Miao Y, Muhammad I, et al. Colistin-induced autophagy and apoptosis involves the JNK-Bcl2-Bax signaling pathway and JNK-p53-ROS positive feedback loop in PC-12 cells. Chem Biol Interact 2017; 277:62-73.
11. van Rijt WG, Nieuwenhuijs-Moeke GJ, van Goor H, et al. ARA290, a non-erythropoietic EPO derivative, attenuates renal ischemia/reperfusion injury. J Transl Med 2013; 11:9.
12 Yan L, Zhang H, Gao S, et al. EPO derivative ARA290 attenuates early renal allograft injury in rats by targeting NF-kappaB pathway. Transplant Proc 2018; 50:1575-82.

LETTER TO THE EDITOR

Downregulation of NPTX1 induces cell cycle progression through Wnt/β-catenin signaling in breast cancer

R.Y. Ye[1], X.Y. Kuang[1], N. Shao[1], S.M. Wang[1] and Y. Lin[1*]

[1]*Department of Thyroid and Breast Surgery, The First Affiliated Hospital of Sun Yat-sen University, Guangzhou, Guangdong, China*

Received February 12, 2021 - Accepted June 9, 2021

To the Editor,

Breast cancer is the most commonly diagnosed cancer and the leading cause of cancer-related death among women (1). Dysregulation of the cell cycle is an important factor that induces cancer cell proliferation leading to tumor development. Therefore, elucidating the molecular mechanisms underlying cell cycle dysfunction may lead to the identification of effective therapeutic strategies for patients with breast cancer.

The eukaryotic cell cycle is controlled by checkpoints in each phase transition to ensure genomic integrity (2). Cancer cells are deficient in the G1/S checkpoint and rely on the G2/M checkpoint to maintain genomic integrity (3, 4). The G2/M checkpoint is regulated by cyclin-dependent kinase 1 (CDK1), cyclin B1, cell division control protein 25C (CDC25C), and WEE1 and MYT1 kinases (5). The activation of CDK1 is indispensable for G2/M phase transition. Therefore, identifying the factors that regulate the G2/M checkpoint is important to prevent tumorigenesis.

Neuronal pentraxin (NPTX1) is a member of the pentraxin family, and was originally identified in the central nervous system (6, 7). NPTX1 is involved in multiple cancers; it promotes metastasis through the integrin/FAK pathway, and knockdown of NPTX1 attenuates the motility of gastric cancer cells (8). NPTX1 is downregulated in hepatocellular carcinoma (HCC), and gain-of-function approaches revealed that NPTX1 suppresses the growth of HCC cells (9). However, the expression and functions of NPTX1 in breast cancer remain to be clarified.

MATERIALS AND METHODS

Cell lines and cancer tissue specimens

The human breast cancer cell line MCF-7 was purchased from American Type Culture Collection. Cells were cultured in Dulbecco's Modified Eagle's Medium (DMEM; HyClone) containing 10% FBS (HyClone). The breast cancer tissues and corresponding adjacent normal breast tissues were collected from The First Affiliated Hospital of Sun Yat-sen University. Patient consent and approval from the Institutional Research Ethics Committee of The First Affiliated Hospital of Sun Yat-sen University were obtained before sample collection. The clinicopathological characteristics of patients are listed in Table I.

Plasmids

Full-length NPTX1 was amplified by PCR and cloned into the pLVX plasmid to obtain the pLVX-NPTX1 plasmid, in which NPTX1 was upregulated. To knock down NPTX1, two human NPTX1 shRNA sequences were

Key words: NPTX1; G2/M arrest; CDC25; G2/M checkpoint

Corresponding Author:
Dr Ying Lin,
Department of Thyroid and Breast Surgery,
The First Affiliated Hospital of Sun Yat-sen University,
58 Zhongshan Road II,
Guangzhou, Guangdong, China
email: linying3@mail.sysu.edu.cn

0393-974X (2021)
Copyright © by BIOLIFE, s.a.s.
This publication and/or article is for individual use only and may not be further reproduced without written permission from the copyright holder.
Unauthorized reproduction may result in financial and other penalties
DISCLOSURE: ALL AUTHORS REPORT NO CONFLICTS OF INTEREST RELEVANT TO THIS ARTICLE.

cloned into the pLKO.1 plasmid. The sequences were as follows: sh#1, CGACGCGCTTCATCTGCACTT; sh#2, CCTGAGCCAGAAGGAGACCAT. The psPAX2 (virus-packaging plasmid), pMD2G (envelope plasmid), and pLVX/pLKO.1 plasmids were transfected into 293T cells to produce pseudo-typed lentiviral particles. After 48 h, the particles were collected to infect MCF-7 cells overnight. Then, the normal culture medium was replaced, and cell lines with stably upregulated or downregulated NPTX1 were screened by exposure to 5 μg/ml puromycin for 7 days.

RNA extraction and quantitative PCR (qPCR)

Total RNA was extracted using the Trizol reagent (Invitrogen) according to the manufacturer's protocol. qPCR was performed using the ABI Prism 7500 Sequence Detection System (Applied Biosystems). The primers used were as follows: NPTX1, forward, 5′-CTCAGCCAACTCGGGCAAACTT-3′, reverse, 5′-ATCCTTGAGGCTGTTGGTCTGG-3′; CDC25A, forward, 5′- TCTGGACAGCTCCTCTCGTCAT-3′, reverse, 5′-ACTTCCAGGTGGAGACTCCTCT-3′; CDC25B, forward, 5′- AGAACCTCCTGGACAGTGACCA-3′, reverse, 5′-GCTGAACTTGCCCGTCAATAGG-3′; CDC25C, forward, 5′- AGAAGCCCATCGTCCCTTTGGA-3′′, reverse, 5′-GCAGGATACTGGTTCAGAGACC-3′; WEE1, forward, 5′- GATGTGCGACAGACTCCTCAAG-3’, reverse, 5′-CTGGCTTCCATGTCTTCACCAC-3′; MYT1, forward, 5′- TTCAGACCAGCGAAACCTCACC-3′, reverse, 5′-TGTGGCTTCGTGCTGAGGTTCT-3′; CCNB1, forward, 5′- GACCTGTGTCAGGCTTTCTCTG-3′, reverse, 5′-GGTATTTTGGTCTGACTGCTTGC-3′; c-Myc, forward, 5’- CCTGGTGCTCCATGAGGAGAC-3′, reverse, 5′-CAGACTCTGACCTTTTGCCAGG-3′; survivin, forward, 5′- CCACTGAGAACGAGCCAGACTT-3′, reverse, 5′-GTATTACAGGCGTAAGCCACCG-3′; c-met, forward, 5′′- TGCACAGTTGGTCCTGCCATGA-3′, reverse, 5′-CAGCCATAGGACCGTATTTCGG-3′; COX-2, forward, 5′- CGGTGAAACTCTGGCTAGACAG-3′, reverse, 5′-GCAAACCGTAGATGCTCAGGGA-3′.

Western blot assay

Total protein was extracted using lysis buffer (Cell Signaling Technology), and incubated on ice for 30 min. Then, the protein was mixed with loading buffer and boiled for 5 min at 95°C. A nuclear extraction kit (Sigma-Aldrich) was used to isolate nuclear protein. Proteins were separated by SDS-PAGE using a protocol described previously (10).

Colony formation and anchorage-independent growth ability assay

A total of 5×10^2 cells were seeded into six-well plates for 10 days. The colonies formed were fixed using 10% formaldehyde and dyed with 0.1% crystal violet. Finally, the colony numbers were counted. The anchorage-independent growth ability assay was performed according to the protocol previously described (10).

Flow cytometry assay

Cells were treated with 75% ethanol for 1 h and then incubated in propidium iodide staining buffer for 10 min

Table I. *Clinicopathological characteristics of breast cancer samples*

Parameters	Number of cases (%)
Age (years)	
< 50	5 (50.0)
≥ 50	5 (50.0)
Tumor size	
≤ 5 cm	6 (60.0)
> 5 cm	4 (40.0)
T classification	
T1_T2	3 (30.0)
T3-T4	7 (70.0)
N classification	
N_0	9 (90.0)
N_1	1 (10.0)
M classification	
M_0	8 (80.0)
M_1	2(20.0)
Histologic grade	
G1-G2	7 (70.0)
G3-G4	3 (30.0)

in the dark. The flow cytometry assay was performed using a FACSCalibur instrument (BD Biosciences). Cell distribution in each cell cycle phase was analyzed using CellQuest 3.3 software (BD Biosciences).

Dual-luciferase reporter assay

To examine the transactivation of β-catenin, cells were seeded into 96-well plates and maintained for 24 h. Subsequently, 100 ng luciferase construct and 10 ng Renilla plasmid were co-transfected into MCF-7 cells using Lipofectamine 3000 (Invitrogen). At 48 h after transfection, luciferase and Renilla signals were detected using a Dual Luciferase Reporter Assay Kit (Promega) according to the manufacturer's instructions.

Statistical analysis

All experiments were performed three times independently. Data were analyzed using SPSS version 21.0 (SPSS) and presented as the mean ± standard deviation. Statistical differences were evaluated by Student's *t*-test, and $p < 0.05$ was considered statistically significant.

RESULTS

NPTX1 is significantly downregulated in breast cancer

Analysis of publicly available data from The Cancer Genome Atlas (TCGA; https://cancergenome.nih.gov/) showed that NPTX1 is dramatically downregulated in breast cancer tissues (tumor, n = 1095) relative to normal breast tissues (normal, n = 113) (Fig. 1a). Analysis of NPTX1 expression in paired breast cancer and normal tissues showed that NPTX1 expression was lower in breast cancer tissues (T) than in normal breast tissues (ANT) (Fig. 1b). NPTX1 expression was then analyzed in fresh breast cancer tissues, which showed that NPTX1 expression was significantly decreased in breast cancer tissues both at the transcription (Fig. 2a) and translation (Fig. 2b) levels.

Taken together, these results indicate that NPTX1 is markedly downregulated in breast cancer tissues.

NPTX1 induces cell cycle G2/M arrest in breast cancer cells

To elucidate the function of NPTX1 in breast cancer, gene set enrichment analysis (GSEA) was performed. The results indicated that NPTX1 might be involved in the regulation of the mitotic cell cycle (Fig. 3a). To confirm this, MCFF-7 cells with stably upregulated and downregulated NPTX1 were generated (Fig. 3b). Flow cytometry showed that overexpression of NPTX1 significantly increased the proportion of cells in G2/M phase, whereas downregulation of NPTX1 dramatically

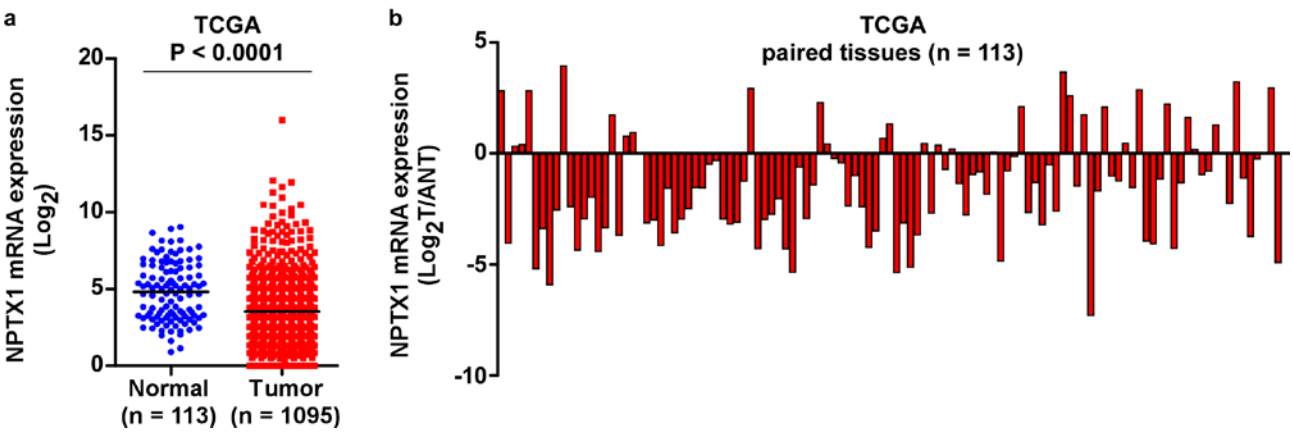


Fig. 1. *NPTX1 mRNA level is significantly downregulated in breast cancer tissues from TCGA.* ***a****) NPTX1 mRNA level is significantly downregulated in breast cancer tissues (tumor, n = 1095) relative to normal breast tissues (normal, n = 113) from TCGA.* ***b****) The expression of NPTX1 was lower in breast cancer tissues (T) than in the corresponding adjacent normal breast tissues (ANT) from TCGA. T: tumor; ANT: corresponding adjacent normal tissues.*

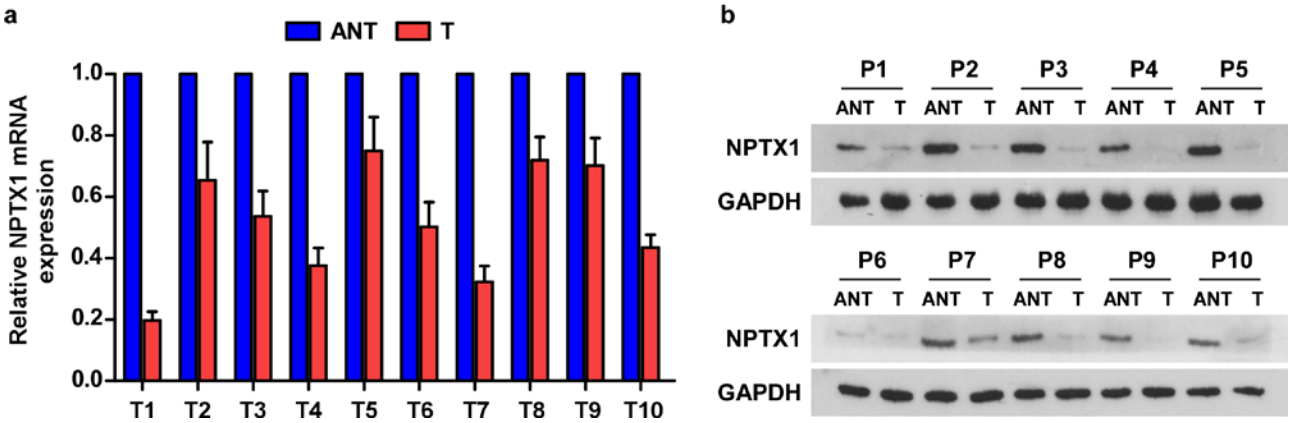


Fig. 2. *NPTX1 expression is significantly decreased in fresh breast cancer tissues both at the mRNA and protein levels.* ***a****) Relative NPTX1 mRNA expression in fresh paired breast cancer tissues.* ***b****) NPTX1 protein expression in fresh paired breast cancer tissues by western blotting. T: tumor; ANT: corresponding adjacent normal tissues.*

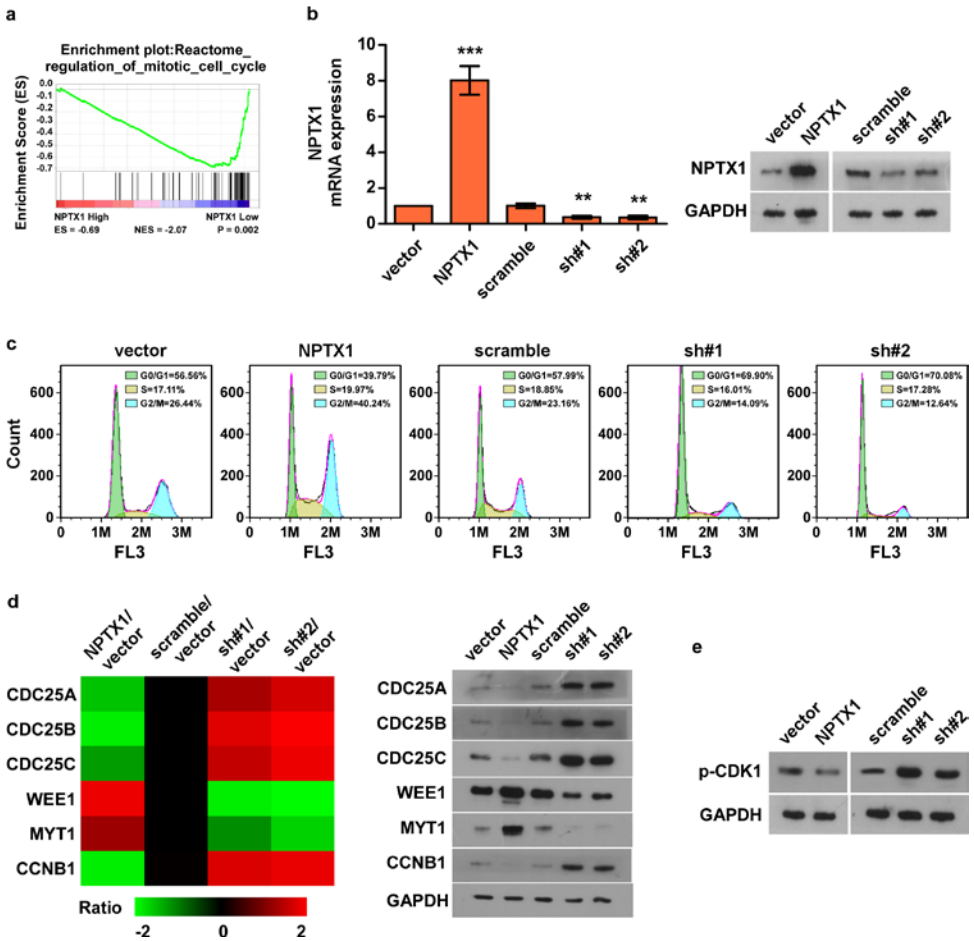


Fig. 3. *NPTX1 induces cell cycle G2/M arrest in breast cancer cells.* ***a****) GSEA demonstrated that NPTX1 is involved in the regulation of the mitotic cell cycle.* ***b****) NPTX1 mRNA (left panel) and protein (right panel) levels in stable cell lines.* ***c****) Flow cytometry assay showed that overexpression of NPTX1 induced cell arrest at G2/M phase, whereas downregulation of NPTX1 dramatically reduced the cell number in the G2/M phase.* ***d****) Analysis of the expression of genes involved in the G2/M checkpoint by qPCR (left panel) and western blotting (right panel).* ***e****) Western blot assay demonstrated that upregulation of NPTX1 significantly inhibited p-CDK2, whereas downregulation of NPTX1 dramatically increased its level. ** P < 0.01, *** P < 0.001.*

reduced the proportion of breast cancer cells in the G2/M phase (Fig. 3c). This suggests that NPTX1 induces G2/M arrest in breast cancer cells. Analysis of the expression of genes involved in the G2/M transition by qPCR and western blotting showed that the mRNA and protein expression of CDC25, CDC25B, CDC25C, and CCNB1 was significantly downregulated in NPTX1-overexpressing cells and dramatically increased in NPTX1-silenced cells (Fig. 3d). However, WEE1 and MYT1 expression showed the opposite trend. Upregulation of NPTX1 significantly decreased the level of phosphorylated CDK2 (p-CDK2), whereas downregulation of NPTX1 dramatically increased it (Fig. 3e). These results taken together indicate that NPTX1 induces breast cancer cell G2/M phase arrest.

Upregulation of NPTX1 inhibits breast cancer cell proliferation

Because NPTX1 induces cell cycle G2/M arrest in breast cancer cells, we examined the effect of NPTX1 on the proliferation of breast cancer cells. The results of the colony formation assay indicated that NPTX1 upregulation decreased, whereas NPTX1 downregulation increased breast cancer cell proliferation (Fig. 4a). Consistent with these results, the *in vitro* anchorage-independent growth ability assay demonstrated that NPTX1 upregulated dramatically inhibited, whereas NPTX1 knockdown promoted breast cancer cell tumorigenesis *in vitro* (Fig. 4b). Taken together, theSE results indicate that NPTX1 decreases the proliferation of breast cancer cells and *in vitro* tumorigenesis.

NPTX1 inhibits cell proliferation and in vitro tumorigenesis through the Wnt pathway

GSEA indicated that NPTX1 may be involved in Wnt/β-catenin signaling (Fig. 5a). To confirm this, we performed the luciferase reporter assay, which showed that overexpression of NPTX1 significantly inhibited, whereas downregulation of NPTX1 dramatically promoted β-catenin trans-activation (Fig. 5b). Western blotting demonstrated that NPTX1 upregulation decreased the level of nuclear β-catenin, whereas NPTX1 knockdown increased it in breast cancer cells (Fig. 5c). Accordingly,

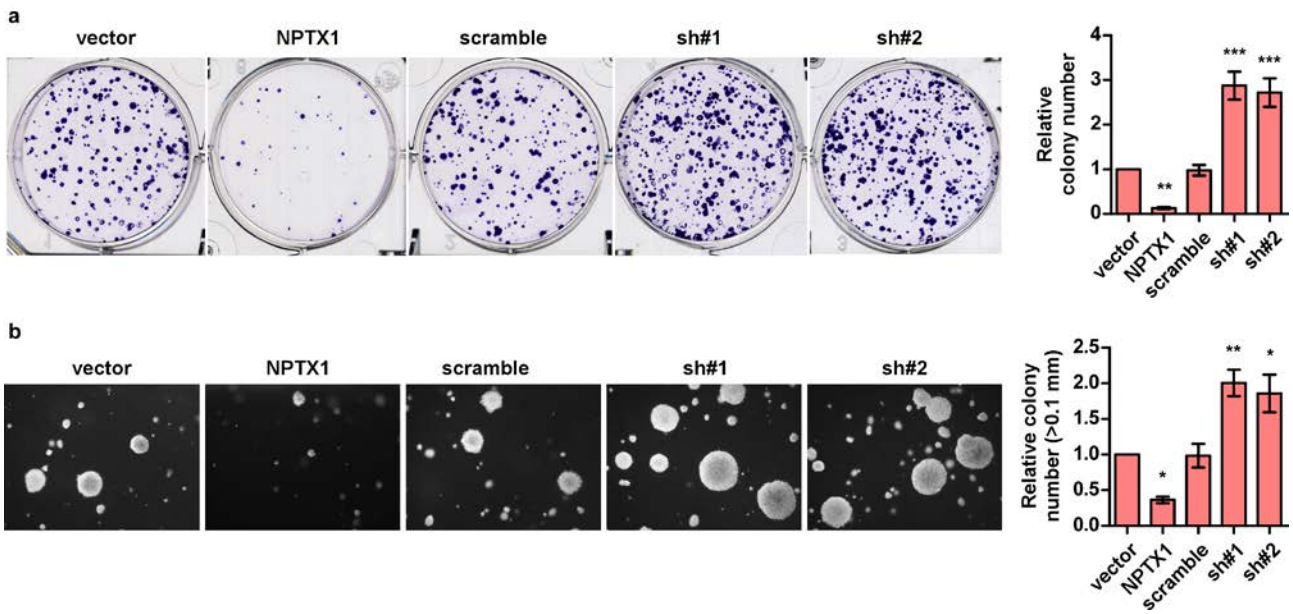


Fig. 4. *NPTX1 decreases cell proliferation and in vitro tumorigenesis.* ***a****) Colony formation assay indicated that upregulation of NPTX1 inhibited, whereas downregulation increased breast cancer cell proliferation.* ***b****) Anchorage-independent growth ability assay showed that NPTX1 dramatically reduced, whereas downregulation of NPTX1 increased in vitro tumorigenesis in breast cancer cells. * P < 0.05, ** P < 0.01, *** P < 0.001.*

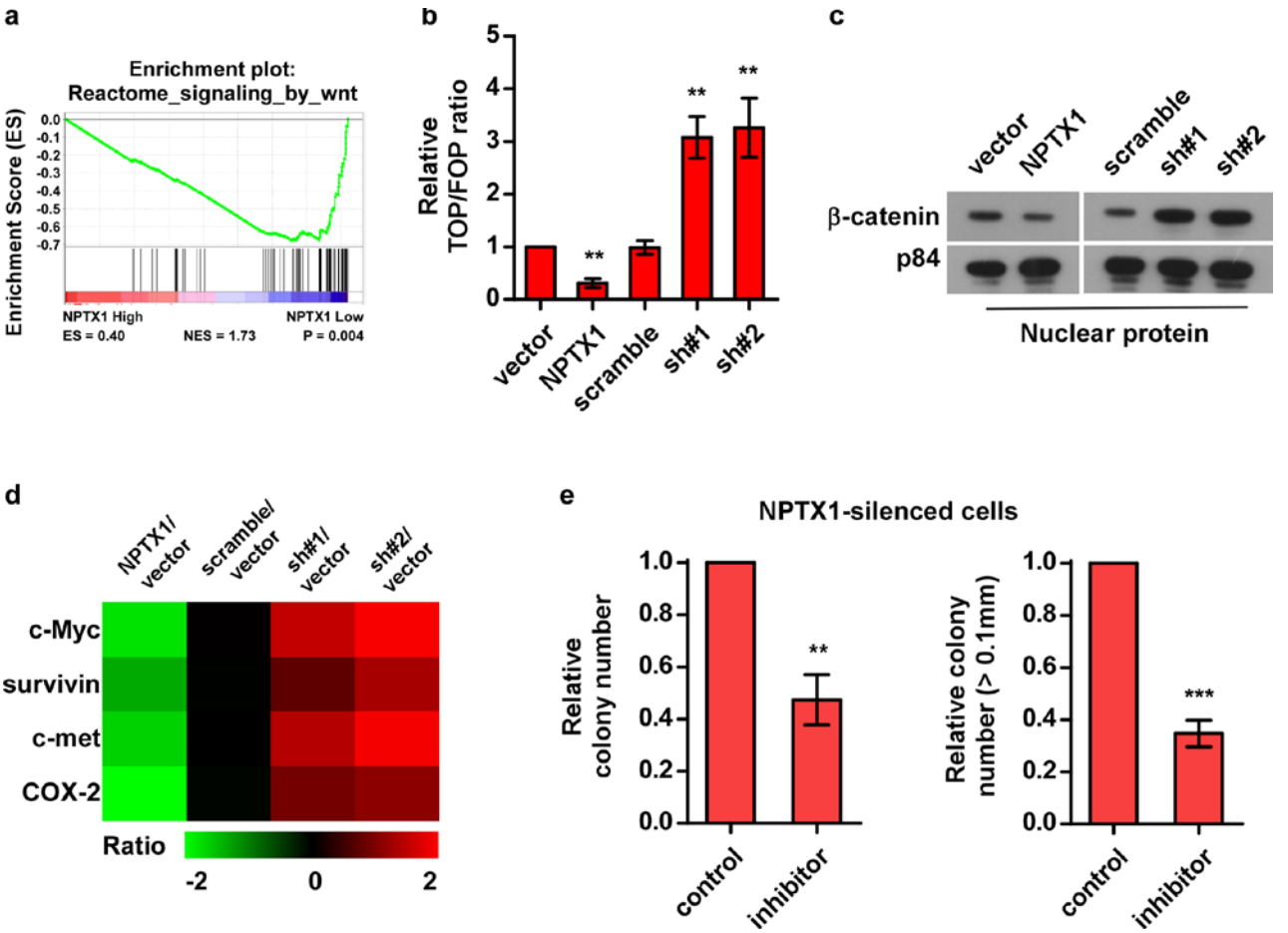


Fig. 5. *NPTX1 inhibits cell proliferation and in vitro tumorigenesis through the Wnt/β-catenin pathway.* ***a****) GSEA revealed that NPTX1 is involved in Wnt/β-catenin signaling.* ***b****) Luciferase reporter assay demonstrated that overexpression of NPTX1 significantly inhibited, whereas downregulation of NPTX1 dramatically promoted β-catenin transactivation.* ***c****) Western blotting showed that nuclear β-catenin was reduced in NPTX1-upregulated breast cancer cells and increased in NPTX1-silenced breast cancer cells.* ***d****) The downstream genes of Wnt/β-catenin analyzed by qPCR.* ***e****) The inhibitor of Wnt/β-catenin signaling, PNU-75654, can counteract the effect of NPTX1 downregulation on promoting cell proliferation (left panel) and in vitro tumorigenesis (right panel). ** $P < 0.01$, *** $P < 0.001$.*

downstream genes of Wnt/β-catenin signaling such as *c-Myc*, *survivin*, *c-met*, and *COX-2* were markedly downregulated in NPTX1-upregulated cells and upregulated in NPTX1-silenced cells, as determined by qPCR (Fig. 5d). Next, we treated NPTX1-silenced cells with 100 μM PNU-75654, a Wnt/β-catenin antagonist that prevents TCF binding to β-catenin. The colony formation assay showed that PNU-75654 decreased the proliferation of NPTX1-silenced cells compared with the controls. The anchorage-independent growth ability assay showed that PNU-75654 inhibited the *in vitro* tumorigenesis of NPTX1-silenced cells compared with the controls (Fig. 5e). These results suggest that Wnt/β-catenin signaling activation is essential for cell proliferation and *in vitro* tumorigenesis induced by NPTX1 downregulation. Taken together, the results indicate that NPTX1 inhibits cell proliferation and *in vitro* tumorigenesis through the Wnt/β-catenin pathway.

DISCUSSION

Herein, we provided evidence that NPTX1 is markedly downregulated in breast cancer and inhibits cell proliferation via the Wnt/β-catenin pathway. The findings suggest that NPTX1 functions as a tumor

suppressor in breast cancer and might represent a vital therapeutic target for the treatment of breast cancer.

The most fundamental character of cancer cells is the ability to sustain chronic proliferation, and cell proliferation is related to cell cycle progression. During cell cycle progression, checkpoints regulate the different cell cycle phase transitions. Dysregulation of checkpoints is responsible for cancer progression (11). The CDC25 family are key components of the G2/M checkpoint. In mammalian cells, there are three isoforms of CDC25: CDC25A, CDC25B, and CDC25C (12). CDC25 can dephosphorylate Thr14 and Tyr15 of CDK1 to activate the CDK1-cyclin B1 complex. In this study, we found that downregulation of NPTX1 upregulated the expression of CDC25A, CDC25B, and CDC25C, suggesting NPTX1 plays an important role in regulating the G2/M checkpoint.

Further study showed that the function of NPTX1 in the G2/M checkpoint is mediated by activation of Wnt/β-catenin signaling. Inhibition of Wnt/β-catenin signaling by treatment with PNU-75654 reversed the effect of NPTX1 downregulation on promoting cell proliferation. PNU-74654 is a non-FDA-approved drug that inhibits the binding of TCF and β-catenin. The present study provides additional evidence supporting the use of PUN-74654 as a drug to treat cancer.

REFERENCES

1. Hao XL, Gao LY, Deng XJ, et al. Identification of TC2N as a novel promising suppressor of PI3K-AKT signaling in breast cancer. Cell Death Dis 2019; 10:424.
2. Elledge SJ. Cell cycle checkpoints: preventing an identity crisis. Science 1996; 274:1664-72.
3. Slipicevic A, Holth A, Hellesylt E, Trope CG, Davidson B, Florenes VA. Wee1 is a novel independent prognostic marker of poor survival in post-chemotherapy ovarian carcinoma effusions. Gynecol Oncol 2014; 135:118-24.
4. Matheson CJ, Backos DS, Reigan P. Targeting WEE1 Kinase in Cancer. Trends Pharmacol Sci 2016; 37:872-81.
5. Malumbres M, Barbacid M. Mammalian cyclin-dependent kinases. Trends Biochem Sci 2005; 30:630-41.
6. Schlimgen AK, Helms JA, Vogel H, Perin MS. Neuronal pentraxin, a secreted protein with homology to acute phase proteins of the immune system. Neuron 1995; 14:519-26.
7. Tsui CC, Copeland NG, Gilbert DJ, Jenkins NA, Barnes C, Worley PF. Narp, a novel member of the pentraxin family, promotes neurite outgrowth and is dynamically regulated by neuronal activity. J Neurosci 1996; 16:2463-78.
8. Yan H, Zheng C, Li Z, et al. NPTX1 promotes metastasis via integrin/FAK signaling in gastric cancer. Cancer Manag Res 2019; 11:3237-51.
9. Zhao Y, Yu Y, Zhao W, et al. As a downstream target of the AKT pathway, NPTX1 inhibits proliferation and promotes apoptosis in hepatocellular carcinoma. Biosci Rep 2019; 39.
10. Zhong Y, Yang J, Xu WW, et al. KCTD12 promotes tumorigenesis by facilitating CDC25B/CDK1/Aurora A-dependent G2/M transition. Oncogene 2017; 36:6177-89.
11. Perner F, Schnoder TM, Fischer T, Heidel FH. Kinomics Screening Identifies Aberrant Phosphorylation of CDC25C in FLT3-ITD-positive AML. Anticancer Res 2016; 36:6249-58.
12. Galaktionov K, Beach D. Specific activation of cdc25 tyrosine phosphatases by B-type cyclins: evidence for multiple roles of mitotic cyclins. Cell 1991; 67:1181-94.

LETTER TO THE EDITOR

Androgen receptor expression in the skin appendages of patients with acne inversa harboring a mutation in the γ-secretase gene NCSTN

T-W. Shi[1,2,3,4#], N. Bai[2], J-A. Zhang[2#], F. Lu[5], X-D. Kong[2], J-B. Yu[2] and S-S. Zhang[1,2,3,4*]

[1]People's Hospital of Henan University of Chinese Medicine, Zhengzhou City, Henan Province, PR China; [2]The First Affiliated Hospital of Zhengzhou University, Zhengzhou City, Henan Province, PR China; [3]The Affiliated Zhengzhou People's Hospital of Xinxiang Medical University. Zhengzhou City, Henan Province, PR China; [4]People's Hospital of Zhengzhou, Southern Medical University, Zhengzhou City, Henan Province, PR China; [5]Southern Medical University Nanfang Hospital, Guangzhou City, Guangdong Province, PR China

Received January 15, 2021 – Accepted June 10, 2021

[#]These Authors contributed equally to this study

To the Editor,

Acne inversa (AI), known as hidradenitis suppurativa (HS), is a chronic, relapsing, and suppuration disorder of the skin (1). It usually affects apocrine gland-bearing regions, such as the axillary fossa, groin, perineum, and the area under the breasts (2). Thus, AI patients often visit many clinicians in several departments, including physicians, surgeons, gynecologists, and dermatologists; however, not all of these medical specialists can identify and manage this disease. Due to the lack of an early diagnosis and effective treatment, a relapsed abscess can lead to sinus tracts and fistulae and subsequent scarring and healing, resulting in disfiguration and disability, necessitating the determination of its etiology to guide the appropriate therapy. In the current model, its pathogenesis begins in the hair follicles, after which the apocrine sweat glands become involved during the later stages (3). The complete etiopathogenesis of AI is unknown (4), but genetic and androgenic factors are considered to be causative agents.

We collected data on a family with AI in an earlier study and found that members who suffered from AI harbored a mutation in the γ-secretase gene NCSTN (5). In this study, we examined the androgenic factors in AI, analyzing androgen receptor (AR) expression in skin specimens of AI patients in this family to determine the function of androgen in AI.

MATERIALS AND METHODS

Participants

In the family that we studied, 17 of 84 members suffered from AI: 9 males and 8 females (5). There were AI patients in each generation, transmitted by autosomal dominant inheritance. Skin specimens were taken from 5 AI patients in this family after informed consent was obtained. Normal skin specimens from 10 persons who underwent breast plastic surgery, excision of melanocytic nevus, or a surgical operation for a wound were collected as controls after informed consent was given. These specimens were obtained from the back, buttock, groin, axillary fossa, and area under the breasts, and the 10 healthy controls had no blood relationship to the family with AI. This study was performed in compliance with the Declaration of Helsinki and was approved by our ethics committee.

Key words: acne inversa; androgen receptor; γ-secretase; gene mutation; NCSTN; skin appendages

**Corresponding Author:*
Dr. Si-Sen Zhang,
People's Hospital of Henan University of Chinese Medicine, Zhengzhou City, 450003, Henan Province, PR China
Tel.: +86 37166295101
e-mail: tougao20210115@163.com

0393-974X (2021)
Copyright © by BIOLIFE, s.a.s.
This publication and/or article is for individual use only and may not be further reproduced without written permission from the copyright holder.
Unauthorized reproduction may result in financial and other penalties
DISCLOSURE: ALL AUTHORS REPORT NO CONFLICTS OF INTEREST RELEVANT TO THIS ARTICLE.

Immunohistochemistry

Skin specimens were embedded in paraffin after fixation in 10% neutral formalin. Then, 4-μm sections were sliced for immunohistochemistry. The tissue sections were deparaffinized, subjected to antigen recovery using citric acid, and incubated in 3% H2O2 to block endogenous peroxidase activity and in goat serum to block endogenous bioepiderm. Then, the sections were incubated with the primary antibody overnight at 4°C. After being rinsed with PBS, the slides were incubated with secondary antibody for 30 min at 37°C and then with horseradish peroxidase-streptavidin for 30 min at 37°C. The reactions were visualized with DAB, and the sections were counterstained with hematoxylin. The average grayscale values of positive signals in hair follicles were analyzed on an image analysis system.

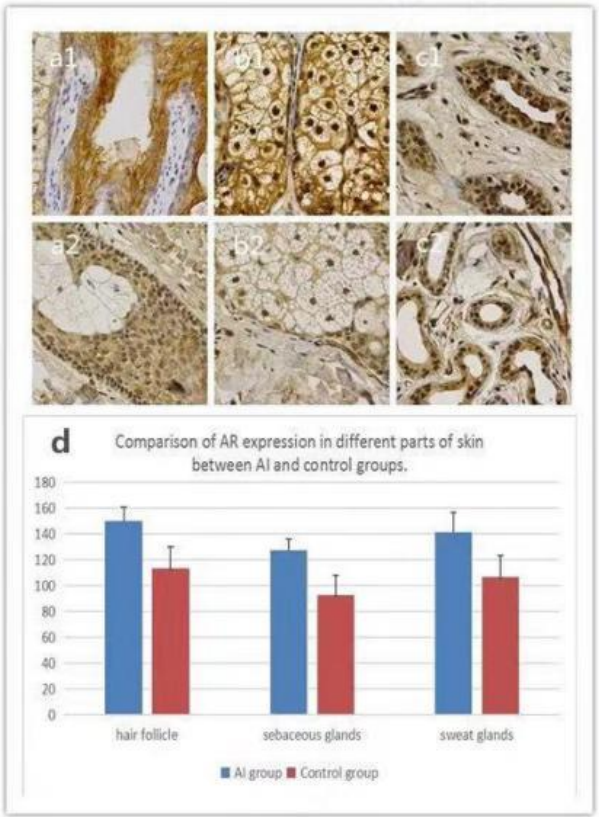


Fig. 1. ***a-c****) AR expression in hair follicles, sebaceous glands, and sweat glands of AI patients (a1, b1, c1) and normal controls (a2, b2, c2) by immunohistochemistry (SP×400).* ***d****) Comparison of AR expression in skin specimens between AI patients and normal controls. The vertical axis is the mean average optical density of AR in skin specimens. t value is 5.026 for hair follicles, 5.449 for sebaceous glands, and 4.072 for sweat glands. P value < 0.05 for all 3 three components of skin specimens.*

Western blot

After electrophoresis, the proteins were transferred to a polyvinylidene difluoride membrane, which was then placed in skim milk, shaken, and sealed for 2 h at room temperature. After being washed with TBS-T (4 times, 8 min each), the membrane was incubated at 4°C overnight in the diluted primary antibody and washed with TBST again, after which it was shaken for 2 h at room temperature in the diluted second antibody. Signals were developed with a chemiluminescence system.

Statistical analysis

The data on the two groups were analyzed by *t*-test using SPSS 17.0. A P value of <0.05 was considered to be the level of statistical significance.

RESULTS

In the skin specimens, brown granules were observed in the cytoplasm and nucleus by immunohistochemistry. The expression of AR was clearly visible in the hair follicles, sebaceous glands, and sweat glands of all AI patients and normal controls. The expression of AR was significantly higher in skin from AI patients than in normal controls (P value < 0.05 for all 3 components) (Fig. 1).

Western blot analysis showed the expression of AR in the skin specimens was also significantly higher in AI patients compared with normal controls (t=6.13, P<0.05) (Fig. 2).

DISCUSSION

Based on other findings, our study (5) supports the genetic etiology in certain patients with AI. However, AI seldom develops before adolescence, even in patients with γ-secretase mutations. The age of onset of AI is often 11–30 years and develops in women before menstruation. Furthermore, AI is chronic, and relief and cessation of AI occur after menopause; the onset of the disease is rare after menopause (6). These instances of AI are not attributed solely to mutations in γ-secretase genes as other etiological factors, such

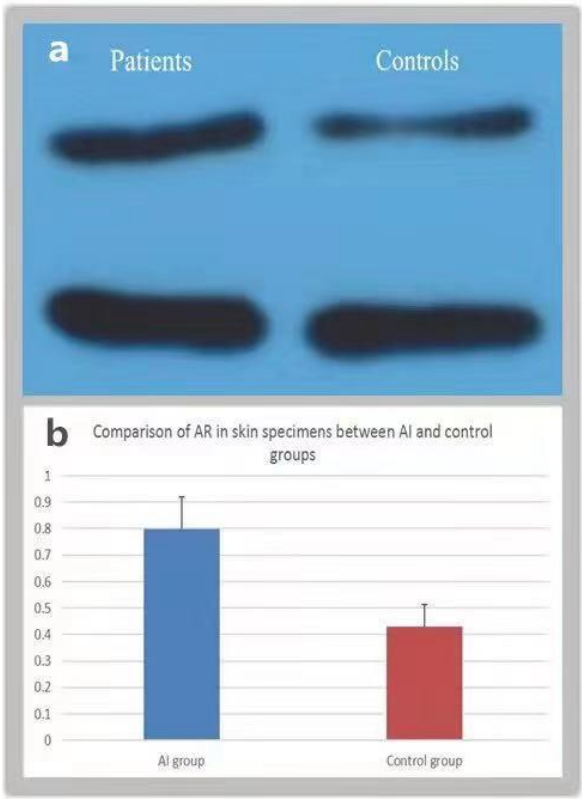


Fig. 2. ***a****) AR expression in skin specimens of AI patients and normal controls by western blot. The top row is AR, and the bottom row is the reference, β-actin.* ***b****) Comparison of AR expression in skin specimens between AI patients and normal controls by western blot. The vertical axis is the mean gray scale of AR in skin specimens. t=6.13, P<0.05.*

as hormones, can induce or aggravate the disease. To examine the pathogenesis of AI in our cohort, we measured AR expression in the hair follicles, sebaceous glands, and sweat glands of rashes in AI patients in this family. Our results implicate androgens in AI, and their involvement is supported by several clinical treatments. Finasteride and spironolactone, antagonists of androgen, improved the symptoms a clinical study (7). These data suggest androgens to be associated with AI, based on the endocrine changes that occur during its onset. Moreover, the transcriptional activity of AR also increases in AI lesions (8), and several genes that are regulated by AR are enriched, as is a genetic locus in familial HS that is linked to Notch signaling (9). In conjunction with our study, these findings implicate an interactive effect of androgen and genetic factors in the onset of AI through Notch signaling. Therefore, we hypothesized that the high expression of ARs heightens the activity of androgens and that hyperkeratinization of hair follicles is induced, based on mutations in γ-secretase genes, resulting in the onset of AI.

ACKNOWLEDGEMENT

This study was supported by the National Natural Science Foundation of China (No. 81773344)

REFERENCES

1. Lu L, Lai H, Pan Z, et al. Clinical and histopathological characteristics in patients with scarring folliculitis type of acne inversa. Dermatoendocrinol 2017; 9(1):e1361575.
2. O'Sullivan Coyne G, Woodring TS, Lee CR, Chen AP, Kong HH. Hidradenitis suppurativa-like lesions associated with pharmacologic inhibition of gamma-secretase. J Invest Dermatol 2018; 138(4):979-81.
3. Kurzen H, Kurokawa I, Jemec GB, et al. What causes hidradenitis suppurativa? Exp Dermatol 2008; 17(5):455-6.
4. Chen W, Plewig G. Should hidradenitis suppurativa/ acne inversa best be renamed as "dissecting terminal hair folliculitis"? Exp Dermatol 2017; 26(6):544-7.
5. Shi TW, Bai N, Zhang JA, et al. Mutations in the γ-secretase genes PSEN1, PSENEN, and NCSTN in a family with acne inversa. Eur J Dermatol 2018; 28(3):374-6.
6. Barth JH, Layton AM, Cunliffe WJ. Endocrine factors in pre-and postmenopausal women with hidradenitis suppurativa.Br J Dermatol 1996; 134(6):1057-9.
7. Lee A, Fischer G.A case series of 20 women with hidradenitis suppurativa treated with spironolactone. Australas J Dermatol 2015; 56(3):192-6.
8. Gauntner TD. Hormonal, stem cell and Notch signalling as possible mechanisms cell and Notch signalling as possible mechanisms of disease in hidradenitis suppurativa: a systems-level transcriptomic analysis. Br J Dermatol 2019; 180(1):203-4.
9. Frew JW, Vekic DA, Woods J, Cains GD. A systematic review and critical evaluation of reported pathogenic sequence variants in hidradenitis suppurativa. Br J Dermatol 2017; 177(4):987-98.

JOURNAL OF BIOLOGICAL REGULATORS & HOMEOSTATIC AGENTS Vol. 35, no. 3, 1189-1194 (2021)

LETTER TO THE EDITOR

Three-year management of hip osteoarthritis with intra-articular polynucleotides: a real-life cohort retrospective study

A. Migliore[1], E. Graziano[2], L.S.M. Martín[3], A. Sorbino[1], M. Raichi[4] and G. Boni[5]

[1]Rheumatology Unit, S. Pietro Fatebenefratelli Hospital, Rome, Italy; [2]Department of Orthopaedics and Traumatology, Cardinal Massaia Hospital, Asti, Italy; [3]Department of Internal Medicine, Sant'Eugenio Hospital, Rome, Italy; [4]Clinical Pharmacology consultant; [5]Italian Sports Medicine Federation, Umbria Region chapter, Perugia, Italy

Received April 15, 2021 – Accepted June 16, 2021

To the Editor,

The Global Burden of Disease 2010 study certified hip and knee osteoarthritis (OA) as the 38th most potent influence on Disability-Adjusted Life Years (DALYs) among 291 disorders investigated (1). The overall prevalence of radiographic hip OA is about 27.0% after 45 years, with a lifetime risk for symptomatic hip OA of 18.5% for men and 28.6% for women (2).

Intra-articular hyaluronic acid (HA) has been the cornerstone of non-surgical OA management since the 1990s. However, as recently as 2019, evidence-based guidelines and consensus reports have long debated its actual value (3). In addition, the strong viscosupplementation efficacy of HA might not be enough, as it is not complemented by similarly strong inflammation-modulating, anti-fibrotic, and pro-trophic properties (4). Natural-origin polynucleotides are fragments of hydrophilic linear DNA chains, highly purified from trout gonads with technologically advanced procedures to minimize contaminants and known with the acronym PN-HPT™ (HPT™, Highly Purified Technology). Both PN-HPT™ and high-molecular-weight HA have persistent viscosupplementation properties (5); PN-HPT™ also have trophic and bio-restructuring properties on chondrocytes, which might conceivably help slow the joint damage progression, while pain control after PN-HPT™ intra-articular injections is also more vigorous and rapid compared with HA (5). PN-HPT™ is thus a candidate as an alternative, or at least a complementary option, to intra-articular HA in addition to the usual OA core treatments such as structured exercise programs, weight management and non-steroidal anti-inflammatory drugs (NSAIDs).

This paper illustrates the real-life clinical evolution over three years of a retrospective cohort of hip OA patients treated with an intra-articular PN-HPT™ formulation as the cornerstone of their non-surgical OA disease management.

MATERIALS AND METHODS

Study design and retrospective cohort population

This is a retrospective cohort post-marketing study on hip OA patients formerly treated with intra-articular single injections (indefinitely about every six months) with a PN-HPT™ Class-III CE-marked (0373) medical device (Condrotide®, Mastelli Srl, Sanremo, Italy), available as pre-filled, single-use, neutral glass 2-mL vial-syringes with a PN-HPT™ concentration of 40 mg in 2 mL. The

Key words: hip osteoarthritis; intra-articular injection; Lequesne index; polynucleotides; PN-HPT™

Corresponding Author:
Prof. Alberto Migliore,
Department of Internal Medicine,
Ospedale S. Pietro Fatebenefratelli,
Via Cassia 600, 00189 Rome, Italy
Tel.: +39 (0)6 33581
e-mail: migliore.alberto60@gmail.com

0393-974X (2021)
Copyright © by BIOLIFE, s.a.s.
This publication and/or article is for individual use only and may not be further reproduced without written permission from the copyright holder.
Unauthorized reproduction may result in financial and other penalties

retrospective review of individual baseline and sequential outcome data archived in the ANTIAGE osteoarthritis management register was the study core (6), with a random selection of hip OA patients who satisfied the predefined inclusion criteria as the retrospective cohort. The selected patients began their treatment with intra-articular PN-HPT™ between January and November 2017 with a three-year follow-up.

The retrospective study design did not consider the stratification of enrolled patients to minimize unknown confounding factors. According to cohort size estimates, the rationale for this design choice was the relatively small number of patients who would be required, even in a real-life setting, to arrive at some preliminary outcomes.

All patients signed an informed consent form and consented to eventual anonymous publication of the study outcomes. A preemptive general ethics approval by the ANTIAGE Institutional Review Board (Ethics Committee of Azienda Ospedaliera San Camillo Forlanini, Rome, Italy) covered all retrospective research activities related to the ANTIAGE register and is available on request.

Patient selection, study procedures and data management

Patients from the ANTIAGE register had to satisfy the following conditions for inclusion in the retrospective cohort: age ≥40 years, monolateral or bilateral symptomatic hip OA according to the ACR criteria (7) of at least 1-year duration or mild to moderate hip OA Kellgren-Lawrence grade 2 or 3 (confirmed on a non-weight bearing X-ray taken no more than six months before the first PN-HPT™ intra-articular injection); baseline score pain at the affected hip more severe than 4.0 (10-cm VAS); up to 36 months of follow-up. Criteria leading to exclusion from the retrospective cohort were concomitant intake of oral anticoagulants, lack of visible articular space at radiological or ultrasound assessment, clinically significant comorbidities (e.g., rheumatologic disease, inflammatory or auto-immune diseases), hypersensitivity to PN-HPT™, chronic systemic steroid treatment, local skin infection or disease at target hip.

Finally, all ANTIAGE patients included in the retrospective cohort should have received ultrasound (US)-guided intra-articular treatment, the entire content of two 2-mL vials of CONDROTIDE® for a total of 4 mL and 80 mg PN-HPT™ every six months (also patients showing improvements in clinical parameters). The protocol allowed up to two additional injections per year if clinically required, with no more than one additional injection in any three months. The US-guided technique avoided all risk of lesions and extra-articular content dispersal (6, 8).

The baseline and follow-up assessments were based on a standard 10-cm Visual Analogue Scale (VAS) for pain, the 11-item Lequesne Index score (9), NSAID intake (days per month), and on the Global Medical Assessment (GMA) and Global Patient Assessment (GPA) scores. Control standard X-rays were taken every 24 months. According to the described inclusion and exclusion criteria, the data extraction from the digital ANTIAGE register occurred in February 2020.

The frequency of pain and functional assessments was every three months for the whole 36-month follow-up period following the standard real-life clinical routine in each author's institution. The paper reports the 6-month pain and functional outcomes. Dropouts were patients lost to control or to the injection sessions; patients referred to other clinical institutions; deceased patients; patients undergoing a total hip replacement.

Previous double-blind studies with intra-articular polynucleotide injections in OA management, with the most careful attention to pain, were the basis for estimating the retrospective cohort size (5). The expected attrition of enrolled cohort patients was also considered, based on available medium-term, real-life-like studies (5). The OA nature and discomfort and the study's exploratory nature tentatively made spontaneous losses to follow-up projected to less than 20% after one year and less than 40% after 24 months acceptable. That assumption led to an estimated 40 hip OA patients at least being retrospectively enrolled to get a reasonable estimate of long-term efficacy over a follow-up period of at least 36 months.

All the authors directly involved carried out all activities with standardized procedures, including baseline and follow-up Lequesne and VAS scoring interviews and registration of outcomes in the ANTIAGE register. The principles of the Declaration of Helsinki were always respected.

Statistical analysis

Estimated descriptive statistics included sample means ± standard error of the means, ranges and numerosity for continuous variables, and count and proportions for discrete variables.

The general linear model for repeated non-parametric

measures (Kruskal–Wallis one-way analysis of variance on ranks) after correction of means for age, body mass index and Kellen-Lawrence grade was the basis of inferential statistics. Pairwise post-hoc Mann-Whitney multiple comparisons identified the study parameters' divergence points during the follow-up (stochastic domination *vs* baseline) without Bonferroni correction. Inferential statistics were applied only to data gathered every six months.

RESULTS

Table I details the demographics of the retrospective cohort of 43 hip OA patients; The number of dropout patients every 12 months and the leading dropout reasons at the end of the 36-month follow-up period are detailed in Table II.

Visual Analogue Scale (VAS, 0-10 cm)

Hip pain (mean VAS scores) almost halved after six months compared with baseline (from a mean of 4.94 to 2.64 or –46.6%, <0.05), and more than halved after 12 months down to a mean of 2.38 or –51.8% (Fig. 1). The pain remained steady on average over the second year of follow-up (mean VAS scores, 2.41 and 2.40 after 18 and 24 months, respectively), then fell steadily again up to the end of the 36-month follow-up (sequential mean VAS scores: 2.19 after 30 months and 2.10 after 36 months or –57.5% ($p < 0.01$ *vs* baseline after 24 and 36 months).

NSAID consumption

The NSAID intake significantly fell from 4.42 days per month at baseline down to 2.74 days per

Table I. *Description of the retrospective cohort at baseline (VAS, visual analogue scale; GMA, Global Medical Assessment; GPA, Global Patient Assessment).*

Retrospective cohort demographics	
Enrolled patients (baseline, n)	43
Males	20 (46.5%)
Females	23 (53.5%)
Cohort mean age (years)	60 ± 18.5
Males (years, mean)	61 ± 18.9
Females (years, mean)	59 ± 17.8
Cohort mean weight (kg)	71 ± 10.1
Males (kg, mean)	72 ± 10.9
Females (kg, mean)	68 ± 9.9
Cohort mean height (cm)	162 ± 7.1
Males (cm, mean)	166 ± 8.4
Females (cm, mean)	157 ± 6.7
Kellgren–Lawrence grades	162 ± 7.1
Second grade	47%
Third grade	53%
Smokers	13 (30.2%)
Lequesne Index (mean)	7.51 ± 2.6
Pain VAS (mean)	4.94 ± 1.3
NSAID intake (days/months, mean)	4.42 ± 4.3
GMA (mean)	4.68 ± 1.34
GPA (mean)	5.23 ± 1.84

Table II. *Reasons leading to drop out over the 36-month retrospective follow-up.*

Dropout history	
Retrospective cohort (baseline, n)	43
Dropped-out patients after:	
12 months	7
24 months	15
36 months	22
THR and surgery	11
Lost to follow-up	9
Deaths	2

month after six months (–38.0% *vs* baseline; p <0.05), 2.41 days per month after 18 months (–45.8% *vs* baseline: p <0.01), 2.17 days per month (–50.9% *vs* baseline; p <0.001) at the end of the 36-month study (Fig. 1). Regarding the NSAIDs administered, diclofenac sodium (50-mg or 100-mg tablets or 75-mg vials) was the agent of choice to control pain; ibuprofen (400-mg or 600-mg tablets or 400-mg vials) or etoricoxib (60-mg or 90-mg tablets or 120-mg vials) were the leading alternatives.

Lequesne Index

The mean Liquesced algofunctional Index score significantly improved over the first six months of follow-up (from 7.51 at baseline down to 4.61 or –38.6% *vs* baseline; p <0.05) (Fig. 1). Differently from the mean VAS scores, the hip function appeared to improve over the second year of follow-up as reflected by the steadily falling mean Lequesne scores (4.43 after 12 months or –41.0% *vs* baseline; p <0.01, 3.98 after 18 months, and finally 3.76 or –49.9% *vs* baseline after 24 months). The hip algofunctional performance slowly kept improving up to the end of the 36-month follow-up period (means of 3.33 after 30 months and 3.29 at the end of the 36-month study (respectively, –55.7% and –56.2% *vs* baseline; p <0.001).

Global medical assessment

The overall structured medical assessment of hip pain and function showed a steady improvement over 36 months (Fig. 2): from a mean GMA score of 4.68 at baseline to 2,67 after six months (–42.9% *vs* baseline; p <0.05), 2.18 after 24 months (–53.4% *vs*

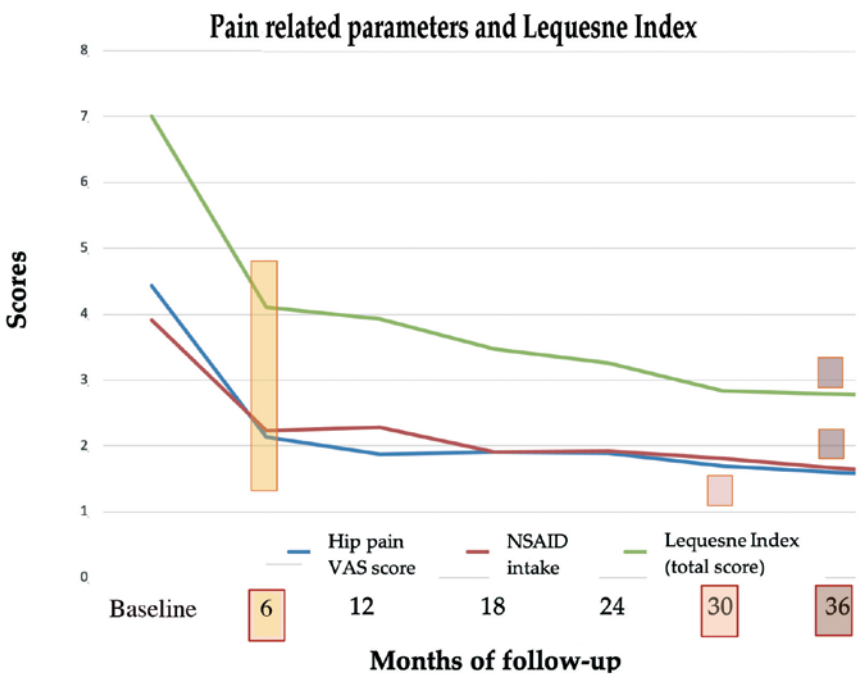


Fig. 1. *Evolution of the mean hip pain VAS scores, mean NSAID consumption (days per month) and mean Lequesne Index scores over the 36 months of the study. Yellow box (month 6, all parameters): p <0.05 vs baseline; light red marker (month 30, VAS score): p <0.01 vs baseline; dark red marker (month 36, Lequesne score): p <0.001 vs baseline.*

baseline; p <0.01), 1.91 after 36 months (–59.2% *vs* baseline; p <0.001).

Global patient assessment

The subjective assessment of their overall condition by the patients of the hip OA cohort also showed a steady improvement over the 36 months of the retrospective study (Fig. 2): from a mean GPA score of 5.23 at baseline to 3.12 after six months (–40.3% *vs* baseline; p <0.05), 2.76 after 24 months (–47.2% *vs* baseline; p <0.01), 2.34 after 36 months (–55.3% *vs* baseline; p <0.001).

Safety

Neither the patients nor the attending physicians reported systemic or severe local side effects. A few minor and transient local pains or burning sensations substantiated all reported side effects. The overall procedure cost, not eligible for reimbursement in Italy, and the concomitant comorbidities were the two main reasons reported in the ANTIAGE register for dropouts.

DISCUSSION

This study is the first to explore the long-term, real-life efficacy and safety data of patients with KL grade 2-3 hip OA treated with intra-articular PN-HPT™. The lack of a retrospective control group is a significant bias, although the extended three-year follow-up might partially compensate. The ANTIAGE-based design might also attenuate the lack-of-control bias; the US-guided technique eliminates a further cause of distortion due to morbidity and extra-articular PN-HPT™ dispersal (6, 8).

The present study confirms the efficacy and safety shown by PN-HPT™ in previous studies, including a recent study on knee and ankle OA (10). These studies were the rationale to recommend PN-HPT™ intra-articular injections in traumatology and sports medicine (11). The dropout rate at the end of the follow-up period (22 over three years out of 43 retrospective patients), although seemingly high, might be compatible with physiological attrition because the cost and

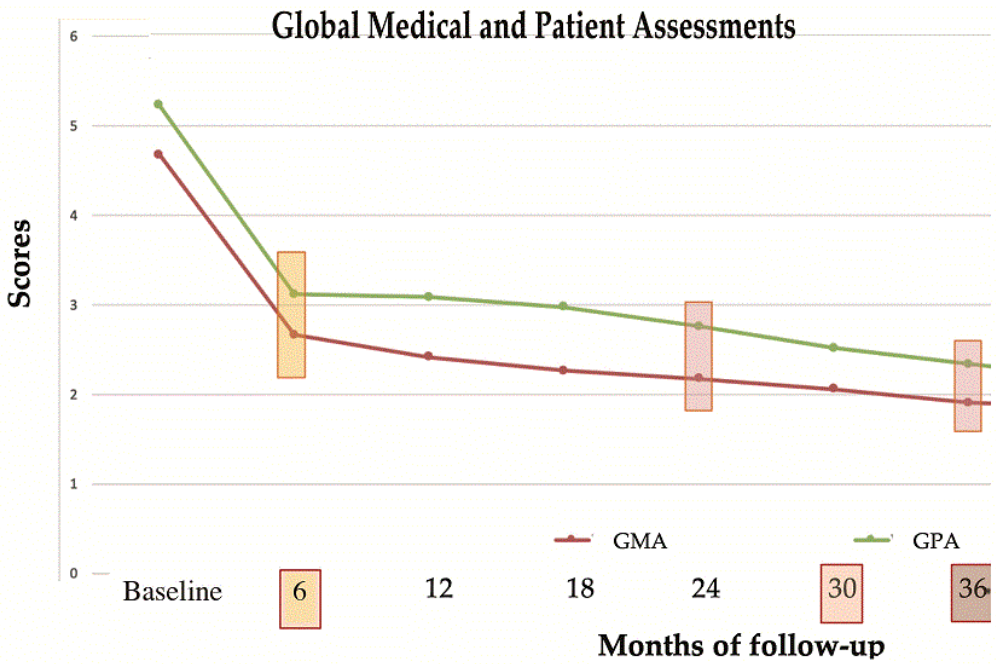


Fig. 2. *Evolution of Global Medical Assessment and Global Patient Assessment (GMA and GPA mean scores, respectively) over the 36 months of the study. Yellow box (month 6, both parameters): p <0.05 vs baseline; light red box (month 30, both parameters): p <0.01 vs baseline; dark red box (month 36, both parameters): p <0.001 vs baseline.*

concomitant comorbidities were the two most common reasons for interrupting treatment.

The study demonstrated that PN-HPT™ does not lose efficacy over time and more than two injection cycles. The steady improvement of all study parameters suggests the adopted injection protocol — 80 mg PN-HPT™ every six months, not excluding patients already showing improvements with up to two additional injections per year if clinically required — allows widely-spaced injections and might be ideal for long hip OA treatments. If needed, the dosage may be increased to 1-2 syringes per month (40-80 mg PN-HPT™ per month).

The rapid and steady improvement of pain and other parameters suggests that PN-HPT™ viscosupplementation and relief of symptoms are likely helpful in all age groups. Pain, NSAID intake, and other parameters rapidly fell over the first six months of follow-up, and all parameters steadily progressed over the residual 30 months of follow-up.

Further studies will be helpful to identify the predictors of response, therapy persistence, and long-term improvements following the short-term progress achieved after six months.

ACKNOWLEDGEMENTS

Mastelli S.r.l., Sanremo, Italy, is the producer of polynucleotides HPT™ (Highly Purified Technology) and Condrotide®, the formulation of polynucleotides for intra-articular injection investigated in this 3-year retrospective study. The authors wish to acknowledge the contribution of Mastelli S.r.l. for financial support of the publication.

Conflict of interest statement

Prof. Alberto Migliore received grants from PFIZER, ABBVIE, MSD, FIDIA, SANOFI, IBSA for national and international studies and courses. All other authors declare they have no conflict of interest. Support with the article processing is the only funding provided by the corporate sponsor, Mastelli S.r.l., Sanremo, Italy.

REFERENCES

1. Cross M, Smith E, Hoy D, et al. The global burden of hip and knee osteoarthritis: estimates from the global burden of disease 2010 study. Ann Rheum Dis 2014; 73(7):1323-30.
2. Lespasio MJ, Sultan AA, Piuzzi NS, Khlopas A, Husni ME, Muschler GF, Mont MA. Hip osteoarthritis: a primer. Perm J 2018; 22:17-084.
3. Bannuru RR, Osani MC, Vaysbrot EE, et al. OARSI guidelines for the non-surgical management of knee, hip, and polyarticular osteoarthritis. Osteoarthritis Cartilage 2019; 27(11):1578-89.
4. Migliore A, Procopio S. Effectiveness and utility of hyaluronic acid in osteoarthritis. Clin Cases Miner Bone Metab 2015; 12(1):31-3.
5. Giarratana LS, Marelli BM, Crapanzano C, et al. A randomized, double-blind clinical trial on the treatment of knee osteoarthritis: the efficacy of polynucleotides compared to standard hyaluronan viscosupplementation. Knee 2014; 21(3):661-8.
6. Migliore A, Tormenta S, Laganà B, et al. Safety of intraarticular hip injection of hyaluronic acid products by ultrasound guidance: an open study from ANTIAGE register. Eur Rev Med Pharmacol Sci 2013; 17(13):1752-9.
7. Altman R, Alarcón G, Appelrouth D, et al. The American College of Rheumatology criteria for the classification and reporting of osteoarthritis of the hip. Arthritis Rheum 1991; 34(5):505-14.
8. Qvistgaard E, Kristoffersen H, Terslev L, Danneskiold-Samsøe B, Torp-Pedersen S, Bliddal H. Guidance by ultrasound of intra-articular injections in the knee and hip joints. Osteoarthr Cartil 2001; 9(6):512-7.
9. Lequesne MG. The algofunctional indices for hip and knee osteoarthritis. J Rheumatology 1997; 24(4):779-81.
10. Guelfi M, Fabbrini R, Guelfi M. Polynucleotide intra-articular treatment of knee and ankle osteoarthritis: prospective case record cohort vs historical controls. J Biol Regul Homeost Agents 2020; 34(5):1949-53.
11. Boni G, Giannini S, Beltrami G, et al. Recommendations by the experts of intra-articular therapy in athletes emerging from the FMSI Consensus Conference. Medicina dello Sport (Official Journal of the European Federation of Sports Medicine Associations) 2020; 73(3):473-502.

LETTER TO THE EDITOR

Contribution of apolipoprotein estimation to cardiovascular risk assessment in women with endometriosis

U. Rafi[1,2], S. Ahmad[3], A. Zia[4], S.S. Bokhari[1,2], M.A. Iqbal[1] and N. Roohi[1]

[1]Institute of Zoology, Physiology/Endocrinology Laboratory, University of the Punjab, Quaid-i-Azam Campus, Lahore, Pakistan; [2]Department of Biology, Lahore Garrison University, Lahore, Pakistan; [3]King Edward Medical University, Lahore, Pakistan; [4]Gynaecologyand Obstetrics Unit, Lady Willingdon Hospital, Lahore, Pakistan

Received May 3, 2021 – Accepted June 16, 2021

To the Editor,

Endometriosis is a widespread anomalous gynecologic disorder whose etiology is unknown. It is characterized by the implantation of endometrial tissue outside the uterus, particularly within the pelvis (1). Randomized clinical trials have improved our knowledge in better understanding the factors involved in the manifestation of cardiovascular disorders. The great achievement in this regard was to find out the association of elevated cholesterol levels with cardiac manifestations (2). Scarce information is available regarding the protein components associated with lipids, the apolipoproteins, which are also documented risk factors of cardiovascular disorders (CVD) (3).

Apolipoprotein B plays a vital role in the body because total cholesterol is the sum of all cholesterol in the HDL-C and Apo-B lipoproteins. Several clinical investigations have shown maximum cardiovascular risks when Apo-B was high and non–HDL-C was normal. Hence, Apo-B is a better biomarker of CVD risk as compared to non–HDL-C (4). Lipoprotein a [Lp(a)] is a lipoprotein full of cholesterol and is different from low-density lipoprotein by having a glycosylated protein apolipoprotein (A) [Apo(A)], that is bonded covalently to it. The direct association between elevated levels of serum Lp(a) and LDL with increased CVD risk has also been reported (5).

The present study aims to demonstrate the concentrations of apolipoproteins Apo-A1, Apo-B, and Apo-B:Apo-A1 ratio in females with endometriosis and healthy subjects and its prognostic efficiency in the establishment of cardiovascular disorders. Thus, the concept that Apo-B, Apo-A1, or Apo-B:Apo-A1 ratio may be exploited as the prognosticator of cardiovascular disorder, can be supported with this study.

MATERIALS AND METHODS

In this study, 81 premenopausal females aged 20 to 40 years, laparoscopically confirmed with endometriosis (revised American Fertility Society 1 [rAFS]) were recruited. As hormonal therapy can derange the lipid metabolism, none of the women had taken any medication or drug during the six months prior to sample collection.

A control group consisting of premenopausal healthy females was matched for body mass index, age, and systolic/diastolic blood pressure. None of the control subjects had taken any medication or oral contraceptives known to modify or upset the metabolic rate of lipids for 6 months. The investigation was permitted by the Ethics

Key words: endometriosis; Apo-A1; Apo-B; endometriosis; cardiovascular disorder

Corresponding Author:
Prof. Nabila Roohi,
Institute of Zoology,
Physiology/ Endocrinology Laboratory,
University of the Punjab, Quaid-i-Azam Campus,
Lahore 54590, Pakistan
e-mail: nabila.physiol@gmail.com

0393-974X (2021)
Copyright © by BIOLIFE, s.a.s.
This publication and/or article is for individual use only and may not be further reproduced without written permission from the copyright holder.
Unauthorized reproduction may result in financial and other penalties
DISCLOSURE: ALL AUTHORS REPORT NO CONFLICTS OF INTEREST RELEVANT TO THIS ARTICLE.

Committee of the tertiary care Hospital and informed written consent was obtained from each of the subjects included in the study. Women with chronic disorders such as diabetes mellitus, cardiovascular and autoimmune diseases were excluded from the study. Likewise, females with a history of pre-eclampsia or having ovarian cysts other than endometrium were also excluded. 5 ml blood samples were taken from each subject by venipuncture, using a sterilized disposable syringe (BD, Becton and Dickinson, Singapore), and were placed in a serum vacutainer. The blood samples were given special IDs marked on each of the blood tubes.

Within 2-3 h of phlebotomy, serum was separated. The blood sample was centrifuged at 3500 rpm for 10 min. RNase-free, 1.5 mL microfuge (Ambion, USA) tubes, were utilized to preserve separated serum which was stored at -80°C until further biochemical assessment. Apolipoprotein (apo) A1 and B levels in serum were analyzed by enzyme-linked immunosorbent assay (ELISA) kits using Glory Biosciences, USA, (cat # PRS-01940hu and cat# PRS-01939hu, respectively). Data obtained by biochemical analysis were subjected to statistical interpretation by applying the unpaired Student's *t*-test using Graph Pad Prism version 6 software.

RESULTS

The levels of various parameters of the study group are shown in Table I. The Apo-A1 level was estimated to be 1245±49.44 **µ**g/mL in the control group, which showed a significant reduction of 22% (P<0.0001) in patients. The level of Apo-A1 in the endometriosis group was 973.8±40.74 **µ**g/mL (Fig. 1). The average level of Apo-B was found to be 885±25.52 and 1484±46.04 **µ**g/mL in the control and patient groups, respectively. A significant difference (P< 0.0001) was observed with a 68% increase of Apo-B in the patient group (Fig. 2).

The average level of Apo-B:Apo-A1 ratio in the endometriosis and control group was found to be

Table I. *Demographic variables and lipid profile of newly diagnosed female patients with endometriosis and healthy controls.*

Parameters	Control (n=80)	Patient (n=81)	*P*-value	Percentage difference
Age (Yrs)	31.01±0.62	32.1±0.58	0.2	3.5
SBP (mmHg)	122.6±0.98	123.1±0.98	0.7	0.4
DBP (mmHg)	80.63±0.98	82.04±0.90	0.2	1.74
Waist (cm)	84.8±0.55	85.17±0.76	0.6	0.4
BMI (kg/m^2)	22.5±0.28	23.26±0.30	0.09	3.3
Apo-A1(µg/mL)	1245±49.44	973.8±40.74	< 0.0001	22↓***
Apo-B (µg/mL)	885.0±25.52	1484±46.04	< 0.0001	68↑***
Apo-B:Apo-A1	0.83±0.05	1.805±0.11	< 0.0001	125↑***

****indicate significance at P< 0.0001, SBP: Systolic BloodPressure,DBP: Diastolic Blood pressure, BMI: Body Mass Index, Apo-A1: Apolipoprotein A1, Apo-B: Apolipoprotein B, Apo-B:Apo-A1 (ratio) Values are mean±SEM.*

1.80±0.11and 0.83±0.05, respectively. A significant difference (P<0.0001) was observed with a 125% increase of Apo-B:Apo-A1 in endometriosis patients (Fig. 3).

DISCUSSION

In the present study, the level of Apo-A1 was significantly reduced, while marked elevation in the Apo-B concentration was found in the patients group, suggesting more cardiovascular risk and associated disorders in these patients. Apo-B is synthesized in the gut and liver and shows the overall atherogenic activity capturing the lipoproteins in the arterial wall (6). It has been documented from clinical trials and epidemiological studies that Apo-B is superior to other cholesterol biomarkers in establishing the risk of cardiovascular disorders and affecting the suitability of therapeutics involved in minimizing the lipids (7).

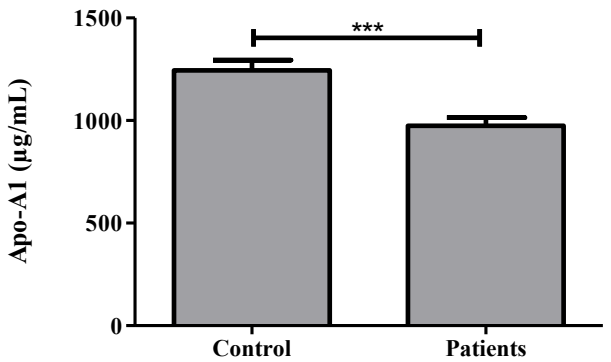


Fig. 1. *Apo-A1 (µg/mL) in control subjects and patients. ***indicates significance at P < 0.0001*

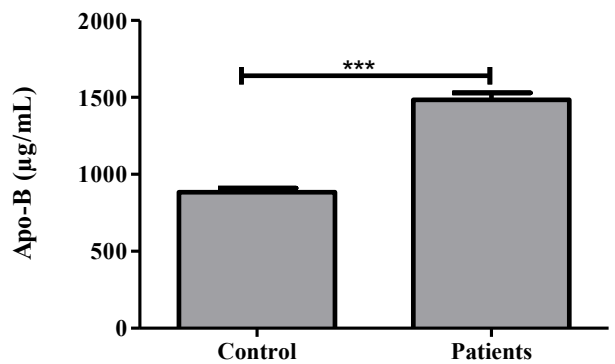


Fig. 2. *Apo-B (µg/mL) in control subjects and patients. ***indicates significance at P < 0.0001*

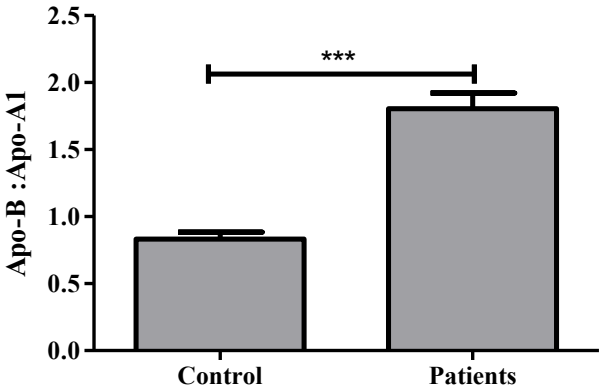


Fig. 3. *Apo B:Apo A1 ratio in control subjects and patients. ***indicates significance at P < 0.0001*

Allan et al. documented that the rate at which Apo-B particles move through the arterial wall and are captured is the number of the Apo-B particles in the lumen of arteries (8). Hence, the higher the Apo-B particles in the arterial lumen, the chances of capturing are higher. Apo-B particles smaller in size will contain a small amount of cholesterol, easily go through the arterial wall, and then keenly attach to the glycosaminoglycans as compared to bigger Apo-B particles (9). Thus, there is a higher number of trapped smaller cholesterol-depleted particles as compared to larger cholesterol-enriched particles in the arterial wall. Conversely, the higher the cholesterol trapped within Apo-B particles in the arterial wall, the higher cholesterol will be delivered at that position to damage the wall. As a result, there is correlation between greater damage per particle from the trapping of cholesterol-depleted as well as cholesterol-richer particles. Eventually, all LDL particles present, approximately, the same risk (2).

In the present study, the endometriosis group demonstrated higher levels of Apo-B as compared to control subjects. By considering the above-mentioned facts, these women may have high cardiovascular risk and may develop cardiovascular disorders in later life.

It has been suggested that Apo-B:Apo-A1 is the most precise diagnostic marker of cardiovascular risk (10). It considers both sides of the risk equation, the Apo-A1 side, which is antiatherogenic and, the Apo-B side which is atherogenic. The higher

Apo-B:Apo-A1 ratio shows the more circulating cholesterol that tends to be accumulated in the arterial wall, inducing the risk of atherosclerosis and CVD (11).

The results specify that the Apo-B:Apo-A1 is a lucid, precise, and novel marker for CVD events, the higher the Apo-B:Apo-A1, the higher the risk of CVD events. In the present investigation, the Apo-B:Apo-A1 ratio is elevated significantly in endometriosis subjects versus healthy controls, demonstrating their risk of CVD. Our investigation reinforces the idea that Apolipoprotein-B, Apolipoprotein-A1, and Apo-B:Apo-A1 can be utilized as strong prognosticators of CVD assessment in subjects with endometriosis.

REFERENCES

1. Zondervan KT, Becker CM, Koga K, Missmer SA, Taylor RN, Viganò P. Endometriosis. Nat Rev Dis Primers 2018; 4(1).
2. Sniderman AD, Pencina M, Thanassoulis G. ApoB: the power of physiology to transform the prevention of cardiovascular disease. Circ Res 2019; 124(10):1425-27.
3. Upadhyay RK. Emerging risk biomarkers in cardiovascular diseases and disorders. J lipids 2015; 2015:971453.
4. Kohli-Lynch CN, Thanassoulis G, Moran AE, Sniderman AD. The clinical utility of apoB versus LDL-C/non-HDL-C. Clin Chim Acta 2020; 508:103-8.
5. Ferretti G, Bacchetti T, Johnston TP, Banach M, Pirro M, Sahebkar A. Lipoprotein (a): A missing culprit in the management of athero thrombosis? J Cell Physiol 2018; 233(4):2966-81.
6. Ghaedi E, Kord-Varkaneh H, Mohammadi H, Askarpour M, Miraghajani M. Phytosterol supplementation could improve atherogenic and anti-Atherogenic apolipoproteins: a systematic review and dose–response meta-analysis of randomized controlled trials. J Am Coll Nutr 2020; 39(1):82-92.
7. Sahebkar A, Watts GF. New therapies targeting apoB metabolism for high-risk patients with inherited dyslipidaemias: what can the clinician expect? Cardiovasc Drugs Ther 2013; 27(6):559-67.
8. Allan R. Psychological Treatment of Cardiac Patients. J Health Psychol 2019; 45(2): 72-78.
9. Björnheden T, Babyi A, Bondjers G, Wiklund O. Accumulation of lipoprotein fractions and subfractions in the arterial wall, determined in an in vitro perfusion system. Atherosclerosis 1996; 123(1-2):43-56.
10. Sathe C. A, Chogle SA, Bharadwaj D. Apo B/Apo A1 ratio: a risk marker in patients with cardiovascular disease. Int J Res Med 2017; 6(2):20-3.
11. Tian M, Li R, Shan Z, Wang DW, Jiang J, Cui G. Comparison of Apolipoprotein B/A1 ratio, Framingham risk score and TC/HDL-c for predicting clinical outcomes in patients undergoing percutaneous coronary intervention. Lipids Health Dis 2019; 18(1):1-9.